Search for new charged bosons and dark matter in final states with one lepton and missing transverse energy with the ATLAS detector at the LHC

Magnar Kopangen Bugge
Department of Physics
University of Oslo
Norway

Dissertation presented for the degree of
Philosophiae Doctor (PhD) in Physics

January 2015

Abstract

The Standard Model (SM), the current theory of elementary particles and interactions, has been extremely successful in predicting and describing experimental results. The prediction of the electron's anomalous magnetic moment served as an early triumph of quantum electrodynamics, and one success after another has followed, including the discovery of the weak interaction gauge bosons $W^{\pm}$ and Z^0, and more recently the discovery of the Higgs boson at CERN's Large Hadron Collider (LHC) in 2012. In spite of the success of the theory, though, there are phenomena which it does not explain, such as the dark matter and dark energy making up most of the universe.

Extensions of the SM aiming to address its shortcomings typically predict observable deviations from the theory. Although theories predicting significant deviations from the SM in the energy regime so far explored can be immediately excluded, theories that predict deviations at higher, unexplored energies are still viable. Therefore, exploring physics at such energies is crucial in order to improve our understanding of nature at the most fundamental level. Currently, experimental data at the energy frontier are provided by the LHC experiments.

In this thesis, we present a search for new physics in final states with one lepton and missing transverse energy using data from the ATLAS detector. No significant deviations from SM predictions are observed in the transverse mass distribution. The search is interpreted in terms of the production of hypothetical heavy, charged bosons, and also in terms of the production of dark matter particles in association with a leptonically decaying W boson. Limits on the cross sections and relevant mass scales of these processes are presented.

In the case of new charged boson signal, the Sequential Standard Model (SSM) and the W^* reference model are considered. The SSM is a reference model widely used to represent new gauge bosons, of which the charged ones are usually denoted W', related to hypothetical symmetries of nature and the associated interactions. The W^* boson is a common occurence in theories addressing the unreasonably large radiative corrections to the Higgs boson mass, and differs significantly from the new gauge bosons in its interactions with the SM fermions. We find that new charged bosons are excluded at 95% CL for masses up to $3.28\,\mathrm{TeV}$ in the case of the SSM W' boson and $3.21\,\mathrm{TeV}$ in the case of the W^* reference model.

As a search for dark matter particles, the analysis is found to be competitive with ATLAS searches in other final states, in particular in the case of constructive interference in the so-called D5 effective field theory (EFT). Limits at 90% CL on the suppression scale in the effective coupling between dark matter particles and quarks are presented. For low dark matter particle masses, where collider searches are particularly sensitive, the limits extend to $1.4\,\mathrm{TeV}$ in the D9 EFT and $1.2\,\mathrm{TeV}$ in the D5 EFT in the case of constructive interference.

Acknowledgements

First of all, I would like to thank my supervisor Farid Ould-Saada, who has been inspirational both as lecturer in particle physics courses and as my supervisor for both my MSc and PhD studies. The projects you gave us in the advanced particle physics course were certainly extensive and time consuming, but I learned a lot from them, and I find myself using them as a convenient and useful resource still today. As a supervisor, you are ambitious, but willing to accept realistic goals. You are always available for discussion and guidance, while still allowing me to work independently.

Thanks also to my subsidiary supervisor Alex Read and the whole particle physics group at the University of Oslo for interesting and useful discussions and for making the group such a nice place to work.

Finally, I would like to thank my parents and the rest of my family for love and support. I thank my wife Vanja Morisbak for the good years we have spent together, and look forward to many more to come. I also thank my daughter Ragnhild for enriching my life with her playfulness and humor.

Contents

Introduction

The Standard Model (SM) of fundamental particles and interactions has been tested to great accuracy at energies up to the TeV scale (corresponding to a distance scale of $10^{-18}\,\mathrm{m}$) and provides in general predictions in excellent agreement with experiment. The theory describes three of the fundamental forces of nature, namely the electromagnetic, strong, and weak forces, but not the fourth one: gravity. At low energies, gravity appears as so much weaker than the other forces that neglecting it has no practical implications when describing the microscopic world. Only at very high energies, of the order of the *Planck scale* ($10^{19}\,\mathrm{GeV}$, corresponding to a distance scale of $10^{-34}\,\mathrm{m}$), is gravity expected to give a significant contribution to the interactions of elementary particles at small distance scales.

Although the discovery of the Higgs boson at the Large Hadron Collider (LHC) in 2012 can be said to have provided the last missing piece of the SM puzzle and thus completed the picture, there are phenomena which are not explained by the SM. An obvious example is gravity, and other important examples are the dark matter and dark energy which are believed to make up most of the universe. Therefore, physicists are busy constructing theories that provide possible explanations of the phenomena that the SM fails to explain. Many such theories exist, and only experiment can reveal which of them – if any – are realized in nature.

On the experimental side, the world's leading results are coming from the LHC at CERN. Located in an underground tunnel on the border between France and Switzerland, close to the city of Geneva, this huge circular accelerator, with a circumference of $27\,\mathrm{km}$, collides protons head on at unprecedented energies. The collisions take place inside huge particle detectors, including the multi-purpose CMS and ATLAS detectors. This thesis deals with the search for physics beyond the SM in final states with one lepton (electron or muon) and missing transverse energy, the latter being an important experimental observable which provides information about particles that are not measured directly in the detector, using ATLAS data. The search is sensitive to, among other things, the production of new heavy, charged gauge bosons (called W' bosons) decaying to a charged lepton and a neutrino.

As a PhD student at the University of Oslo, I have had the opportunity to work with the subgroup of the ATLAS exotics working group dealing with the search in the one lepton and missing transverse energy final state – the "W' group" – more or less since the arrival of the first high energy collision data. The size of actual contributions I have made to the analyses of the different subsets of data has varied because of variations in the workload associated with university teaching duties, exams, and my qualification task within the ATLAS Monte Carlo generators group associated with becoming an ATLAS author, decribed in appendix B. I have also had the chance to work on bringing ATLAS data to school students via the International Masterclasses and the "Z path", see appendix C.

The original plan was to perform the full data analysis in both the electron and muon channels. For the analysis of the 2010 data at a proton-proton center of mass energy $\sqrt{s} = 7\,\mathrm{TeV}$, ref. [104], manpower was needed on the electron channel to a larger extent than on the muon channel, and I focused on this channel during the fall of 2010. My main contribution on the data analysis side was an estimate of the jet background in the electron channel based on the Matrix Method (see chapter 6), which was used together with three other estimates to obtain a fit and extrapolated jet background levels at high transverse mass. Because of a general interest in search statistics, I also kept up with this aspect of the analysis, and contributed one of two independent cross checks of the final CL_s exclusion limits.

In the early stages of the analysis of the 2011 data, my involvement was insignificant due to high workload with teaching and following courses at the university. However, during the summer of 2011, I got up to speed on the analysis in both the electron and muon channels, and provided Matrix Method jet background estimates in the $1\,\mathrm{fb}^{-1}$ subset of data used for ref. [106]. The results were provided somewhat "after the fact" and were not included in the results for ref. [106]. The work did, however, serve as preparation for the analysis of the full 2011 dataset presented in ref. [107]. For this analysis, manpower was desperately needed on the muon channel, and I took the leading role in terms of practical data analysis for this channel.

During the fall of 2012 and spring of 2013, I stayed involved on the muon channel side of the analysis of the 2012 data at $\sqrt{s} = 8\,\mathrm{TeV}$, although with limited time to spend because I was working part time while also doing my service task and teaching. I did provide the muon channel jet background estimate, and kept up with this channel in general. In the later stages of the analysis, I had more time to spend, and my contributions became more significant. Having kept up with the statistical analysis, which was by now based on a Bayesian prescription, I could contribute transverse mass threshold optimizations for the muon channel (see sections 8.4 and 9.4) and exclusion limit cross checks, and I gradually took over the responsibility for the statistical analysis. I also helped with the integration of the dark matter signal models in the analysis (see chapter 9).

The proper handling of uncertainties related to the shape of the invariant mass distributions of hypothetical new gauge boson signal was introduced in the 2012 data analysis. This turned out to be problematic within the existing statistical analysis because of large signal uncertainty at high mass, and triggered my study of "fiducial cross section limits" which is presented in section 8.8 and reflected in ref. [108]. It also led to some more detailed investigation of the statistical analysis itself, in particular related to the choice of informative priors for nuisance parameters and proper handling of correlations between signal and background and between the signal in the two channels, and this work is documented in section 7.3. All cross section limits and significances given in refs. [108] and [109] were provided by me.

During the course of my PhD studies, I have also had the opportunity to travel to several conferences, and in particular I have presented physics talks at the "Spåtind Nordic Conference on Particle Physics"[1] in 2012 and 2014 and at the conference "LHC Days in Split"[2] in 2014,

[1] https://indico.nbi.ku.dk/conferenceDisplay.py?ovw=True&confId=380
http://indico.hep.lu.se//conferenceDisplay.py?confId=1361

[2] http://indico.cern.ch/event/287996/overview
http://cds.cern.ch/record/1957570

and an outreach related talk at the "International Conference on New Frontiers in Physics"[3] in 2013.

In this thesis, only the analysis of the 2012 data at $\sqrt{s} = 8\,\mathrm{TeV}$ is presented in detail. The final results of the analysis of the 2011 data at $\sqrt{s} = 7\,\mathrm{TeV}$ are briefly presented in section 8.9.1. The analysis is described with emphasis on the muon channel, as this is the channel I have been working on in the last analysis iterations. Only at the stage of the statistical analysis are electron channel results included, which are taken directly from the official analysis corresponding to ref. [109].

The thesis is structured as follows. First, some particle physics theory is presented in chapter 1, serving as background and motivation before we continue with the description of the experimental analysis. The LHC and the ATLAS detector are presented in chapter 2. Then we proceed with a description of the heavy, charged boson signal and relevant backgrounds in chapters 3 and 4. The implementation of the muon channel analysis is presented in chapter 5, with details on the jet background estimate following in chapter 6. We then proceed with a description of the statistical analysis in chapter 7, before applying it to search for new heavy, charged bosons in chapter 8. Finally, the search is interpreted as a search for dark matter production in association with a leptonically decaying W boson in chapter 9.

[3] https://indico.cern.ch/event/198153/overview

Chapter 1

Particle Physics Theory – The Standard Model and Beyond

1.1 Introduction

The Standard Model (SM) of particle physics is the immensely successful theory describing the elementary particles of nature and three of the fundamental forces acting between them. The fundamental forces described by the theory are the strong force, the weak force, and the electromagnetic force. While the latter two are collectively described by the electroweak theory (a part of the SM), they appear to be two separate forces at low energy. The SM is a relativistic quantum field theory, meaning that it combines the fundamental principles of quantum mechanics with those of special relativity. Gravity is the only fundamental force not described by the SM, and in fact, it is not (yet) described by a quantum mechanical theory at all, but by the general theory of relativity.

1.1.1 Particles of the Standard Model

Ordinary matter is built up of atoms, with negatively charged electrons surrounding a positively charged nucleus. The electrons are bound together with the nucleus by the electromagnetic force. The nucleus consists of the nucleons; the positively charged protons and the electrically neutral neutrons. These consist in turn of quarks bound together by the strong force. The proton consists of two up quarks and one down quark, while the neutron consists of two down quarks and one up quark. Ordinary matter, then, consists only of three elementary matter particles; the electron, the up quark, and the down quark. Together with the electron neutrino, an electrically neutral, very light particle which was first proposed to solve the apparent problem of energy and momentum non-conservation in radioactive β-decay, the electron and the up and down quarks make up the first generation of the SM matter particles.

These four matter particles have heavier[1] versions of themselves making up the second and third generations of matter particles. The heavier versions have exactly the same properties as the first generation particles, except for the mass. Each matter particle has its respective

[1] An exception may be the neutrinos – the ordering of the neutrino masses is not known, and the mass eigenstates do not correspond exactly to the flavor (electron, muon, and tau) eigenstates. Such a mismatch between flavor and mass eigenstates occurs also in the quark sector.

antiparticle, which has exactly the same mass, but opposite electric charge. For example, the antiparticle of the negatively charged electron is the positively charged positron. A particle and its antiparticle may annihilate, for example into a pair of photons. All the elementary matter particles of the SM are spin-1/2[2] fermions[3].

The neutrinos are special. They are matter particles in the sense that they are fermions, but even the first generation neutrino (the electron neutrino) is not a building block of ordinary (atomic) matter. It takes part in weak interaction processes where matter is transformed, as for example the transformation of a proton to a neutron or vice versa in nuclear β-decay or in the "burning" of the Sun.

In addition to the matter particles, the SM contains force particles mediating the interactions between them. The force particles are all spin-1 bosons[4]. The electromagnetic force is mediated by the photon (γ), which is the quantum of electromagnetic radiation. The weak force is mediated by the $W^{\pm}$ and Z^0 bosons, while the strong force is mediated by the gluon (g). It is worth noting that, while the photon and the gluon are massless, the $W^{\pm}$ and Z^0 bosons are very heavy, with masses of 80 and $91\,\mathrm{GeV}$ [1]. This is indeed the reason why the weak force appears to be much weaker than electromagnetism at low energies, while it has in principle a fundamental strength of the same order as electromagnetism (see section 1.3.3).

Finally, the only particle of the SM which is neither a matter particle nor a force particle, is the Higgs boson (H). It is the only fundamental spin-0 particle of the SM. The Higgs boson has to do with the reason why the $W^{\pm}$ and Z^0 bosons as well as the fermions are massive (see section 1.3.4). Discovered in 2012 [2, 3], it was the last particle of the SM to be observed in experiment.

The particle content of the SM is summarized in table 1.1. The charged leptons are the electron (e^-), muon (μ^-), and tau lepton (τ^-), all of which have electric charge $-e$ where e is the elementary electric charge. There is one electrically neutral neutrino (ν_l) for each charged lepton. The quarks with electric charge $+(2/3)e$ are the up (u), charm (c), and top (t) quarks, and those with electric charge $-(1/3)e$ are the down (d), strange (s), and bottom (b) quarks.

Composite particles

The fundamental matter particles of the SM that are not quarks, are referred to as leptons. These include the charged leptons and the neutrinos. All the leptons can be observed in nature as free particles, as they do not experience the strong force. Quarks have never been seen as free particles, because they are *confined* by the strong force. They form bound states called mesons (consisting of one quark and one antiquark) and baryons (consisting of three quarks). The complete classification of mesons and baryons, collectively referred to as hadrons, will not be reviewed here.

Examples of mesons are the pions and the kaons. Pions consist only of the lightest quark flavors, up and down. For example, the π^+ meson consists of one up quark and one down antiquark. The kaons contain one strange quark (antiquark) in combination with one light (up

[2]The shorthand spin-1/2 means that the total spin quantum number of the particle is $s = 1/2$. The magnitude of the intrinsic angular momentum of a particle with total spin quantum number s is $\sqrt{s(s+1)}\hbar$.

[3]Fermions are particles with half-integral total spin quantum numbers. They follow Fermi-Dirac statistics and obey the Pauli exclusion principle.

[4]Bosons are particles with integral total spin quantum numbers. They follow Bose-Einstein statistics.

Spin-1/2 fermions

	1st generation	2nd generation	3rd generation
Leptons	e^-	μ^-	τ^-
	ν_e	ν_μ	ν_τ
Quarks	u	c	t
	d	s	b

Spin-1 (gauge) bosons

Electromagnetic force	γ
Weak force	$W^\pm$, Z^0
Strong force	g

Spin-0 bosons

H

Table 1.1: The elementary particles of the SM. The matter particles (fermions) appear in three generations. Each matter particle has its respective antiparticle with opposite electric charge. The gauge bosons mediate the SM forces. There is only one spin-0 boson, the Higgs boson H, related to the masses of other elementary particles.

or down) antiquark (quark). There are also dozens of mesons with heavier quarks (charm and bottom) in combination with lighter quarks as well as with each other. The J/ψ meson is an example of charmonium, with one charm quark and one charm antiquark, giving zero total charm quantum number.

Examples of baryons are the nucleons (protons and neutrons) and the Λ baryons. While the nucleons contain only the up and down quarks, the Λ baryons contain one strange quark in combination with the lighter quarks. A large number of baryons exist, with different numbers of strange, charm, and bottom quarks.

The *baryon number* is a useful concept because it is conserved. It takes the value $+1$ for any baryon and -1 for any antibaryon. It is analogous to the *lepton number*, which takes the value $+1$ for leptons and -1 for antileptons. For example, the neutron decay process $n \to p\, e^- \,\overline{\nu_e}$ is allowed as it conserves electric charge ($q = 0$), baryon number ($B = +1$), and lepton number ($L = 0$). The individual electron, muon, and tau lepton numbers are also conserved, so that e.g. the $\overline{\nu_e}$ is not interchangeable with a $\overline{\nu_\mu}$ in the neutron decay process.

The top quark, with a mass of $174\,\mathrm{GeV}$ [1], is so heavy that it decays before it can form bound states with the lighter quarks. Therefore, there are no mesons or baryons containing the top quark. The top quark decays almost exclusively to a W boson and a bottom quark.

1.2 Relativistic quantum mechanics

In this section, the basic ingredients of relativistic quantum field theory will be reviewed, without reference to any particular interaction. In section 1.3, the details of the various interactions of the SM will be presented.

1.2.1 Wave equations

In quantum mechanics, the time evolution of the state vector $|\Psi(t)\rangle$ is given by the Schrödinger equation,

$$\hat{H}\,|\Psi(t)\rangle = i\frac{d}{dt}\,|\Psi(t)\rangle\,, \tag{1.1}$$

where $\hat{H}$ is the Hamiltonian (operator), corresponding usually to the total energy. Written out in the position basis in terms of the wavefunction $\Psi(\mathbf{x},t)$ of a particle, the Schrödinger equation is often seen on the form

$$\left(-\frac{1}{2m}\nabla^2 + V(\mathbf{x})\right)\Psi(\mathbf{x},t) = i\frac{\partial}{\partial t}\Psi(\mathbf{x},t), \tag{1.2}$$

where m is the mass of the particle and $V(\mathbf{x})$ is the potential energy. This equation is, however, not relativistically valid because the form of the Hamiltonian is derived from the classical (non-relativistic) relation between kinetic energy T and momentum $\mathbf{p}$,

$$T = \frac{\mathbf{p}^2}{2m}, \tag{1.3}$$

where the momentum vector is replaced by the momentum operator $\hat{\mathbf{p}} = -i\nabla$.

For a free particle, the relativistic energy-momentum relation has the form

$$E^2 = \mathbf{p}^2 + m^2, \tag{1.4}$$

and the classical wave equation (1.2) needs to be replaced by one derived from this relation. Dirac wanted to construct such a wave equation, first order in both space and time derivatives, and postulated a Hamiltonian on the form [4]

$$\hat{H}_D = \alpha_i \hat{p}_i + \beta m \tag{1.5}$$

(note the conventional summation over the repeated index i). This Hamiltonian satisfies

$$\hat{H}_D^2 = \hat{\mathbf{p}}^2 + m^2 \tag{1.6}$$

given that the matrices α_i and β satisfy the relations[5]

$$\beta^2 = 1, \quad \alpha_i^2 = 1 \text{ (all } i\text{)}, \quad \alpha_i\alpha_j + \alpha_j\alpha_i = 0 \text{ (all } i \neq j\text{)}, \quad \alpha_i\beta + \beta\alpha_i = 0 \text{ (all } i\text{)}. \tag{1.7}$$

These relations are fulfilled by certain 4×4 matrices which can be constructed from the Pauli matrices (see ref. [4]). The Dirac equation takes the form

$$\hat{H}_D\psi(\mathbf{x},t) = i\frac{\partial}{\partial t}\psi(\mathbf{x},t), \tag{1.8}$$

where the wavefunction $\psi(\mathbf{x},t)$ is now a 4-component spinor (column matrix). Defining the

[5]Note that in these relations, 1 represents the identity matrix, and to be very precise, one could make the appearance of the identity matrix explicit in eq. (1.6).

γ-matrices

$$\gamma^0 = \beta, \quad \gamma^i = \beta\alpha_i, \tag{1.9}$$

the Dirac equation can be written very compactly in four-vector notation as

$$(i\gamma^\mu \partial_\mu - m)\,\psi(x) = 0. \tag{1.10}$$

It describes the wave function of a spin-1/2 particle [4].

Another, quite different, way of obtaining a wave equation from the energy-momentum relation (1.4), is to simply replace the momentum $\mathbf{p}$ by the momentum operator $\hat{\mathbf{p}} = -i\nabla$, and replace the energy E by the operator $i\partial/\partial t$ [5]. The latter substitution can be motivated by the Schrödinger equation (1.2) since the action of $i\partial/\partial t$ on the wave function yields the same result as the action of the Hamiltonian on that same wave function. With these substitutions, the energy-momentum relation (1.4) leads to the wave equation

$$\frac{\partial^2\phi(\mathbf{x},t)}{\partial t^2} = \nabla^2\phi(\mathbf{x},t) - m^2\phi(\mathbf{x},t) \tag{1.11}$$

when multiplied by a wave function $\phi(\mathbf{x},t)$ from the right. This equation is called the Klein-Gordon equation, and it describes the wave function of a spin-0 particle, such as the Higgs boson [4]. It too can be conveniently formulated in four-vector notation:

$$\left(\partial_\mu\partial^\mu + m^2\right)\phi(x) = 0. \tag{1.12}$$

Each component of the Dirac spinor $\psi(x)$ satisfies the Klein-Gordon equation, as do the components $V^\mu(x)$ of a vector (spin-1) boson field such as that of the Z^0 and $W^\pm$ bosons or the photon (in the case of the photon, $m = 0$).

1.2.2 Lagrangian field theory

In classical mechanics, Newton's second law on the form $\mathbf{F} = m\mathbf{a}$ or $\mathbf{F} = d\mathbf{p}/dt$ applies to point particles and does not facilitate an easy description of a system with constraints (where the individual point particles are constrained to move along certain trajectories or in a particular way with respect to one another). Lagrange's formulation of classical mechanics is mathematically equivalent to Newton's laws of motion, but is much better suited for a system with constraints. The system is described in terms of generalized coordinates q_i, of which there is one for each degree of freedom of the system. The time evolution of the generalized coordinates is given by the Euler-Lagrange equations [6]

$$\frac{d}{dt}\left(\frac{\partial L}{\partial \dot{q}_i}\right) - \frac{\partial L}{\partial q_i} = 0 \tag{1.13}$$

(with $\dot{q}_i = dq_i/dt$), one equation for each degree of freedom. Here, the Lagrangian $L(q,\dot{q},t)$[6] is defined as the difference between the kinetic and potential energy of the system, $L = T - V$.

[6]The Lagrangian depends on all the generalized coordinates q_i and their time derivatives $\dot{q}_i$, and we denote this simply by $L(q,\dot{q},t)$. Correspondingly, the Hamiltonian depends on all the generalized coordinates and generalized momenta.

We also define the generalized momenta

$$p_i = \frac{\partial L}{\partial \dot{q}_i}, \tag{1.14}$$

which enter in the definition of the Hamiltonian

$$H(q, p, t) = p_i \dot{q}_i - L. \tag{1.15}$$

The Hamiltonian is the basis of the Hamiltonian formulation of classical mechanics, where the time evolution of the system is given by Hamilton's equations, which are equivalent to Lagrange's equations. The Hamiltonian is also important because it is constant in time whenever the Lagrangian is not explicitly time dependent[7], and because it is the classical analogue of the Hamiltonian operator in quantum mechanics.

Making the transition to a field theory, we consider the fields $\phi_i(x)$ and the Lagrangian density $\mathcal{L}(\phi, \partial_\mu \phi)$, which is a function of all the fields and their space-time derivatives. The fields satisfy the Euler-Lagrange equations [5]

$$\partial_\mu \left(\frac{\partial \mathcal{L}}{\partial(\partial_\mu \phi_i)} \right) - \frac{\partial \mathcal{L}}{\partial \phi_i} = 0. \tag{1.16}$$

The Lagrangian density corresponding to a free (relativistic) spin-1/2 particle is[8]

$$\mathcal{L}_{\text{Dirac}} = \overline{\psi} \left(i\gamma^\mu \partial_\mu - m \right) \psi. \tag{1.17}$$

Here $\overline{\psi} = \psi^\dagger \gamma^0$, and the corresponding Euler-Lagrange equations lead to the Dirac equation (1.10). The Lagrangian density of a neutral spin-0 particle is

$$\mathcal{L}_{\text{scalar}} = \frac{1}{2}(\partial_\mu \phi)(\partial^\mu \phi) - \frac{1}{2} m^2 \phi^2, \tag{1.18}$$

for which the Euler-Lagrange equation leads to the Klein-Gordon equation (1.12). Furthermore, the Lagrangian density corresponding to a neutral vector boson is

$$\mathcal{L}_{\text{neutral,vector}} = -\frac{1}{4} F_{\mu\nu} F^{\mu\nu} + \frac{1}{2} m^2 V_\mu V^\mu, \tag{1.19}$$

where V^μ is the real vector field associated with the particle, and we have defined the corresponding field tensor[9]

$$F_{\mu\nu} = \partial_\nu V_\mu - \partial_\mu V_\nu. \tag{1.20}$$

[7] Explicit time dependence has a precise meaning in Lagrangian mechanics. The explicit time dependence of the Lagrangian is the time dependence which does not enter via the generalized coordinates and their time derivatives.

[8] The explicit examples of Lagrangian densities given in this section are not unique – different forms of the Lagrangian density can lead to the same Euler-Lagrange equations.

[9] The sign of $F_{\mu\nu}$ is arbitrary, and cancels in the Lagrangian density (1.19). We follow generally the convention of ref. [5], except for in the treatment of QCD (section 1.3.2), where we rely on ref. [8] and follow the convention used there.

The Euler-Lagrange equations lead to the Proca equation [5]

$$\partial_\alpha \partial^\alpha V^\mu + m^2 V^\mu - \partial^\mu \partial_\alpha V^\alpha = 0. \tag{1.21}$$

By applying ∂_μ on this equation, one finds that, for $m \neq 0$, V^μ satisfies the two separate equations

$$\left(\partial_\alpha \partial^\alpha + m^2\right) V^\mu = 0, \tag{1.22}$$

corresponding to the Klein-Gordon equation (1.12), and $\partial_\mu V^\mu = 0$. Finally, for a charged vector boson, we have the Lagrangian density

$$\mathcal{L}_{\text{charged,vector}} = -\frac{1}{2} F^*_{\mu\nu} F^{\mu\nu} + m^2 V^*_\mu V^\mu, \tag{1.23}$$

which leads to exactly the same equations of motion for the now complex field V^μ as in the case of a neutral vector boson.

Analogous to the generalized momenta p_i, we define the conjugate fields

$$\pi_i = \frac{\partial \mathcal{L}}{\partial \dot{\phi}_i}. \tag{1.24}$$

The Hamiltonian density is defined as

$$\mathcal{H} = \pi_i \dot{\phi}_i - \mathcal{L}. \tag{1.25}$$

Furthermore, the Lagrangian and Hamiltonian are the volume integrals of the respective densities over all space:

$$L = \int \mathcal{L}(x)\, d^3\mathbf{x}, \quad H = \int \mathcal{H}(x)\, d^3\mathbf{x}. \tag{1.26}$$

1.2.3 Quantized Lagrangian field theory

The Hamiltonian defined in eq. (1.26) is not an operator when considering a classical Lagrangian field theory. To have a quantum mechanical theory, where the Hamiltonian governs the evolution of a quantum mechanical state, the Hamiltonian needs to become an operator. This is achieved by letting the fields themselves become operators[10], and demand certain commutation relations between the fields and their conjugate fields. The equal time commutation relations for a boson field are [5]

$$[\phi_k(\mathbf{x}, t), \pi_j(\mathbf{x}', t)] = i\delta_{kj}\delta(\mathbf{x} - \mathbf{x}'), \quad [\phi_i(\mathbf{x}, t), \phi_j(\mathbf{x}', t)] = [\pi_i(\mathbf{x}, t), \pi_j(\mathbf{x}', t)] = 0. \tag{1.27}$$

The field operator ϕ_i is taken to be time dependent in anticipation of the fact that the time evolution will be studied in the interaction picture, in which both operators and states are time dependent. For the case of a fermion field, the commutation relations are replaced by anticommutation relations.

The commutation relations (1.27) can be satisfied by fields written out as expansions of

[10]From here on, operators are not marked with a hat. It should be clear from the context which quantities are operators.

plane wave solutions to the field equations if the expansion coefficients are taken to be creation and annihilation operators satisfying similar relations. For example, the Klein-Gordon field can be expanded as[11] [5]

$$\phi(x) = \phi^+(x) + \phi^-(x) \tag{1.28}$$

with

$$\phi^+(x) = \sum_{\mathbf{k}} \frac{1}{\sqrt{2V\omega_{\mathbf{k}}}}\, a(\mathbf{k})\, e^{-ik_\mu x^\mu} \tag{1.29}$$

and

$$\phi^-(x) = \sum_{\mathbf{k}} \frac{1}{\sqrt{2V\omega_{\mathbf{k}}}}\, a^\dagger(\mathbf{k})\, e^{+ik_\mu x^\mu}, \tag{1.30}$$

where V is the normalization volume, k is the wave four-vector, and

$$\omega_{\mathbf{k}} = k^0 = \sqrt{\mathbf{k}^2 + m^2}. \tag{1.31}$$

In this expansion, the exponentials ensure that $\phi(x)$ satisfies the Klein-Gordon equation (1.12), while the creation and annihilation operators $a^\dagger(\mathbf{k})$ and $a(\mathbf{k})$ ensure that the commutation relations (1.27) are satisfied as long as these operators themselves satisfy

$$\left[a(\mathbf{k}), a^\dagger(\mathbf{k}')\right] = \delta_{\mathbf{k}\mathbf{k}'}, \quad [a(\mathbf{k}), a(\mathbf{k}')] = \left[a^\dagger(\mathbf{k}), a^\dagger(\mathbf{k}')\right] = 0. \tag{1.32}$$

The quantum mechanical states dealt with in the quantized Lagrangian field theory are characterized by the particles present. For example, the vacuum state[12] $|0\rangle$ is the state containing no particles, and the action of an annihilation operator on this state gives zero, $a(\mathbf{k})\,|0\rangle = 0$. Other states can be created from the vacuum state by the action of one or more creation operators. For example, the state containing one particle (the kind of particle represented by the Klein-Gordon field ϕ) with momentum $\mathbf{k}$ is $a^\dagger(\mathbf{k})\,|0\rangle$.

1.2.4 Time evolution

Since a particle physics theory is primarily tested in the context of a collider experiment, one can think of the main goal of such a theory as being able to predict the probabilities of certain final state particle configurations given the initial state particle configuration, i.e. given the beam particles' species and momenta (and possibly also their spin states). Such probabilities can be defined precisely in terms of cross sections, and the main goal of the theory is thus to predict the correct cross section for any scattering process[13].

The time evolution in a quantized field theory with interactions between the fields, is most conveniently considered in the interaction picture. The Hamiltonian is split into a part describing the free fields, H_0, and a part describing their interactions, H_{int}, so that $H = H_0 + H_{\text{int}}$. The state vectors and observables (operators) are related to those in the Schrödinger picture (the

[11] These expansions are for normalization within a finite volume V with boundary conditions at the edge of the volume, in which case the allowed momenta $\mathbf{k}$ are discrete.

[12] Technically, $|0\rangle$ is the vacuum state of the free field theory, while the vacuum state of a theory with interactions is more complex. It will not be necessary to make the distinction for our purpose.

[13] Predictions of decay widths (i.e. lifetimes) of unstable particles are also important tests of a theory, and they are calculated in a similar manner as cross sections.

"standard" view) by

$$|\Psi(t)\rangle_{\rm IP} = e^{iH_0(t-t_0)}\,|\Psi(t)\rangle\,, \quad O^{\rm IP}(t) = e^{iH_0(t-t_0)}Oe^{-iH_0(t-t_0)} \tag{1.33}$$

where $|\Psi(t)\rangle_{\rm IP}$ ($O^{\rm IP}(t)$) is the state vector (observable) in the interaction picture. The equation determining the time evolution looks very much like the ordinary Schrödinger equation (1.1), but involves only the interaction part of the Hamiltonian [5]:

$$H_{\rm int}^{\rm IP}(t)\,|\Psi(t)\rangle_{\rm IP} = i\frac{d}{dt}\,|\Psi(t)\rangle_{\rm IP}\,. \tag{1.34}$$

Here, the interaction Hamiltonian in the interaction picture is, as one would expect,

$$H_{\rm int}^{\rm IP}(t) = e^{iH_0(t-t_0)}H_{\rm int}e^{-iH_0(t-t_0)}. \tag{1.35}$$

In the following, all states and operators are considered in the interaction picture, but the label IP is dropped to make the notation less cumbersome.

The cross section is found by evolving the initial state $|i\rangle$, characterized by the beam particles' species, momenta and polarization, through time to find the quantum mechanical state at some time after the collision. Formally, we take the initial time to be $-\infty$ and the final time to be $+\infty$, which physically means that we consider the time evolution from the time when the beam particles are far enough apart that they do not interact, to the time when the final state particles are far enough apart that they do not interact. We define the S-matrix (or S-operator) to be the time evolution operator relating the initial state to the state at $t = \infty$:

$$|\Psi(\infty)\rangle = S\,|\Psi(-\infty)\rangle = S\,|i\rangle\,. \tag{1.36}$$

The probability density to measure certain particles with certain momenta, spins, etc. after the collision, is $|\langle f|\Psi(\infty)\rangle|^2$, where $|f\rangle$ is the state containing exactly these particles (with these momenta, spins, etc.).

The time evolution equation (1.34) can be integrated from the initial time $t_i = -\infty$ to obtain the result

$$|\Psi(t)\rangle = |\Psi(t_i)\rangle - i\int_{t_i}^{t} H_{\rm int}(t')\,|\Psi(t')\rangle\;dt'. \tag{1.37}$$

This is not really a solution, as the desired state vector enters on both sides of the equation. However, we can insert

$$|\Psi(t')\rangle = |\Psi(t_i)\rangle - i\int_{t_i}^{t'} H_{\rm int}(t'')\,|\Psi(t'')\rangle\;dt'' \tag{1.38}$$

for $|\Psi(t')\rangle$ on the right hand side of eq. (1.37) and so on, giving an iterative solution with the S-operator on the form

$$S = \sum_{n=0}^{\infty}(-i)^n\int_{-\infty}^{+\infty}dt_1\int_{-\infty}^{t_1}dt_2\,\cdots\int_{-\infty}^{t_{n-1}}dt_n\,H_{\rm int}(t_1)H_{\rm int}(t_2)\cdots H_{\rm int}(t_n). \tag{1.39}$$

Furthermore, all the integrations over time can be extended to $+\infty$ by noting that the interac-

tion Hamiltonians are time ordered, and introducing a combinatorial factor $1/n!$ to account for double counting. Finally, the integrals can be extended over all space-time by writing the interaction Hamiltonian as the integral of the respective density. The final result for the S-operator takes the form [5]

$$S = \sum_{n=0}^{\infty} \frac{(-i)^n}{n!} \int \cdots \int d^4x_1\, d^4x_2 \cdots d^4x_n \mathrm{T}\left\{\mathcal{H}_{\mathrm{int}}(x_1)\mathcal{H}_{\mathrm{int}}(x_2)\cdots\mathcal{H}_{\mathrm{int}}(x_n)\right\} \tag{1.40}$$

where the T denotes a time ordered product (later times to the left of earlier times).

The expansion (1.40) is only useful if it can to a good approximation be truncated after a small number of terms. This is the case whenever the coupling constant of the interaction under consideration is small, because the higher order terms in (1.40) contain higher powers of the coupling constant (not explicit in eq. (1.40), but contained in the interaction Hamiltonian densities). For example, the coupling constant of the electromagnetic force is the fine structure constant $\alpha_{\mathrm{em}} \approx 1/137$, and higher powers of this number become quickly small.

Feynman rules

The actual computation of cross sections from the expansion (1.40) is very cumbersome. Feynman discovered that the result of this computation could be anticipated by drawing so-called Feynman diagrams and writing down particular factors corresponding to the various parts of the diagrams following the Feynman rules[14]. The Feynman diagrams also provide a physical interpretation of scattering processes in terms of exchanges of force particles and the production and decays of short lived particles.

Feynman diagrams are built from the basic vertices of a given theory, which are found by inspection of the interaction Hamiltonian density (or the interaction Lagrangian density). While the interaction Lagrangian density specifies the factors associated with each vertex, the factors associated with the lines between the vertices and external lines are found from the Lagrangian density terms corresponding to the free particles. Examples of the basic vertices of the SM will be shown in the next sections.

To illustrate the use of the Feynman diagram approach, we show in fig. 1.1 the lowest order Feynman diagram for the process $e^+e^- \to \tau^+\tau^-$ in QED (Quantum Electrodynamics, the theory of electromagnetic interaction). The Feynman diagram provides an interpretation of the process as the annihilation of the electron-positron pair into a (virtual) photon which subsequently decays to the $\tau^+\tau^-$ pair. The factors associated with the various parts of the diagram are shown. The dynamics of the process is encoded in the *Feynman amplitude* $\mathcal{M}$, whose absolute square is proportional to the cross section. Once the Feynman amplitude is known, the cross section calculation is reduced to pure kinematics which is independent of the theory of the interaction (i.e. independent of the Lagrangian density).

The initial and final state leptons are associated with Dirac spinors u and v that appear in plane wave expansions of the full Dirac spinor ψ. These are labeled with the momenta and spin states of the particles, and the calculation of an unpolarized cross section involves averaging over initial spins and summing over final spins. The Feynman rules state that the factors along

[14]Feynman rules for the Standard Electroweak Theory can be found in the appendix of ref. [5]. Feynman rules for QCD (the strong interaction) can be found in the appendix of ref. [8].

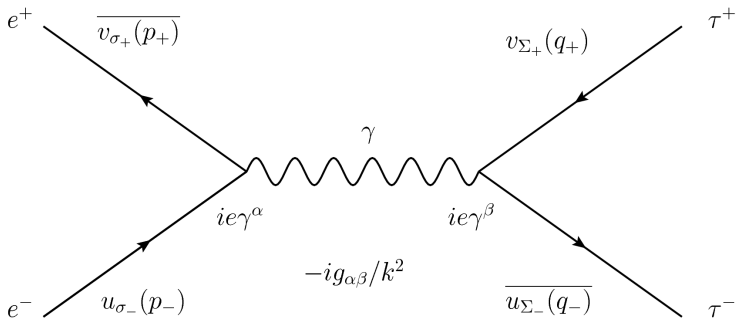

Figure 1.1: The lowest order Feynman diagram for the process $e^+e^- \to \tau^+\tau^-$ in QED. The factors associated with the various parts of the diagram are shown.

a fermion line are written down in the opposite direction of the arrows, and the full Feynman amplitude takes the form

$$\mathcal{M} = \overline{v_{\sigma_+}(p_+)}\, ie\gamma^\alpha\, u_{\sigma_-}(p_-)\, \frac{-ig_{\alpha\beta}}{k^2}\, \overline{u_{\Sigma_-}(q_-)}\, ie\gamma^\beta\, v_{\Sigma_+}(q_+) \tag{1.41}$$

where $k = p_+ + p_- = q_+ + q_-$ is the four-momentum of the virtual photon and e is the elementary charge. We note that the organization of Dirac spinors and γ-matrices gives just an ordinary (complex) number without spinor or matrix structure, and that the arbitrary space-time indices α and β associated with the two vertices are fully contracted via the factor $g_{\alpha\beta}$ in the photon propagator. Finally, we note that the Feynman amplitude contains a factor e^2, and that the corresponding cross section is proportional to e^4 or $\alpha_{\rm em}^2$ ($\alpha_{\rm em} = e^2/(4\pi)$).

1.3 Interactions of the Standard Model

We have reviewed the main ingredients involved in going from a theory, formulated in terms of a Lagrangian density, to actual cross sections measurable in experiment. This tells us nothing about how we can actually find a good Lagrangian density to describe the world we live in. The Lagrangian density is really the basic part of a particle physics theory, summarizing all particle species and their interactions. It must to a certain extent be *postulated*, but the principle of *gauge invariance* provides an extremely powerful guide to postulating a good Lagrangian density (one which is mathematically possible to deal with and possibly leads to finite cross sections in good agreement with experiment). First, we will present a classical motivation for the Lagrangian density of Quantum Electrodynamics (QED), before seeing how the Lagrangian density could instead be found by the principle of gauge invariance. Then, the Lagrangian densities of the SM are presented.

1.3.1 Quantum Electrodynamics

The Dirac Lagrangian[15] (1.17) describes a free spin-1/2 particle, such as a free electron. Electromagnetic interactions can be introduced into this Lagrangian by the "minimal substitution", which will now be motivated.

[15]The Lagrangian density is from now on referred to simply as "the Lagrangian" following standard convention to avoid cumbersome language.

Consider a (non-relativistic) particle of charge q in an electromagnetic field described in terms of the four-potential $A^\mu = (\phi, \mathbf{A})$. The standard form of the Lagrangian, $L = T - V$ cannot describe the general electromagnetic force, as only the electrostatic part can be described in terms of a potential energy function. The classical Lagrangian is extended to include a "velocity dependent potential" term [6]:

$$L = \frac{1}{2}m\dot{\mathbf{x}}^2 + q\dot{\mathbf{x}} \cdot \mathbf{A}(\mathbf{x}, t) - q\phi(\mathbf{x}, t). \tag{1.42}$$

It can be verified that this Lagrangian indeed correctly describes the electromagnetic force by checking that the Euler-Lagrange equations take the form

$$m\ddot{\mathbf{x}} = q\mathbf{E} + q\dot{\mathbf{x}} \times \mathbf{B} \tag{1.43}$$

with the usual relations between the electromagnetic potential A^μ and the electric and magnetic fields $\mathbf{E}$ and $\mathbf{B}$:

$$\mathbf{E} = -\nabla\phi - \frac{\partial \mathbf{A}}{\partial t}, \quad \mathbf{B} = \nabla \times \mathbf{A}. \tag{1.44}$$

Using the ordinary cartesian coordinates as generalized coordinates, the generalized momentum components corresponding to the Lagrangian (1.42) are

$$p_i = \frac{\partial L}{\partial \dot{x}_i} = m\dot{x}_i + qA_i. \tag{1.45}$$

The Hamiltonian is found from the definition (1.15):

$$H = \frac{1}{2m}\left(\mathbf{p} - q\mathbf{A}\right)^2 + q\phi \tag{1.46}$$

where $\mathbf{p}$ is the generalized momentum, not the mechanical momentum $m\dot{\mathbf{x}}$. In fact, this Hamiltonian is nothing but the total energy $T + V$. Creating a quantum mechanical Hamiltonian operator, we replace $\mathbf{p}$ with $\hat{\mathbf{p}} = -i\nabla$, yielding[16]

$$\hat{H} = \frac{1}{2m}\left(i\nabla + q\mathbf{A}\right)^2 + q\phi. \tag{1.47}$$

Writing out the non-relativistic Schrödinger wave equation with this Hamiltonian and comparing to the non-relativistic wave equation for a free particle (eq. (1.2) with $V(\mathbf{x}) = 0$), we see that the electromagnetic interaction is introduced into the free particle wave equation by the substitutions

$$i\nabla \;\rightarrow\; i\nabla + q\mathbf{A} \quad \text{and} \quad i\frac{\partial}{\partial t} \;\rightarrow\; i\frac{\partial}{\partial t} - q\phi, \tag{1.48}$$

or in four-vector notation:

$$\partial_\mu \;\rightarrow\; D_\mu = \partial_\mu + iqA_\mu \tag{1.49}$$

where the covariant derivative D_μ is defined. This is exactly the "minimal substitution" as presented in ref. [5]. It turns out that this substitution can be used to introduce electromagnetic interactions also in the relativistic case, and we will shortly see how it can be derived from the

[16]The "hat" notation for operators is here briefly reintroduced to distinguish them from the classical quantities.

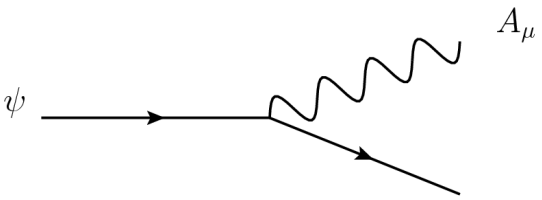

Figure 1.2: The basic vertex of QED in which a fermion couples to a photon. The vertex can be oriented as to represent a fermion emitting a photon (shown), an antifermion emitting a photon, a fermion and an antifermion annihilating into a photon, a photon splitting into a fermion and an antifermion, or a fermion or an antifermion absorbing a photon.

principle of gauge invariance.

Using the minimal substitution (1.49) in the Dirac Lagrangian (1.17) we obtain

$$\mathcal{L} = \overline{\psi}\left(i\gamma^\mu\partial_\mu - m\right)\psi - q\overline{\psi}\gamma^\mu\psi A_\mu = \mathcal{L}_0 + \mathcal{L}_{\text{int}}. \tag{1.50}$$

The interaction Lagrangian $\mathcal{L}_{\text{int}} = -q\overline{\psi}\gamma^\mu\psi A_\mu$ describes the interaction between the charged particle and the electromagnetic field. It corresponds to the basic Feynman diagram vertex shown in fig. 1.2. Finally, we add in the Lagrangian a term describing the free electromagnetic field to obtain the complete QED Lagrangian

$$\mathcal{L} = \overline{\psi}\left(i\gamma^\mu\partial_\mu - m\right)\psi - \frac{1}{4}F_{\mu\nu}F^{\mu\nu} - q\overline{\psi}\gamma^\mu\psi A_\mu = \mathcal{L}_0 + \mathcal{L}_{\text{int}} \tag{1.51}$$

where the new term $-(1/4)F_{\mu\nu}F^{\mu\nu}$ enters in $\mathcal{L}_0$, $\mathcal{L}_{\text{int}}$ remains as previously defined, and

$$F_{\mu\nu} = \partial_\nu A_\mu - \partial_\mu A_\nu \tag{1.52}$$

is the electromagnetic field tensor. To include several fermion species, the terms involving the fermion spinor ψ in the Lagrangian must be summed over all fermion species. (There is then one spinor for each fermion species.)

The basic QED vertex in fig. 1.2 is associated with a particular vertex factor when one uses the Feynman diagram approach to calculate a cross section. One obtains the vertex factor from the interaction Lagrangian by multiplying by the imaginary unit i and erasing the field variables. In the QED case, we find

$$i\mathcal{L}_{\text{int}} = -iq\overline{\psi}\gamma^\mu\psi A_\mu, \tag{1.53}$$

and erasing the field variables $\overline{\psi}$, ψ, and A_μ, we find the vertex factor $-iq\gamma^\mu$. For the electron, $q = -e$, so the vertex factor is $ie\gamma^\mu$ in accordance with fig. 1.1.

Gauge invariance in QED

From the definition of the electromagnetic four-potential (1.44), it is clear that the transformation

$$A_\mu(x) \;\rightarrow\; A'_\mu(x) = A_\mu(x) - \partial_\mu\alpha(x) \tag{1.54}$$

leaves the electric and magnetic fields unchanged, i.e. $\mathbf{E}' = \mathbf{E}$ and $\mathbf{B}' = \mathbf{B}$, for any (well-behaved) function $\alpha(x)$. Thinking of $\mathbf{E}$ and $\mathbf{B}$ as the physical quantities[17], it is clear that the

[17] In classical electrodynamics, it is clear that $\mathbf{E}$ and $\mathbf{B}$ are the physical quantities, since the force on a charged particle is written in terms of them. In the quantum regime this is no longer really the case, as it can be shown

transformation has no real effect in terms of forces acting on charged particles, and we could expect the QED Lagrangian (1.51) to be left unchanged by such a transformation (called a gauge transformation). This is, however, not the case unless we demand that the fermion field undergoes the coupled transformation

$$\psi(x) \;\rightarrow\; \psi'(x) = e^{iq\alpha(x)}\psi(x). \tag{1.55}$$

Turning the argument the other way around, we can *derive* the QED Lagrangian from the free fermion Lagrangian (1.17) by the requirement of gauge invariance. This is very important, because this is the way that the exact form of all the interactions in the SM is derived. Let us start from the free fermion Lagrangian (1.17). We note that it is invariant under a *global* phase transformation

$$\psi(x) \;\rightarrow\; \psi'(x) = e^{iq\beta}\psi(x) \tag{1.56}$$

where β is a constant, and *demand* that it be invariant under the *local* transformation (1.55). To obtain such an invariance, we must introduce the field $A_\mu(x)$, demand that it undergoes the coupled transformation (1.54), and add the interaction term $\mathcal{L}_{\text{int}}$ to the free fermion Lagrangian. Finally, to arrive to the full QED Lagrangian, we would need to observe that the quantity $F_{\mu\nu}$ is also invariant under the transformation (1.54) and argue that this means that also a Lorentz invariant contraction of this quantity, such as $-(1/4)F_{\mu\nu}F^{\mu\nu}$, should be added to the Lagrangian[18] to describe the propagation of the free A_μ field (the photon).

1.3.2 Quantum Chromodynamics

Quarks carry a quantum number, color (or color charge), which is not carried by leptons. Without such a property of quarks, the quark content of the Δ^{++} baryon (uuu) would violate the Pauli exclusion principle. Furthermore, the ratio of the cross sections for the processes $e^+e^- \rightarrow \mu^+\mu^-$ and $e^+e^- \rightarrow q\overline{q}$ at low energies, with the latter process observed as a final state of hadrons, can only be correctly predicted assuming that the quarks come in three different versions. This triples the number of physically distinct $q\overline{q}$ final states, thus affecting the ratio.

In Quantum Chromodynamics (QCD), the theory describing the strong interaction, quarks are placed in color triplets. The Lagrangian for a free quark of one specific flavor is [8]

$$\mathcal{L}_0 = \overline{\psi}\left(i\gamma^\mu\partial_\mu - m\right)\psi \tag{1.57}$$

where

$$\psi = \begin{pmatrix}\psi_1\\ \psi_2\\ \psi_3\end{pmatrix}, \quad \overline{\psi} = \begin{pmatrix}\overline{\psi_1} & \overline{\psi_2} & \overline{\psi_3}\end{pmatrix}, \tag{1.58}$$

and ψ_i is a regular Dirac spinor for a quark of color i. This Lagrangian is invariant under the $\mathrm{SU(3)_C}$ transformations

$$\psi \;\rightarrow\; \psi' = U\psi, \quad U = e^{\frac{1}{2}ig_s\alpha_k\lambda_k} \tag{1.59}$$

that a quantum particle is sensitive to the electromagnetic field even when it is in a region where $\mathbf{E} = \mathbf{B} = \mathbf{0}$, see ref. [9].

[18] One can also construct Lagrangian terms from $F_{\mu\nu}$ other than $F_{\mu\nu}F^{\mu\nu}$. In ref. [10], it is briefly mentioned why these can be disregarded.

where λ_k ($k = 1, 2, \ldots, 8$) are the Gell-Mann matrices and g_s is the strong coupling constant, as long as the real numbers α_k are constants. This invariance follows from the unitarity of the $\mathrm{SU}(3)_\mathrm{C}$ transformations (or matrices), $U^\dagger U = 1$.

If we consider a *local* $\mathrm{SU}(3)_\mathrm{C}$ transformation, i.e. eq. (1.59) with α_k as a function of space-time, then the Lagrangian $\mathcal{L}_0$ is no longer invariant, but transforms as

$$\mathcal{L}_0 \;\rightarrow\; \mathcal{L}_0' = \mathcal{L}_0 + \overline{\psi} i\gamma^\mu U^\dagger (\partial_\mu U)\psi. \tag{1.60}$$

Invariance of the Lagrangian can be restored by the introduction of eight gluon fields $A_\mu^k(x)$ through the interaction Lagrangian

$$\mathcal{L}_\mathrm{int} = -\frac{g_\mathrm{s}}{2}\overline{\psi}\gamma^\mu \lambda_k \psi A_\mu^k. \tag{1.61}$$

The fields A_μ^k transform under infinitesimal $\mathrm{SU}(3)_\mathrm{C}$ transformations (eq. (1.59) with infinitesimal α_k) as [8]

$$A_\mu^k \;\rightarrow\; A_\mu'^k = A_\mu^k - \partial_\mu \alpha_k - g_\mathrm{s} f_{klm} \alpha_l A_\mu^m \tag{1.62}$$

where f_{klm} are the $\mathrm{SU}(3)$ structure constants. The last term in eq. (1.62) arises because the $\mathrm{SU}(3)_\mathrm{C}$ matrices do not commute, i.e. $\mathrm{SU}(3)$ is a non-Abelian group. Eq. (1.61) gives rise to the basic quark-gluon vertex.

We need also the Lagrangian describing the free gluon field. The straight forward generalization of $F_{\mu\nu}$ from eq. (1.52) is not gauge invariant because of the non-Abelian nature of $\mathrm{SU}(3)$. The free gluon Lagrangian takes the form [8]

$$\mathcal{L}_\mathrm{gluons} = -\frac{1}{4} F_{\mu\nu}^k F_k^{\mu\nu} \tag{1.63}$$

where

$$F_{\mu\nu}^k = \partial_\mu A_\nu^k - \partial_\nu A_\mu^k - g_\mathrm{s} f_{klm} A_\mu^l A_\nu^m. \tag{1.64}$$

When written out explicitly in terms of the gluon fields A_μ^k, the Lagrangian (1.63) contains terms involving

$$g_\mathrm{s} f_{klm} (\partial_\mu A_\nu^k - \partial_\nu A_\mu^k) A_l^\mu A_m^\nu \quad \text{and} \quad g_\mathrm{s}^2 f_{klm} f_{kij} A_\mu^l A_\nu^m A_i^\mu A_j^\nu, \tag{1.65}$$

giving rise to three and four gluon vertices respectively.

To sum up QCD, the full Lagrangian for gluons and a quark of one specific flavor is

$$\mathcal{L} = \overline{\psi}\left(i\gamma^\mu \partial_\mu - m\right)\psi - \frac{1}{4} F_{\mu\nu}^k F_k^{\mu\nu} - \frac{g_\mathrm{s}}{2}\overline{\psi}\gamma^\mu \lambda_k \psi A_\mu^k. \tag{1.66}$$

For the complete Lagrangian, simply sum the terms involving ψ over all flavors. The basic vertices of QCD are shown in fig. 1.3, and while the vertex factor for the quark-gluon coupling is simply $-ig_\mathrm{s}\gamma^\mu \lambda_k/2$, the gluon self-coupling vertex factors are somewhat more complex and are not given here explicitly. In particular, the derivatives in the three gluon vertex give a four-momentum dependent factor.

Note that while quark masses are not a problem in QCD alone (meaning that the Dirac mass term is $\mathrm{SU}(3)_\mathrm{C}$ gauge invariant), they must be omitted when fitting QCD into the SM,

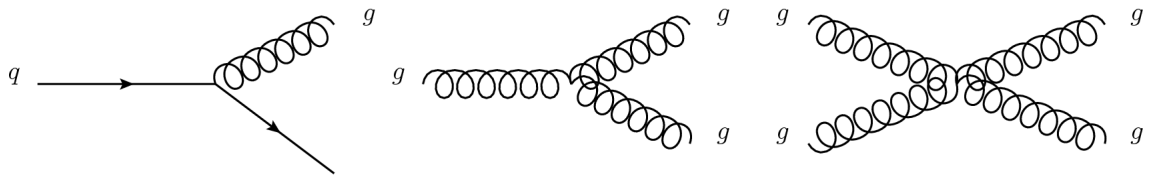

Figure 1.3: The basic Feynman diagram vertices of QCD.

and they are reinserted into the Lagrangian through the Brout-Englert-Higgs mechanism (see section 1.3.4). The Dirac mass term is also invariant under the gauge transformation of QED.

1.3.3 The Standard Electroweak Theory

In the Standard Electroweak Theory, the concept of chirality or handedness is central. It is closely related to the concept of helicity, defined by the projection of the spin $\boldsymbol{\sigma}$ of a particle on its direction of motion:

$$\sigma_{\mathbf{p}} = \frac{\boldsymbol{\sigma} \cdot \mathbf{p}}{|\mathbf{p}|}. \tag{1.67}$$

A left-handed massless spin-$1/2$ particle has helicity $\sigma_{\mathbf{p}} = -1/2$, while a right-handed one has helicity $\sigma_{\mathbf{p}} = +1/2$. The helicity and the chirality coincide in this way for massless particles, and to good approximation for all particles moving at highly relativistic speeds. For massive particles, the helicity is not Lorentz invariant, as boosting to a reference frame in which the direction of motion of the massive particle is reversed does not change the direction of the spin.

If the operation of space inversion, parity, were a symmetry of nature, no distinction would be made between left-handed and right-handed particles. Since this symmetry is violated in weak interactions, we will see that left-handed and right-handed particles are treated differently in the electroweak theory.

In the electroweak theory, the left-handed components of quark and lepton fields are grouped into doublets. One such doublet is the electron and its neutrino, which will be used as the example in introducing the theory. The theory is identical for the other lepton generations, and also more or less identical for the three quark generations (for the quarks, the values of the weak hypercharge, which will soon be introduced, differ from those of the leptons).

We define $\psi_L = L\psi$ and $\psi_R = R\psi$, where L and R are the left-handed and right-handed chirality projection matrices[19]:

$$L = \frac{1}{2}\left(1 - \gamma_5\right) \quad \text{and} \quad R = \frac{1}{2}\left(1 + \gamma_5\right). \tag{1.68}$$

Because $\{\gamma^\mu, \gamma_5\} = 0$, we have $\gamma^\mu L = R\gamma^\mu$ and $L\gamma^\mu = \gamma^\mu R$. Furthermore, $L^2 = L$, $R^2 = R$, $R + L = 1$, $R^\dagger = R$, and $L^\dagger = L$. Using these relations, we may decompose the Dirac Lagrangian (1.17) as

$$\mathcal{L} = \overline{\psi_L} i\gamma^\mu \partial_\mu \psi_L + \overline{\psi_R} i\gamma^\mu \partial_\mu \psi_R - m\overline{\psi_R}\psi_L - m\overline{\psi_L}\psi_R. \tag{1.69}$$

[19]The "fifth γ matrix" is defined as $\gamma_5 = i\gamma^0\gamma^1\gamma^2\gamma^3$. It satisfies $\gamma_5^\dagger = \gamma_5$ and $\gamma_5^2 = 1$.

The mass term is troublesome because it mixes the left-handed and right-handed components of the field. Neglecting the masses, we may write the Lagrangian describing the free electron and electron neutrino as

$$\mathcal{L}_0 = \overline{\psi_L^e} i\gamma^\mu \partial_\mu \psi_L^e + \overline{\psi_R^e} i\gamma^\mu \partial_\mu \psi_R^e + \overline{\psi_L^\nu} i\gamma^\mu \partial_\mu \psi_L^\nu + \overline{\psi_R^\nu} i\gamma^\mu \partial_\mu \psi_R^\nu. \tag{1.70}$$

In constructing the electroweak Lagrangian, one next makes a distinction between left-handed and right-handed components, and writes the Lagrangian as

$$\mathcal{L}_0 = \overline{\chi_L} i\gamma^\mu \partial_\mu \chi_L + \overline{\psi_R^e} i\gamma^\mu \partial_\mu \psi_R^e + \overline{\psi_R^\nu} i\gamma^\mu \partial_\mu \psi_R^\nu \tag{1.71}$$

where

$$\chi_L = \begin{pmatrix} \psi_L^\nu \\ \psi_L^e \end{pmatrix} \quad \text{and} \quad \overline{\chi_L} = \begin{pmatrix} \overline{\psi_L^\nu} & \overline{\psi_L^e} \end{pmatrix}. \tag{1.72}$$

We have now grouped the left-handed components in a weak isospin doublet, where ψ_L^ν has $I_3 = +1/2$ and ψ_L^e has $I_3 = -1/2$, while the right-handed components are isospin singlets ($I_3 = 0$). Furthermore, we assign a weak hypercharge Y to each field (individually for right-handed and left-handed components) such that the electric charge is

$$q = \left(I_3 + \frac{Y}{2} \right) e \tag{1.73}$$

with e as the elementary electric charge. Hence, the left-handed components have $Y = -1$, the right-handed component of the electron has $Y = -2$, and the right-handed component of the neutrino has $Y = 0$.

The electroweak Lagrangian (1.71) is invariant under the $\mathrm{SU(2)_L}$ transformations

$$\chi_L \;\rightarrow\; \chi_L' = U\chi_L, \quad U = e^{\frac{1}{2} i g \omega_k \tau_k} \tag{1.74}$$

where τ_k ($k = 1, 2, 3$) are the Pauli matrices, ω_k are real constants, and g is the coupling constant associated with the transformation. Furthermore, it is invariant under the $\mathrm{U(1)}_Y$ transformations

$$\psi \;\rightarrow\; \psi' = e^{\frac{Y}{2} i g' \beta} \psi \tag{1.75}$$

where Y is the weak hypercharge and g' is the corresponding coupling constant, as long as the real number β is constant.

To make the Lagrangian invariant under *local* $\mathrm{U(1)}_Y$ transformations, (eq. (1.75) with β as a function of space-time) we must add a term (for each spinor)

$$\mathcal{L}_{\text{int}}^B = -\frac{Y}{2} g' \overline{\psi} \gamma^\mu \psi B_\mu \tag{1.76}$$

where the field $B_\mu(x)$ transforms as

$$B_\mu \;\rightarrow\; B_\mu' = B_\mu - \partial_\mu \beta. \tag{1.77}$$

Furthermore, to make the Lagrangian invariant under local $\mathrm{SU(2)_L}$ transformations (eq. (1.74)

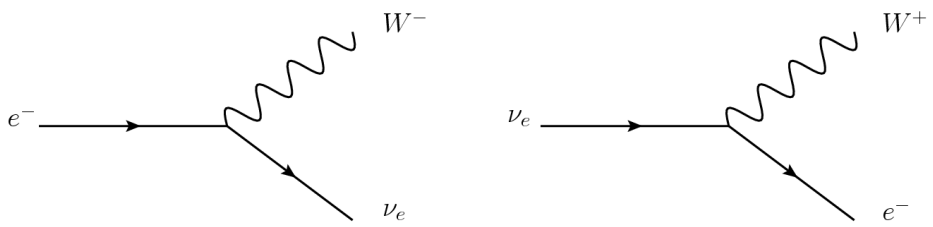

Figure 1.4: The basic charged current vertices for the electron and electron neutrino.

with ω_k as functions of space-time) we must add a term

$$\mathcal{L}_{\text{int}}^{W} = -\frac{1}{2} g \overline{\chi_L} \gamma^\mu \tau_k \chi_L W_\mu^k, \tag{1.78}$$

where the three fields $W_\mu^k(x)$ transform under infinitesimal $\mathrm{SU(2)_L}$ transformations as [5]

$$W_\mu^i \;\rightarrow\; W_\mu'^i = W_\mu^i - \partial_\mu \omega_i - g \varepsilon_{ijk} \omega_j W_\mu^k \tag{1.79}$$

with ε_{ijk} as the Levi-Civita tensor (the structure constants of $\mathrm{SU(2)}$).

The full interaction Lagrangian for the electron and electron neutrino can now be written out, inserting the correct hypercharge values:

$$\mathcal{L}_{\text{int}} = \mathcal{L}_{\text{int}}^{W} + \mathcal{L}_{\text{int}}^{B} = -\frac{1}{2} g \overline{\chi_L} \gamma^\mu \tau_k \chi_L W_\mu^k + \frac{1}{2} g' \overline{\chi_L} \gamma^\mu \chi_L B_\mu + g' \overline{\psi_R^e} \gamma^\mu \psi_R^e B_\mu. \tag{1.80}$$

We consider first the terms involving W_μ^1 and W_μ^2. Defining the physical $W^\pm$-field

$$W_\mu = \frac{1}{\sqrt{2}} \left(W_\mu^1 - i W_\mu^2 \right) \tag{1.81}$$

with Hermitian conjugate

$$W_\mu^\dagger = \frac{1}{\sqrt{2}} \left(W_\mu^1 + i W_\mu^2 \right) \tag{1.82}$$

and using explicit expressions for τ_1 and τ_2, we find

$$\mathcal{L}_{\text{int}}^{W^{1,2}} = -\frac{g}{\sqrt{2}} \left[\overline{\psi_L^\nu} \gamma^\mu \psi_L^e W_\mu + \overline{\psi_L^e} \gamma^\mu \psi_L^\nu W_\mu^\dagger \right], \tag{1.83}$$

giving rise to the basic charged current vertices shown in fig. 1.4. We see that the $W^\pm$ bosons couple only to left-handed components – the symmetry of space inversion is violated 100% in charged current weak interactions.

When writing out the terms involving W_μ^3 and B_μ, we define the physical photon A_μ and Z^0 boson Z_μ:

$$A_\mu = \cos\theta_{\mathrm{W}} B_\mu + \sin\theta_{\mathrm{W}} W_\mu^3, \tag{1.84}$$

$$Z_\mu = -\sin\theta_{\mathrm{W}} B_\mu + \cos\theta_{\mathrm{W}} W_\mu^3 \tag{1.85}$$

Fermion	e^-, μ^-, τ^-	ν_e, ν_μ, ν_τ	u, c, t	d, s, b
g_{V}	$2\sin^2\theta_{\mathrm{W}} - \frac{1}{2}$	$\frac{1}{2}$	$\frac{1}{2} - \frac{4}{3}\sin^2\theta_{\mathrm{W}}$	$\frac{2}{3}\sin^2\theta_{\mathrm{W}} - \frac{1}{2}$
g_{A}	$-\frac{1}{2}$	$\frac{1}{2}$	$\frac{1}{2}$	$-\frac{1}{2}$

Table 1.2: The vector and axial vector Z^0 couplings to quarks and leptons. From ref. [8].

where θ_{W} is the weak mixing angle. Demanding that A_μ couples to the electromagnetic current, one obtains the restrictions $g\sin\theta_{\mathrm{W}} = g'\cos\theta_{\mathrm{W}} = e$. The resulting neutral current terms are

$$\mathcal{L}_{\mathrm{int}}^{W^3B} = e\overline{\psi^e}\gamma^\mu\psi^e A_\mu - \frac{g}{2\cos\theta_{\mathrm{W}}}\left(\overline{\chi_L}\gamma^\mu\tau_3\chi_L + 2\sin^2\theta_{\mathrm{W}}\overline{\psi^e}\gamma^\mu\psi^e\right)Z_\mu, \tag{1.86}$$

where

$$\overline{\chi_L}\gamma^\mu\tau_3\chi_L = \overline{\psi_L^\nu}\gamma^\mu\psi_L^\nu - \overline{\psi_L^e}\gamma^\mu\psi_L^e. \tag{1.87}$$

These terms give the neutral current vertices shown in fig. 1.5. The Z^0 couples only to the left-handed component of the neutrino field. It couples not only to the left-handed component of the electron field, but also to the right-handed one. However, the left-handed and right-handed couplings are not equal.

The vertex factor for a fermion coupling to the Z^0 is customarily written as

$$\frac{-ig\gamma^\mu}{2\cos\theta_{\mathrm{W}}}\left(g_{\mathrm{V}} - g_{\mathrm{A}}\gamma_5\right) \tag{1.88}$$

where g_{V} (g_{A}) is the vector (axial vector) coupling. By comparison with equation (1.86), we find $g_{\mathrm{V}} = 2\sin^2\theta_{\mathrm{W}} - 1/2$ and $g_{\mathrm{A}} = -1/2$ for the electron, and $g_{\mathrm{V}} = g_{\mathrm{A}} = 1/2$ for the electron neutrino. Values of g_{V} and g_{A} for quarks and leptons are given in table 1.2. The vertex factor for $W^\pm$ coupling to electron and electron neutrino is from equation (1.83)

$$\frac{-ig\gamma^\mu}{2\sqrt{2}}\left(1 - \gamma_5\right). \tag{1.89}$$

This factor is the same for the $W^\pm$ coupling to the other lepton generations, but slightly different for the quark generations. (In the case of quarks, it is the left-handed up-type quark that is assigned $I_3 = +1/2$ while the left-handed down-type quark is assigned $I_3 = -1/2$.) In the $W^\pm$ coupling to quarks, the CKM matrix element for the relevant transition enters (see section 1.3.4). This means that the W^+ can couple for example to $u\overline{s}$, with an amplitude proportional to the relevant CKM matrix element.

We see that because it has hypercharge $Y = 0$, the right-handed component of the neutrino field has dropped out of the interaction Lagrangian. Hence, the right-handed neutrino does not take part in any SM interaction, and it is a technicality that we included it in the first place. As long as neutrinos are considered massless, there is no need for a right-handed neutrino in the SM. Since it seems that neutrinos do have mass (see section 1.7.1), the exact nature of the neutrinos is today still an open question.

The complete electroweak Lagrangian contains also a free gauge field part, giving rise to gauge boson self-interactions as in the case of QCD, since $\mathrm{SU}(2)$ is a non-Abelian group. This

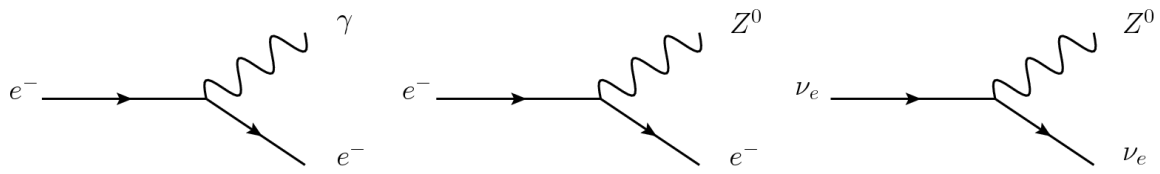

Figure 1.5: The basic neutral current vertices for the electron and electron neutrino.

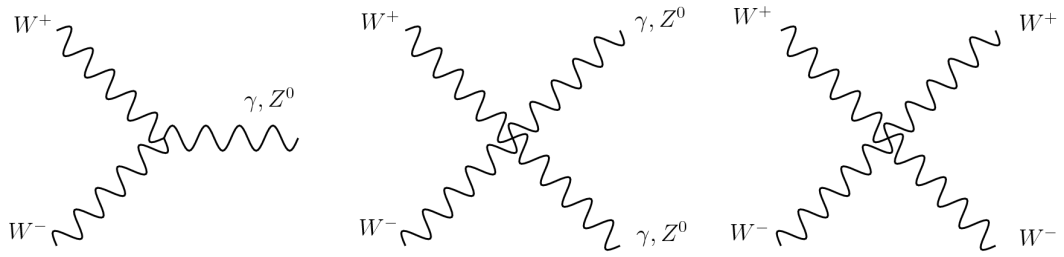

Figure 1.6: The gauge boson self-interaction vertices in the electroweak theory. As long as we allow vertex in the middle to represent also the $W^+W^- \to \gamma\, Z^0$ vertex, there are no other gauge boson self-interaction vertices than those shown here.

part has the form [5]

$$\mathcal{L}_{\text{bosons}} = -\frac{1}{4}B_{\mu\nu}B^{\mu\nu} - \frac{1}{4}F^i_{\mu\nu}F_i^{\mu\nu} \tag{1.90}$$

where

$$B_{\mu\nu} = \partial_\nu B_\mu - \partial_\mu B_\nu \tag{1.91}$$

and

$$F^i_{\mu\nu} = \partial_\nu W^i_\mu - \partial_\mu W^i_\nu + g\varepsilon_{ijk}W^j_\mu W^k_\nu. \tag{1.92}$$

To obtain the exact gauge boson self-interactions, these terms must be written in terms of the physical fields W_μ, Z_μ, and A_μ. The gauge boson self-interaction vertices in the electroweak theory are shown in fig. 1.6.

1.3.4 The Brout-Englert-Higgs mechanism

The fermion mass terms had to be neglected in constructing the electroweak Lagrangian because they are not gauge invariant on account of the left-right mixing. Furthermore, mass terms for the $W^\pm$ and Z^0 bosons,

$$m_W^2 W_\mu^\dagger W^\mu + \frac{1}{2}m_Z^2 Z_\mu Z^\mu \tag{1.93}$$

(cf. eqs. (1.23) and (1.19)), are not gauge invariant either. The way gauge boson and fermion masses are incorporated into the Standard Electroweak Theory is the Brout-Englert-Higgs (BEH) mechanism.

An additional scalar isospin doublet $\Phi(x)$ with hypercharge $Y = 1$ is introduced in the

Lagrangian through the terms [5]

$$\mathcal{L}_\Phi = (iD^\mu\Phi)^\dagger(iD_\mu\Phi) - \left[\mu^2\Phi^\dagger\Phi + \lambda(\Phi^\dagger\Phi)^2\right] \tag{1.94}$$

where the covariant derivative

$$D^\mu = \partial^\mu + \frac{1}{2}ig\tau_k W_k^\mu + \frac{1}{2}ig'B^\mu \tag{1.95}$$

ensures gauge invariance. The term in square brackets is the "mexican hat" potential, which for $\mu^2 < 0$ has a minimum at $\Phi^\dagger\Phi = v^2/2$ where $v = \sqrt{-\mu^2/\lambda}$. The Higgs field therefore chooses a ground state on the circle $\Phi^\dagger\Phi = v^2/2$. In the electroweak theory, this ground state is written as

$$\Phi_0 = \frac{1}{\sqrt{2}}\begin{pmatrix}0\\ v\end{pmatrix}. \tag{1.96}$$

This choice is motivated by the fact that the lower component ($I_3 = -1/2$) corresponds to zero electric charge (see eq. (1.73)), and we do not want to give mass to the photon. Allowing for small oscillations around the ground state value Φ_0, one writes

$$\Phi = \frac{1}{\sqrt{2}}\begin{pmatrix}\eta_1(x) + i\eta_2(x)\\ v + H(x) + i\eta_3(x)\end{pmatrix}. \tag{1.97}$$

It is possible to find an $\mathrm{SU(2)_L} \times \mathrm{U(1)}_Y$ gauge transformation which brings us to the unitary gauge, in which the Higgs doublet has the form

$$\Phi = \frac{1}{\sqrt{2}}\begin{pmatrix}0\\ v + H(x)\end{pmatrix} \tag{1.98}$$

where $H(x)$ is the field corresponding to the Higgs boson.

With the form (1.98) of the doublet Φ, the "kinetic" terms of $\mathcal{L}_\Phi$ become

$$(iD^\mu\Phi)^\dagger(iD_\mu\Phi) = \frac{1}{2}(\partial_\mu H)(\partial^\mu H) + \frac{1}{4}(v+H)^2 g^2\left(W_\mu^\dagger W^\mu + \frac{1}{2\cos^2\theta_\mathrm{W}}Z_\mu Z^\mu\right). \tag{1.99}$$

The first term is the kinetic part of the scalar Lagrangian (1.18), describing in this context the Higgs boson. Among the remaining terms, those proportional to v^2 constitute mass terms for the $W^\pm$ and Z^0 bosons, and we find $m_W = vg/2$ and $m_Z = vg/(2\cos\theta_\mathrm{W})$. With the choice (1.96) for the ground state, no mass term is generated for the photon, as desired.

The parameter v is related to the Fermi coupling constant G_F. Written in terms of this constant and the fine structure constant α, the $W^\pm$ and Z^0 masses are

$$m_W = \frac{1}{\sin\theta_\mathrm{W}}\sqrt{\frac{\alpha\pi}{G_\mathrm{F}\sqrt{2}}} \quad \text{and} \quad m_Z = \frac{2}{\sin 2\theta_\mathrm{W}}\sqrt{\frac{\alpha\pi}{G_\mathrm{F}\sqrt{2}}} \tag{1.100}$$

giving $m_W = 76.9\,\mathrm{GeV}$ and $m_Z = 87.9\,\mathrm{GeV}$ with $\sin^2\theta_\mathrm{W} = 0.235$ obtained from neutrino scattering [5]. When the $W^\pm$ and Z^0 bosons were discovered in the early 1980s with masses in reasonable agreement with this prediction, this was a huge success for the theory [11–14]. The predicted masses are in excellent agreement with experiment when higher order corrections are

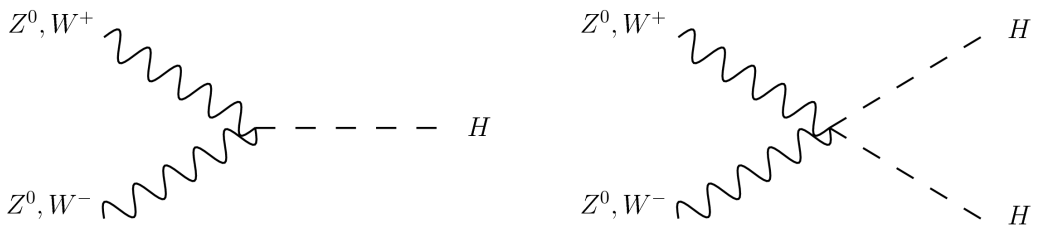

Figure 1.7: The basic vertices of the interaction of the Higgs boson with the $W^{\pm}$ and Z^0 bosons. The vertices depict in their current orientation the annihilation of either two Z^0 bosons or a W^+W^- pair into one or two Higgs bosons.

taken into account. The Higgs boson itself was not discovered until about 30 years later with the ATLAS and CMS detectors at the CERN Large Hadron Collider (LHC) [2, 3].

The remaining terms of eq. (1.99) give rise to interactions between the Higgs boson and the $W^{\pm}$ and Z^0 bosons via the basic vertices of fig. 1.7. The vertex factors for the vertices involving only one Higgs boson are[20] [5] $ig^2vg^{\mu\nu}/2$ for the $W^{\pm}$ case and $ig^2vg^{\mu\nu}/(2\cos^2\theta_{\mathrm{W}})$ for the Z^0 case. Written in terms of the gauge boson masses and the vacuum expectation value v, they are $2im_W^2g^{\mu\nu}/v$ and $2im_Z^2g^{\mu\nu}/v$ respectively. Dividing by v, one obtains the corresponding vertex factors for the vertices involving two Higgs bosons.

We consider finally the terms in square brackets of eq. (1.94). With the form (1.98) of the doublet Φ, these are

$$-\left[\mu^2\Phi^\dagger\Phi+\lambda(\Phi^\dagger\Phi)^2\right]=-\frac{1}{2}\mu^2(v+H)^2-\frac{1}{4}\lambda(v+H)^4. \tag{1.101}$$

The term proportional to H^2 is the Higgs boson mass term, and we find $m_H=\sqrt{-2\mu^2}=\sqrt{2v^2\lambda}$. Although the value of $v=\sqrt{-\mu^2/\lambda}$ was known long before the discovery of the Higgs boson at the LHC, the Higgs boson mass was not known because one did not know the individual μ^2 and λ parameters. The Higgs mass is today known quite precisely, and is very close to $125\,\mathrm{GeV}$ [15, 16]. The higher order (in H) terms of eq. (1.101) give rise to the Higgs boson self-interactions via the vertices shown in fig. 1.8, where three and four Higgs bosons couple. The corresponding vertex factors are $-6i\lambda v$ and $-6i\lambda$ respectively. Finally, eq. (1.101) contains a constant term. If interpreted as a contribution to the dark energy of the universe (see section 1.7.2), it gives a contribution which is more than 50 orders of magnitude larger than the observed value [17].

Mass terms for the fermions are also introduced by the BEH mechanism through additional terms of the form (taking the electron as an example)

$$\mathcal{L}_{e\Phi}=-G_e\left[\overline{\chi_L}\Phi\psi_R^e+\overline{\psi_R^e}\Phi^\dagger\chi_L\right]. \tag{1.102}$$

[20]Except for the $W^+W^-\to H$ vertex, the vertex factors for the vertices of fig. 1.7 differ from what one might naively expect from eq. (1.99) because of combinatorial factors due to the presence of identical particles. The same is true for the vertex factors corresponding to the vertices of fig. 1.8.

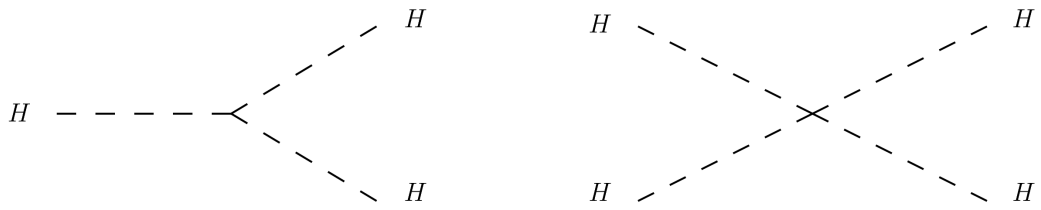

Figure 1.8: The basic vertices of the Higgs boson self-interactions.

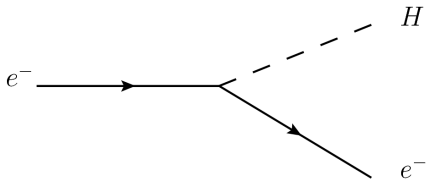

Figure 1.9: The basic vertex of the interaction of the Higgs boson with the electron.

With the form (1.98) of the doublet Φ, this gives

$$\mathcal{L}_{e\Phi} = -\frac{G_e}{\sqrt{2}}(v+H)\overline{\psi^e}\psi^e, \tag{1.103}$$

and the electron mass is thus $m_e = G_e v/\sqrt{2}$. This is not a prediction of the BEH theory, as G_e is a free parameter which is given by the experimentally measured electron mass. However, eq. (1.103) clearly also gives rise to the interaction of the electron with the Higgs boson via the basic vertex of fig. 1.9. This vertex is associated with a factor $-iG_e/\sqrt{2} = -im_e/v$. The BEH theory thus predicts a relation between the electron mass and its coupling to the Higgs boson, and equivalent relations are also obtained for the other fermions. As in the case of the Higgs boson interactions with the $W^\pm$ and Z^0 bosons, we see that the Higgs boson "couples to mass", i.e. couples more strongly to heavier particles.

We note that the Lagrangian terms of eq. (1.102) may only be used to give mass to down-type ($I_3 = -1/2$) fermions. To give masses to up-type ($I_3 = +1/2$) quarks (u, c, and t), similar terms involving $\tilde{\Phi} = -i(\Phi^\dagger \tau_2)^{\mathrm{T}}$ are added [5]. The doublet $\tilde{\Phi}$ transforms under $\mathrm{SU}(2)_{\mathrm{L}}$ transformations as Φ, but transforms under $\mathrm{U}(1)_Y$ transformations as if it had opposite hypercharge. In the unitary gauge, it has the non-zero component in the upper position, so that it "picks out" the up-type fermion instead of the down-type, so a mass term for the up quark can be written as

$$\mathcal{L}_{u\Phi} = -G_u\left[\overline{Q_L}\tilde{\Phi}\psi^u_R + \overline{\psi^u_R}\tilde{\Phi}^\dagger Q_L\right] \tag{1.104}$$

with Q_L as the doublet of left-handed up and down quarks (analogous to χ_L for leptons) and ψ^u as the up quark Dirac spinor. Such terms can also provide masses for the neutrinos, but adding neutrino masses goes already somewhat beyond the SM as discussed in section 1.7.1.

The term (1.104) couples the left-handed and right-handed components of the up quark field and provides a mass term. However, the term remains gauge invariant also if we replace Q_L with the corresponding doublet of the second or third generation or if we replace ψ^u_R with ψ^c_R or ψ^t_R – the right-handed spinors of the charm and top quarks. Assuming that all possible combinations

are a priori present in the Lagrangian, one can make a suitable unitary transformation, [7]

$$\begin{pmatrix} \psi_L^u \\ \psi_L^c \\ \psi_L^t \end{pmatrix} \rightarrow U_u \begin{pmatrix} \psi_L^u \\ \psi_L^c \\ \psi_L^t \end{pmatrix} \quad \text{and} \quad \begin{pmatrix} \psi_L^d \\ \psi_L^s \\ \psi_L^b \end{pmatrix} \rightarrow U_d \begin{pmatrix} \psi_L^d \\ \psi_L^s \\ \psi_L^b \end{pmatrix}, \tag{1.105}$$

(and corresponding transformations on the right-handed fields involving corresponding unitary matrices W_u and W_d) in flavor space to bring the mass terms on diagonal form, i.e. with couplings only between left-handed and right-handed fields of the same flavor. In all the previously described Lagrangian terms coupling up-type to up-type or down-type to down-type fermions, such a transformation makes no difference because each unitary matrix such as U_u comes together in a product with its Hermitian conjugate and gives just the unit matrix. The situation is different for the charged current weak interaction, where up-type left-handed fields couple to down-type left-handed fields. Here, the Lagrangian term will after the transformation contain a factor $U_u^\dagger U_d \equiv V$ – the CKM matrix. The vertex factor corresponding to (1.89) for the coupling of the up-type quark of generation k to the down-type quark of generation l is therefore

$$\frac{-iV_{kl}g\gamma^\mu}{2\sqrt{2}}\left(1-\gamma_5\right). \tag{1.106}$$

The magnitudes $|V_{kl}|$ of the CKM matrix elements are close to unity on the diagonal ($k = l$), about 0.23 for coupling between the first and second generation, about 0.04 for coupling between the second and third generations, and smaller than 0.01 for coupling between the first and third generations [1].

Experimental status

After the discovery of the Higgs-like resonance with a mass of $125\,\mathrm{GeV}$, measurements have been performed to test the compatibility of the observed particle with being the (SM) Higgs boson. In particular, the spin-0 nature of the boson has been confirmed [18], and the amount of observed signal is in agreement with SM predictions both in the diphoton [19], four lepton [20], and two leptons plus missing transverse energy [21] final states. The amount of observed signal in the various channels probes indirectly the Higgs boson's couplings to top quarks, Z bosons, and W bosons, as the dominant production mechanisms and the relevant branching fractions are sensitive to these couplings because they are described by the Feynman diagrams shown in fig. 1.10.

Recently, the direct coupling of the Higgs boson to leptons has been confirmed in final states with two tau leptons [22]. The Higgs boson decay to a muon pair is so far not observed [23], which is consistent with SM expectations. The vector boson fusion production process (fig. 1.10(b)) is observed at a significance level of about 3σ [21, 24].

Further tests of the SM predictions for the Higgs sector will certainly be an important part of the LHC physics program throughout the lifetime of the experiments. Precision Higgs measurements are also a motivation for a possible future linear electron-positron collider [25], which could act as a "Higgs factory" with very clean final states.

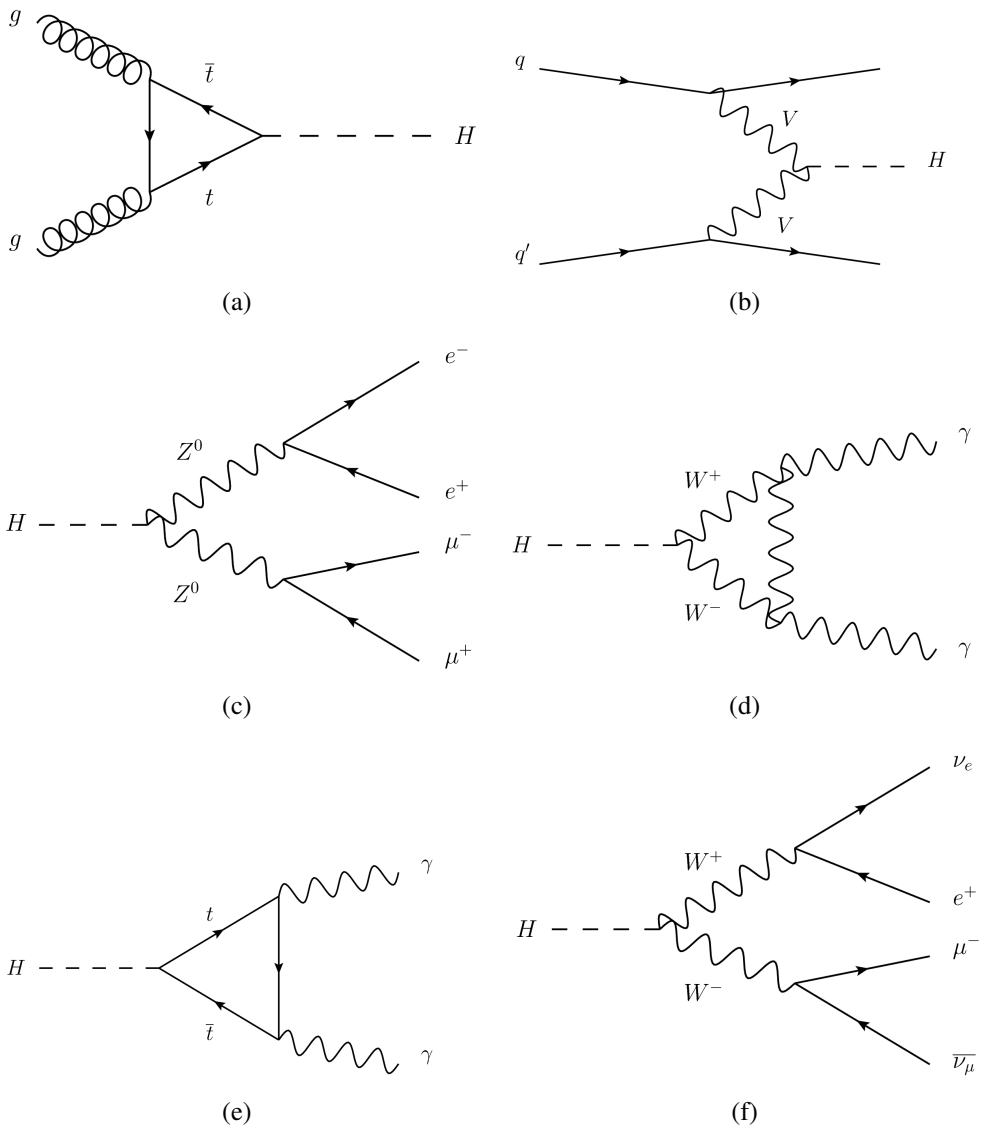

Figure 1.10: Feynman diagrams for Higgs boson production in proton-proton collisions via gluon-gluon (a) and vector boson (b) fusion, and for the decay of the Higgs boson to four charged leptons (c), two photons ((d) and (e)), and two charged leptons and two neutrinos (f). The gluon-gluon fusion (a) is the dominant production mode. The vector bosons V that annihilate to the Higgs boson in (b) may be a W^+W^- pair or a pair of Z^0 bosons. In the diagrams for decays to leptons, only example flavor combinations are shown.

1.4 Summary of the Standard Model interactions

The SM describes the strong, weak, and electromagnetic interactions. The strong interaction is related to the $\mathrm{SU}(3)_{\mathrm{C}}$ transformation in color space. The weak and electromagnetic interactions are entangled, and they are related to the $\mathrm{SU}(2)_{\mathrm{L}}$ transformation acting on the weak isospin doublets of left-handed quarks and leptons, and the $\mathrm{U}(1)_Y$ transformation related to weak hypercharge. Still, one does in general consider the electromagnetic and weak interactions as two separate forces. While the coupling constants g and g' are related via the weak mixing angle – a measurable parameter – a true unification of the electromagnetic and weak forces would require a description in terms of only one coupling constant, which is not the case in the electroweak theory.

The SM is often summarized symbolically as $\mathrm{SU}(3)_{\mathrm{C}} \times \mathrm{SU}(2)_{\mathrm{L}} \times \mathrm{U}(1)_Y$, referring to the gauge symmetries related to color, weak isospin, and weak hypercharge respectively.

1.5 Higher order corrections and renormalization

From the above sections, it would seem that an in principle straightforward procedure for the calculation of any cross section, to any desired accuracy, is to draw the Feynman diagrams corresponding to the process under consideration, and simply follow the Feynman rules for all Feynman diagrams up to the order dictated by the desired accuracy. This is not really the case, because once we go beyond the leading order in the S-matrix expansion (1.40), loop diagrams are encountered. As the Feynman rules state that each four-momentum which is not fixed by four-momentum conservation must be integrated over, these diagrams lead to divergent integrals, and finite results to be compared with experiment can only be obtained after some *renormalization* of the theory. Renormalization is a vast subject, and will here only be briefly touched upon.

When drawing the higher order Feynman diagrams of a given process, some of them can be obtained from the leading order diagrams by replacing propagators or vertices with modified counterparts (see explicit examples for QED in fig. 1.11), for example replacing a simple photon propagator with a photon propagator which includes a fermion loop. The net effect of this is the replacement of the free particle propagators with the corresponding propagators in the interacting theory, and the replacement of the lowest order vertex function (basically just a γ-matrix in QED) with one that includes higher order corrections. As suggested in fig. 1.11 the mathematical expressions corresponding to the higher order correction diagrams are added to the leading order propagators and vertex functions – they are corrections which are of order α (the fine structure constant of the theory under study) relative to the leading order propagators and vertex functions. However, the correction diagrams to propagators and vertex functions are typically divergent. For example, the fermion self-energy diagram (fig. 1.11(a)) contains the photon four-momentum k which is not fixed by four-momentum conservation, and must therefore be integrated over. Higher order diagrams which are not obtained from the leading order diagrams by replacing propagators or vertices with modified counterparts, are finite and well defined [5].

Renormalization can be performed in three steps. First, identify some quantities (couplings, fields, and masses) in the Lagrangian under study as "bare" (non-interacting, classical) quan-

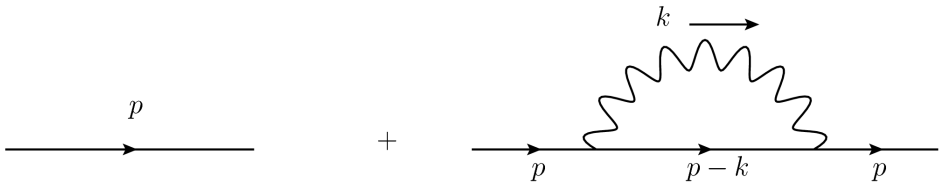

(a) Lowest order fermion propagator correction in QED.

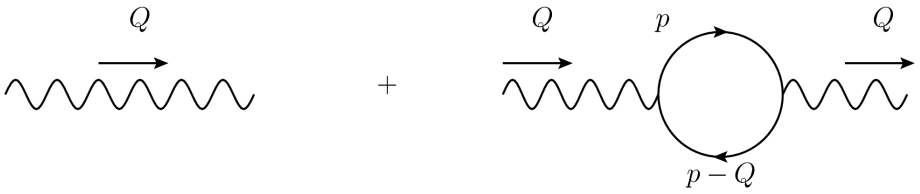

(b) Lowest order photon propagator correction in QED.

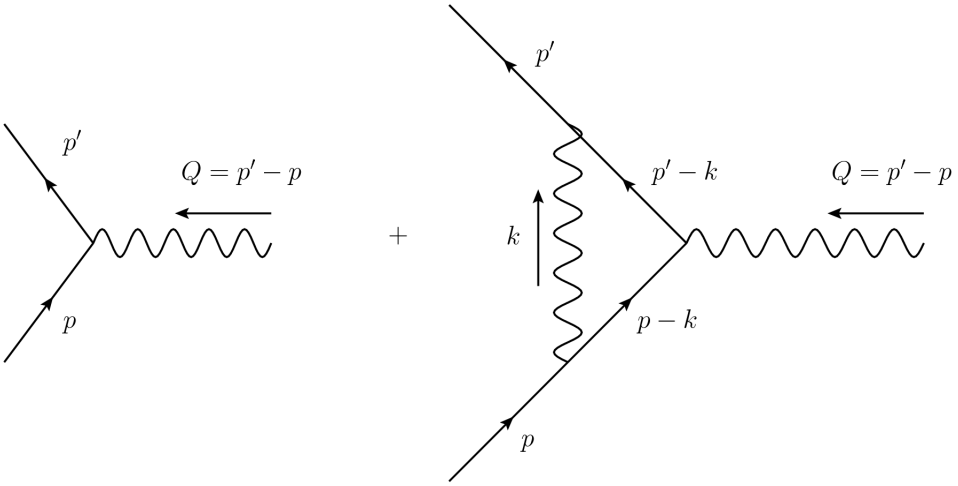

(c) Lowest order vertex correction in QED.

Figure 1.11: The lowest order corrections to the fermion propagator (a), the photon propagator (b), and vertex function (c) in QED. The plus signs indicate that the mathematical expressions corresponding to the correction diagrams on the right hand side are added to the free propagators and vertex function.

tities and rewrite the Lagrangian as function of the physical (interacting) quantities. A set of *counter-terms* can then be identified, which depend on a set of *renormalization constants*. These terms can be considered as interactions, and must be included when calculating propagator and vertex corrections. The second step is to *regularize* the divergent integrals, i.e. parametrize the divergence in such a way that a finite result is obtained for some values of a regularization parameter, while the original divergent integral is restored in some limit of this parameter. Finally, the renormalization constants are determined by imposing a set of *renormalization conditions*, for example that the pole of a particle's propagator should appear at that particle's physical (measured) mass. The procedure is best illustrated by an example, and we will now sketch the renormalization of QED.

1.5.1 Outline of the renormalization of QED

We identify the QED Lagrangian (1.51) as the "bare" Lagrangian

$$\mathcal{L} = \overline{\psi}_0 \left(i\gamma^\mu \partial_\mu - m_0\right) \psi_0 - \frac{1}{4} F_{0,\mu\nu} F_0^{\mu\nu} - q_0 \overline{\psi}_0 \gamma^\mu \psi_0 A_{0,\mu} \tag{1.107}$$

where m_0 is the bare fermion mass, q_0 is the bare fermion charge, ψ_0 is the bare fermion field, A_0^μ is the bare photon field, and

$$F_0^{\mu\nu} = \partial^\nu A_0^\mu - \partial^\mu A_0^\nu. \tag{1.108}$$

The renormalization constants Z_i are defined by the relations

$$\psi_0 = \sqrt{Z_2}\psi, \quad A_0^\mu = \sqrt{Z_3} A^\mu, \quad Z_2 m_0 = Z_0 m, \quad \text{and} \quad Z_2 \sqrt{Z_3} q_0 = Z_1 q, \tag{1.109}$$

where ψ, A^μ, m, and q are renormalized (physical) quantities. Using these relations, we can rewrite the QED Lagrangian on the form

$$\begin{aligned} \mathcal{L} = {} & \overline{\psi} \left(i\gamma^\mu \partial_\mu - m\right) \psi - \frac{1}{4} F_{\mu\nu} F^{\mu\nu} - q \overline{\psi} \gamma^\mu \psi A_\mu \\ & + (Z_2 - 1) \overline{\psi} i \gamma^\mu \partial_\mu \psi - (Z_0 - 1) m \overline{\psi} \psi - \frac{1}{4} (Z_3 - 1) F_{\mu\nu} F^{\mu\nu} - (Z_1 - 1) q \overline{\psi} \gamma^\mu \psi A_\mu, \end{aligned} \tag{1.110}$$

where the terms on the second line are taken as part of the interaction Lagrangian and referred to as counter-terms. The first line is just the ordinary QED Lagrangian written in terms of physical quantities. We note that the definitions (1.109) lead to a simple structure for the counter-terms, where each term depends on only one renormalization constant.

Interpreting the counter-terms as interactions, we see that these give rise to Feynman diagram vertices where the fermion couples to itself (strength determined by Z_0 and Z_2) and the photon couples to itself (strength determined by Z_3), as well as an additional fermion-photon coupling vertex of the same form as the original one (strength determined by Z_1). The photon self-coupling gives an extra term in the photon propagator calculation, as illustrated in fig. 1.12. This term can be made to cancel the divergence in the fermion loop diagram by assigning a divergent value to Z_3. It is not a problem that Z_3 is divergent, as it represents an unobservable relation between the bare and physical photon field. In a similar manner, the fermion propagator

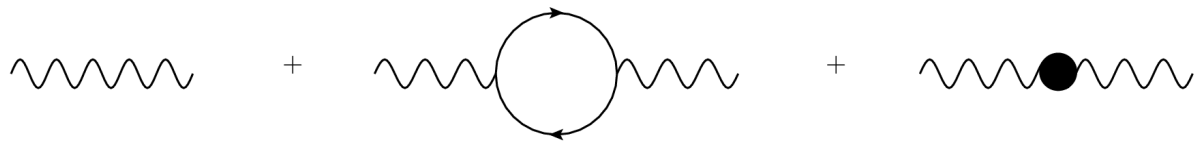

Figure 1.12: The leading order corrections to the photon propagator, including the correction from the counter-term which depends on the renormalization constant Z_3.

receives counter-term corrections depending on Z_0 and Z_2, while the vertex function receives a correction depending on Z_1.

To explain how the renormalization constants are finally determined, we must give the expressions for the interacting fermion propagator[21] [7]

$$S(\not{p}) = \frac{1}{\not{p} - m - \Sigma(\not{p})}\,, \tag{1.111}$$

the interacting photon propagator [7]

$$D_{\mu\nu}(Q) = \frac{-g_{\mu\nu}}{Q^2\left[1 - \Pi(Q^2)\right]}\,, \tag{1.112}$$

and the interacting vertex function [7]

$$\Gamma^\mu(p', p) = \gamma^\mu F_1(Q^2) + \frac{i\sigma^{\mu\nu}Q_\nu}{2m}F_2(Q^2), \quad (Q = p' - p), \tag{1.113}$$

where $\sigma^{\mu\nu} = (i/2)[\gamma^\mu, \gamma^\nu]$. In these expressions, the functions $\Sigma(\not{p})$, $\Pi(Q^2)$, $F_1(Q^2)$, and $F_2(Q^2)$ are calculated from the Feynman diagrams in fig. 1.11 and corresponding counter-term diagrams. In eq. (1.113), the first term is related to the electric charge of the fermion, and the second term is related to its magnetic moment.

Finally, we have a set of renormalization conditions, given below [7].

- The pole of the fermion propagator must be at the physical fermion mass, i.e. $\Sigma(m) = 0$.
- The fermion propagator should have the form $1/(\not{p} - m)$ in the immediate vicinity of the pole $p^2 = m^2$. This fixes the derivative $\Sigma'(\not{p}) = d\Sigma(\not{p})/d\not{p}$, i.e. $\Sigma'(m) = 0$.
- The photon propagator should have the form $-g_{\mu\nu}/Q^2$ close to $Q^2 = 0$, i.e. $\Pi(0) = 0$.
- Finally, we must fix the vertex function so that the fermion electric charge measured in a low energy experiment is the physical charge q, giving the condition $\Gamma^\mu(Q = 0) = \gamma^\mu$.

These conditions fix the values of the renormalization constants in terms of some regularization parameter. Finally, taking the limit of the regularization parameter that restores the original

[21] Some conventional notation is here used. First of all, the slash notation means a contraction between a four-vector and the γ-matrices, $\not{p} = \gamma^\mu p_\mu$. Furthermore, fractions with γ-matrices in the denominator can be interpreted properly by multiplying a suitable (common) factor in both the numerator and the denominator. For example, $\frac{1}{\not{p}-m} = \frac{\not{p}+m}{p^2-m^2}$ because $\not{p}^2 = p^2$.

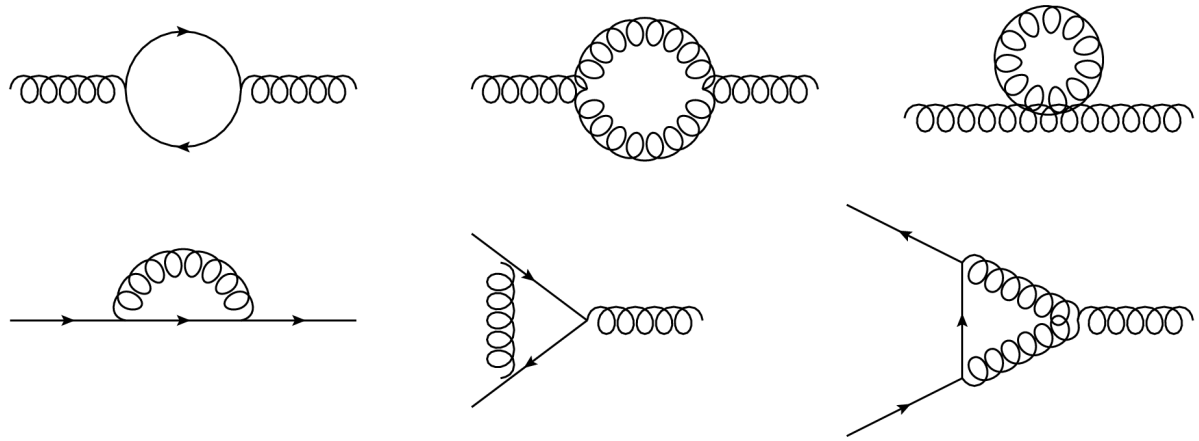

Figure 1.13: Some propagator and vertex corrections in QCD.

divergent integrals causes divergence in the renormalization constants, but not in any observable quantities.

1.5.2 Running coupling constants

Although one of the renormalization conditions in the renormalization of QED forced the function $\Pi(Q^2)$ in the photon propagator (1.112) to be zero for $Q^2 = 0$, the function changes the propagator for $Q^2 \neq 0$. Since the photon propagator is always connected to a fermion at both ends, calculations involve the quantity

$$q^2 D_{\mu\nu}(Q) = \frac{-q^2 g_{\mu\nu}}{Q^2 \left[1 - \Pi(Q^2)\right]}. \tag{1.114}$$

Thus, the effect of the higher order corrections to the photon propagator can be taken into account by swapping the electric charge of the fermion with an effective electric charge, $q_{\text{eff}}(Q^2)$, where

$$q^2_{\text{eff}}(Q^2) = \frac{q^2}{1 - \Pi(Q^2)}. \tag{1.115}$$

In terms of the fine structure constant[22] $\alpha = q^2/(4\pi)$,

$$\alpha_{\text{eff}}(Q^2) = \frac{\alpha}{1 - \Pi(Q^2)}. \tag{1.116}$$

This is an example of a running coupling constant. It is often explained qualitatively as the effect of virtual fermion-antifermion pairs in the vacuum around the fermion shielding its electric charge as seen from a distance. Thus, the electric charge seen at small distances (high energies) is larger than the one seen from large distances (low energies).

Within the context of the Callan-Symanzik equation (see ref. [7], chapter 12), the running of the coupling constant λ in any theory as function of the energy scale μ, is described in terms

[22]For QED, the fermions considered are usually only the electron and the muon, so $|q| = e$ with e as the elementary charge.

of the β-function

$$\beta = \mu \frac{d\lambda}{d\mu}. \tag{1.117}$$

This function is calculable in terms of the renormalization constants of the theory, i.e. it can be calculated from the correction diagrams to propagators and vertices. In QED, the β-function can, due to a particular cancellation, be calculated from the vacuum polarization diagram shown in fig. 1.12 only. To find the β-function in QCD, both propagator and vertex correction diagrams must be considered, some of which are shown in fig. 1.13. The result is [7]

$$\beta_{\mathrm{QCD}} = -\frac{g_{\mathrm{s}}^3}{(4\pi)^2}\left(\frac{11}{3}N_{\mathrm{C}} - \frac{2}{3}N_{\mathrm{f}}\right) \tag{1.118}$$

where g_{s} is the strong coupling constant, $N_{\mathrm{C}} = 3$ is the number of colors, and N_{f} is the number of quark species (flavors). This β-function is *negative*, which means that the coupling constant decreases as the energy scale increases. For sufficiently high energies, then, the quarks behave as free particles – a phenomenon known as *asymptotic freedom*. An important consequence of the negative β-function, is that QCD can be described perturbatively at high energies.

At low energies, the strong force behaves in a very different manner. Quarks are *confined* in bound states (baryons and mesons), and cannot be separated. One can imagine trying to pull the quark and antiquark in a meson apart, but at some point one will have supplied enough energy to create a quark-antiquark pair from the vacuum. The result is then two mesons, not two free quarks. Strongly interacting elementary particles (quarks and gluons) are never observed as free particles.

1.5.3 Unstable particles

As a final remark on higher order corrections, we consider schematically how the propagator of a particle of mass M is changed as a result of higher order corrections,

$$\frac{1}{p^2 - M^2} \quad \rightarrow \quad \frac{1}{p^2 - M^2 - \Sigma(p^2)}. \tag{1.119}$$

Assume that the correction $\Sigma(p^2)$ is calculated from a loop diagram as illustrated in fig. 1.14(a), and that the particle running in the loop has mass m. If $p^2 > (2m)^2$, then $\Sigma(p^2)$ gets a non-zero imaginary part. The cross section for s-channel[23] production and decay of the particle of mass M has exactly the form of a relativistic Breit-Wigner distribution,

$$\sigma \propto \left|\frac{1}{p^2 - M^2 + iM\Gamma}\right|^2, \tag{1.120}$$

whenever $\mathrm{Im}\,\Sigma(p^2) \approx \mathrm{Im}\,\Sigma(M^2)$ over the full resonance peak of the particle [7], i.e. if the resonance is not too wide. The width Γ of the particle is related to the imaginary part of the correction Σ, while the real part of Σ is a mass shift (the position of the pole is fixed to be at the

[23]The term s-channel refers to a Feynman diagram configuration such as the one shown in fig. 1.15, where the horizontal propagator carries a four-momentum equal to the sum of the four-momenta of the initial state (or final state) particles.

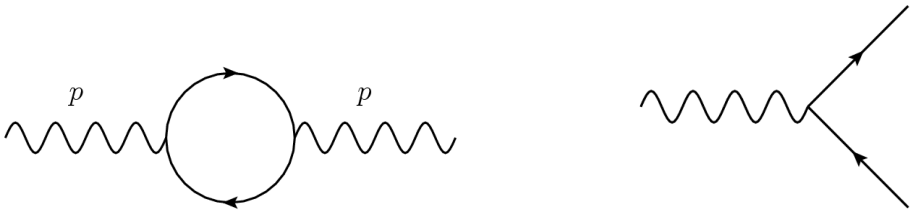

(a) A loop diagram correction to a propagator.

(b) The decay diagram obtained by cutting the loop diagram (a) in half.

Figure 1.14: The imaginary part of a loop diagram correction (a) to the propagator of a particle is closely related to the corresponding decay diagram (b) for that particle obtained by cutting the loop diagram in half.

physical mass by the renormalization condition $\mathrm{Re}\,\Sigma(M^2) = 0$).

The Heisenberg uncertainty principle for energy and time, $\Delta E\,\Delta t \geq 1/2$, can be used to argue that there should be a relation between a particle's width (thought of as ΔE) and its lifetime (thought of as Δt). Indeed such a relation exists. The imaginary part of the loop diagram in fig. 1.14(a) is closely related to the decay diagram in fig. 1.14(b) (see ref. [7], section 7.3). In the actual calculation of the width of a particle, the particle's decay diagrams are considered.

1.6 Proton-proton collisions

As the SM assigns a well defined set of interactions to the quarks and gluons, we know in principle how to calculate cross sections for collisions between free quarks and gluons, and we know in principle how to calculate cross sections involving free quarks and gluons as final state particles. It would, however, seem that we could never relate such calculations to experimental results, as free quarks and gluons do not exist in nature. Strongly interacting particles are confined by the strong force.

There is, however, a modification to this grim picture. As QCD is an asymptotically free theory, quarks and gluons are essentially free particles over the time scale of a scattering with large momentum transfer, i.e. a *hard scattering*. When colliding hadrons, such as protons, we do indeed observe such hard scatterings between quarks and gluons, and the quarks and gluons do indeed appear to act essentially as free particles in such scatterings. The quarks going into the hard scattering in a proton-proton (pp) collision are not only up and down quarks (called the *valence quarks* of the proton). Since the gluons mediating the strong force between the valence quarks can split into quark-antiquark pairs, other quark species may enter as well, and they are referred to as *sea quarks*.

Furthermore, we can "almost" observe final state quarks and gluons experimentally. They give rise to collimated "squirts" of hadrons, known as jets. Individual jets can to some extent be identified with individual "final state" quarks and gluons from hard scatterings. Even if that picture may be a bit too simple, it is at least possible to evolve theoretically "final state" quarks and gluons from a hard scattering into a set of observable final state particles by e.g. the *parton shower* and the subsequent *hadronization*.

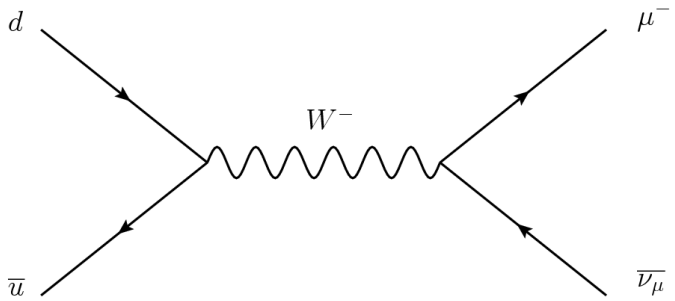

Figure 1.15: A lowest order Feynman diagram for the production of a muon-neutrino pair in a pp collision. The Feynman diagram depicts only the hard scattering, i.e. it enters in the calculation of the hard scattering cross section.

The idea of the hard scattering between individual partons (quarks and gluons) allows the *factorization* of the cross section for the production of high transverse momentum (w.r.t. the beam line) final state particles in pp collisions. For example, the cross section for the production of a high mass muon-neutrino pair in a symmetric pp collision, takes the form [7]

$$\sigma(p\,p \to \mu^-\,\overline{\nu_\mu} + X) = \int_0^1 dx_1 \int_0^1 dx_2 \sum_{q,q'} f_q(x_1) f_{q'}(x_2)\,\hat{\sigma}[q(x_1P)\,q'(x_2P) \to \mu^-\,\overline{\nu_\mu}]. \tag{1.121}$$

Here, $\hat{\sigma}[q(x_1P)\,q'(x_2P) \to \mu^-\,\overline{\nu_\mu}]$ is the hard scattering cross section, calculable at lowest order from Feynman diagrams such as the one shown in fig. 1.15 as if the initial state quarks were free particles. The quarks have momenta x_1P and x_2P (in opposite directions) along the beam line where P is the proton momentum, i.e. x is the fraction of the proton momentum carried by the constituent going into the hard scattering. The Parton Distribution Function (PDF) $f_i(x)$ gives the probability that a parton of species i goes into the hard scattering with momentum fraction x. The sums run over all quark species, i.e. $q, q' = u, \overline{u}, d, \overline{d}, ...$ In general, the sums must run also over the gluon, but terms with gluons as initial state particles do not contribute to this process at the lowest order. The dominating terms in this particular case are $(q, q') = (\overline{u}, d)$ and $(q, q') = (d, \overline{u})$. The term $(q, q') = (\overline{c}, s)$ is smaller because both quarks are necessarily sea quarks, while the term $(q, q') = (\overline{c}, d)$ is smaller because $\overline{c}$ is a sea quark and the off-diagonal CKM matrix element corresponding to the coupling between $\overline{c}$ and d is small.

A qualitative picture of the complete process $p\,p \to \mu^-\,\overline{\nu_\mu} + X$ via the hard scattering $\overline{u}\,d \to \mu^-\,\overline{\nu_\mu}$ is shown in fig. 1.16. In this picture we see how the antiquark going into the hard scattering emerges from the splitting of a gluon emitted from one of the "original" quarks in the proton. In the picture, this gluon is emitted from the up quark, but it could of course equally well have been emitted from one of the down quarks. The "spectator quarks" that do not go into the hard scattering give rise to hadrons (included in the "$+X$") in the final state.

The PDF $f_i(x)$ does in fact also have a slow dependence on the momentum transfer Q in the hard scattering, so one may write $f_i(x, Q)$ instead of just $f_i(x)$. While the PDFs cannot themselves be calculated from first principles – they need to be experimentally determined – one can evolve the PDFs between different momentum transfers Q from first principles. This evolution is described by the Altarelli-Parisi (or DGLAP) equations [7]. Qualitatively, one can say that these equations tell us how e.g. a gluon on one energy scale can be split into a quark-antiquark pair when viewed at a larger energy scale (corresponding to finer spatial resolution). The PDF evolution is governed by the *splitting functions* corresponding to the three vertices shown in fig. 1.17. Fig. 1.18 shows a particular set of PDFs at two different energy scales. It

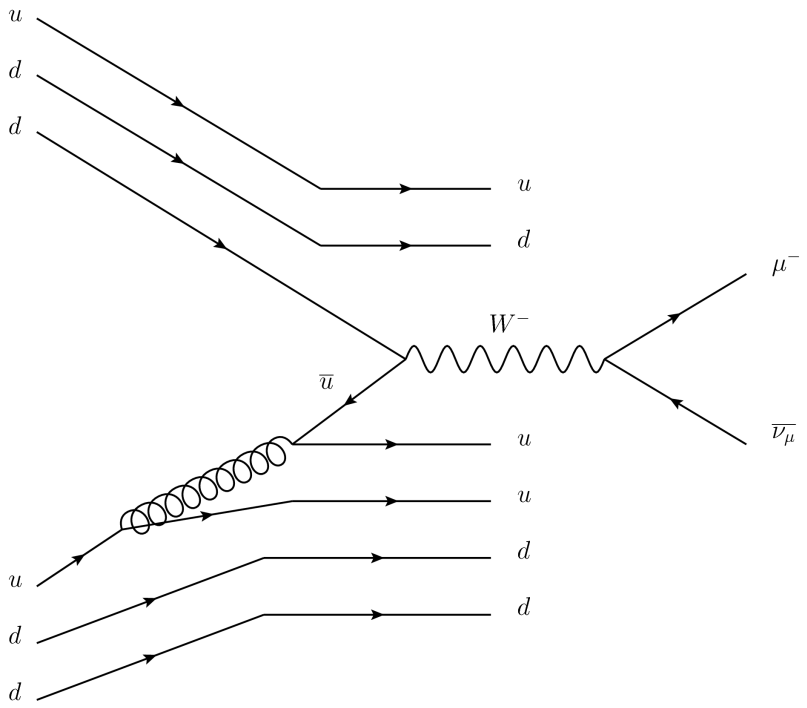

Figure 1.16: A qualitative picture of the complete process $p\ p \rightarrow \mu^-\ \overline{\nu_\mu} + X$ via the hard scattering $\overline{u}\, d \rightarrow \mu^-\ \overline{\nu_\mu}$. The "spectator quarks" that do not go into the hard scattering give rise to hadrons (included in the "$+X$") in the final state.

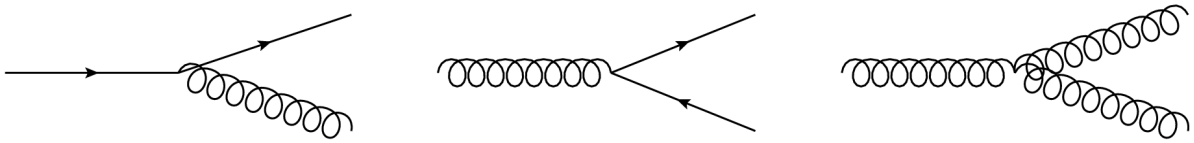

Figure 1.17: The Feynman diagram vertices corresponding to the splitting functions in QCD. The splitting functions are used to derive the evolution of the parton distribution functions (PDFs) from one energy scale to another.

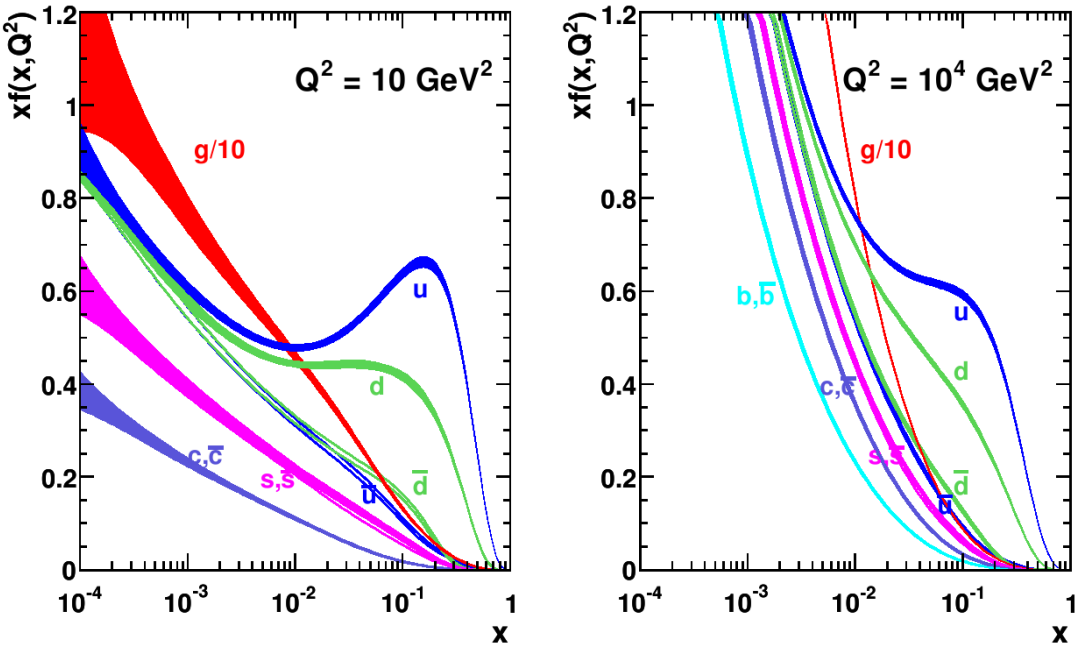

Figure 1.18: Plots of a PDF set (MSTW 2008, NLO) at $Q^2 = 10\,\mathrm{GeV}^2$ and $Q^2 = 10^4\,\mathrm{GeV}^2$, from ref. [26]. The values of the PDFs at low momentum fractions x increase as the energy scale increases. It is not the parton density $f(x)$ itself which is plotted, but rather the product $xf(x)$.

can be seen in this plot that the values of the PDFs at low momentum fractions x increase as the energy scale increases. This can be qualitatively understood as more partons being seen at a higher energy (finer spatial resolution), and therefore each of the partons carry less momentum.

1.6.1 Parton shower, hadronization, and underlying event

The "final state" quarks and gluons from the hard scattering must be evolved into a set of observable final state hadrons. This is usually done by the *parton shower* and subsequent *hadronization*. Note that the parton shower may also be applied to the initial state quarks and gluons to generate initial state radiation of jets. For a detailed description of both parton showers, hadronization, and underlying event (as implemented in PYTHIA 6), see ref. [27].

The parton shower is based on the splittings of one particle into two. The evolution from a quark or gluon from the hard scattering into a set of observable final state hadrons is governed by the splittings shown in fig. 1.17. The parton shower approach is good for soft and collinear emissions in particular. The evolution from a quark or gluon to a corresponding jet is therefore well described by this model. However, if the quark or gluon were to radiate a hard quark or gluon, giving rise to another jet well separated from the one corresponding to the original quark or gluon, such emissions are not expected to be well described by the parton shower. The parton shower should do well in describing the structure within a jet, but not in describing an event topology with several energetic and well separated jets.

Hadronization turns a set of quarks and gluons into a set of colorless hadrons. Since this

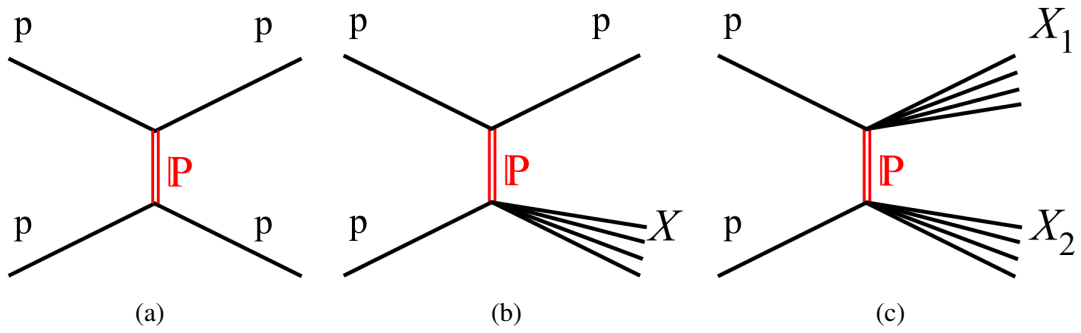

Figure 1.19: Illustrations of elastic (a), single diffractive (b), and double diffractive (c) pp scattering via the exchange of a color singlet object called a Pomeron. From ref. [28].

happens in the low energy regime, the strong coupling is large, and perturbation theory is not applicable. Indeed, hadronization models are not constructed from first principles – they are phenomenological.

For a complete description of a pp event, the *underlying event* must also be simulated. The partons going into the hard scattering leave behind proton remnants which are not colorless, and therefore color connected to the hard scattering process. Multiple interactions, in general much softer than the hard scattering, may also occur between the proton constituents that do not go into the hard scattering. Although the resulting final state particles are in general soft compared to the final state particles from the hard scattering, the underlying event may make a non-negligible contribution to missing transverse energy (see section 2.3.6) or lepton isolation energies used to distinguish prompt leptons from those associated with jet activity.

Finally, the event topology at the LHC may receive additional contributions from non-perturbative interactions between the other protons in the colliding bunches. These interactions include elastic and diffractive scattering (see fig. 1.19). They are of the most common kinds (with the highest cross sections), since the recording of the event is triggered by the particles resulting from the hard scattering. These are the same kinds of interactions that are observed in "minimum bias" events, where an event is recorded at the time of a bunch crossing without requiring any particles to trigger the recording, or with only a very loose trigger selection. Again, the final state particles resulting from these additional interactions are in general soft compared to the final state particles from the hard scattering, but may contribute significantly to missing transverse energy and lepton isolation energies.

1.7 Beyond the Standard Model

The SM has been extremely successful in its description of more or less all experimental data within its domain to date. For example, the *anomalous magnetic moment* of the electron shows agreement between theory and experiment to an accuracy of order one part in a billion [29]. There are, however, reasons to believe that there is physics "beyond" the SM, i.e. that measurements will at some energy scale start to deviate from the SM predictions. The most obvious reason for such a claim, is that gravity is not included in the SM. At some energy scale, gravitational interactions between the elementary particles will become important, and the SM will no longer be able to correctly describe nature. This must happen at the latest when the Compton

wavelength of a black hole becomes of the same order as its Schwarzschild radius, since this means that quantum mechanical and gravitational effects are observed at the same length scale. The corresponding energy scale is the *Planck scale*, of order $10^{19}\,\mathrm{GeV}$.

1.7.1 Neutrino masses

We saw in section 1.3.3 that the right-handed neutrino does not participate in any SM interaction. As long as neutrinos are massless, there is thus no reason to include it in the model at all. If neutrinos are massive, though, then the Dirac mass term necessitates the inclusion of the right-handed neutrino. Observations of neutrino oscillations – oscillations between the different neutrino flavors – are interpreted as meaning that the neutrinos do indeed have some small masses. Neutrino oscillations can then be explained by assuming that the flavor eigenstates are not the same as the mass eigenstates. Since the mass eigenstates are the eigenstates of the Hamiltonian, oscillations can then occur between the flavor eigenstates.

The first hint of neutrino oscillations came from observation of the neutrino flux from the Sun. The observed flux was smaller than that expected from the theoretical model of the Sun [30]. Solar neutrinos are electron neutrinos, primarily from the fusion of two protons into a deuterium nucleus, involving the conversion of a proton into a neutron. Further evidence that the observed deficit was due to oscillations came from the fact that the disappearance of electron neutrinos was apparently accompanied by an appearance of other neutrino flavors, as measured through neutral current interactions [31]. The total neutrino flux was as expected from the theoretical model of the Sun.

Striking evidence of oscillations has also been seen in the angular distribution of upward going atmospheric neutrinos, where the angle can be related to the distance traveled through the Earth by the neutrinos, over which they have had time to oscillate [32]. Atmospheric neutrinos are primarily muon neutrinos as they are produced, because charged pions decay almost exclusively to a muon and a muon neutrino. This is related to the 100% parity violation in charged current weak interactions.

Since neutrinos are apparently massive, the right-handed neutrino spinor must be included in the SM. It seems unsatisfactory to have a state in the theory that does not enter any of the interactions, and this strongly suggests some extension of the SM that allows the right-handed neutrino component to take part in interactions. The neutrinos are the only electrically neutral fermions in the SM, and could in principle be of Majorana nature, meaning that the neutrino could be its own antiparticle.

1.7.2 Dark matter and dark energy

Matter consisting of ordinary atoms is believed to account for only about 5% of the energy in the universe. The rest is accounted for by dark matter (27%) and dark energy (68%). Dark matter is required to explain the rotation of galaxies around their centers (i.e. the orbital velocities of stars around each galaxy's center). The amount of luminous matter does not alone account for the observed orbital velocity of stars as function of their distance to the center of the galaxy. Dark matter has also been observed in a more direct manner by gravitational lensing. In a collision between two galaxy clusters, it is observed that luminous matter has been slowed down due to

its electromagnetic interaction and accumulated in some region of space, while the gravitational lensing data suggest that most of the matter is actually outside this region [33]. This is explained by the fact that dark matter does not have electromagnetic interactions, so it is not slowed down in the collision.

Dark energy is needed to account for the observed acceleration of the expansion of the universe. Mathematically it is described very well in terms of the *cosmological constant* introduced by Einstein in order for him to be able to construct static universe models [34].

Neither dark matter nor dark energy is explained by the SM. The only candidates for dark matter within the SM would be the neutrinos, since these interact only through the weak interaction. The SM neutrinos are, however, ruled out as dark matter candidates [35] because they are so light.

One theory beyond the SM which can potentially shed some light on the nature of dark matter is *supersymmetry*. In this theory, a symmetry between fermions and bosons exists, and there is a supersymmetric boson partner to each SM fermion and a supersymmetric fermion partner to each SM boson. If so-called R-parity, a quantum number which is $+1$ for SM particles and -1 for their supersymmetric partners, is conserved, then a supersymmetric particle cannot decay to a pair of SM particles, and the lightest supersymmetric particle would in this case be stable. It could then potentially constitute dark matter. Searches for supersymmetry are an important part of the LHC physics program.

1.7.3 Grand unification

It would be theoretically pleasing if it were possible to describe all the forces of nature as different manifestations of the same force, in the same way as the electric and magnetic forces can be seen as different manifestations of the electromagnetic force. A grand unification theory is one that proposes a single gauge symmetry as the source of all the SM interactions, for example $\mathrm{SU}(5)$ [36]. This means that all the SM forces are described in terms of the same coupling constant. The running coupling constants of the SM (see section 1.5.2) should thus become equal at some energy scale where the unification is realized. However, plotting the coupling constants of the SM as function of energy, they do not quite meet [35]. This is often used to argue in favor of supersymmetry, because the inclusion of supersymmetric particles in the calculations of the running couplings allow them to become equal at an energy scale of about $10^{16}\,\mathrm{GeV}$ [35], suggesting that a unification of the SM forces is realized at this scale.

The idea of grand unification is a key motivation for searches for new, heavy gauge bosons. If grand unification is indeed part of nature, then the grand unification symmetry must be broken, so that physics at low energy is well described by the SM. After various symmetry breakings, the SM gauge groups may appear in conjunction with additional symmetry groups, in particular extra $\mathrm{U}(1)$ groups which would lead to new neutral gauge bosons, commonly denoted Z'. This can happen for example in the context of $\mathrm{SO}(10)$ or E_6 grand unification [37, 38]. Current experimental limits on E_6 motivated Z' bosons are 2.5-$2.6\,\mathrm{TeV}$ [39, 40].

1.7.4 The hierarchy problem

In our discussion of renormalization (section 1.5), we mentioned that divergent integrals have to be regularized, so that divergence happens only in a particular limit of some regularization parameter. Depending on the regularization method employed, the regularization parameter may have the dimension of energy. Referring to such a dimensionful regularization parameter as Λ, the original divergent integral would typically be restored in the limit $\Lambda \to \infty$.

While most loop diagrams in the SM diverge logarithmically as $\ln \Lambda$, the corrections to the Higgs mass squared are quadratic in Λ, i.e. the correction to m_H^2 goes as Λ^2 [7]. Whether the divergence in some correction is logarithmic or quadratic should not matter if the cutoff scale is just thought of as a way to parametrize the divergence of the integral, i.e. just as a piece of mathematical trickery. The divergence is in any case removed by renormalization, and the limit $\Lambda \to \infty$ can finally be taken without divergence in any observable quantity.

However, the cutoff scale Λ is usually considered to be more than just a regularization parameter – it is thought of as the energy scale at which the theory being normalized (i.e. the SM in this case) stops being valid, i.e. the scale at which deviations from the model will be observed. One could hope that the SM would be valid up to energies of the order of the grand unification scale or even the Planck scale (at the Planck scale, we know that the theory is no longer valid as gravity cannot be neglected). This means that one would assign Λ values of the order 10^{16}-$10^{19}\,\mathrm{GeV}$. This leads to huge corrections to the Higgs mass. These corrections enter in the (unobservable) relation between the bare Higgs mass and the physical one, and leads to a relation which can be schematically written as

$$m_H^2 = m_{0,H}^2 + O(\Lambda^2) \tag{1.122}$$

with $m_{0,H}$ as the bare Higgs mass and $O(\Lambda^2)$ denoting a correction of order Λ^2. With m_H around $125\,\mathrm{GeV}$, there must be an extremely precise cancellation between $m_{0,H}^2$ and the $O(\Lambda^2)$ correction term. This seems to require an unnatural *fine tuning* of the bare Higgs mass, and the corresponding philosophical quandary is referred to as the *hierarchy problem*.

In supersymmetric models, the quadratic divergence of the squared Higgs mass can be tamed to a logarithmic divergence because of cancellations between the loop diagrams involving standard model particles and those involving the respective supersymmetric partners. For example, the fermion loop diagram of fig. 1.20(a) has a quadratic divergence which could be exactly canceled by the corresponding scalar boson loop diagram of fig. 1.20(b) if the scalar boson running in the loop had a coupling to the Higgs boson related in a particular way to the fermion's coupling. Relating the couplings in such a precise way does not introduce another fine tuning problem because the relation between the couplings could be enforced by a symmetry – supersymmetry [41].

1.7.5 An example of theory beyond the Standard Model: Left-right symmetric models

In constructing the electroweak Lagrangian, one makes an a priori distinction between left- and right-handed fields when one groups the left-handed fields according to $\mathrm{SU}(2)$, but not the right-handed ones. This results in the parity violating nature of the weak interactions, which is

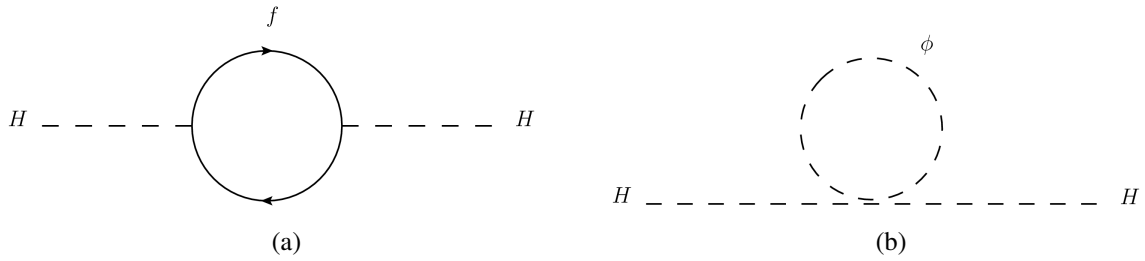

Figure 1.20: Corrections to the Higgs boson propagator from a fermion loop (a) and from a loop with a hypothetical scalar supersymmetric partner ϕ of the fermion (b).

an experimental fact. In left-right symmetric models, one groups also the right-handed fields according to $\mathrm{SU}(2)$, and arrives at a structure such as

$$\mathrm{SU}(2)_\mathrm{R} \times \mathrm{SU}(2)_\mathrm{L} \times \mathrm{U}(1). \tag{1.123}$$

The Lagrangian is required to be invariant under the discrete symmetry operation of interchanging left-handed and right-handed fields. As parity is violated in weak interactions, the left-right symmetry must be broken.

As the gauge group $\mathrm{SU}(2)_\mathrm{L}$ in the SM is associated with gauge bosons $W^\pm$ and Z^0, the gauge group $\mathrm{SU}(2)_\mathrm{R}$ of the left-right symmetric theory is also associated with gauge bosons $W_R^\pm$ and Z'. The new gauge bosons W_R couple only to right-handed currents, in contrast to the regular W-bosons, which couple only to left-handed currents.

The left-right symmery is broken spontaneously analogously to the symmetry breaking in the Standard Electroweak Theory [42]. The Higgs content in left-right symmetric models is more complex than in the SM, and contains charged Higgs bosons. First, the symmetry is broken down to the symmetry of the SM:

$$\mathrm{SU}(2)_\mathrm{R} \times \mathrm{SU}(2)_\mathrm{L} \times \mathrm{U}(1) \quad \rightarrow \quad \mathrm{SU}(2)_\mathrm{L} \times \mathrm{U}(1)_Y. \tag{1.124}$$

In this process, the gauge bosons W_R and Z' obtain masses. Then the SM symmetry is further broken, and the regular gauge bosons W and Z obtain masses. At this point, also the fermions acquire masses.

The $\mathrm{U}(1)$-symmetry in left-right symmetric models is, at least in some cases, related to baryon and lepton number (B and L). The charge formula of the Standard Model,

$$Q = I_3 + \frac{Y}{2} \tag{1.125}$$

is then replaced by

$$Q = I_3^L + I_3^R + \frac{B-L}{2}, \tag{1.126}$$

where the somewhat unintuitive weak hypercharge has been replaced by the familiar baryon and lepton numbers.

Initially, no parity violation is present in left-right symmetric models. Parity violation may only occur after the breaking of the initial left-right symmetry. The requirement of 100% parity violation in weak interactions at the energies so far probed, translates to the right-handed gauge

bosons $W_R^{\pm}$ being much heavier than the left-handed $W^{\pm}$. In this case, W_R does not play an important role at low energies, and parity is violated in this regime. The parity symmetry would in this case be restored at energies of the same order of magnitude as the mass of the W_R. Instead of parity violation being put in "by hand", as in the SM, the parity symmetry is spontaneously broken by the Higgs fields in left-right symmetric models.

A further interesting feature of left-right symmetric models is the seesaw mechanism [43]. In the SM, there is no explanation for the non-vanishing but extremely small neutrino mass. In left-right symmetric models, the breaking of the left-right symmetry gives a large mass to the right-handed neutrino. The breaking of the $\mathrm{SU}(2)_{\mathrm{L}} \times \mathrm{U}(1)_Y$ symmetry relates the masses of the left-handed and right-handed neutrinos in such a way that a heavy right-handed neutrino gives a light left-handed one. The mass of the right-handed neutrino is further related to the mass of the W_R, since these masses are both given by the breaking of the left-right symmetry.

The result of this is that the left-handed neutrino acquires a mass [43]

$$m_{\nu_l} \sim \frac{m_l^2}{m_{W_R}}. \tag{1.127}$$

We see that the maximal parity violation observed in weak interactions at low energies is closely related to the very small neutrino mass. As the mass of the W_R tends to infinity, parity violation becomes maximal and the neutrino mass tends to zero.

1.8 Summary

In this chapter, some particle physics theory has been introduced. We have seen how the elementary matter particles interact through forces mediated by gauge bosons in the gauge theory that is the Standard Model. Furthermore, we have reviewed some shortcomings of the theory, which serve as motivation for new physics searches in general, including the search in the one lepton and missing transverse energy final state which is the subject of this thesis.

While many ideas for physics beyond the Standard Model exist, with different theoretically pleasing features and promises to improve on the shortcomings of the Standard Model, only experiment can reveal which – if any – of these are realized in nature. On the experimental side, the world's leading results are coming from the Large Hadron Collider at CERN. In the next chapter we will describe this machine, as well as the ATLAS detector, which has provided the data analyzed in this thesis.

Chapter 2

The experimental setup at CERN

2.1 Introduction

To study the smallest constituents of nature, we need the finest spatial resolution. When probing a target by scattering some particle (be it a photon, an electron, or something else) off it, the target is resolved with a spatial resolution of the order of the (de Broglie) wavelength of that particle, $\lambda = h/p$. As the wavelength is inversely proportional to the momentum of the particle, it is clear that fine spatial resolution requires particles of high momenta (high energies). The study of the smallest constituents of nature is therefore done to large extent using particle accelerators, whose purpose is to accelerate beams of particles to as high energies as possible. The high energy particles can then be scattered off a target to resolve the target at a spatial resolution as given by the beam particles' energies.

Colliding a beam of high energy particles on a target at rest is in general not optimal for a particle physics experiment, as one would like to study interactions with high invariant masses, allowing the production of heavy particles such as the Z^0 and $W^{\pm}$ bosons, the Higgs boson, or even much heavier particles such as hypothetical new gauge bosons. When colliding beam particles of energies E_1 and E_2 and corresponding momenta $\mathbf{p}_1$ and $\mathbf{p}_2$, the heaviest particle one can possibly produce has a mass m equal to the *invariant mass* of the collision,

$$\sqrt{s} = m = \sqrt{(E_1 + E_2)^2 - (\mathbf{p}_1 + \mathbf{p}_2)^2}. \tag{2.1}$$

This is the total energy in the center of mass (or center of momentum) frame, defined as the reference frame in which the sum of all spatial momenta is zero. To maximize $\sqrt{s}$, it is clear that one would like to have $\mathbf{p}_1 = -\mathbf{p}_2$, so that $\sqrt{s} = E_1 + E_2$, meaning that the laboratory fixed reference frame *is* the center of mass frame. This is achieved by accelerating beams of particles in opposite directions and colliding them head on.

CERN, Conseil Européen pour la Recherche Nucléaire, or the European Organization for Nuclear Research, is an organization for fundamental research with a focus on particle physics in particular. It is a fantastic example of international collaboration, with scientists and engineers from all over the world working together on some of the biggest experiments in the history of physics, with the goal of shedding light on some of the biggest mysteries in fundamental science. The CERN laboratory, located at the border between France and Switzerland, close to the city of Geneva, has housed some of the most important particle colliders used to

gain understanding of the microscopic world of fundamental particles, including the SPS (Super Proton Synchrotron), where the $W^{\pm}$ and Z^0 bosons were discovered[1], and LEP (the Large Electron-positron Collider) where SM physics was studied with great accuracy.

Today, CERN houses the LHC (Large Hadron Collider) which accelerates and collides protons and heavy ions. The LHC is placed underground in a circular tunnel previously used to accomodate LEP. Four main detectors are situated at the interactions points (where the protons or heavy ions are made to collide) around the LHC ring. The CMS (Compact Muon Solenoid) and ATLAS (A Toroidal LHC ApparatuS) are multi-purpose detectors, designed to be able to do a wide variety of physics measurements and searches, including both precision SM measurements, searches for the SM Higgs boson, and searches for physics beyond the SM. The LHCb experiment is designed to do measurements on b-hadrons in particular, in order to shed light on the matter-antimatter asymmetry of the universe. Finally, the ALICE (A Large Ion Collider Experiment) detector is designed specifically to cope with the crowded enviroment of heavy ion collisions and for the study of quark-gluon plasma.

2.2 The Large Hadron Collider

The LHC is a circular accelerator with a circumference of $27\,\mathrm{km}$. While it collides both protons and heavy ions, it is the pp collisions which are relevant to this thesis, and the LHC will mainly be referred to as pp collider. As a pp collider, the LHC design parameters are a center of mass energy $\sqrt{s} = 14\,\mathrm{TeV}$ and a luminosity $L = 1.0 \cdot 10^{34}\,\mathrm{cm}^{-2}\,\mathrm{s}^{-1}$ [44]. The luminosity L essentially measures the collision rate, and given the cross section σ for some process, we find the number of expected events per unit of time from the relation

$$\frac{dN}{dt} = \sigma L. \tag{2.2}$$

The total amount of collisions collected in a given data sample is quantified by the integrated luminosity

$$L_{\mathrm{int}} = \int L\,dt. \tag{2.3}$$

Clearly, eq. (2.2) implies that the total number of expected events is $N = \sigma L_{\mathrm{int}}$ for a process of cross section σ.

The acceleration of the protons in the LHC is achieved when the protons pass through so-called RF (Radio-Frequency) cavities containing oscillating electric fields. The protons are grouped together in bunches, 2808 bunches in total when the machine is filled completely, and the oscillation frequency in the RF cavities is tuned in such a way that each bunch of protons always sees an accelerating (rather than decelerating) field when passing through a cavity. The advantage of using a circular accelerator is that each bunch of protons can be passed through each RF cavity as many times as one would like. The only limitation on the accessible energy, from the acceleration point of view, is then given by the fact that particles in a circular orbit experience a centripetal acceleration, and accelerated charged particles radiate energy in the

[1]For the discovery of the $W^{\pm}$ and Z^0 bosons the SPS was used as a proton-antiproton collider, accelerating protons and antiprotons in opposite directions. The SPS is still in use today, as the final step in the LHC injection chain.

form of electromagnetic radiation (called synchrotron radiation in this context). The maximum accessible energy, from the acceleration point of view, is thus given by the condition that the RF cavities must in each revolution replace the energy the beam particles radiate during one revolution. This limited the accessible energy at LEP to $\sqrt{s} = 209\,\mathrm{GeV}$.

2.2.1 Synchrotron radiation

The power P radiated by an accelerated particle of charge q is given by the relativistic generalization of the Larmor formula[2] [45]:

$$P = \frac{q^2 a_0^2}{6\pi\varepsilon_0 c^3}. \tag{2.4}$$

Here, ε_0 is the vacuum permittivity, c is the speed of light in vacuum, and a_0 is the particle's *proper acceleration*, i.e. the acceleration of the particle as measured in its instantaneous inertial rest frame. For a particle in a circular orbit, we have $a_0 = \gamma^2 a$ [46] with γ as the relativistic γ-factor, $\gamma = 1/\sqrt{1 - v^2/c^2}$, a as the particle's acceleration, and v as its velocity. For a particle in a circular accelerator, we have $a = v^2/r$ with r as the radius of the accelerator, and we find

$$P = \frac{q^2 c(\gamma^2 - 1)^2}{6\pi\varepsilon_0 r^2} \approx \frac{q^2 c\gamma^4}{6\pi\varepsilon_0 r^2} \tag{2.5}$$

where the latter expression is valid for highly relativistic particles, i.e. $\gamma^2 \gg 1$. Finally, we can use the expression for the beam particle's energy E as function of its mass m, $E = \gamma mc^2$, to find

$$P = \frac{q^2 E^4}{6\pi\varepsilon_0 c^7 r^2 m^4}. \tag{2.6}$$

It is clear then why the LHC can reach a much higher energy than LEP did: While the radius is approximately the same for the LHC as for LEP (since the LEP tunnel is used also for the LHC), the mass of the beam particles is almost two thousand times larger for the LHC than for LEP. Since the power loss to synchrotron radiation depends on the ratio E/m, the energy can be made almost two thousand times larger before a similar synchrotron radiation power loss is seen. However, the beam particle energy at the LHC is limited to much lower values than suggested by the electron-proton mass ratio by the strength of the magnetic field needed to keep the protons in orbit (see section 2.2.2).

The energy loss of each beam particle per turn is given by

$$\Delta E = P \times \frac{2\pi r}{c} = \frac{q^2 E^4}{3\varepsilon_0 c^8 r m^4}. \tag{2.7}$$

The LHC is not truely circular – there are both straight sections and bends around the LHC ring. Using the bending radius in the main bends[3], $r = 2.8\,\mathrm{km}$ [44], we find $\Delta E \approx 7\,\mathrm{keV}$ for the

[2]The non-relativistic Larmor formula is given in section 14.2 of ref. [45], and can be converted to ordinary SI units with the conversion rules in the appendix of that book. As argued in section 14.2 of ref. [45], the radiated power is a Lorentz invariant. We can therefore simply replace the acceleration a with the proper acceleration a_0 to get a result valid in any reference frame.

[3]When we use this value for the radius, eq. (2.6) gives the (instantaneous) synchtrotron radiation power in the

protons in the LHC at the design energy $E = 7\,\mathrm{TeV}$. For LEP at the highest energy achieved, we have the beam energy $E = 104.5\,\mathrm{GeV}$ and the bending radius $r = 3.1\,\mathrm{km}$ [47], and we find the synchrotron radiation loss per turn $\Delta E \approx 3\,\mathrm{GeV}$, approximately half a million times larger than for the LHC.

2.2.2 Magnetic field

The protons in the LHC are kept on their circular orbit by the magnetic field from dipole magnets. Consider a particle of charge q moving in the plane perpendicular to a homogeneous magnetic field of magnetic flux density $\mathbf{B}$. The relativistic equation of motion is

$$\frac{d\mathbf{p}}{dt} = \mathbf{F} = q\mathbf{v} \times \mathbf{B} \tag{2.8}$$

where the relativistic momentum is $\mathbf{p} = \gamma m\mathbf{v}$. Since the force $\mathbf{F}$ is at all times perpendicular to the velocity $\mathbf{v}$, no work is done, and the particle's energy $E = \gamma mc^2$ remains constant, i.e. γ is constant. Hence,

$$\frac{d\mathbf{p}}{dt} = \gamma m\mathbf{a}, \tag{2.9}$$

and taking the magnitude of the equation of motion (2.8), we find

$$\gamma ma = |q|vB. \tag{2.10}$$

Since the acceleration $\mathbf{a}$ is at all times perpendicular to the velocity $\mathbf{v}$, the motion is circular, and the centripetal acceleration is $a = v^2/r$ with r as the radius of the circle. Inserting this into eq. (2.10) and identifying the expression for the relativistic momentum, we find

$$p = |q|rB. \tag{2.11}$$

With the beam particle momentum corresponding to the LHC design energy, $p = 7\,\mathrm{TeV}/c$ ($p \approx E/c$ in the relativistic limit), and the bending radius in the main bends, $r = 2.8\,\mathrm{km}$, the corresponding magnetic flux density is $B = 8.3\,\mathrm{T}$. Such an immensely strong field must be realized in all of the 1232 main bends, each of length $14.3\,\mathrm{m}$, around the LHC ring. This field is realized by the use of superconducting magnets operating at the temperature $1.9\,\mathrm{K}$ with a current of $12\,\mathrm{kA}$. Two coils provide magnetic fields in opposite directions as required when protons are circulating in both directions around the ring. These are "side by side", such that the return field of each of them contributes to the field inside the other one. This is illustrated in fig. 2.1. In addition to the dipole magnets used for the "brute force" bending of the beams around the LHC, there are higher multipole magnets which are used for focusing and beam control.

We note finally that the dependencies of eqs. (2.11), (2.6), and (2.7) on the accelerator radius favor large radii. This is indeed the reason why the LEP/LHC tunnel is as large as it is. It is also the reason why future possibilities for the particle physics community include not only linear

bends, and the expression $2\pi r/c$ in eq. (2.7) corresponds to the time spent in the bends (not the total time spent on a full turn of the accelerator). Thus, eq. (2.7) gives the correct total synchrotron radiation energy loss per turn.

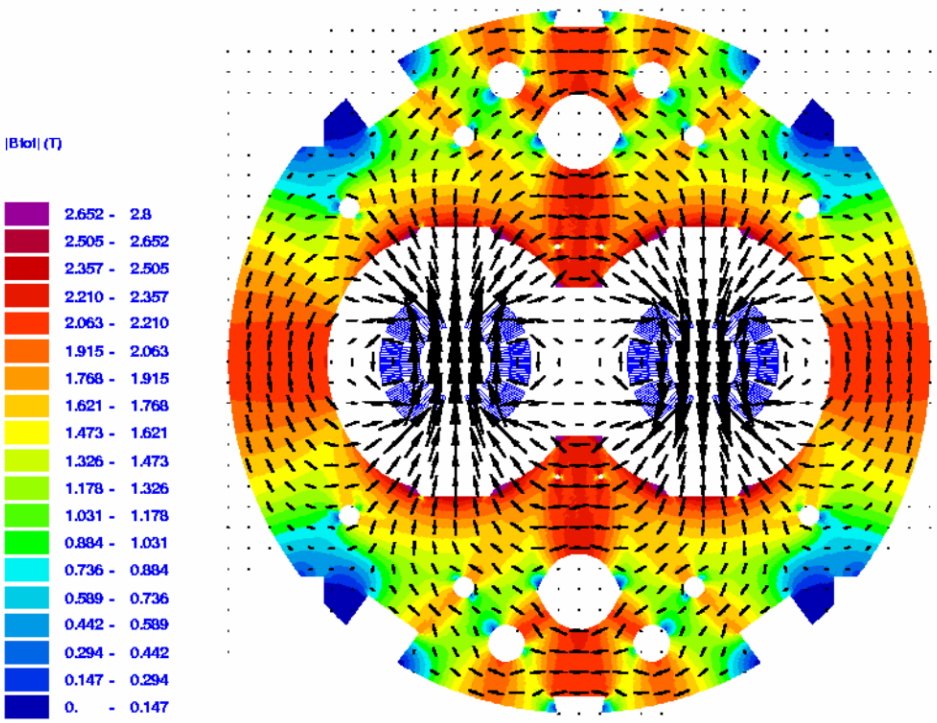

Figure 2.1: The magnetic field configuration in a dipole magnet in the LHC. Two sets of coils provide fields in opposite directions, and the return field of each of them contributes to the field inside the other one. From ref. [44].

colliders [48, 49], but also a circular accelerator[4] with a circumference of 80-100 km.

2.2.3 Pile-up

As mentioned briefly in section 1.6.1, there may be more than one inelastic pp interaction giving rise to final state particles in a given bunch crossing. The expected number of interactions per bunch crossing depends on the beam characteristics, such as the number of protons per bunch and the geometry of the bunches. In general, one must cope with more pile-up to achieve a higher luminosity.

In addition to the so-called in-time pile-up resulting from multiple pp interactions in each bunch crossing, there is also out-of-time pile-up due to interactions in neighboring bunch crossings at the LHC when collisions are taking place with high enough frequency. The design bunch crossing rate of the LHC is one every 25 ns, and this number is achieved when the accelerator is filled with the full 2808 bunches.

2.2.4 Actual LHC performance

So far, the design parameters of the LHC have been presented. We now proceed to review briefly how the LHC has been performing since the initial start-up in 2008. After beams had

[4] https://espace2013.cern.ch/fcc/Pages/default.aspx
http://press.web.cern.ch/press-releases/2014/02/cern-prepares-its-long-term-future

for the first time been successfully circulated in the LHC ring in September 2008, a magnet quench[5] caused severe damage to many superconducting magnets and a long delay of further LHC operation.

LHC operation was resumed in November 2009, and since then, the LHC has been operating very successfully. Collision data at $\sqrt{s} = 7\,\mathrm{TeV}$ were collected by the experiments in 2010 and 2011, amounting to about $5\,\mathrm{fb}^{-1}$ of integrated luminosity. In 2012, the energy was ramped up to $\sqrt{s} = 8\,\mathrm{TeV}$, and about $20\,\mathrm{fb}^{-1}$ of integrated luminosity was delivered to the experiments. The energy was kept well below design energy as the electrical connections between the superconducting magnets were not believed to be able to withstand operation at design energy.

Fig. 2.2 shows some numbers characterizing LHC operation and performance during the period 2010-2012, as seen from the ATLAS point of view. As seen in fig. 2.2(a), the luminosity delivered to ATLAS came close to $8 \cdot 10^{33}\,\mathrm{cm}^{-2}\,\mathrm{s}^{-1}$. This is indeed very close to the design luminosity $1.0 \cdot 10^{34}\,\mathrm{cm}^{-2}\,\mathrm{s}^{-1}$, but this luminosity was achieved with a number of colliding bunches around half the design number (fig. 2.2(b)). To achieve this, the number of protons in each bunch was made higher than the design value. This resulted in more in-time pile-up than the design value (fig. 2.2(c)). The number of interactions per bunch crossing was around 30-35 in late 2012, providing a challenging environment for the ATLAS detector, designed to cope with the design value of 19 interactions per bunch crossing [44].

2.3 The general layout of a detector for a collider experiment

Before presenting the layout of the ATLAS detector in detail, let us review the general layout of a detector for use in a particle physics collider experiment. Such a detector is in general comprised of many layers performing different measurements. In the so-called barrel section (the central part of the detector), the detector layers are arranged in cylindrical symmetry around the beam line. At both ends of the detector, there are so-called end-caps, which provide the measurements of particles moving with a small angle with respect to the beam line. The detector layers in the end-caps are perpendicular to the beam line, so that a particle moving with a small angle with respect to the beam line traverses all the different detector layers in the end-cap, just as a particle moving perpendicular to the beam line traverses all the different detector layers in the barrel.

The only (known) particles living long enough to reach the detector after a high energy collision are photons, electrons, muons, and neutrinos, as well as a few different baryons and mesons. The neutrinos, feeling only the weak interaction, have tiny cross sections for interacting with anything, and escape most of the time out of any detector without leaving any trace. This leaves the photons, electrons, muons, and hadrons to be measured in the detector of a collider experiment. The detector must be constructed in such a way that it can as accurately as possible measure the momenta and energies of these particles, since all the dynamics of the initial collision must be inferred from these measurements. In addition, it should be able to identify some of these particles, in particular the electrons, muons, and photons.

If we imagine moving outwards from the interaction region (where the beam particles are

[5] A magnet quench is what happens when a superconducting magnet loses its superconductivity and the energy associated with the magnetic field is released in an uncontrolled way.

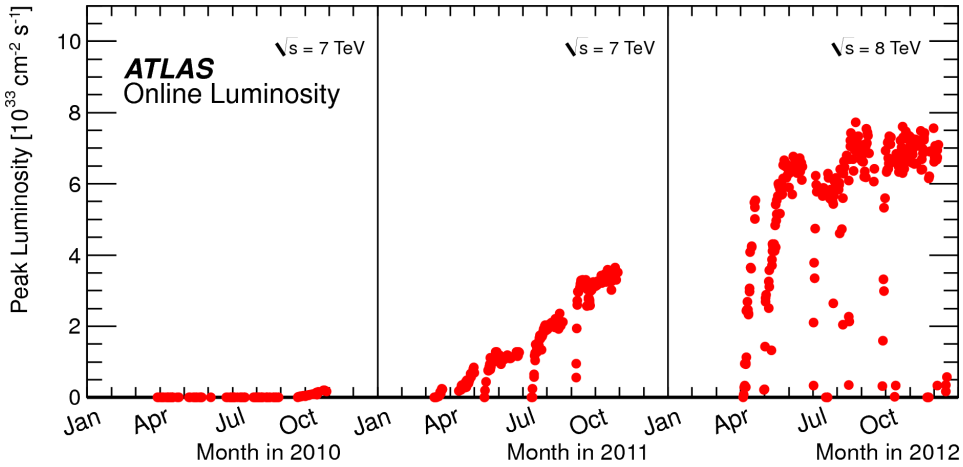

(a) Luminosity as function of time.

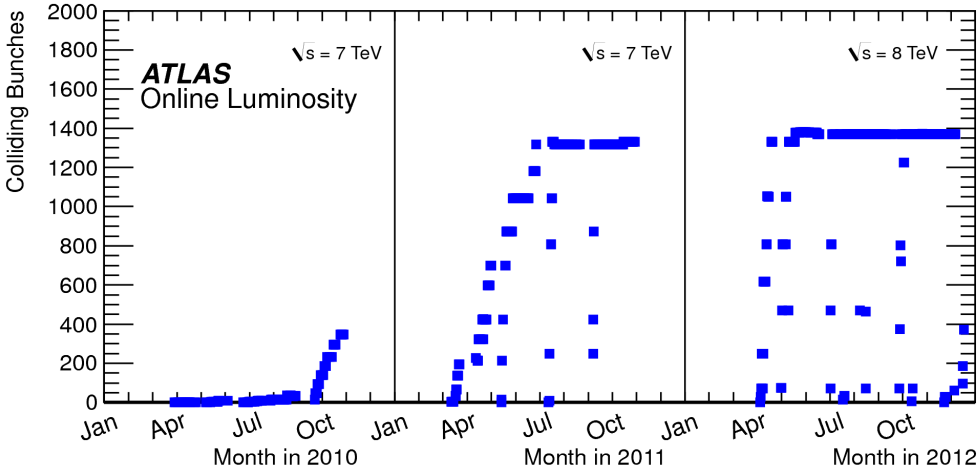

(b) Number of bunches as function of time.

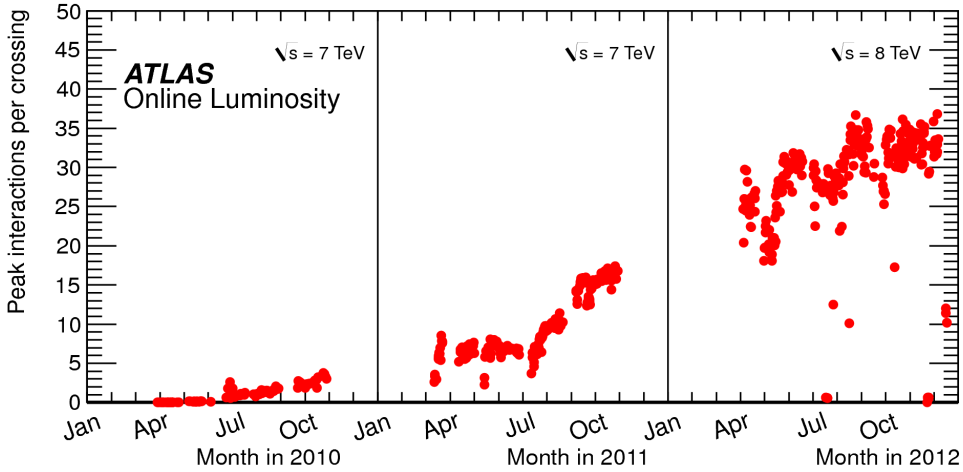

(c) Number of interactions per bunch crossing as function of time.

Figure 2.2: Luminosity (a), number of bunches (b), and number of interactions per bunch crossing (c) in ATLAS as functions of time for LHC operation in the period 2010-2012.

made to collide), we would in general traverse the following detector systems:

- the inner detector tracking system,
- the electromagnetic (EM) calorimeter,
- the hadronic calorimeter, and
- the muon spectrometer.

2.3.1 Inner detector tracking

A tracking detector consists of many modules which each give a signal when a charged particle passes through. When a signal (known as a *hit*) is registered in a certain module, we know that a charged particle has passed through a corresponding region in space. Combining several hits, we can reconstruct the trajectory of the charged particle, and we have what is called a track. Ideally, each charged particle leaves a track in the inner detector tracking system, and we can identify each particle's trajectory through the inner detector. In general, a tracking detector is immersed in a magnetic field, allowing the determination of the charge and momentum of each charged particle[6]. The direction of the track at the closest approach to the beam line gives the direction of the particle's initial momentum as it emerged from the collision.

After reconstruction of the tracks of all charged particles, we can identify vertices. These are identified as points in space to which several tracks seem to converge. The vertices can be *primary vertices*, which tell us where the inelastic pp interactions have occurred, or they can be *secondary vertices*. A secondary vertex is displaced from the primary vertex or the beam line, and indicates the decay in flight of an unstable particle whose lifetime is long enough to allow a measurable displacement from the primary vertex or the beam line, but short enough that the particle decays within the confines of the inner detector tracking system.

Ideally, the inner detector tracking measurement should not in any way disturb the particles being measured. Hence, the material in the inner detector should not be too dense.

2.3.2 Momentum measurement in a homogeneous magnetic field

As derived in section 2.2.2, a charged particle in a homogeneous magnetic field moves in a circle, the radius of which is related to the charge and momentum of the particle. It is not hard to convince one self that the derivation still holds when the particle has a velocity component along the magnetic field, and that eq. (2.11) must be replaced by

$$p_\perp = |q| r B \tag{2.12}$$

with $p_\perp$ as the magnitude of the momentum component in the plane perpendicular to the magnetic field and r as the radius of the circle which is now the projection of the particle's trajectory into this plane. Clearly, we can measure $p_\perp$ by tracking if we know B and $|q|$, since r is the radius of curvature of the track. The direction of curvature gives the sign of the charge q. For most interesting final state particles in a collider experiment, $|q|$ is the elementary charge. With

[6] Actually, the charge and momentum are not measured individually, as explained in section 2.3.2.

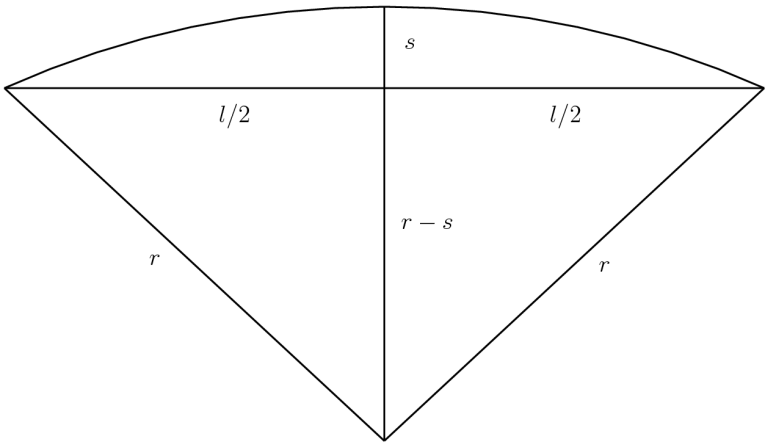

Figure 2.3: Illustration of the geometry of a momentum measurement in a homogeneous magnetic field. The particle's trajectory is a segment of a circle of radius r, and the sagitta s is measured. The magnetic field is perpendicular to the plane of the paper. The sagitta is greatly exaggerated relative to the radius.

the reconstruction of a full three-dimensional track, the complete momentum vector $\mathbf{p}$ at any point along the track can be reconstructed.

Consider now a particle passing through an instrumented region of length l where there is a homogeneous magnetic field. The particle's trajectory is a segment of a circle, and the sagitta s is measured[7], see fig. 2.3. The Pythagorean theorem gives

$$(r - s)^2 + \left(\frac{l}{2}\right)^2 = r^2, \tag{2.13}$$

giving

$$r = \frac{l^2/4 + s^2}{2s} \approx \frac{l^2}{8s} \tag{2.14}$$

when $l \gg s$, i.e. when only a small segment of the circle is measured. Combining with eq. (2.12), we find the perpendicular momentum

$$p_\perp = \frac{|q|B\,l^2}{8s}. \tag{2.15}$$

The corresponding uncertainty is

$$\delta p_\perp = \left|\frac{\partial p_\perp}{\partial s}\right| \delta s = \frac{|q|B\,l^2}{8s^2}\delta s = p_\perp \frac{\delta s}{s}, \tag{2.16}$$

where δs is the uncertainty on the sagitta, which is related to the spatial resolution of the tracking detector. Finally, the relative uncertainty on $p_\perp$ is

$$\frac{\delta p_\perp}{p_\perp} = \frac{\delta s}{s} = \frac{8p_\perp \delta s}{|q|B\,l^2}. \tag{2.17}$$

Several important conclusions can be drawn from this simple expression. First of all, it is clear that good momentum resolution is achieved by having

- good spatial resolution in the tracking detector (small δs),

[7]The following derivation is based on the one found here: `http://cbooth.staff.shef.ac.uk/phy6040det/magfield.html`.

- a strong magnetic field (large B), and
- a long "lever arm", i.e. a long distance l over which the track is measured.

Furthermore, we see that the relative momentum uncertainty is proportional to the momentum itself – particles with large momenta are more difficult to measure precisely as their tracks have small sagittae.

Finally, it should be noted that, in general, the magnetic field in an actual experimental setup is not necessarily homogeneous. Furthermore, it may be necessary to take into account effects of the fact that the particles are passing through some detector material. Some refined track fitting algorithm is in general used, and the momentum (or rather the ratio $q/p_\perp$) is one of the parameters in the fit. Even in such a general case, the conclusions of this section regarding the main factors which affect the momentum resolution, still apply.

2.3.3 The calorimeters

A calorimeter is a dense detector which is supposed to completely contain the *shower* of secondary particles produced when a particle enters the calorimeter material. The shower of secondary particles produces measurable signals in active detector material. In order for the calorimeter to fully contain the shower, it should have a thickness which is many radiation lengths[8] X_0/ρ for an EM calorimeter or many nuclear interaction lenghts λ_I/ρ for a hadronic calorimeter. These are the characteristic length scales for the development of EM and hadronic showers.

In a *homogeneous* calorimeter, only active detector material is present, which serves both the purpose of measurement and containment of the shower. In a *sampling* calorimeter, on the other hand, the active detector material is interleaved with inactive material (absorbers) whose sole purpose is to contain the shower, i.e. to contribute to the thickness of the calorimeter as measured in interaction lengths or radiation lengths. While a homogeneous calorimeter provides in general the best energy measurements, a sampling calorimeter may be necessary due to cost and size constraints, and may also provide superior angular resolution.

An EM shower is a cascade of electrons, positrons, and photons, which is caused by the processes called bremsstrahlung and pair production. Bremsstrahlung is the emission of a photon from an electron or positron in the presence of some material (the process can not happen in vacuum due to energy and momentum conservation). Pair production is the creation of an electron-positron pair from a photon in the presence of some material (also this process is impossible in vacuum). To understand the development of an EM shower, consider an electron entering the material of an EM calorimeter. The electron emits a photon by bremsstrahlung. Furthermore, this photon produces an electron-positron pair, and the original electron emits another photon by bremsstrahlung. The shower development continues in this way, creating more and more electrons, positrons, and photons with lower and lower energy until the single particle energies are too low for bremsstrahlung and pair production. A shower initiated by a photon entering the calorimeter material develops in the same way, with the first step being pair

[8]Here, ρ is the mass density of the material with which the particles interact. It is X_0/ρ and λ_I/ρ which have the dimension of length. However, the quantities X_0 and λ_I are also referred to as radiation and interaction lengths, as seen for example in ref. [1], section 31.9.

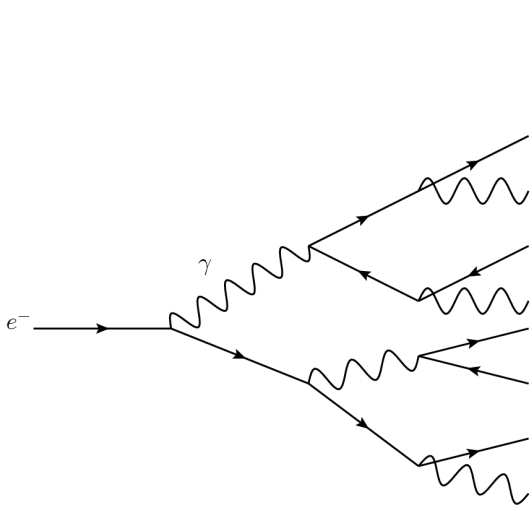

(a)

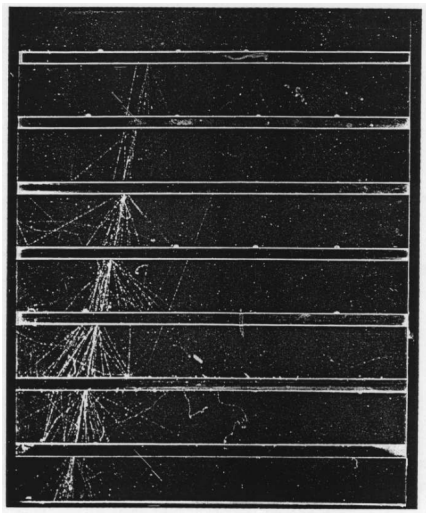

(b)

Figure 2.4: A sketch of the development of an EM shower initiated by an electron (a) and a picture (from ref. [50]) of an EM shower in a cloud chamber with lead absorbers (b).

production rather than bremsstrahlung. A sketch of an EM shower initiated by an electron and a picture of an EM shower in a cloud chamber is shown in fig. 2.4.

A hadronic shower results from the strong interaction of an incident particle with the nuclei in the calorimeter material. Such a shower is more complex than an EM shower, with the production of a variety of hadrons, and with the decays of neutral pions into photons contributing to the EM component of the shower.

The EM calorimeter of a detector in a collider experiment has a lower density than the hadronic calorimeter. In principle, it is mainly the electrons, positrons, and photons which induce showers in the EM calorimeter. As the cross section for bremsstrahlung is strongly mass dependent, hadrons, being much heavier than electrons and positrons, do not induce showers in the EM calorimeter to the same extent. They pass through to the more dense hadronic calorimeter, where they induce hadronic showers due to their strong interaction with nuclei.

The relative energy resolution of a calorimeter can be parametrized as [1]

$$\frac{\delta E}{E} = \frac{a}{\sqrt{E}} \oplus b \oplus \frac{c}{E}, \tag{2.18}$$

where $\oplus$ represents addition in quadrature, i.e. $x \oplus y = \sqrt{x^2 + y^2}$. For high energies, the term $a/\sqrt{E}$ dominates over the term c/E. As long as one does not reach the limit where the resolution is limited by the constant term, we have $\delta E/E \propto 1/\sqrt{E}$. I.e. the relative resolution improves with increasing energy, exactly the opposite behavior of the relative momentum resolution in a magnetic field, which becomes worse as the momentum increases.

2.3.4 The muon spectrometer

The only particle (except neutrinos) which passes through both the EM and hadronic calorimeters without being stopped, is the muon. The muon's bremsstrahlung in the EM calorimeter is

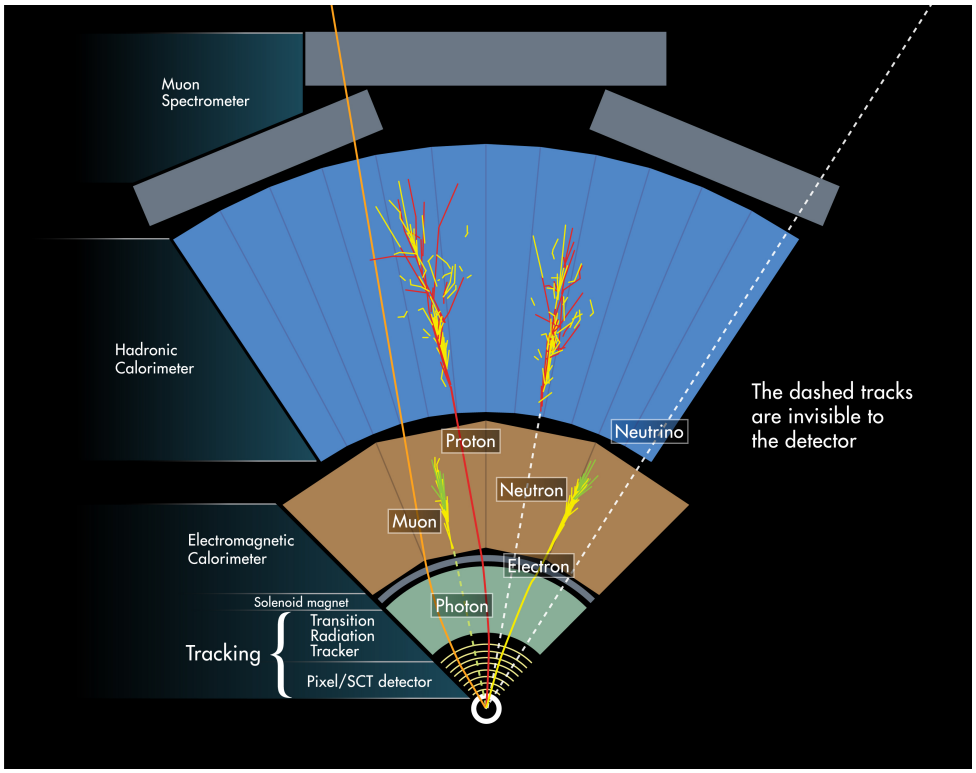

Figure 2.5: This illustration shows a cross section of a section of the ATLAS detector barrel and how the different particles interact in the different layers of the detector.

negligible because of the its large mass, and the muon does not experience the strong interaction, so it is not stopped in the hadronic calorimeter (although it does leave a signal characteristic of a *minimum ionizing particle*). The outermost part of a detector is therefore the muon spectrometer, dedicated to the detection of muons. This is an additional layer of tracking, which gives an additional measurement of the muon momentum and which provides muon identification, since in principle only muons can reach this part of the detector (assuming that the hadronic calorimeter is thick enough to effectively contain the hadronic showers).

2.3.5 Interactions of various particles with the detector

Fig. 2.5 shows how different particles are seen in the different parts of a detector for a collider experiment – in this particular case, the ATLAS detector[9]. The neutrinos do not interact with the detector, as they experience only the weak interaction. They can, however, to some extent be indirectly measured, since their momentum shows up as missing, in the sense that any apparent violation of the conservation of momentum may be attributed to the neutrinos (or to other, yet unknown, weakly interacting particles).

[9]The illustration is taken from `https://cds.cern.ch/record/1505342` (CERN).

2.3.6 The missing transverse energy

Particles that do not interact with any parts of the detector can in pp collisions be indirectly measured using the concept of the missing transverse energy ($\not{E}_{\mathrm{T}}$), a quantity motivated by the conservation of momentum. The only examples of such particles within the SM are the neutrinos. Due to the fact that these are electrically neutral leptons, i.e. experience neither the electromagnetic nor the strong force, they have tiny, in practice vanishing, cross sections for interacting with the detector material. Unknown particles not included in the SM could also have very small interaction cross sections, and thus contribute to the missing transverse energy. For example, dark matter is most likely comprised of such *weakly interacting massive particles* (WIMPs).

Let us assume that all the final state particles with significant momentum components in the plane perpendicular to the beam axis in a pp collision result from a hard scattering process. The plane perpendicular to the beam axis is referred to as the *transverse* plane, and the momentum components in this plane are referred to as transverse momenta and denoted $\mathbf{p}_{\mathrm{T}}$. The beam axis is chosen to be the z-axis, so that $\mathbf{p} = \mathbf{p}_{\mathrm{T}} + p_z\mathbf{e}_z$ with $\mathbf{e}_z$ as the unit vector in the z-direction.

The total momentum of the final state particles along the beam axis is equal to that of the colliding partons, $p_z = (x_1 - x_2)P$, where P is the proton momentum, x_i is the momentum fraction of parton number i, and parton number 1 is defined as the one coming from the proton moving in the positive z-direction. In general, $x_1 \neq x_2$, so there is a non-zero total momentum along the beam axis.

The transverse momenta of the colliding partons are in general small compared to the energy scale of the collision. Using the uncertainty principle, one can get an order of magnitude estimate of the transverse momenta of the partons, knowing that they are confined within the proton, which has a size of order $1\,\mathrm{fm}$. The uncertainty principle,

$$\Delta x\, \Delta p_x \sim \hbar, \tag{2.19}$$

gives the order of magnitude of the transverse momentum,

$$\Delta p_x \sim \frac{\hbar}{\Delta x} \approx \frac{0.2\,\mathrm{GeV\,fm}}{1\,\mathrm{fm}} = 0.2\,\mathrm{GeV}, \tag{2.20}$$

which is negligible compared to the TeV scale of the pp collisions at the LHC. One can therefore assume that the total transverse momentum of the final state particles in a pp collision should be zero. This can be used to observe particles that do not interact with the detector, since their existence can be inferred when the total transverse momentum of the measured particles is different from zero. In particular, the condition that the total transverse momentum of all final state particles be zero,

$$\sum_{\text{invisible}} \mathbf{p}_{\mathrm{T}} + \sum_{\text{visible}} \mathbf{p}_{\mathrm{T}} = \mathbf{0}, \tag{2.21}$$

leads directly to an expression for the total transverse momentum of "invisible" final state particles in terms of the measured transverse momenta of the "visible" ones:

$$\sum_{\text{invisible}} \mathbf{p}_{\mathrm{T}} = -\sum_{\text{visible}} \mathbf{p}_{\mathrm{T}}. \tag{2.22}$$

Here, the "invisible" particles are those that do not interact with the detector, while the "visible" particles are all the others.

Eq. (2.22) shows that one can find the total transverse momentum of "invisible" particles in a given collision event by summing up the measured transverse momenta of all the "visible" particles and reversing the sign. The missing transverse energy is defined as

$$\not{\mathbf{E}}_{\mathrm{T}} = -\sum_{\text{visible}} \mathbf{p}_{\mathrm{T}}^{\mathrm{reco}} \tag{2.23}$$

with $\mathbf{p}_{\mathrm{T}}^{\mathrm{reco}}$ as reconstructed (measured) transverse momenta of "visible" particles. Generally, the reconstructed transverse momenta going into the sum (2.23) are to a large extent taken from calorimeter measurements, hence the term missing transverse *energy* is used. As long as the final state particles are highly relativistic, their energies and momenta are to good approximation equal (when working in natural units). Even with the presence of less relativistic final state particles, one can choose to *define* the missing transverse energy in terms of calorimeter measurements, as the effect of these particles is also present in the simulation to which data are compared.

The only final state particles that are not accounted for in a pure calorimeter based missing transverse energy measurement are the muons. For any identified muons, the transverse momenta as measured by the tracking detectors must be added into the sum (2.23). Schematically, the missing transverse energy becomes then

$$\not{\mathbf{E}}_{\mathrm{T}} = -\sum_{\text{calo}} \mathbf{E}_{\mathrm{T}}^{\mathrm{calo}} - \sum_{\text{muons}} \mathbf{p}_{\mathrm{T}}^{\mu} \tag{2.24}$$

with $\mathbf{E}_{\mathrm{T}}^{\mathrm{calo}}$ denoting "transverse energy" measurements[10] in the calorimeters and $\mathbf{p}_{\mathrm{T}}^{\mu}$ denoting the measured transverse momenta of muons. The calorimetric part of the missing transverse energy can be refined using information about reconstructed jets, electrons, photons, and tau leptons, taking into account differences in calorimeter response to the different objects and using information from the inner tracking detectors.

The assumption that all the final state particles with significant transverse momenta come from the hard scattering may be violated to a certain extent due to final state particles from the underlying event and pile-up interactions. However, it is clear that the assumption of vanishing total transverse momentum should hold also when these are included, since the transverse momenta of the colliding protons vanish. Thinking of the collision as one between two protons instead of two partons, one could imagine that even the total momentum along the beam axis should vanish. However, proton remnants can escape the detector very close to the beam line, and indirect reconstruction of the total z-component of the momentum of "invisible" particles is not possible.

[10]Even though energy is not a vector, it is customary in this context to define an "energy vector" with magnitude equal to the measured energy and direction equal to the direction of motion of the particle that supposedly deposited the energy in the calorimeter. This direction can for example be taken to be from the reconstructed primary vertex to the position of the energy deposit in the calorimeter. Such an "energy vector" is to good approximation equal to the momentum vector for highly relativistic particles (when working in natural units).

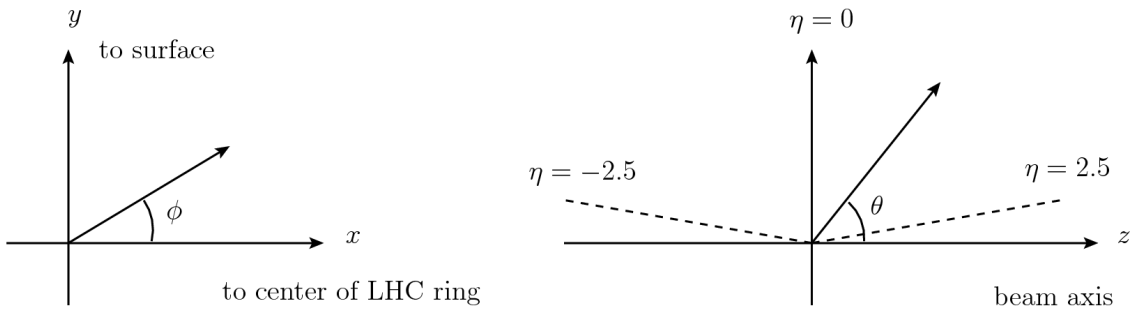

Figure 2.6: Illustration of the ATLAS coordinate system showing two projections. The definitions of the azimuthal and polar angles ϕ and θ are shown, as well as sample values of the pseudorapidity η.

2.4 The ATLAS detector

In this section, the specific layout of the ATLAS detector will be presented. Only an overview is given, and the reader is referred to ref. [51] for further details.

2.4.1 The ATLAS coordinate system

The ATLAS coordinate system (fig. 2.6) is oriented with the z-axis along the beam pipe, the positive x-direction towards the center of the LHC ring, and the positive y-direction upwards (opposite of the acceleration of gravity). The origin is located at the nominal interaction point.

The spherical coordinates ϕ and θ are defined in the standard way, with ϕ as the angle between the x-axis and the x,y-projection of the position vector and θ as the angle between the position vector and the positive z-axis. The angle ϕ increases counter-clockwise when observed from the positive z-axis and is zero on the positive x-axis. The range of θ is $\theta \in [0, \pi]$, while the range of ϕ is chosen as $\phi \in [-\pi, \pi]$. We also define the pseudorapidity

$$\eta = -\ln\left(\tan\frac{\theta}{2}\right), \tag{2.25}$$

which is usually quoted instead of the polar angle θ. The pseudorapidity is zero when $\theta = \pi/2$, i.e. in the direction perpendicular to the beam axis.

The transverse component of any vector, e.g. $\mathbf{p}_{\mathrm{T}}$, is defined as its projection in the x,y-plane (transverse to the beam axis). To quantify the separation between two directions, the distance ΔR in the η,ϕ-plane is used:

$$\Delta R = \sqrt{(\Delta\eta)^2 + (\Delta\phi)^2}\,. \tag{2.26}$$

2.4.2 The magnets

The magnetic field of ATLAS is provided by the central solenoid in the inner detector and the barrel and end-cap toroids in the muon spectrometer. The configuration is illustrated in fig. 2.7.

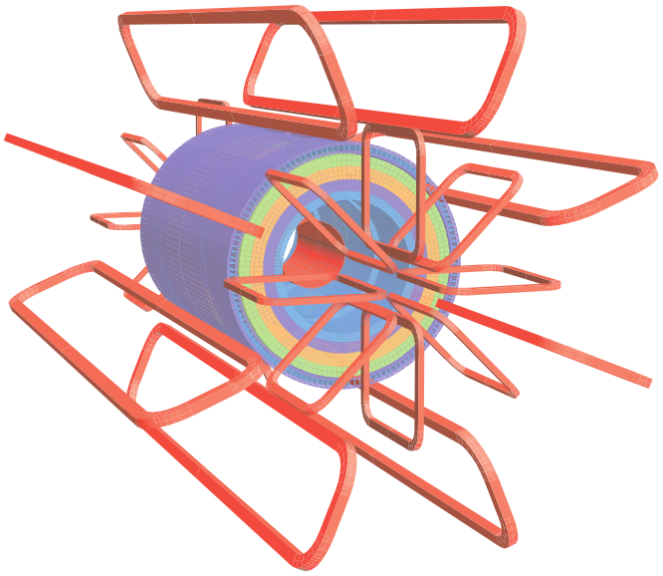

Figure 2.7: Illustration of the magnet configuration of ATLAS. Current loops are red, and also shown is the material of the tile calorimeter. The current loops for the barrel and end-cap toroids are outside the calorimeters, and provide a magnetic field circulating around the beam line. The central solenoid is inside the calorimeters. With the current circulating around the beam line, it provides a magnetic field parallel to the beam line. From ref. [51].

The central solenoid provides a magnetic flux density of $2\,\mathrm{T}$ [51] directed along the beam axis in the inner detector. The barrel and end-cap toroids provide the magnetic field for the muon spectrometer. The field is here tangential to a circle parallel to the x,y-plane around the beam axis. The magnetic flux density is around $0.5\,\mathrm{T}$ in the barrel and $1\,\mathrm{T}$ in the end-caps [51].

2.4.3 The inner detector

The ATLAS inner detector tracking system consists of three separate detectors. From the beam pipe and outwards, these are the pixel detector, the semiconductor tracker (SCT), and the transition radiation tracker (TRT). The geometry of the inner detector is shown in figs. 2.8 and 2.9. In fig. 2.9, one can see which parts of the inner detector measure particles with different pseudorapidities.

The pixel and SCT detectors

The pixel and SCT detectors are both silicon based semiconductor detectors. In such detectors, p-doped silicon is brought in contact with n-doped silicon, and this results in a p-n junction. The *depletion zone*, which is almost free of holes and free electrons, is extended by the application of a *bias voltage*. When a charged particle passes through such a p-n junction, it creates electron-hole pairs, and the electrons and holes drift in opposite directions because of the bias voltage. This creates a measurable pulse on the electrodes. The sensors are arranged on concentric cyliders in the barrel and on disks perpendicular to the beam line in the end-caps.

The basic sensor of the pixel detector is a pixel of size $50 \times 400\,\mu\mathrm{m}^2$ in $R\phi \times z$ in the barrel ($R\phi \times R$ in the end-caps) where R is the distance from the beam axis[11]. Each hit in a pixel defines a space point. The intrinsic accuracy of the pixel detector is $10\,\mu\mathrm{m}$ in $R\phi$ and $115\,\mu\mathrm{m}$ in z (barrel) or R (end-caps) [51]. Typically, three pixel layers are crossed by each track.

[11] An accuracy in $R\phi$ refers to the spatial accuracy in the direction tangent to a cirle of radius R around the beam axis.

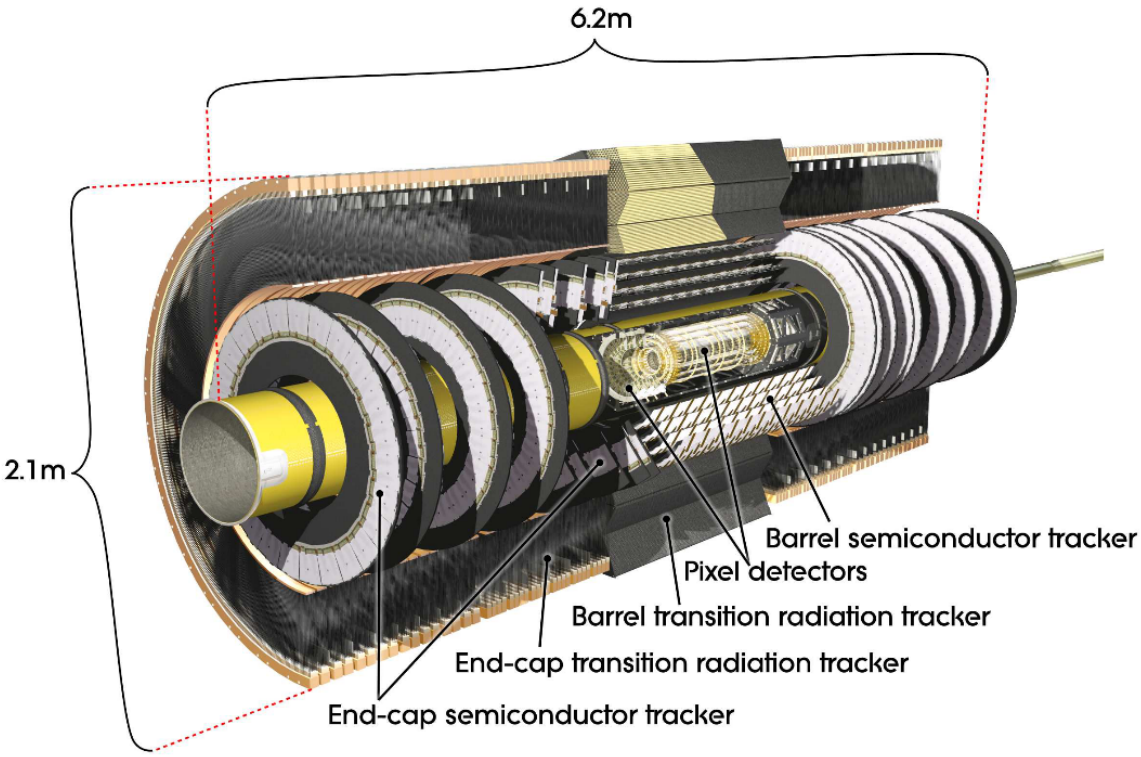

Figure 2.8: Layout of the ATLAS inner detector. From ref. [51].

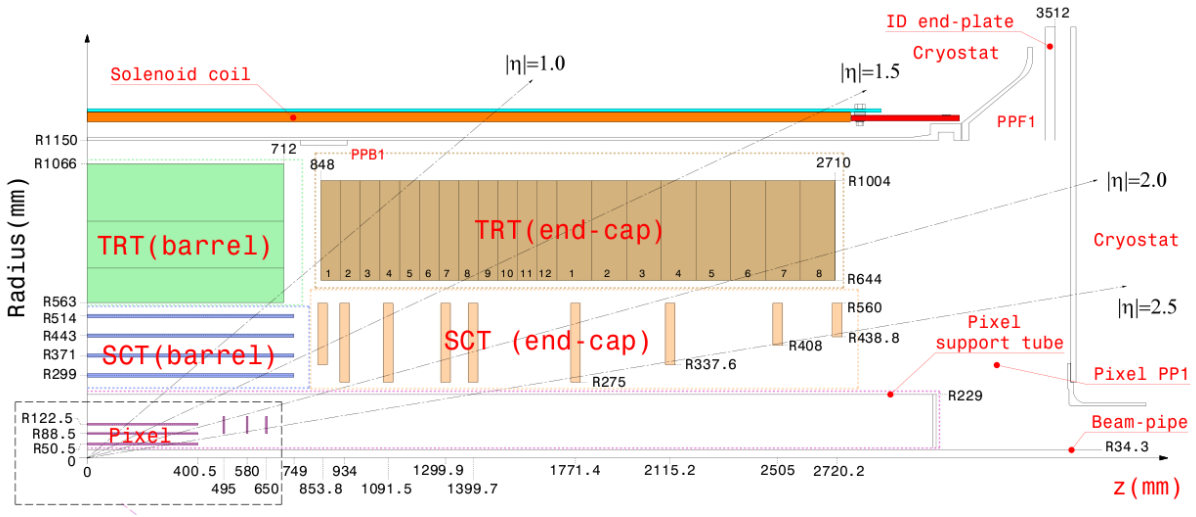

Figure 2.9: Illustration showing the geometry of the inner detector in the barrel-end-cap transition region. In this illustration, it is clearly seen which parts of the inner detector measure particles with different pseudorapidities. From ref. [51].

In the SCT, silicon strips are used. Each strip provides an accurate measurement in one dimension only, and two hits are required for one space point. Eight strip layers are crossed by each track (providing four space points). The intrinsic accuracy per module for the SCT is $17\,\mu\mathrm{m}$ in $R\phi$ and $580\,\mu\mathrm{m}$ in z (barrel) or R (end-caps) [51].

Both the pixel and SCT detectors cover the pseudorapidity region $|\eta| < 2.5$.

The Transition Radiation Tracker

In the TRT, straw tubes of diameter $4\,\mathrm{mm}$ are used to provide many measurements of $R\phi$ with an accuracy of $130\,\mu\mathrm{m}$ per straw [51]. The straw tubes' length direction is parallel to the beam axis in the barrel and radial in the end caps, and the TRT therefore does not provide any measurement of η. The TRT provides up to 36 measurements per track within its pseudorapidity acceptance $|\eta| < 2.0$.

A straw tube consists of a central anode wire surrounded by a cylindrical tube. When a charged particle ionizes the gas in the TRT tube, the electrons start to drift towards the central wire, where they produce a signal. The drift time, i.e. the time the electrons use to reach the central wire, is measured, and gives a measurement of the radius (distance from central wire) at which the charged particle passed. See fig. 2.13(a) for an illustration of a charged particle passing through a drift tube (in that case, in the ATLAS muon spectrometer).

Transition radiation is the emission of a photon when a charged particle passes between two media of different dielectric constants. The phenomenon occurs only for particles with very high relativistic factors, i.e. $\beta\gamma \gtrsim 1000$ [52]. In the TRT, there are layers of materials with different dielectric constants, which cause electrons to emit transition radiation photons. These photons are measured in the TRT tubes, and provide electron identification, since heavier particles in general do not produce transition radiation because of their smaller relativistic factors. A transition radiation hit in the TRT is identified as a hit where the signal exceeds a higher threshold than for ordinary hits.

2.4.4 The calorimeters

The ATLAS calorimeter layout is shown in figs. 2.10 and 2.11. The calorimeters cover the region $|\eta| < 4.9$, and are all sampling calorimeters.

The EM calorimeter of ATLAS uses liquid argon as its active detector material, and lead plates as absorbers. The ionization in the liquid argon is measured directly by electrodes. Over the pseudorapidity range corresponding to the acceptance of the inner detector, the EM calorimeter has an especially fine granularity, so that precision measurements of photons and electrons can be made. Over the rest of the pseudorapidity range, the granularity is coarser, but still fine enough for jet reconstruction and missing transverse energy measurements.

The hadronic calorimeter of ATLAS consists of the tile calorimeter in the barrel and extended barrel regions, and the liquid argon end-cap calorimeters and liquid argon forward calorimeters. The tile calorimeter uses steel as absorber and scintillators as active detector material. Here, the particles of a hadronic shower produce photons in tiles of scintillating material, and these photons are read out through wavelength shifters and photomultiplier tubes.

The hadronic end-cap calorimeter consists of two wheels for each end-cap, using copper

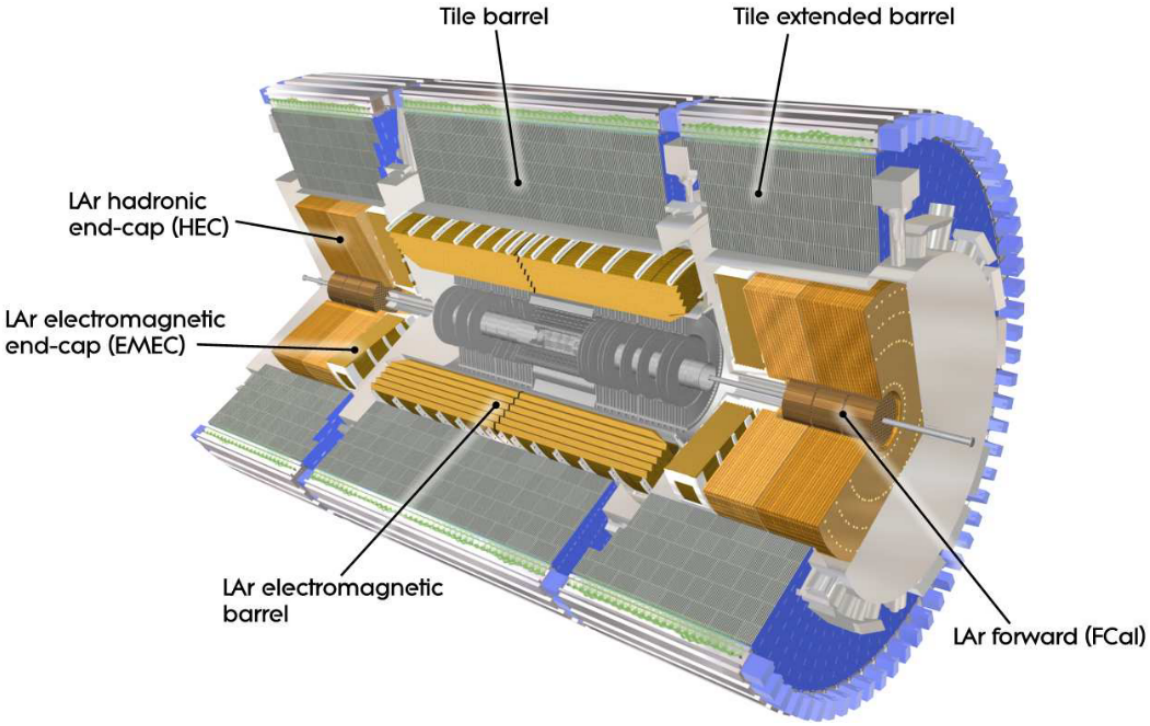

Figure 2.10: Layout of the ATLAS calorimeter system. From ref. [51].

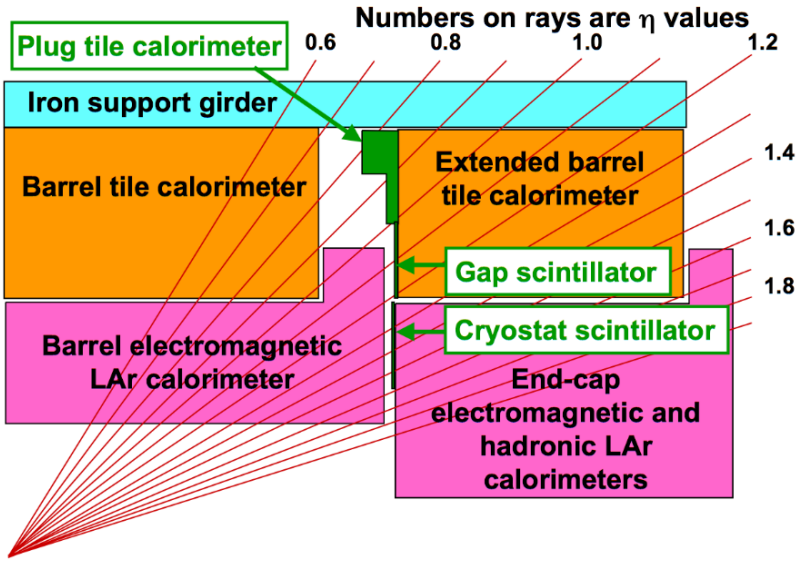

Figure 2.11: Illustration showing the geometry of the calorimeters in the barrel-end-cap transition region. In this illustration, one can clearly see which calorimeter units contribute to containing the showers of particles with different pseudorapidities. The forward calorimeters are not shown. From ref. [51].

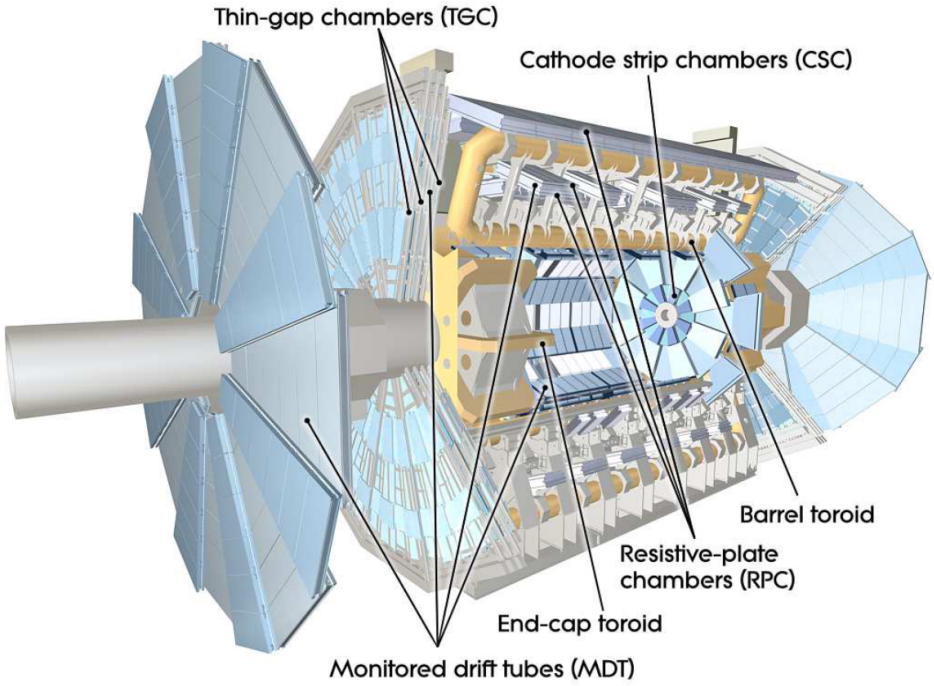

Figure 2.12: Layout of the ATLAS muon spectrometer. From ref. [51].

plates as absorbers and liquid argon as active detector medium. Inside the center of the hadronic end-cap calorimeters, we find the forward calorimeters, covering the region closest to the beam pipe, assuring an as hermetic as possible detector. The detector needs to be as hermetic as possible to do good missing transverse energy measurements. The forward calorimeters use copper and tungsten as absorbers and liquid argon as active detector material.

The total thickness of the EM calorimeter is at least 22 radiation lengths in the barrel and at least 24 radiation lengths in the end-caps [51]. The total calorimeter thickness is about 9.7 (nuclear) interaction lengths in the barrel and 10 interaction lengths in the end-caps. Including the inactive material between the calorimeters and the muon spectrometer, at least 11 interaction lengths of material contribute to the effective shielding of the muon spectrometer over the pseudorapidity range which it covers.

2.4.5 The muon spectrometer

The layout of the ATLAS muon spectrometer is shown in fig. 2.12. It consists, as the inner detectors and calorimeters, of a barrel part and end-caps. There are different kinds of sensors used in the muon spectrometer, serving different purposes. These are the monitored drift tubes (MDTs), the cathode strip chambers (CSCs), the resistive plate chambers (RPCs), and the thin gap chambers (TGCs).

The main precision tracking sensors in the ATLAS muon spectrometer are the MDTs. These are gaseous ionisation detectors with drift time measurement as in the case of the TRT. An illustration of an MDT is shown in fig. 2.13. The tubes are oriented with their length direction tangential to circles parallel to the x,y-plane around the beam axis. They thus provide good precision in η, but not in ϕ. They are oriented in this way because this makes the tube length

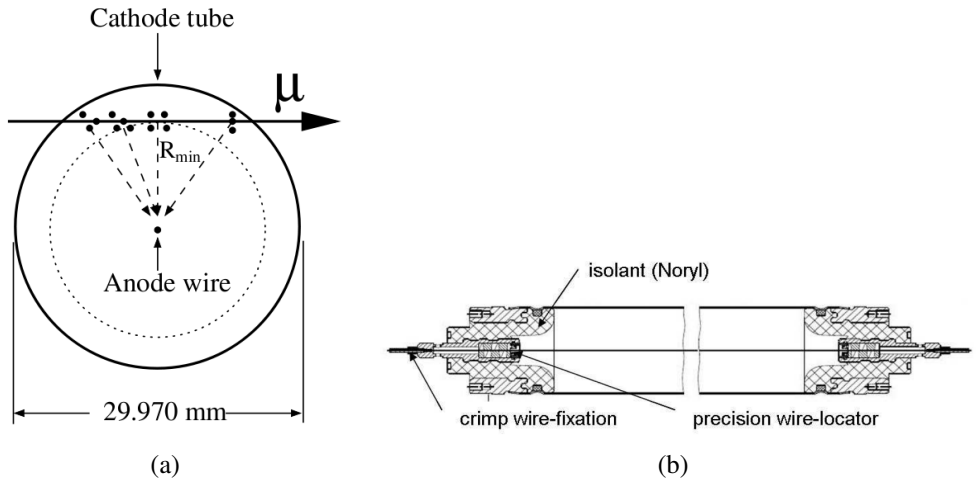

Figure 2.13: Illustration of a monitored drift tube from the ATLAS muon spectrometer. The tube is shown in a transverse (a) and a longitudinal (b) projection. From ref. [51].

direction parallel to the toroidal magnetic field, so that the MDTs provide as good as possible momentum resolution. Several layers of tubes are put together in chambers, and the MDTs can provide a resolution of about $80\,\mu\mathrm{m}$ per tube, or $35\,\mu\mathrm{m}$ per chamber [51].

In the first end-cap layer for $|\eta| > 2$, the particle flux was expected to be too large for the MDTs to cope with. The MDTs are therefore replaced by the CSCs in this region. The CSCs are multiwire proportional chambers, which are gaseous ionization detectors, and they serve the same purpose as the MDTs.

The trigger is the system that, for each collision event, decides whether the data from this particular event should be stored. It is needed because keeping all events is not feasible in terms of bandwidth and data storage. The muon chambers must provide information to the trigger very fast, and the MDTs are not feasible for this. For the trigger, faster detectors are needed, and these are the RPCs in the barrel and the TGCs in the end-caps. The RPCs and TGCs are both gaseous ionization detectors. In addition to trigger information, they provide measurements of ϕ, which is not accurately measured by the MDTs. Clearly, they must also provide measurements in η in order to provide momentum measurements to the trigger system. The muon spectrometer covers the pseudorapidity range $|\eta| < 2.7$ with trigger capability within $|\eta| < 2.4$.

The MDTs are in the barrel arranged in chambers in three concentric cylindrical layers. In the azimuthal angle ϕ, there are 16 sectors. Even numbered sectors are fitted with smaller chambers which overlap in acceptance with both the neighboring sectors' larger chambers, as shown in fig. 2.14(a). The layout is symmetric in ϕ, except for the region around sectors 12 and 14, where we find the feet of the detector. The three layers are labeled "inner", "middle", and "outer". In fig. 2.14(a), one can for example see the labels BIL, meaning Barrel Inner Large, and BOS, meaning Barrel Outer Small. In addition, there is some special labeling of the chambers around the feet of the detector.

In the end-caps, the MDTs are arranged in four layers perpendicular to the beam line, see fig. 2.14(b). Also here, there are three main layers, the "inner", "middle", and "outer" ones. In addition, the EE (End-cap Extra) layer is needed to ensure three measurements for muons close to the barrel-end-cap transition region. As seen in fig. 2.14(b), a high momentum (almost

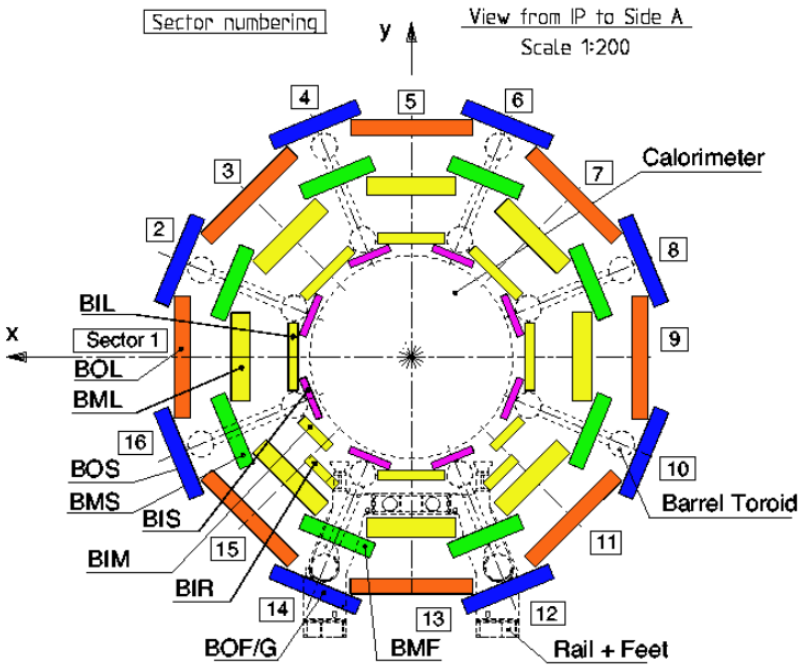

(a)

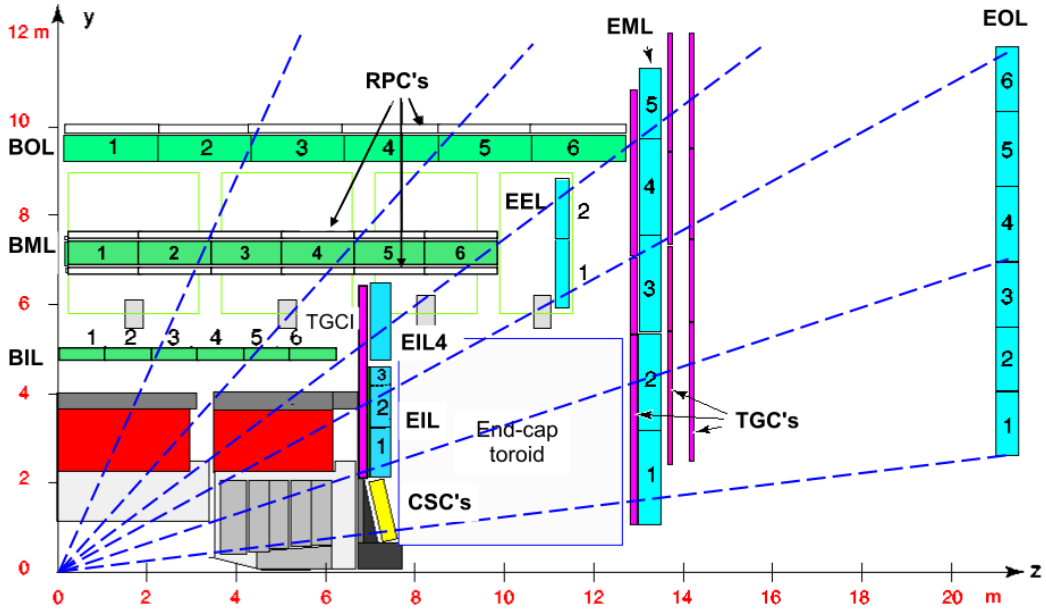

(b)

Figure 2.14: Transverse (a) and longitudinal (b) cross sections of the muon spectrometer. From ref. [51].

Subdetector	Relative resolution	Acceptance
Inner detector	$\delta p_{\mathrm{T}}/p_{\mathrm{T}} = 0.05\% \cdot p_{\mathrm{T}}/(1\,\mathrm{GeV}) \oplus 1\%$	$\lvert\eta\rvert < 2.5$
EM calorimeter	$\delta E/E = 10\%/\sqrt{E/(1\,\mathrm{GeV})} \oplus 0.7\%$	$\lvert\eta\rvert < 3.2$ (trigger: $\lvert\eta\rvert < 2.5$)
Hadronic calorimeter		
barrel and end-cap	$\delta E/E = 50\%/\sqrt{E/(1\,\mathrm{GeV})} \oplus 3\%$	$\lvert\eta\rvert < 3.2$
forward	$\delta E/E = 100\%/\sqrt{E/(1\,\mathrm{GeV})} \oplus 10\%$	$3.1 < \lvert\eta\rvert < 4.9$
Muon spectrometer	$\delta p_{\mathrm{T}}/p_{\mathrm{T}} = 10\%$ at $p_{\mathrm{T}} = 1\,\mathrm{TeV}$	$\lvert\eta\rvert < 2.7$ (trigger: $\lvert\eta\rvert < 2.4$)

Table 2.1: The resolution performance goals of the ATLAS detector. From ref. [51]. The symbol $\oplus$ denotes addition in quadrature.

straight) muon track passing through the outer (in the radial direction) parts of the end-cap inner layer (EIL) and end-cap middle layer (EML) does not hit the end-cap outer layer (EOL), so the end-cap extra layer is needed. The installation of the EE layer was, however, not completed until just before summer 2013[12].

As explained in section 2.3.2, the "lever arm", i.e. the distance over which a track is measured, is important for the momentum resolution. It should therefore be clear that the ultimate momentum resolution is achieved only for muons which are measured in all layers of the muon spectrometer. The need for a proper "lever arm" makes the muon spectrometer, and the whole of the ATLAS detector, very large.

2.4.6 Subdetector resolutions

We summarize the performance goals of the ATLAS detector in terms of the momentum/energy resolutions of the individual subdetectors in table 2.1. From the point of view of the search for new physics in the one lepton (electron or muon) and missing transverse energy final state, it is worth noting that the electron channel has superior resolution at high mass (high p_{T} of the final state lepton). In particular, the design resolution of the muon spectrometer is 10% for $p_{\mathrm{T}} = 1\,\mathrm{TeV}$, while the EM calorimeter achieves a resolution at the sub-percent level for $E = 1\,\mathrm{TeV}$.

2.4.7 The trigger system

As mentioned in section 2.4.5, a trigger system is needed to decide very fast whether a given event is interesting and should be read out and stored on tape and disk. Storing the data from each bunch crossing is not feasible in terms of bandwidth or storage capacity. One therefore needs to make a selection of interesting events already before the data is read out from the detector. All the data for any given event is buffered while the trigger system processes event data in order to decide whether the event should be read out.

The ATLAS trigger system has three levels, level 1 (L1), level 2 (L2), and the event filter (EF). Each level provides a more refined selection than the previous ones, and processes events at a lower rate than the previous ones. The level 1 trigger reduces the rate from the bunch crossing rate of $40\,\mathrm{MHz}$ to about $75\,\mathrm{kHz}$ [51]. The level 2 trigger reduces the rate further to

[12]See here: `http://atlas.ch/news/2013/full-coverage-for-ATLAS-muons.html`.

about $3.5\,\mathrm{kHz}$, and events finally pass the event filter selections and go into permanent storage at a rate of about $200\,\mathrm{Hz}$.

The L1 trigger searches for high p_{T} muons, electrons, photons, and hadronically decaying tau leptons, as well as events with large missing transverse energy or a large scalar sum of transverse energy. It uses information from the trigger chambers in the muon spectrometer and reduced granularity calorimeter information. Information about *regions of interest* (RoIs) is passed to the L2 trigger for events passing the L1 selection. The L2 trigger then uses full granularity detector information within the regions of interest only. Finally, the EF reconstructs events using the same algorithms as used in offline analysis before the final decision is made to discard or permanantly store the event.

At any given time, the trigger system must know which criteria should be passed in order for an event to proceed to the next level. The list of criteria is referred to as the trigger menu, which can for example state that all events with reconstructed muons with a p_{T} above a certain threshold should be kept. This threshold needs to be selected in such a way that the available bandwidth is not wasted while also making sure that the rate does not exceed the limitation on the bandwidth. The trigger menu therefore evolves with the luminosity delivered by the LHC. As the luminosity increases, so must the thresholds in order for the rate not to become too large. One can include also trigger menu items that give too large rates, as long as they are *prescaled*, meaning that only a certain fraction of such events are passed to the next level. Putting together a good trigger menu is a complex task, and requires input from all the analysis groups within the collaboration. While searches for new, heavy particles demand high threshold unprescaled triggers, detailed studies of the lower mass SM particles may require lower threshold triggers, which may need to be prescaled to be accomodated by the bandwidth. The available bandwidth must be shared in a reasonable way between a variety of experimental signatures.

2.4.8 Muon reconstruction in ATLAS

Muon reconstruction in ATLAS can be done stand-alone by the muon spectrometer, or by combining muon spectrometer and inner detector information. There are three main reconstruction strategies: [51]

- reconstructing a track stand-alone in the muon spectrometer (stand-alone muon),
- matching a muon spectrometer track to an inner detector track and using information from both subdetectors (combined muon), or
- matching an inner detector track to a track segment in the first layer of the muon spectrometer (segment-tagged muon).

Segment-tagging is primarily used for low p_{T} muons, which may not even reach the second and third layers of the muon spectrometer. For combined muons, the combination of muon spectrometer and inner detector information improves the momentum resolution. The requirement of finding an inner detector track to which the muon spectrometer track can be matched can also reject backgrounds from non-prompt muons.

There are two procedures for combining inner detector and muon spectrometer information for the combined muons. Either, a new track fit is performed using the hits associated with both

the inner detector and muon spectrometer tracks, or the muon spectrometer and inner detector track parameters are combined statistically. The former procedure is used for so-called MuID muons, while the latter is used for STACO muons. The muon spectrometer information is expected to dominate the momentum measurement at high p_{T}.

2.4.9 Missing transverse energy reconstruction

As mentioned in section 2.3.6, the missing transverse energy is in general reconstructed using primarily measurements from the calorimeters and the muon spectrometer. A simple definition of the missing transverse energy is

$$\not{\mathbf{E}}_{\mathrm{T}} = -\sum_{\text{clusters}} \mathbf{E}_{\mathrm{T}}^{\text{cluster}} - \sum_{\text{muons}} \mathbf{p}_{\mathrm{T}}^{\mu}. \tag{2.27}$$

The use of energy clusters, i.e. extended calorimeter areas of significant activity, instead of all calorimeter cells, reduces the noise contribution. Such a simple definition was in fact used in early ATLAS publications, when studies of the missing transverse energy performance and particle identification and reconstruction were just getting underway. For the data used in this thesis, the recommendation from the ATLAS jet/$\not{E}_{\mathrm{T}}$ working group is to use the *refined* missing transverse energy, which is based on the identification of various physics objects, such as electrons, photons, and jets. The use of such identified objects allows one to take into account differences in calorimeter response to the different kinds of objects, and to use all available detector information, e.g. taking the track information into account for electrons.

The following calorimeter objects go into the missing transverse energy:

- electrons with $p_{\mathrm{T}} > 10\,\mathrm{GeV}$,
- photons with $p_{\mathrm{T}} > 10\,\mathrm{GeV}$,
- hadronically decayed tau leptons,
- jets with $p_{\mathrm{T}} > 20\,\mathrm{GeV}$,
- calorimeter clusters.

Obviously, there is overlap between these objects. For example, the calorimeter deposit associated with an electron object could also be associated to a jet, and certainly also to a cluster. The objects are prioritized in the order given above. For example, if an electron with $p_{\mathrm{T}} > 10\,\mathrm{GeV}$ is identified, the calorimeter cells associated with this electron are not entered into the calculation later in the context of jets or clusters. A single calorimeter cell can also be associated to several objects of the same kind, for example two electrons close to each other in the calorimeter. If so, the energy sharing is treated properly, and double counting is avoided also in this case. Obviously, the identification of each of the above kinds of objects is a complicated procedure, but further details will not be given here.

Finally, the muon contribution must be added. The contribution is separated in that from *non-isolated* muons and that from *isolated* muons. A non-isolated muon is defined to be one which is close to a jet, with $\Delta R_{\mu,\mathrm{jet}} < 0.3$. For such muons, the stand-alone muon spectrometer

momentum measurement is used. Since the momentum measured in the muon spectrometer is smaller than the original muon momentum by an amount corresponding to the muon's energy deposit in the calorimeters, this deposit should also be part of the missing transverse energy calculation, but must obviously not be double counted if also present as an individual cluster or as part of the nearby jet.

For isolated muons, the STACO combined momentum is used, which is taken at *perigee*, i.e. at the point of closest approach to the reconstructed primary vertex. In this case, the energy deposited by the muon in the calorimeters should *not* be present in the missing transverse energy calculation, as it is already included in the muon's momentum.

The procedure, as implemented for the 2010 $\sqrt{s} = 7\,\mathrm{TeV}$ data, is documented in ref. [53], where the performance of the missing transverse energy reconstruction is also investigated.

2.5 Summary

In this chapter, we have presented the Large Hadron Collider and the ATLAS detector. We will present a search for new physics using ATLAS data, and understanding the experimental signature of hypothetical new physics signal is obviously crucial. In the next chapter, the new charged, heavy boson signal will be presented.

Chapter 3

New charged, heavy boson signal

3.1 Experimental signature

The key to the discovery of any new physics process in a particle collider experiment is to identify an *experimental signature* which can be used to separate events resulting from the new physics process (the *signal*) from events resulting from known processes (the *background*). The experimental signature of the production of a new heavy particle is the presence of a set of final state particles with a large invariant mass. These particles will also typically have high transverse momenta.

As described in section 1.5.3, the s-channel production and decay of an unstable particle leads to a peak in the differential cross section $d\sigma/dm$, and this is a telltale sign of such production and of the existence of the short lived particle. Here, the invariant mass m is the Lorentz invariant "magnitude" of the four-momentum carried by the short lived particle, i.e. $m = \sqrt{(p_1 + p_2)^2}$ with p_1 and p_2 as the four-momenta of the particles annihilating into the short lived particle or the four-momenta of the short lived particle's decay products. If one can experimentally reconstruct the invariant mass m from measurements of the decay products, a peak in the invariant mass spectrum reveals the existence of the short lived particle.

When searching for a new charged, heavy boson decaying to a charged lepton and a neutrino, one would ideally like to reconstruct the invariant mass of the lepton-neutrino pair. This is, however, not possible, as only the transverse component of the neutrino momentum can be reconstructed (see section 2.3.6). In this case, a related variable is used instead: the *transverse mass*. The experimental signature is then one high p_{T} charged lepton, large missing transverse energy, and large transverse mass as reconstructed from the charged lepton momentum and the missing transverse energy.

3.1.1 The transverse mass

We consider a particle decaying into two lighter particles, labeled 1 and 2. The invariant mass of the decay products is

$$m = \sqrt{(E_1 + E_2)^2 - (\mathbf{p}_1 + \mathbf{p}_2)^2}, \tag{3.1}$$

with E_i ($\mathbf{p}_i$) as the energy (momentum) of decay product number i. When searching for heavy particles, we can in general assume that the decay products are highly relativistic, such that

$E_i \approx |\mathbf{p}_i|$. In this case, the invariant mass is

$$m = \sqrt{(|\mathbf{p}_1| + |\mathbf{p}_2|)^2 - (\mathbf{p}_1 + \mathbf{p}_2)^2}. \tag{3.2}$$

If one of the decay products is a neutrino, this expression can not be calculated because not all components of the neutrino momentum are known. We define the transverse mass as

$$m_{\mathrm{T}} = \sqrt{(|\mathbf{p}_{\mathrm{T},1}| + |\mathbf{p}_{\mathrm{T},2}|)^2 - (\mathbf{p}_{\mathrm{T},1} + \mathbf{p}_{\mathrm{T},2})^2}. \tag{3.3}$$

The transverse mass is always smaller than or equal to the invariant mass, i.e. $m_{\mathrm{T}} \leq m$. When searching for a new charged, heavy boson decaying to a charged lepton and a neutrino, there is irreducible background from the production and decay of the W boson. In most of the W events, the resulting lepton-neutrino pair has an invariant mass close to the W boson mass of $80\,\mathrm{GeV}$. The inequality $m_{\mathrm{T}} \leq m$ guarantees that these events do not contribute to the background at higher transverse mass as long as the charged lepton and neutrino transverse momenta are correctly measured. Any upward migration of background events from low invariant mass to high transverse mass is solely due to measurement uncertainty on the charged lepton and neutrino transverse momenta. Hence, the irreducible background at high transverse mass comes only from events where the W boson is far off the *mass shell*, and the resulting background is therefore small.

The inequality $m_{\mathrm{T}} \leq m$ will now be proven. From eqs. (3.2) and (3.3), some vector algebra leads to the relation

$$m^2 - m_{\mathrm{T}}^2 = 2\left(|\mathbf{p}_1||\mathbf{p}_2| - |\mathbf{p}_{\mathrm{T},1}||\mathbf{p}_{\mathrm{T},2}| - p_{z,1}p_{z,2}\right). \tag{3.4}$$

Rewritten in terms of the polar angle θ,

$$m^2 - m_{\mathrm{T}}^2 = 2|\mathbf{p}_1||\mathbf{p}_2|\left(1 - \sin\theta_1 \sin\theta_2 - \cos\theta_1 \cos\theta_2\right). \tag{3.5}$$

Finally, we use the trigonometric identity

$$\sin\theta_1 \sin\theta_2 + \cos\theta_1 \cos\theta_2 = \cos(\theta_1 - \theta_2), \tag{3.6}$$

and arrive to

$$m^2 - m_{\mathrm{T}}^2 = 2|\mathbf{p}_1||\mathbf{p}_2|\left[1 - \cos(\theta_1 - \theta_2)\right] \geq 0. \tag{3.7}$$

Hence, $m_{\mathrm{T}} \leq m$, as we set out to prove. We also see that the transverse mass and the invariant mass are equal when both decay products are emitted with the same polar angle, i.e. $\theta_1 = \theta_2$. We identify a special case: $\theta_1 = \theta_2 = \pi/2$. In this case, $\mathbf{p}_{\mathrm{T},i} = \mathbf{p}_i$, so the relation $m_{\mathrm{T}} = m$ clearly holds.

Finally, we note that

$$\mathbf{p}_{\mathrm{T},1} \cdot \mathbf{p}_{\mathrm{T},2} = |\mathbf{p}_{\mathrm{T},1}||\mathbf{p}_{\mathrm{T},2}| \cos\Delta\phi_{1,2} \tag{3.8}$$

with $\Delta\phi_{1,2}$ as the opening angle between the decay products in the transverse plane. Hence,

$$m_{\mathrm{T}} = \sqrt{2|\mathbf{p}_{\mathrm{T},1}||\mathbf{p}_{\mathrm{T},2}|\left(1 - \cos\Delta\phi_{1,2}\right)}. \tag{3.9}$$

When searching for a new charged, heavy boson decaying to a charged lepton and a neutrino, we define

$$m_{\mathrm{T}} = \sqrt{2p_{\mathrm{T},l}\not{E}_{\mathrm{T}}\left(1 - \cos\Delta\phi_{l,\not{E}_{\mathrm{T}}}\right)} \tag{3.10}$$

with $p_{\mathrm{T},l}$ as the transverse momentum of the charged lepton, $\not{E}_{\mathrm{T}}$ as the missing transverse energy, and $\Delta\phi_{l,\not{E}_{\mathrm{T}}}$ as the angle between the charged lepton and the missing transverse energy in the transverse plane. This is the form in which the transverse mass is usually seen.

3.2 Signal models

The search for new charged, heavy bosons can be thought of as a test of the SM, where one searches for any deviation from the SM prediction in the high mass tail of the transverse mass distribution. Ideally, the search should be *model independent*, as there is not one particular theoretical model predicting such bosons which is in particular anticipated to be realized in nature. This can be thought of as in contrast to the search for the SM Higgs boson, whose detailed properties, except for the mass, were known long before the experimental verification of its existence.

Although one would ideally like to think of the search for new charged, heavy bosons as a model independent search, it is necessary, or at least very useful, to consider particular examples of signal models. In this thesis, we consider two reference models, based on two classes of origins of the new bosons. The first one is the Sequential Standard Model (SSM), which is a reference model for gauge bosons arising from new, broken gauge symmetries. In this model, the new gauge boson is defined to have the same couplings to fermions as the W boson and no coupling to the W and Z bosons. This corresponds almost[1] to the second reference model in ref. [54]. The corresponding interaction Lagrangian terms are thus given by eq. (1.83) with the W field replaced by the field corresponding to the new gauge boson, and with the relevant extension to other lepton and quark generations. The corresponding vertex factor is given by eq. (1.89) for leptons and (1.106) for quarks. In the case of the quarks, the CKM matrix elements are assumed to be the same as for the W. We stress that fixing the couplings in this way is arbitrary, but that the resulting model is a useful benchmark for presenting limits and comparing between different experiments. Obviously, the Lagrangian of the extended model still includes the W terms.

The left-right symmetric models described in section 1.7.5 give rise to a new gauge boson with right-handed couplings to quarks and leptons. However, purely left-handed and purely right-handed couplings lead to identical differential cross sections for $pp \to W' + X \to l\,\nu + X$ [55] as long as the handedness of the couplings to quarks and leptons are equal. Hence, the SSM W', although it inherits the left-handed couplings of the W boson, can also be used to represent a hypothetical new boson with right-handed couplings, as long as the right-handed boson decays to a light neutrino. In the case of a heavy right-handed neutrino, the neutrino can decay to visible particles, and one can search for this scenario in final states with e.g. two leptons and two jets [56].

The second reference model considered in this thesis is motivated by various solutions to

[1] The second reference model of ref. [54] contains couplings of the new gauge boson W' to the W and Z bosons, suppressed by a factor of order $(m_W/m_{W'})^2$. In the SSM, these couplings are rather set exactly to zero.

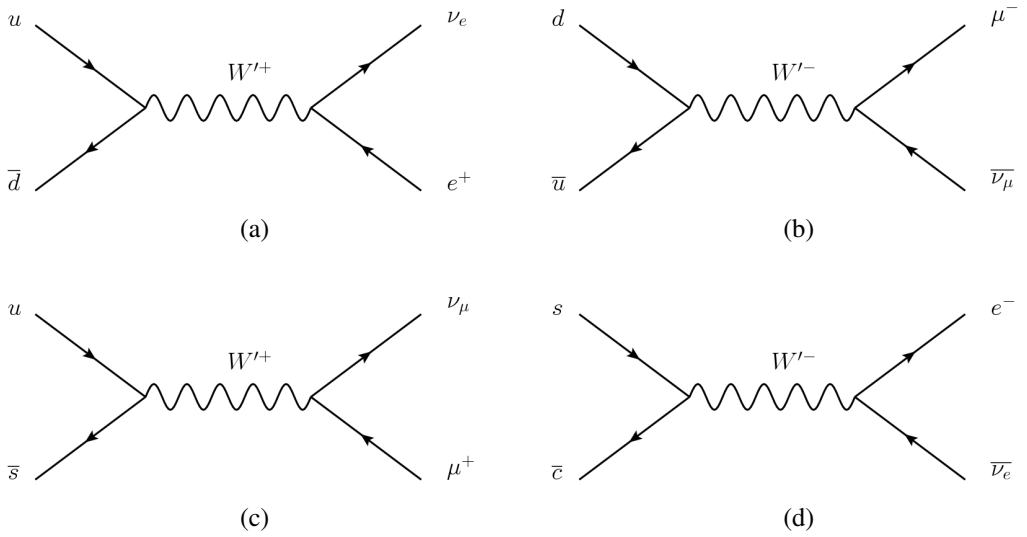

Figure 3.1: Feynman diagrams for SSM W' production and leptonic decay in pp collisions. The diagrams (a) and (b) show the dominant production modes, and less important production modes are shown in the diagrams (c) and (d).

the hierarchy problem, as described in ref. [57]. In these models, the new charged boson, called the W^*, interacts with fermions via "anomalous" couplings involving the space-time derivatives of the W^* fields. Such couplings lead to four-momentum dependent vertex factors, and hence important differences in the invariant mass dependence of the cross section wrt. the SSM W' case. In the reference model [58], the exact form and strength of the coupling of the W^* to fermions is fixed in such a way that the total decay width of the W^* is the same as that of the SSM W' boson in the limit of large boson mass. As the SSM W', the W^* is spin-1.

3.2.1 W'/W^* production in proton-proton collisions

Fig. 3.1 shows some Feynman diagrams for SSM W' production and leptonic decay in pp collisions. Figs. 3.1(a) and 3.1(b) show the dominant production modes, and examples of less important production modes are shown in figs. 3.1(c) and 3.1(d). The production mode shown in fig. 3.1(c) is *CKM suppressed*, as the $u\overline{s} \rightarrow W'^{+}$ vertex is associated with an off-diagonal CKM matrix element. The process shown in 3.1(d) is suppressed because s and $\overline{c}$ are both necessarily sea quarks, and are associated with small parton densities in the proton. One can also draw Feynman diagrams involving the b quark, but the corresponding contributions to the cross section are even smaller.

The W^* boson is produced in the same way as the SSM W' boson, except that the W^* reference model does not include couplings that mix the different quark generations. Hence, the CKM suppressed process in fig. 3.1(c) is not possible with the W' boson replaced by a W^*. The other processes in fig. 3.1 *are* possible with the W' boson replaced by a W^*, and it is the production modes shown in figs. 3.1(a) and 3.1(b) which dominate, as in the SSM W' case.

Process	Generator	Full/Fast	N_{evts}	σ_{gen}
$W' \to l\,\nu$, $m_{W'} = 500\,\text{GeV}$	PYTHIA 8	Fast	180000	$50.2\,\text{pb}$
$W' \to l\,\nu$, $m_{W'} = 1000\,\text{GeV}$	PYTHIA 8	Fast	180000	$2.81\,\text{pb}$
$W' \to l\,\nu$, $m_{W'} = 3000\,\text{GeV}$	PYTHIA 8	Fast	180000	$3.87\,\text{fb}$
$W' \to l\,\nu$, template	PYTHIA 8	Fast	1988999	$25.7\,\text{pb}$
$W^* \to \mu\,\nu$, $m_{W^*} = 500\,\text{GeV}$	CalcHEP + PYTHIA 8	Fast	20000	$16.3\,\text{pb}$
$W^* \to \mu\,\nu$, $m_{W^*} = 1000\,\text{GeV}$	CalcHEP + PYTHIA 8	Fast	20000	$884\,\text{fb}$
$W^* \to \mu\,\nu$, $m_{W^*} = 3000\,\text{GeV}$	CalcHEP + PYTHIA 8	Fast	20000	$0.490\,\text{fb}$
$W^* \to \mu\,\nu$, template	CalcHEP + PYTHIA 8	Full	699798	$8.45\,\text{pb}$

Table 3.1: Signal MC samples used in the analysis. The column labeled "Full/Fast" indicates whether full or fast detector simulation has been used. The columns labeled "N_{evts}" and "σ_{gen}" contain respectively the numbers of generated events and the cross sections calculated by the generators.

3.2.2 Monte Carlo samples

SSM W' signal Monte Carlo (MC) samples have been generated with PYTHIA 8 [27, 59] using the AU2 tune [60] and MSTW 2008 LO PDFs [26]. There is one high statistics template sample with a relatively flat distribution of the lepton-neutrino invariant mass, which can be reweighted to represent any desired W' mass at analysis time by applying an invariant mass dependent weight on an event-by-event basis. In addition, three ordinary W' samples are generated for fixed W' masses of $500\,\text{GeV}$, $1\,\text{TeV}$, and $3\,\text{TeV}$. These are used for validation of the reweighting procedure. The fixed mass samples include all leptonic decays of the W' (including the τ lepton), while the template sample includes only electron and muon decays.

For the mass range considered in this analysis, the total width of the W' boson increases almost linearly with the W' mass, with just a small correction from the fact that the top quark cannot be considered massless at low W' mass. The width-to-mass ratio $\Gamma_{W'}/m_{W'}$ is 3.0% at $m_{W'} = 300\,\text{GeV}$ and approaches 3.4% in the limit $m_{W'} \gg m_t$. The branching fraction of the W' to each lepton generation is 8.2% at high W' mass, slightly lower than the 11% for the W because of the additional top quark decay channel for the W'.

Signal samples for the W^* model have been generated at the hard scattering level with CalcHEP [61] using the CTEQ6L1 PDFs [62] and interfaced to PYTHIA 8 with the AU2 tune and CTEQ6L1 PDFs for the parton shower, hadronization, and underlying event. Also in the case of the W^*, a high statistics template sample is generated in addition to three ordinary W^* samples for fixed W^* masses of $500\,\text{GeV}$, $1\,\text{TeV}$, and $3\,\text{TeV}$. Both the fixed mass samples and the template sample include only muon decays.

The response of the ATLAS detector to the final state particles is simulated using Geant4 [63]. We distinguish between full simulation and fast simulation (Atlfast-II [64]). The latter uses a parametrized description of the development of showers in the calorimeters, which is tuned against data. All the signal MC samples described here are fast simulation, except the W^* template sample, which is full simulation. All the signal MC samples are generated for a pp center of mass energy $\sqrt{s} = 8\,\text{TeV}$, and are listed in table 3.1. For all samples, final state photon radiation from leptons is handled by PHOTOS [65].

$m_{W'}$ [GeV]	σ_{LO} [fb]	k-factor	σ_{NNLO} [fb]	$(\Delta\sigma/\sigma)^{\mathrm{up}}_{\mathrm{NNLO}}$ [%]	$(\Delta\sigma/\sigma)^{\mathrm{down}}_{\mathrm{NNLO}}$ [%]
300	$1.14 \cdot 10^5$	1.31	$1.49 \cdot 10^5$	6.8	3.2
400	$3.84 \cdot 10^4$	1.31	$5.02 \cdot 10^4$	6.6	3.2
500	$1.65 \cdot 10^4$	1.30	$2.14 \cdot 10^4$	6.3	4.2
600	$8.08 \cdot 10^3$	1.29	$1.04 \cdot 10^4$	5.9	5.8
750	$3.27 \cdot 10^3$	1.27	$4.16 \cdot 10^3$	5.5	8.2
1000	930	1.25	$1.16 \cdot 10^3$	6.6	12
1250	316	1.23	389	8.1	15
1500	120	1.21	145	9.7	17
1750	48.7	1.19	58.1	11	18
2000	20.7	1.17	24.3	13	16
2250	9.34	1.16	10.8	14	15
2500	4.46	1.14	5.09	14	15
2750	2.28	1.13	2.58	15	15
3000	1.26	1.14	1.43	15	14
3250	0.765	1.16	0.885	14	13
3500	0.497	1.18	0.587	13	11
3750	0.348	1.21	0.420	11	10
4000	0.255	1.23	0.313	10	9.1

Table 3.2: Cross sections for the process $pp \to W' + X \to l\,\nu + X$ at a pp center of mass energy $\sqrt{s} = 8\,\mathrm{TeV}$. The cross sections are for a single decay channel, i.e. not a sum over the three lepton generations. Both the LO cross section, the NNLO cross section, and the ratio between the two (the k-factor) are shown. The uncertainties on the NNLO cross sections are derived from variations of the invariant mass dependent k-factor as described in section 4.1.1 and are dominated by PDF uncertainties. They are presented here as relative uncertainties in percent.

3.2.3 Cross sections

Cross sections for the process $pp \to W' + X \to l\,\nu + X$ at a pp center of mass energy $\sqrt{s} = 8\,\mathrm{TeV}$ have been calculated at leading order (LO) with PYTHIA 8 using the AU2 tune and MSTW 2008 LO PDFs. These are corrected to next-to-next-to leading order (NNLO) using an invariant mass dependent k-factor which will be described in more detail in section 4.1.1. Only QCD corrections are applied, as the details of higher order electroweak corrections in general vary between different extended gauge models. The cross sections are shown in table 3.2.

Cross sections for the process $pp \to W^* + X \to l\,\nu + X$ at a pp center of mass energy $\sqrt{s} = 8\,\mathrm{TeV}$ have been calculated at LO with CalcHEP using the CTEQ6L1 PDFs. The cross sections are kept at LO due to the non-renormalizable nature of the W^* interactions. No uncertainties are evaluated because they are expected to be dominated by PDF uncertainties, which are known to be too optimistic for LO PDFs. Not evaluating these uncertainties is merely a matter of presentation, as they would appear only as a band around the theoretical cross section curve in the W^* limit plots to be presented in chapter 8. The cross section uncertainties do not affect the derived cross section limits or signal significances. The cross sections are shown in table 3.3.

m_{W^*} [GeV]	σ_{LO} [fb]	m_{W^*} [GeV]	σ_{LO} [fb]
400	$3.76 \cdot 10^4$	2250	7.00
500	$1.62 \cdot 10^4$	2500	2.90
600	$7.95 \cdot 10^3$	2750	1.20
750	$3.17 \cdot 10^3$	3000	0.490
1000	882	3250	0.199
1250	294	3500	0.0797
1500	108	3750	0.0317
1750	42.3	4000	0.0126
2000	17.1		

Table 3.3: Cross sections for the process $pp \rightarrow W^* + X \rightarrow l\,\nu + X$ at a pp center of mass energy $\sqrt{s} = 8\,\mathrm{TeV}$. The cross sections are for a single decay channel, i.e. not a sum over the three lepton generations.

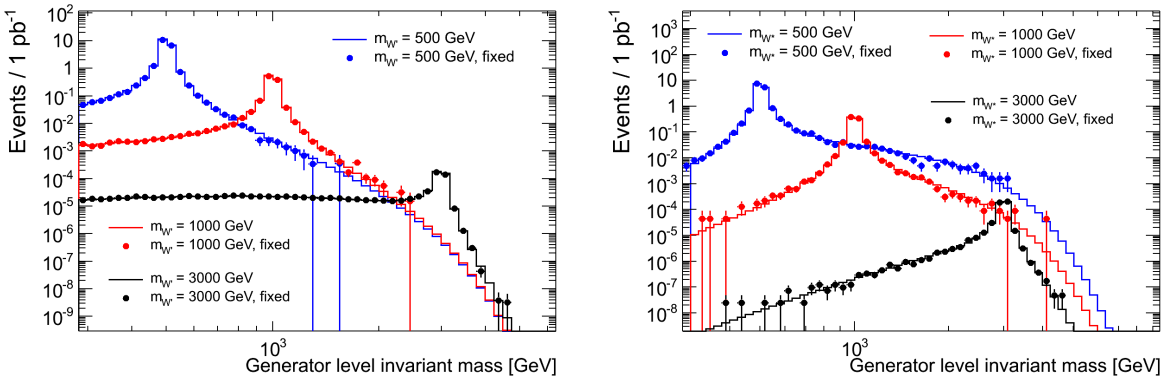

(a) (b)

Figure 3.2: Generator level invariant mass distributions for W' (a) and W^* (b) bosons of different masses. The solid lines are obtained by reweighting the template samples, while the points represent the ordinary "fixed mass" samples.

3.2.4 Validation of the resonance reweighting

The W' and W^* template samples are generated with a lepton-neutrino invariant mass distribution that provides sufficient statistics across the whole range of interest to the analysis. This is achieved by removing the Breit-Wigner propagator and additional mass dependent factors in the hard scattering calculation, and these factors are reintroduced at the analysis stage through invariant mass[2] dependent event weights. The ordinary MC samples generated with fixed W'/W^* masses are used to validate the procedure.

Fig. 3.2 shows the generator level invariant mass distributions for W' and W^* bosons of different masses both as obtained from reweighting the template samples and as obtained from the ordinary "fixed mass" samples. Good agreement is observed between the ordinary samples and the reweighted template samples.

Fig. 3.3 shows the same comparison for the muon channel reconstructed transverse mass distribution after the full event selection to be described in chapter 5. Good agreement is observed also in this distribution.

[2]From here on, the term invariant mass is used to refer to the invariant mass of the lepton-neutrino pair resulting from the W'/W^* decay. Strictly speaking it refers to the mass of the W'/W^* propagator in the MC event record, and corresponds therefore to the lepton-neutrino invariant mass before final state radiation.

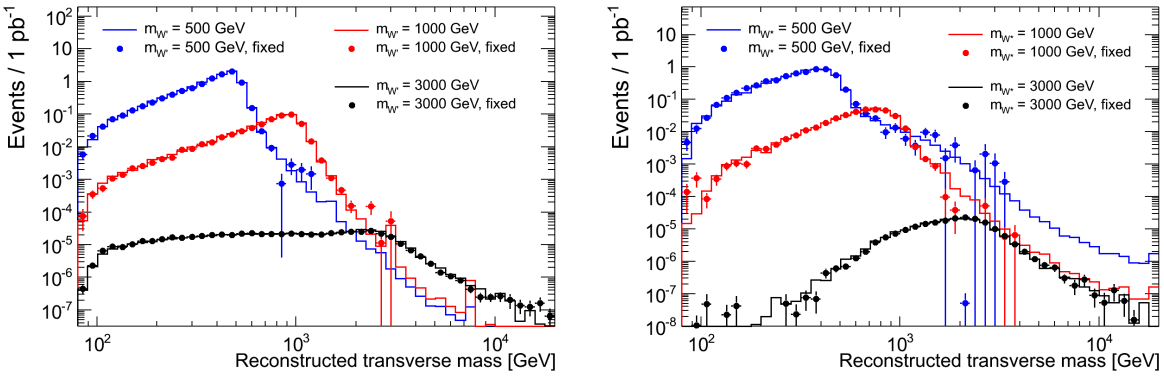

(a) (b)

Figure 3.3: Muon channel reconstructed transverse mass distributions for W' (a) and W^* (b) bosons of different masses. The solid lines are obtained by reweighting the template samples, while the points represent the ordinary "fixed mass" samples.

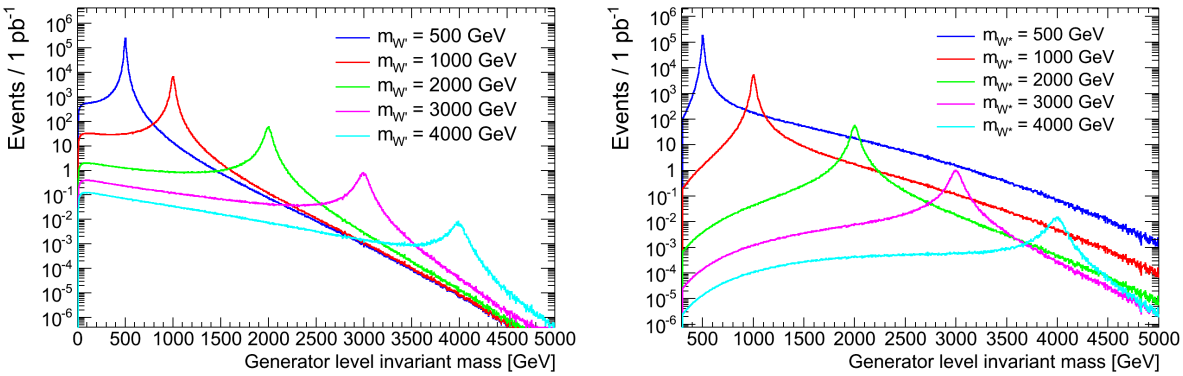

(a) (b)

Figure 3.4: Generator level invariant mass distributions for W' (a) and W^* (b) bosons of different masses.

3.2.5 Transverse mass distributions

The transverse mass m_{T} is the primary variable used to distinguish a potential new heavy boson signal from the SM background. Clearly, it is interesting to investigate the m_{T} distributions from the W' and W^* signal processes. We consider first the corresponding invariant mass distributions shown in fig. 3.4. As expected, each distribution is peaked around the mass of the W'/W^* boson. However, the tails far away from the peak regions behave differently in the W' and W^* cases. For the W', a significant tail of low mass off-shell production is present for the higher W' masses. This is because the *parton luminosity* is higher for lower invariant masses, i.e. the lower masses are favored by the PDFs. The low mass tail is much less significant in the case of the W^* because the derivative couplings lead to a different mass dependence of the hard scattering cross section.

Having discussed briefly the invariant mass distributions, we now turn our attention to the m_{T} distributions. As it turns out, the main features of the W' and W^* m_{T} distributions can be derived using knowledge of the respective angular distributions in the heavy boson rest frame.

Consider a W'/W^* boson of mass $m_{W'}$ produced on-shell and at rest in the detector frame of reference and decaying to a lepton-neutrino pair. As the boson is at rest, conservation of momentum implies that the lepton and neutrino will have equal and opposite momenta, $\mathbf{p}_l = -\mathbf{p}_\nu$. Assuming that the lepton and neutrino can be considered massless, conservation of energy gives $|\mathbf{p}_l| = |\mathbf{p}_\nu| = m_{W'}/2$. The lepton and neutrino go "back to back" in the transverse plane, and identifying the neutrino with the missing transverse energy $\not{E}_{\mathrm{T}}$, eq. (3.10) reduces to $m_{\mathrm{T}} = 2p_{\mathrm{T},l}$. Defining θ as the angle of the lepton direction of motion w.r.t. the beam line, we have

$$m_{\mathrm{T}} = 2p_{\mathrm{T},l} = m_{W'} \sin\theta. \tag{3.11}$$

The differential cross section $d\sigma/dm_{\mathrm{T}}$ can be expanded using the chain rule:

$$\frac{d\sigma}{dm_{\mathrm{T}}} = \frac{d\sigma}{d\cos\theta}\frac{d\cos\theta}{dm_{\mathrm{T}}}. \tag{3.12}$$

Rewriting eq. (3.11) in terms of the cosine and differentiating, we find

$$\left|\frac{dm_{\mathrm{T}}}{d\cos\theta}\right| = \frac{m_{W'}}{m_{\mathrm{T}}}\sqrt{m_{W'}^2 - m_{\mathrm{T}}^2}. \tag{3.13}$$

Neglecting a potential forward-backward asymmetric term, the angular distribution of the SSM W' boson has the form [66]

$$\frac{d\sigma}{d\cos\theta} \propto 1 + \cos^2\theta, \tag{3.14}$$

while the corresponding expression for the W^* boson is [66]

$$\frac{d\sigma}{d\cos\theta} \propto \cos^2\theta. \tag{3.15}$$

Combining eqs. (3.12) and (3.13) with these angular distributions and noting that

$$\cos^2\theta = 1 - \left(\frac{m_{\mathrm{T}}}{m_{W'}}\right)^2, \tag{3.16}$$

the m_{T} differential cross section takes the form

$$\frac{d\sigma}{dm_{\mathrm{T}}} \propto \frac{m_{\mathrm{T}}}{m_{W'}^2}\frac{\kappa + 1 - \left(\frac{m_{\mathrm{T}}}{m_{W'}}\right)^2}{\sqrt{1 - \left(\frac{m_{\mathrm{T}}}{m_{W'}}\right)^2}} \tag{3.17}$$

with $\kappa = 1$ for the SSM W' and $\kappa = 0$ for the W^*.

As noted in ref. [67], the difference between the angular distributions (3.14) and (3.15) leads to striking differences in the SSM W' and W^* experimental signatures. For the SSM W', the divergence in the expression (3.17) as m_{T} approaches $m_{W'}$ leads to the well known "Jacobian peak" in the m_{T} distribution close to the W' mass. For the W^*, on the other hand, the divergence is absent, and there is no such peak.

Fig. 3.5 shows the generator level m_{T} distributions resulting from W' and W^* production and leptonic decay with a W'/W^* mass of $1\,\mathrm{TeV}$. The difference between the SSM W' and

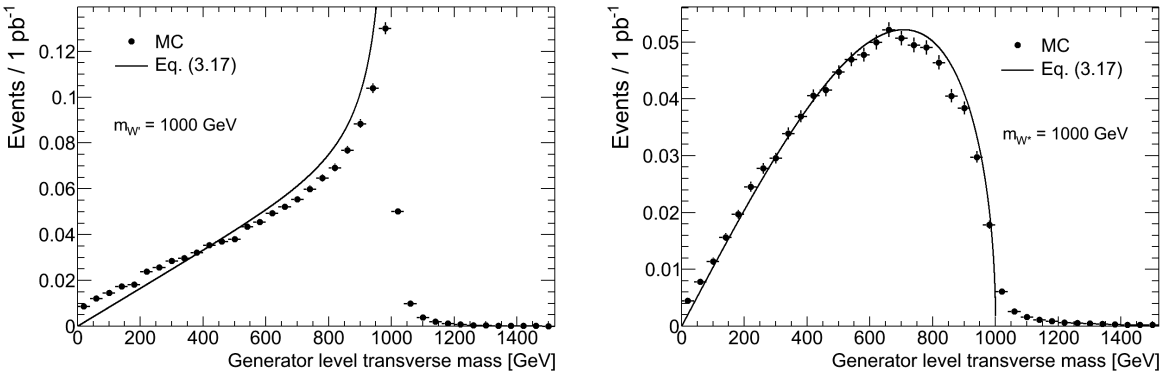

(a) (b)

Figure 3.5: Generator level transverse mass distributions for W' (a) and W^* (b) bosons of mass $1\,\mathrm{TeV}$. The points represent the distribution obtained from the signal MC samples, and the solid line corresponds to eq. (3.17) with the normalization fitted to the MC distribution below $m_{\mathrm{T}} = 800\,\mathrm{GeV}$.

the W^* distributions is clearly visible, with the pronounced Jacobian peak present in the SSM W' distribution, but not in the W^* distribution. Also shown is the distribution as obtained from eq. (3.17) with the normalization fitted to the MC distribution below $m_{\mathrm{T}} = 800\,\mathrm{GeV}$. It is interesting to note that this simple formula does such a good job describing the shape of the W^* m_{T} distribution below the boson mass of $1\,\mathrm{TeV}$. In the W' case, the formula reproduces roughly the shape of the m_{T} distribution below the boson mass of $1\,\mathrm{TeV}$, although this plot is clearly less convincing.

As we are considering W'/W^* production in pp collisions, both the assumptions leading to eq. (3.17) are violated: the W'/W^* is in general not produced on-shell and not at rest. Bearing this in mind, the agreement observed between the analytical result and the MC distributions in fig. 3.5 is surprisingly good. As it turns out, most of the shape mismatch in fig. 3.5(a) comes from low mass off-shell W' production which prevents the m_{T} distribution from vanishing at $m_{\mathrm{T}} = 0$. The same plots are shown in fig. 3.6 with the requirement that the invariant mass be above $700\,\mathrm{GeV}$, i.e. with the low mass off-shell production removed. In this case, eq. (3.17) describes the distribution well almost all the way up to $1\,\mathrm{TeV}$. To properly describe the behavior of the m_{T} distribution near the kinematical end-point $m_{\mathrm{T}} = m_{W'}$, one would need to account for the width of the W'/W^* boson.

We show finally the generator level m_{T} distributions for a selection of W' and W^* masses in fig. 3.7.

3.2.6 Interference

When calculating the (differential) cross section for a given hard scattering process, defined by a set of initial state and final state particles, the *Feynman amplitudes* corresponding to all Feynman diagrams connecting the initial and final state particles are added together. The observable (differential) cross section depends finally on the absolute square of the sum. For example, the hard scattering process $u\,\overline{d} \to e^+\,\nu_e$ is in the SM associated with the Feynman diagram of fig. 3.1(a) with the W boson replacing the W', and in an extended model with a heavy W' boson,

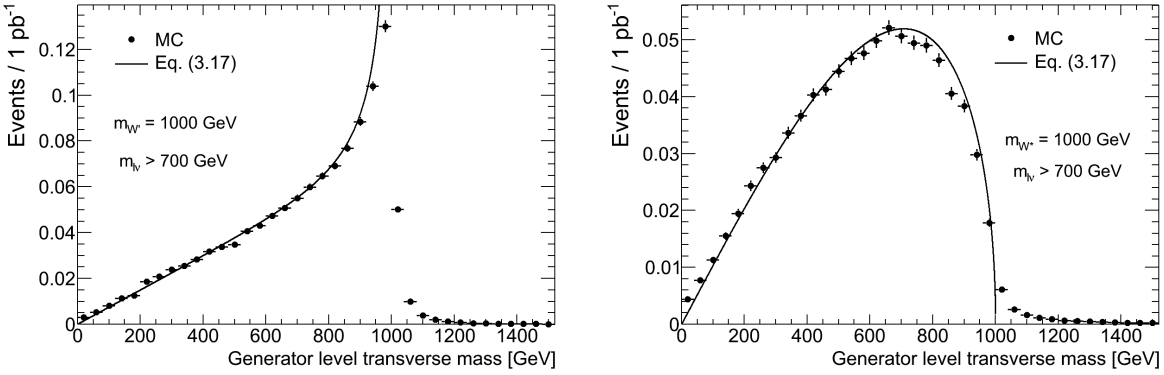

(a) (b)

Figure 3.6: Generator level transverse mass distributions for W' (a) and W^* (b) bosons of mass $1\,\mathrm{TeV}$ with a lower invariant mass cut of $700\,\mathrm{GeV}$. The points represent the distribution obtained from the signal MC samples, and the solid line corresponds to eq. (3.17) with the normalization fitted to the MC distribution below $m_{\mathrm{T}} = 800\,\mathrm{GeV}$.

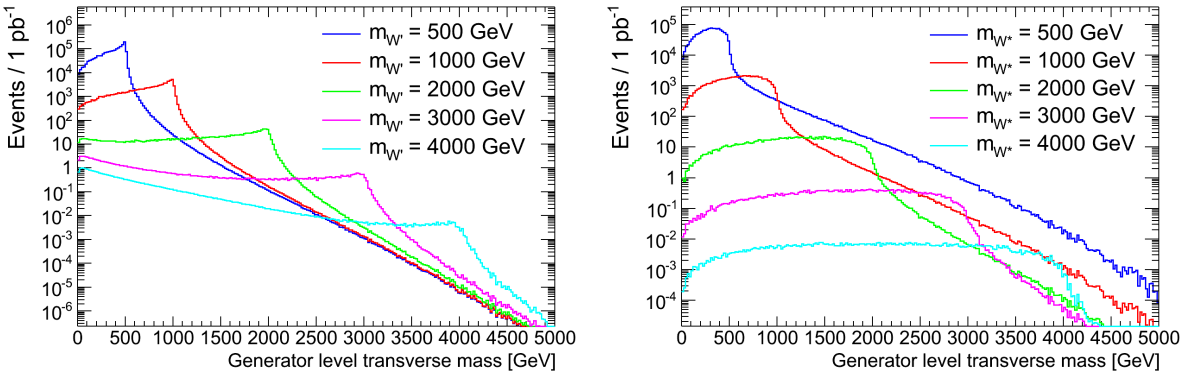

(a) (b)

Figure 3.7: Generator level transverse mass distributions for W' (a) and W^* (b) bosons of different masses.

the diagram of fig. 3.1(a) comes in addition. The hard scattering cross section is proportional to

$$|\mathcal{M}_W + \mathcal{M}_{W'}|^2 = |\mathcal{M}_W|^2 + |\mathcal{M}_{W'}|^2 + \mathcal{M}_W \mathcal{M}_{W'}^* + \mathcal{M}_W^* \mathcal{M}_{W'} \tag{3.18}$$

with $\mathcal{M}_W$ and $\mathcal{M}_{W'}$ as the Feynman amplitudes corresponding to the W and W' Feynman diagrams respectively. The two first terms correspond to the cross sections one would obtain in the presence of only the W boson or only the W' boson respectively, but the cross section in the presence of both particles is not simply the sum of these two. The remaining terms are called *interference terms*.

A W' boson with left-handed couplings to quarks and leptons (as the W boson) can lead to constructive (enhanced cross section) or destructive (reduced cross section) interference with the W boson in the invariant mass range between the W mass and the W' mass [68, 69]. The constructive or destructive nature of the interference depends on the relative sign of the W' couplings to quarks and leptons.

Interference with the W boson is not included in the PYTHIA SSM W' signal model, and is thus not considered in this analysis. As noted in ref. [70], the inclusion of interference makes a W' search more complicated both from a purely technical point of view (event generation can not trivially be performed for signal and backgrounds individually) and from the point of view of the statistical search interpretation (the new physics contribution is not necessarily positive). It is worth noting that CMS interpreted their 2012 data results [71] both in terms of the standard SSM scenario without interference and in terms of the corresponding model where the W' is allowed to interfere with the W. The mass limit is reported to improve wrt. the no interference scenario both in the case of constructive and destructive interference. The effect on the expected mass limit for the electron and muon channel combination is an increase from approximately $3.3\,\mathrm{TeV}$ in the no interference case to approximately $3.8\,\mathrm{TeV}$ in both the constructive and destructive interference cases.

3.3 Summary

In this chapter, the new charged, heavy boson signal has been presented. We have seen that such signal leads to an experimental signature with one lepton and missing transverse energy combining to form high transverse mass. A Jacobian peak is present in the transverse mass distribution in the case of a new gauge boson similar to the W boson, but not in the case of a different kind of spin-1 resonance known as the W^*.

A final state with one lepton and missing transverse energy combining to form high transverse mass can occur also within the Standard Model in the absence of new physics. The corresponding processes are *backgrounds* to our search, and in order to make a statement about the presence of new physics, we must first carefully evaluate the different backgrounds, which are introduced in the next chapter.

Chapter 4

Backgrounds to the one lepton and missing transverse energy final state

Having established that a potential signal from the production and leptonic decay of a new charged, heavy boson results in an experimental signature with one high p_{T} (charged) lepton and large missing transverse energy, we must consider all known processes resulting in such a final state, as they constitute background to the heavy boson search. The contribution of all backgrounds to the transverse mass spectrum must be examined, so that a potential *excess* over the background expectations can be established.

In this chapter, the various SM backgrounds to the one lepton and missing transverse energy final state are presented. Detailed information about MC samples are given only for the muon channel, as this channel is the main focus of this thesis. However, the same background processes are in general relevant also for the electron channel, and they are generated with the same generators as used in the muon channel.

4.1 The W boson

The (SM) W boson production and leptonic decay produces the one lepton and missing transverse energy ($\not{E}_{\mathrm{T}}$) final state with transverse masses predominantly in the Jacobian peak region around $80\,\mathrm{GeV}$. There is, however, a high mass off-shell production tail which covers in principle all of the kinematically allowed transverse masses, and thus contributes background to the search for a heavier boson. Production and leptonic decay of the W boson in pp collisions proceeds through exactly the same Feynman diagrams as that of the SSM W' boson, some of which are shown in fig. 3.1, although obviously with the W boson in place of the W'.

MC samples for the W background are generated at NLO with POWHEG BOX [72–74] using the CT10 NLO PDFs [75] interfaced to PYTHIA 8 with the AU2 tune for parton shower, hadronization, and underlying event. Both the muon and tau decay channels are used in the muon channel analysis, as the tau channel can contribute to the muon final state via the tau lepton's decay into a muon and two neutrinos, e.g. $\tau^- \rightarrow \mu^- \overline{\nu_\mu} \nu_\tau$. Samples are generated with different requirements on the lepton-neutrino invariant mass ($m_{l\nu}$) and the lepton p_{T} at the generator level in order to ensure sufficient statistics at high mass and high p_{T}. All MC samples are listed in table 4.1. For these and all other MC samples used in this analysis, final

state photon radiation from leptons is handled by PHOTOS.

Overlap between samples with different generator level requirements is removed by

- removing events with $p_{\mathrm{T}}^{\mu} > 100\,\mathrm{GeV}$ or $m_{l\nu} > 200\,\mathrm{GeV}$ from the $W \to \mu\,\nu$ unfiltered samples and
- removing events with $m_{l\nu} > 200\,\mathrm{GeV}$ from the $W \to \mu\,\nu\;p_{\mathrm{T}}$ filtered samples and the $W \to \tau\,\nu$ unfiltered samples.

The cross sections and numbers of events given in table 4.1 refer to the quantities before this overlap removal.

4.1.1 Higher order corrections

The W background MC samples are at NLO already from the POWHEG BOX event generator. The invariant mass differential cross section $d\sigma/dm_{l\nu}$ is further corrected to NNLO using an invariant mass dependent k-factor. The differential cross section is obtained at NNLO in QCD using ZWPROD [76] with the MSTW 2008 NNLO PDFs. Consistent results are obtained using Vrap [77] and FEWZ [78, 79]. Higher order electroweak corrections are obtained with mcsanc [80]. The QCD and electroweak corrections are assumed to factorize so that the final k-factor is the product of a QCD k-factor and an electroweak k-factor. The k-factor is derived separately for W^+ and W^-. Also the LO SSM W' signal samples are corrected to NNLO using the results of the ZWPROD calculations, but electroweak corrections beyond final state radiation are not included as these would require the specification of the complete gauge theory in which the W' arises.

PDF uncertainties on the NNLO differential cross section are evaluated from the MSTW 2008 NNLO eigenvector and α_s variations, both at 90% confidence level, following the prescription of ref. [81] for Hessian PDF sets and asymmetric errors. In addition, a scale uncertainty is evaluated from simultaneous variations of the factorization and renormalization scales of a factor 2 up or down from their nominal value, which is the invariant mass. The scale and PDF uncertainties are added in quadrature. Finally, the NNLO differential cross section is evaluated with different PDF choices, namely CT10 NNLO, NNPDF 2.3 NNLO [82], ABM11 5N NNLO [83], and HERAPDF 1.5 NNLO [84], all evaluated with the same choice of α_s as in the nominal MSTW 2008 NNLO case. If any of these PDFs provides a prediction falling outside the error band of the original MSTW 2008 NNLO prediction, the error band is extended to this prediction.

The final k-factor and its uncertainty are shown as function of the invariant mass in fig. 4.1, separately for the two charges and the W and SSM W' cases. In the case of the W, the k-factor at low mass is close to unity, meaning that additional corrections when going from NLO to NNLO are small. These corrections become significant at high invariant mass, where they reduce the differential cross section. For both the W and the SSM W', the uncertainties at high invariant mass are dominated by PDF uncertainties. Large differences are seen between the two charges at high invariant mass, in particular for the W'. These arise from the very large PDF uncertainties in this region combined with the fact that the two charges have different sensitivities to the various proton constituents. There is huge spread between the central values of different PDF choices in this region.

Process	Filter	Full/Fast	N_{evts}	σ_{gen}
$W^- \to \mu^- \overline{\nu_\mu}$	None	Full	$17.0 \cdot 10^6$	4.79 nb
$W^+ \to \mu^+ \nu_\mu$	None	Full	$23.0 \cdot 10^6$	6.89 nb
$W^- \to \mu^- \overline{\nu_\mu}$	$200 < m_{l\nu}/\text{GeV} < 500$	Fast	$45.0 \cdot 10^3$	1.45 pb
$W^+ \to \mu^+ \nu_\mu$	$200 < m_{l\nu}/\text{GeV} < 500$	Fast	$45.0 \cdot 10^3$	2.51 pb
$W^- \to \mu^- \overline{\nu_\mu}$	$500 < m_{l\nu}/\text{GeV} < 1500$	Fast	$45.0 \cdot 10^3$	34.2 fb
$W^+ \to \mu^+ \nu_\mu$	$500 < m_{l\nu}/\text{GeV} < 1500$	Fast	$45.0 \cdot 10^3$	76.7 fb
$W^- \to \mu^- \overline{\nu_\mu}$	$1500 < m_{l\nu}/\text{GeV} < 2500$	Fast	$45.0 \cdot 10^3$	99.8 ab
$W^+ \to \mu^+ \nu_\mu$	$1500 < m_{l\nu}/\text{GeV} < 2500$	Fast	$45.0 \cdot 10^3$	320 ab
$W^- \to \mu^- \overline{\nu_\mu}$	$2500 < m_{l\nu}/\text{GeV} < 3000$	Fast	$45.0 \cdot 10^3$	1.47 ab
$W^+ \to \mu^+ \nu_\mu$	$2500 < m_{l\nu}/\text{GeV} < 3000$	Fast	$44.0 \cdot 10^3$	4.37 ab
$W^- \to \mu^- \overline{\nu_\mu}$	$3000 < m_{l\nu}/\text{GeV} < 3500$	Fast	$44.0 \cdot 10^3$	0.213 ab
$W^+ \to \mu^+ \nu_\mu$	$3000 < m_{l\nu}/\text{GeV} < 3500$	Fast	$45.0 \cdot 10^3$	0.554 ab
$W^- \to \mu^- \overline{\nu_\mu}$	$m_{l\nu} > 3500\,\text{GeV}$	Fast	$45.0 \cdot 10^3$	0.0346 ab
$W^+ \to \mu^+ \nu_\mu$	$m_{l\nu} > 3500\,\text{GeV}$	Fast	$45.0 \cdot 10^3$	0.0774 ab
$W^- \to \mu^- \overline{\nu_\mu}$	$100 < p_{\text{T}}^{\mu}/\text{GeV} < 150$	Fast	$500 \cdot 10^3$	13.7 pb
$W^+ \to \mu^+ \nu_\mu$	$100 < p_{\text{T}}^{\mu}/\text{GeV} < 150$	Fast	$399 \cdot 10^3$	14.4 pb
$W^- \to \mu^- \overline{\nu_\mu}$	$150 < p_{\text{T}}^{\mu}/\text{GeV} < 200$	Fast	$99.0 \cdot 10^3$	2.17 pb
$W^+ \to \mu^+ \nu_\mu$	$150 < p_{\text{T}}^{\mu}/\text{GeV} < 200$	Fast	$100 \cdot 10^3$	2.26 pb
$W^- \to \mu^- \overline{\nu_\mu}$	$200 < p_{\text{T}}^{\mu}/\text{GeV} < 300$	Fast	$50.0 \cdot 10^3$	668 fb
$W^+ \to \mu^+ \nu_\mu$	$200 < p_{\text{T}}^{\mu}/\text{GeV} < 300$	Fast	$50.0 \cdot 10^3$	695 fb
$W^- \to \mu^- \overline{\nu_\mu}$	$p_{\text{T}}^{\mu} > 300\,\text{GeV}$	Fast	$10.0 \cdot 10^3$	105 fb
$W^+ \to \mu^+ \nu_\mu$	$p_{\text{T}}^{\mu} > 300\,\text{GeV}$	Fast	$10.0 \cdot 10^3$	117 fb
$W^- \to \tau^- \overline{\nu_\tau}$	None	Full	$2.99 \cdot 10^6$	4.79 nb
$W^+ \to \tau^+ \nu_\tau$	None	Full	$4.00 \cdot 10^6$	6.89 nb
$W^- \to \tau^- \overline{\nu_\tau}$	$200 < m_{l\nu}/\text{GeV} < 500$	Fast	$45.0 \cdot 10^3$	1.45 pb
$W^+ \to \tau^+ \nu_\tau$	$200 < m_{l\nu}/\text{GeV} < 500$	Fast	$45.0 \cdot 10^3$	2.51 pb
$W^- \to \tau^- \overline{\nu_\tau}$	$500 < m_{l\nu}/\text{GeV} < 1500$	Fast	$45.0 \cdot 10^3$	34.2 fb
$W^+ \to \tau^+ \nu_\tau$	$500 < m_{l\nu}/\text{GeV} < 1500$	Fast	$45.0 \cdot 10^3$	76.7 fb
$W^- \to \tau^- \overline{\nu_\tau}$	$1500 < m_{l\nu}/\text{GeV} < 2500$	Fast	$45.0 \cdot 10^3$	99.8 ab
$W^+ \to \tau^+ \nu_\tau$	$1500 < m_{l\nu}/\text{GeV} < 2500$	Fast	$45.0 \cdot 10^3$	320 ab
$W^- \to \tau^- \overline{\nu_\tau}$	$2500 < m_{l\nu}/\text{GeV} < 3000$	Fast	$45.0 \cdot 10^3$	1.47 ab
$W^+ \to \tau^+ \nu_\tau$	$2500 < m_{l\nu}/\text{GeV} < 3000$	Fast	$45.0 \cdot 10^3$	4.37 ab
$W^- \to \tau^- \overline{\nu_\tau}$	$3000 < m_{l\nu}/\text{GeV} < 3500$	Fast	$45.0 \cdot 10^3$	0.213 ab
$W^+ \to \tau^+ \nu_\tau$	$3000 < m_{l\nu}/\text{GeV} < 3500$	Fast	$45.0 \cdot 10^3$	0.554 ab
$W^- \to \tau^- \overline{\nu_\tau}$	$m_{l\nu} > 3500\,\text{GeV}$	Fast	$45.0 \cdot 10^3$	0.0346 ab
$W^+ \to \tau^+ \nu_\tau$	$m_{l\nu} > 3500\,\text{GeV}$	Fast	$45.0 \cdot 10^3$	0.0774 ab

Table 4.1: MC samples used for the W boson background. All samples are generated at NLO with POWHEG BOX using the CT10 NLO PDFs with PYTHIA 8 handling the parton shower, hadronization, and underlying event. The column labeled "Filter" gives the generator level cuts applied in the event generation. The column labeled "Full/Fast" indicates whether full or fast detector simulation has been used. The columns labeled "N_{evts}" and "σ_{gen}" contain respectively the numbers of generated events and the cross sections calculated by the generator.

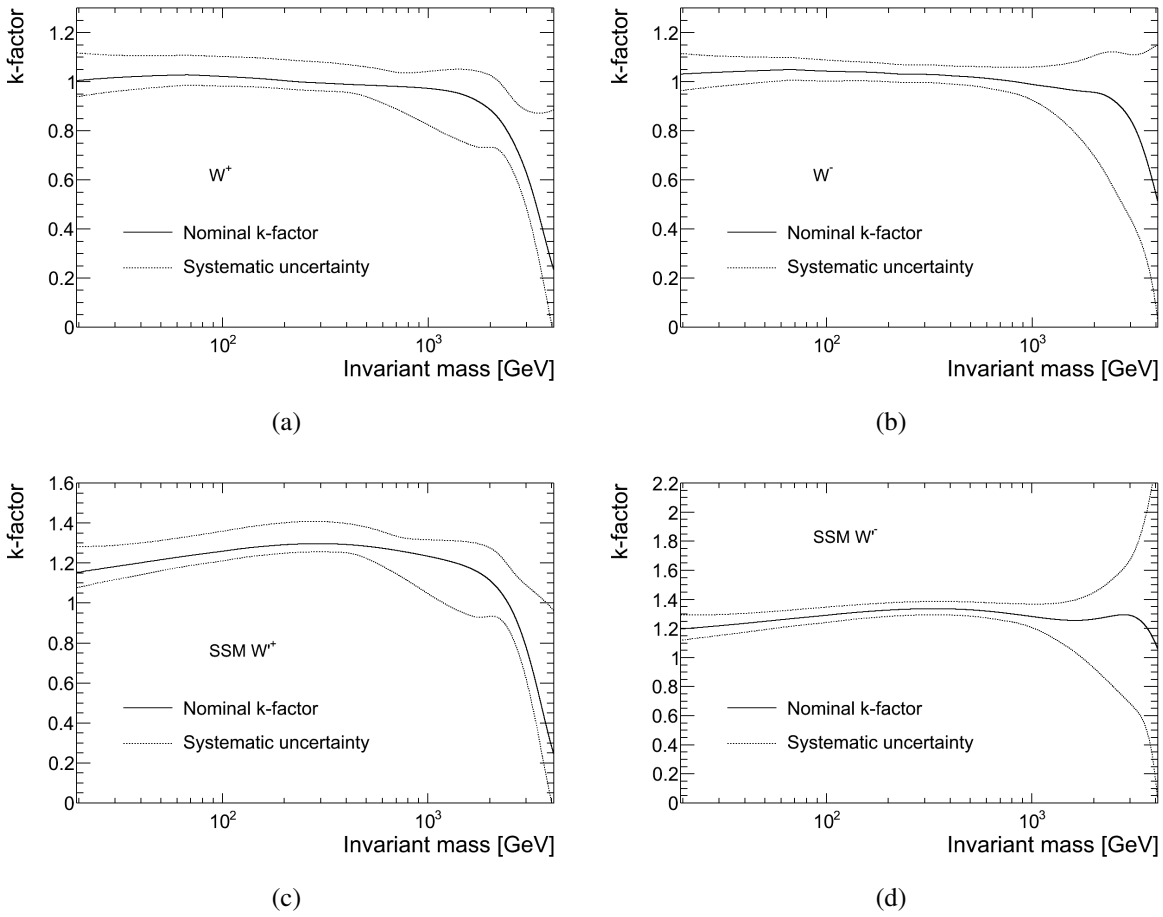

Figure 4.1: The final k-factor and its uncertainty as function of the invariant mass for the W^+ (a), the W^- (b), the SSM W'^+ (c), and the SSM W'^- (d). The SSM W' k-factors are LO to NNLO, while the W k-factors are NLO to NNLO. Higher order electroweak corrections are not taken into account for the SSM W'.

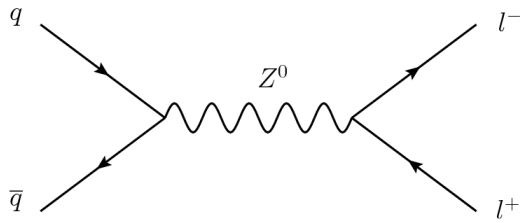

Figure 4.2: The most important Feynman diagram for Z boson production and leptonic decay in pp collisions.

4.2 The Z boson

Production of the Z boson and decay to the dilepton final state may constitute background to the one lepton and $\not{E}_{\mathrm{T}}$ final state if one of the leptons from the Z decay is not properly reconstructed. In particular, this is true in the muon channel, because a muon which is not identified as such will be absent from the $\not{E}_{\mathrm{T}}$ calculation, thus appearing as $\not{E}_{\mathrm{T}}$. With the other muon from the Z decay properly identified and measured, a high invariant mass $Z \to \mu^+ \mu^-$ event mimics very closely a high mass $W \to \mu \nu$ or $W' \to \mu \nu$ event. The same is not true for the electron channel, where the energy deposit of an electron which is not identified as such will still be present in the $\not{E}_{\mathrm{T}}$ calculation as a jet or a cluster. Hence, the $\not{E}_{\mathrm{T}}$ in $Z \to e^+ e^-$ events is in general small.

The most important lowest order Feynman diagram for Z boson production and leptonic decay is shown in fig. 4.2. Technically, this is a Feynman diagram for the neutral current Drell-Yan process, and the same Feynman diagram with the Z boson replaced by a photon also enters the calculation of the Drell-Yan differential cross section. Both the photon diagram and its interference with the Z diagram are included in the background samples used in this analysis, but the background is for simplicity referred to simply as the Z boson background. The Z boson provides the dominant contribution to the cross section at high invariant mass.

The Z boson background MC samples are listed in table 4.2. They are generated with POWHEG BOX using the CT10 NLO PDFs interfaced to PYTHIA 8 with the AU2 tune for parton shower, hadronization, and underlying event, exactly as the W background samples. As in the W boson case, samples are generated with different generator level cuts to improve statistics at high invariant mass and high p_{T}, and overlap between the samples is removed.

The Z boson background invariant mass differential cross section $d\sigma/dm_{ll}$ is corrected to NNLO using a set of invariant mass dependent k-factors which are derived following exactly the same methodology as in the W case.

4.3 The top quark

Being the heaviest particle of the SM with a mass of about $170\,\mathrm{GeV}$, the top quark is an obvious candidate background for searches involving high masses and high transverse momenta. It decays immediately to a W boson and a b quark, and contributes to leptonic final states predominantly when the W boson decays leptonically[1].

Top quarks can be pair produced in pp collisions via the strong interaction (see figs. 4.3 and 4.4). The production of single top quarks is also possible, but only via the weak interaction

[1]Final state jets in $t\bar{t}$ events may also give rise to lepton candidates. This is part of the jet background or "fake" lepton background which is estimated from the data.

Process	Filter	Full/Fast	N_{evts}	σ_{gen}
$Z \to \mu^+ \mu^-$	$m_{ll} > 60\,\text{GeV}$	Full	$9.99 \cdot 10^6$	1.11 nb
$Z \to \mu^+ \mu^-$	$250 < m_{ll}/\text{GeV} < 400$	Full	$99.9 \cdot 10^3$	549 fb
$Z \to \mu^+ \mu^-$	$400 < m_{ll}/\text{GeV} < 600$	Full	$99.9 \cdot 10^3$	89.7 fb
$Z \to \mu^+ \mu^-$	$600 < m_{ll}/\text{GeV} < 800$	Full	$100 \cdot 10^3$	15.1 fb
$Z \to \mu^+ \mu^-$	$800 < m_{ll}/\text{GeV} < 1000$	Full	$100 \cdot 10^3$	3.75 fb
$Z \to \mu^+ \mu^-$	$1000 < m_{ll}/\text{GeV} < 1250$	Full	$99.9 \cdot 10^3$	1.29 fb
$Z \to \mu^+ \mu^-$	$1250 < m_{ll}/\text{GeV} < 1500$	Full	$100 \cdot 10^3$	358 ab
$Z \to \mu^+ \mu^-$	$1500 < m_{ll}/\text{GeV} < 1750$	Full	$99.9 \cdot 10^3$	112 ab
$Z \to \mu^+ \mu^-$	$1750 < m_{ll}/\text{GeV} < 2000$	Full	$100 \cdot 10^3$	38.4 ab
$Z \to \mu^+ \mu^-$	$2000 < m_{ll}/\text{GeV} < 2250$	Full	$100 \cdot 10^3$	13.9 ab
$Z \to \mu^+ \mu^-$	$2250 < m_{ll}/\text{GeV} < 2500$	Full	$99.8 \cdot 10^3$	5.23 ab
$Z \to \mu^+ \mu^-$	$2500 < m_{ll}/\text{GeV} < 2750$	Full	$99.8 \cdot 10^3$	2.02 ab
$Z \to \mu^+ \mu^-$	$2750 < m_{ll}/\text{GeV} < 3000$	Full	$100 \cdot 10^3$	0.789 ab
$Z \to \mu^+ \mu^-$	$m_{ll} > 3000\,\text{GeV}$	Full	$99.7 \cdot 10^3$	0.504 ab
$Z \to \mu^+ \mu^-$	$100 < p_{\text{T}}^{\mu}/\text{GeV} < 150$	Fast	$1.40 \cdot 10^6$	8.55 pb
$Z \to \mu^+ \mu^-$	$150 < p_{\text{T}}^{\mu}/\text{GeV} < 200$	Fast	$300 \cdot 10^3$	1.36 pb
$Z \to \mu^+ \mu^-$	$200 < p_{\text{T}}^{\mu}/\text{GeV} < 300$	Fast	$99.0 \cdot 10^3$	428 fb
$Z \to \mu^+ \mu^-$	$p_{\text{T}}^{\mu} > 300\,\text{GeV}$	Fast	$20.0 \cdot 10^3$	70.7 fb
$Z \to \tau^+ \tau^-$	$m_{ll} > 60\,\text{GeV}$	Full	$5.00 \cdot 10^6$	1.11 nb
$Z \to \tau^+ \tau^-$	$250 < m_{ll}/\text{GeV} < 400$	Full	$20.0 \cdot 10^3$	549 fb
$Z \to \tau^+ \tau^-$	$400 < m_{ll}/\text{GeV} < 600$	Full	$19.9 \cdot 10^3$	89.7 fb
$Z \to \tau^+ \tau^-$	$600 < m_{ll}/\text{GeV} < 800$	Full	$20.0 \cdot 10^3$	15.1 fb
$Z \to \tau^+ \tau^-$	$800 < m_{ll}/\text{GeV} < 1000$	Full	$20.0 \cdot 10^3$	3.75 fb
$Z \to \tau^+ \tau^-$	$1000 < m_{ll}/\text{GeV} < 1250$	Full	$20.0 \cdot 10^3$	1.29 fb
$Z \to \tau^+ \tau^-$	$1250 < m_{ll}/\text{GeV} < 1500$	Full	$20.0 \cdot 10^3$	358 ab
$Z \to \tau^+ \tau^-$	$1500 < m_{ll}/\text{GeV} < 1750$	Full	$20.0 \cdot 10^3$	112 ab
$Z \to \tau^+ \tau^-$	$1750 < m_{ll}/\text{GeV} < 2000$	Full	$20.0 \cdot 10^3$	38.4 ab
$Z \to \tau^+ \tau^-$	$2000 < m_{ll}/\text{GeV} < 2250$	Full	$20.0 \cdot 10^3$	13.9 ab
$Z \to \tau^+ \tau^-$	$2250 < m_{ll}/\text{GeV} < 2500$	Full	$20.0 \cdot 10^3$	5.23 ab
$Z \to \tau^+ \tau^-$	$2500 < m_{ll}/\text{GeV} < 2750$	Full	$20.0 \cdot 10^3$	2.02 ab
$Z \to \tau^+ \tau^-$	$2750 < m_{ll}/\text{GeV} < 3000$	Full	$20.0 \cdot 10^3$	0.789 ab
$Z \to \tau^+ \tau^-$	$m_{ll} > 3000\,\text{GeV}$	Full	$20.0 \cdot 10^3$	0.504 ab

Table 4.2: MC samples used for the Z boson background. All samples are generated at NLO with POWHEG BOX using the CT10 NLO PDFs with PYTHIA 8 handling the parton shower, hadronization, and underlying event. The column labeled "Filter" gives the generator level cuts applied in the event generation. The column labeled "Full/Fast" indicates whether full or fast detector simulation has been used. The columns labeled "N_{evts}" and "σ_{gen}" contain respectively the numbers of generated events and the cross sections calculated by the generator.

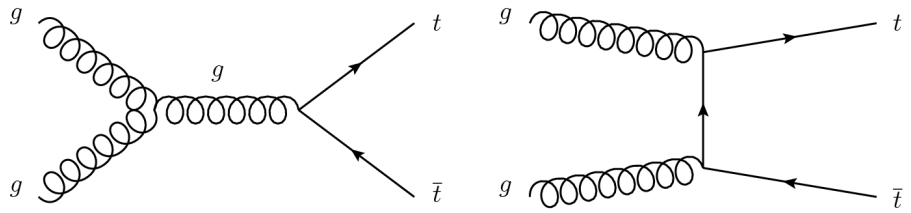

Figure 4.3: Feynman diagrams for the production of top quark pairs via the strong interaction.

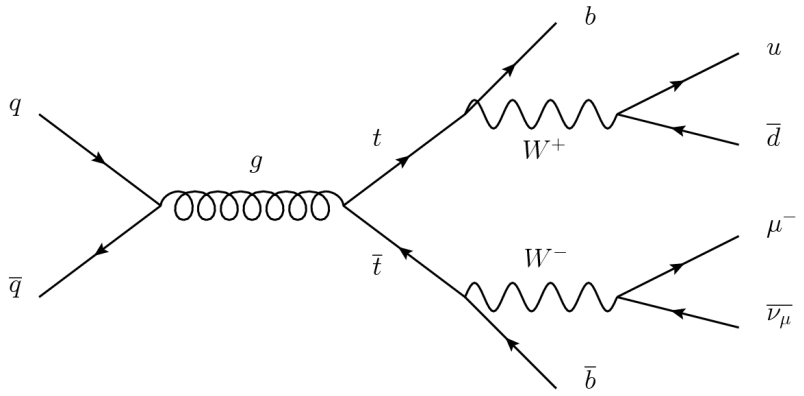

Figure 4.4: Feynman diagram for the production of a top quark pair via the strong interaction and subsequent decays leading to a final state with one muon.

(see fig. 4.5). When top quarks are pair produced, the possible contribution to the one lepton final state comes from events where one W boson decays leptonically and the other one hadronically. In such events the lepton is expected to be accompanied by significant jet activity, and $\not{E}_{\mathrm{T}}$ may arise from jet mismeasurements and neutrinos from weak interaction hadron decays within jets in addition to the neutrino from the W boson decay. Fig. 4.4 shows a Feynman diagram for the production of a top quark pair via the strong interaction and subsequent decays leading to a final state with one muon.

A top pair production MC sample with a filter requiring at least one lepton in the final state is generated using POWHEG BOX with the CT10 NLO PDFs and PYTHIA 6 [27] with the AUET2B tune [85] for the parton shower, hadronization, and underlying event. For single top production in the t-channel, AcerMC [86] and the CTEQ6L1 PDFs are used in combination with PYTHIA 6 and the AUET2B tune. Finally, the single top s-channel and $W + t$ associated production processes are generated with MC@NLO [87] and the CT10 NLO PDFs using HERWIG [88] for the parton shower and hadronization and Jimmy [89] for the underlying event. All top background MC samples are listed in table 4.3.

For normalization of the $t\bar{t}$ MC samples we make use of the cross section calculated with Top++, see ref. [90] and the references therein. For the single top samples, the cross sections are based on refs. [91–93]. All normalization cross sections are at NNLO, and are presented in table 4.4. The values given in the last column of table 4.3 correspond to these cross sections when a W boson leptonic branching fraction of 10.8% [1] (for each lepton generation) is taken into account. All cross sections were calculated for a top quark mass of $172.5\,\mathrm{GeV}$, and the uncertainties include a contribution from a $\pm 1\,\mathrm{GeV}$ variation of the mass.

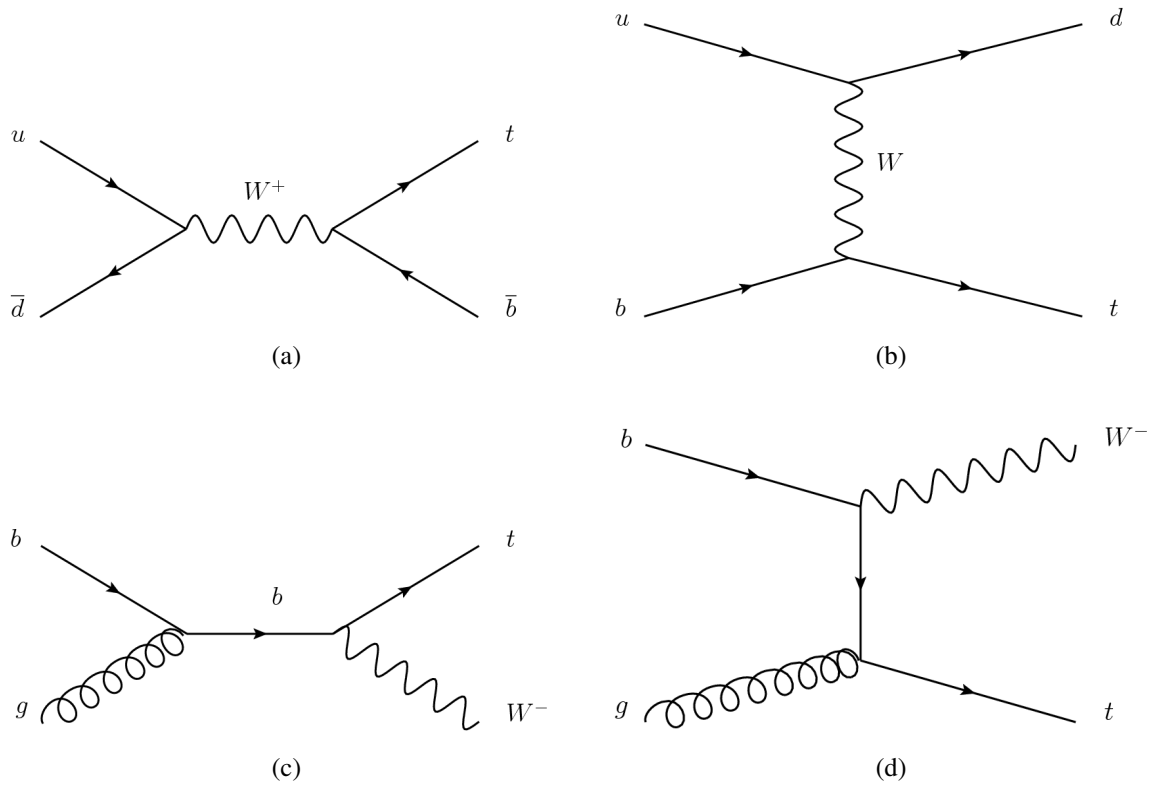

Figure 4.5: Feynman diagrams for single top production in the s-channel (a), the t-channel (b), and the $W+t$ associated production mode ((c) and (d)). The charge conjugate processes leading to antitop production are of course equally relevant.

Process	Generator	Full/Fast	N_{evts}	σ_{gen}	σ_{norm}
$t\bar{t} \to l + X$	POWHEG BOX + PYTHIA 6	Fast	$29.9 \cdot 10^6$	114 pb	137 pb
t-channel, $\mu + X$	AcerMC + PYTHIA 6	Full	$300 \cdot 10^3$	8.59 pb	9.48 pb
t-channel, $\tau + X$	AcerMC + PYTHIA 6	Full	$293 \cdot 10^3$	8.58 pb	9.48 pb
s-channel, $\mu + X$	MC@NLO + HERWIG	Full	$200 \cdot 10^3$	0.564 pb	0.606 pb
s-channel, $\tau + X$	MC@NLO + HERWIG	Full	$200 \cdot 10^3$	0.564 pb	0.606 pb
$W + t$ inclusive	MC@NLO + HERWIG	Full	$2.00 \cdot 10^6$	20.7 pb	22.4 pb

Table 4.3: MC samples used for the top background. The column labeled "Full/Fast" indicates whether full or fast detector simulation has been used. The columns labeled "N_{evts}" and "σ_{gen}" contain respectively the numbers of generated events and the cross sections calculated by the generators. Finally, the column σ_{norm} gives the cross sections used for the sample normalizations.

Process	Cross section [pb]
$t\bar{t}$ inclusive	253^{+15}_{-16}
t-channel inclusive	$87.8^{+3.5}_{-2.1}$
s-channel inclusive	$5.61^{+0.26}_{-0.25}$
$W + t$ inclusive	22.4 ± 1.6

Table 4.4: Cross sections and uncertainties for top pair production and single top production in pp collisions at $\sqrt{s} = 8\,\text{TeV}$ assuming a top mass of $172.5\,\text{GeV}$. The uncertainties include a contribution from a top mass variation of $\pm 1\,\text{GeV}$.

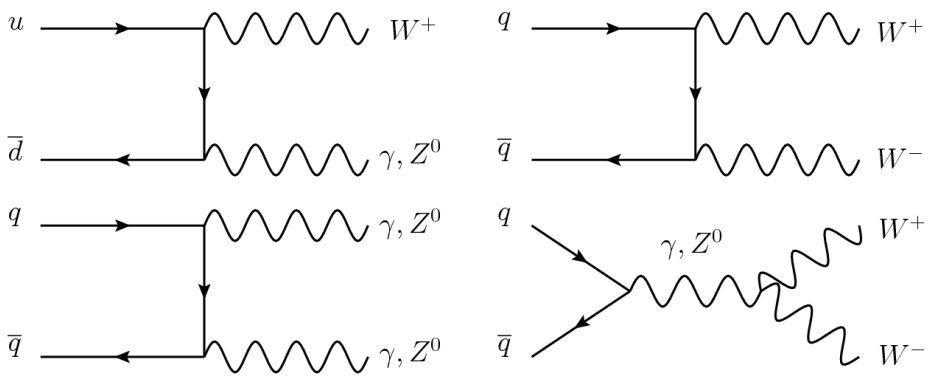

Figure 4.6: Feynman diagrams for diboson production in pp collisions.

Process	Full/Fast	N_{evts}	σ_{gen}	σ_{norm}
$W\,W \to l\,\nu\,l\,\nu$	Full	$2.59 \cdot 10^6$	5.28 pb	5.60 pb
$W\,Z \to l\,\nu\,l^+\,l^-$	Full	$2.70 \cdot 10^6$	9.75 pb	10.2 pb
$W\,Z \to l\,\nu\,\nu\,\overline{\nu}$	Full	$400 \cdot 10^3$	1.40 pb	1.47 pb
$Z\,Z \to l^+\,l^-\,l^+\,l^-$	Full	$3.80 \cdot 10^6$	8.74 pb	8.74 pb
$Z\,Z \to l^+\,l^-\,\nu\,\overline{\nu}$	Full	$900 \cdot 10^3$	0.496 pb	0.521 pb
$V\,V \to \mu^+\mu^-\,q\,q$	Full	$200 \cdot 10^3$	1.69 pb	1.69 pb
$V\,V \to \mu\,\nu\,q\,q$	Full	$918 \cdot 10^3$	8.77 pb	8.77 pb
$V\,V \to \tau^+\tau^-\,q\,q$	Full	$200 \cdot 10^3$	1.70 pb	1.70 pb
$V\,V \to \tau\,\nu\,q\,q$	Full	$918 \cdot 10^3$	8.78 pb	8.78 pb

Table 4.5: MC samples used for the diboson background. All samples are generated with SHERPA at LO with the inclusion of up to three QCD jets radiated off the initial and final state partons in the hard scattering process. The symbol V is used to represent either a W or Z boson. The column labeled "Full/Fast" indicates whether full or fast detector simulation has been used. The columns labeled "N_{evts}" and "σ_{gen}" contain respectively the numbers of generated events and the cross sections calculated by the generator. Finally, the column σ_{norm} gives the cross sections used for the sample normalizations.

4.4 Dibosons

More than one SM gauge boson may be produced in a single hard scattering interaction. Events where two SM gauge bosons are produced are referred to as diboson events. Depending on the decays of the bosons, such events can contribute to the one lepton and $\not{E}_{\text{T}}$ final state, e.g. via decays such as $W\,Z \to l\,\nu\,\nu\,\nu$ and $W\,Z \to l\,\nu\,q\,\overline{q}$. Some Feynman diagrams for diboson production in pp collisions are shown in fig. 4.6.

Diboson MC samples are generated with SHERPA [94] at LO with the inclusion of up to three QCD jets radiated off the initial and final state partons in the hard scattering process using the CT10 NLO PDFs. The samples are listed in table 4.5. In processes involving a Z boson, the corresponding contribution from the photon is taken into account in the event generation.

The normalization cross sections for all the samples not labeled "$VV \to X$" are corrected to NLO based on NLO cross sections calculated with MCFM [95] and the MSTW 2008 NLO PDFs. Relating the "$VV \to X$" samples to the MCFM cross sections is non-trivial, and for

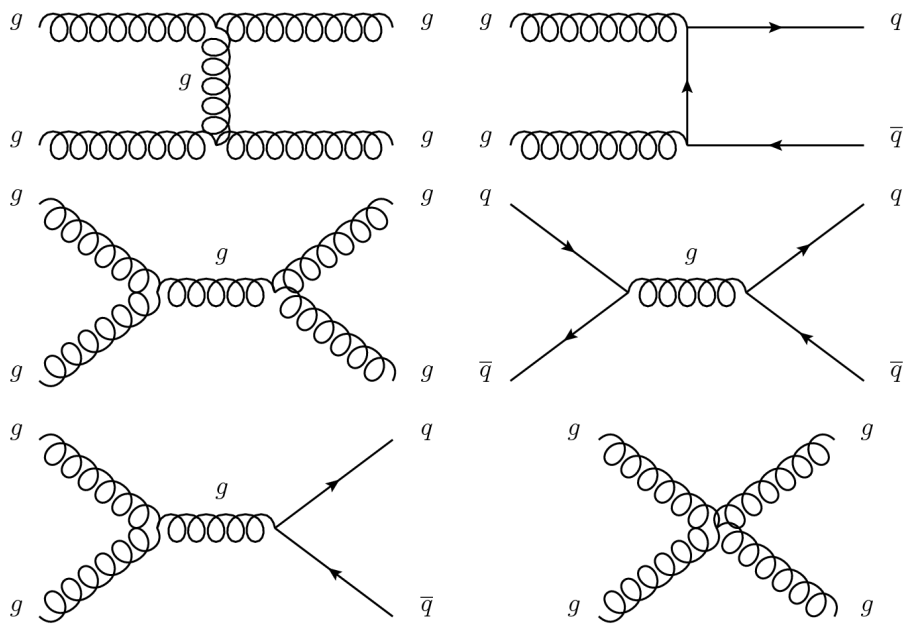

Figure 4.7: Feynman diagrams for dijet production in pp collisions via the strong interaction.

these samples the cross section calculated by SHERPA is used for normalization. As seen in table 4.5, the SHERPA cross sections are already close to the NLO corrected ones.

4.5 Jets

As briefly mentioned in section 1.6, quarks or gluons produced with high momentum in some interaction can give rise to a jet: a collimated "squirt" of particles, mainly hadrons. This is because of confinement – the strong force does not allow a quark or gluon to go off on its own, so the quarks and gluons produced in the interaction evolve into a set of colorless hadrons.

The production of jets in pp collisions proceeds mainly via the strong interaction, and has therefore a huge cross section. For example, the cross section for dijet production at $\sqrt{s} = 7\,\mathrm{TeV}$ is of the order of $1\,\mu\mathrm{b}$ with p_{T} cuts of $80\,\mathrm{GeV}$ and $60\,\mathrm{GeV}$ for the leading and subleading jet respectively and a jet rapidity cut of 2.8 [96]. With such huge cross sections, jet production may constitute an important background for searches involving leptons even though the probability for a given jet event to lead to a reconstructed lepton is small. Some Feynman diagrams for dijet production in pp collisions via the strong interaction are shown in fig. 4.7.

Real electrons and muons can originate from weak or electromagnetic interaction decays of the hadrons inside jets. The light mesons decay predominantly to muons, with branching fractions of 99.9% for $\pi^+ \to \mu^+ \nu_\mu$ and 64% for $K^+ \to \mu^+ \nu_\mu$ [1]. They are, however, pretty much stable over the time it takes them to traverse the ATLAS detector, and muons from pion and kaon decays are expected to be efficiently rejected by requiring hits in the pixel detector and requiring that the muon track points to the reconstructed primary vertex of the event. "Heavy flavor" mesons containing c and b quarks have significant branching fractions for electron and muon decays and characteristic decay lengths ($c\tau$) of the order of a few hundred $\mu\mathrm{m}$, and are thus candidate contributors to the jet background to lepton searches. Some Feynman diagrams

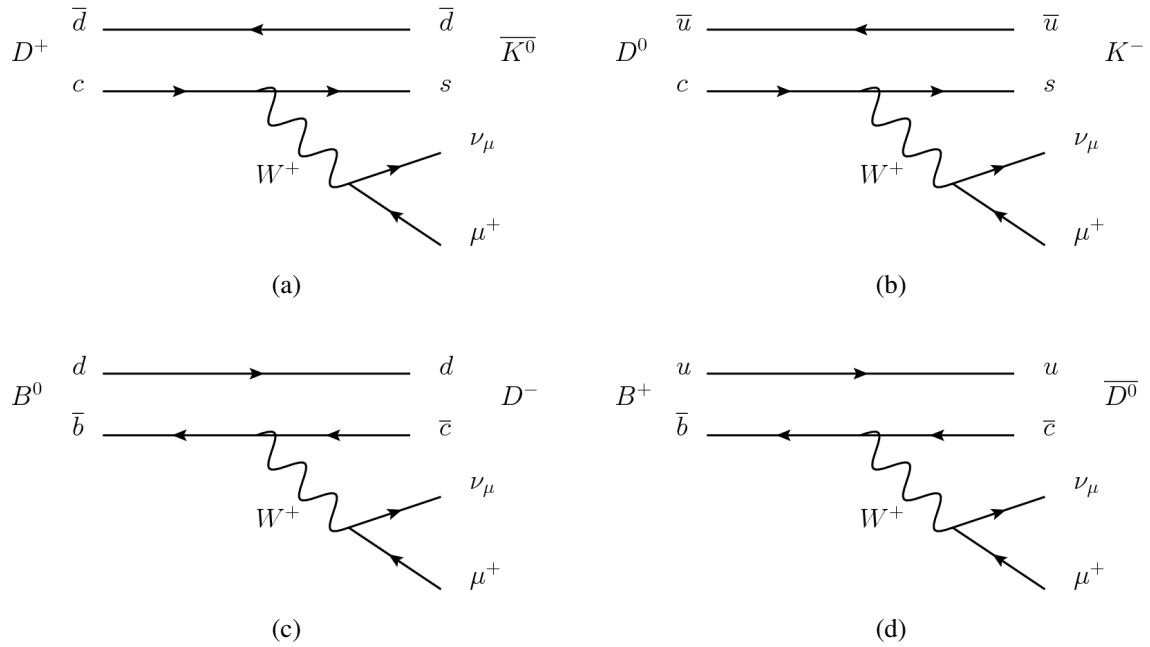

Figure 4.8: Feynman diagrams for heavy flavor meson decays to muons. The corresponding branching fractions from ref. [1] are 9% for (a), 3% for (b), and 2% for (c) and (d).

for heavy flavor meson decays are shown in fig. 4.8.

Fake electrons in jets can be reconstructed from EM calorimeter energy deposits and tracks, where the tracks are created by charged hadrons and the calorimeter deposits are created by charged hadrons or e.g. photons from the decay $\pi^0 \to \gamma\gamma$. While it is in principle possible to produce also fake muons because of hadrons penetrating all the way through the calorimeters, detailed jet background studies in ATLAS supersymmetry searches suggest that good ATLAS muon candidates originating from jet activity are mostly real muons [98]. In particular, it was found that a heavy flavor filtered jet MC sample with a lepton filter could reasonably well describe the jet background in the muon channel (see ref. [98], section C.2). The same was not true for the electron channel, suggesting that fake electrons are a significant contribution from the jet background in this channel.

Because of the huge cross section for jet production in pp collisions and difficulties describing the data properly with jet MC samples, the jet background is estimated from data in this analysis (see chapter 6).

4.6 Summary

We have in this chapter reviewed the different backgrounds to the search in the one lepton and missing transverse energy final state. Understanding the background is a crucial step in any search for new physics. The details of the MC generators used to model the different background processes have been given, and we have mentioned that a special approach will be used to estimate the jet background. Before we can proceed with the details of the jet background estimation in chapter 6, we need to introduce the event selection and review some data driven corrections which are applied to the MC samples. This will be done in the next

chapter, where we will also take a first look at how well the MC describes the data in relevant kinematical distributions.

Chapter 5

Event selection and initial data/MC comparisons

5.1 Data sample and integrated luminosity

The data used for this analysis were recorded with the ATLAS detector during the 2012 LHC run with pp collisions at an $8\,\mathrm{TeV}$ center of mass energy. They were recorded between April and December 2012, with instantaneous luminosities up to $7.6 \cdot 10^{33}\,\mathrm{cm}^{-2}\,\mathrm{s}^{-1}$ and with the average number of interactions per bunch crossing up to 36.

Only data passing a certain data quality selection, requiring that all detector systems were operating properly at the time of data taking, are used[1]. The integrated luminosity corresponding to these data quality requirements is determined to be $20.3\,\mathrm{fb}^{-1}$ with an associated 2.8% relative uncertainty derived following the methodology of ref. [99].

5.2 Event selection

Each event in both data and MC is required to have set off at least one of two triggers[2]:

- A trigger requiring matching tracks in the inner detector (ID) and muon spectrometer (MS) with an approximate p_{T} cut of $36\,\mathrm{GeV}$, and

- a trigger requiring a track in the MS barrel section with an approximate p_{T} cut of $40\,\mathrm{GeV}$.

Furthermore, the event is required to have at least one primary vertex reconstructed from at least three tracks located within $20\,\mathrm{cm}$ of the nominal interaction point along the beam axis. *The* primary vertex is defined to be the one with the highest sum of track p_{T}^2. So-called "jet cleaning" requirements are imposed to suppress the noise contribution to the missing transverse energy ($\not{E}_{\mathrm{T}}$) measurement by rejecting events containing jets with properties that suggest

[1] ATLAS internal readers may be interested in the exact data quality requirements, summarized by the Good Runs List (GRL) name: data12_8TeV.periodAllYear_DetStatus-v61-pro14-02_DQDefects-00-01-00_PHYS_StandardGRL_All_Good. In addition to the GRL requirement, the standard removal of corrupted events due to "LArError", "TileError", "Tile Trips" and "TTC restart" is performed.

[2] For ATLAS internal readers: the trigger names are EF_mu36_tight and EF_mu40_MSonly_barrel_tight.

significant noise contributions. The jet cleaning follows the recommendations of the ATLAS Jet/$\not\!\!E_{\mathrm{T}}$ working group, i.e. the "looser" selection documented in ref. [100].

STACO muons (see section 2.4.8) in the event are selected requiring:

- that the muon is combined, i.e. it must have matching tracks in the ID and MS,
- $p_{\mathrm{T}} > 20\,\mathrm{GeV}$,
- ID hits following the ATLAS Muon Combined Performance (MCP) recommendations (see section 5.2.1),
- transverse and longitudinal impact parameters $|d_0| < 0.2\,\mathrm{mm}$ and $|z_0| < 1.0\,\mathrm{mm}$ respectively wrt. the reconstructed primary vertex.

The event is required to have exactly one such muon. Furthermore, for this muon, it is required:

- $p_{\mathrm{T}} > 45\,\mathrm{GeV}$, ensuring that the triggers are fully effective,
- MS hits as detailed in section 5.2.1,
- that it is the one that triggered the event, i.e. that it fits with the measured parameters from the trigger system,
- that it is isolated,
- that the ID and MS momentum measurements are within 5σ of each other.

The last cut removes a few "outlier" events where something is obviously wrong with either the matching between ID and MS tracks or at least one of the ID and MS measurements. The isolation cut is based on the track activity in the region around the muon, and has the exact form

$$\sum_{\Delta R_{\mathrm{trk},\mu}<0.3} p_{\mathrm{T}}^{\mathrm{trk}} < 0.05\, p_{\mathrm{T}}^{\mu}. \tag{5.1}$$

The sum runs over all tracks with $p_{\mathrm{T}} > 1\,\mathrm{GeV}$ and $\Delta R < 0.3$ wrt. the muon, and the scaling of the isolation threshold with the muon p_{T} reduces potential efficiency losses for high p_{T} muons.

It is worth noting that, even if there is only one muon passing the full selection, the event is not accepted if there is an additional muon passing the cuts corresponding to the first set of bullets. This reduces the background from dimuon events, and is incidentally also advantageous for the data driven jet background estimate to be described in chapter 6.

Finally, a cut is imposed on the $\not\!\!E_{\mathrm{T}}$ of the event, $\not\!\!E_{\mathrm{T}} > 45\,\mathrm{GeV}$.

5.2.1 Muon hit requirements

The cuts that are imposed on the muon hits in the ID and MS are now described in detail. The ID hit requirements are:

- at least one hit in the pixel detector,
- at least 5 hits in the SCT detector,

- at most two holes in total for the pixel and SCT detectors,
- a successful TRT extension for muons within the pseudorapidity range $0.1 < |\eta| < 1.9$.

A hole means that the track crosses a working module which has not registered a hit. The muon track is said to have a "successful TRT extension" if there is at least 6 TRT hits of which at most 90% are identified as outliers.

The MS hit requirements are designed to provide a very robust momentum measurement. The muon is required to have

- at least three MDT hits in each of the inner, middle, and outer layers,
- no overlap between the barrel and end-caps (i.e. the muon is not allowed to have hits in both),
- at least one hit measuring the ϕ coordinate in at least two different layers.

In addition, muons with hits in certain chambers which are not linked to the optical alignment system are vetoed[3]. Muons with hits in the EE chambers and the CSCs (see fig. 2.14(b)) are also vetoed, with a corresponding loss of acceptance around the barrel-end-cap transition and at high $|\eta|$. This selection is slightly stricter than the default MCP recommendations for high p_{T} searches with the 2012 data, but this analysis is also particularly sensitive to mismeasurements, as the muon in the event also dominates the $\not{E}_{\mathrm{T}}$.

5.2.2 Treatment of the missing transverse energy

The strict muon selection requirements described in the past sections ensure that the muon momentum is measured as accurately as possible. Muons failing some of these requirements may, however, be included in the default $\not{E}_{\mathrm{T}}$ calculation. To ensure a consistent treatment, the $\not{E}_{\mathrm{T}}$ is corrected to include only the muon contribution from the muon in the event passing the full selection (there is only one such muon). The default muon contributions are removed from the $\not{E}_{\mathrm{T}}$, leaving a purely calorimeter based $\not{E}_{\mathrm{T}}$, and the contribution from the selected muon is added in:

$$\not{\mathbf{E}}_{\mathrm{T}} = \not{\mathbf{E}}_{\mathrm{T}}^{\mathrm{calo}} - (\mathbf{p}_{\mathrm{T}}^{\mu} - \mathbf{E}_{\mathrm{T}}^{\mu}). \tag{5.2}$$

Here, $\mathbf{E}_{\mathrm{T}}^{\mu}$ is the vector associated with the calorimeter deposit of the muon, which must be subtracted from the muon p_{T} to avoid double counting, as it is already part of the calorimeter term $\not{\mathbf{E}}_{\mathrm{T}}^{\mathrm{calo}}$. Its magnitude is taken from a parametrization of the muon's calorimeter energy loss, and it constitutes a negligible correction to the $\not{E}_{\mathrm{T}}$ of the order of a few GeV. We refer to the pure calorimeter term $\not{\mathbf{E}}_{\mathrm{T}}^{\mathrm{calo}}$ as the calorimeter $\not{E}_{\mathrm{T}}$.

5.2.3 Cut flows for signal MC samples

The effect of the event selection on potential heavy boson signal is here presented in the form of cut flow tables. Cuts are applied in the order used for cut flow comparisons within the W' analysis team. All numbers are event counts, i.e. each event is only counted once even if more

[3]For ATLAS internal readers: These are the so-called BIS7 and BIS8.

Cut	$m_{W'} = 500\,\mathrm{GeV}$	$m_{W'} = 1000\,\mathrm{GeV}$	$m_{W'} = 3000\,\mathrm{GeV}$
Truth muon decay	59912	59728	59752
Trigger	40948	41562	37954
Primary vertex	40667	41292	37689
Jet cleaning	40538	41162	37546
Combined muon	39255	39526	35723
$p_{\mathrm{T}} > 45\,\mathrm{GeV}$	38731	39263	34723
ID hits	38668	39182	34662
$\lvert d_0 \rvert < 0.2\,\mathrm{mm}$	38654	39173	34654
$\lvert z_0 \rvert < 1.0\,\mathrm{mm}$	37918	38550	34042
MS hits	27973	29939	25964
Trigger matching	27798	29744	25747
Isolation	27376	29366	25419
Exactly one tight muon	27376	29366	25419
Exactly one loose muon	27367	29346	25409
$\not{E}_{\mathrm{T}} > 45\,\mathrm{GeV}$	27054	29249	24977
ID/MS consistency	26916	29124	24837
Final cut efficiency	45%	49%	42%

Table 5.1: Cut flows for the "fixed mass" SSM W' signal MC samples. The final cut efficiency quoted in the last row is simply the last event count divided by the first one, and does not include the corrections described in sections 5.3.1-5.3.3.

than one muon passes the relevant cuts. The "loose" muons referred to in the tables are those passing the cuts listed in the first set of bullets on page 98, while the "tight" muons are required to pass all cuts up to the relevant row in the tables.

Tables 5.1 and 5.2 show cut flows for the "fixed mass" W' and W^* signal MC samples respectively. The final cut efficiency is seen to be about 40% for W^* and 40-50% for the SSM W', with most of the loss in both cases occuring at the trigger cut and at the MS hits cut.

5.3 Corrections to the MC samples

The signal and background MC samples are corrected to better describe the data. In this section, the different corrections are reviewed.

5.3.1 Primary vertex z position reweighting

The MC samples used in this analysis were generated with a wider beam spot than that of the data. Therefore, the z coordinate of the primary vertex has a wider distribution in MC than in data and the MC is reweighted back to the data distribution. The weights are derived by matching the generator level hard scattering vertex z position distribution in MC to the distribution of the position of the reconstructed primary vertex in data.

Fig. 5.1 shows the effect of the reweighting on the distribution of the z position of the reconstructed primary vertex in the $W^+ \to \mu^+ \nu_\mu$ unfiltered MC sample. The reweighted MC distribution is seen to reproduce closely the distribution in data.

Cut	$m_{W^*} = 500\,\text{GeV}$	$m_{W^*} = 1000\,\text{GeV}$	$m_{W^*} = 3000\,\text{GeV}$
None	20000	20000	20000
Trigger	12504	13578	13968
Primary vertex	12412	13479	13874
Jet cleaning	12371	13422	13824
Combined muon	12017	12922	12886
$p_{\text{T}} > 45\,\text{GeV}$	11833	12866	12835
ID hits	11806	12841	12818
$\lvert d_0 \rvert < 0.2\,\text{mm}$	11805	12838	12815
$\lvert z_0 \rvert < 1.0\,\text{mm}$	11592	12620	12573
MS hits	8041	8625	8439
Trigger matching	7978	8525	8270
Isolation	7858	8425	8229
Exactly one tight muon	7858	8425	8229
Exactly one loose muon	7854	8418	8224
$\not{E}_{\text{T}} > 45\,\text{GeV}$	7715	8396	8224
ID/MS consistency	7675	8353	8194
Final cut efficiency	38%	42%	41%

Table 5.2: Cut flows for the "fixed mass" W^* signal MC samples. The final cut efficiency quoted in the last row is simply the last event count divided by the first one, and does not include the corrections described in sections 5.3.1-5.3.3.

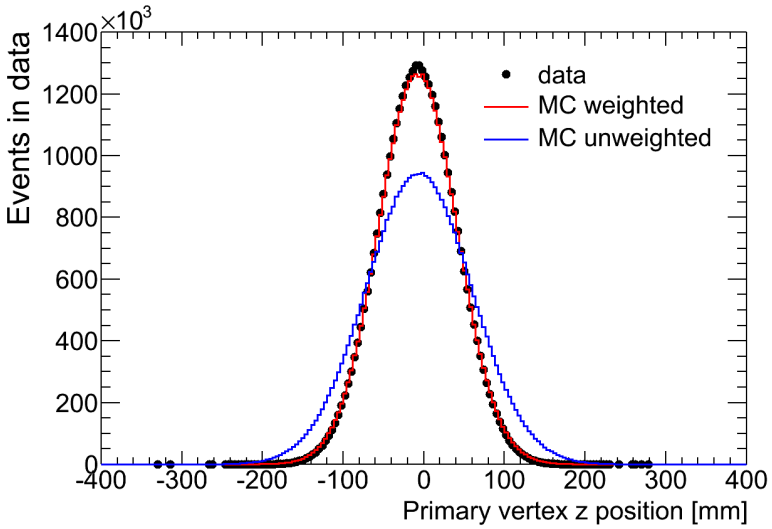

Figure 5.1: The effect of primary vertex z position reweighting on the $W^+ \to \mu^+ \nu_\mu$ unfiltered MC sample in terms of the z position of the reconstructed primary vertex. The MC distributions are normalized to the data for a pure shape comparison.

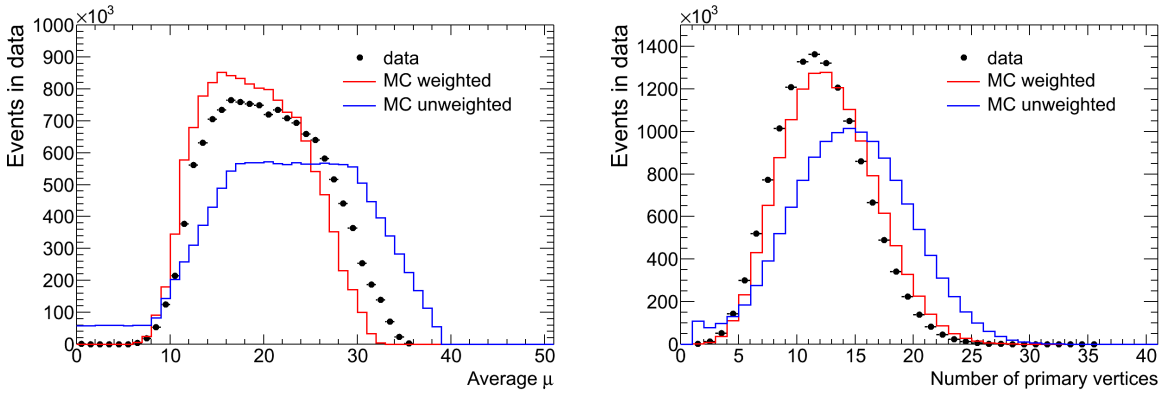

(a) (b)

Figure 5.2: The effect of pile-up reweighting on the $W^+ \to \mu^+ \nu_\mu$ unfiltered MC sample in terms of the average number of interactions per bunch crossing $\langle\mu\rangle$ (a) and the number of reconstructed primary vertices with at least two tracks (b). The MC distributions are normalized to the data for a pure shape comparison.

5.3.2 Pile-up reweighting

The ATLAS MC samples are produced with a distribution of the average number of interactions per bunch crossing $\langle\mu\rangle$ which is meant to reflect the distribution in data. However, the MC is usually produced before or during the data taking, and the exact final distribution of $\langle\mu\rangle$ in data is not known. Furthermore, even if the MC is produced after the data taking is finished, different analyses may use different subsets of the data with different pile-up conditions. Hence, the distribution of $\langle\mu\rangle$ needs to be corrected to match the data using event weights.

In fact, the pile-up reweighting is also used to correct for data/MC differences in the minimum bias vertex multiplicity by systematically mismatching the data and MC $\langle\mu\rangle$ distributions by a suitable amount. In this analysis, the relation $\langle\mu\rangle_{\text{data}} = 1.09\,\langle\mu\rangle_{\text{MC}}$ is enforced as recommended by the ATLAS ID tracking performance group[4].

Fig. 5.2 shows the effect of pile-up reweighting on the $W^+ \to \mu^+ \nu_\mu$ unfiltered MC sample. The effect on the $\langle\mu\rangle$ distribution is shown in fig. 5.2(a), and it is clear that the weighted MC distribution displays the intentional mismatch with data. The effect on the number of reconstructed primary vertices with at least two tracks is shown in fig. 5.2(b). Clearly, the pile-up reweighting improves the agreement in this variable, but perfect agreement cannot be expected because the wider beam spot in MC than in data means that nearby vertices are more likely to be reconstructed together as one vertex in data than in MC. Hence, there should be on average more primary vertices in MC than in data, and forcing a match in the number of primary vertices would lead to a mismatch in the actual pile-up event activity.

5.3.3 Muon efficiency corrections

The muon reconstruction efficiency has been measured in data by the MCP group using the tag and probe technique on Z, J/ψ, and Υ decays (see also section 6.3.1). It was measured as

[4] ATLAS internal readers, see `https://twiki.cern.ch/twiki/bin/viewauth/AtlasProtected/InDetTrackingPerformanceGuidelines`

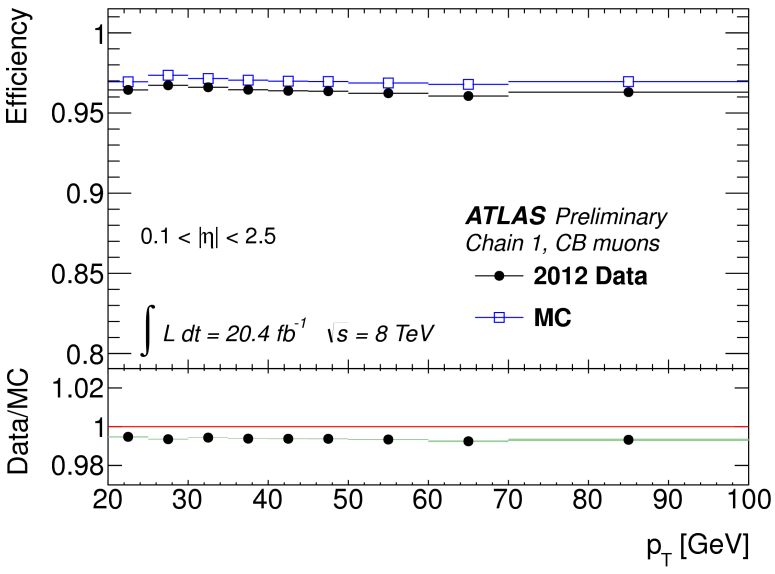

Figure 5.3: The measured muon reconstruction efficiency as function of p_{T} in data compared to the corresponding MC estimate. The ratio in the panel below the plot is the correction weight which is applied to the MC averaged over the considered range of η, and is seen to be close to unity. The plot is taken from ref. [101], where "Chain 1" is used to refer to STACO muons and "CB" means combined.

function of η and p_{T}, and MC was found to reproduce the data very well [101]. A set of event weights is used to correct the MC for the small data/MC disagreement. The muon selection used in this analysis is stricter than the selection used in ref. [101], for which the corrections were derived. The effect of the additional requirements in this analysis is effectively to exclude certain η regions, and the corrections derived in ref. [101] are therefore applicable as they are η dependent.

A corresponding set of trigger efficiency correction weights is also derived and applied to the MC. These are derived for the exact muon selection and trigger requirements used in this analysis.

Fig. 5.3 shows the measured reconstruction efficiency as function of p_{T} in data compared to the corresponding MC estimate. The ratio in the panel below the plot is the correction weight which is applied to the MC averaged over the considered range of η. The mismatch between the efficiencies in data and MC is seen to be very small, and the efficiency corrections have therefore a marginal impact on final results. The same is true for the trigger efficiency correction, although a plot corresponding to fig. 5.3 has not been made public by ATLAS.

5.3.4 Muon momentum corrections

The muon momentum resolution and scale have also been studied in data [101]. Corrections have been derived to correct the MC by smearing and scaling the muon momentum to match the observed distributions in data. Fig. 5.4 shows the effect of the smearing for the $W^+ \to \mu^+ \nu_\mu$ unfiltered MC sample and for the "fixed mass" $m_{W'} = 3\,\mathrm{TeV}$ W' sample with a p_{T} cut of $500\,\mathrm{GeV}$. The results of varying the amount of smearing within its associated uncertainty are also shown. The high p_{T} cut for the W' sample is imposed to study the smearing for high p_{T} muons without contamination from low p_{T}. Distributions for the $W^- \to \mu^- \overline{\nu_\mu}$ unfiltered MC sample are almost identical to the ones for the $W^+ \to \mu^+ \nu_\mu$ sample and are therefore not shown.

For the W' high p_{T} sample, the effect of smearing is shown in terms of the charge-to-momentum ratio q/p, which is proportional to the measured track sagitta and therefore better

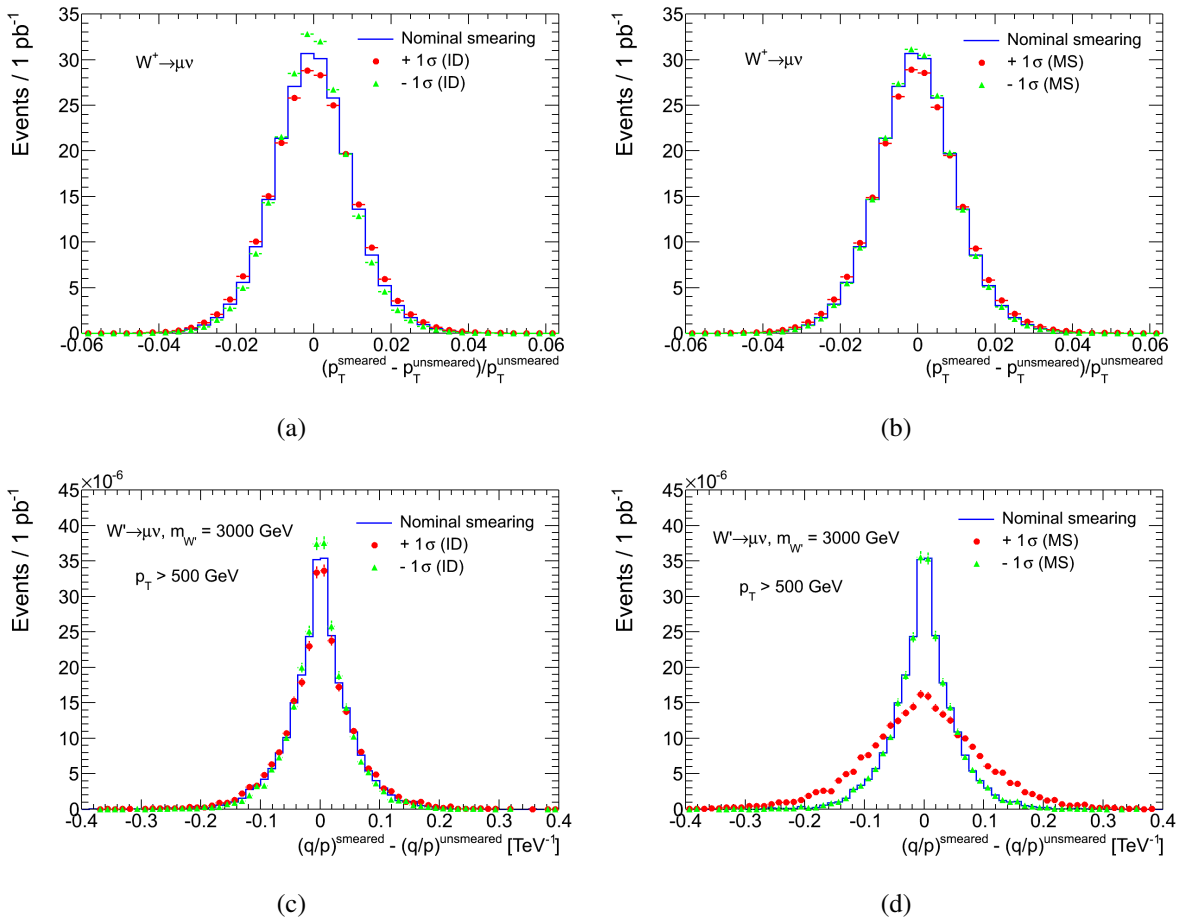

Figure 5.4: The effect of the muon momemtum smearing for the $W^+ \to \mu^+ \nu_\mu$ unfiltered MC sample ((a) and (b)) and for the "fixed mass" W' sample with a W' mass of $3\,\mathrm{TeV}$ and a p_T cut of $500\,\mathrm{GeV}$ ((c) and (d)). The results of varying the amount of smearing within its associated uncertainty are also shown, with ID variations in (a) and (c) and MS variations in (b) and (d).

described by a Gaussian distribution than the momentum itself. The plots look qualitatively the same in terms of q/p_T. For the $W^+ \to \mu^+ \nu_\mu$ MC sample, the relative amount of smearing is smaller and even the momentum itself is well described by a Gaussian distribution. The effect of smearing on this sample is therefore shown in terms of the p_T itself, although the plots look qualitatively the same in terms of q/p_T. The effects of smearing the ID and MS momenta are shown separately. The uncertainty on the MS smearing is seen to have the most significant impact on the W' sample and is therefore expected to give the most important contribution to the resolution uncertainty for this analysis.

5.4 Initial data/MC comparisons

With all MC corrections in place, we proceed by comparing the MC predictions to data for some important distributions. One should note that comparisons at this point are done without any estimate of the jet background. The contribution labeled "Top" is the sum of the $t\bar{t}$ and single top MC samples.

Fig. 5.5 shows the muon η and ϕ distributions at final selection. The W boson is seen to be

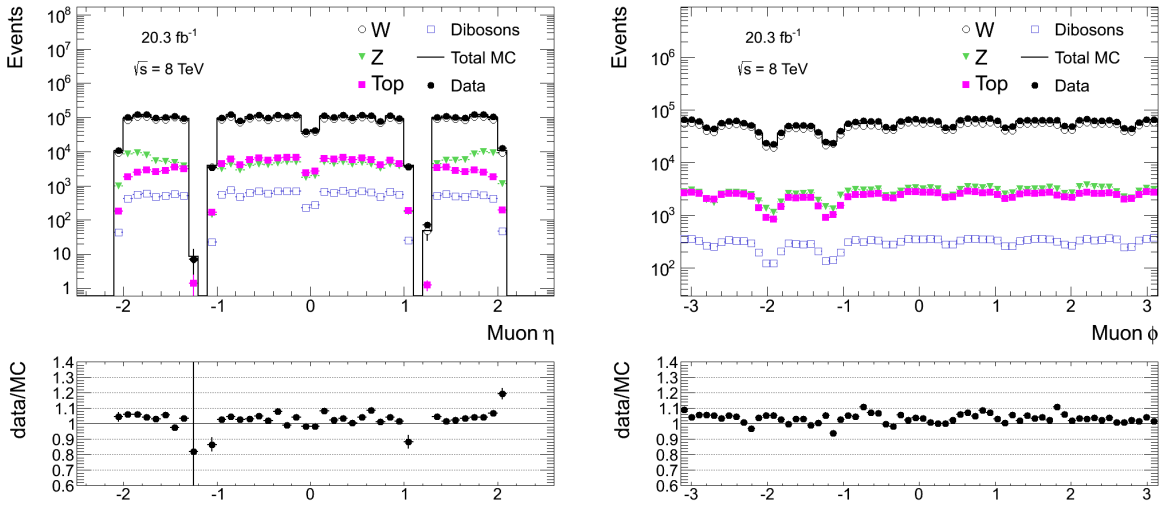

(a) (b)

Figure 5.5: The muon η (a) and ϕ (b) distributions at final selection. The MC predictions with all corrections applied are shown as well as data. The ratio of data to the total MC prediction is shown in the panel below each plot with error bars reflecting the statistical uncertainty of the data and MC.

by far the dominant background. The data/MC ratio is already close to unity, suggesting that the additional contribution from the jet background is not large. The "holes" in the η distribution (fig. 5.5(a)) for $|\eta|$ slightly above 1 result from the veto on barrel-end-cap overlap in the muon selection. Furthermore, the dip around $\eta = 0$ reflects a loss of acceptance for the most central muons because of a gap in MS coverage which allows services to the solenoid magnet, the calorimeters, and the ID. In the ϕ distribution, regular dips are seen which reflect the sector structure of the MS, and the somewhat more pronounced dips at $\phi \approx -1.2$ and $\phi \approx -2$ correspond to the feet of the detector.

The muon p_{T} and $\not\!\!E_{\mathrm{T}}$ distributions are shown in fig. 5.6, and reasonable agreement is observed between data and the total MC prediction also in these variables. Some overall excess of data over MC is seen, which could be due to the missing jet background contribution. Finally, the calorimeter $\not\!\!E_{\mathrm{T}}$ (see section 5.2.2) and m_{T} distributions are shown in fig. 5.7. The calorimeter $\not\!\!E_{\mathrm{T}}$ distribution shows reasonable agreement between data and MC, with a relatively flat data/MC ratio. In the m_{T} distribution, it is clear that something is missing at the low end, and we expect this to be the jet background. It seems also that the background, even without the jet contribution, is somewhat overestimated at high m_{T}.

Even though results at this point hint that the jet background is probably quite small, a careful evaluation of this background is necessary. While its overall contribution appears to be small, we already suspect that it makes a significant contribution at low m_{T}, and the results of a search for new physics at high m_{T} would hardly be trustworthy if good understanding of the background in the low m_{T} region could not be demonstrated. Furthermore, a complete picture of all contributing backgrounds is necessary in order to reveal potential problems with the normalization of the MC backgrounds.

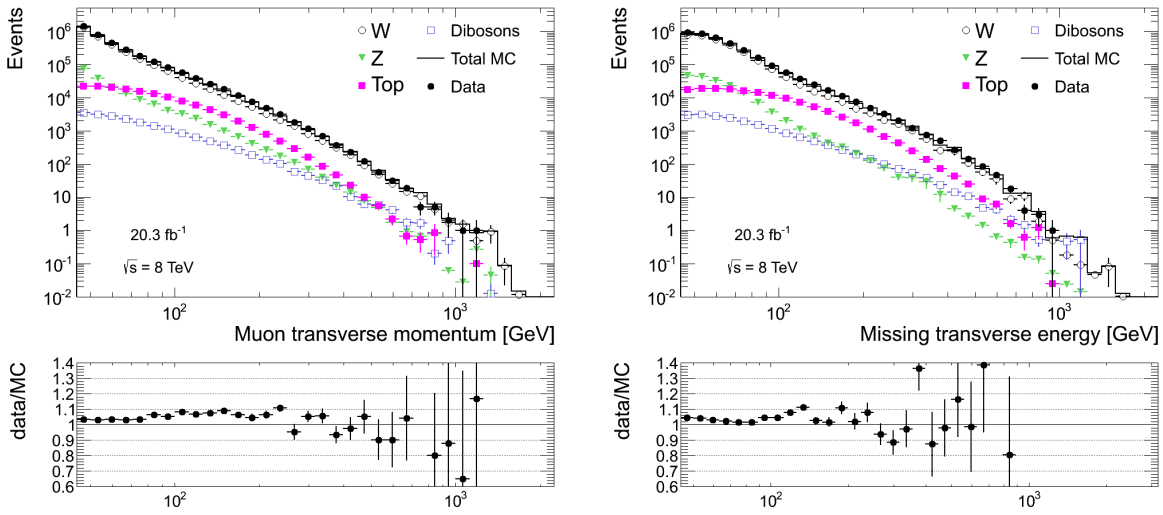

(a) (b)

Figure 5.6: The muon p_{T} (a) and $\not{E}_{\mathrm{T}}$ (b) distributions at final selection. The MC predictions with all corrections applied are shown as well as data. The ratio of data to the total MC prediction is shown in the panel below each plot with error bars reflecting the statistical uncertainty of the data and MC.

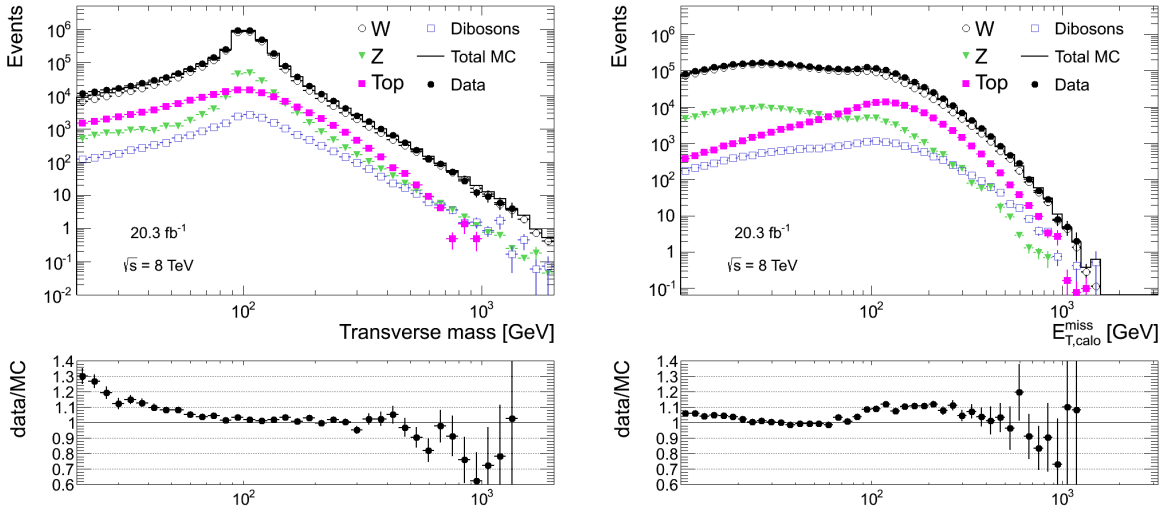

(a) (b)

Figure 5.7: The m_{T} (a) and calorimeter $\not{E}_{\mathrm{T}}$ (b) distributions at final selection. The MC predictions with all corrections applied are shown as well as data. The ratio of data to the total MC prediction is shown in the panel below each plot with error bars reflecting the statistical uncertainty of the data and MC.

5.5 Summary

In this chapter, the muon channel event selection has been introduced, as well as various corrections to the MC samples. We have taken a first look at important kinematical distributions, which are already looking very promising in terms of data/MC agreement. A clear trend is seen in the data/MC ratio in the very low transverse mass region, which we expect to be due to the jet background which is at this point not included. In the next chapter, we proceed with a description of the data driven estimation of this background.

Chapter 6

Data driven jet background estimate

6.1 Introduction

Because of the huge cross section for jet production in pp collisions, typical jet MC samples correspond only to a small fraction of the integrated luminosity of the data, and would therefore need to be scaled up by huge factors in order to be used for background estimation. Such scaling introduces large statistical uncertainties. Furthermore, the probability for a jet event to pass a typical lepton channel event selection may depend on the details of the parton shower and/or hadronization models in the event generators. In the analysis of the very early ATLAS data, it was already clear that jet MC samples did not describe the data satisfactory, and many ATLAS analyses have been relying on data driven jet background estimates.

This chapter describes the estimation of the jet background in the muon channel using the Matrix Method. The idea of the method is simple: Consider some lepton quality cut that is imposed in order to reduce the jet background in a lepton search. We expect leptons (or rather, *lepton candidates*) that originate from jets to have a low probability to pass such a cut, while prompt leptons from e.g. W or Z decays or potential signal should have a high probability to pass the cut. When applying the cut to data, there will be a corresponding reduction of the number of events reflecting the data's composition in terms of jets and prompt leptons. If the data is mostly jet events, a large fraction of the data events should be removed by the cut. Correspondingly, if the data is mostly consisting of prompt leptons, few events should be removed by the cut. Thus, by looking at the effect of the cut on the data, one can get an idea of the jet background content.

We will consider the isolation cut in our application of the Matrix Method, and we therefore show a plot of the normalized track based isolation variable $\sum_{\Delta R_{\mathrm{trk},\mu}<0.3} p_{\mathrm{T}}^{\mathrm{trk}}/p_{\mathrm{T}}^{\mu}$ in fig. 6.1. The distribution is considered right before the application of the isolation cut in the muon selection. We see that the muons selected from the MC samples tend to have very small values of the normalized isolation variable, but that a large number of events with rather high values is present in data. These events come from the jet background which we want to estimate. As a reminder, the cut value on the normalized isolation for the baseline muon selection is 0.05.

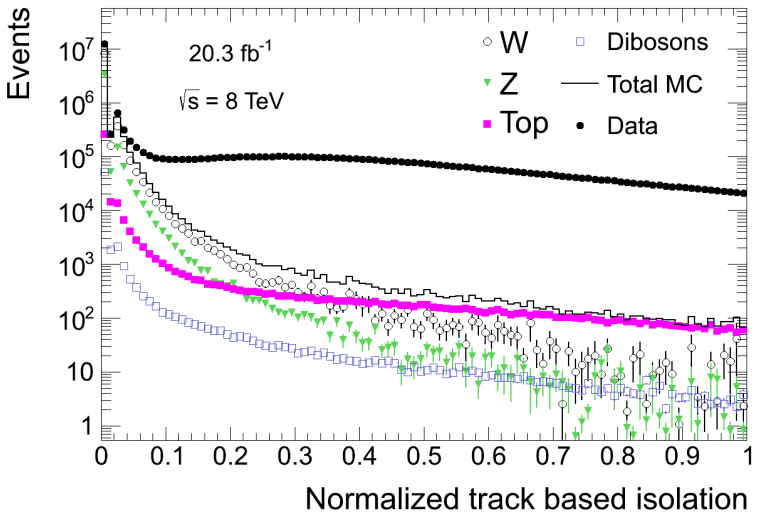

Figure 6.1: The distribution of the normalized track based isolation variable $\sum_{\Delta R_{\mathrm{trk},\mu}<0.3} p_{\mathrm{T}}^{\mathrm{trk}}/p_{\mathrm{T}}^{\mu}$. The large number of data events with rather high values come from the jet background which we want to estimate.

6.2 The Matrix Method

As previously stated, the Matrix Method is based on considering the effect of some jet background suppression cut on data. In the following, we consider the muon isolation cut, but the description of the method is obviously valid for any choice of cut, and for electrons as well as muons.

We define first two classes of muons:

- A "real" muon is defined as a prompt, real muon.
- A "fake" muon is defined as a muon candidate originating from a jet.

The "fake" muon can clearly be a real muon from a heavy flavor hadron decay within a jet, and as mentioned in section 4.5, we actually expect most of the "fake" muons to be real, hence the use of the quotation marks. The "real" muons are those we are primarily interested in selecting in the analysis, typically those from W or Z decays or from W' or W^* signal. They do not originate from within jets, and are a priori expected to be isolated. A muon from a W boson originating from top quark decay is also considered "real" in this context. Muons from τ lepton decays such as $\tau^- \rightarrow \mu^- \overline{\nu_\mu}\, \nu_\tau$ are classified in the same way based on the origin of the τ. For example, a prompt τ lepton from a W or Z boson decay gives rise to a "real" muon, while the muon is classified as "fake" if the τ lepton arose from e.g. a B meson decay inside a jet. The jet background which we want to estimate is the number of "fake" muons in data.

The numbers of "real" and "fake" muons in data[1] is what we want to know, and we have to relate these to what we can measure directly: the number of muons that pass and do not pass the isolation cut respectively. We define a *loose* muon as one that passes all muon selection cuts except the isolation cut. A loose muon may or may not pass the isolation cut, and a loose muon that does pass the isolation cut is defined as a *tight* muon. Tight muons form thus a subset of

[1]Here, "the data" is the data sample in which we want to measure the "fake" muon content. The term may be slightly misleading, as we will see that separate control regions of the data are used for the "real" and "fake" muon efficiency measurements. One could use instead the term "signal region", but we will in general reserve this term for a region defined by a lower transverse mass threshold, while we would like to measure the "fake" muon content also at lower transverse mass.

the loose muons. We further define the probability, or efficiency, that a loose, "real" muon is also tight,

$$\varepsilon_{\text{real}} = \frac{N_{\text{tight}}^{\text{real}}}{N_{\text{loose}}^{\text{real}}}, \tag{6.1}$$

and the corresponding efficiency for a "fake" muon:

$$\varepsilon_{\text{fake}} = \frac{N_{\text{tight}}^{\text{fake}}}{N_{\text{loose}}^{\text{fake}}}. \tag{6.2}$$

Clearly, we expect $\varepsilon_{\text{real}}$ to be high, close to 100%, while we expect $\varepsilon_{\text{fake}}$ to be much lower. These efficiencies need to be measured and fed as inputs to the Matrix Method. Measuring these efficiencies is the main challenge when applying the method.

We proceed by writing the number of loose and tight muons in data, denoted respectively N_{loose} and N_{tight}, in terms of the "real" and "fake" contributions:

$$N_{\text{loose}} = N_{\text{loose}}^{\text{real}} + N_{\text{loose}}^{\text{fake}} \tag{6.3}$$

and

$$N_{\text{tight}} = N_{\text{tight}}^{\text{real}} + N_{\text{tight}}^{\text{fake}} = \varepsilon_{\text{real}} N_{\text{loose}}^{\text{real}} + \varepsilon_{\text{fake}} N_{\text{loose}}^{\text{fake}}. \tag{6.4}$$

In the last equation, the tight contributions have been written in terms of the loose contributions and the "real" and "fake" muon efficiencies. Assuming $\varepsilon_{\text{real}}$ and $\varepsilon_{\text{fake}}$ to be known, this set of equations can be solved for the "fake" content in the data. We find for the number of "fake" muons in the loose sample,

$$N_{\text{loose}}^{\text{fake}} = \frac{\varepsilon_{\text{real}} N_{\text{loose}} - N_{\text{tight}}}{\varepsilon_{\text{real}} - \varepsilon_{\text{fake}}}, \tag{6.5}$$

and the corresponding expression for the tight sample,

$$N_{\text{tight}}^{\text{fake}} = \varepsilon_{\text{fake}} N_{\text{loose}}^{\text{fake}} = \varepsilon_{\text{fake}} \frac{\varepsilon_{\text{real}} N_{\text{loose}} - N_{\text{tight}}}{\varepsilon_{\text{real}} - \varepsilon_{\text{fake}}}. \tag{6.6}$$

Introducing the average efficiency measured in the data,

$$\varepsilon_{\text{data}} = \frac{N_{\text{tight}}}{N_{\text{loose}}}, \tag{6.7}$$

alternative forms of eqs. (6.5),

$$N_{\text{loose}}^{\text{fake}} = N_{\text{loose}} \frac{\varepsilon_{\text{real}} - \varepsilon_{\text{data}}}{\varepsilon_{\text{real}} - \varepsilon_{\text{fake}}}, \tag{6.8}$$

and (6.6),

$$N_{\text{tight}}^{\text{fake}} = \varepsilon_{\text{fake}} N_{\text{loose}} \frac{\varepsilon_{\text{real}} - \varepsilon_{\text{data}}}{\varepsilon_{\text{real}} - \varepsilon_{\text{fake}}}, \tag{6.9}$$

illustrate that the composition of the data in terms of "real" and "fake" muons is measured essentially by comparing the average efficiency in data to the known efficiencies for "real" and "fake" muons.

We identify some special cases. First, if $\varepsilon_{\text{data}} = \varepsilon_{\text{real}}$, then $N_{\text{loose}}^{\text{fake}} = N_{\text{tight}}^{\text{fake}} = 0$, i.e. the data

consists purely of "real" muons. It is worth noting that this conclusion does not depend on the measured value of $\varepsilon_{\text{fake}}$. Furthermore, if $\varepsilon_{\text{data}} = \varepsilon_{\text{fake}}$, then $N_{\text{loose}}^{\text{fake}} = N_{\text{loose}}$ and $N_{\text{tight}}^{\text{fake}} = N_{\text{tight}}$, i.e. the data consists purely of "fake" muons. This conclusion does not depend on the measured value of $\varepsilon_{\text{real}}$. Finally, we note that the expressions for $N_{\text{tight}}^{\text{fake}}$ and $N_{\text{loose}}^{\text{fake}}$ become ill-defined when $\varepsilon_{\text{real}} = \varepsilon_{\text{fake}}$, as the cut used for the loose and tight definitions in this case has no discriminating power between "real" and "fake" muons.

It is important to note that "the data" referred to in the previous paragraphs does not need to be the inclusive sample of all data events. In general, one is interested in the jet background as function of various variables, in our case m_{T} in particular, and the "fake" contributions $N_{\text{loose}}^{\text{fake}}$ and $N_{\text{tight}}^{\text{fake}}$ are in this case estimated one bin at a time using the event counts N_{loose} and N_{tight} in the given bin.

Uncertainties in the measurements of $\varepsilon_{\text{real}}$ and $\varepsilon_{\text{fake}}$ lead to uncertainties in the final jet background estimates. From eqs. (6.8) and (6.9), we see that $N_{\text{loose}}^{\text{fake}}$ and $N_{\text{tight}}^{\text{fake}}$ are both particularly sensitive to the value of $\varepsilon_{\text{real}}$ when $\varepsilon_{\text{data}} \approx \varepsilon_{\text{real}}$, i.e. when the data consist mostly of "real" muons. The dependence on the value of $\varepsilon_{\text{fake}}$ is seen to be different for $N_{\text{loose}}^{\text{fake}}$ and $N_{\text{tight}}^{\text{fake}}$. For $N_{\text{loose}}^{\text{fake}}$, the dependence on $\varepsilon_{\text{fake}}$ enters only in the denominator, where $\varepsilon_{\text{fake}}$ is subtracted from $\varepsilon_{\text{real}}$. Hence, the resulting relative uncertainty on $N_{\text{loose}}^{\text{fake}}$ is typically smaller than that on $\varepsilon_{\text{fake}}$ itself in the typical situation that $\varepsilon_{\text{fake}} \ll \varepsilon_{\text{real}}$. For $N_{\text{tight}}^{\text{fake}}$, on the other hand, there is also the dependence from the factor $\varepsilon_{\text{fake}}$ in front, leading to the same relative uncertainty on $N_{\text{tight}}^{\text{fake}}$ as on $\varepsilon_{\text{fake}}$ when the contribution from the $\varepsilon_{\text{fake}}$ in the denominator is neglected. As the baseline selection for the analysis corresponds to tight muons, it is $N_{\text{tight}}^{\text{fake}}$ that is the jet background we are primarily interested in.

We conclude this section by noting that the event selection described in section 5.2 ensures that there is only one loose muon in each event selected in the analysis. If the "exactly one muon" requirement applied only to tight muons, there would in principle be a severe complication due to the possibility for events with two loose muons where only one muon would pass the tight requirement and therefore end up in the final selection sample. We also note that the Matrix Method is applicable also to searches in final states with more than one lepton, although the equation sets corresponding to eqs. (6.3) and (6.4) in this case become more complicated. The interested reader is referred to refs. [97, 98] for an example of the application of the method to dilepton final states.

6.2.1 Taking into account dependencies

The efficiencies $\varepsilon_{\text{real}}$ and $\varepsilon_{\text{fake}}$ may depend on the muon's p_{T}, η, or other parameters. Such dependencies can be taken into account as long as the dependencies of the efficiencies on the parameters can be measured. Consider as an example the dependence of $\varepsilon_{\text{real}}$ and $\varepsilon_{\text{fake}}$ on the muon's p_{T}. If one is interested in the p_{T} spectrum of the jet background, one can obviously insert in eq. (6.6) the values $\varepsilon_{\text{real}}(p_{\text{T}}^i)$ and $\varepsilon_{\text{fake}}(p_{\text{T}}^i)$ when estimating the jet background in bin i of the distribution, where p_{T}^i can for example be taken to be the center of the bin. However, when estimating the jet background in the m_{T} distribution, the full p_{T} spectrum of each m_{T} bin needs to be taken into account. This is most easily done with the event-by-event approach which will now be described.

We rewrite N_{loose} and N_{tight} as

$$N_{\text{loose}} = \sum_{i \in \text{loose}} 1 \quad \text{and} \quad N_{\text{tight}} = \sum_{i \in \text{loose}} N^i_{\text{tight}} \tag{6.10}$$

with the sums running over all events in the loose muon sample and $N^i_{\text{tight}} = 0$ if the muon in event number i does not pass the isolation cut and $N^i_{\text{tight}} = 1$ if it does. Eq. (6.6) can then be written on the form

$$N^{\text{fake}}_{\text{tight}} = \sum_{i \in \text{loose}} \varepsilon_{\text{fake}} \frac{\varepsilon_{\text{real}} - N^i_{\text{tight}}}{\varepsilon_{\text{real}} - \varepsilon_{\text{fake}}}. \tag{6.11}$$

With $\varepsilon_{\text{real}}$ and $\varepsilon_{\text{fake}}$ as constants, this is just a trivial rewrite of eq. (6.6), but dependencies of $\varepsilon_{\text{real}}$ and $\varepsilon_{\text{fake}}$ on e.g. p_{T} can now be easily taken into account by inserting for each event i the value of the efficiencies evaluated at the value p^i_{T} in that event, i.e.

$$N^{\text{fake}}_{\text{tight}} = \sum_{i \in \text{loose}} \varepsilon_{\text{fake}}(p^i_{\text{T}}) \frac{\varepsilon_{\text{real}}(p^i_{\text{T}}) - N^i_{\text{tight}}}{\varepsilon_{\text{real}}(p^i_{\text{T}}) - \varepsilon_{\text{fake}}(p^i_{\text{T}})}. \tag{6.12}$$

Here, $N^{\text{fake}}_{\text{tight}}$ could be the jet background in some bin of m_{T}, with the sum then running over all loose muons in that bin. This approach corresponds to estimating the jet background in the given m_{T} bin by summing over individual p_{T} bins in the limit of infinitely fine p_{T} binning. However, the determination of $\varepsilon_{\text{real}}$ and $\varepsilon_{\text{fake}}$ as functions of p_{T} or any other variable involves in general some binning. Obviously, the described method can be used to take into account efficiency dependence on any variable while estimating the jet background in bins of this or any other variable.

6.2.2 Measuring the efficiencies

With reliable measurements of the "real" and "fake" muon efficiencies $\varepsilon_{\text{real}}$ and $\varepsilon_{\text{fake}}$ at hand, estimating the jet background by the Matrix Method is trivial. The main challenge is thus to measure these efficiencies, and the uncertainties on the measurements lead to corresponding uncertainties in the jet background estimate. Clearly, the "fake" muon efficiency must be measured in a control region in data with a high purity of "fake" muons. The "real" muon efficiency, on the other hand, could be measured in MC samples, as it is the jet MC samples that we want to avoid dependence on by the data driven jet background estimate. However, in the spirit of the data driven approach, the "real" muon efficiency is also measured in data in this analysis, with a MC based measurement serving only as a systematics variation[2].

6.3 The real muon efficiency

To measure the "real" muon efficiency in data, a control region with a high purity of "real" muons is needed, and the Z boson invariant mass peak is an obvious choice. The measurement of efficiencies based on the selection of lepton pairs consistent with originating from Z boson

[2]The term *systematics variation* is used to refer to some variation from the baseline approach that finally goes into the estimate of the systematic uncertainty on the jet background.

decays (or decays of another known resonance) is in general referred to as the tag and probe approach.

6.3.1 The tag and probe approach

The tag and probe approach is based on selecting lepton pairs with an invariant mass close to the Z peak. Consider the set of all loose muon pairs within the chosen invariant mass window. We select from this set all pairs where at least one muon is tight (the "tag" muon), and refer to the number of such events as N_{lt}. Finally, we count the number of events N_{tt} in which also the "probe" muon passes the tight selection, i.e. where both muons are tight. The ratio of these numbers is not the efficiency $\varepsilon_{\text{real}}$. To see that, we relate both event counts to the number of loose-loose muon pairs N_{ll}. The number N_{lt} is the number of loose-loose events in which not both muons fail the tight requirement, i.e.[3]

$$N_{lt} = N_{ll}\left[1 - (1 - \varepsilon_{\text{real}})^2\right] = N_{ll}\left[2\varepsilon_{\text{real}} - \varepsilon_{\text{real}}^2\right]. \tag{6.13}$$

Furthermore, N_{tt} is the number of loose-loose events in which both muons pass the tight requirement:

$$N_{tt} = N_{ll}\varepsilon_{\text{real}}^2. \tag{6.14}$$

We define the ratio as $\tilde{\varepsilon}$,

$$\tilde{\varepsilon} = \frac{N_{tt}}{N_{lt}} = \frac{\varepsilon_{\text{real}}}{2 - \varepsilon_{\text{real}}}, \tag{6.15}$$

and invert the equation to find the efficiency we seek:

$$\varepsilon_{\text{real}} = \frac{2\tilde{\varepsilon}}{1 + \tilde{\varepsilon}}. \tag{6.16}$$

We now proceed by noting that the efficiency could be calculated directly as a ratio of muon counts if the muons are counted in a particular way. In each dimuon event, we refer in turn to each tight muon as the tag muon and the other one as the probe muon. In an event with two tight muons, then, they are both counted once as the tag muon and once as the probe muon. We count the number of times N_t that the probe muon is tight and the number of times N_l it is loose, i.e. the total number of probe muons. These are now muon counts rather than event counts. In events with two tight muons, we receive a contribution of 2 to both N_t and N_l. Furthermore, events with one loose muon that does not pass tight (an "exclusive loose" muon, denoted by $\bar{l}$) and one tight muon contributes 1 to N_l and nothing to N_t. Finally, we find that the efficiency is simply the ratio of the tight and loose probe muon counts:

$$\frac{N_t}{N_l} = \frac{2N_{tt}}{N_{\bar{l}t} + 2N_{tt}} = \frac{2N_{ll}\varepsilon_{\text{real}}^2}{N_{ll} \cdot 2(1 - \varepsilon_{\text{real}})\varepsilon_{\text{real}} + 2N_{ll}\varepsilon_{\text{real}}^2} = \varepsilon_{\text{real}}. \tag{6.17}$$

The change from event counts to muon counts is, considering the average efficiency in the Z boson invariant mass window as given by eqs. (6.16) and (6.17), unimportant. The approach with the muon counts is, however, favorable when the efficiency is measured as function of p_{T}

[3] Of course, equations such as eq. (6.13) are true only in terms of expectation values. Resulting expressions for the desired efficiency in terms of the relevant counts are estimators.

or some other muon characteristic. In this case, the number of tight and loose probe muons are counted in bins of e.g. p_{T}, and the efficiency in bin i is obtained simply as the ratio of the number of tight probe muons within the bin, N_t^i, to the number of loose probe muons N_l^i in the same bin. Obviously, it is the p_{T} of the probe muon that decides the bin, not the p_{T} of the tag muon. We conclude this section by verifying that the ratio N_t^i/N_l^i is indeed the efficiency in bin i as claimed.

We denote the number of events with one loose muon in bin i of the p_{T} distribution and another one in bin j by $N_{l_i l_j}$. The notation is extended in the obvious way to events with different combinations of loose and tight muons. Furthermore, we define the probability P_{ij} that the two muons in a selected loose-loose Z boson candidate event have transverse momenta within bin i and j respectively. The tight probe muon count in a given bin i receives a contribution of 1 from each tight-tight pair with only one of the muons in bin i and a contribution of 2 from each tight-tight pair with both muons in the given bin, i.e.

$$N_t^i = \sum_{j\neq i} N_{t_i t_j} + 2N_{t_i t_i} = \sum_{j\neq i} N_{ll} P_{ij} \varepsilon^i_{\mathrm{real}} \varepsilon^j_{\mathrm{real}} + 2N_{ll} P_{ii} (\varepsilon^i_{\mathrm{real}})^2 \tag{6.18}$$

with $\varepsilon^i_{\mathrm{real}}$ denoting the efficiency for a "real" muon in p_{T} bin i to pass the isolation cut. The loose probe muon count in bin i receives

- a contribution of 1 from each event with a loose muon in bin i and a tight muon in any other bin,
- a contribution of 1 from each event with an *exclusive* loose muon in bin i and a tight muon in the same bin, and finally
- a contribution of 2 from each event with two tight muons in bin i.

This results in the relation

$$\begin{aligned} N_l^i &= \sum_{j\neq i} N_{l_i t_j} + N_{\bar{l}_i t_i} + 2N_{t_i t_i} \\ &= \sum_{j\neq i} N_{ll} P_{ij} \varepsilon^j_{\mathrm{real}} + N_{ll} P_{ii} \cdot 2(1-\varepsilon^i_{\mathrm{real}})\varepsilon^i_{\mathrm{real}} + 2N_{ll} P_{ii} (\varepsilon^i_{\mathrm{real}})^2 \\ &= \sum_{j\neq i} N_{ll} P_{ij} \varepsilon^j_{\mathrm{real}} + 2N_{ll} P_{ii} \varepsilon^i_{\mathrm{real}}. \end{aligned} \tag{6.19}$$

Clearly, eqs. (6.18) and (6.19) lead to the required relation

$$\frac{N_t^i}{N_l^i} = \varepsilon^i_{\mathrm{real}}. \tag{6.20}$$

6.3.2 The invariant mass window

To decide on a reasonable invariant mass window for the tag and probe selection, we plot the distribution of the dimuon invariant mass for loose-tight muon pairs. The distribution is shown on both logarithmic and linear y-axis scales in fig. 6.2. A few things should be noted about this distribution. First of all, the Z peak is not symmetric around $91\ \mathrm{GeV}$ as one might have expected

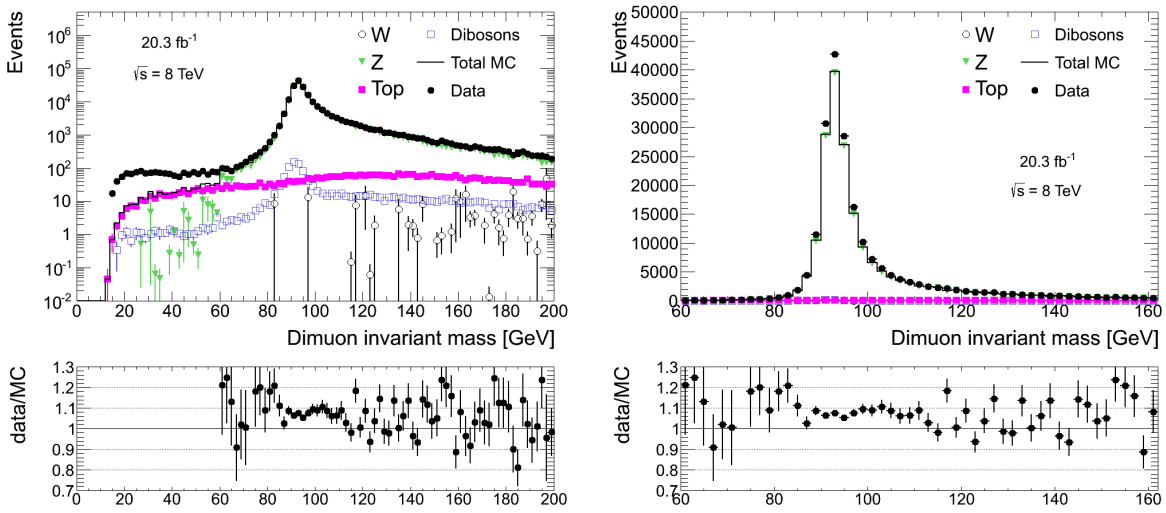

(a) (b)

Figure 6.2: The dimuon invariant mass distribution for loose-tight muon pairs on logarithmic (a) and linear (b) y-axis scales. The ratio of data to the total MC prediction is shown in the panel below each plot with error bars reflecting the statistical uncertainty of the data and MC.

it to be. This is, however, not unreasonable, as the muon p_{T} cut of $45\,\mathrm{GeV}$ is already right at the top of the Jacobian peak one would expect from on-shell Z boson production with small Z boson transverse momentum, and the cut therefore creates a preference for higher invariant masses. We will see in section 6.4.1 that the peak is more symmetric when the p_{T} cut is not applied to both muons (fig. 6.9(a)). We further note that the sum of SM MC samples describes the data relatively well, with the Z boson contribution dominating over most of the considered invariant mass range. There is an obvious problem with the MC description of the data below an invariant mass of $60\,\mathrm{GeV}$, but this is of course expected from the fact that this is the lower invariant mass cut used for the low mass Z boson MC samples.

Clearly, the MC does not *perfectly* describe the data. In particular, there is a bit more than 5% discrepancy in the peak region where most of the events are located. One could worry that this indicates the presence of significant jet background contamination. If so, one would expect the data/MC ratio in the peak region to be significantly different for the tight-tight muon pairs, as much of the jet background would be expected to be removed by the isolation cut. The invariant mass distribution for such pairs is shown in fig. 6.3. While the data/MC discrepancy in the peak region is slightly smaller for these pairs, it is quite close to that observed for the loose-tight pairs, and we conclude that the data/MC discrepancy is for the most part not caused by jet background contamination. The uncertainty on the mass dependent k-factor for the Z background is 5% in the Z peak region, and therefore almost covers the observed data/MC discrepancy.

Based on the observed invariant mass distributions, we choose the range $[86\,\mathrm{GeV}, 110\,\mathrm{GeV}]$ as the nominal tag and probe mass window for the "real" efficiency determination. For systematics variations, we consider a "low mass" window $[86\,\mathrm{GeV}, 94\,\mathrm{GeV}]$, a "high mass" window $[94\,\mathrm{GeV}, 110\,\mathrm{GeV}]$, and a "narrow" window $[90\,\mathrm{GeV}, 98\,\mathrm{GeV}]$.

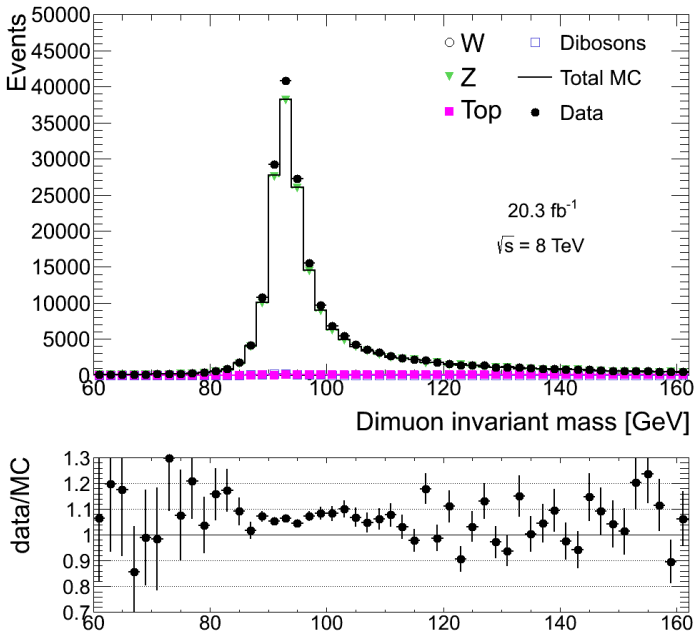

Figure 6.3: The dimuon invariant mass distribution for tight-tight muon pairs. The ratio of data to the total MC prediction is shown in the panel below the plot with error bars reflecting the statistical uncertainty of the data and MC.

6.3.3 Results

The "real" muon efficiency $\varepsilon_{\text{real}}$ is shown as function of muon p_{T} and η in fig. 6.4. As expected, the efficiency is high, and it is seen to increase as function of p_{T}, as one might expect from the explicit p_{T} dependence in eq. (5.1). The average efficiency for all muons in the tag and probe selection is $(97.63 \pm 0.03)\%$, with the quoted uncertainty being purely statistical. The η dependent "real" muon efficiency is used when the jet background is estimated in the η distribution.

Fig. 6.5(a) shows the "real" muon efficiency with different systematics variations. In addition to the efficiency measurements under variations of the tag and probe mass window mentioned in section 6.3.2, the efficiency as obtained from the W MC samples is also shown. When the efficiency is measured in the MC samples, no tag and probe is performed, and the efficiency is calculated according to eq. (6.1). The MC based efficiency is seen to be a bit higher than that measured in data. This could be due to jet background contamination in the tag and probe selection, but it could also be due to imperfection in the MC modeling. Whatever the reason, the resulting uncertainty on the estimated jet background is found to be negligible compared to the uncertainty due to the "fake" muon efficiency.

The jet background is also estimated with a variation of the loose muon definition where the loose muons are required to pass an isolation preselection,

$$\sum_{\Delta R_{\text{trk},\mu}<0.3} p_{\text{T}}^{\text{trk}} < 0.4\, p_{\text{T}}^{\mu}, \tag{6.21}$$

which is of course looser than the baseline isolation cut (5.1) used to define the tight muons. The "real" muon efficiency for this variation is shown in fig. 6.5(b). It is seen to be very close to the baseline efficiency, as the isolation preselection has a marginal impact on "real" muons.

We finally show the "real" muon efficiency in the p_{T},η-plane and as function of the muon ϕ in fig. 6.6. The efficiency binned in the two-dimensional p_{T},η-plane is used as a systematics

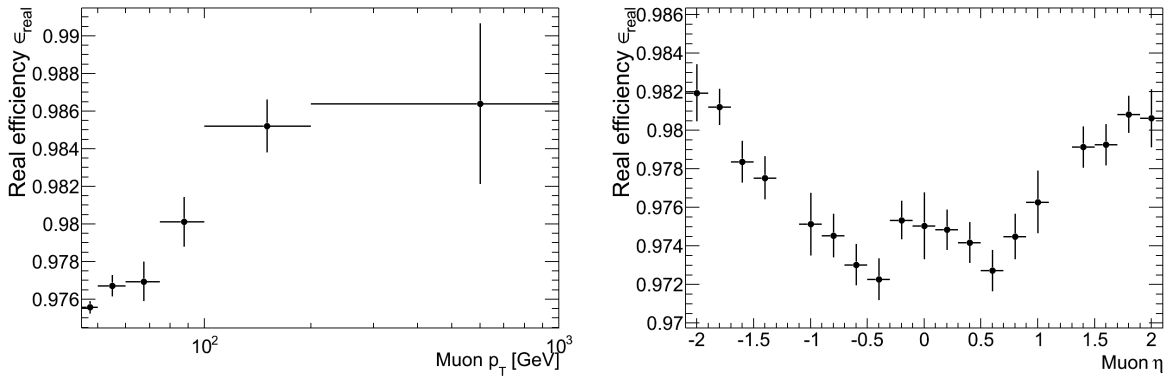

(a) (b)

Figure 6.4: The "real" muon efficiency $\varepsilon_{\text{real}}$ as function of muon p_{T} (a) and η (b). The "missing points" in the η plot correspond to the barrel-end-cap transition region where there are few muons and the estimated efficiency is 100%. The error bars represent statistical uncertainty.

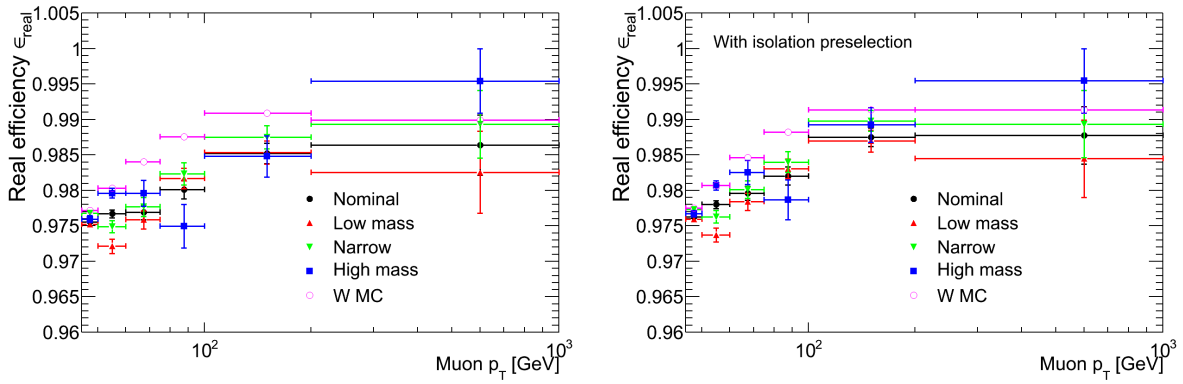

(a) (b)

Figure 6.5: The "real" muon efficiency $\varepsilon_{\text{real}}$ as function of muon p_{T}. The measured efficiency is shown for variations of the tag and probe mass window as described in section 6.3.2, and the efficiency as obtained from the W boson MC samples is also shown. The efficiency for the baseline Matrix Method implementation is shown in (a), while (b) shows the efficiency for a variation of the method where the loose muons are defined with an isolation preselection. The error bars represent statistical uncertainty.

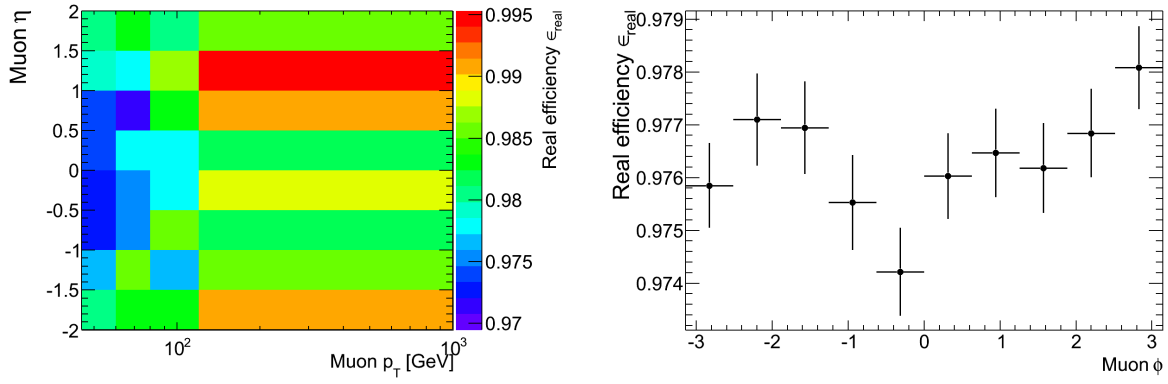

(a) (b)

Figure 6.6: The "real" muon efficiency $\varepsilon_{\text{real}}$ in the p_{T},η-plane (a) and as function of muon ϕ (b). The error bars represent statistical uncertainty.

variation, while the ϕ dependent efficiency is used when estimating the jet background in the ϕ distribution. As expected, not much dependence of the efficiency on the muon ϕ is observed.

When the jet background is estimated in distributions other than the η and ϕ distributions, the p_{T} dependent "real" muon efficiency is in general used.

6.4 The fake muon efficiency

The "fake" muon efficiency $\varepsilon_{\text{fake}}$ is measured in a control region of data with a high purity of "fake" muons. The control region is defined by a set of cuts that reduce the "real" muon contamination, but getting this contamination to a level where it is really negligible is difficult. Therefore, the "real" muon contamination as obtained from the MC samples is subtracted when calculating the "fake" muon efficiency, i.e.

$$\varepsilon_{\text{fake}} = \frac{N_{\text{tight}} - N_{\text{tight}}^{\text{MC}}}{N_{\text{loose}} - N_{\text{loose}}^{\text{MC}}}, \tag{6.22}$$

where all event counts refer to those in the "fake" muon control region, typically also within some given bin of e.g. the muon p_{T}. Obviously, the MC numbers are predictions scaled to the integrated luminosity of the data. Although one would ideally like the data driven jet background estimate to be fully data driven, with no MC dependence, subtracting the "real" muon contamination as obtained from MC seems to be necessary, and it is acceptable because we trust that the MC samples properly model "real" muon contributions – it is the jet MC samples that we want to avoid.

It is worth noting that the "real" muon contribution that we subtract is the sum of the contributions from *all* the MC samples used in the analysis. No generator level selection is made to ensure that only "real" muon contributions are subtracted, but the "fake" muon contribution in the considered MC samples is expected to be negligible. It is true that the MC samples include jet activity, and could therefore in principle contain "fake" muons. However, all the MC events contain at least one "real" muon, and an event with a "fake" muon can only be selected if the

"real" muon is not reconstructed or fails the selection requirements in the first set of bullets on page 98. If a fully hadronic $t\bar{t}$ sample were used in addition to the lepton filtered one, this sample would include *only* "fake" muons. Including such a sample would thus lead to an error[4] in the MC subtraction, and it would also lead to double counting in the background level, as fully hadronic $t\bar{t}$ events are part of the jet background that we estimate with the data driven approach.

While we do in principle trust the MC samples for "real" muons, the MC subtraction in the "fake" muon control region is obviously associated with some uncertainty. At the very least, small uncertainties due to cross sections and efficiencies are expected, but we may also expect that some of the cut variables used for the control region definition are not perfectly modeled in the MC. We consider several systematics variations of the control region definition, with varying levels of "real" muon contamination, and we expect that these variations cover any uncertainty due to the MC subtraction.

6.4.1 Defining the control region

The "fake" muon control region must be defined by a set of cuts that reduce the contribution from "real" muons. The cuts should ideally be uncorrelated with the isolation cut, as this is the cut for which we want to probe the "fake" muon efficiency. It is, however, not easy to know which cuts are truely uncorrelated with the isolation cut – if any – so systematics variations of the control region definition are crucial.

Events for the "fake" muon control region are selected after requiring exactly one good, isolated muon in the event, but before the application of the $\not{E}_{\mathrm{T}}$ threshold ($\not{E}_{\mathrm{T}} > 45\,\mathrm{GeV}$). Some candidate variables for the control region definition are plotted at this stage in the event selection in fig. 6.7. Fig. 6.7(a) shows the distribution of the number of jets with $p_{\mathrm{T}} > 25\,\mathrm{GeV}$ and $\Delta R > 0.2$ wrt. the muon, reconstructed with the anti-k_t algorithm [102] with a radius parameter $R = 0.4$. In jet events, we assume that the "fake" muon is associated with one jet, and we expect that there is at least one other jet in the event balancing the p_{T} of the jet associated with the muon. There is an obvious data/MC discrepancy for $N_{\mathrm{jet}} \geq 2$, which we assume to be due to jet events.

Fig. 6.7(b) shows the opening angle between the muon and the $\not{E}_{\mathrm{T}}$ in the transverse plane. We see that W events tend to have a large opening angle, and this is due to the fact that the W bosons are often produced with relatively small p_{T}. When the W boson is produced with low p_{T}, the muon and the neutrino go approximately "back to back" ($\Delta\phi_{\mu,\not{E}_{\mathrm{T}}} \approx \pi$) as dictated by the conservation of momentum in the transverse plane. There is a data/MC discrepancy at low $\Delta\phi_{\mu,\not{E}_{\mathrm{T}}}$, which we assume again to be due to jet events.

Finally, we consider the muon transverse impact parameter d_0 wrt. the reconstructed primary vertex. In events with "real" (prompt) muons, the impact parameter is small, which is indeed the motivation for using the d_0 cut in the event selection in the first place. However, we see in fig. 6.7(c) that the cut $|d_0| < 0.2\,\mathrm{mm}$ is rather loose, and there is a large region of

[4] Actually, the subtraction of a certain "fake" muon component as obtained from MC should only lead to an error to the extent that the MC does not properly describe the "fake" muons. For example, if one had a perfect MC description of the "fake" muons in fully hadronic $t\bar{t}$ events, then subtracting this contribution from the "fake" muon control region simply means that the control region is left consisting only of all other types of "fake" muon events besides fully hadronic $t\bar{t}$ events. Assuming that the isolation characteristics of "fake" muons are independent of their origin, no change would be seen in the estimated "fake" muon efficiency.

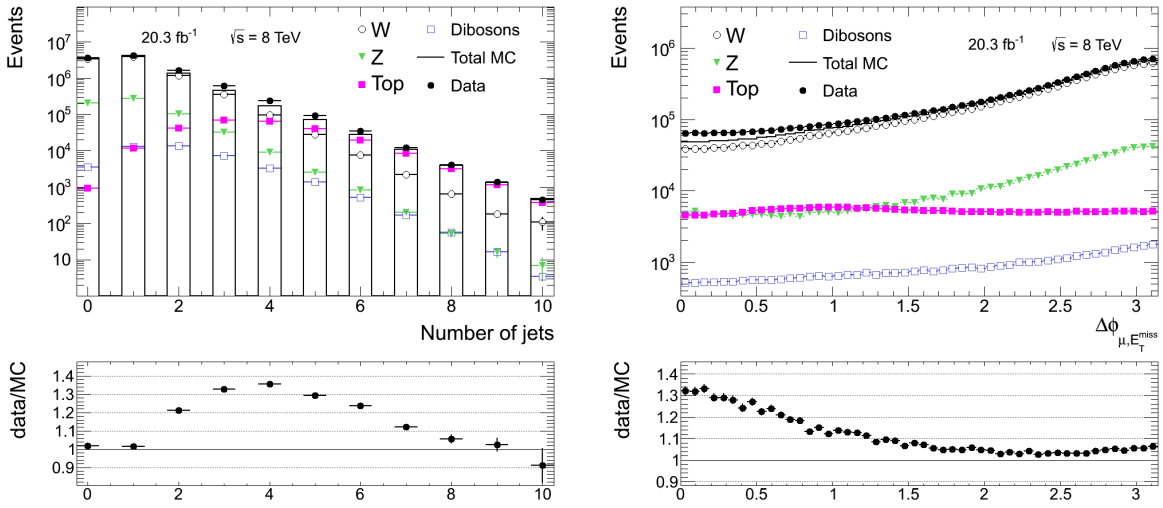

(a)

(b)

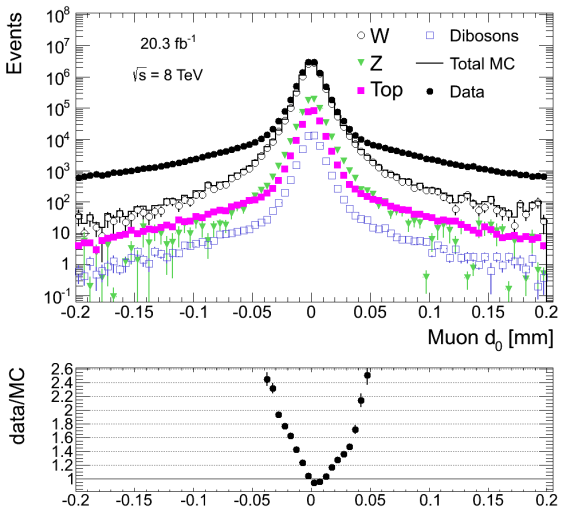

(c)

Figure 6.7: Variables used in the definition of the "fake" muon control region: the number of jets with $p_{\mathrm{T}} > 25\,\mathrm{GeV}$ (a), the azimuth angle between the muon and the $\not{E}_{\mathrm{T}}$ (b), and the muon transverse impact parameter d_0 wrt. the reconstructed primary vertex (c).

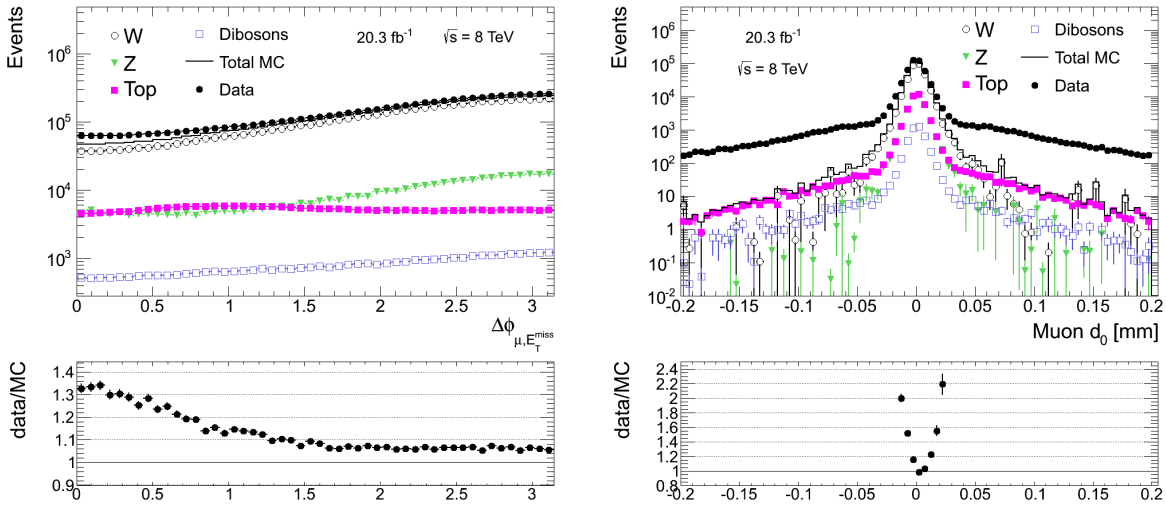

(a) (b)

Figure 6.8: The distribution of $\Delta\phi_{\mu,\not{E}_{\mathrm{T}}}$ after the requirement $N_{\mathrm{jet}} \geq 1$ (a) and the d_0 distribution after the cuts $N_{\mathrm{jet}} \geq 1$ and $\Delta\phi_{\mu,\not{E}_{\mathrm{T}}} < 0.5$ (b).

significant data/MC discrepancy, assumed to be due to jet events.

It is by now clear that the "fake" muon control region can be constructed with some combination of cuts on N_{jet}, $\Delta\phi_{\mu,\not{E}_{\mathrm{T}}}$, and d_0. The exact combination of cuts is necessarily somewhat arbitrary, and variations are done to estimate systematic uncertainties. For the nominal definition of the control region, we require:

- $N_{\mathrm{jet}} \geq 1$,
- $\Delta\phi_{\mu,\not{E}_{\mathrm{T}}} < 0.5$, and
- $|d_0| > 0.01\,\mathrm{mm}$.

Obviously, the cut on N_{jet} is rather minimal, and $N_{\mathrm{jet}} \geq 2$ seems more well motivated from the distribution in fig. 6.7(a). Tightening the cut in this way is, however, not found to improve the purity of the control region significantly when the $\Delta\phi_{\mu,\not{E}_{\mathrm{T}}}$ and d_0 cuts are in place. One could use the cut $N_{\mathrm{jet}} \geq 2$ instead of $\Delta\phi_{\mu,\not{E}_{\mathrm{T}}} < 0.5$, which would lead to a control region with better statistics, but somewhat inferior purity. The cut $N_{\mathrm{jet}} \geq 2$ is used both instead of and in addition to the cut $\Delta\phi_{\mu,\not{E}_{\mathrm{T}}} < 0.5$ for systematics variations.

To give a better idea of the flow of the control region definition, we make first the cut $N_{\mathrm{jet}} \geq 1$ and show the resulting distribution of $\Delta\phi_{\mu,\not{E}_{\mathrm{T}}}$ in fig. 6.8(a). Then we apply also the cut $\Delta\phi_{\mu,\not{E}_{\mathrm{T}}} < 0.5$, and show finally the d_0 distribution with both these cuts in place in fig. 6.8(b).

It is clear that $Z \to \mu^+\,\mu^-$ events may pass the exactly one muon requirement if the additional muon is outside the muon spectrometer acceptance or fails any of the cuts listed in the first set of bullets on page 98. If the additional muon is outside the muon spectrometer acceptance, there is not much that can be done. If, on the other hand, the additional muon is removed by the cuts, then we can still consider the invariant mass of that muon and the selected muon, to see if there is an obvious Z candidate in the event.

The distribution of the invariant mass of all combinations of reconstructed muons in the event is shown after the requirements $N_{\text{jet}} \geq 1$ and $\Delta\phi_{\mu,\not{E}_{\text{T}}} < 0.5$ in fig. 6.9(a) and after the additional requirement $|d_0| > 0.01\,\text{mm}$ in fig. 6.9(b). The Z peak is clearly visible, even after the d_0 cut, and we make a "Z veto", requiring that there be no muon pairs with invariant mass in the range $[80\,\text{GeV}, 100\,\text{GeV}]$, to suppress the Z contamination in the "fake" muon control region. We note that this invariant mass window is symmetric around $90\,\text{GeV}$, as opposed to that used for the tag and probe selection. This is due to the fact that the high p_{T} cut ($p_{\text{T}} > 45\,\text{GeV}$) is only applied to the selected muon, so that the p_{T} cut is not biasing the invariant mass distribution so much. We also note that the two bins just around an invariant mass of $10\,\text{GeV}$ display an upward fluctuation in data, indicating the presence of $\Upsilon \to \mu^+\mu^-$ decays in the jet events of the "fake" muon control region. Some structure seems also to be present around an invariant mass of 30-35 GeV in fig. 6.9(b), which may be a threshold effect. Finally, it is also worth mentioning that the Z veto has a relatively small impact on the control region purity. It has, however, also a small impact on the amount of statistics in the control region, and the cut seems warranted by the fact that such a large fraction of the Z events are concentrated in such a narrow invariant mass range.

We finally consider the $\not{E}_{\text{T}}$ distribution after all other cuts used for the "fake" muon control region, shown in fig. 6.9(c). Jet events are expected to be found predominantly at low $\not{E}_{\text{T}}$. We make a cut $\not{E}_{\text{T}} < 60\,\text{GeV}$, which has an overall small effect on the purity of the control region, but which is seen to increase the purity at high muon p_{T} in particular.

In summary, the cuts used to define the "fake" muon control region are:

- $N_{\text{jet}} \geq 1$,
- $\Delta\phi_{\mu,\not{E}_{\text{T}}} < 0.5$,
- $|d_0| > 0.01\,\text{mm}$,
- no muon pair with invariant mass in the range $[80\,\text{GeV}, 100\,\text{GeV}]$, and
- $\not{E}_{\text{T}} < 60\,\text{GeV}$.

6.4.2 Results

Fig. 6.10 shows the "fake" muon efficiency as function of muon p_{T} and η. It is seen to increase significantly as function of the muon p_{T}, as might be expected from the explicit p_{T} dependence in the isolation cut definition (eq. (5.1)). One would expect an isolation cut without such explicit p_{T} dependence to have an associated "fake" muon efficiency decreasing as function of p_{T}, as higher p_{T} muons would in general be expected to originate from higher p_{T} jets, giving rise to more activity around the muon. The η dependent "fake" muon efficiency is used when the jet background is estimated in the η distribution, and correspondingly the ϕ dependent "fake" muon efficiency shown in fig. 6.11(a) is used when the jet background is estimated in the ϕ distribution. For all other distributions, including the m_{T} distribution, the p_{T} dependent "fake" muon efficiency is used.

The average "fake" muon efficiency for all muons in the "fake" muon control region is $\varepsilon_{\text{fake}} = (5.57 \pm 0.07)\%$. The quoted uncertainty is purely statistical and includes the uncertainty

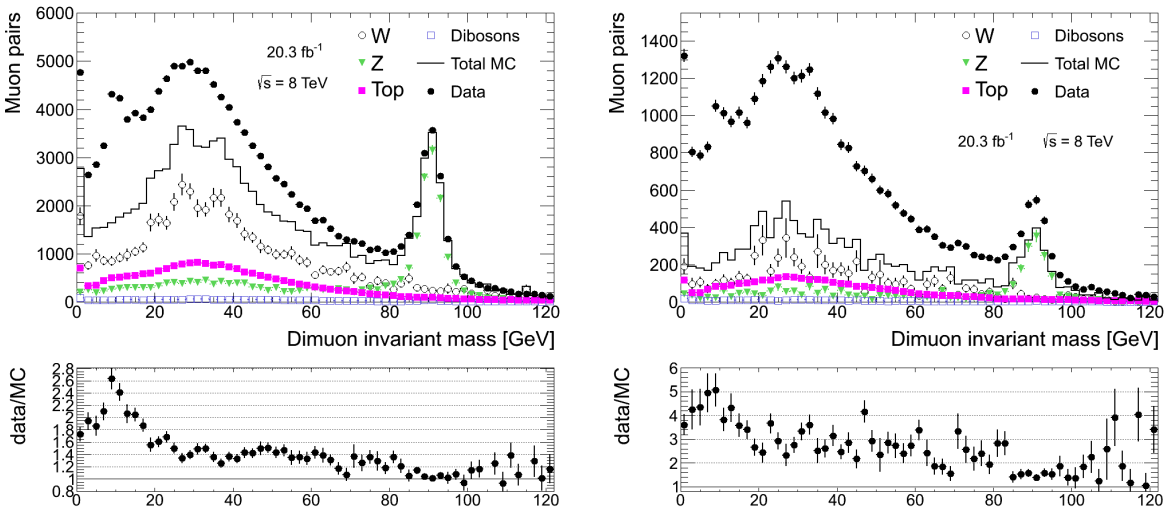

(a)

(b)

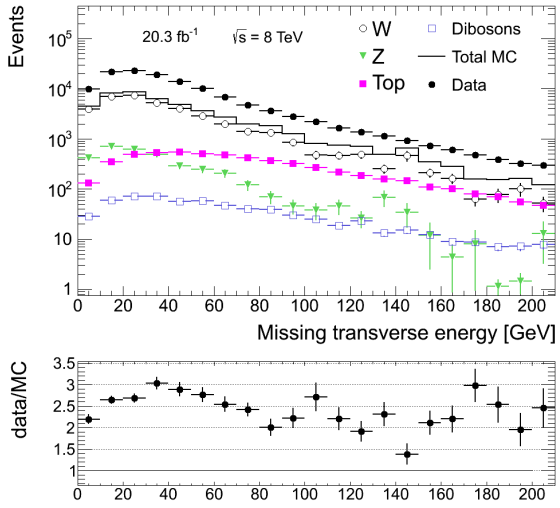

(c)

Figure 6.9: The distribution of the invariant mass of all combinations of reconstructed muons in the event after the requirements $N_{\text{jet}} \geq 1$ and $\Delta\phi_{\mu,\not{E}_{\text{T}}} < 0.5$ (a) and after the additional requirement $|d_0| > 0.01\,\text{mm}$ (b), and the $\not{E}_{\text{T}}$ distribution after all other cuts used for the "fake" muon control region (including the Z veto) (c).

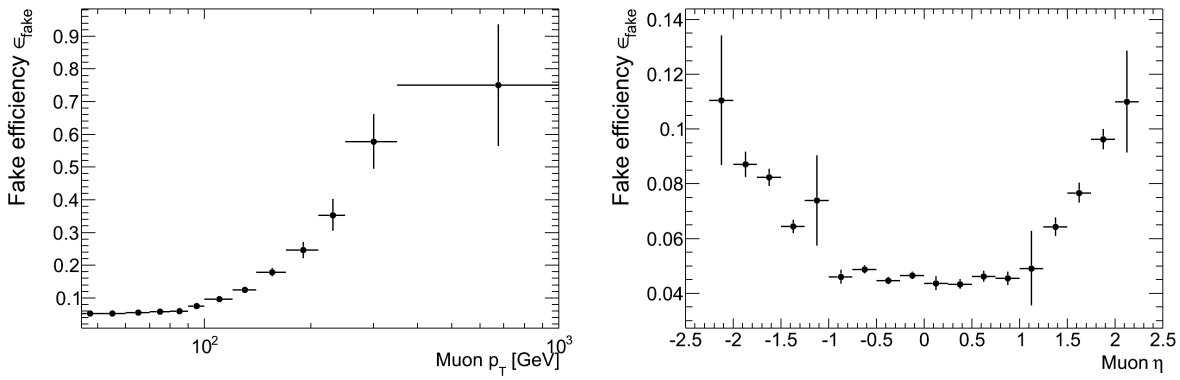

(a) (b)

Figure 6.10: The "fake" muon efficiency as function of muon p_{T} (a) and η (b). The error bars represent statistical uncertainty and include the uncertainty in the MC subtraction.

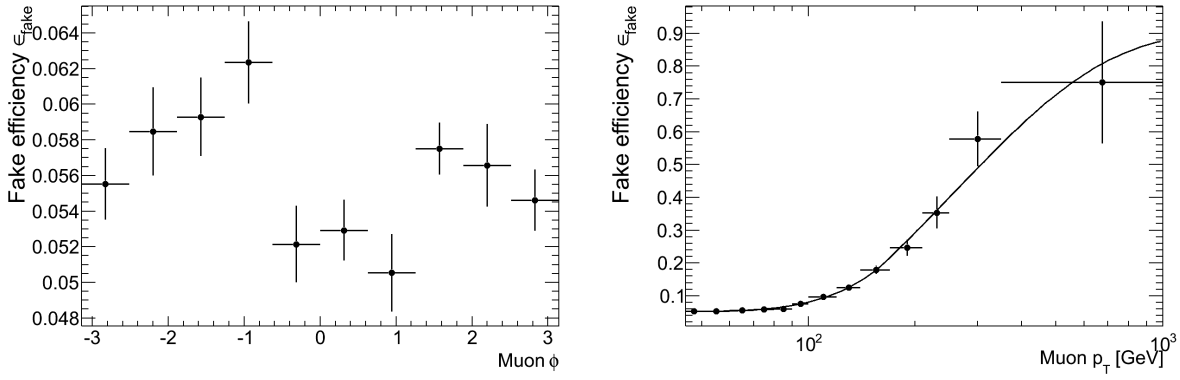

(a) (b)

Figure 6.11: The "fake" muon efficiency as function of the muon ϕ (a) and the "fake" muon efficiency as function of p_{T} with a fit (b). The fit function is used for the nominal estimate of the jet background p_{T} distribution to avoid obvious discontinuities due to the p_{T} binning. The error bars represent statistical uncertainty and include the uncertainty in the MC subtraction.

in the MC subtraction. The same goes for the error bars in fig. 6.10 and all further plots of the "fake" muon efficiency. The estimated "real" muon contamination in the "fake" muon control region is $N^{\mathrm{MC}}_{\mathrm{loose}}/N_{\mathrm{loose}} = (3.27 \pm 0.06)\%$ in the loose muon sample and $N^{\mathrm{MC}}_{\mathrm{tight}}/N_{\mathrm{tight}} = (36.9 \pm 0.7)\%$ in the tight muon sample, again with uncertainties being purely statistical. The contamination in the tight muon sample does not exceed 65% in any p_{T} bin used for the p_{T} dependent "fake" muon efficiency shown in fig. 6.10(a). We summarize the contamination in both the loose and tight muon samples in fig. 6.13 for all systematics variations of the "fake" muon control region.

We finally show a fit of the "fake" muon efficiency as function of muon p_{T} in fig. 6.11(b). The fit function is motivated simply by the fact that the p_{T} dependence at low p_{T} looks like it can be properly described by a simple low order polynomial, while the "fake" muon efficiency most likely displays some saturation at high p_{T}, as it can not grow larger than unity. The function has

the form

$$\varepsilon_{\text{fake}}(p_{\text{T}}) = \begin{cases} a + b\,p_{\text{T}} + c\,p_{\text{T}}^2 & \text{for } p_{\text{T}} < p_{\text{T}}^0 \\ d - ke^{-p_{\text{T}}/f} & \text{for } p_{\text{T}} > p_{\text{T}}^0 \end{cases}, \tag{6.23}$$

and the requirements that its derivative and the function itself both be continuous at $p_{\text{T}} = p_{\text{T}}^0$ lead to the relations

$$a + b\,p_{\text{T}}^0 + c\,(p_{\text{T}}^0)^2 = d - ke^{-p_{\text{T}}^0/f} \tag{6.24}$$

and

$$b + 2c\,p_{\text{T}}^0 = \frac{k}{f}e^{-p_{\text{T}}^0/f}. \tag{6.25}$$

These are used to eliminate a and b as free parameters, and c, d, f, p_{T}^0, and k are the free parameters in the fit. Obviously, the fit function is rather arbitrary, and should be thought of primarily as a "smoothing aid" that is used to produce aesthetically more pleasing p_{T} plots. It is needed because the "fake" muon efficiency binned in p_{T} leads to obvious discontinuities when estimating the jet background p_{T} distribution. When using the binned p_{T} dependent "fake" muon efficiency to estimate the jet background in other distributions, e.g. the m_{T} distribution, discontinuities are washed out because the effective weighting of each p_{T} bin changes gradually as function of the variable of interest. When using the fit function for the "fake" muon efficiency as function of p_{T}, the statistical uncertainty is still taken directly from the relevant p_{T} bin instead of from the fit, since the form of the fit function strongly constrains the p_{T} dependence of $\varepsilon_{\text{fake}}$, but this constraint is arbitrary.

6.4.3 Systematics variations

The systematic uncertainty on the "fake" muon efficiency is expected to give the dominant contribution to the systematic uncertainty on the jet background estimate. The systematic uncertainty is estimated by performing variations of the "fake" muon control region. These are as follows:

- Using no $\not{E}_{\text{T}}$ cut.
- Using a tighter $\not{E}_{\text{T}}$ cut of $40\,\text{GeV}$.
- Using a tighter d_0 cut, $|d_0| > 0.02\,\text{mm}$.
- Using no Z veto.
- Using no Z veto and no $\Delta\phi_{\mu,\not{E}_{\text{T}}}$ cut.
- Using a cut $N_{\text{jet}} \geq 2$ in addition to all other cuts.
- Using a cut $N_{\text{jet}} \geq 2$ instead of the Z veto and $\Delta\phi_{\mu,\not{E}_{\text{T}}}$ cut.

Fig. 6.12 shows the "fake" muon efficiency under the different systematics variations of the "fake" muon control region. As mentioned earlier, the jet background is also estimated with an alternative definition of the loose muons where these are required to pass an isolation preselection defined in eq. (6.21), and fig. 6.12 shows the "fake" muon efficiency for both the

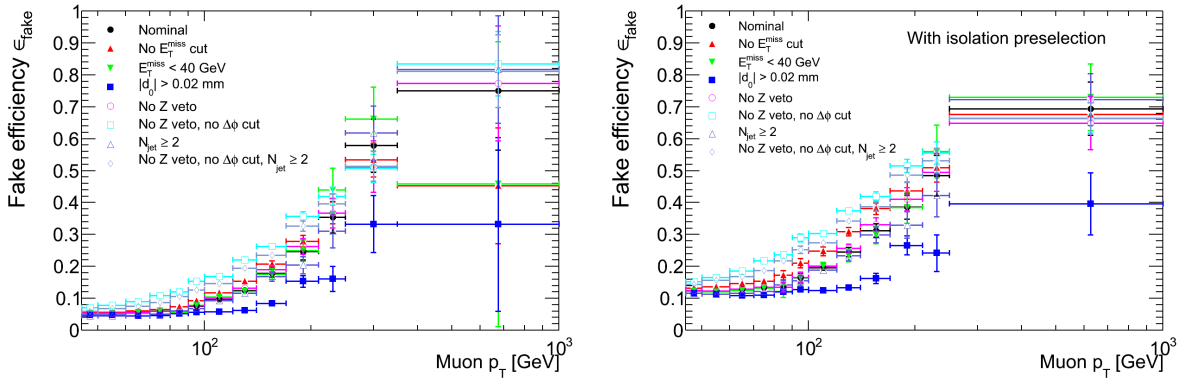

(a) (b)

Figure 6.12: The "fake" muon efficiency under the different systematics variations of the "fake" muon control region for the baseline loose muon definition (a) and the alternative definition with an isolation preselection (b). The two last bins are merged in the latter case because of the loss of statistics associated with the isolation preselection. The error bars represent statistical uncertainty and include the uncertainty in the MC subtraction.

baseline loose muon definition and the alternative definition. The "fake" muon efficiency is higher with the isolation preselection, as one would expect. However, it should be noted that differences between the "fake" muon efficiencies obtained with the two definitions are not to be interpreted as systematic uncertainty, as the efficiencies themselves are not comparable, only the resulting jet background estimates in the tight muon sample.

The plots in fig. 6.12 are quite crowded, and it is not easy to see each individual variation's impact on the efficiency. One should rather focus on the spread between the different variations, as this represents the systematic uncertainty. It is clear that the systematic uncertainty becomes quite large at intermediate and high p_{T}. Rather than assigning a systematic uncertainty to the "fake" muon efficiency as an intermediate step to obtain the systematic uncertainty on the jet background, we estimate the jet background under each efficiency variation and obtain the systematic uncertainty from the resulting jet background variation.

The "real" muon contamination in the "fake" muon control region under the various systematics variations is plotted as function of p_{T} in fig. 6.13. The contamination stays in general below 70% for all variations, with only a couple of counterexamples in the highest p_{T} bin. We see that an exceptionally pure control region is achieved with the cut $|d_0| > 0.02\,\mathrm{mm}$. It is clear from fig. 6.8(b) that the control region can be made very pure with a strict cut on this variable. However, any cut will in general change the composition of the control region and therefore affect the measured "fake" muon efficiency. Cutting very hard on $|d_0|$ may therefore introduce a mismatch between the control region and the inclusive "fake" muon sample and bias the "fake" muon efficiency. We therefore keep $|d_0| > 0.01\,\mathrm{mm}$ as the nominal cut for the control region definition.

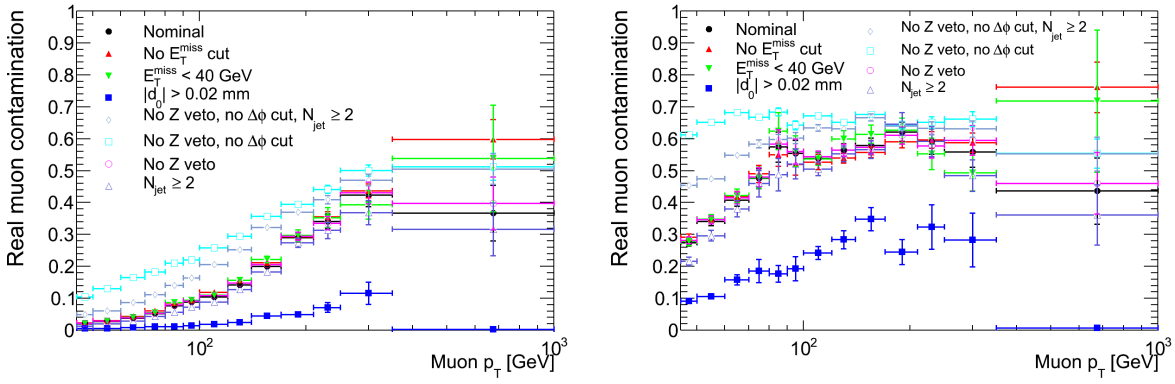

(a) (b)

Figure 6.13: The "real" muon contamination in the "fake" muon control region in the different p_{T} bins used to determine the p_{T} dependent "fake" muon efficiency. The contamination is shown for the loose (a) and tight (b) muon samples.

6.5 Jet background results

The main result of the jet background analysis is the estimate of the jet background for the high m_{T} region which is used to search for new physics. Obviously, though, it is also interesting to see the jet background contribution in various important distributions and evaluate the agreement between data and the total background prediction in regions where the jet background is significant. This serves as validation, as disagreement between data and the total background prediction in regions of significant jet background may point to problems with the jet background estimate. Clearly, such validation is only possible in regions where potential signal is expected to be negligible.

6.5.1 The jet background contribution in various distributions

We begin the results section by showing various distributions with the jet background estimate together with the MC based background estimates and data. Distributions are shown both for the loose muon sample (referring here to the baseline definition of loose muons, i.e. without any isolation cut) and the tight muon sample. The distributions in the loose muon sample are interesting because of the more significant jet background contribution, while the tight muon sample is obviously interesting because it corresponds to the baseline analysis selection, i.e. the tight muon sample is used to search for new physics.

The distributions are shown with error bars on the jet background estimate representing the total uncertainty, including both systematic and statistical uncertainty. The systematic uncertainty is evaluated from the before mentioned variations of the "real" and "fake" muon efficiencies. Separate estimates are performed under all variations, and asymmetric uncertainties are assigned to each bin as the absolute difference between the maximal/minimal estimate and the nominal. In other words, the error bars are set to span all the obtained estimates under the different variations. Finally, the systematic uncertainty is made symmetric by taking the maximum of the upward and downward uncertainties, and the statistical and systematic uncertainties are added in quadrature.

In the case of the estimates in the tight muon sample, all variations are done also with the alternative definition of the loose muon sample, leading to a total of 26 different estimates (5 $\varepsilon_{\mathrm{real}}$ variations, 7 $\varepsilon_{\mathrm{fake}}$ variations, the nominal estimate, and all of these again for the alternative loose muon definition). For the loose muon sample, results obtained with the alternative and default loose muon definitions are not comparable, so only 13 different estimates enter the systematic uncertainty calculation.

Figs. 6.14 and 6.15 show various kinematical distributions, with a panel below each distribution showing the ratio of data to the total background prediction (labeled "data/SM"). The error bars on the ratio include the statistical uncertainty of the data and MC as well as the total uncertainty on the jet background estimate (systematic and statistical uncertainty added in quadrature). Systematic uncertainties on the MC backgrounds, e.g. due to efficiency uncertainties and cross section uncertainties, are not shown in the plots. We note that the jet background constitutes a significant fraction of the total background in the loose muon sample. The good agreement observed between data and the total background prediction in this sample inspires confidence in the data driven jet background estimate.

In the tight muon sample, the jet background is reduced to a small contribution at the percent level to the total background. Hence, the data to total background ratio here does not reveal much in terms of the validity of the jet background estimate. An exception is the low transverse mass region, where we see that the estimated jet background covers the discrepancy observed in fig. 5.7(a), so that the resulting data to total background ratio in fig. 6.15(f) is equal to unity within the uncertainty.

We note that the relative uncertainty on the jet background estimate is much larger in the tight than the loose muon sample. This is primarily due to the different sensitivities of the loose and tight muon jet background estimates to the "fake" muon efficiency (see eqs. (6.8) and (6.9)). It is not due to the fact that the estimates in the loose muon sample are lacking the variations with the alternative loose muon definition, i.e. that only 13 different estimates enter the uncertainty calculation for this sample.

In section 6.4, the assumption was made that data/MC disagreements in fig. 6.7 were due to the missing jet background estimate in these distributions. With the data driven jet background estimate at hand, this assumption can now be put to the test. We consider the corresponding distributions after all event selection cuts, both in the loose and tight muon samples, in fig. 6.16. While the distributions of figs. 6.16(a)-6.16(d) display reasonable agreement between the data and the total background prediction, there is an obvious problem with the d_0 distribution (figs. 6.16(e) and 6.16(f)). In particular, the discrepancy in the peak region suggests problems with the modeling of this variable in the "real" muon MC samples. Such problems would affect the MC subtraction in the determination of the "fake" muon efficiency, and some more investigation will therefore be presented in section 6.5.5.

6.5.2 The transverse mass distribution

The transverse mass distribution shown in fig. 6.15(f) is used to search for new physics. The distribution is examined from approximately $m_{\mathrm{T}} = 250\,\mathrm{GeV}$ and out to very high transverse mass to test the compatibility of the data with the background-only hypothesis and various signal+background hypotheses. For this purpose, it is not optimal that the jet background estimate

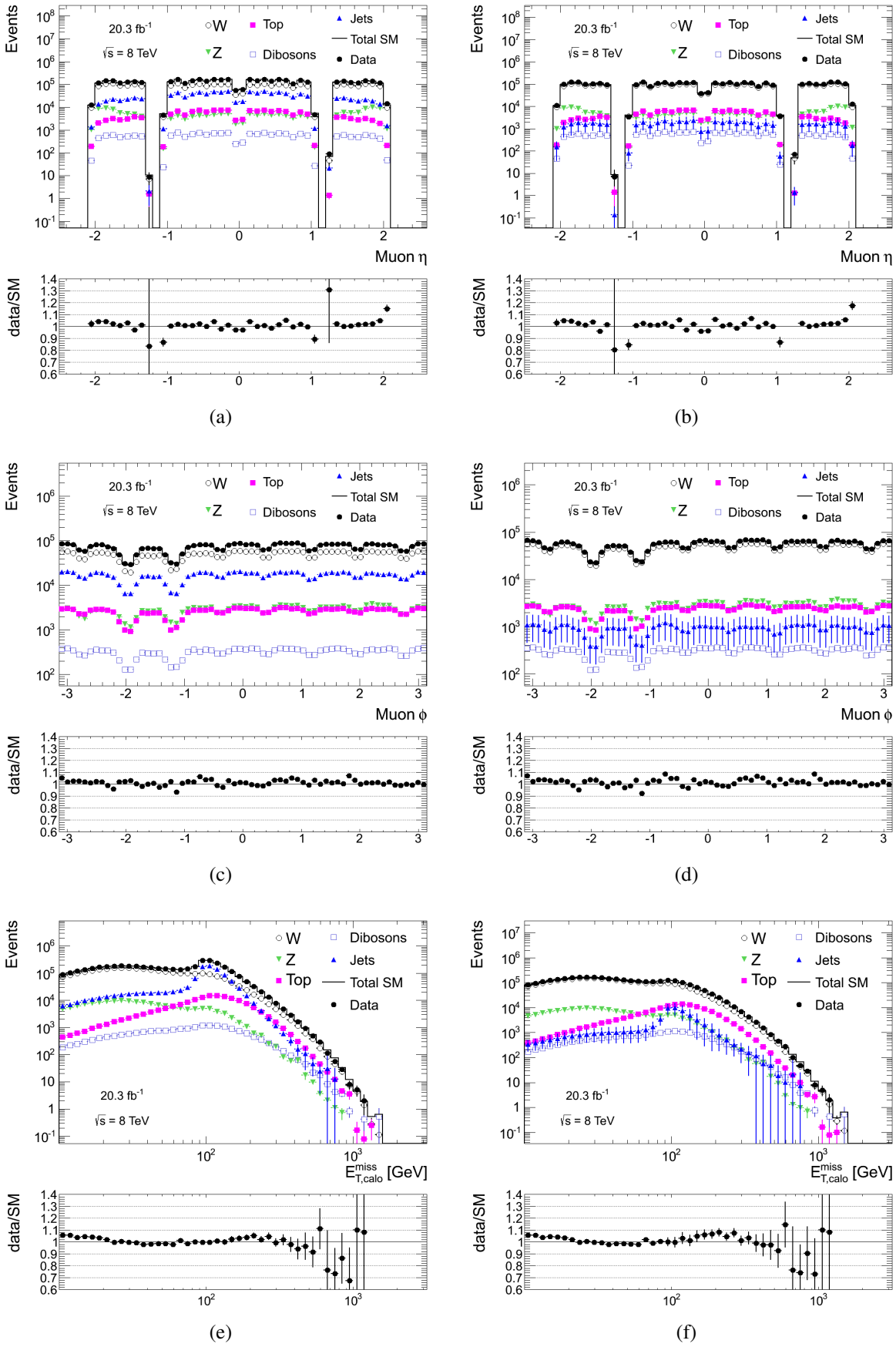

Figure 6.14: Distributions of the muon η ((a) and (b)) and ϕ ((c) and (d)) and the calorimeter $\not{E}_{\mathrm{T}}$ ((e) and (f), see section 5.2.2) in the loose (left) and tight (right) muon samples.

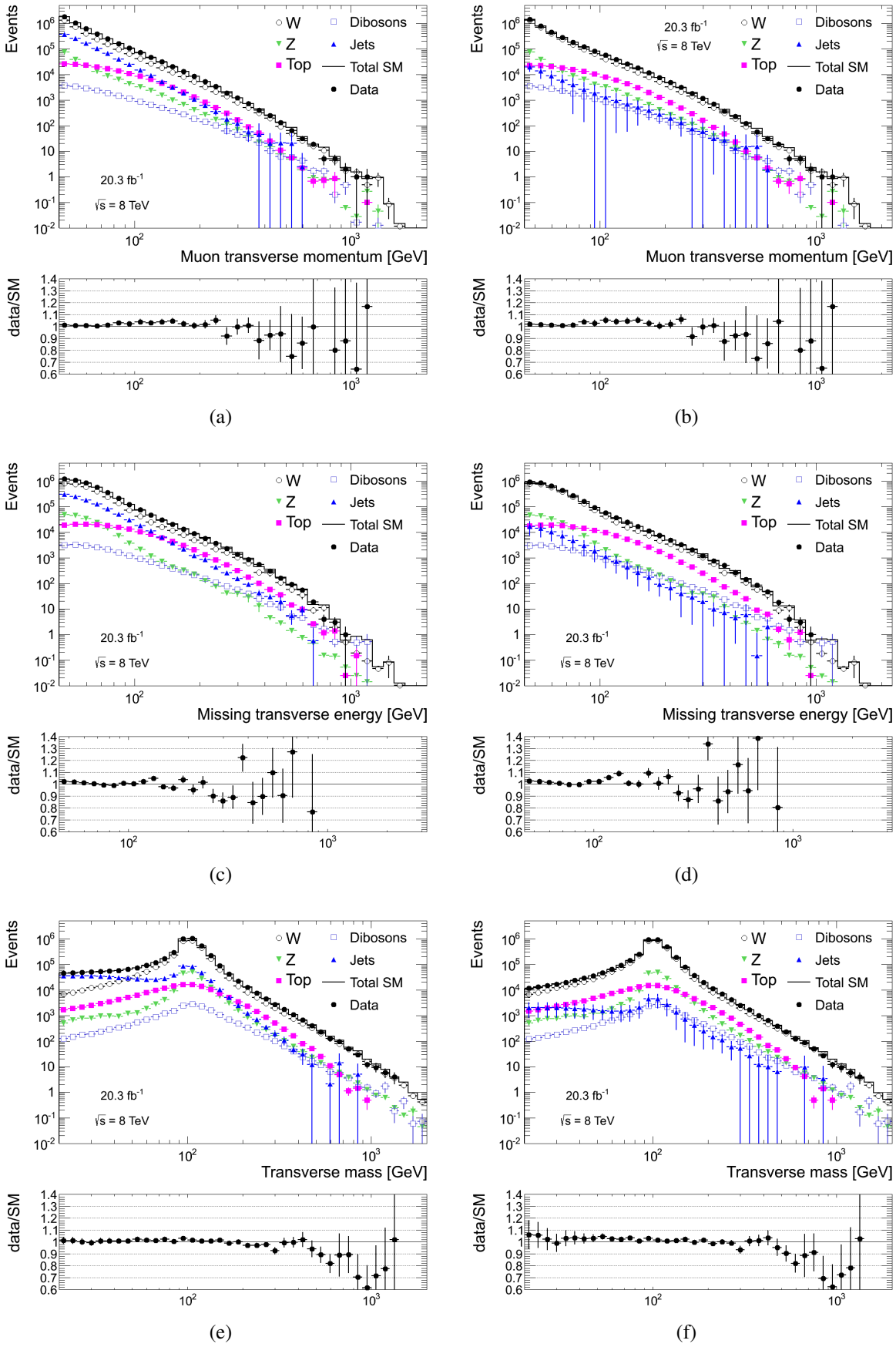

Figure 6.15: Distributions of the muon p_{T} ((a) and (b)), the $\not{E}_{\mathrm{T}}$ ((c) and (d)), and the m_{T} ((e) and (f)) in the loose (left) and tight (right) muon samples.

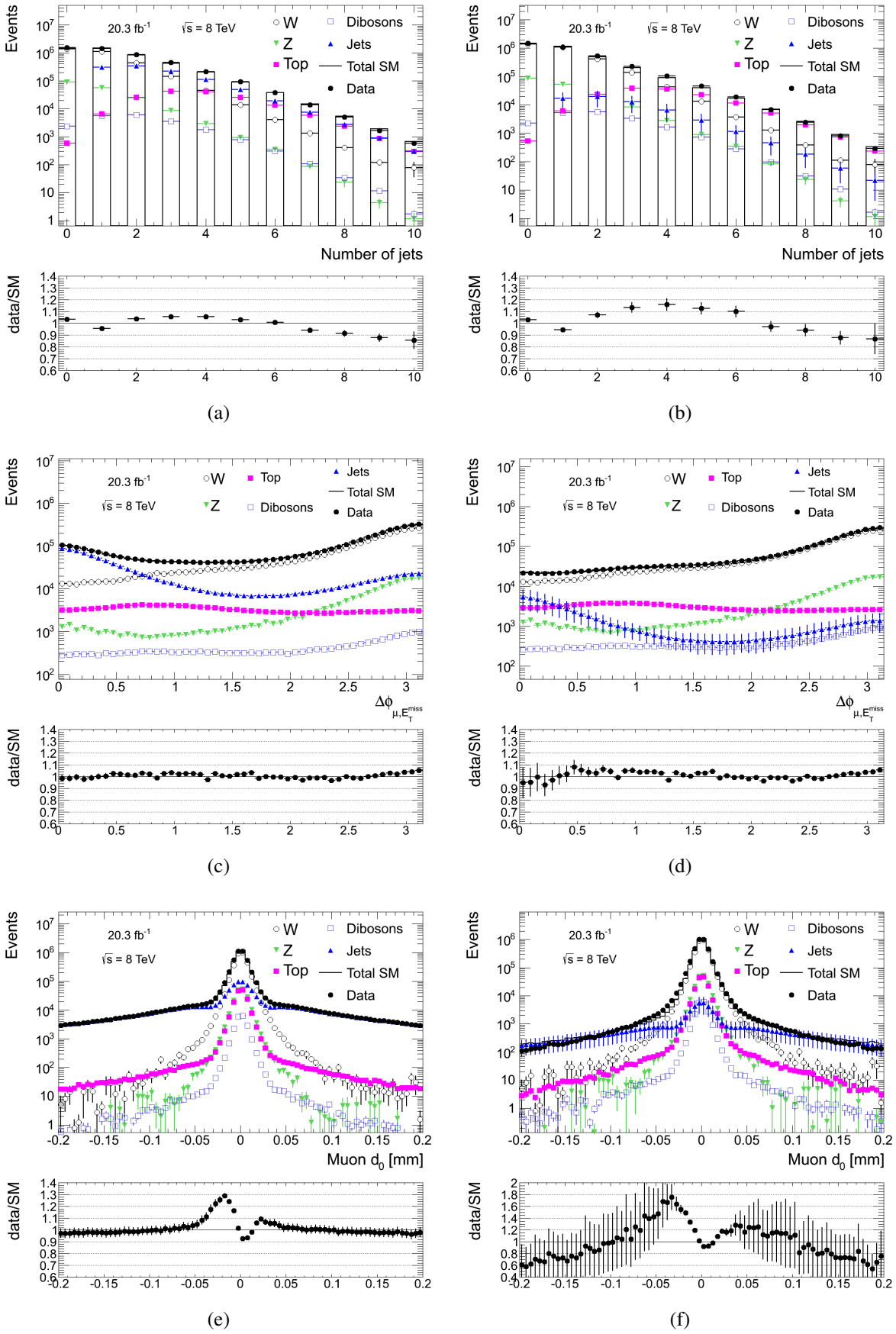

Figure 6.16: Distributions of the variables used in the "fake" muon control region definition in the loose (left) and tight (right) muon samples with the data driven jet background estimate.

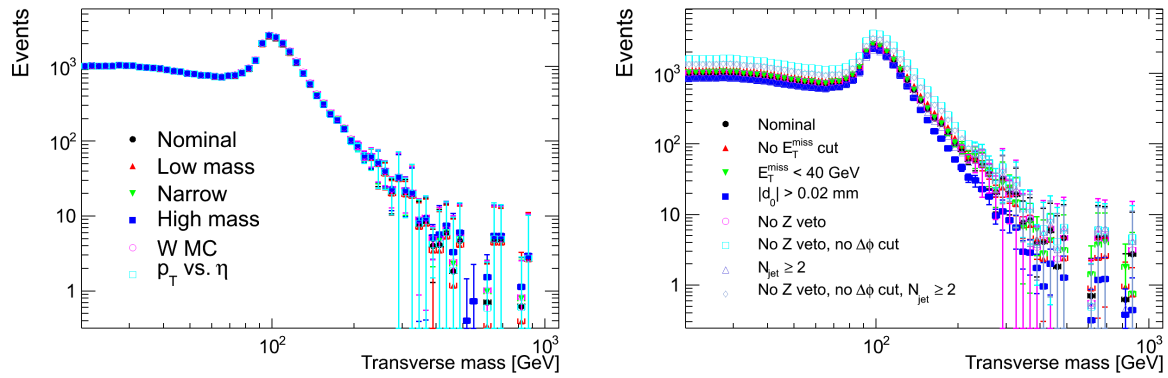

(a) (b)

Figure 6.17: The estimated jet background m_{T} distribution under variations of the "real" muon efficiency (a) and the "fake" muon efficiency (b).

runs out of statistics already as we approach $m_{\mathrm{T}} = 400\,\mathrm{GeV}$. Therefore, the estimated jet background as function of m_{T} is fitted, and the expected jet background event counts for the statistical analysis are taken from the fits. Clearly, the fits need to be extrapolated beyond the region used for the fitting.

In fig. 6.15(f), the error bars on the jet background estimate summarize the results of all systematics variations. It is, however, interesting to know in some more detail how the different variations affect the transverse mass distribution. Before proceeding to the fitting and extrapolation, we therefore show some plots illustrating exactly this.

We show first the estimated jet background m_{T} distribution[5] under variations of the "real" and "fake" muon efficiencies in fig. 6.17. Clearly, the systematic uncertainty on the "real" muon efficiency has a very small impact on the estimated m_{T} distribution, while the systematic uncertainty on the "fake" muon efficiency leads to more significant variations. Although the plots look very similar to those in fig. 6.17, the same variations are plotted under the alternative loose muon definition in fig. 6.18 for completeness. Finally, the nominal estimates with the nominal and alternative loose muon definitions are compared directly in fig. 6.19. We see that the shape of the jet background m_{T} distribution differs slightly between the two estimates, but variations are significantly smaller than those due to the "fake" muon efficiency variations.

6.5.3 Fitting and extrapolation to high transverse mass

The background-only and various signal+background hypotheses are tested by comparing (in a statistical manner) the number of data events above certain transverse mass thresholds to the corresponding predictions under the various hypotheses. In order to obtain an estimate of the expected jet background event counts above these thresholds, we fit the jet background m_{T} distribution with a simple power law function,

$$\frac{dN}{dm_{\mathrm{T}}} = a m_{\mathrm{T}}^{-b}, \tag{6.26}$$

[5]Unless stated otherwise, all plots from here on show the m_{T} distribution in the tight muon sample.

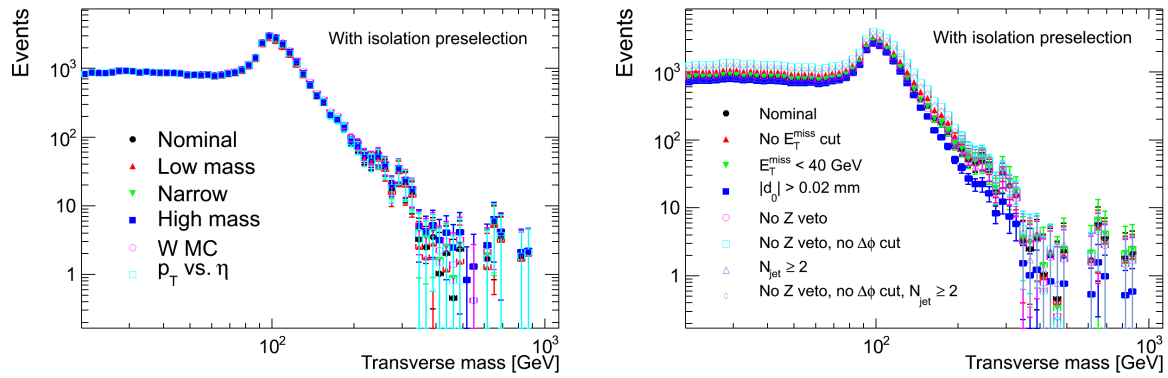

(a) (b)

Figure 6.18: The estimated jet background m_{T} distribution under variations of the "real" muon efficiency (a) and the "fake" muon efficiency (b) for the alternative loose muon definition where these are required to pass the isolation preselection (eq. (6.21)).

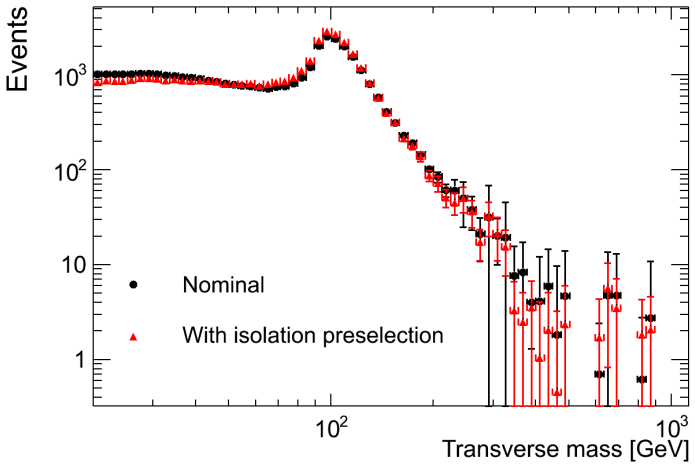

Figure 6.19: The estimated jet background m_{T} distribution with the nominal loose muon definition and with the alternative definition where the loose muons are required to pass the isolation preselection (eq. (6.21)).

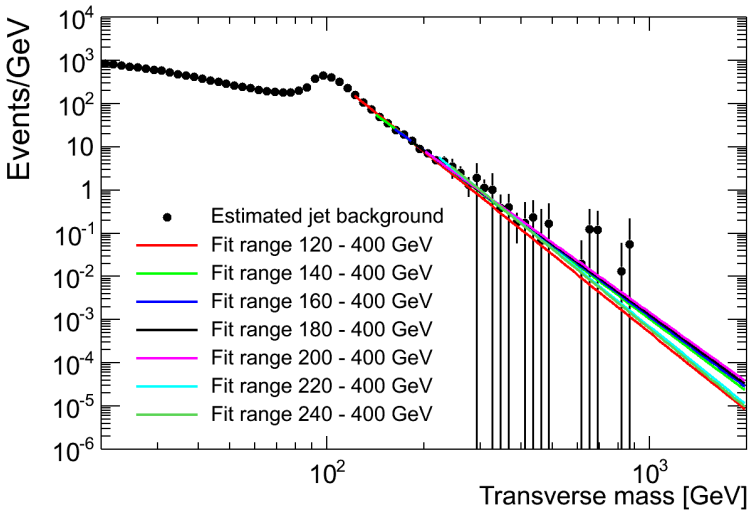

Figure 6.20: The nominal jet background m_{T} distribution with power law fits.

where a and b are the fitted parameters. The range which is considered in the actual fitting must be chosen in a somewhat arbitrary way, and the range is varied to obtain an estimate of the associated systematic uncertainty. The upper edge of the range is kept at $m_{\mathrm{T}} = 400\,\mathrm{GeV}$, motivated by the fact that this is approximately where the jet background m_{T} distribution runs out of statistics. The lower edge is varied from $120\,\mathrm{GeV}$ to $240\,\mathrm{GeV}$ in steps of $20\,\mathrm{GeV}$. Both the nominal jet background m_{T} distribution and the systematics variations are fitted.

For each transverse mass threshold, a nominal jet background estimate is obtained from the fit to the nominal jet background m_{T} distribution with the fit range $[180\,\mathrm{GeV}, 400\,\mathrm{GeV}]$ (the nominal fit). Each individual fit of each systematics variation of the m_{T} distribution provides a different estimate of the jet background for the given transverse mass threshold, and an asymmetric systematic uncertainty is assigned to the nominal estimate to span all these estimates. In other words, the upward systematic uncertainty is the difference between the highest estimate and the nominal, while the downward uncertainty is the difference between the nominal and the lowest estimate. The nominal estimate is also assigned a statistical uncertainty which is taken from the nominal fit.

Fig. 6.20 shows the nominal jet background m_{T} distribution and the seven associated fits. The different fit functions can be thought of as forming a band which represents the systematic uncertainty associated with the choice of fit range. The estimated jet background expected event counts for the different transverse mass thresholds are presented in table 6.1. The thresholds themselves are given by an optimization to be described in section 8.4. Each threshold corresponds to one of the logarithmically spaced thresholds sampled in the optimization procedure, rounded to the nearest GeV, and the numbers are not in any way meant to reflect the precision of the optimization procedure.

The last column of table 6.1 shows the fraction that the jet background constitutes of the total background. We see that this is a very small fraction at the 1% level, which can be compared to the uncertainty on the total background level due to the mass dependent k-factor alone, starting from 5% at the lowest m_{T} threshold and increasing to 19% for the highest threshold. Hence, the jet background contributes negligibly to the total background level. Even though the relative uncertainty on the jet background estimate itself is large, the resulting uncertainty on the total background level is approximately 1% for most transverse mass thresholds, and is at

Search region	Jet background	Fraction of total background [%]
$m_{\mathrm{T}} > 252\,\mathrm{GeV}$	$1.3 \cdot 10^2 \pm 25(\mathrm{stat})^{+72}_{-1.0\cdot 10^2}(\mathrm{sys})$	1.2
$m_{\mathrm{T}} > 317\,\mathrm{GeV}$	$48 \pm 13(\mathrm{stat})^{+23}_{-41}(\mathrm{sys})$	1.1
$m_{\mathrm{T}} > 336\,\mathrm{GeV}$	$37 \pm 11(\mathrm{stat})^{+17}_{-33}(\mathrm{sys})$	1.1
$m_{\mathrm{T}} > 377\,\mathrm{GeV}$	$22 \pm 7.6(\mathrm{stat})^{+9.3}_{-20}(\mathrm{sys})$	1.1
$m_{\mathrm{T}} > 423\,\mathrm{GeV}$	$14 \pm 5.2(\mathrm{stat})^{+5.1}_{-12}(\mathrm{sys})$	1.0
$m_{\mathrm{T}} > 448\,\mathrm{GeV}$	$10 \pm 4.2(\mathrm{stat})^{+3.8}_{-9.7}(\mathrm{sys})$	1.0
$m_{\mathrm{T}} > 502\,\mathrm{GeV}$	$6.3 \pm 2.8(\mathrm{stat})^{+2.6}_{-5.9}(\mathrm{sys})$	0.99
$m_{\mathrm{T}} > 564\,\mathrm{GeV}$	$3.8 \pm 1.9(\mathrm{stat})^{+1.8}_{-3.6}(\mathrm{sys})$	0.99
$m_{\mathrm{T}} > 597\,\mathrm{GeV}$	$2.9 \pm 1.5(\mathrm{stat})^{+1.4}_{-2.8}(\mathrm{sys})$	0.98
$m_{\mathrm{T}} > 710\,\mathrm{GeV}$	$1.4 \pm 0.79(\mathrm{stat})^{+0.77}_{-1.3}(\mathrm{sys})$	0.97
$m_{\mathrm{T}} > 796\,\mathrm{GeV}$	$0.82 \pm 0.51(\mathrm{stat})^{+0.51}_{-0.80}(\mathrm{sys})$	0.98
$m_{\mathrm{T}} > 843\,\mathrm{GeV}$	$0.64 \pm 0.41(\mathrm{stat})^{+0.41}_{-0.62}(\mathrm{sys})$	0.99
$m_{\mathrm{T}} > 1002\,\mathrm{GeV}$	$0.30 \pm 0.21(\mathrm{stat})^{+0.22}_{-0.29}(\mathrm{sys})$	1.0
$m_{\mathrm{T}} > 1062\,\mathrm{GeV}$	$0.23 \pm 0.17(\mathrm{stat})^{+0.18}_{-0.23}(\mathrm{sys})$	1.0
$m_{\mathrm{T}} > 1191\,\mathrm{GeV}$	$0.14 \pm 0.11(\mathrm{stat})^{+0.11}_{-0.14}(\mathrm{sys})$	1.2
$m_{\mathrm{T}} > 1416\,\mathrm{GeV}$	$0.064 \pm 0.054(\mathrm{stat})^{+0.059}_{-0.064}(\mathrm{sys})$	1.4
$m_{\mathrm{T}} > 1500\,\mathrm{GeV}$	$0.050 \pm 0.043(\mathrm{stat})^{+0.047}_{-0.049}(\mathrm{sys})$	1.4
$m_{\mathrm{T}} > 1683\,\mathrm{GeV}$	$0.030 \pm 0.027(\mathrm{stat})^{+0.030}_{-0.030}(\mathrm{sys})$	1.9
$m_{\mathrm{T}} > 1888\,\mathrm{GeV}$	$0.018 \pm 0.017(\mathrm{stat})^{+0.019}_{-0.018}(\mathrm{sys})$	2.8

Table 6.1: The estimated jet background expected event counts with uncertainties for the different transverse mass regions used to search for new physics. The final column shows the fraction that the jet background constitutes of the total background.

most comparable to the MC statistical uncertainty.

A final feature that may be worth noting in table 6.1, is that the jet background fraction of the total background starts out decreasing as function of the m_{T} threshold, but then starts to increase again for m_{T} thresholds above $710\,\mathrm{GeV}$. This is most likely not physical, but rather a consequence of the fact that the simple power law fits do not capture the inevitable change in slope as the parton luminosities diminish at high mass. We conclude that the jet background at very high transverse mass is most likely significantly overestimated, but that this is conservative. It is not in general true that overestimating backgrounds is conservative, but the overestimation of a background can be said to be conservative when the background is found to have a negligible impact on final results. This is indeed found to be the case.

The jet background transverse mass distribution is estimated using the p_{T} dependent "fake" muon efficiency. While there is clearly some η dependence of the efficiency (fig. 6.10(b)), and the muon η is expected to have some correlation with the transverse mass, the impact of neglecting η dependence on top of the p_{T} dependence is assumed to be negligible for the transverse mass distribution. In particular, we find that taking the η dependence into account *instead of* the p_{T} dependence, leads to a transverse mass distribution with a slightly steeper slope than that obtained using a *constant* "fake" muon efficiency, with 10-30% differences in the extrapolated background levels. Using the p_{T} dependence, on the other hand, changes the background levels compared to those obtained with the constant efficiency much more significantly, as seen by comparing tables 6.1 and 6.2. Taking both the η and p_{T} dependencies into account simultaneously requires a two-dimensional determination of the efficiency, as shown for "real" muons

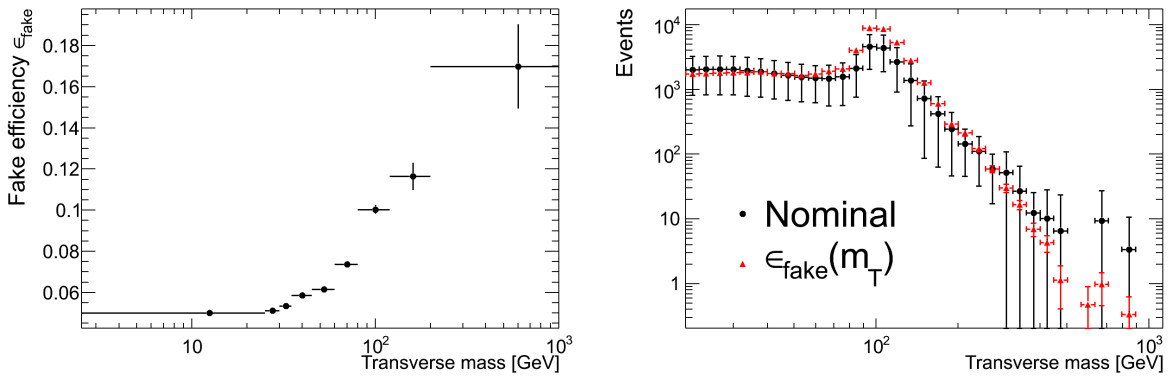

(a) (b)

Figure 6.21: The "fake" muon efficiency as function of the transverse mass (a) and the resulting jet background m_{T} distribution compared to the nominal one (b). In (b), systematic uncertainty is shown for the nominal estimate, but only statistical uncertainty is shown for the estimate with the m_{T} dependent "fake" muon efficiency.

in fig. 6.6(a), and leads to problems due to limited statistics in the control region and the MC subtraction.

6.5.4 Transverse mass dependent "fake" muon efficiency

In the jet background estimation, we have assumed that the "fake" muon efficiency depends only on the muon p_{T}, so that the transverse mass dependence can be inferred by taking into account the full p_{T} spectrum inside each m_{T} bin. We now finally put this assumption to the test by doing the estimate of the jet background transverse mass distribution with a transverse mass dependent "fake" muon efficiency. This efficiency is measured in the same way as the p_{T} dependent one, but the $\not{E}_{\mathrm{T}}$ and $\Delta\phi_{\mu,\not{E}_{\mathrm{T}}}$ cuts are removed from the definition of the "fake" muon control region because of their obvious correlation with the transverse mass. The cut on d_0 is therefore tightened to $|d_0| > 0.02\,\mathrm{mm}$ in order to keep the "real" muon contamination at the same level as for the p_{T} dependent "fake" muon efficiency.

The m_{T} dependent "fake" muon efficiency is shown in fig. 6.21(a), and the resulting jet background m_{T} distribution is compared to the nominal one in fig. 6.21(b), where the error bars on the nominal estimate include systematic uncertainty. The estimated jet background m_{T} distribution with the m_{T} dependent "fake" muon efficiency is seen to agree rather well with the nominal one when taking into account the systematic uncertainty.

The use of the m_{T} dependent "fake" muon efficiency leads in principle to an unfortunate mixing of signal and control regions. In the high transverse mass bins, signal may be present in data, in which case the MC subtraction does not work properly, as only SM processes are subtracted. With the nominal estimate using the p_{T} dependent "fake" muon efficiency, the problem is avoided, as the $\not{E}_{\mathrm{T}}$ and $\Delta\phi_{\mu,\not{E}_{\mathrm{T}}}$ cuts reduce overlap of the jet background control region with the high transverse mass signal region. The jet background estimate with the m_{T} dependent "fake" muon efficiency is therefore only included as a cross check.

6.5.5 Investigation of the d_0 discrepancy

From fig. 6.16 it is clear that the most problematic variable in the "fake" muon control region definition is the transverse impact parameter d_0. The distribution in MC has a clear asymmetry, with more events with positive than with negative d_0 values. The data is much more symmetric, but seems in fact to have a slight asymmetry in the opposite direction of the MC. In addition, it seems that the distribution in MC is more sharply peaked than in data. Obviously, the large data/MC discrepancy in this variable could make a significant impact on the jet background estimate because it affects the estimate of the "real" muon contamination which is subtracted when the "fake" muon efficiency is determined. The variation of the d_0 cut value in the "fake" muon control region definition already provides an estimate of the resulting uncertainty as part of the total uncertainty on the jet background estimate, but some more investigation seems necessary due to the size of the discrepancy in figs. 6.16(e) and 6.16(f).

We show the "fake" muon efficiency as function of p_{T} obtained with different cuts on d_0 in fig. 6.22(a). As the d_0 cut is increased, the "fake" muon efficiency becomes more flat or even a bit decreasing as function of p_{T}. One possible interpretation of this is that the true "fake" muon efficiency is actually much less p_{T} dependent than what we have been using in the nominal jet background estimate, and that this becomes apparent with the tighter d_0 cuts because of smaller "real" muon contamination in the "fake" muon control region. On the other hand, the "fake" muon efficiency could depend on the d_0 variable, so it is not obvious that the "fake" muon efficiency estimated with a tighter d_0 cut provides a better description of the inclusive muon sample even though the estimated "real" muon contamination is smaller with a tighter cut.

We proceed to investigate the effect of a flat, i.e. p_{T} independent, "fake" muon efficiency on the estimated jet background transverse mass distribution. In fig. 6.22(b), the jet background m_{T} distribution obtained with a constant "fake" muon efficiency is compared to the nominal one. As one might have expected, the estimated jet background decreases more rapidly as function of m_{T} when a constant "fake" muon efficiency is used. The corresponding estimated jet background expected event counts in the different transverse mass search regions are shown in table 6.2. Obviously, these are smaller than those presented in table 6.1, but they are within the uncertainties of the latter.

It is worth noting that the jet background transverse mass distribution obtained with the constant "fake" muon efficiency is in good agreement with the estimate we obtain using the standard "shape method" where the shape of the jet background m_{T} distribution is obtained from a jet enriched control region defined by an "inverted" isolation cut. This shape is then assumed to describe the jet background m_{T} distribution also in the isolated muon sample, and this assumption is pretty much equivalent to the assumption of an m_{T} independent "fake" muon efficiency in the Matrix Method. When estimating the jet background with the "shape method", we determine the normalization of the jet background in the isolated muon sample by fitting the sum of the MC and jet backgrounds to the data in the low $\not\!\!E_{\mathrm{T}}$ region.

The data/MC discrepancy in the d_0 distribution is not investigated further in this work. A better MC description of this variable may be needed in order to make a more precise jet background estimate, as its discriminating power seems necessary to obtain a reasonably pure "fake" muon control region. Investigation of the p_{T} dependence of the "fake" muon efficiency obtained from heavy flavor enriched MC samples, such as those used in ref. [98], would be

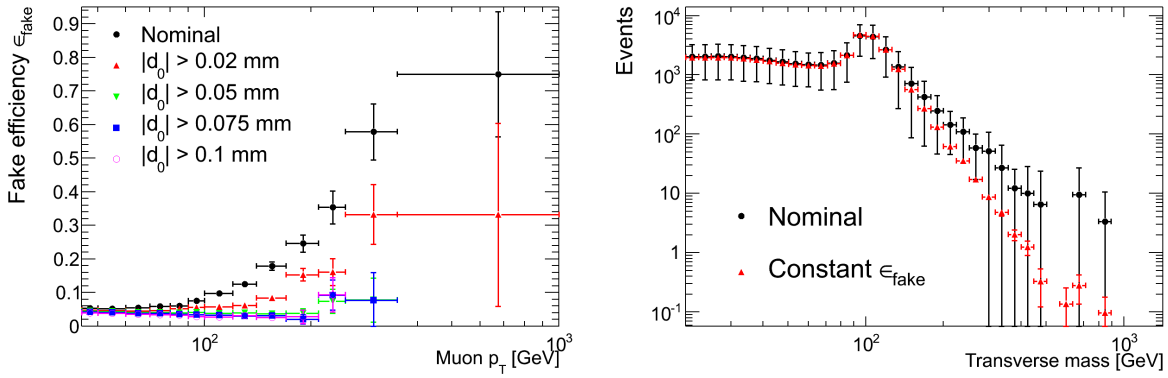

(a) (b)

Figure 6.22: The "fake" muon efficiency as function of p_{T} obtained with different cuts on d_0 (a) and the jet background m_{T} distribution obtained with a constant "fake" muon efficiency compared to the nominal one (b). In (b), systematic uncertainty is shown for the nominal estimate, but only statistical uncertainty is shown for the estimate with a constant "fake" muon efficiency.

Search region	Jet background	Fraction of total background [%]
$m_{\mathrm{T}} > 252\,\mathrm{GeV}$	34 ± 1.6(stat)	0.31
$m_{\mathrm{T}} > 317\,\mathrm{GeV}$	8.8 ± 0.61(stat)	0.21
$m_{\mathrm{T}} > 336\,\mathrm{GeV}$	6.3 ± 0.47(stat)	0.19
$m_{\mathrm{T}} > 377\,\mathrm{GeV}$	3.2 ± 0.28(stat)	0.15
$m_{\mathrm{T}} > 423\,\mathrm{GeV}$	1.6 ± 0.16(stat)	0.12
$m_{\mathrm{T}} > 448\,\mathrm{GeV}$	1.1 ± 0.12(stat)	0.11
$m_{\mathrm{T}} > 502\,\mathrm{GeV}$	0.59 ± 0.070(stat)	0.092
$m_{\mathrm{T}} > 564\,\mathrm{GeV}$	0.30 ± 0.039(stat)	0.077
$m_{\mathrm{T}} > 597\,\mathrm{GeV}$	0.21 ± 0.029(stat)	0.07
$m_{\mathrm{T}} > 710\,\mathrm{GeV}$	0.076 ± 0.012(stat)	0.054
$m_{\mathrm{T}} > 796\,\mathrm{GeV}$	0.039 ± 0.0066(stat)	0.046
$m_{\mathrm{T}} > 843\,\mathrm{GeV}$	0.028 ± 0.0049(stat)	0.043
$m_{\mathrm{T}} > 1002\,\mathrm{GeV}$	0.0099 ± 0.0020(stat)	0.035
$m_{\mathrm{T}} > 1062\,\mathrm{GeV}$	0.0070 ± 0.0014(stat)	0.032
$m_{\mathrm{T}} > 1191\,\mathrm{GeV}$	0.0036 ± 0.00078(stat)	0.032
$m_{\mathrm{T}} > 1416\,\mathrm{GeV}$	0.0013 ± 0.00031(stat)	0.029
$m_{\mathrm{T}} > 1500\,\mathrm{GeV}$	0.00092 ± 0.00022(stat)	0.025
$m_{\mathrm{T}} > 1683\,\mathrm{GeV}$	0.00046 ± 0.00012(stat)	0.029
$m_{\mathrm{T}} > 1888\,\mathrm{GeV}$	0.00024 ± 0.000064(stat)	0.037

Table 6.2: The estimated jet background expected event counts obtained using a constant "fake" muon efficiency. Only the statistical uncertainty is shown.

interesting. However, special generator level filters may be needed in order to obtain sufficient statistics at high p_{T}, as the "fake" muon efficiencies obtained from MC in ref. [98], are seen to be severly statistics limited already from $p_{\mathrm{T}} = 50\,\mathrm{GeV}$. Relying on the description of "fake" muons in MC was also what we wanted to avoid in the first place when introducing the data driven jet background estimate.

In summary, the transverse impact parameter d_0 used in the definition of the "fake" muon control region seems to be not well described in MC. The cut value is seen to have a large impact on the p_{T} dependence of the "fake" muon efficiency, but even a constant "fake" muon efficiency provides jet background levels which are within the uncertainties of the nominal estimate. Keeping in mind that the main result of the jet background estimation is that this background is negligible at high transverse mass, we argue that further investigation is not necessary.

6.6 Summary

In this chapter, the data driven estimation of the jet background in the muon channel has been described. This background covers the discrepancy between data and MC in the very low transverse mass region. Distributions in the loose muon sample, i.e. without the isolation cut applied, show good agreement between the data and the total background prediction, and the jet background in this sample is significant. This inspires confidence in the data driven estimate, but distributions in the tight muon sample are much more sensitive to the "fake" muon efficiency. The jet background levels in the high transverse mass search regions are found to be negligible, although associated with a relatively speaking very large uncertainty.

With estimates at hand for all backgrounds, we can proceed with testing the background-only hypothesis and constraining possible contributions from new physics. This necessarily involves some statistical analysis, which is the topic of the next chapter.

Chapter 7

Statistical analysis for discovery and exclusion

In the search for new heavy, charged bosons, we want ultimately to draw some conclusion about the presence or absence of such new physics in nature. This is done by comparing the observed transverse mass distribution to the predictions from background alone and from the combination of background and hypothetical signal. The observed event count in any interval of the transverse mass distribution must in this context be thought of as the realization of a stochastic variable whose expectation value is related to the presence or absence of new physics.

It is clear that each bunch crossing in the ATLAS detector has some finite probability to produce an event that passes the event selection and has a reconstructed transverse mass in a given interval. After a certain number of bunch crossings, the observed event count in the given interval is therefore a realization of a binomially distributed stochastic variable. However, if we consider many bunch crossings, each with a very small probability to produce an event in the given transverse mass interval, the binomial distribution is well approximated by the Poisson distribution. The latter plays therefore a central role in the statistical analysis of search results in high energy physics. The probability for a Poisson distributed stochastic variable with expectation value λ to take the value k is

$$P(k|\lambda) = \frac{\lambda^k e^{-\lambda}}{k!}. \tag{7.1}$$

In the absence of significant evidence for the presence of signal, search results are usually presented in the form of exclusion limits on the cross section for the sought after new physics process or on other relevant theory parameters. Both *frequentist* and *Bayesian* limit setting procedures are widely used in high energy physics. A Bayesian exclusion limit is a statement about the probability that certain parameter values are realized in nature, i.e. excluded parameter values are those that are sufficiently improbable after gaining knowledge from the observed data. Such probabilities cannot be defined precisely in terms of the relative frequency of occurence of some outcome when repeating an experiment many times – they are not well defined frequentist probabilities. In a frequentist analysis, one tries to stick only to such well defined probabilities, and the excluded parameter values are those that would make the observed data sufficiently improbable.

7.1 Single bin counting experiment

All the published ATLAS W' searches [103–109] have been interpreted statistically in the framework of the single bin counting experiment. Events are counted above certain transverse mass thresholds, and the expected number of events above a given threshold is written as

$$\lambda = L_{\mathrm{int}} \left(\varepsilon_{\mathrm{sig}} \sigma + \sigma_{\mathrm{bg}}^{\mathrm{eff}} \right) \tag{7.2}$$

with L_{int} as the integrated luminosity, σ as the signal cross section[1], $\varepsilon_{\mathrm{sig}}$ as the signal efficiency, and $\sigma_{\mathrm{bg}}^{\mathrm{eff}}$ as the number of expected background events per unit of integrated luminosity. The signal cross section σ is usually defined to be the total cross section for W' production and decay to a single lepton generation, but we will also consider definitions where the cross section is restricted to more interesting parts of the total phase space. When describing the limit setting itself, no explicit choice needs to be made. We only need to know that the number of selected signal events (above the transverse mass threshold) per unit of integrated luminosity is the product of the signal efficiency and the signal cross section, and we can think of this relation as the definition of the signal efficiency.

The signal cross section σ is the parameter of interest in the analysis. The expected number of events λ depends also on the nuisance parameters L_{int}, $\varepsilon_{\mathrm{sig}}$, and $\sigma_{\mathrm{bg}}^{\mathrm{eff}}$. All of these are constrained by external measurements summarized as a central value and an uncertainty. The signal efficiency is determined with the signal MC samples, and the background level is primarily also measured with MC samples, except for the small jet contribution estimated using the data. All MC predictions include obviously all corrections such as smearing, efficiency corrections, etc.

We combine the results of the electron and muon channel searches assuming a common signal cross section for the two channels. The expected number of events in a channel labeled with the index i is then

$$\lambda_i = L_{\mathrm{int}} \left(\varepsilon_{\mathrm{sig}}^{i} \sigma + \sigma_{\mathrm{bg},i}^{\mathrm{eff}} \right) . \tag{7.3}$$

Channels are assumed to be statistically independent so that the probability for a given set of observations in the different channels is a simple product of the individual channel Poisson probabilities.

7.2 Frequentist/hybrid analysis

A frequentist hypothesis test is based on a chosen *test statistic*, a function that maps the observed data (in our case the observed event counts in the electron and/or muon channels) into a single real number. The test statistic defines how background-like or signal-like the observed data are. Agreement between the observed data and a particular hypothesis is quantified by a p-value, which is the relevant tail of the distribution of the test statistic above or below the observed value under the given hypothesis. For example, the p-value quantifying the deviation of the

[1] If interference is taken into account, the signal cross section is not necessarily a well defined quantity, but we do not include in the statistical interpretation models in which the new physics is allowed to interfere with SM processes. See section 3.2.6.

observed data from the background-only prediction is

$$p = \sum_{X \geq X_{\mathrm{obs}}} P_{\mathrm{bg}}(X) \tag{7.4}$$

where X is the test statistic, assumed here to take discrete values and higher values for more signal-like results, X_{obs} is the observed value of the test statistic, and $P_{\mathrm{bg}}(X)$ is the probability to obtain the test statistic value X under the background-only hypothesis. This p-value is the probability under the background-only hypothesis to obtain an as signal-like or more signal-like result than the observed result, and smaller values correspond to stronger evidence for the presence of signal. The corresponding *significance* Z of the deviation from the background-only hypothesis is defined by the relation

$$p = \int_Z^\infty \frac{e^{-x^2/2}}{\sqrt{2\pi}}\, dx, \tag{7.5}$$

i.e. it is the number of standard deviations one has to go into the tail of a Gaussian distribution to find the same p-value. In high energy physics, one ususally does not claim "discovery" or "observation" with significance less than 5, corresponding to a p-value of about $3 \cdot 10^{-7}$.

In the absence of uncertainties on the nuisance parameters, the probability $P_{\mathrm{bg}}(X)$ is a pure Poisson probability. When nuisance parameter uncertainties are included, we modify the probability to account for the uncertainties, as described in section 7.2.2.

7.2.1 Exclusion

Exclusion limits are in the frequentist setting determined by considering the p-value of the signal+background hypothesis in the direction of more background-like results, i.e.

$$\mathrm{CL}_{s+b} = \sum_{X \leq X_{\mathrm{obs}}} P(X|\sigma). \tag{7.6}$$

We follow here the notation of ref. [110], denoting the p-value under the signal+background hypothesis CL_{s+b}. We have defined the probability $P(X|\sigma)$ to obtain a test statistic value X in the presence of signal with cross section σ. Clearly, $P_{\mathrm{bg}}(X) = P(X|\sigma = 0)$.

It is obvious that smaller values of CL_{s+b} inspire less confidence in the signal+background hypothesis, and in a pure frequentist analysis one would exclude any signal cross section giving $\mathrm{CL}_{s+b} \leq \delta$ at confidence level (CL) $1-\delta$.[2] This approach leads to very counter-intuitive results, which can be illustrated by considering the case of no observed events in a single bin (and single channel) counting experiment without systematic uncertainty. In this case, we can take the test statistic to be the number of events n, and we find

$$\mathrm{CL}_{s+b} = P(n = 0|\sigma) = e^{-\lambda(\sigma)} = e^{-[s(\sigma)+b]} \tag{7.7}$$

with $s(\sigma)$ and b as the expected number of signal and background events respectively, i.e.

[2] It is customary to use $\delta = 5\%$ in high energy physics, thus quoting exclusion at 95% CL.

$s(\sigma) = L_{\mathrm{int}}\varepsilon_{\mathrm{sig}}\sigma$ and $b = L_{\mathrm{int}}\sigma_{\mathrm{bg}}^{\mathrm{eff}}$. We would place an upper limit on σ, σ_{up}, satisfying

$$e^{-[s(\sigma_{\mathrm{up}})+b]} = \delta \quad \Rightarrow \quad s(\sigma_{\mathrm{up}}) + b = -\ln\delta \approx 3 \tag{7.8}$$

with $\delta = 5\%$. Any signal+background hypothesis predicting 3 events can be excluded, and the limit on σ becomes stronger if b is increased. Obviously unreasonable results are obtained in the limit $b \to 3$, where one can exclude signal hypotheses giving arbitrarily small contributions to the expected event count.

To avoid such unreasonably strong exclusion in the cases of overestimated backgrounds and/or statistical fluctuations, the CL_s prescription [110] is widely used in high energy physics. The p-value CL_{s+b} is supplemented with the corresponding tail of the background-only distribution,

$$\mathrm{CL}_b = \sum_{X \leq X_{\mathrm{obs}}} P(X|\sigma = 0), \tag{7.9}$$

and the ratio

$$\mathrm{CL}_s = \frac{\mathrm{CL}_{s+b}}{\mathrm{CL}_b} \tag{7.10}$$

is finally considered as the relevant p-value for exclusion, i.e. the signal is considered excluded if $\mathrm{CL}_s \leq \delta$. In the case of no observed events and no systematic uncertainty, we find

$$\mathrm{CL}_s = \frac{P(n=0|\sigma)}{P(n=0|\sigma=0)} = e^{-s(\sigma)}, \tag{7.11}$$

and the limit on the signal cross section is given by $s(\sigma_{\mathrm{up}}) = -\ln\delta \approx 3$ with no dependence of the background b – the signal itself must contribute at least three expected events to be considered excluded.

7.2.2 Frequentist/hybrid implementation

For each of the nuisance parameters θ_i, we have a measured value $\overline{\theta_i}$ and an estimated uncertainty σ_{θ_i}. The uncertainty is in general dominated by systematic effects, and does not have an immediate statistical interpretation. In order to incorporate the uncertainty in the limit setting, we assign a probability density function[3] (PDF) $g_i(\theta_i)$ to each nuisance parameter, and "smear" the distributions of the test statistic by integrating over the nuisance parameters. This is essentially a Bayesian treatment where $g_i(\theta_i)$ is interpreted as the prior probability density for the nuisance parameter θ_i, and the resulting prescription is often referred to as *hybrid*. An obvious choice for the probability density is a Gaussian with mean equal to $\overline{\theta_i}$ and standard deviation σ_{θ_i}.

We calculate frequentist p-values and exclusion limits using as test statistic

$$X = \sum_{i=1}^{N_{\mathrm{chan}}} n_i \ln\left(1 + \frac{\overline{s_i}(\sigma)}{\overline{b_i}}\right), \tag{7.12}$$

[3]The abbreviation "PDF" is used for both parton density functions and probability density functions, but it should always be clear from the context which is the correct interpretation.

which is equal to the logarithm of the likelihood ratio except for an offset that is independent of $\mathbf{n}$ and therefore does not affect the ordering of potential outcomes of the experiment. Here, $\mathbf{n}$ is a vector with components n_i, the number of events in channel i, and N_{chan} is the number of channels, equal to 2 for the electron and muon channel combination and 1 for the analysis of each individual channel. The expected signal and background event counts $\overline{s_i}(\sigma) = \overline{L_{\text{int}}}\overline{\varepsilon^i_{\text{sig}}}\sigma$ and $\overline{b_i} = \overline{L_{\text{int}}}\overline{\sigma^{\text{eff}}_{\text{bg},i}}$ are evaluated at the measured values of the nuisance parameters.

We assume that the probability to observe a test statistic value X when the signal cross section is σ is

$$P(X|\sigma) = \int P(X|\sigma, \boldsymbol{\theta}) \prod_i g_i(\theta_i)\, d\boldsymbol{\theta} \tag{7.13}$$

with $P(X|\sigma, \boldsymbol{\theta})$ as the probability to observe this test statistic value for given values of the nuisance parameters contained in the vector $\boldsymbol{\theta}$. In practice, we calculate such probabilities by generating pseudo-experiments. In such a pseudo-experiment, the values of the nuisance parameters are first generated according to their PDFs, and the event count n_i in each channel is then generated according to a Poisson distribution with the expectation value given by eq. (7.3) for the generated values of the nuisance parameters. The fraction of such pseudo-experiments that lead to the test statistic value X is the probability defined in eq. (7.13). These probabilities and corresponding p-values can be calculated for any value of σ, including the background-only case $\sigma = 0$. They are used both in the cases of discovery significance and exclusion. In the case of exclusion, the limit σ_{up} is found by solving the equation $\text{CL}_s(\sigma_{\text{up}}) = \delta$ by the bisection method. When there are many expected events, keeping track of each individual discrete test statistic value becomes computationally intractable. In this case, the test statistic becomes "almost continuous", and sums such as eq. (7.4) are replaced by integrals of a histogrammed test statistic distribution.

The implementation described here resembles closely that described in ref. [111], except that the test statistic evaluation itself involves integration over the nuisance parameters in that prescription. It is also very similar to the implementation used for limit computation in ref. [104], and was used as a cross check for that paper. It does not correspond to "LHC style CL_s" as used e.g. in ATLAS Higgs publications, where the *profile likelihood ratio* (see ref. [115]) is used and no integration over nuisance parameters is performed.

7.3 Bayesian analysis

Bayes' theorem relates the probability for A given B, $P(A|B)$, to the probability for B given A, $P(B|A)$. It has the form

$$P(A|B) = \frac{P(B|A)\, P(A)}{P(B)}. \tag{7.14}$$

While the theorem itself is valid regardless of the interpretation of probability, it forms the starting point for Bayesian analysis with a Bayesian interpretation of probability as a "degree of belief". In a Bayesian analysis of the single bin counting experiment, we are interested in the probability density of the parameter of interest σ given the data, which is given by Bayes' theorem as

$$p(\sigma|\mathbf{n}_{\text{obs}}) = \frac{P(\mathbf{n}_{\text{obs}}|\sigma)\, p(\sigma)}{P(\mathbf{n}_{\text{obs}})} \tag{7.15}$$

with lowercase p denoting probability density and uppercase P denoting probability. The vector $\mathbf{n}_{\text{obs}}$ (with components n^i_{obs}) holds the observed event counts in the different channels. The probability $P(\mathbf{n}_{\text{obs}})$ does not depend on the signal cross section σ and is determined by the normalization requirement[4]

$$\int_0^\infty p(\sigma|\mathbf{n}_{\text{obs}})\, d\sigma = 1. \tag{7.16}$$

The *prior* probability density for the parameter of interest, $p(\sigma)$, represents our knowledge about the parameter before seeing the data. It should reflect that we do not know whether new physics is present, but that we are open to the possibility. We choose the "flat" prior which is zero for $\sigma < 0$ and constant for $\sigma \geq 0$, thus reflecting that a negative cross section is unphysical, but that any positive (including zero) value is possible as far as we know. The choice can be interpreted as meaning that we a priori do not favor any positive value of σ over another, i.e. that we want to provide as little information as possible. This might seem at first like a very good motivation for the flat prior, but the argument is not so clear, as a flat prior in a different, related variable, for example a coupling strength, would correspond to a non-flat prior in the cross section. A better motivation is that the flat cross section prior is standard in high energy physics, thus facilitating comparison between limits from different experiments, and that the flat prior in many cases leads to results in good agreement with CL_s limits.

The flat prior is independent of σ (for $\sigma \geq 0$), and can therefore be absorbed into a normalization constant together with $P(\mathbf{n}_{\text{obs}})$. The expression for the posterior probability density takes then the form

$$p(\sigma|\mathbf{n}_{\text{obs}}) = NP(\mathbf{n}_{\text{obs}}|\sigma) = N \prod_{i=1}^{N_{\text{chan}}} \frac{\lambda_i^{n^i_{\text{obs}}} e^{-\lambda_i}}{n^i_{\text{obs}}!} \tag{7.17}$$

with λ_i as defined in eq. (7.3) and N determined by the condition (7.16).

Dependence on the nuisance parameters enters through λ_i, and if these are not assumed to be known precisely, they should be included already in eq. (7.15), which then takes the form

$$p(\sigma, \boldsymbol{\theta}|\mathbf{n}_{\text{obs}}) = \frac{P(\mathbf{n}_{\text{obs}}|\sigma, \boldsymbol{\theta})\, p(\sigma, \boldsymbol{\theta})}{P(\mathbf{n}_{\text{obs}})}. \tag{7.18}$$

As before, $P(\mathbf{n}_{\text{obs}})$ acts only as a normalization constant, and the posterior probability density for the parameter of interest alone is found by integrating over the nuisance parameters:

$$p(\sigma|\mathbf{n}_{\text{obs}}) = \int p(\sigma, \boldsymbol{\theta}|\mathbf{n}_{\text{obs}})\, d\boldsymbol{\theta} = N \int P(\mathbf{n}_{\text{obs}}|\sigma, \boldsymbol{\theta})\, p(\sigma, \boldsymbol{\theta})\, d\boldsymbol{\theta} \tag{7.19}$$

with N as before determined by eq. (7.16) and

$$P(\mathbf{n}_{\text{obs}}|\sigma, \boldsymbol{\theta}) = \prod_{i=1}^{N_{\text{chan}}} \frac{\lambda_i^{n^i_{\text{obs}}}(\sigma, \boldsymbol{\theta})\, e^{-\lambda_i(\sigma,\boldsymbol{\theta})}}{n^i_{\text{obs}}!}. \tag{7.20}$$

We assume a factorized (uncorrelated) form for the prior probability density of the nuisance

[4] In principle, the integration should extend to $-\infty$ at this point, but the condition $p(\sigma|\mathbf{n}_{\text{obs}}) = 0$ for any $\sigma < 0$ will be ensured by our choice of prior $p(\sigma)$.

parameters and the parameter of interest,

$$p(\sigma, \boldsymbol{\theta}) = p(\sigma) \prod_i g_i(\theta_i), \tag{7.21}$$

with $p(\sigma)$ as the prior probability density of the signal cross section (chosen to be flat) and $g_i(\theta_i)$ as the prior for the nuisance parameter θ_i. The function $g_i(\theta_i)$ is meant to represent the available information after the measurement of the nuisance parameter θ_i and could ideally be thought of as the posterior probability density after that measurement. The measurements of the nuisance parameters are, however, summarized simply as a central value and an uncertainty, and some PDF must be chosen to represent this information.

With the posterior probability density for the signal cross section at hand, the upper limit σ_{up} on the signal cross section at credibility level (CL) $1 - \delta$ is defined by

$$\int_0^{\sigma_{\mathrm{up}}} p(\sigma|\mathbf{n}_{\mathrm{obs}})\, d\sigma = 1 - \delta \tag{7.22}$$

or equivalently

$$\int_{\sigma_{\mathrm{up}}}^{\infty} p(\sigma|\mathbf{n}_{\mathrm{obs}})\, d\sigma = \delta, \tag{7.23}$$

i.e. it is the cross section value above which there is a probability δ for the true signal cross section to be found.

7.3.1 The case of no observed events

In section 7.2.1, we saw that in the absence of uncertainty on the nuisance parameters, the CL_s exclusion limit for a single channel with no observed events corresponds to three expected signal events. We derive the corresponding limit in the Bayesian case starting from eq. (7.17). For ease of notation, we define $s = L_{\mathrm{int}}\varepsilon_{\mathrm{sig}}\sigma$ and $b = L_{\mathrm{int}}\sigma_{\mathrm{bg}}^{\mathrm{eff}}$, with s as the parameter of interest, described by a flat prior (which is equivalent to the choice of flat prior for σ). With $n_{\mathrm{obs}} = 0$ in the single channel case, eq. (7.17) is reduced to

$$p(s|n_{\mathrm{obs}} = 0) = Ne^{-(s+b)}. \tag{7.24}$$

The normalization constant is determined by the condition

$$\int_0^{\infty} p(s|n_{\mathrm{obs}} = 0)\, ds = 1, \tag{7.25}$$

giving $N = e^b$ so that the dependence of the posterior $p(s|n_{\mathrm{obs}} = 0)$ on the background level is canceled out. The posterior is thus simply $p(s|n_{\mathrm{obs}} = 0) = e^{-s}$ and the upper limit s_{up} on s is given by

$$\int_0^{s_{\mathrm{up}}} e^{-s}\, ds = 1 - \delta \tag{7.26}$$

leading to $s_{\mathrm{up}} = -\ln\delta$ exactly as in the case of CL_s. As noted before, $s_{\mathrm{up}} \approx 3$ for $\delta = 5\%$.

We see that the Bayesian limit in the case $n_{\mathrm{obs}} = 0$ is naturally independent of the back-

ground level, and no extra protection is necessary to avoid unreasonably strong exclusion in the case of overestimated backgrounds or downward fluctuations. The limit is also independent of the uncertainty on the background level, as the integral of the factor e^{-b} over the background level PDF does not depend on s and can therefore be absorbed into the normalization constant. In the context of the complete statistical model with uncertainty also on the signal efficiency, this is no longer strictly true if correlations between the signal efficiency and background level are taken into account.

The flat prior as an improper prior

The uniform distribution can only be defined for finite intervals, and the flat cross section prior is really ill-defined or *improper* – no constant function can yield a unit integral from zero to infinity. To have a well-defined prior for the signal cross section, we could define some cutoff $\sigma_{\max}$, in which case the value of the prior would be $1/\sigma_{\max}$ in the range $[0, \sigma_{\max}]$ and zero elsewhere. In the simplified notation, we would then use a cutoff $s_{\max}$ for the parameter s. The constant value $1/s_{\max}$ would already be absorbed in the normalization constant in eq. (7.24), but the cutoff would appear as the upper limit on the integral (7.25), leading to a normalization constant

$$N = \frac{e^b}{1 - e^{-s_{\max}}} \tag{7.27}$$

and finally a limit

$$s_{\mathrm{up}} = -\ln\left[1 - (1-\delta)(1 - e^{-s_{\max}})\right]. \tag{7.28}$$

As the cutoff $s_{\max}$ is an arbitrary parameter, we would need to ensure that the limit were not significantly affected by its value, leading intuitively to the requirement $s_{\max} \gg s_{\mathrm{up}}$. Fortunately, the limit of s_{up} as $s_{\max} \to \infty$ exists, and gives back the result $s_{\mathrm{up}} = -\ln\delta$ from before. As long as the convergence properties of the resulting posterior are satisfactory, we can live with the flat prior being improper, and no explicit choice of $\sigma_{\max}$ needs to be made in the limit calculations. Some numerical truncation of the calculation of the posterior needs however to be made, and plays effectively the role of $\sigma_{\max}$. Obviously, we must ensure that this truncation does not significantly affect the obtained limits.

Convergence problem with the Gaussian efficiency prior

We continue to consider the simple single channel zero event case, but extend the analysis now to include uncertainty on the signal efficiency $\varepsilon_{\mathrm{sig}}$. We therefore consider $s' = L_{\mathrm{int}}\sigma$ as parameter of interest, and write the equation corresponding to (7.24) as

$$p(s'|n_{\mathrm{obs}} = 0) \propto \int_0^1 g_{\varepsilon_{\mathrm{sig}}}(\varepsilon_{\mathrm{sig}})\, e^{-\varepsilon_{\mathrm{sig}} s'}\, d\varepsilon_{\mathrm{sig}} \tag{7.29}$$

with the proportionality symbol indicating that any factors that are independent of s' are omitted as they can be absorbed into the normalization constant. The integration range corresponds to the allowed range for $\varepsilon_{\mathrm{sig}}$, outside which any reasonable prior $g_{\varepsilon_{\mathrm{sig}}}(\varepsilon_{\mathrm{sig}})$ must be zero[5]. Choosing

[5] In fact, if the parameter of interest is taken to be the signal cross section within some restricted phase space region, then the signal efficiency could be greater than one. This is, however, not an important point for the present

a truncated Gaussian prior for the signal efficiency,

$$g_{\varepsilon_{\mathrm{sig}}}(\varepsilon_{\mathrm{sig}}) \propto e^{-\frac{(\varepsilon_{\mathrm{sig}}-\overline{\varepsilon_{\mathrm{sig}}})^2}{2\sigma^2_{\varepsilon_{\mathrm{sig}}}}} \quad \text{(for } \varepsilon_{\mathrm{sig}} \in [0,1],\, g_{\varepsilon_{\mathrm{sig}}}(\varepsilon_{\mathrm{sig}}) = 0 \text{ elsewhere)} \tag{7.30}$$

with $\overline{\varepsilon_{\mathrm{sig}}}$ as the measured efficiency value and $\sigma_{\varepsilon_{\mathrm{sig}}}$ as the associated uncertainty, we find the following expression for the posterior:

$$p(s'|n_{\mathrm{obs}}=0) = N\, e^{\frac{1}{2}\sigma^2_{\varepsilon_{\mathrm{sig}}} s'^2 - \overline{\varepsilon_{\mathrm{sig}}} s'} \left[\mathrm{erf}\, \frac{\sigma^2_{\varepsilon_{\mathrm{sig}}} s' - \overline{\varepsilon_{\mathrm{sig}}} + 1}{\sqrt{2}\,\sigma_{\varepsilon_{\mathrm{sig}}}} - \mathrm{erf}\, \frac{\sigma^2_{\varepsilon_{\mathrm{sig}}} s' - \overline{\varepsilon_{\mathrm{sig}}}}{\sqrt{2}\,\sigma_{\varepsilon_{\mathrm{sig}}}} \right] \tag{7.31}$$

with N as a normalization constant and "erf" denoting the error function. Using L'Hôpital's rule repeatedly, we find

$$\lim_{s'\to\infty} s'\, p(s'|n_{\mathrm{obs}}=0) = \frac{N}{\sigma_{\varepsilon_{\mathrm{sig}}}} \sqrt{\frac{2}{\pi}}\, e^{-\frac{\overline{\varepsilon_{\mathrm{sig}}}^2}{2\sigma^2_{\varepsilon_{\mathrm{sig}}}}}, \tag{7.32}$$

which means that $p(s'|n_{\mathrm{obs}}=0)$ goes asymptotically as $1/s'$ for large s' and that the normalization integral

$$\int_0^\infty p(s'|n_{\mathrm{obs}}=0)\, ds' \tag{7.33}$$

diverges. Hence, no mathematically well defined limit can be calculated unless a cutoff is introduced for the flat prior.

The fact that the truncated Gaussian efficiency prior together with the flat cross section prior leads to ill-defined results was in the context of the ATLAS W' analysis discovered during the analysis of the 2012 data, and the ATLAS publications [106] and [107] were published with such prior choices. While the corresponding limits are in principle ill-defined, numerical calculations appear relatively stable and results reasonable with the small efficiency uncertainties encountered in those analyses. The convergence problem itself was already noted in ref. [112].

As the posterior goes asymptotically as $1/\sigma$, convergence is assured if any prior is used which decreases asymptotically as function of σ. A well motivated example is the reference prior [113] with an asymptotic $1/\sqrt{\sigma}$ behavior. However, any such prior leads to stronger limits than the customary flat prior and hence makes comparison between experiments more difficult. In the single channel zero event case without nuisance parameter uncertainties, the reference prior is for example found to give a limit of about 1.95 expected events when the expected background is zero and to approach the standard 3 event limit when the background becomes large. The result depends on the background because it explicitly enters the reference prior via a factor $1/\sqrt{s+b}$ for which the background dependence does not factor out.

As noted in ref. [112], the divergence problem is associated with efficiency values close to zero, and can be viewed as a $1/\varepsilon_{\mathrm{sig}}$ divergence if the integral over σ is performed before that over $\varepsilon_{\mathrm{sig}}$. A possible solution is therefore to use an efficiency prior that approaches zero as the efficiency approaches zero, and the *log-normal* distribution is suggested in ref. [112]. The log-normal prior can be said to give a more physical description of the signal efficiency, as negative values are automatically avoided, and the prior smoothly approaches zero in the limit $\varepsilon_{\mathrm{sig}} \to 0$.

discussion.

As also the background level and the integrated luminosity are restricted to positive values, the log-normal distribution is an appealing candidate prior also for these nuisance parameters.

7.3.2 Choice of priors for the nuisance parameters

As it is clear that the naive choice of the truncated Gaussian as prior for the signal efficiency is not valid, a different function must be chosen, and some investigation of the limit's dependence on the choice seems warranted. Therefore, some different priors are tried out both for the signal efficiency and the background level. The integrated luminosity is associated with a very small uncertainty, and the dependence on its prior is therefore not explicitly investigated. Since the integrated luminosity multiplies the signal cross section in the statistical model (7.2), a prior that approaches zero as the integrated luminosity approaches zero is required based on the same argument of convergence and consistency as applies to the efficiency. For the background level, on the other hand, a truncated Gaussian prior is an acceptable choice.

Log-normal prior

A log-normal distributed random variable is obtained by the exponentiation of a Gaussian variable. In other words, if Z is a standard normal distributed variable, then

$$X = e^{\mu+\Sigma Z} \tag{7.34}$$

is log-normal distributed. The distribution can be characterized by the mean μ and standard deviation Σ of the exponentiated Gaussian variable, and these parameters must be related to the measured value $\overline{\theta}$ of the nuisance parameter θ that we wish to describe by the log-normal distribution and the associated uncertainty σ_θ. The log-normal distribution has a mean $\langle X\rangle = e^{\mu+\Sigma^2/2}$, median e^{μ}, and variance $\operatorname{Var} X = (e^{\Sigma^2}-1)e^{2\mu+\Sigma^2}$. The mode, i.e. the value at which the maximum of the probability density occurs, is $e^{\mu-\Sigma^2}$.

Following the ATLAS Higgs search procedure as documented in ref. [114][6], we require

$$\frac{\operatorname{Var} X}{\langle X\rangle^2} = \left(\frac{\sigma_\theta}{\overline{\theta}}\right)^2, \tag{7.35}$$

which fixes the parameter Σ:

$$\Sigma = \sqrt{\ln\left[1+\left(\frac{\sigma_\theta}{\overline{\theta}}\right)^2\right]}. \tag{7.36}$$

For fixing the parameter μ, we consider three possibilities:

- requiring $\langle X\rangle = \overline{\theta}$ as suggested in ref. [112],
- requiring that the median of X be equal to $\overline{\theta}$ as done in ATLAS Higgs searches and documented in ref. [114], or
- requiring that the mode of X be equal to $\overline{\theta}$.

[6] See appendix C of ref. [114].

We refer to these prescriptions as "mean", "median", and "mode" respectively, and the corresponding expressions for μ are

$$\mu = \begin{cases} \ln \frac{\overline{\theta}}{\sqrt{1+\left(\frac{\sigma_\theta}{\overline{\theta}}\right)^2}} & \text{(mean)} \\ \ln \overline{\theta} & \text{(median)} \\ \ln\left(\overline{\theta}\left[1+\left(\frac{\sigma_\theta}{\overline{\theta}}\right)^2\right]\right) & \text{(mode)} \end{cases}. \tag{7.37}$$

To avoid concerns about the fact that θ is not necessarily dimensionless, we note that a factor $\overline{\theta}$ can always be factored out from the expression (7.34), leaving only dimensionless numbers in the exponent.

It is built into the log-normal distribution that θ is never negative, which is the case for both background level, integrated luminosity, and signal efficiency. For the signal efficiency, truncation at 1 is required as in the Gaussian prior case.

Gamma prior

The gamma distribution with shape parameter k and scale parameter Θ has the PDF

$$f(x) \propto x^{k-1} e^{-x/\Theta}. \tag{7.38}$$

It has mean $k\Theta$, variance $k\Theta^2$, and mode $(k-1)\Theta$ (for $k > 1$). We associate the parameters to the measured value of the nuisance parameter and the associated uncertainty in the same way as for the log-normal distribution. In the gamma case, the requirement (7.35) fixes the parameter k:

$$k = \left(\frac{\overline{\theta}}{\sigma_\theta}\right)^2. \tag{7.39}$$

There is no simple closed form expression for the median of the gamma distribution, but the values of the scale parameter are easily found for the "mean" and "mode" cases:

$$\Theta = \begin{cases} \frac{\sigma_\theta^2}{\overline{\theta}} & \text{(mean)} \\ \frac{\overline{\theta}}{\left(\frac{\overline{\theta}}{\sigma_\theta}\right)^2 - 1} & \text{(mode)} \end{cases}. \tag{7.40}$$

Also the gamma distribution is restricted to positive numbers.

Results

In fig. 7.1, histogram representations of the various candidate priors are shown. The priors are plotted for the signal efficiency with a central value $\overline{\varepsilon_{\text{sig}}} = 0.3$ and relative uncertainties of 5% and 30%. The truncated Gaussian is not really a candidate prior for the signal efficiency, but is included because it may in any case be interesting to include it in the visual prior comparison, and because it *is* a candidate prior for the background level. (An independent plot of background level priors is not made, as the same general features would be seen as in fig. 7.1.)

With the smaller relative uncertainty of 5%, it is clear that all priors are very similar. Only

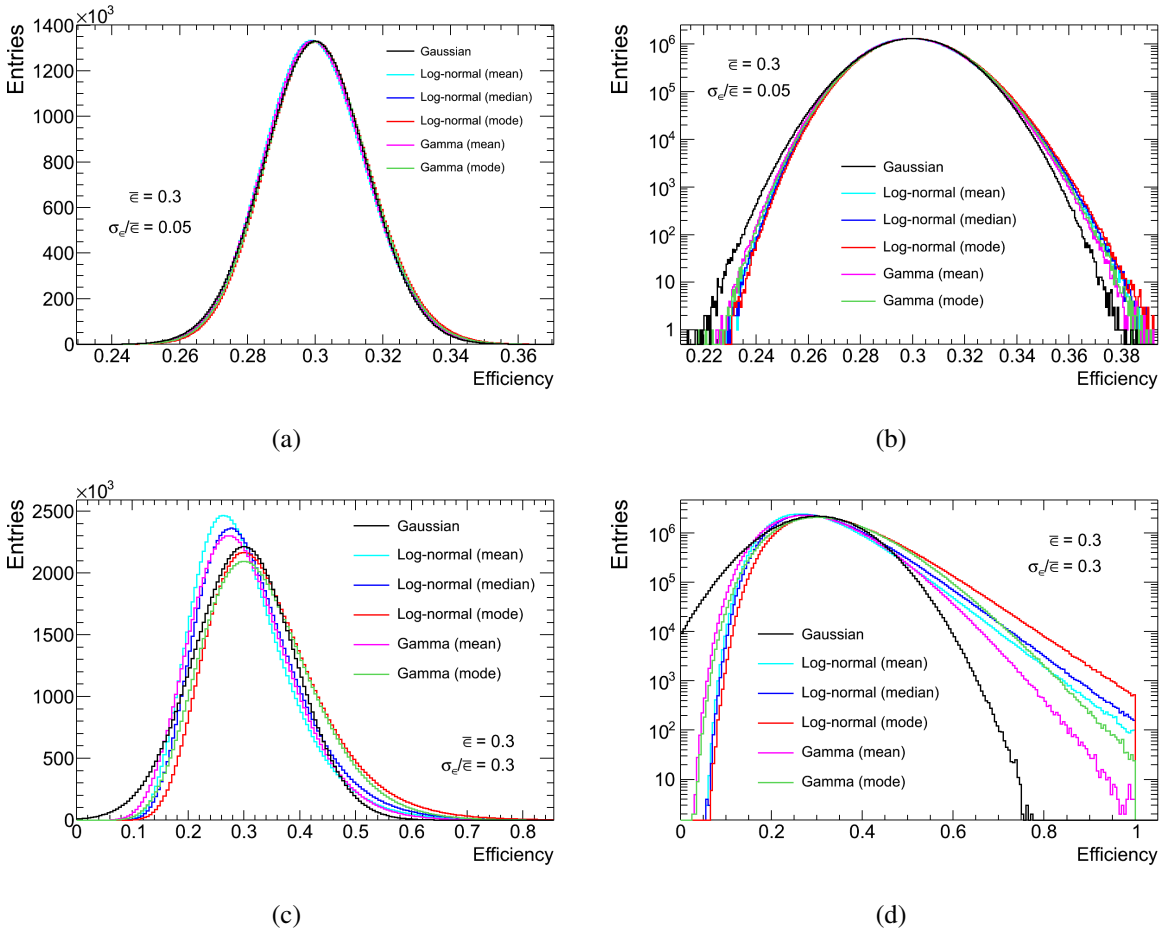

Figure 7.1: Histogram representations of the various candidate priors for the signal efficiency with a central value $\overline{\varepsilon_{\text{sig}}} = 0.3$ and relative uncertainties of 5% ((a) and (b)) and 30% ((c) and (d)). The priors look similar for the 5% relative uncertainty, but differ clearly for the 30% relative uncertainty. They are shown on linear ((a) and (c)) and logarithmic ((b) and (d)) y-axis scales.

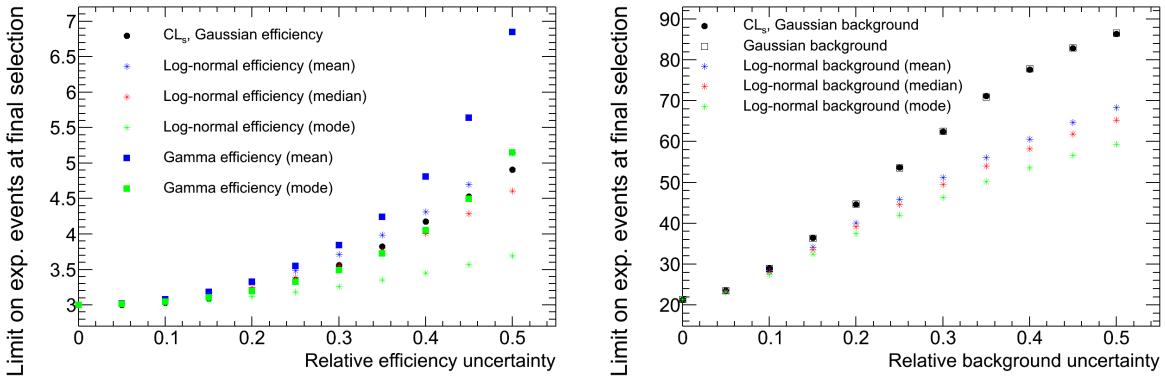

(a) (b)

Figure 7.2: The 95% CL exclusion limit on the expected number of signal events at final selection as function of the relative signal efficiency uncertainty (a) and the relative background level uncertainty (b) for different nuisance parameter prior choices. In (a) we assume no observed events and a signal efficiency of 0.3, and results are independent of the expected background. In (b) we assume 100 observed events and 100 expected background events, and results are independent of the signal efficiency. In both cases, uncertainty is included on the investigated nuisance parameter only.

the Gaussian is seen to be slighthly separated from the other priors on the logarithmic scale. With a relative uncertainty of 30%, differences between the different priors are clearly visible. In particular, we see that the "mean" and "median" prescriptions give distributions which are peaked somewhat below the central efficiency value $\overline{\varepsilon_{\text{sig}}} = 0.3$, while the Gaussian and the "mode" prescription give distributions peaked exactly at 0.3 as expected. Differences in the tails are visible on the logarithmic scale, and here the truncation at $\varepsilon_{\text{sig}} = 1$ is also clearly seen.

Fig. 7.2 shows the dependence of the exclusion limit at 95% CL on the signal efficiency and background level uncertainties. In fig. 7.2(a), the dependence on the signal efficiency uncertainty is investigated for the situation of zero observed events, representative typically of limits for the highest W' masses considered in a W' search. In fig. 7.2(b), the dependence on the background uncertainty is investigated for the case of 100 observed events and 100 expected background events, because the background uncertainty has a more pronounced effect in the higher statistics regime. In both cases, uncertainty is included on the investigated nuisance parameter only, and results are presented in terms of the expected number of signal events at final selection, so that the familiar limit of three events occurs in fig. 7.2(a) at zero uncertainty. Results are shown for the Bayesian approach with different priors for the nuisance parameter under study, and the hybrid/frequentist result with Gaussian nuisance parameter description is also shown.

It is clear that significant dependence on the choice of prior is observed for both the signal efficiency and the background level when the corresponding relative uncertainties become large. We note the remarkable agreement between the CL_s and Bayesian results in fig. 7.2(b) when they are both using the Gaussian background prior. The agreement is also found to persist for the log-normal prior choices.

As the baseline prescription for the 2012 ATLAS W' analysis [108, 109], log-normal priors with the "median" prescription were used for all nuisance parameters. This was motivated by

arguments of consistency, as log-normal priors seem now to be relatively standard, and are used for example in the CMS 2012 data W' search [71]. The "median" prescription is motivated by the fact that the same prior for the background level is used also when calculating the expected limit under the background-only hypothesis, which is defined to be the median.

7.3.3 Correlation between nuisance parameters

As will be argued in chapter 8, some correlation between the nuisance parameters should be taken into account due to common sources of uncertainty affecting the different nuisance parameters. In particular, the theoretical uncertainty on the differential cross sections should be correlated between the electron and muon channels and also between the signal efficiency and background level, leading to a set of four partly correlated nuisance parameters (signal efficiencies and background levels in the two channels) for the combination of the electron and muon channel results.

We denote an arbitrary one of these parameters by θ_i and calculate separately the uncertainty $\sigma_{\theta_i}^{\mathrm{uc}}$ due to the uncorrelated uncertainty sources and $\sigma_{\theta_i}^{\mathrm{c}}$ due to the correlated ones. We assume a product form of the stochastic variable θ_i,

$$\theta_i = \overline{\theta_i} X_i Y_i, \tag{7.41}$$

where the stochastic variable X_i is related to correlated uncertainty sources and Y_i to uncorrelated ones. Clearly, we want the "central value" of both X_i and Y_i to be unity, and we want their associated relative uncertainties to be $\sigma_{\theta_i}^{\mathrm{c}}/\overline{\theta_i}$ and $\sigma_{\theta_i}^{\mathrm{uc}}/\overline{\theta_i}$ respectively, so that standard error propagation leads to a total uncertainty

$$\sigma_{\theta_i}^{\mathrm{tot}} = \sqrt{(\sigma_{\theta_i}^{\mathrm{c}})^2 + (\sigma_{\theta_i}^{\mathrm{uc}})^2} \tag{7.42}$$

on θ_i.

Since we want θ_i to be log-normal distributed, we associate log-normal distributions to X_i and Y_i following the "median" prescription, i.e.

$$X_i = e^{\Sigma_{\theta_i}^{\mathrm{c}} Z^{\mathrm{c}}} \quad \text{with} \quad \Sigma_{\theta_i}^{\mathrm{c}} = \sqrt{\ln\left[1 + \left(\frac{\sigma_{\theta_i}^{\mathrm{c}}}{\overline{\theta_i}}\right)^2\right]} \tag{7.43}$$

and

$$Y_i = e^{\Sigma_{\theta_i}^{\mathrm{uc}} Z_i^{\mathrm{uc}}} \quad \text{with} \quad \Sigma_{\theta_i}^{\mathrm{uc}} = \sqrt{\ln\left[1 + \left(\frac{\sigma_{\theta_i}^{\mathrm{uc}}}{\overline{\theta_i}}\right)^2\right]}. \tag{7.44}$$

Here Z^{c} and Z_i^{uc} are standard normal distributed, and the lack of index on Z^{c} indicates that this is a single variable entering the expressions for all the partly correlated variables θ_i, thus imposing the desired correlation. We note that the introduction of such correlation increases the dimensionality of the marginalization integral (7.19) by one, leading to a total number of effective nuisance parameters equal to 4 in the single channel case and 6 in the electron and

muon channel combination[7].

It would be reasonable to expect that the distribution of θ_i in the case of correlation is the same as that obtained by the log-normal "median" prescription in the case without correlations (described in section 7.3.2) as long as the uncertainty in the latter case is

$$\sigma_{\theta_i} = \sigma_{\theta_i}^{\mathrm{tot}} = \sqrt{(\sigma_{\theta_i}^{\mathrm{c}})^2 + (\sigma_{\theta_i}^{\mathrm{uc}})^2}. \tag{7.45}$$

Writing eq. (7.41) on the form

$$\theta_i = e^{\mu_i + \Sigma_{\theta_i}^{\mathrm{c}} Z^{\mathrm{c}} + \Sigma_{\theta_i}^{\mathrm{uc}} Z_i^{\mathrm{uc}}} \tag{7.46}$$

with $\mu_i = \ln \overline{\theta_i}$ and comparing to eqs. (7.34), (7.36), and (7.37), we see that the distributions match if

$$(\Sigma_{\theta_i}^{\mathrm{c}})^2 + (\Sigma_{\theta_i}^{\mathrm{uc}})^2 = \ln \left[1 + \left(\frac{\sigma_{\theta_i}^{\mathrm{tot}}}{\overline{\theta_i}} \right)^2 \right], \tag{7.47}$$

which is found by Taylor expansions to be approximately valid when the relative uncertainties are small. The impact on calculated limits of the non-validity of eq. (7.47) can be investigated by comparing limits which are in principle not affected by correlation[8] calculated with all uncertainty put into either the correlated or uncorrelated part to those calculated with a democratic division $\sigma_{\theta_i}^{\mathrm{c}} = \sigma_{\theta_i}^{\mathrm{uc}} = \sigma_{\theta_i}^{\mathrm{tot}}/\sqrt{2}$, and is found to be only about 2% for a total relative uncertainty as high as 50%. It is also worth noting that no such "extreme" case will be encountered in the following applications of the statistical prescription – the correlated part of the uncertainty can become very large, but the uncorrelated part will then be much smaller and essentially negligible.

7.3.4 Numerical implementation

The Bayesian limit calculation prescription is implemented numerically as follows. A step length is chosen in the parameter of interest σ. For each step along the σ-axis, the marginalization (7.19) is performed by MC integration where the nuisance parameters are generated according to their PDFs and the likelihood (7.20) is sampled. This is done for all discrete σ-values starting from $\sigma = 0$ and up to some σ_{max} where the integrated likelihood is observed to be sufficiently small as defined by a numerical convergence criterion. With the discretized version of the unnormalized posterior for σ at hand, the normalization integral (7.16) is easily evaluated, and eq. (7.22) is easily solved for the limit σ_{up}.

It is interesting to know not only the observed limit of an experiment, but also how the observed limit compares with the limit that was expected in the absence of signal based on the estimated backgrounds and efficiencies. The expected limit itself is a measure of the sensitivity of the experiment, and the position of the observed limit in the probability distribution of possible limits under the background-only hypothesis can tell us whether the experiment was

[7] In the dark matter interpretation in chapter 9, the theoretical uncertainty will be treated as correlated between the background levels and signal efficiencies of the two channels, but not between signal and background, leading to a total of 7 effective nuisance parameters for the combination.

[8] An example of such a limit would be that calculated for a single channel with the correlated part of the signal efficiency uncertainty equal to zero. In this case, one would intuitively not expect a difference whether the background uncertainty is put into the correlated or uncorrelated part or divided between the two.

"lucky" or "unlucky" with their limit and reveal problems with background estimations and/or hints of new physics. We follow the standard high energy physics convention of representing all this information visually in the limit plot, where both the observed and expected limits are shown, as well as the customary green and yellow bands representing the one and two sigma quantiles of the background-only limit distribution. Also following standard convention, we define the expected limit to be the *median* of the background-only limit distribution (see also refs. [116] and [117]).

The distribution of possible limits under the background-only hypothesis is determined by MC sampling. In each MC cycle, the nuisance parameters are drawn from their PDFs and the background levels are evaluated. Pseudo-data is generated by generating a Poisson distributed random variable as the "observed" event count in each channel with mean given by the background level in that channel as evaluated with the generated nuisance parameter values. These event counts are treated as if they were the real data, and a limit is calculated following the above prescription. After many MC cycles, the median and the $\pm 1\sigma$ and $\pm 2\sigma$ limits are extracted. For a single channel, the limit has a simple monotonic one-to-one correspondence with the "observed" event count, and the median, $\pm 1\sigma$, and $\pm 2\sigma$ event counts are first obtained, and limits calculated only for these "observations", leading to considerable savings in computation time.

The distribution of possible limits under the background-only hypothesis is discrete. The median limit corresponds to one of the possible, discrete limits, and we fix the position of the green and yellow bands by requiring that

- the edge of the $\pm 1\sigma$ ($\pm 2\sigma$) band corresponds to an observable limit value, and
- if the observed limit falls exactly on the band edge, then the data corresponds to *at most* a 1σ (2σ) deviation from the background-only hypothesis as determined from the relevant p-value using the limit as test statistic, while if it falls outside the band edge, then the deviation is more significant than 1σ (2σ).

7.4 Summary

In this chapter, the statistical prescriptions which will be used to test the background-only hypothesis and place limits on hypothetical new physics contributions have been introduced. Limits on new physics will be calculated using the Bayesian prescription, and we have seen that the choice of informative priors for the nuisance parameters can significantly impact the evaluated limits if the relative nuisance parameter errors are large. In particular, the combination of a truncated Gaussian signal efficiency prior and a flat signal cross section prior is found to give an improper, i.e. not normalizable, posterior for the signal cross section.

We proceed in the next chapters to apply the statistical prescription in the search for new physics in the form of charged, heavy bosons or dark matter production.

Chapter 8

Search for new charged, heavy boson signal

In this chapter, we pursue the search for new charged, heavy boson production. Systematic uncertainties must be evaluated in order to quantify the agreement of the data with the background-only hypothesis and constrain contributions from new physics. In the first part of this chapter, we follow closely the final ATLAS analysis of the 2012 data, as presented in ref. [109]. Then, in section 8.8, we investigate possible choices of parameter of interest in the statistical analysis other than the customary total signal cross section. The work presented in this section is also reflected in the preliminary ATLAS analysis of the 2012 data, ref. [108].

While this thesis is focused on the muon channel, some results will also be presented for the electron channel and the combination of the electron and muon channels. For the electron channel, inputs to the statistical analysis are taken directly from the official ATLAS analysis corresponding to ref. [109], while the inputs for the muon channel are rederived for the thesis. Small discrepancies may be observed wrt. the official ATLAS results in the muon channel because of some minor analysis differences detailed in section A.1 of appendix A. As we will make use of the electron channel results from the official ATLAS analysis, we begin this chapter with a brief summary of the electron channel event selection.

8.1 Electron channel event selection

The data quality, "jet cleaning", and primary vertex requirements are exactly the same in the electron channel as described for the muon channel in chapter 5. A single photon trigger[1] with a p_{T} threshold of approximately $120\,\mathrm{GeV}$ is required. The higher p_{T} threshold compared to the muon channel is needed to keep the trigger rate at an acceptable level because of higher "fake" electron background rate from jet activity. A lower threshold can be achieved with the use of tighter identification criteria at the trigger level, but keeping the trigger selection as loose as possible is desirable for the data driven jet background estimate.

Electron candidates are formed from energy clusters in the electromagnetic (EM) calorimeter with matching tracks found in the inner detector (ID). The electron cluster is required to be within the high-granularity acceptance of the EM calorimeter, $|\eta| < 2.47$, but not in the

[1] For ATLAS internal readers: the trigger name is EF_g120_loose.

barrel-end-cap transition region $1.37 < |\eta| < 1.52$.

Cuts are placed on the ID track associated with the electron and its matching with the EM energy cluster. In particular, the track is required to have at least 7 hits[2] in total in the pixel and SCT detectors. Furthermore, at least one hit is required in the innermost pixel layer for $|\eta| < 2.37$ and at least one hit in the pixel detector is required for all η. Tracks within the acceptance of the TRT detector are required to have a large fraction of so-called high threshold hits, indicating transition radiation. Cuts are imposed on the transverse and longitudinal impact parameters, $|d_0| < 1\,\mathrm{mm}$ and $|z_0| < 5\,\mathrm{mm}$ respectively. Finally, the track is required to point towards the EM energy cluster in η, with a cut $|\Delta\eta| < 0.005$.

Cuts are also placed on "shower shape" variables characterizing the electron candidate's calorimeter deposits. These include the width of the EM shower as well as the leakage into the hadronic calorimeter, and the cuts employed[3] depend on p_{T} and η. The electron is finally required to be matched to the trigger, have $p_{\mathrm{T}} > 125\,\mathrm{GeV}$, and be isolated. A calorimeter based isolation criterion is applied,

$$\sum_{\Delta R<0.2} E_{\mathrm{T}}^{\mathrm{calo}} < 0.007\, p_{\mathrm{T}}^{e} + 5\,\mathrm{GeV}, \tag{8.1}$$

where the energy deposited by the electron is excluded from the sum.

Events are required not to have any additional electron candidates passing the above requirements, although without the trigger matching cut and with a lower p_{T} cut of $20\,\mathrm{GeV}$. The default missing transverse energy definition is used without the muon channel specific correction described in section 5.2.2, and $\not{E}_{\mathrm{T}} > 125\,\mathrm{GeV}$ is required. The $\not{E}_{\mathrm{T}}$ cut is thus equal to the lepton p_{T} cut, as in the muon channel.

The jet background in the electron channel is estimated using the Matrix Method[4]. The loose electron is defined by loosening the shower shape cuts and removing the isolation and track matching cuts, and the "fake" and "real" electron efficiencies are estimated as function of p_{T} in four bins of $|\eta|$. A cross check is provided by the "shape method", where the shape of the jet background transverse mass distribution is obtained from a jet enriched sample obtained by inverting the isolation cut or shower shape cuts.

8.2 Transverse mass distributions

The basis for the statistical analysis is the transverse mass distributions, as shown for the muon channel case in fig. 6.15(f). We show again the muon channel m_{T} distribution in fig. 8.1, now with the jet background shown in the form of a histogram representation of the power law fit at high transverse mass and with only statistical uncertainty. Example signal contributions from SSM W' bosons and W^* bosons are also shown in fig. 8.1.

We also show the electron channel m_{T} distribution as presented in ref. [109], and we include for completeness also the muon channel plot from the same publication. Both distributions are

[2]For all cuts on numbers of hits, the numbers include outlier hits.

[3]For ATLAS internal readers, the cuts used correspond to the "medium++" definition, and more details can be found here: `https://twiki.cern.ch/twiki/bin/view/AtlasProtected/TechnicalitiesForMedium1`

[4]The method is described in the muon channel context in chapter 6.

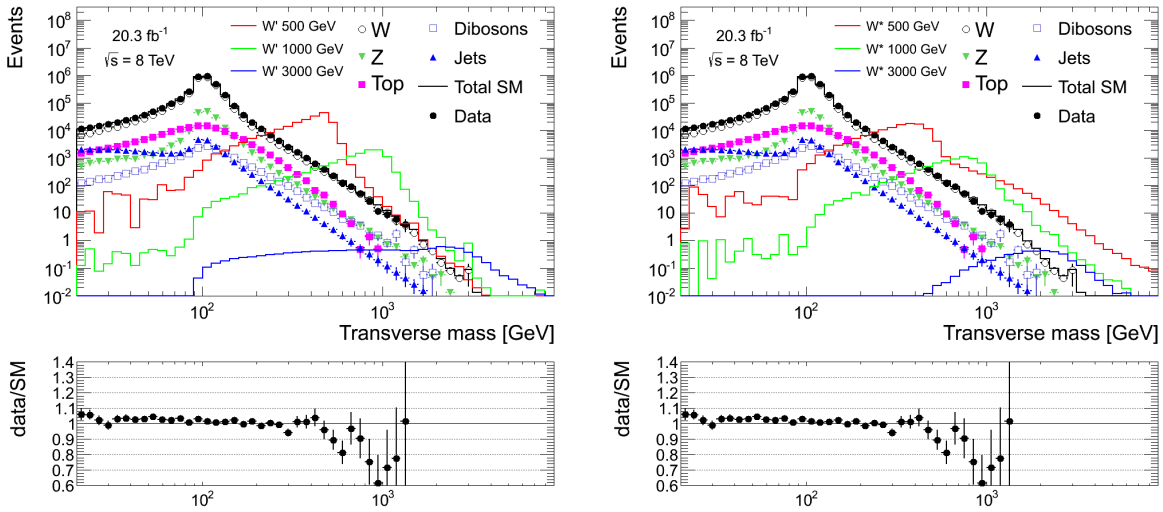

(a) (b)

Figure 8.1: Transverse mass distributions in the muon channel with example signal contributions from SSM W' bosons (a) and W^* bosons (b) of different masses. The ratio of the data to the total background prediction is shown in the panels below the plots with error bars representing statistical uncertainty.

shown in fig. 8.2. Note that histograms are stacked in fig. 8.2, but not in fig. 8.1 and other figures of the same style found in this thesis[5]. Some differences are visible between the electron and muon channel plots, most notably due to the difference in resolution (cf. section 2.4.6) and due to the higher p_{T} and $\not{E}_{\mathrm{T}}$ cuts of $125\,\mathrm{GeV}$ employed in the electron channel. The difference in resolution is especially visible for the $3\,\mathrm{TeV}$ W' signal distribution, where the superior resolution in the electron channel at high p_{T} leads to a sharp end-point, which is seen to be heavily smeared in the muon channel. The difference in p_{T} cuts is primarily visible at low m_{T}, where a threshold at approximately $250\,\mathrm{GeV}$ is apparent in the electron channel.

In both channels, the data are seen to agree reasonably well with the expected background, although there seems to be some deficit of data compared to the background prediction in the muon channel around $m_{\mathrm{T}} = 1\,\mathrm{TeV}$, the significance of which will be evaluated in section 8.6. In order to proceed with the statistical analysis to quantify the agreement of the data with the background-only and various signal+background hypotheses, we must evaluate systematic uncertainties.

8.3 Systematic uncertainties

We employ the single bin counting experiment formalism with a lower threshold on the transverse mass, meaning that we consider the number of events above some threshold $m_{\mathrm{T}}^{\mathrm{min}}$ in the m_{T} distribution as the observable. For each candidate W'/W^* mass, the statistical analysis is based on the following inputs:

[5] We choose not to employ the stacked presentation, as it has some obvious disadvantages. First of all, one can not easily see the shape of individual histograms in a stacked plot. Furthermore, when the y-axis is logarithmic, even reading off the relative sizes of the different histograms in a given bin is difficult.

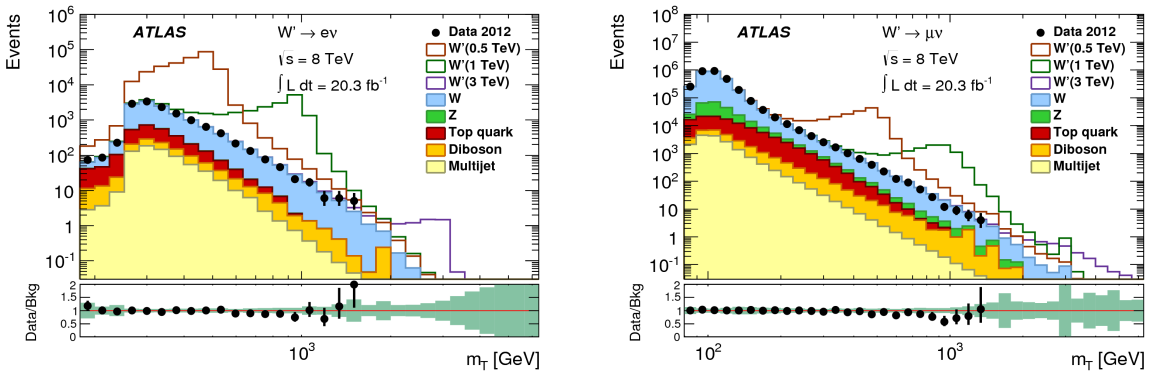

(a) (b)

Figure 8.2: Transverse mass distributions in the electron (a) and muon (b) channels with example signal contributions from SSM W' bosons of different masses. The ratio of the data to the total background prediction is shown in the panels below the plots with error bars representing the statistical uncertainty of the data and with bands around unity representing the total uncertainty in the background estimate. The plots are from ref. [109].

- the event count observed in data,
- the signal efficiency and its uncertainty (correlated and uncorrelated parts),
- the background level and its uncertainty (correlated and uncorrelated parts),
- and the integrated luminosity and its uncertainty ($(20.3 \pm 0.6)\,\mathrm{fb}^{-1}$).

The signal efficiencies and background levels are evaluated from the relevant MC samples, with the exception of the jet background contribution, which is measured in a data driven manner (described for muons in chapter 6). The signal efficiency estimate is in principle just a ratio of event counts in a signal MC sample before and after the reconstruction and event selection, but event weights must be included to account for pile-up and vertex position reweighting, lepton efficiency corrections, and invariant mass dependent k-factors. In addition, the use of template samples for the signal necessitates the use of "Breit-Wigner weights" to reproduce the resonance structure of the signal from the template sample. The efficiency is estimated as

$$\overline{\varepsilon_{\mathrm{sig}}} = \frac{\sum_{i \in \mathrm{final}} w_i}{\sum_{i \in \mathrm{initial}} w_i} \tag{8.2}$$

where w_i is the event weight of event i, which is itself a product of the individual weights mentioned above. In general, the same weights are applied in the numerator and the denominator of eq. (8.2), as is in particular important when it comes to the k-factor and the Breit-Wigner weight, but the efficiency weights are applied in the numerator only. The sum in the numerator (denominator) runs over all events at final (initial) selection, where "final selection" means that the event has to pass all selection cuts including the m_{T} threshold, while "initial selection" refers to the selection of electron (muon) decays of the W'/W^* at the generator level when calculating the signal efficiency in the electron (muon) channel as is appropriate because we take the cross section for an individual decay channel as parameter of interest in the statistical analysis.

Detector related experimental systematic uncertainties due to the lepton efficiency, scale, and resolution as well as due to uncertainties on the hadronic contributions to the missing transverse energy are calculated with the help of tools from the relevant ATLAS combined performance groups. For example, the smearing tool from the MCP group can provide smeared momenta under variations where the resolution is shifted according to its uncertainty. Any given background level or signal efficiency can be calculated under the default smearing procedure as well as under the up and down variations, leading to three estimates; the nominal and two variations. Asymmetric uncertainties are then assigned to the nominal estimate as the differences between the variation estimates and the nominal, and the uncertainty is finally made symmetric by taking the symmetric uncertainty to be the maximum of the up and down uncertainties.

Theoretical uncertainties due to the W and Z (for the background level) and W'/W^* (for the signal efficiency) differential cross sections are calculated in the same manner via up and down variations of the relevant invariant mass dependent k-factors (see section 4.1.1). The W' mass dependent k-factor is not applicable to the W^* due to the non-renormalizability of the W^* interactions, but the relative uncertainty on the k-factor is propagated to the W^* signal efficiency[6] because the large uncertainty on the k-factor at high mass is primarily due to PDF uncertainties, which are assumed to be representative also for the W^* production process. An additional uncertainty is evaluated by propagating the 0.66% relative uncertainty on the beam energy [118] to the W boson differential cross section and assuming the same relative mass dependent uncertainty to be valid for W'/W^*.

The $t\bar{t}$ and single top cross section uncertainties given in table 4.4 are propagated to the background levels by the appropriate scaling of the background contribution from the relevant MC samples. The uncertainties on the data driven jet background estimates, as given for the muon channel in table 6.1, are also taken into account.

Finally, a statistical uncertainty is calculated within the Poisson approximation, meaning that a sum of event weights $s = \sum_i w_i$ is assigned an uncertainty

$$\sigma_s = \sqrt{\sum_i w_i^2}. \tag{8.3}$$

Special formulae based on the binomial distribution exist for the calculation of efficiency uncertainties, but the application to the case of weighted events is nontrivial. We make sure not to include the uncertainty in the denominator of eq. (8.2) when calculating the signal efficiency uncertainty and in the corresponding total MC event count entering the scale factor used to scale the background histograms to the integrated luminosity of the data.

8.3.1 The k-factor uncertainty

The invariant mass dependent k-factors shown in fig. 4.1 are applied to the W'/W^* signal and to the dominant W boson irreducible background. Their uncertainties are propagated to both the background levels and signal efficiencies via the up and down variations corresponding

[6] In practical terms, this means that the central value of the W^* signal efficiency is evaluated with a k-factor $k_{W^*}(m_{l\nu}) = 1$ for all invariant masses $m_{l\nu}$, while the upward variation for example is evaluated with a k-factor $k^{\mathrm{up}}_{W^*}(m_{l\nu}) = k^{\mathrm{up}}_{W'}(m_{l\nu})/k_{W'}(m_{l\nu})$.

to the dashed curves in fig. 4.1. For the uncertainty on the background levels, a subleading contribution comes from the variation of the mass dependent Z boson k-factors which are varied simultaneously with the W boson k-factors. Clearly, different response to variations in the mass dependent k-factors is expected from the signal efficiency than from the background level. In particular, the background level is affected by an amount which reflects an average of the k-factor variation within the signal region defined by the cut $m_{\mathrm{T}} > m_{\mathrm{T}}^{\mathrm{min}}$, while the situation is different for the signal efficiency.

In the case of the signal efficiency, cancellation can occur between the variations in the numerator and denominator of eq. (8.2), leading to a smaller uncertainty than what may naively be expected from the degree of variation of the k-factor itself. For example, it is clear that a *mass independent* relative uncertainty of any size leads to no uncertainty at all on the signal efficiency due to exact cancellation. We see, however, that the uncertainties depicted in fig. 4.1 are strongly mass dependent. Since the (reconstructed) transverse mass and the (generator level) invariant mass are strongly correlated, the signal region $m_{\mathrm{T}} > m_{\mathrm{T}}^{\mathrm{min}}$ corresponds to high invariant mass. As the uncertainty at high invariant mass is typically higher than at lower invariant mass, the k-factor induced variation in the numerator of eq. (8.2) can become significantly larger than that in the denominator when the total cross section receives significant contributions from invariant masses much below the cut value $m_{\mathrm{T}}^{\mathrm{min}}$. This is the case for very high boson masses, and for the W' in particular, due to the low mass off-shell tails in the invariant mass distributions as shown in fig. 3.4.

In fig. 8.3, we see the generator level invariant mass and transverse mass[7] distributions before event selection as well as the distribution of the reconstructed transverse mass after full event selection (except for the m_{T} threshold) in the muon channel for an SSM W' boson of mass $3.5\,\mathrm{TeV}$. In the generator level invariant mass distribution, fig. 8.3(a), we note that a significant fraction of the total cross section comes from the low mass off-shell production tail, and that this tail is associated with smaller k-factor induced variations than the peak region around $3.5\,\mathrm{TeV}$. In the generator level m_{T} distribution, fig. 8.3(b), the same features are seen, although some of the on-shell production around $3.5\,\mathrm{TeV}$ has migrated to lower m_{T} as expected from the usual tail of the m_{T} distribution below the Jacobian peak (see e.g. fig. 3.6(a)). When turning the attention finally to the reconstructed m_{T} distribution, fig. 8.3(c), we note that significant smearing is observed from the finite resolution of the muon momentum reconstruction, but that a clear mass dependence of the k-factor variation is still seen. The distribution in fig. 8.3(c) is used to define the signal region $m_{\mathrm{T}} > m_{\mathrm{T}}^{\mathrm{min}}$, with the threshold $m_{\mathrm{T}}^{\mathrm{min}} \approx 1.9\,\mathrm{TeV}$ as obtained by the optimization procedure documented in section 8.4. Since the numerator of eq. (8.2) receives contributions only from the region $m_{\mathrm{T}} > m_{\mathrm{T}}^{\mathrm{min}}$ and the denominator receives contributions from the whole transverse mass spectrum, it is clear that cancellation of the k-factor uncertainty is only partial and that the uncertainty on the signal efficiency is nonzero.

Fig. 8.4 shows the relative uncertainty on the signal efficiencies and background levels resulting from propagating the uncertainty on the k-factor to these quantities. We refer to this uncertainty simply as "the k-factor uncertainty", but we keep in mind that it is comprised of several sources (see section 4.1.1) and dominated by PDF uncertainties at high mass. The

[7]Note that the generator level invariant mass is defined as in chapter 3, i.e. as the mass of the boson propagator in the MC event record, while the generator level transverse mass is calculated from the momenta of the generator level muon and neutrino labeled as final state particles.

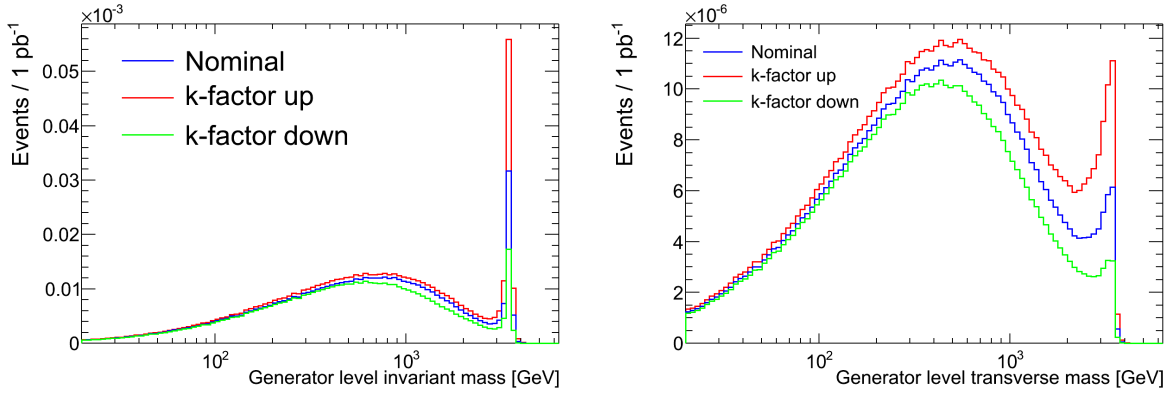

(a) (b)

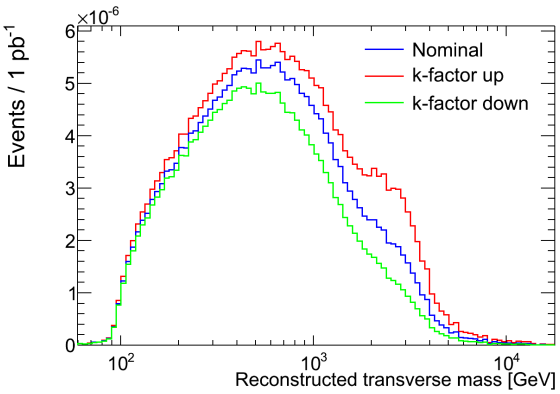

(c)

Figure 8.3: Generator level invariant mass (a) and transverse mass (b) distributions before event selection and the distribution of the reconstructed transverse mass (c) after full event selection (except for the m_{T} threshold) for an SSM W' boson of mass $3.5\,\mathrm{TeV}$. The distributions are shown with the nominal mass dependent k-factor applied as well as with its up and down variations.

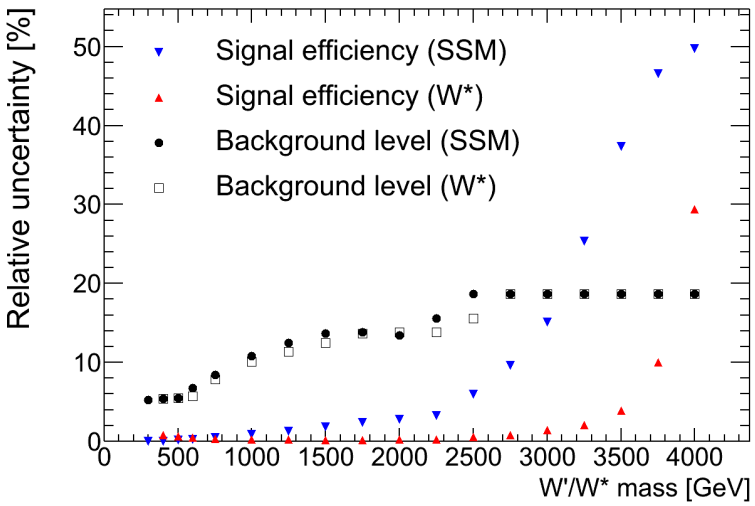

Figure 8.4: The k-factor uncertainty on the signal efficiency and the background level for the SSM W' and the W^*. The background level uncertainty depends only on the transverse mass threshold $m_{\mathrm{T}}^{\mathrm{min}}$, but is plotted separately for the SSM W' and the W^* because the sets of optimal thresholds differ between the two signal models.

uncertainty is shown for the SSM W' and W^* signal efficiencies and the corresponding background levels. We note that the background level uncertainty depends only on the m_{T} threshold $m_{\mathrm{T}}^{\mathrm{min}}$, but is plotted separately for the SSM W' and the W^* because the sets of optimal thresholds differ between the two signal models. The uncertainties are evaluated with the optimal m_{T} thresholds to be presented in section 8.4.

We note that the k-factor uncertainty on the background level ranges from about 5% at low mass to about 20% for the highest m_{T} threshold which is used for the highest W'/W^* masses. For the SSM W', the k-factor uncertainty on the signal efficiency starts to become important for W' masses around $2.5\,\mathrm{TeV}$ and quickly grows to become the by far dominant uncertainty on the signal efficiency for the higher W' masses, reaching a relative uncertainty of 50% for $m_{W'} = 4\,\mathrm{TeV}$. A similar trend is seen for the W^* signal efficiency, but it is clear that the k-factor uncertainty becomes significant for the W^* model only for the very highest W^* masses, and that the uncertainty is smaller than for the SSM W' for all W'/W^* masses. The difference is due to the suppression of low mass off-shell production in the W^* case, as seen in fig. 3.4.

8.3.2 Correlation

The k-factor up and down variations distort the shapes of the W and the W'/W^* invariant mass distributions, and we have seen that this distortion can lead to significant changes in both background levels and signal efficiencies. A k-factor up variation leads to both higher background levels and higher signal efficiencies, and it seems natural to treat this uncertainty as 100% correlated between signal and background. Invariant mass distributions are distorted in the same way for the electron and muon channels, and 100% correlation between channels seems an obvious choice.

Subdominant correlation arises from the beam energy uncertainty, and in the context of correlation between background levels only, also the top cross section should be handled in a correlated way. Detector related experimental uncertainties are dominated by the lepton efficiencies, resolutions, and scales, which are obviously uncorrelated between the electron and muon channels, but correlated between signal and background.

We follow the approximation discussed in section 7.3.3 with a correlated and uncorrelated uncertainty for each signal efficiency and background level, and group the uncertainties as follows: The correlated uncertainty on the signal efficiency is calculated from the k-factor and beam energy uncertainties, while all other sources contribute to the uncorrelated uncertainty. For the background level, the k-factor, beam energy, and top cross section uncertainties are put in the correlated uncertainty, while the rest of the sources contribute to the uncorrelated uncertainty.

Technically, the top cross section uncertainty should be handled separately, as it is correlated between the background levels in the two channels only, and not correlated with the signal efficiency. We argue, however, that the chosen correlation scheme is good enough because the top cross section uncertainty is found to be essentially negligible, and the only region where it even comes close to making a significant contribution is in the low mass region, where the signal efficiency uncertainty is also very small.

We note that correlation between signal and background due to detector related experimental uncertainties is neglected. This is warranted by the fact that these uncertainties never become

large enough to significantly affect final results via the signal efficiencies. We note in particular that the total detector related experimental uncertainty on the signal efficiency never exceeds 5-6%, and this leads to negligible impact on e.g. cross section limits as the example result in fig. 7.2(a) indicates.

8.4 Transverse mass threshold optimization

The m_{T} threshold used in the single bin counting experiment formalism is chosen by an optimization to obtain the lowest possible expected (i.e. median) limit on the new physics cross section under the background-only hypothesis, i.e. the optimal exclusion potential in the absence of signal. The optimization is run individually for each candidate mass and individually for the W' and W^* models. For a given signal model (with a specified boson mass), the signal efficiency, background level, and their uncertainties are functions of the m_{T} threshold. A scan is performed where logarithmically spaced thresholds are sampled. For each threshold, the inputs to the statistical analysis are calculated and passed to the limit setting framework to obtain the median limit under the background-only hypothesis. The threshold providing the lowest median limit is chosen for the subsequent limit evaluation based on the observed data. As the optimization is based on the median limit under the background-only hypothesis, the optimal threshold does not depend on the observed data.

Results presented in this section are for the muon channel. A separate optimization has been performed for the electron channel, and for the publications, refs. [108, 109], the lower one of the electron and muon channel thresholds were used for both channels for each candidate mass. In this thesis, we use the muon channel optimized thresholds for all muon channel results. This means that the thresholds may differ from those used in the publications, but only a couple of thresholds differ in practice, because the lowest threshold came in most cases from the muon channel optimization in the first place. When combining with the electron channel, we use electron channel inputs to the statistical analysis from ref. [109]. This means that for most candidate masses, the electron channel and muon channel m_{T} thresholds are the same, but in a couple of cases they differ. No separate threshold optimization has been performed for the electron and muon channel combination.

Fig. 8.5 shows the median limit under the background-only hypothesis as function of the m_{T} threshold for the SSM W' for a few chosen candidate masses. For the W' masses of $500\,\mathrm{GeV}$ (fig. 8.5(a)) and $1000\,\mathrm{GeV}$ (fig. 8.5(b)), the median limit appears as a smooth function of the m_{T} threshold. For the higher W' masses of $3000\,\mathrm{GeV}$ (fig. 8.5(c)) and $4000\,\mathrm{GeV}$ (fig. 8.5(d)), this is clearly not the case. While we do not completely rule out the possibility that some discontinuity is due to the propagation of MC statistical fluctuations in the signal efficiencies, background levels, and their uncertainties to the median limit, we note that discontinuities are expected in the low statistics region even if MC statistical uncertainty is completely absent. This is because the median limit is a discrete function of the background level. For example, the pronounced structure leading up to $m_{\mathrm{T}}^{\mathrm{min}} = 1888\,\mathrm{GeV}$ is explained as follows: At $m_{\mathrm{T}}^{\mathrm{min}} = 1589\,\mathrm{GeV}$, the median background event count is 2, and the median limit corresponds to what would be obtained if 2 events were observed in data. Increasing the threshold to $m_{\mathrm{T}}^{\mathrm{min}} = 1683\,\mathrm{GeV}$, the median background event count drops to 1. Even though the signal efficiency obviously decreases,

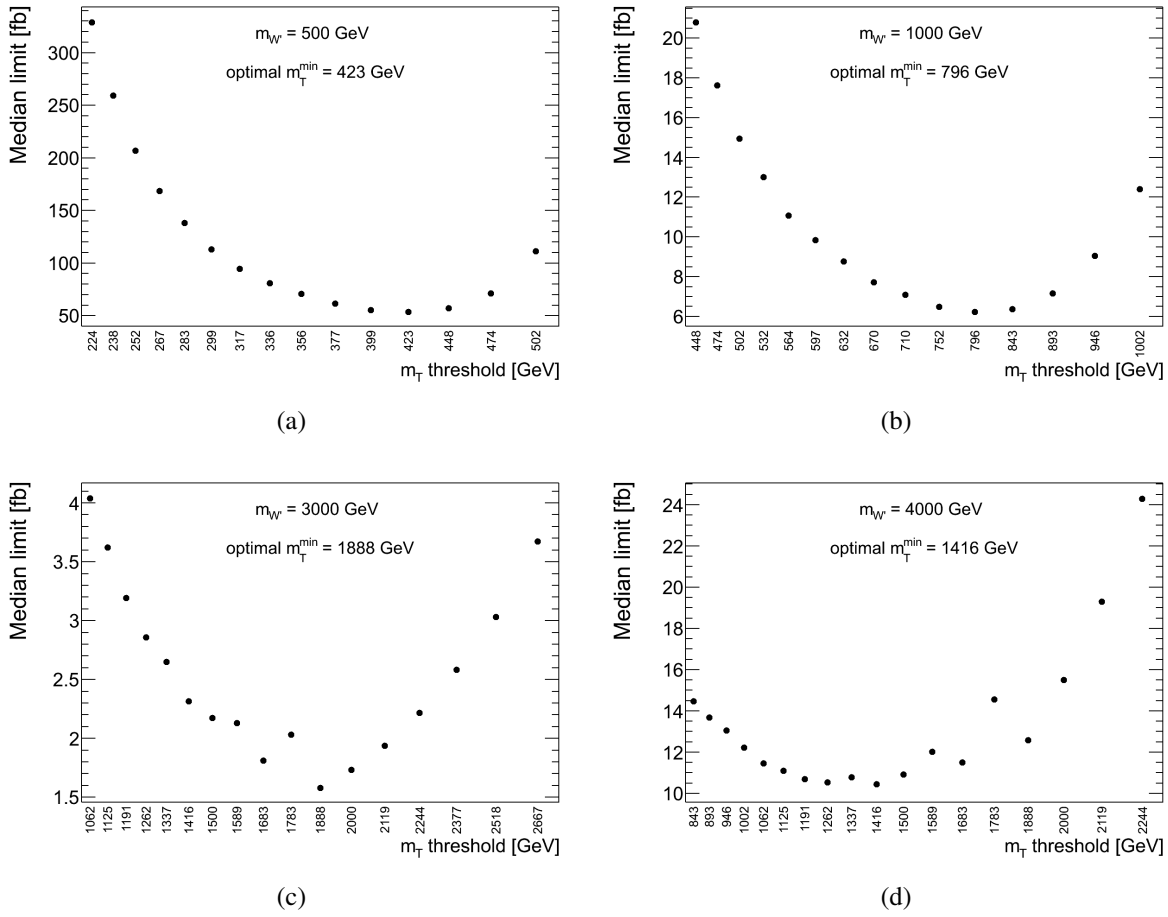

Figure 8.5: The median limit under the background-only hypothesis as function of the m_{T} threshold for the SSM W' for a few chosen candidate masses. We note the difference between the high statistics region ((a) and (b)), in which the median limit appears as a smooth function of the threshold, and the low statistics region ((c) and (d)), where obvious discontinuities are observed.

the overall effect is an improvement in the median limit. Going from $m_{\mathrm{T}}^{\mathrm{min}} = 1683\,\mathrm{GeV}$ to $m_{\mathrm{T}}^{\mathrm{min}} = 1783\,\mathrm{GeV}$, the median background event count is unchanged. As the signal efficiency decreases, the median limit increases[8]. Going from $m_{\mathrm{T}}^{\mathrm{min}} = 1783\,\mathrm{GeV}$ to $m_{\mathrm{T}}^{\mathrm{min}} = 1888\,\mathrm{GeV}$, the median background event count drops from 1 to 0, and the limit improves once again. Further increases in the m_{T} threshold beyond $m_{\mathrm{T}}^{\mathrm{min}} = 1888\,\mathrm{GeV}$ impacts the median limit primarily through the decrease of the signal efficiency, leading to a monotonically increasing median limit. This discussion also explains why this particular threshold, $m_{\mathrm{T}}^{\mathrm{min}} = 1888\,\mathrm{GeV}$, is preferred, as we will see, for so many of the high boson masses both in the SSM W' and the W^* cases. It is special because it is the lowest threshold corresponding to a median background event count of zero.

We note finally that in fact a lower threshold is preferred for the SSM W' of mass $4\,\mathrm{TeV}$ than for that of mass $3\,\mathrm{TeV}$. This has to do with the off-shell production tail becoming more important at the highest masses. The preference for $m_{\mathrm{T}}^{\mathrm{min}} = 1416\,\mathrm{GeV}$ over $m_{\mathrm{T}}^{\mathrm{min}} = 1888\,\mathrm{GeV}$

[8]In this explanation, we neglect the fact that the median limit does depend on the background level not only through the median background event count, but also through the explicit appearance of the background level in the limit calculation. This dependence is found to be subdominant in the low statistics region.

Mass [GeV]	Optimal threshold (SSM) [GeV]	Optimal threshold (W^*) [GeV]
300	252	
400	336	317
500	423	377
600	502	448
750	597	564
1000	796	710
1250	1002	843
1500	1191	1062
1750	1416	1191
2000	1500	1416
2250	1683	1416
2500	1888	1683
2750	1888	1888
3000	1888	1888
3250	1888	1888
3500	1888	1888
3750	1888	1888
4000	1888	1888

Table 8.1: The optimal m_{T} thresholds for the SSM W' and the W^*. Each threshold corresponds to one of the logarithmically spaced thresholds sampled in the optimization procedure, rounded to the nearest GeV, and the numbers are not in any way meant to reflect the precision of the optimization procedure. Every threshold corresponds to the minimum median limit under the background-only hypothesis, except the one for the SSM W' of mass $4\,\mathrm{TeV}$ as discussed in the text.

is not very strong (about a 20% effect on the expected limit), and if k-factor uncertainty is neglected, then $m_{\mathrm{T}}^{\mathrm{min}} = 1888\,\mathrm{GeV}$ is in fact the optimal threshold. To avoid a counter-intuitive appearance of the limit plot at the high mass end, we proceed with $m_{\mathrm{T}}^{\mathrm{min}} = 1888\,\mathrm{GeV}$ as the threshold for the $4\,\mathrm{TeV}$ W' limit evaluation. This threshold was also used in the publications (refs. [108, 109]). It is also worth noting that we will investigate alternative definitions of the signal cross section, for which the k-factor uncertainty on the signal efficiency will be greatly reduced, so that the preference for the lower threshold will be reduced or absent.

We show the optimization plots for the same selection of masses in the W^* case in fig. 8.6. The same general features are seen as in the case of the SSM W', except that the preference for a lower threshold for the $4\,\mathrm{TeV}$ mass is absent in the W^* case because of the suppression of the low mass off-shell tail. Finally, the chosen thresholds for all W' and W^* masses are shown in table 8.1. All thresholds in the table correspond to the optimal one as defined by the minimum median limit under the background-only hypothesis, except for the SSM W' of mass $4\,\mathrm{TeV}$ as already discussed. The thresholds for the W^* are in general a bit lower than those for the SSM W', as expected from the difference in the m_{T} distributions as seen for example in fig. 3.5. The complete sets of optimization plots for both the SSM W' and the W^* are given in section A.2 of appendix A.

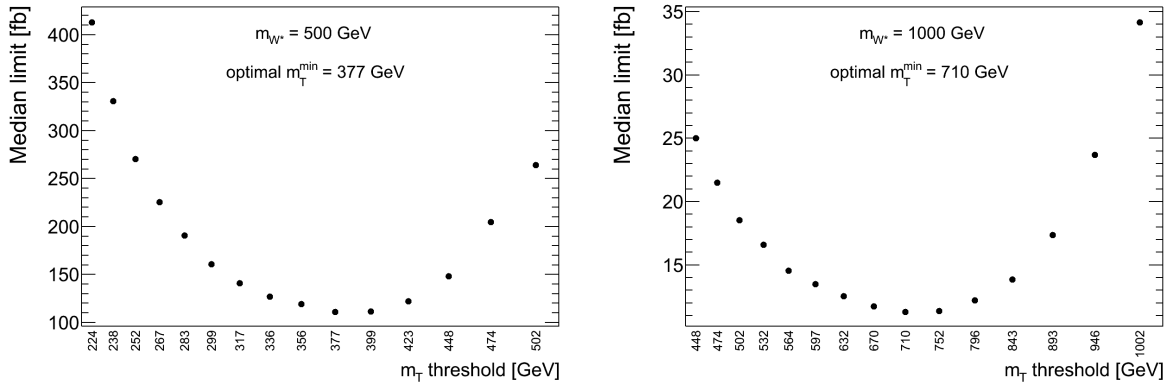

(a) (b)

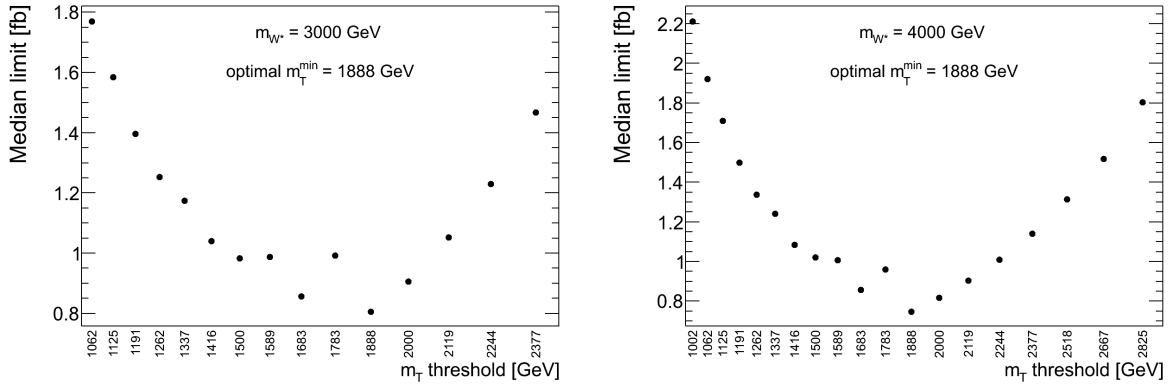

(c) (d)

Figure 8.6: The median limit under the background-only hypothesis as function of the m_{T} threshold for the W^* for a few chosen candidate masses. We note the difference between the high statistics region ((a) and (b)), in which the median limit appears as a smooth function of the threshold, and the low statistics region ((c) and (d)), where obvious discontinuities are observed.

8.5 Summary of systematic uncertainties

The systematic uncertainties on the signal efficiencies and background levels are summarized in tables 8.2-8.7. The "efficiency", "resolution", and "scale" entries refer to those of the relevant lepton (i.e. electron or muon depending on the channel considered). The "efficiency" entry includes both reconstruction and trigger efficiencies. In the muon channel case, the "resolution" entry includes contributions from both ID and MS smearing variations. The jet resolution and scale entries are self-explanatory, and the $\not\!\!E_{\mathrm{T}}$ entry represents uncertainty on the soft (non-jet, non-leptonic) contributions to the $\not\!\!E_{\mathrm{T}}$. It is clear that the uncertainties on the non-leptonic contributions to the $\not\!\!E_{\mathrm{T}}$ are in general negligible for both background levels and signal efficiencies.

The dominant correlated uncertainty is due to the k-factor, and a subdominant contribution with a similar mass dependence comes from the beam energy uncertainty. Separate entries in the tables give the total uncertainty contributions going into the correlated and uncorrelated parts in the statistical analysis.

We note some significant statistical fluctuations in the muon channel resolution, scale, jet, and $\not\!\!E_{\mathrm{T}}$ uncertainties on the background levels at high mass. The variations used to derive these uncertainties change the reconstructed kinematics on an event-by-event basis, causing events to migrate into and out of a given signal region, and the resulting uncertainty estimate is sensitive to statistical fluctuations. Fortunately, the observed fluctuations occur only at high mass, where the background level itself is relatively small, so that results are less sensitive to the background level uncertainty.

Finally, we present the inputs to the statistical analysis for the SSM W' and W^* in tables 8.8-8.11. The inputs are the integrated luminosity central value and uncertainty as well as the central value and correlated and uncorrelated uncertainties for the signal efficiency and background level[9] and the event count observed in data. The integrated luminosity has a central value $\overline{L_{\mathrm{int}}} = 20.3\,\mathrm{fb}^{-1}$ and a relative uncertainty of 2.8% for all calculations, and is therefore not given in the tables. The central value of the number of expected background events per unit of integrated luminosity, $\overline{\sigma_{\mathrm{bg}}^{\mathrm{eff}}}$, is presented in the form of the product with the integrated luminosity central value for convenience. The column labeled $\overline{L_{\mathrm{int}}}\overline{\varepsilon_{\mathrm{sig}}}\sigma_{\mathrm{th}}$ gives the predicted number of signal events at final selection with the predicted cross section[10] σ_{th} of the relevant signal model as presented in tables 3.2 and 3.3. While σ_{th} is not an input to the statistical analysis, this column is included because it is useful for understanding the sensitivity to the theoretical signal prediction.

It is clear from tables 8.8-8.11 that no significant excess of events in data over the expected background is observed for any m_{T} threshold. On the contrary, the observed event counts in the muon channel are somewhat lower than the expected background event counts, and we therefore proceed to evaluate the significances of downward deviations.

[9]The contributions of the individual backgrounds to the total background level are given in section A.3 of appendix A.

[10]The symbol σ_{theory} will later be used for this quantity. There is no distinction between σ_{theory} and σ_{th}. The latter is used here simply to fit the tables within the page margins.

	$m_{\mathrm{T}}^{\mathrm{min}}$ [GeV]									
Source	252	317	336	377	423	448	474	564	597	710
Efficiency	2.5	2.5	2.5	2.5	2.6	2.6	2.6	2.5	2.5	2.5
Resolution	0.022	0.10	0.17	0.11	0.31	0.80	0.28	0.26	0.28	0.26
Scale	1.7	3.0	3.4	2.7	3.9	3.9	3.0	3.3	3.6	3.5
$\not\!\!E_{\mathrm{T}}$	0.31	0.23	0.41	0.17	0.38	0.44	0.13	0.21	0.14	0.35
Jet resolution	0.23	0.39	0.29	0.087	0.50	0.18	0.087	0.11	0.14	0.30
Jet scale	0.65	0.46	0.41	0.25	0.36	0.17	0.28	0.33	0.076	0.40
All experimental	3.1	3.9	4.3	3.7	4.7	4.7	3.9	4.2	4.5	4.4
MC statistics	0.92	1.2	1.3	1.4	1.5	1.4	1.1	1.0	1.1	1.7
Jet background	0.58	0.32	0.36	0.58	0.83	0.85	1.0	0.96	1.1	1.2
All uncorrelated	3.3	4.1	4.5	4.0	5.0	5.0	4.2	4.4	4.7	4.8
Top cross section	0.66	0.65	0.62	0.55	0.46	0.43	0.38	0.28	0.23	0.17
Beam energy	0.85	0.91	0.93	0.99	1.1	1.1	1.1	1.3	1.3	1.5
k-factor	5.3	5.1	5.1	5.2	5.2	5.6	6.2	7.9	8.6	11
All correlated	5.4	5.2	5.2	5.3	5.3	5.7	6.3	8.0	8.7	11
Total	6.3	6.7	6.9	6.6	7.3	7.6	7.6	9.2	9.9	12
	$m_{\mathrm{T}}^{\mathrm{min}}$ [GeV]									
Source	796	843	1002	1062	1191	1337	1416	1500	1683	1888
Efficiency	2.5	2.5	2.5	2.5	2.5	2.6	2.7	2.7	2.9	2.4
Resolution	0.93	0.52	0.64	0.77	0.72	3.0	1.2	1.9	0.37	0.29
Scale	3.6	3.6	3.8	3.6	2.9	3.1	3.3	3.5	3.1	3.9
$\not\!\!E_{\mathrm{T}}$	0.37	0.38	0.83	0.21	1.3	0.26	0.74	1.2	0.080	0.12
Jet resolution	0.43	0.35	0.28	0.61	0.30	3.0	0.98	0.072	0.079	0.13
Jet scale	0.33	0.15	0.63	0.18	0.54	0.62	0.94	0.025	0.14	0.092
All experimental	4.6	4.5	4.8	4.5	4.1	5.9	4.7	5.0	4.2	4.6
MC statistics	2.1	2.4	3.7	4.3	5.1	6.7	7.2	8.5	17	1.8
Jet background	0.53	0.27	0.98	1.2	1.6	1.8	2.0	2.2	2.5	4.2
All uncorrelated	5.0	5.1	6.1	6.4	6.8	9.1	8.8	10	18	6.4
Top cross section	0.14	0.095	0.0	0.0	0.0	0.0	0.0	0.0	0.0	0.0
Beam energy	1.7	1.8	2.0	2.1	2.4	2.5	2.7	2.8	2.8	3.9
k-factor	12	13	15	16	17	17	18	18	16	20
All correlated	12	13	15	16	17	17	18	18	16	20
Total	13	14	16	17	19	19	20	21	24	21

Table 8.2: Electron channel background level relative uncertainties in percent.

	$m_{\mathrm{T}}^{\mathrm{min}}$ [GeV]									
Source	252	317	336	377	423	448	502	564	597	710
Efficiency	3.3	3.3	3.3	3.3	3.3	3.3	3.3	3.3	3.3	3.3
Resolution	0.83	0.90	1.2	0.78	1.5	2.0	1.3	2.0	3.5	3.6
Scale	1.0	1.0	1.1	1.1	1.1	0.97	1.6	1.8	1.5	2.3
$\not\!\!E_{\mathrm{T}}$	0.82	0.30	0.77	0.47	0.69	0.43	0.35	0.84	0.28	0.44
Jet resolution	0.70	0.43	0.65	0.50	0.36	0.50	0.84	0.59	0.18	0.046
Jet scale	1.7	1.2	0.98	1.0	0.77	0.51	0.67	0.45	0.67	0.34
All experimental	4.1	3.8	3.9	3.8	4.0	4.1	4.1	4.4	5.1	5.4
MC statistics	0.94	1.4	1.5	1.7	1.8	1.8	1.5	1.4	1.5	2.2
Jet background	0.96	1.0	1.0	1.0	1.0	1.0	1.0	1.1	1.1	1.1
All uncorrelated	4.3	4.2	4.3	4.3	4.5	4.6	4.5	4.8	5.4	6.0
Top cross section	0.90	0.72	0.67	0.54	0.43	0.41	0.30	0.23	0.19	0.084
Beam energy	0.75	0.86	0.89	0.96	1.0	1.1	1.1	1.2	1.3	1.4
k-factor	5.3	5.4	5.4	5.5	5.5	5.7	6.7	7.9	8.4	10
All correlated	5.4	5.5	5.5	5.6	5.6	5.9	6.8	8.0	8.5	10
Total	6.9	6.9	7.0	7.0	7.2	7.4	8.2	9.3	10	12

	$m_{\mathrm{T}}^{\mathrm{min}}$ [GeV]								
Source	796	843	1002	1062	1191	1416	1500	1683	1888
Efficiency	3.4	3.4	3.4	3.3	3.4	3.4	3.4	3.4	3.5
Resolution	1.2	2.9	0.68	0.47	9.5	16	12	3.9	8.8
Scale	2.3	2.0	2.8	1.8	7.8	7.6	3.3	8.0	29
$\not\!\!E_{\mathrm{T}}$	0.30	0.71	0.29	0.28	5.1	0.26	0.39	0.075	0.059
Jet resolution	0.34	0.061	0.30	0.91	0.46	0.14	3.6	0.066	0.038
Jet scale	0.94	0.88	0.30	1.0	0.64	0.17	3.3	0.14	0.098
All experimental	4.4	5.0	4.5	4.1	14	18	13	9.5	30
MC statistics	3.0	3.5	5.4	6.6	7.8	12	14	12	11
Jet background	1.1	1.2	1.3	1.3	1.6	1.9	1.8	2.6	4.0
All uncorrelated	5.4	6.2	7.1	7.8	16	21	19	16	33
Top cross section	0.11	0.10	0.0004	0.0006	0.001	0.0	0.0	0.0	0.0
Beam energy	1.5	1.5	1.6	1.6	1.8	1.9	1.8	2.1	2.7
k-factor	11	11	13	12	14	14	13	16	19
All correlated	11	11	13	13	14	14	14	16	19
Total	12	13	14	15	21	25	24	22	38

Table 8.3: Muon channel background level relative uncertainties in percent.

Source	$m_{W'}$, $m_{\mathrm{T}}^{\mathrm{min}}$ [GeV]								
	300	400	500	600	750	1000	1250	1500	1750
	252	336	423	474	597	796	1002	1191	1416
Efficiency	2.7	2.7	2.7	2.6	2.6	2.5	2.5	2.5	2.5
Resolution	0.096	0.19	0.25	0.096	0.19	0.10	0.12	0.13	0.15
Scale	2.2	2.4	2.8	1.8	1.7	1.5	1.5	1.6	1.5
$\not\!\!E_{\mathrm{T}}$	1.3	0.11	0.060	0.14	0.056	0.087	0.034	0.081	0.051
Jet resolution	0.52	0.17	0.028	0.12	0.073	0.064	0.060	0.090	0.029
Jet scale	0.70	0.25	0.073	0.21	0.12	0.022	0.043	0.091	0.021
All experimental	3.8	3.6	3.9	3.2	3.1	3.0	2.9	3.0	2.9
MC statistics	1.4	1.2	1.2	1.1	1.0	1.0	0.97	0.93	0.94
All uncorrelated	4.1	3.8	4.1	3.4	3.3	3.1	3.1	3.1	3.1
Beam energy	0.012	0.015	0.018	0.020	0.030	0.056	0.10	0.17	0.31
k-factor	0.13	0.13	0.21	0.45	0.49	0.69	1.2	1.9	2.5
All correlated	0.13	0.13	0.21	0.45	0.50	0.69	1.2	1.9	2.5
Total	4.1	3.8	4.1	3.4	3.3	3.2	3.3	3.6	3.9

Source	$m_{W'}$, $m_{\mathrm{T}}^{\mathrm{min}}$ [GeV]								
	2000	2250	2500	2750	3000	3250	3500	3750	4000
	1500	1683	1888	1888	1888	1888	1888	1888	1888
Efficiency	2.5	2.5	2.5	2.5	2.5	2.5	2.5	2.5	2.5
Resolution	0.19	0.13	0.11	0.018	0.048	0.091	0.040	0.049	0.041
Scale	1.2	1.1	1.3	1.2	1.0	0.96	1.0	1.2	1.5
$\not\!\!E_{\mathrm{T}}$	0.068	0.027	0.043	0.026	0.020	0.030	0.014	0.015	0.018
Jet resolution	0.062	0.024	0.065	0.019	0.022	0.006	0.008	0.009	0.018
Jet scale	0.022	0.007	0.036	0.018	0.022	0.024	0.006	0.016	0.004
All experimental	2.8	2.8	2.8	2.8	2.7	2.7	2.7	2.8	2.9
MC statistics	0.85	0.87	0.90	0.85	0.81	0.78	0.73	0.65	0.54
All uncorrelated	2.9	2.9	3.0	2.9	2.8	2.8	2.8	2.9	3.0
Beam energy	0.52	0.90	1.5	2.3	3.3	4.3	5.1	5.4	5.2
k-factor	2.9	3.6	5.9	9.7	15	26	39	51	56
All correlated	3.0	3.7	6.1	10	16	26	40	51	57
Total	4.2	4.7	6.8	10	16	27	40	52	57

Table 8.4: Electron channel SSM W' relative signal efficiency uncertainties in percent.

Source	$m_{W'}$, $m_{\mathrm{T}}^{\mathrm{min}}$ [GeV]								
	300	400	500	600	750	1000	1250	1500	1750
	252	336	423	502	597	796	1002	1191	1416
Efficiency	3.3	3.3	3.3	3.4	3.4	3.4	3.4	3.5	3.5
Resolution	0.15	0.21	0.12	0.95	0.44	0.98	0.69	0.44	1.2
Scale	0.53	0.48	0.84	0.81	0.79	1.1	1.4	1.8	2.4
$\not{E}_{\mathrm{T}}$	0.65	0.27	0.20	0.12	0.19	0.19	0.096	0.13	0.083
Jet resolution	0.44	0.065	0.38	0.30	0.18	0.11	0.15	0.065	0.21
Jet scale	0.19	0.015	0.12	0.041	0.034	0.023	0.15	0.13	0.18
All experimental	3.4	3.4	3.5	3.6	3.5	3.7	3.7	3.9	4.4
MC statistics	1.6	1.6	1.6	1.5	1.4	1.3	1.3	1.3	1.3
All uncorrelated	3.8	3.7	3.8	3.9	3.8	3.9	4.0	4.1	4.5
Beam energy	0.009	0.012	0.017	0.022	0.030	0.053	0.099	0.17	0.30
k-factor	0.010	0.026	0.14	0.26	0.44	0.88	1.2	1.8	2.4
All correlated	0.013	0.029	0.14	0.26	0.44	0.88	1.2	1.8	2.4
Total	3.8	3.7	3.8	3.9	3.8	4.0	4.1	4.5	5.1

Source	$m_{W'}$, $m_{\mathrm{T}}^{\mathrm{min}}$ [GeV]								
	2000	2250	2500	2750	3000	3250	3500	3750	4000
	1500	1683	1888	1888	1888	1888	1888	1888	1888
Efficiency	3.5	3.5	3.6	3.5	3.5	3.6	3.9	3.8	3.7
Resolution	1.4	0.74	1.3	0.92	1.1	0.60	0.40	0.40	1.3
Scale	1.8	2.3	2.8	2.3	1.9	1.9	2.1	2.5	3.3
$\not{E}_{\mathrm{T}}$	0.064	0.055	0.064	0.071	0.083	0.030	0.018	0.011	0.015
Jet resolution	0.038	0.023	0.051	0.060	0.017	0.006	0.047	0.023	0.036
Jet scale	0.039	0.033	0.099	0.096	0.054	0.051	0.028	0.024	0.032
All experimental	4.2	4.3	4.7	4.3	4.2	4.1	4.5	4.6	5.1
MC statistics	1.2	1.2	1.2	1.1	1.1	1.0	0.97	0.85	0.71
All uncorrelated	4.3	4.4	4.9	4.5	4.3	4.2	4.6	4.6	5.1
Beam energy	0.52	0.89	1.5	2.3	3.3	4.2	4.9	5.0	4.7
k-factor	2.8	3.3	5.9	9.6	15	25	37	47	50
All correlated	2.8	3.4	6.1	9.8	15	26	38	47	50
Total	5.2	5.6	7.8	11	16	26	38	47	50

Table 8.5: Muon channel SSM W' relative signal efficiency uncertainties in percent.

Source	m_{W^*}, $m_{\mathrm{T}}^{\mathrm{min}}$ [GeV]								
	400	500	600	750	1000	1250	1500	1750	2000
	317	377	448	564	710	843	1062	1191	1337
Efficiency	2.9	3.0	3.0	2.9	2.8	2.8	2.7	2.7	2.7
Resolution	0.22	0.28	0.24	0.23	0.094	0.21	0.18	0.17	0.36
Scale	3.4	2.7	2.7	2.6	2.8	2.4	2.4	2.4	2.4
$\not\!\!E_{\mathrm{T}}$	0.15	0.25	0.13	0.076	0.17	0.12	0.087	0.12	0.083
Jet resolution	0.84	0.083	0.35	0.058	0.019	0.077	0.085	0.17	0.066
Jet scale	0.53	0.32	0.14	0.14	0.15	0.053	0.074	0.094	0.091
All experimental	4.6	4.0	4.0	3.9	4.0	3.7	3.6	3.6	3.6
MC statistics	1.7	1.6	1.5	1.6	1.4	1.3	1.3	1.3	1.2
All uncorrelated	4.9	4.3	4.3	4.2	4.2	3.9	3.9	3.9	3.8
Beam energy	0.079	0.051	0.045	0.044	0.036	0.033	0.044	0.049	0.059
k-factor	0.81	0.58	0.53	0.50	0.24	0.16	0.18	0.20	0.23
All correlated	0.82	0.59	0.54	0.50	0.25	0.17	0.19	0.20	0.24
Total	4.9	4.4	4.3	4.2	4.2	3.9	3.9	3.9	3.9

Source	m_{W^*}, $m_{\mathrm{T}}^{\mathrm{min}}$ [GeV]							
	2250	2500	2750	3000	3250	3500	3750	4000
	1416	1683	1888	1888	1888	1888	1888	1888
Efficiency	2.7	2.6	2.6	2.6	2.6	2.6	2.6	2.6
Resolution	0.074	0.15	0.20	0.14	0.055	0.17	0.18	0.088
Scale	2.1	2.4	2.5	2.1	1.9	1.7	1.5	1.3
$\not\!\!E_{\mathrm{T}}$	0.044	0.031	0.071	0.077	0.038	0.054	0.013	0.031
Jet resolution	0.16	0.060	0.098	0.044	0.057	0.086	0.037	0.068
Jet scale	0.079	0.076	0.076	0.083	0.066	0.018	0.037	0.096
All experimental	3.4	3.6	3.6	3.4	3.3	3.1	3.0	2.9
MC statistics	1.1	1.2	1.3	1.2	1.2	1.3	1.3	1.4
All uncorrelated	3.6	3.8	3.9	3.6	3.5	3.4	3.3	3.3
Beam energy	0.068	0.10	0.15	0.20	0.28	0.43	0.66	1.0
k-factor	0.27	0.48	0.89	1.4	2.2	3.9	10	30
All correlated	0.27	0.49	0.90	1.4	2.2	3.9	10	31
Total	3.6	3.8	4.0	3.9	4.1	5.2	11	31

Table 8.6: Electron channel W^* relative signal efficiency uncertainties in percent.

Source	m_{W^*}, $m_{\mathrm{T}}^{\mathrm{min}}$ [GeV]								
	400	500	600	750	1000	1250	1500	1750	2000
	317	377	448	564	710	843	1062	1191	1416
Efficiency	3.3	3.3	3.3	3.4	3.3	3.4	3.4	3.4	3.5
Resolution	0.76	0.59	0.19	0.58	0.19	0.88	0.30	0.90	0.86
Scale	0.94	0.54	0.46	0.86	0.86	1.2	1.5	2.1	2.8
$\not\!\!E_{\mathrm{T}}$	0.66	0.32	0.25	0.47	0.36	0.24	0.13	0.17	0.12
Jet resolution	0.29	0.62	0.19	0.22	0.17	0.075	0.14	0.14	0.090
Jet scale	0.27	0.41	0.009	0.22	0.22	0.12	0.030	0.033	0.10
All experimental	3.6	3.5	3.4	3.6	3.5	3.7	3.7	4.1	4.5
MC statistics	2.2	2.1	2.1	2.1	1.9	1.7	1.8	1.7	1.8
All uncorrelated	4.2	4.1	4.0	4.1	3.9	4.1	4.1	4.4	4.9
Beam energy	0.074	0.049	0.049	0.046	0.032	0.029	0.044	0.045	0.059
k-factor	0.79	0.60	0.45	0.35	0.24	0.23	0.18	0.18	0.24
All correlated	0.79	0.60	0.45	0.35	0.24	0.23	0.18	0.18	0.25
Total	4.3	4.1	4.0	4.1	3.9	4.1	4.1	4.4	4.9

Source	m_{W^*}, $m_{\mathrm{T}}^{\mathrm{min}}$ [GeV]							
	2250	2500	2750	3000	3250	3500	3750	4000
	1416	1683	1888	1888	1888	1888	1888	1888
Efficiency	3.5	3.5	3.5	3.5	3.8	3.8	3.7	3.6
Resolution	0.38	0.66	0.36	0.28	1.1	1.4	1.2	0.35
Scale	2.2	2.5	4.7	2.8	2.3	1.8	2.1	1.9
$\not\!\!E_{\mathrm{T}}$	0.26	0.099	0.12	0.057	0.052	0.15	0.11	0.17
Jet resolution	0.14	0.073	0.25	0.15	0.14	0.052	0.064	0.033
Jet scale	0.18	0.040	0.042	0.044	0.026	0.087	0.039	0.027
All experimental	4.1	4.3	5.9	4.6	4.6	4.4	4.4	4.1
MC statistics	1.6	1.7	1.8	1.8	1.8	1.8	1.8	2.0
All uncorrelated	4.4	4.7	6.2	4.9	4.9	4.7	4.8	4.6
Beam energy	0.065	0.088	0.14	0.17	0.27	0.38	0.62	0.95
k-factor	0.25	0.59	0.79	1.4	2.1	3.9	10	29
All correlated	0.25	0.60	0.80	1.4	2.1	3.9	10	29
Total	4.4	4.7	6.2	5.1	5.3	6.1	11	30

Table 8.7: Muon channel W^* relative signal efficiency uncertainties in percent.

$m_{W'}$ [GeV]	$m_{\mathrm{T}}^{\mathrm{min}}$ [GeV]	$\overline{\varepsilon_{\mathrm{sig}}}$	$\frac{(\Delta\varepsilon_{\mathrm{sig}})_{\mathrm{uc}}}{\overline{\varepsilon_{\mathrm{sig}}}}$ [%]	$\frac{(\Delta\varepsilon_{\mathrm{sig}})_{\mathrm{c}}}{\overline{\varepsilon_{\mathrm{sig}}}}$ [%]	$\overline{L_{\mathrm{int}}}\,\overline{\varepsilon_{\mathrm{sig}}}\sigma_{\mathrm{th}}$	$\overline{L_{\mathrm{int}}}\,\overline{\sigma_{\mathrm{bg}}^{\mathrm{eff}}}$	$\frac{(\Delta\sigma_{\mathrm{bg}}^{\mathrm{eff}})_{\mathrm{uc}}}{\overline{\sigma_{\mathrm{bg}}^{\mathrm{eff}}}}$ [%]	$\frac{(\Delta\sigma_{\mathrm{bg}}^{\mathrm{eff}})_{\mathrm{c}}}{\overline{\sigma_{\mathrm{bg}}^{\mathrm{eff}}}}$ [%]	n_{obs}
300	252	0.228	4.1	0.13	$6.9 \cdot 10^5$	$1.29 \cdot 10^4$	3.3	5.4	12717
400	336	0.319	3.8	0.13	$3.2 \cdot 10^5$	$5.28 \cdot 10^3$	4.5	5.2	5176
500	423	0.325	4.1	0.21	$1.4 \cdot 10^5$	$2.07 \cdot 10^3$	5.0	5.3	2017
600	474	0.397	3.4	0.45	$8.4 \cdot 10^4$	$1.26 \cdot 10^3$	4.2	6.3	1214
750	597	0.393	3.3	0.50	$3.3 \cdot 10^4$	456	4.7	8.7	414
1000	796	0.386	3.1	0.69	$9.1 \cdot 10^3$	116	5.0	12	101
1250	1002	0.378	3.1	1.2	$3.0 \cdot 10^3$	35.3	6.1	15	34
1500	1191	0.376	3.1	1.9	$1.1 \cdot 10^3$	13.2	6.8	17	14
1750	1416	0.336	3.1	2.5	$4.0 \cdot 10^2$	4.56	8.8	18	5
2000	1500	0.370	2.9	3.0	$1.8 \cdot 10^2$	2.99	10	18	3
2250	1683	0.327	2.9	3.7	71	1.38	18	16	0
2500	1888	0.262	3.0	6.1	27	0.432	6.4	20	0
2750	1888	0.235	2.9	10	12	0.432	6.4	20	0
3000	1888	0.183	2.8	16	5.3	0.432	6.4	20	0
3250	1888	0.124	2.8	26	2.2	0.432	6.4	20	0
3500	1888	0.0769	2.8	40	0.92	0.432	6.4	20	0
3750	1888	0.0474	2.9	51	0.40	0.432	6.4	20	0
4000	1888	0.0311	3.0	57	0.20	0.432	6.4	20	0

Table 8.8: Electron channel inputs to the statistical analysis for the SSM W'.

$m_{W'}$ [GeV]	$m_{\mathrm{T}}^{\mathrm{min}}$ [GeV]	$\overline{\varepsilon_{\mathrm{sig}}}$	$\frac{(\Delta\varepsilon_{\mathrm{sig}})_{\mathrm{uc}}}{\overline{\varepsilon_{\mathrm{sig}}}}$ [%]	$\frac{(\Delta\varepsilon_{\mathrm{sig}})_{\mathrm{c}}}{\overline{\varepsilon_{\mathrm{sig}}}}$ [%]	$\overline{L_{\mathrm{int}}}\,\overline{\varepsilon_{\mathrm{sig}}}\sigma_{\mathrm{th}}$	$\overline{L_{\mathrm{int}}}\,\overline{\sigma_{\mathrm{bg}}^{\mathrm{eff}}}$	$\frac{(\Delta\sigma_{\mathrm{bg}}^{\mathrm{eff}})_{\mathrm{uc}}}{\overline{\sigma_{\mathrm{bg}}^{\mathrm{eff}}}}$ [%]	$\frac{(\Delta\sigma_{\mathrm{bg}}^{\mathrm{eff}})_{\mathrm{c}}}{\overline{\sigma_{\mathrm{bg}}^{\mathrm{eff}}}}$ [%]	n_{obs}
300	252	0.183	3.8	0.013	$5.6 \cdot 10^5$	$1.11 \cdot 10^4$	4.3	5.4	10886
400	336	0.193	3.7	0.029	$2.0 \cdot 10^5$	$3.36 \cdot 10^3$	4.3	5.5	3306
500	423	0.186	3.8	0.14	$8.1 \cdot 10^4$	$1.30 \cdot 10^3$	4.5	5.6	1214
600	502	0.196	3.9	0.26	$4.1 \cdot 10^4$	640	4.5	6.8	548
750	597	0.226	3.8	0.44	$1.9 \cdot 10^4$	301	5.4	8.5	255
1000	796	0.220	3.9	0.88	$5.2 \cdot 10^3$	84.2	5.4	11	58
1250	1002	0.210	4.0	1.2	$1.7 \cdot 10^3$	28.8	7.1	13	19
1500	1191	0.206	4.1	1.8	$6.1 \cdot 10^2$	11.1	16	14	6
1750	1416	0.182	4.5	2.4	$2.1 \cdot 10^2$	4.49	21	14	0
2000	1500	0.198	4.3	2.8	98	3.60	19	14	0
2250	1683	0.173	4.4	3.4	38	1.59	16	16	0
2500	1888	0.140	4.9	6.1	14	0.643	33	19	0
2750	1888	0.127	4.5	9.8	6.7	0.643	33	19	0
3000	1888	0.100	4.3	15	2.9	0.643	33	19	0
3250	1888	0.0689	4.2	26	1.2	0.643	33	19	0
3500	1888	0.0439	4.6	38	0.52	0.643	33	19	0
3750	1888	0.0278	4.6	47	0.24	0.643	33	19	0
4000	1888	0.0191	5.1	50	0.12	0.643	33	19	0

Table 8.9: Muon channel inputs to the statistical analysis for the SSM W'.

m_{W^*} [GeV]	$m_{\mathrm{T}}^{\mathrm{min}}$ [GeV]	$\overline{\varepsilon_{\mathrm{sig}}}$	$\frac{(\Delta\varepsilon_{\mathrm{sig}})_{\mathrm{uc}}}{\overline{\varepsilon_{\mathrm{sig}}}}$ [%]	$\frac{(\Delta\varepsilon_{\mathrm{sig}})_{\mathrm{c}}}{\overline{\varepsilon_{\mathrm{sig}}}}$ [%]	$\overline{L_{\mathrm{int}}}\,\overline{\varepsilon_{\mathrm{sig}}}\sigma_{\mathrm{th}}$	$\overline{L_{\mathrm{int}}}\,\overline{\sigma_{\mathrm{bg}}^{\mathrm{eff}}}$	$\frac{(\Delta\sigma_{\mathrm{bg}}^{\mathrm{eff}})_{\mathrm{uc}}}{\overline{\sigma_{\mathrm{bg}}^{\mathrm{eff}}}}$ [%]	$\frac{(\Delta\sigma_{\mathrm{bg}}^{\mathrm{eff}})_{\mathrm{c}}}{\overline{\sigma_{\mathrm{bg}}^{\mathrm{eff}}}}$ [%]	n_{obs}
400	317	0.196	4.9	0.82	$1.5 \cdot 10^5$	$6.63 \cdot 10^3$	4.1	5.2	6448
500	377	0.246	4.3	0.59	$8.1 \cdot 10^4$	$3.32 \cdot 10^3$	4.0	5.3	3275
600	448	0.257	4.3	0.54	$4.1 \cdot 10^4$	$1.63 \cdot 10^3$	5.0	5.7	1582
750	564	0.248	4.2	0.50	$1.6 \cdot 10^4$	593	4.4	8.0	524
1000	710	0.302	4.2	0.25	$5.4 \cdot 10^3$	203	4.8	11	177
1250	843	0.337	3.9	0.17	$2.0 \cdot 10^3$	85.6	5.1	13	79
1500	1062	0.296	3.9	0.19	$6.5 \cdot 10^2$	25.8	6.4	16	26
1750	1191	0.324	3.9	0.20	$2.8 \cdot 10^2$	13.2	6.8	17	14
2000	1337	0.341	3.8	0.24	$1.2 \cdot 10^2$	6.75	9.1	17	9
2250	1416	0.391	3.6	0.27	55	4.56	8.8	18	5
2500	1683	0.337	3.8	0.49	20	1.38	18	16	0
2750	1888	0.322	3.9	0.90	7.8	0.432	6.4	20	0
3000	1888	0.382	3.6	1.4	3.8	0.432	6.4	20	0
3250	1888	0.437	3.5	2.2	1.8	0.432	6.4	20	0
3500	1888	0.474	3.4	3.9	0.77	0.432	6.4	20	0
3750	1888	0.498	3.3	10	0.32	0.432	6.4	20	0
4000	1888	0.487	3.3	31	0.12	0.432	6.4	20	0

Table 8.10: Electron channel inputs to the statistical analysis for the W^*.

m_{W^*} [GeV]	$m_{\mathrm{T}}^{\mathrm{min}}$ [GeV]	$\overline{\varepsilon_{\mathrm{sig}}}$	$\frac{(\Delta\varepsilon_{\mathrm{sig}})_{\mathrm{uc}}}{\overline{\varepsilon_{\mathrm{sig}}}}$ [%]	$\frac{(\Delta\varepsilon_{\mathrm{sig}})_{\mathrm{c}}}{\overline{\varepsilon_{\mathrm{sig}}}}$ [%]	$\overline{L_{\mathrm{int}}}\,\overline{\varepsilon_{\mathrm{sig}}}\sigma_{\mathrm{th}}$	$\overline{L_{\mathrm{int}}}\,\overline{\sigma_{\mathrm{bg}}^{\mathrm{eff}}}$	$\frac{(\Delta\sigma_{\mathrm{bg}}^{\mathrm{eff}})_{\mathrm{uc}}}{\overline{\sigma_{\mathrm{bg}}^{\mathrm{eff}}}}$ [%]	$\frac{(\Delta\sigma_{\mathrm{bg}}^{\mathrm{eff}})_{\mathrm{c}}}{\overline{\sigma_{\mathrm{bg}}^{\mathrm{eff}}}}$ [%]	n_{obs}
400	317	0.111	4.2	0.79	$8.5 \cdot 10^4$	$4.28 \cdot 10^3$	4.2	5.5	4227
500	377	0.140	4.1	0.60	$4.6 \cdot 10^4$	$2.09 \cdot 10^3$	4.3	5.6	2002
600	448	0.144	4.0	0.45	$2.3 \cdot 10^4$	$1.04 \cdot 10^3$	4.6	5.9	936
750	564	0.143	4.1	0.35	$9.2 \cdot 10^3$	383	4.8	8.0	321
1000	710	0.173	3.9	0.24	$3.1 \cdot 10^3$	140	6.0	10	109
1250	843	0.191	4.1	0.23	$1.1 \cdot 10^3$	64.4	6.2	11	40
1500	1062	0.164	4.1	0.18	$3.6 \cdot 10^2$	22.2	7.8	13	12
1750	1191	0.182	4.4	0.18	$1.6 \cdot 10^2$	11.1	16	14	6
2000	1416	0.160	4.9	0.25	55	4.49	21	14	0
2250	1416	0.204	4.4	0.25	29	4.49	21	14	0
2500	1683	0.178	4.7	0.60	10	1.59	16	16	0
2750	1888	0.161	6.2	0.80	3.9	0.643	33	19	0
3000	1888	0.185	4.9	1.4	1.8	0.643	33	19	0
3250	1888	0.218	4.9	2.1	0.88	0.643	33	19	0
3500	1888	0.230	4.7	3.9	0.37	0.643	33	19	0
3750	1888	0.244	4.8	10	0.16	0.643	33	19	0
4000	1888	0.242	4.6	29	0.062	0.643	33	19	0

Table 8.11: Muon channel inputs to the statistical analysis for the W^*.

8.6 Significance of downward deviations

Significances are calculated following the hybrid prescription detailed in section 7.2. The p-value relevant for downward deviations is

$$p = \sum_{X \leq X_{\mathrm{obs}}} P_{\mathrm{bg}}(X), \tag{8.4}$$

and it is evaluated, along with the corresponding significance, with Gaussian PDFs for the nuisance parameters.

Results are shown in fig. 8.7. Both p-values and significances are shown for the SSM W' and the W^* searches for both the electron and muon channels and the combination. Significances are seen to be in general below 2, with the exceptions being in the muon channel with the thresholds[11] $m_{\mathrm{T}}^{\mathrm{min}} = 1416\,\mathrm{GeV}$, corresponding to a significance of 2.02, and $m_{\mathrm{T}}^{\mathrm{min}} = 843\,\mathrm{GeV}$, corresponding to a significance of 2.15. We see that the significances for the electron and muon channel combination are in general below those for the muon channel alone, which is due to the fact that the observation in the electron channel is generally in good agreement with the background prediction.

With a highest *local* significance of 2.15, we conclude that the observed data are in reasonable agreement with the background-only hypothesis. The term local significance is used here to indicate that the significances are not corrected for the "look elsewhere effect", i.e. the fact that one is more likely to find a high significance the more different search regions (m_{T} thresholds in this context) one considers.

We note that, while the test statistic (7.12) has a simple one-to-one correspondence with the event count for a single channel, p-values and significances for the combination are in principle dependent on the value of the signal cross section used for the significance evaluation. The results in fig. 8.7 were obtained with a signal cross section of $1\,\mathrm{fb}$, and results with a signal cross section of $500\,\mathrm{fb}$ were found to give p-values differing by up to 30% from these. Such dependence could be avoided with the use of the profile likelihood ratio as test statistic, but a new calculation of the combined significances seems hardly warranted considering the fact that the muon channel significances are in any case higher. It is also worth noting that the highest muon channel significance, corresponding to $m_{\mathrm{T}}^{\mathrm{min}} = 843\,\mathrm{GeV}$, can be approximately reproduced by the simple formula

$$Z \approx \frac{\left| n_{\mathrm{obs}} - \overline{L_{\mathrm{int}}}\,\overline{\sigma_{\mathrm{bg}}^{\mathrm{eff}}} \right|}{\sqrt{\overline{L_{\mathrm{int}}}\,\overline{\sigma_{\mathrm{bg}}^{\mathrm{eff}}} + \left[\overline{L_{\mathrm{int}}}(\Delta\sigma_{\mathrm{bg}}^{\mathrm{eff}})_{\mathrm{uc}}\right]^2 + \left[\overline{L_{\mathrm{int}}}(\Delta\sigma_{\mathrm{bg}}^{\mathrm{eff}})_{\mathrm{c}}\right]^2}}\,, \tag{8.5}$$

giving $Z \approx 2.1$ with the inputs from the relevant row of table 8.11. In this formula, the numerator is the deviation of the observed data event count from the background prediction, while the denominator is the sum in quadrature of the correlated and uncorrelated background uncertainties and the standard deviation of the Poisson distribution with expectation value equal to the

[11] Note that the significance evaluated for a single channel only depends on the background estimate and uncertainty and the observed event count. Therefore, the significance of 2.02 appears for the SSM W' of mass $1750\,\mathrm{GeV}$ as well as the W^* of masses $2000\,\mathrm{GeV}$ and $2250\,\mathrm{GeV}$. The significance of 2.15 corresponds to the W^* of mass $1250\,\mathrm{GeV}$.

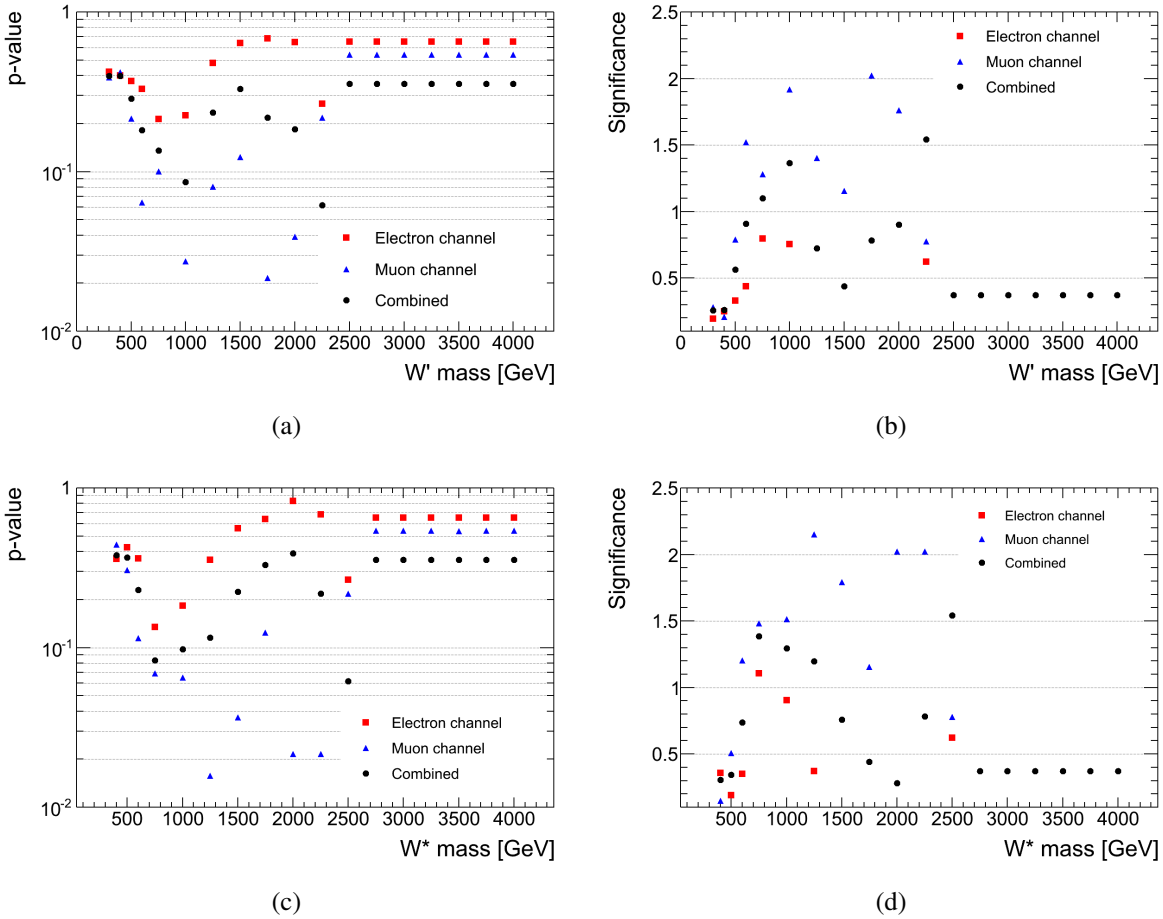

Figure 8.7: The p-values ((a) and (c)) and significances ((b) and (d)) of downward deviations for the SSM W' ((a) and (b)) and the W^* ((c) and (d)) searches.

	$m_{W'}$ [TeV]		m_{W^*} [TeV]	
Channel	Expected	Observed	Expected	Observed
Electron	3.13	3.13	3.08	3.08
Muon	2.97	2.97	2.84	2.84
Combined	3.17	3.24	3.12	3.21

Table 8.12: Mass limits for the SSM W' (left) and the W^* (right) signal models.

expected background event count.

8.7 Limits on the W' and W^* cross sections

Limits on the total cross sections for production of the SSM W' and W^* bosons and decay to a single lepton generation are shown in fig. 8.8. All limits are at 95% CL and are calculated following the Bayesian prescription (see section 7.3). A prominent feature in both the SSM W' and W^* cases is a drastic increase in the limits towards low masses, corresponding to the fact that the lower m_{T} thresholds used for lower W'/W^* masses admit higher background levels. In the SSM W' case, limits increase also significantly towards the highest masses, which is due to the low mass off-shell production tails in the invariant mass distributions for the higher mass W' bosons. As the low invariant mass events have vanishing probability to be reconstructed with $m_{\mathrm{T}} > m_{\mathrm{T}}^{\mathrm{min}}$, they contribute only to the denominator of eq. (8.2) and thus reduce the signal efficiency. This leads to an increase in the cross section limit. This feature is pretty much absent in the W^* case due to the natural suppression of the low mass off-shell tails in this model.

The cross section predicted by the given signal model, σ_{theory}, is also shown in the limit plots. The cross sections correspond to tables 3.2 and 3.3. No uncertainty band is included in the W^* case because of the non-renormalizability of this model as mentioned in section 3.2.3. The mass limit is defined to be at the intersection between the observed limit (labeled "Excluded at 95% CL" in the plots) and the (central) theory prediction σ_{theory}. Mass limits for the SSM W' and the W^* are shown in table 8.12. The mass limits obtained for the electron and muon channel combination are $3.24\,\mathrm{TeV}$ for the SSM W' and $3.21\,\mathrm{TeV}$ for the W^*. The combined SSM W' mass limit is slightly weaker than the limit of $3.28\,\mathrm{TeV}$ presented in ref. [71].

The limits presented here are in good agreement with those presented in the ATLAS publication based on the 2012 data, ref. [109]. In particular, the electron channel cross section limits agree to better than 0.2%, which is at the level of the precision of the limit calculation, since exactly the same electron channel limit calculation inputs are used here as in the paper. The muon channel limit inputs are recalculated for this thesis, and even for the W'/W^* masses where the same m_{T} threshold is used here as in the paper, small differences are seen wrt. the published results. In particular, cross section limits differ by up to 10-20% at low mass, where the limits are sensitive to small differences in the background levels and their uncertainties, because a few background MC samples are not the same between this work and the publication. For W' (W^*) masses starting from $1750\,\mathrm{GeV}$ ($2250\,\mathrm{GeV}$), the cross section limits agree to better than 0.4%. A smaller effect is seen for the combined limits, which differ only by up to 6% at low mass. We note also a difference in the mass limit for the W^* in the muon channel, which is $2.84\,\mathrm{TeV}$ here and $2.83\,\mathrm{TeV}$ in ref. [109]. This is caused by the marginal sub-percent differences in the high mass limits combined with the fact that the precise number is very close to $2.835\,\mathrm{TeV}$, and

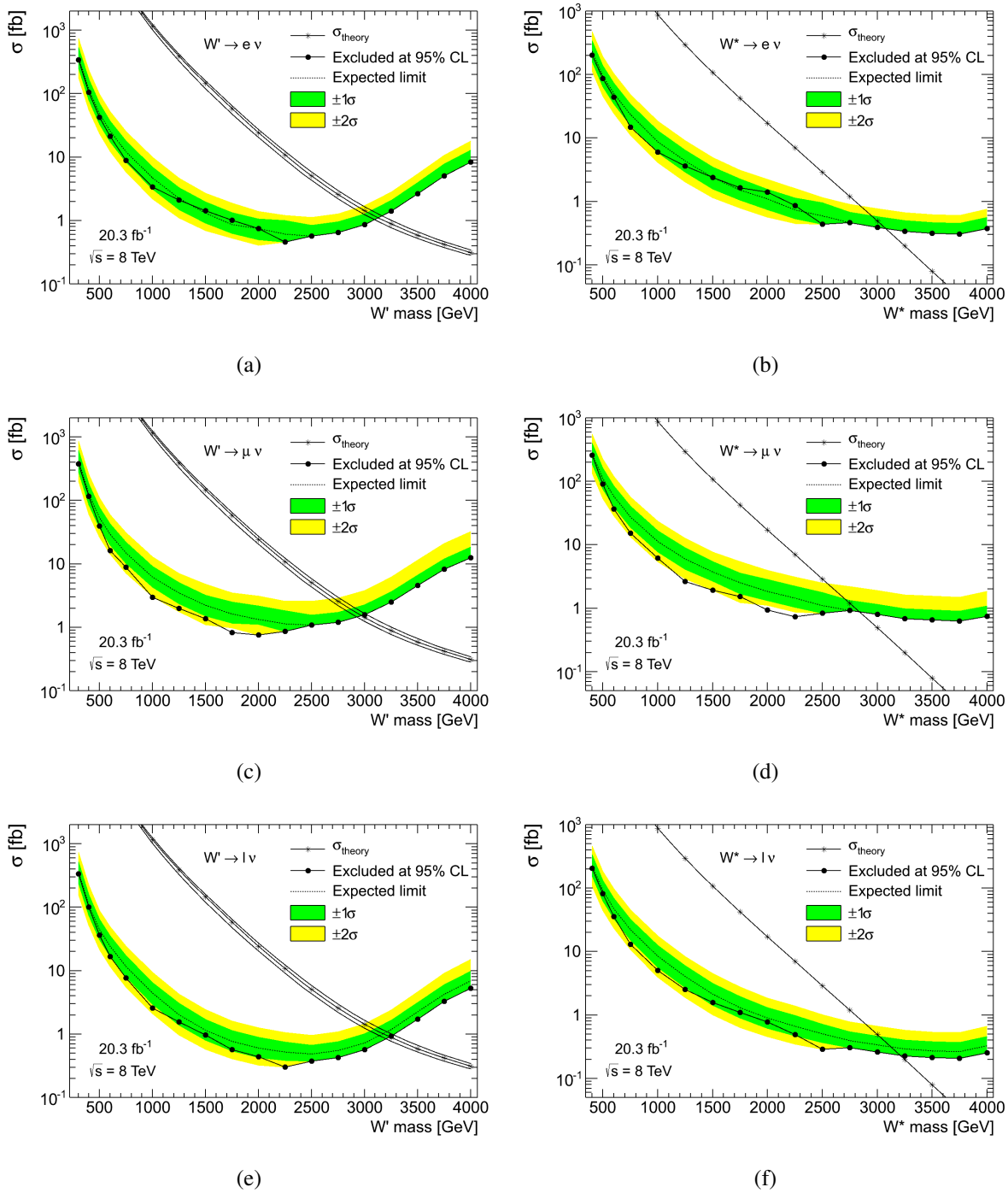

Figure 8.8: Limits on the cross sections for SSM W' ((a), (c), and (e)) and W^* ((b), (d), and (f)) production and decay to a single lepton generation. Limits are shown for the electron channel ((a) and (b)), the muon channel ((c) and (d)), and their combination ((e) and (f)). The parameter σ is here the total cross section for W'/W^* production and decay to a single lepton generation, and the theory cross section σ_{theory} corresponds to tables 3.2 and 3.3, with the uncertainties in the SSM W' case represented by the band formed by the immediately adjacent curves to the central theory prediction.

different rounding seems appropriate here than with the published results. The mass limit is in any case based on simple interpolation between the different W'/W^* mass points as shown in fig. 8.8, and should not be considered as very precise.

It is interesting to know to which extent the final cross section limits are affected by the various nuisance parameter uncertainties and their correlations. We follow here the standard ATLAS W' presentation with tables showing the cross section limits calculated with different subsets of the relevant uncertainties. The cross section limits are presented for W' in table 8.13 and for W^* in table 8.14. The headers in the tables indicate which uncertainties are included in the limit calculation, with "S", "B", and "L" indicating respectively that the uncertainties on the signal efficiency, background level, and integrated luminosity are taken into account. The subscript "c" means that correlation is included, e.g. in the column labeled $(\mathrm{SB})_\mathrm{c}$, both signal and background uncertainties are included with correlation between them and between channels (for the combination). All limits are quoted with three significant digits, reflecting the sub-percent numerical precision of the limit calculation.

We note that the background uncertainty has a very large impact on the limits in the low mass region, where the expected background event counts are large, and a much smaller impact at high mass. The signal efficiency uncertainty has negligible impact at low mass, and only starts to become important for masses above $3\,\mathrm{TeV}$. This uncertainty has the dominant impact on the cross section limits for the highest masses, where the limits are affected at the level of more than 50% for the SSM W'. The uncertainty on the integrated luminosity has an impact of about 10-15% at low mass and is negligible at high mass. Finally, correlations affect the combined cross section limits by up to 35% at low mass due to correlation between the background levels and up to 45% at high mass for the SSM W' due to correlation between the signal efficiencies. There is an intermediate mass region where correlations have only a marginal impact because neither the background level nor signal efficiency uncertainties significantly impact the limits.

The effect of the nuisance parameter uncertainties on the derived mass limits is of the order of 20-$50\,\mathrm{GeV}$ for the SSM W' and marginal for the W^* due to the smaller signal efficiency uncertainty for this model. For the SSM W', shifting the theoretical cross section prediction within its uncertainty changes the mass limit by a similar amount as the effect of the nuisance parameter uncertainties.

We comment finally on the fact that, for the very highest W' masses in table 8.13, the column labeled $\mathrm{S_c}$ does in some cases differ from the one labeled S even for the individual channels. Such an effect is intuitively not expected, but can arise because of the product ansatz for the nuisance parameters used when correlation is included, as discussed in the last paragraph of section 7.3.3. Considering the limit numbers before they are rounded for the table, this effect is at most at the level of 0.1%.

8.7.1 Numerical accuracy

There are three numerical accuracy parameters in the limit evaluation (see section 7.3.4), namely the step length in the signal cross section σ, the number of MC cycles in the marginalization, and the numerical convergence criterion used to cut off the posterior. The numerical accuracy of the observed limits presented here (and also those to be presented in chapter 9) has been investigated and is estimated to be in general better than half a percent. When the expected limits

$m_{W'}$		95% CL limit on the signal cross section [fb]						
[GeV]	Channel	none	S	SB	SBL	S_c	$(SB)_c$	$(SB)_cL$
	Electron	29.0	29.1	304	342	29.1	305	343
300	Muon	27.7	27.8	339	376	27.8	340	376
	Combined	16.2	16.3	224	274	16.3	294	334
	Electron	14.0	14.1	94.8	105	14.1	95.1	105
400	Muon	21.4	21.5	105	116	21.5	105	116
	Combined	10.2	10.3	69.9	83.7	10.3	88.6	100
	Electron	9.14	9.18	38.6	42.3	9.18	38.8	42.4
500	Muon	9.30	9.32	35.6	39.3	9.32	35.8	39.4
	Combined	5.34	5.35	24.9	29.7	5.35	32.1	36.3
	Electron	5.67	5.69	19.5	21.2	5.69	19.7	21.4
600	Muon	4.63	4.65	14.7	16.1	4.65	14.8	16.1
	Combined	2.87	2.87	10.8	12.7	2.87	15.0	16.7
	Electron	2.95	2.95	8.26	8.72	2.95	8.35	8.80
750	Muon	3.48	3.49	8.36	8.82	3.49	8.45	8.90
	Combined	1.77	1.77	5.24	5.82	1.77	7.16	7.66
	Electron	1.84	1.85	3.25	3.34	1.85	3.30	3.38
1000	Muon	1.86	1.87	2.83	2.92	1.87	2.88	2.97
	Combined	1.03	1.04	1.84	1.95	1.04	2.47	2.57
	Electron	1.63	1.64	2.06	2.09	1.64	2.09	2.12
1250	Muon	1.59	1.60	1.92	1.95	1.60	1.95	1.98
	Combined	0.980	0.981	1.27	1.30	0.981	1.51	1.55
	Electron	1.27	1.28	1.40	1.41	1.28	1.42	1.43
1500	Muon	1.20	1.20	1.33	1.34	1.20	1.35	1.36
	Combined	0.771	0.771	0.873	0.884	0.772	0.962	0.973
	Electron	0.964	0.967	0.993	0.997	0.967	1.01	1.01
1750	Muon	0.813	0.817	0.817	0.821	0.817	0.827	0.831
	Combined	0.521	0.522	0.533	0.537	0.522	0.563	0.567
	Electron	0.721	0.724	0.735	0.738	0.724	0.743	0.746
2000	Muon	0.747	0.751	0.751	0.754	0.751	0.760	0.763
	Combined	0.415	0.416	0.422	0.425	0.417	0.439	0.442
	Electron	0.453	0.455	0.455	0.456	0.455	0.458	0.459
2250	Muon	0.853	0.859	0.859	0.861	0.859	0.865	0.868
	Combined	0.296	0.297	0.297	0.298	0.297	0.302	0.303
	Electron	0.564	0.569	0.569	0.570	0.569	0.572	0.573
2500	Muon	1.06	1.07	1.07	1.07	1.07	1.08	1.08
	Combined	0.368	0.370	0.370	0.371	0.371	0.376	0.377
	Electron	0.629	0.643	0.643	0.644	0.643	0.648	0.649
2750	Muon	1.16	1.19	1.19	1.19	1.19	1.21	1.21
	Combined	0.409	0.413	0.413	0.413	0.417	0.425	0.426
	Electron	0.809	0.852	0.852	0.853	0.852	0.863	0.865
3000	Muon	1.47	1.55	1.55	1.55	1.55	1.58	1.58
	Combined	0.523	0.535	0.535	0.535	0.549	0.565	0.567
	Electron	1.20	1.37	1.37	1.37	1.37	1.40	1.40
3250	Muon	2.15	2.44	2.44	2.45	2.44	2.51	2.52
	Combined	0.768	0.814	0.814	0.816	0.877	0.919	0.921
	Electron	1.93	2.56	2.56	2.56	2.56	2.64	2.64
3500	Muon	3.37	4.37	4.37	4.38	4.38	4.55	4.56
	Combined	1.22	1.38	1.38	1.38	1.61	1.72	1.73
	Electron	3.12	4.90	4.90	4.91	4.90	5.07	5.08
3750	Muon	5.32	7.83	7.83	7.85	7.84	8.19	8.21
	Combined	1.97	2.37	2.37	2.38	3.01	3.26	3.27
	Electron	4.76	8.07	8.07	8.08	8.08	8.38	8.40
4000	Muon	7.75	11.9	11.9	12.0	12.0	12.5	12.6
	Combined	2.95	3.66	3.66	3.66	4.81	5.23	5.25

Table 8.13: Cross section limits for the SSM W' with different subsets of the nuisance parameter uncertainties included in the limit calculation.

m_{W^*}		95% CL limit on the signal cross section [fb]						
[GeV]	Channel	none	S	SB	SBL	S_c	$(SB)_c$	$(SB)_cL$
	Electron	20.7	20.8	180	201	20.8	183	204
400	Muon	44.4	44.5	232	256	44.5	235	259
	Combined	16.6	16.7	141	170	16.7	180	204
	Electron	17.3	17.3	78.0	86.5	17.3	79.0	87.5
500	Muon	18.0	18.0	81.5	90.0	18.0	82.5	91.1
	Combined	10.6	10.6	55.0	66.2	10.6	72.0	81.6
	Electron	10.4	10.4	40.0	43.5	10.4	40.5	43.9
600	Muon	8.60	8.62	32.9	36.3	8.62	33.2	36.7
	Combined	5.36	5.37	23.6	28.2	5.37	31.6	35.7
	Electron	4.23	4.25	13.8	14.8	4.25	13.9	14.9
750	Muon	5.48	5.50	14.3	15.2	5.50	14.4	15.4
	Combined	2.57	2.57	8.57	9.76	2.57	12.0	13.1
	Electron	2.69	2.70	5.75	5.97	2.70	5.79	6.01
1000	Muon	3.17	3.18	5.87	6.09	3.18	5.91	6.12
	Combined	1.61	1.61	3.58	3.85	1.61	4.77	5.01
	Electron	2.29	2.30	3.56	3.63	2.30	3.57	3.64
1250	Muon	1.80	1.81	2.57	2.63	1.81	2.58	2.64
	Combined	1.17	1.17	1.85	1.94	1.17	2.45	2.54
	Electron	1.99	2.00	2.36	2.38	2.00	2.37	2.39
1500	Muon	1.65	1.65	1.88	1.91	1.65	1.89	1.91
	Combined	1.11	1.11	1.34	1.37	1.11	1.55	1.58
	Electron	1.48	1.48	1.62	1.63	1.48	1.62	1.64
1750	Muon	1.36	1.37	1.51	1.52	1.37	1.51	1.52
	Combined	0.885	0.885	1.00	1.01	0.885	1.08	1.09
	Electron	1.34	1.34	1.39	1.40	1.35	1.39	1.40
2000	Muon	0.925	0.929	0.929	0.933	0.929	0.931	0.935
	Combined	0.718	0.720	0.732	0.739	0.720	0.771	0.777
	Electron	0.830	0.832	0.855	0.858	0.832	0.856	0.859
2250	Muon	0.726	0.729	0.729	0.732	0.729	0.730	0.733
	Combined	0.457	0.458	0.467	0.471	0.458	0.484	0.488
	Electron	0.438	0.439	0.439	0.441	0.439	0.440	0.441
2500	Muon	0.828	0.833	0.833	0.834	0.833	0.833	0.836
	Combined	0.287	0.287	0.287	0.288	0.287	0.288	0.289
	Electron	0.459	0.461	0.461	0.461	0.461	0.461	0.462
2750	Muon	0.917	0.924	0.924	0.925	0.924	0.925	0.926
	Combined	0.306	0.307	0.307	0.307	0.307	0.307	0.308
	Electron	0.387	0.388	0.388	0.389	0.388	0.389	0.389
3000	Muon	0.798	0.802	0.802	0.803	0.802	0.803	0.805
	Combined	0.261	0.261	0.261	0.262	0.261	0.262	0.263
	Electron	0.338	0.339	0.339	0.340	0.339	0.340	0.340
3250	Muon	0.678	0.681	0.681	0.683	0.682	0.683	0.685
	Combined	0.226	0.226	0.226	0.227	0.226	0.227	0.228
	Electron	0.312	0.314	0.314	0.314	0.314	0.315	0.315
3500	Muon	0.644	0.649	0.649	0.650	0.649	0.651	0.653
	Combined	0.210	0.211	0.211	0.211	0.211	0.213	0.213
	Electron	0.297	0.304	0.304	0.305	0.304	0.307	0.307
3750	Muon	0.605	0.619	0.619	0.621	0.619	0.627	0.628
	Combined	0.199	0.202	0.202	0.202	0.204	0.208	0.208
	Electron	0.304	0.363	0.363	0.364	0.363	0.371	0.372
4000	Muon	0.612	0.723	0.723	0.725	0.723	0.746	0.747
	Combined	0.203	0.220	0.220	0.221	0.242	0.255	0.255

Table 8.14: Cross section limits for the W^* with different subsets of the nuisance parameter uncertainties included in the limit calculation.

and the green and yellow bands are calculated, an additional numerical precision parameter enters, namely the number of background-only pseudo-experiments. The trick of considering the distribution of the "observed" event counts in the background-only pseudo-experiments and exploiting the one-to-one correspondence with the limits is not applicable to the two channel combination, so for the combination, the numerical precision of the median, $\pm 1\sigma$, and $\pm 2\sigma$ is at the level of a few percent in the high statistics (low mass) regime.

8.7.2 Quantitative effect of various approximations

We have claimed in various sections that some approximations or effects are negligible. With the non-observation of new physics confirmed, the cross section limits presented here can be thought of as the final result of the analysis, and we can make the statements quantitative by considering the effect on the cross section limits.

In section 6.5.3, we claimed that the percent level jet contribution to the total background in the muon channel was negligible. The argument was based on comparing this contribution to the uncertainty on the total background from the W boson k-factor. We can now make a quantitative statement about the effect of the jet background on the cross section limits. The jet background is found to affect the muon channel cross section limits obtained for the SSM W' by at most 5% at low W' mass and by less than 1% for W' masses starting from $1250\,\mathrm{GeV}$ (corresponding to m_{T} thresholds starting from $1002\,\mathrm{GeV}$). It is worth noting that the 5% effect at low W' mass comes primarily from the central value of the jet background estimate, with the accompanying uncertainty affecting the limit by at most 1%.

In section 8.3.2, it was mentioned that some correlations were not handled correctly in the statistical analysis. In particular, the top cross section was taken as a contribution to the correlated background uncertainty, which means that it is treated as correlated also with the signal efficiency. We find, however, that the addition of signal-background correlation on top of background-only correlation impacts the limits for the lowest masses by less than 2%, and the low mass region is the only region where the top cross section uncertainty even comes close to making a significant contribution to the total background uncertainty. We argued also in section 8.3.2 that correlation between signal and background due to detector related experimental uncertainties could be neglected because the up to 5-6% contributions from these sources to the signal efficiency uncertainty affected results negligibly. Considering tables 8.13 and 8.14, we see that the signal efficiency uncertainty has a negligible impact on limits in the low mass region where the detector related experimental uncertainties dominate.

Finally, we mentioned in section 8.5 some large statistical fluctuations in the muon channel resolution, scale, jet, and $\not\!\!E_{\mathrm{T}}$ uncertainties on the background levels at high mass. We find that excluding completely the resolution, scale, jet, and $\not\!\!E_{\mathrm{T}}$ uncertainties on the background level from the limit setting gives cross section limits differing from the baseline ones by about 3% for the limits evaluated with the threshold $m_{\mathrm{T}}^{\mathrm{min}} = 1191\,\mathrm{GeV}$ and by less than half a percent for the higher thresholds. We conclude that the calculated cross section limits are not significantly affected by the observed statistical fluctuations.

8.8 Alternative definitions of the signal cross section

It is common in searches for exotic new physics to take the parameter of interest in the limit setting procedure to be the signal cross section. In the context of new particle searches, this is usually defined as the total cross section for the new particle production and decay to the relevant final state. The signal cross section has the advantage, when used as parameter of interest in the limit setting, that it is closer to the raw observable (the number of reconstructed events passing the full event selection) than e.g. a coupling or some other fundamental theory parameter. Therefore, less theoretical "extrapolation" is needed to relate the raw event count to the parameter of interest, and the uncertainty related to this "extrapolation" is thus reduced.

To the extent that the cross section limits are *model independent*, they can be used to obtain a mass limit for a model that differs from the one used in the limit setting. For example, if one had a particular theory predicting a new gauge boson with a particular set of couplings to fermions, one could calculate the theoretical cross section as function of mass and obtain a mass limit as the intersection between this cross section and the cross section limits. One would then use the SSM W' cross section limits, and simply replace the theoretical cross section curve in e.g. fig. 8.8(e) with the newly calculated cross sections. The underlying assumption would be that the different couplings of the particular model considered would not lead to different kinematical distributions than those of the SSM reference model, but only change the cross section. Even if the Dirac matrix structure of the couplings considered would be the same as in the SSM, this assumption would be violated to some extent because of the fact that the width of the new gauge boson depends on the couplings to its decay products (see section 1.5.3).

The quantitative effect of such model dependence has been studied in the context of the ATLAS Z' search [39], and it is clear that the cross section limit for any of the models considered there can be used at least as an order of magnitude estimate also for the other models. In particular, the difference between the cross section limits for the various Z' models is at most approximately a factor of 2 for the highest mass considered, $m_{Z'} = 3.5\,\mathrm{TeV}$, where differences in off-shell production rates are important, and much smaller at lower mass ($m_{Z'} \lesssim 2\,\mathrm{TeV}$)[12]. The three Z' models considered are the SSM Z', which has the same couplings to fermions as the Z boson, and two E_6 motivated examples. Also the neutral equivalent of the W^*, the Z^*, is considered. The cross section limits for this model are close to the corresponding ones for the SSM Z' at low mass ($m_{Z'/Z^*} \lesssim 2\,\mathrm{TeV}$), but the difference grows at high mass because of the suppression of the low mass off-shell production in the Z^* case, and is approximately a factor of 3 at $m_{Z'/Z^*} = 3.5\,\mathrm{TeV}$.

When using the signal cross section as parameter of interest, the uncertainty on the theoretical cross section is naturally absent from the actual limit calculation, and it is customary to display this uncertainty as a band around the theoretical cross section prediction in the usual limit plots, such as those displayed in fig. 8.8. Theoretical uncertainty may also affect the signal efficiency, in which case the uncertainty has a natural place in the limit calculation. In our case, the theoretical uncertainty from the mass dependent k-factor affects in practice only the theoretical cross section for low W' masses, but becomes the dominant source of uncertainty on the signal efficiency for the highest W' masses, where its effect on the theoretical cross section is actually reduced compared to intermediate masses (see table 3.2). We will see that this can be

[12] See fig. 5 of ref. [39].

changed with alternative definitions of the signal cross section, which lead to different divisions of the k-factor uncertainty between signal efficiency and signal cross section.

All results in this section are shown for the muon channel only unless stated otherwise.

8.8.1 The fiducial cross section

We follow the nomenclature used within the ATLAS W' search team, and refer to the parameter of interest in the limit setting as the *fiducial* signal cross section, or just the fiducial cross section. The term "fiducial" is often used about phase space regions that are truncated in a manner that mimics detector acceptance, but it is used more loosely in this context. The fiducial cross section is defined by a generator level (truth level) cut (or set of cuts). When calculating the signal efficiency according to eq. (8.2), the fiducial cut must be imposed as part of the "initial selection" in the denominator, so that the signal efficiency correctly relates the expected number of signal events per unit of integrated luminosity to the fiducial cross section. A sensible definition of the fiducial cross section leads to a better match between the event samples in the denominator and numerator, so that the k-factor uncertainty variations to a larger extent cancel and the resulting uncertainty on the signal efficiency is smaller.

Two definitions of the signal efficiency are investigated, distinguished by whether or not the fiducial cut is employed also in the numerator of eq. (8.2). If it is, then the signal efficiency is a true efficiency, i.e. it is necessarily between 0 and 1 and is the probability for an event in the fiducial region[13] to fire the necessary trigger(s) and pass the full event selection (including the m_{T} threshold) after reconstruction. This definition means that signal events outside the fiducial region are not allowed to contribute to the signal strength, and limits are more conservative than necessary by an amount determined by the extent to which the fiducial region does not fully encompass the set of events that have non-vanishing probabilities to be reconstructed and pass the full event selection. If the fiducial cut is not included in the numerator of eq. (8.2), then all signal is accounted for, and the signal efficiency is not a true efficiency. The two definitions are equivalent when the fiducial region fully encompasses the set of events that have non-vanishing probabilities to be reconstructed and pass the full event selection.

It is in this context interesting to note that the exclusion of less relevant decay modes from the signal samples can be thought of as a fiducial cut. When new charged, heavy bosons are searched for in the electron and muon channels, one gets in principle a contribution to the signal yield also from the tau decays of the boson, because the tau lepton can decay to an electron or a muon (and neutrinos). This signal contribution[14] is often neglected, which might be considered natural, as the parameter of interest is usually taken to be the cross section for the electron (muon) decay mode in the electron channel (muon channel) search. While one could of course use the alternative definition of the signal efficiency, with the contribution from tau decays present in the numerator but not the denominator of eq. (8.2), it has been chosen in ATLAS searches to exclude the tau decays also in the numerator. This approach has the philosophical advantage that no assumption needs to be made that electron, muon, and tau channel cross sections are equal. The resulting electron and muon channel limits are valid independently of

[13]The term "fiducial region" is used to denote the phase space region defined by the fiducial cut.

[14]The magnitude of this contribution has been quantified in previous ATLAS publications, and is at the level of 3-4% for the highest SSM W' masses [107].

the coupling of the new boson to the tau lepton up to effects of the contribution from tau decays to the boson's width. A practical advantage of this approach is that tau decays can be excluded already at the stage of signal MC generation, but this has not been the motivation in ATLAS, as signal samples have usually been generated for all three lepton decay modes inclusively.

8.8.2 Invariant mass fiducial cut

The primary motivation for the study of fiducial cross section limits in the ATLAS W' analysis of the 2012 data was the appearance of large signal efficiency uncertainty due to the invariant mass dependent k-factor uncertainty. The mass dependent k-factors were applied to the signal for the first time in the analysis of the 2012 data, leading to uncertainties much larger than the few percent which were found in previous analyses.

As discussed in section 8.3.1, the uncertainty arises from incomplete cancellation of k-factor variations in the numerator and denominator of the signal efficiency because the numerator contains only events with high reconstructed m_{T}, corresponding primarily to the high end tail of the invariant mass distribution, while the denominator contains the whole invariant mass spectrum and is in fact dominated by invariant masses much below the new boson mass for the highest masses considered. The uncertainty arises, in other words, from the large contribution of events with $m_{l\nu} \ll m_{W'}$ to the denominator, and a fiducial cut on the form $m_{l\nu} > \kappa m_{W'}$ with κ as a common constant for all W' masses comes to mind as a simple definition which may effectively reduce the signal efficiency uncertainty. The uncertainty is reduced because the fiducial cut is present in the denominator of the signal efficiency, so that the phase space overlapping with the numerator becomes more dominant. The parameter of interest in the limit setting is thus defined as

$$\sigma = \int_{m_{l\nu}^{\mathrm{min}}}^{\infty} \frac{d\sigma(pp \to W' + X \to l\,\nu + X)}{dm_{l\nu}}\, dm_{l\nu} \tag{8.6}$$

with $m_{l\nu}^{\mathrm{min}} = \kappa m_{W'}$. As usual, l denotes a single lepton generation.

Fig. 8.9 shows the signal efficiencies and associated k-factor uncertainties obtained for the SSM W' with different values of κ ranging from 0 (corresponding to the total cross section used in section 8.7) to 0.4. The signal efficiencies are calculated without the fiducial cut present in the numerator, but results would be almost identical with the alternative definition as the fiducial region almost fully encloses the final selection event sample for all these values of κ. This enclosure is clearly due to the fact that the fiducial cut for the highest W' mass, $m_{l\nu}^{\mathrm{min}}(m_{W'} = 4\,\mathrm{TeV}) = 1.6\,\mathrm{TeV}$, is significantly below the corresponding m_{T} threshold $m_{\mathrm{T}}^{\mathrm{min}}(m_{W'} = 4\,\mathrm{TeV}) \approx 1.9\,\mathrm{TeV}$, so that events from outside the fiducial region can only enter the final selection event sample if the reconstructed m_{T} is off by at least about $300\,\mathrm{GeV}$ compared to the generator level value.

Considering first the signal efficiencies themselves, as shown in fig. 8.9(a), we see that they are not at all affected by the fiducial cut for the lowest W' masses. This is because the cross section for these masses is mostly contained in the peak region, and the invariant mass cut has only a marginal impact. Going to higher masses, the fiducial cut is seen to increase the signal efficiency. This is not to be considered as an improvement in itself, because the signal efficiencies evaluated with different fiducial cuts differ in their interpretation, and a direct

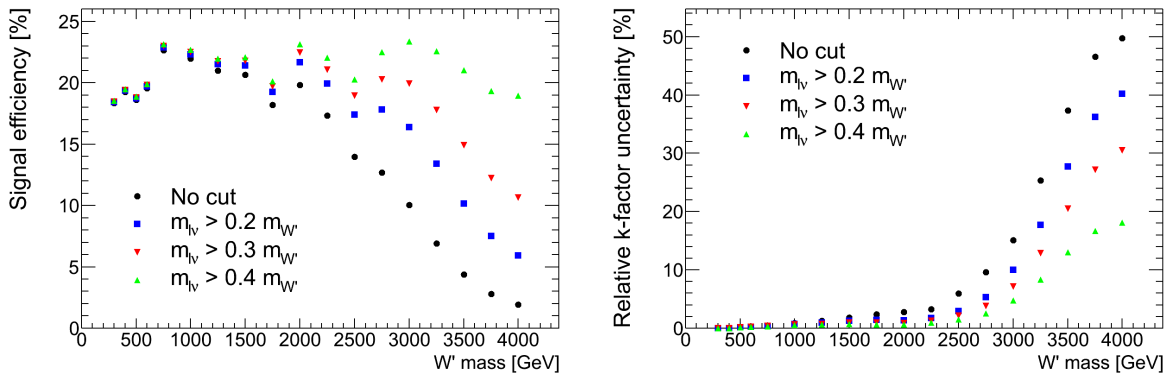

(a) (b)

Figure 8.9: The signal efficiencies (a) and associated k-factor uncertainties (b) obtained for the SSM W' with a fiducial cut $m_{l\nu} > \kappa m_{W'}$ with different values of κ ranging from 0 to 0.4.

quantitative comparison is not necessarily meaningful. However, the more constant signal efficiency achieved with the highest invariant mass cut in fig. 8.9(a) may be considered appealing. In particular one gets rid of the drastic decrease in signal efficiency as off-shell production becomes dominant for the highest W' masses. This decrease is a bit of a technicality and may be misinterpreted as a real loss of sensitivity due to problems with muon momentum resolution and trigger/reconstruction efficiencies at high p_{T}. The efficiencies evaluated with the highest invariant mass cut show that the sensitivity to the relevant part of the invariant mass spectrum is retained even for the highest W' masses. Events at low invariant mass are essentially irrelevant because of their much less favorable signal-to-background ratio.

Fig. 8.9(b) shows the relative uncertainty on the signal efficiency due to the k-factor uncertainty. The uncertainty is clearly reduced by the application of the invariant mass fiducial cut, and is below 20% for the cut $m_{l\nu} > 0.4\, m_{W'}$. The reduced uncertainty indicates a better match between the cross section definition used in the limit setting and the cross section to which the analysis is sensitive. It allows for stronger limits and a reduced dependence of the limits on the treatment of the signal efficiency uncertainty in the limit setting.

We proceed to consider the relative uncertainty on the signal efficiency due to the k-factor uncertainty for the higher invariant mass cuts. In this case, results are shown separately for the two definitions of the signal efficiency with and without the fiducial cut present in the numerator in fig. 8.10. When the fiducial cut is not present in the numerator, the uncertainty starts to increase when κ is increased beyond 0.5. The reason is that the mismatch between numerator and denominator is then reintroduced, although in this case with the denominator restricted to higher invariant mass than what is representative of the numerator. With the fiducial cut present in the numerator, the numerator is always restricted to as high invariant mass as the denominator, and the uncertainty is not reintroduced as the cut value becomes high. We show for completeness also the corresponding signal efficiencies in fig. 8.11.

The extent to which the fiducial region does not fully encompass the final selection event sample is quantified in the form of the relative contribution of non-fiducial events in this sample, i.e. the fraction of events in the final selection event sample which have $m_{l\nu} < \kappa m_{W'}$. This fraction is shown in fig. 8.12(a), and is seen to be at most 3.1% for $\kappa = 0.4$ and at most 17% for

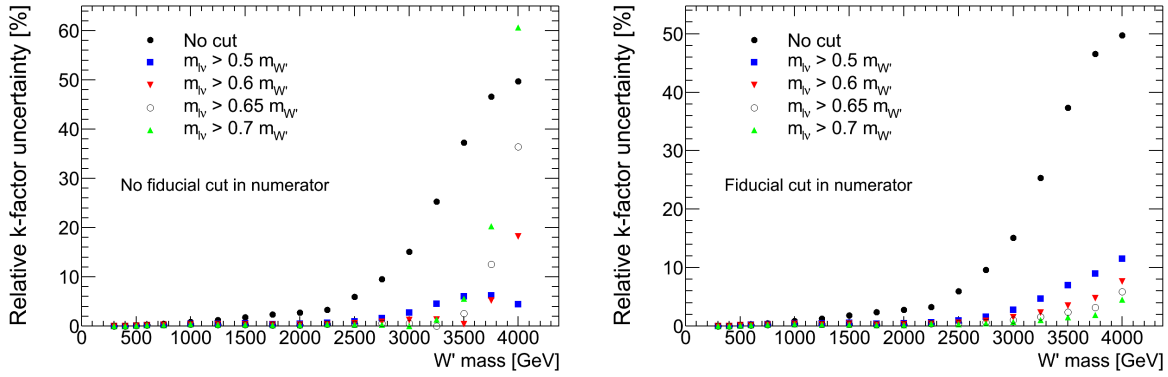

(a) (b)

Figure 8.10: The relative uncertainty on the signal efficiency due to the k-factor uncertainty obtained for the SSM W' with a fiducial cut $m_{l\nu} > \kappa m_{W'}$ with different values of κ. Results are shown without (a) and with (b) the fiducial cut present in the numerator of the signal efficiency.

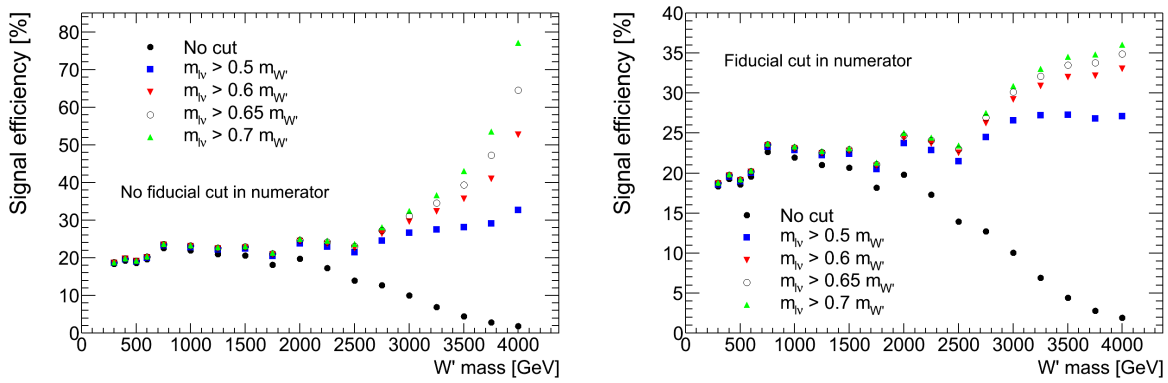

(a) (b)

Figure 8.11: The signal efficiencies obtained for the SSM W' with a fiducial cut $m_{l\nu} > \kappa m_{W'}$ with different values of κ. Results are shown without (a) and with (b) the fiducial cut present in the numerator of the signal efficiency.

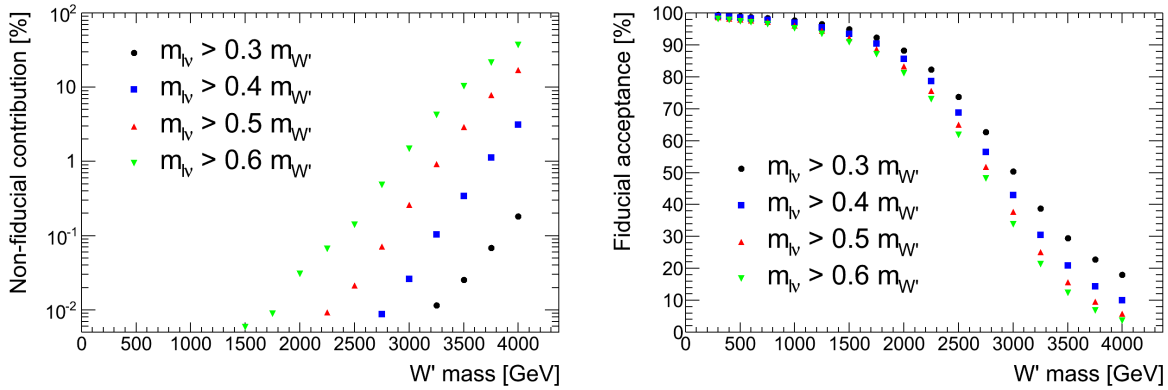

(a) (b)

Figure 8.12: The relative non-fiducial contribution to the final selection event sample (a) and the fiducial acceptance (b), both for the SSM W'.

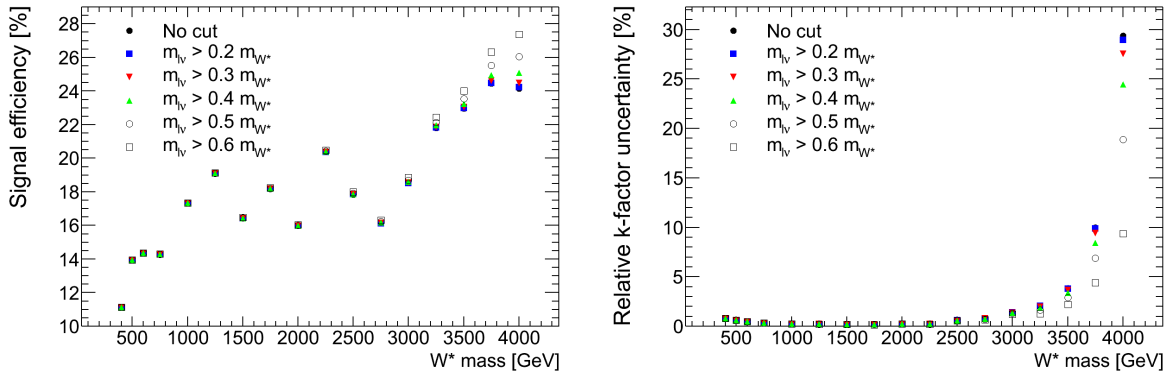

(a) (b)

Figure 8.13: The signal efficiencies (a) and associated k-factor uncertainties (b) obtained for the W^* with a fiducial cut $m_{l\nu} > \kappa m_{W^*}$ with different values of κ ranging from 0 to 0.6.

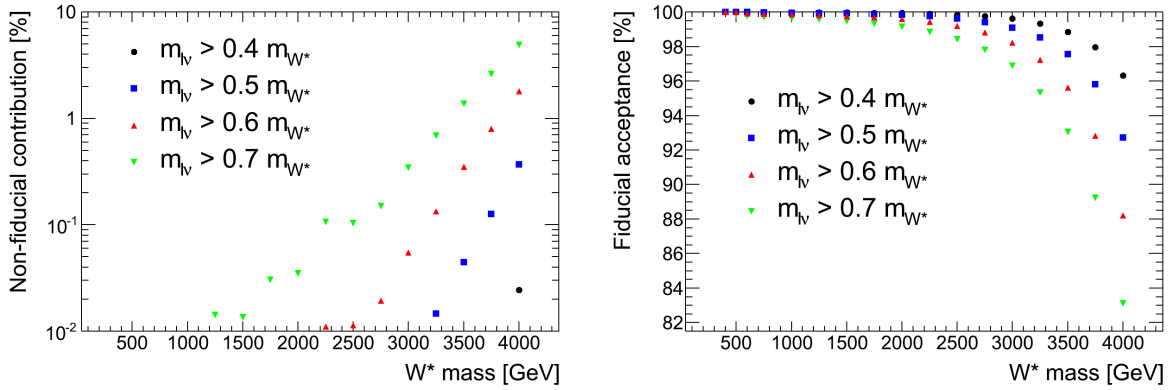

(a) (b)

Figure 8.14: The relative non-fiducial contribution to the final selection event sample (a) and the fiducial acceptance (b), both for the W^*.

$\kappa = 0.5$.

It is also interesting to know the fraction of the total cross section which is contained in the fiducial region, which we will refer to as the fiducial acceptance. The fiducial acceptance is shown in fig. 8.12(b). It is close to 100% for low W' masses and decreases drastically for the highest W' masses. For the value $\kappa = 0.4$ and the highest W' mass, the fiducial acceptance is 10%. The fiducial acceptance is evaluated from the k-factor corrected generator level invariant mass distribution, and it is needed to calculate the theoretical cross section to which one can compare the fiducial cross section limit, which is the product of the total cross section and the fiducial acceptance.

We consider finally the equivalents of figs. 8.9 and 8.12 for the W^* signal model. Fig. 8.13 shows the signal efficiencies and associated k-factor uncertainties for the W^* with a fiducial cut $m_{l\nu} > \kappa m_{W^*}$. The signal efficiency is here calculated without the fiducial cut present in the numerator, but results would be almost identical with the alternative definition as the fiducial region almost fully encloses the final selection event sample for all these values of κ. The only notable exception is the uncertainty for the highest mass and $\kappa = 0.6$, which is 14% when the

fiducial cut is present in the numerator. We see that the efficiencies are much less significantly affected by the fiducial cut than in the SSM W' case, as expected from the strong suppression of low mass off-shell production in the W^* model. As for the SSM W', we see that the signal efficiency uncertainty may be reduced for the W^* with an invariant mass fiducial cut. Finally, the small non-fiducial contributions and high fiducial acceptances seen in fig. 8.14 both reflect the suppression of low mass off-shell production in the W^* model.

Limit strength

We proceed to calculate limits with different invariant mass fiducial cuts. Both signal efficiency definitions are considered. As mentioned earlier, the efficiency is a true efficiency (probability) when the fiducial cut is imposed also in the numerator, and truncation of the efficiency distribution at unity is thus appropriate. For the definition without the fiducial cut in the numerator, the appropriate truncation is the inverse of the fiducial acceptance, corresponding to the case that all generated signal MC events pass the full selection including the m_{T} threshold. It is worth noting that for all calculated limits, the upper truncation of the signal efficiency is not found to have any significant effect, and limits are equal to those calculated without any upper truncation within the precision of the limit calculation.

The cross section limits calculated with different fiducial cuts are not directly comparable. We consider therefore the ratio of the cross section limit to the theoretical signal cross section as a measure of limit strength which is comparable between different fiducial cut definitions. Smaller values of the ratio correspond to stronger limits, and the mass limit is the mass at which the ratio is equal to unity. The ratio is shown as function of the W' mass for the SSM W' in fig. 8.15 both for the observed and expected limits obtained without the fiducial cut imposed in the numerator of the signal efficiency. It is clear that the limit strength is independent of the fiducial cut for low W' masses, where the k-factor uncertainty is negligible. For the highest masses, some difference is observed in the limit strength between different fiducial cut definitions, and we make the results in this region easier to read with the alternative presentation shown in fig. 8.16. Here, all ratios are normalized to the ratio obtained without any fiducial cut ($\kappa = 0$), and the values for $\kappa = 0$ are thus equal to unity by construction. The other fiducial cuts are seen in general to provide stronger limits for the highest W' masses, except for the highest values of κ.

The results for the highest W' masses are finally presented in a different way in fig. 8.17, where the ratio of the cross section limit to the theoretical signal cross section is shown as function of the relative invariant mass cut $\kappa = m_{l\nu}^{\mathrm{min}}/m_{W'}$ for each of the four highest W' masses. Results are shown for both definitions of the signal efficiency. With the fiducial cut not imposed in the numerator, the evolution of the limit ratio as function of the invariant mass cut simply reflects the corresponding evolution of the (relative) signal efficiency uncertainty, which is dominated by the k-factor uncertainty. When the fiducial cut *is* imposed in the numerator, the evolution of the limit ratio is composed of two effects. The reduction of the signal efficiency uncertainty as the invariant mass cut is increased leads to improved limit strength, but limits start to deteriorate as the fiducial cut $m_{l\nu}^{\mathrm{min}}$ approaches the m_{T} threshold $m_{\mathrm{T}}^{\mathrm{min}}$ because the non-fiducial contribution to the final selection event sample becomes non-negligible.

It is worth noting that the effect of the fiducial cut on the ratio of the cross section limit to

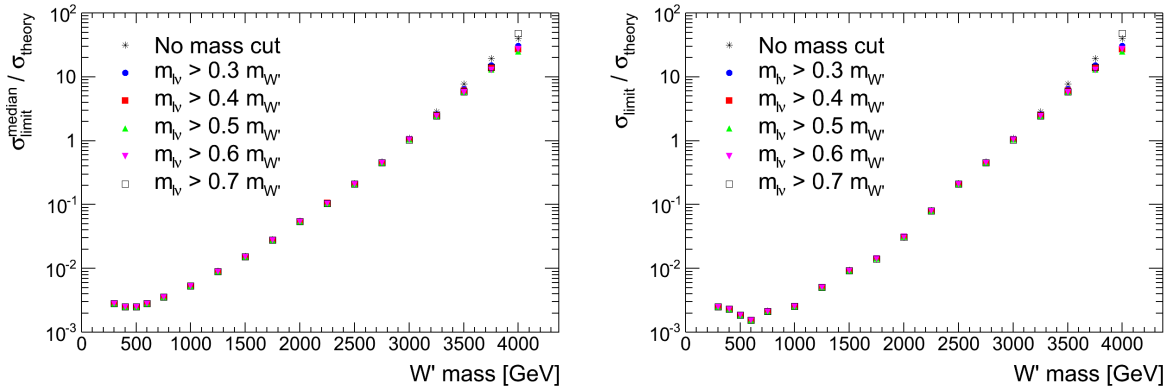

(a) (b)

Figure 8.15: The ratio of the cross section limit to the theoretical signal cross section for expected (a) and observed (b) limits for the SSM W'. The ratio is plotted for different invariant mass fiducial cuts.

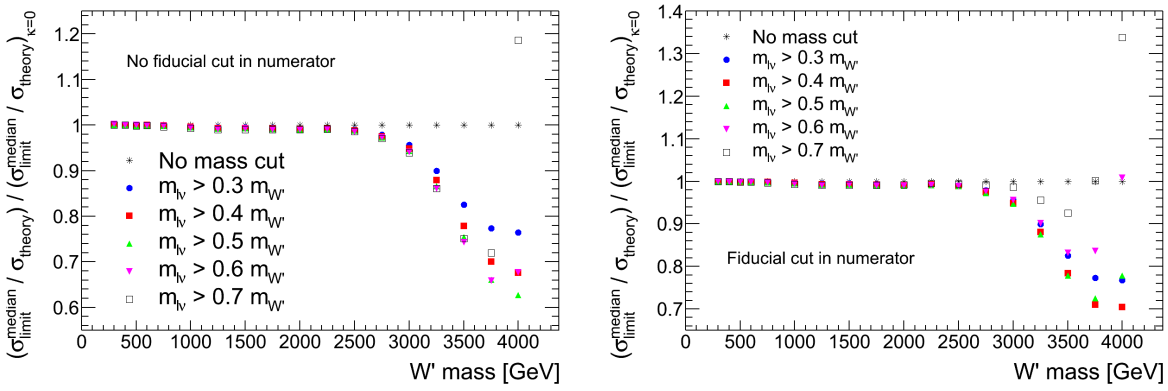

(a) (b)

Figure 8.16: The ratio of the cross section limit to the theoretical signal cross section normalized to the ratio obtained without any fiducial cut for the SSM W'. Results are shown without (a) and with (b) the fiducial cut present in the numerator of the signal efficiency for different invariant mass fiducial cuts. The results are here shown for the expected limits, but the plots would look almost indistinguishable if observed limits were considered. In particular, results would be identical starting from $m_{W'} = 2.5\,\mathrm{TeV}$.

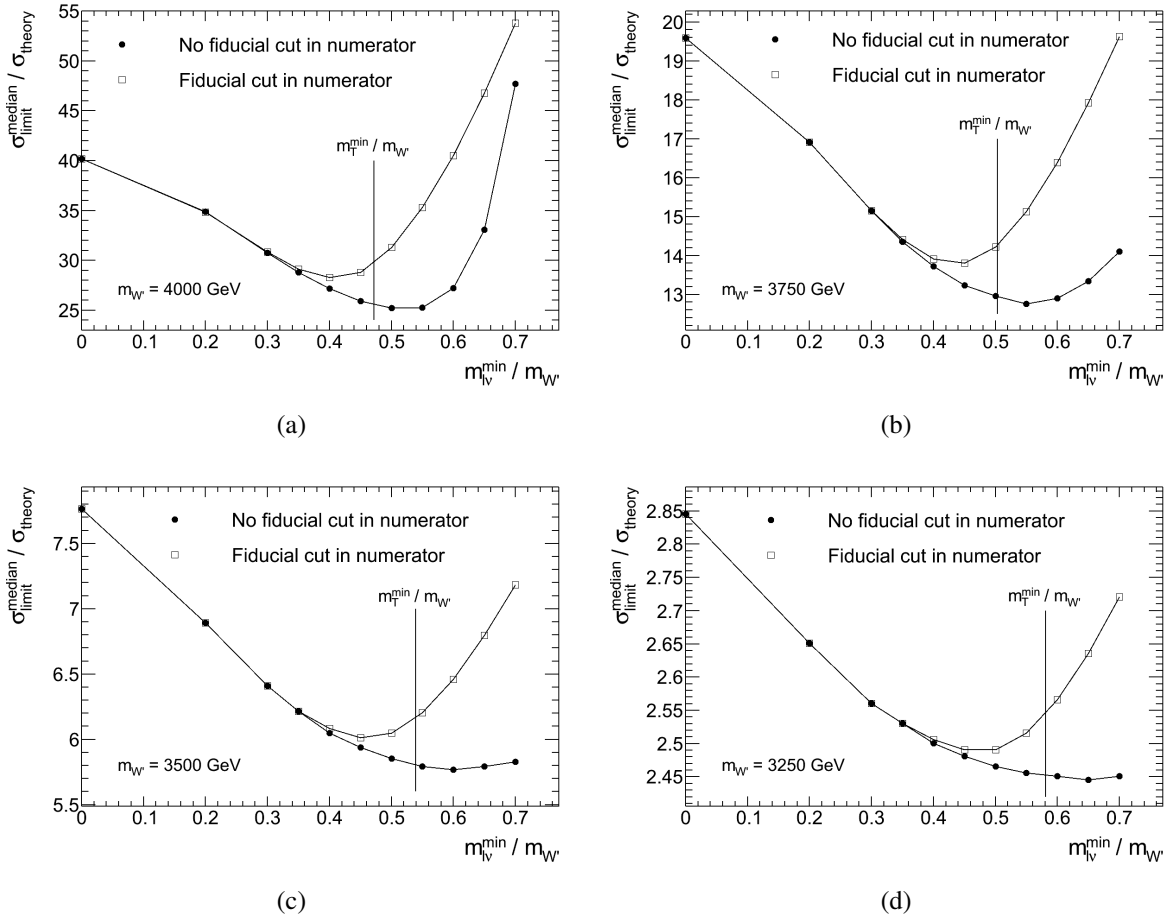

Figure 8.17: The ratio of the cross section limit to the theoretical signal cross section as function of the relative invariant mass cut $\kappa = m_{l\nu}^{\min}/m_{W'}$ for W' masses of $4\,\mathrm{TeV}$ (a), $3.75\,\mathrm{TeV}$ (b), $3.5\,\mathrm{TeV}$ (c), and $3.25\,\mathrm{TeV}$ (d). The vertical line indicates the point along the horizontal axis where $m_{l\nu}^{\min} = m_{\mathrm{T}}^{\min}$.

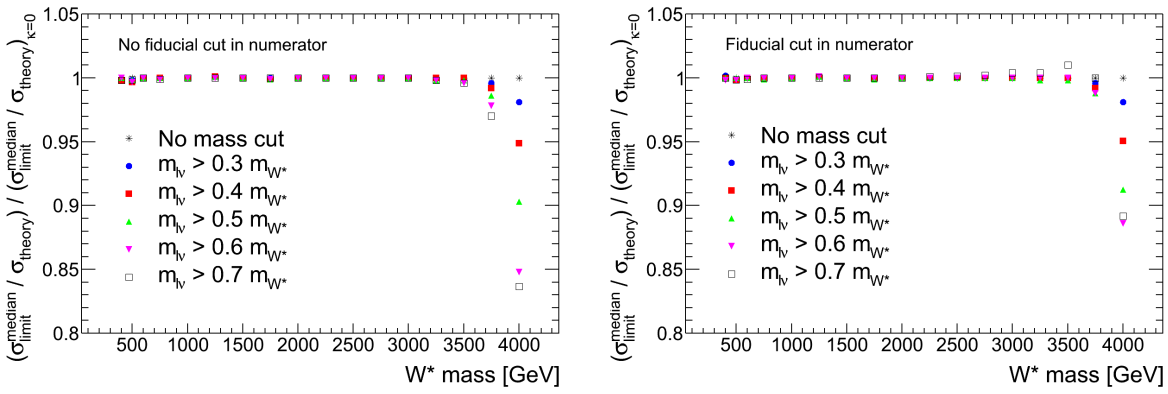

(a) (b)

Figure 8.18: The ratio of the cross section limit to the theoretical signal cross section normalized to the ratio obtained without any fiducial cut for the W^*. Results are shown without (a) and with (b) the fiducial cut present in the numerator of the signal efficiency for different invariant mass fiducial cuts. The results are here shown for the expected limits, but the plots would look almost indistinguishable if observed limits were considered. In particular, results would be identical starting from $m_{W^*} = 2.75\,\mathrm{TeV}$.

the theoretical signal cross section is solely due to the change in the (relative) signal efficiency uncertainty when the fiducial cut is not imposed in the numerator of the signal efficiency. It has been checked that all the points in fig. 8.16(a) are equal to unity within the precision of the limit calculation when the signal efficiency uncertainty is not included in the limit calculations.

We have already seen that the effect of fiducial cuts on the W^* model results is much smaller than in the case of the SSM W'. However, we present finally the equivalent of fig. 8.16 for the W^* model in fig. 8.18. Some improvement in the limit strength is seen for the very highest W^* mass, but the effect is much smaller than in the case of the SSM W'.

Limit plots

We proceed to present some standard limit plots for different fiducial cut definitions. All limits are calculated without the fiducial cut in the numerator of the signal efficiency, but results would be almost identical *with* the cut in the numerator for the lower invariant mass cuts, with differences reaching the few percent level for $\kappa = 0.4$ in the W' case and $\kappa = 0.6$ for the W^*.

Limit plots for the SSM W' are shown for four different invariant mass cuts in fig. 8.19. A few features are worth noting. First of all, the increase of the cross section limit at high W' mass becomes less obvious as the invariant mass cut is increased, and the limit at high mass is almost flat for the highest relative mass cuts $\kappa = 0.4$ and $\kappa = 0.5$. This corresponds to what is seen for the efficiencies in fig. 8.9, and as argued before, the flattening at high W' mass is a nice feature because it demonstrates that the sensitivity to the relevant signal is fully retained even for the highest W' masses.

A second feature which is worth noting is that the uncertainty on the theoretical cross section at high mass becomes larger as the invariant mass cut is increased. In practice, the invariant mass fiducial cut shifts the uncertainty from the signal efficiency to the (fiducial) signal cross section. It is because the uncertainty on the cross section has no place in the limit setting

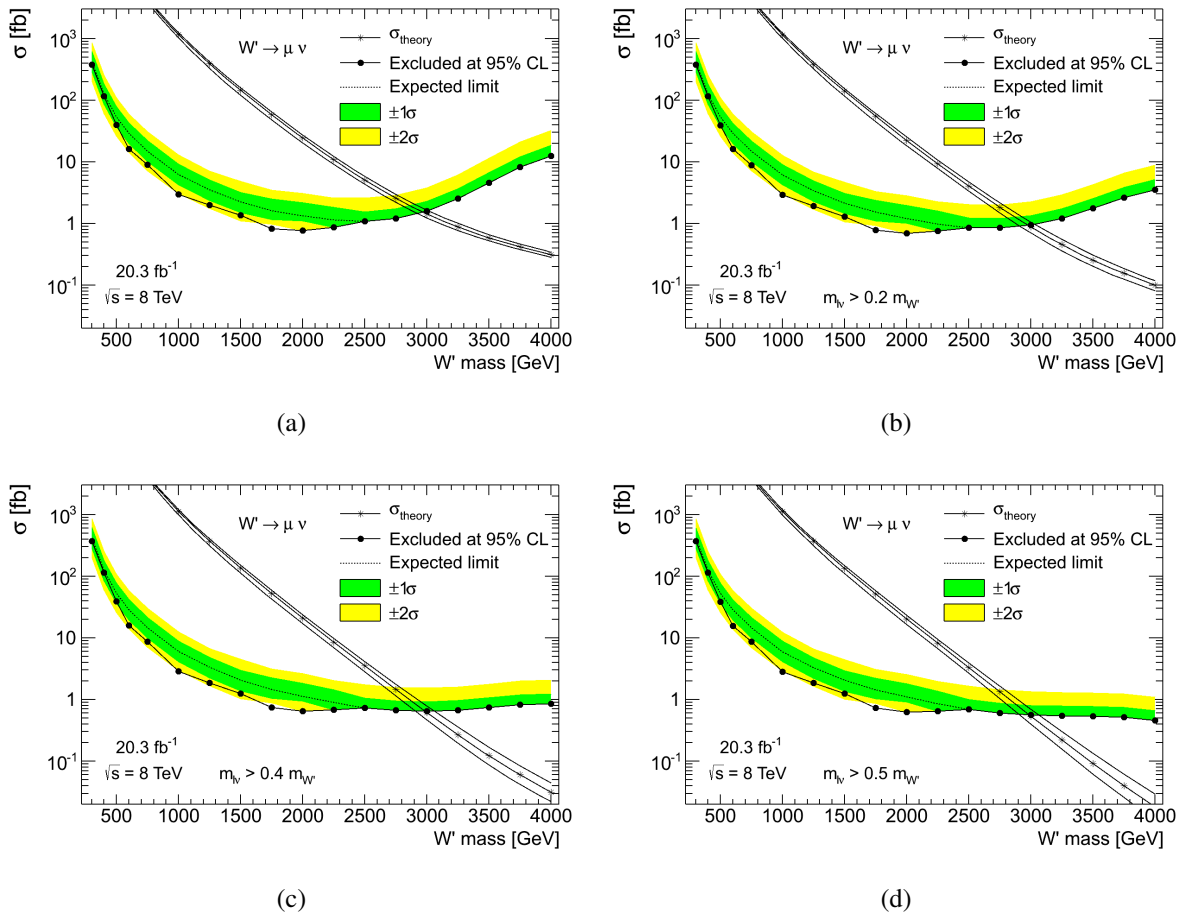

Figure 8.19: Limit plots for the SSM W' for four different invariant mass fiducial cuts. In (a) there is no fiducial cut and the results are the same as shown in fig. 8.8(c), but they are shown again here for convenience. In (b), (c), and (d), the relative cut values are $\kappa = 0.2$, $\kappa = 0.4$, and $\kappa = 0.5$ respectively.

that the limit strength, quantified as the ratio of the cross section limit to the theoretical cross section, improves with the application of the invariant mass fiducial cut. Corresponding to this improvement is an improvement of the mass limit, as defined by the intersection of the limit curve with the central theoretical prediction. The mass limit, read off and rounded in the same way as for table 8.12, is $2.97\,\mathrm{TeV}$ for $\kappa = 0$, $2.98\,\mathrm{TeV}$ for $\kappa = 0.2$, and $2.99\,\mathrm{TeV}$ for $\kappa = 0.4$ and $\kappa = 0.5$.

We do not make the claim that the improvement in the limit strength and the corresponding improvement in the mass limit is a strong argument in favor of the invariant mass cut fiducial cross section limits over the more conventional total cross section limits. Some uncertainty on the signal efficiency is certainly removed, but the uncertainty is in a sense moved to the theoretical cross section. If the parameter of interest were taken to be a fundamental parameter, such as a coupling constant, or if it were taken to be the mathematical construct known as the signal strength parameter[15], the uncertainty on the cross section itself would also enter the limit setting.

[15]The signal strength parameter is a dimensionless number quantifying the extent to which the signal is present. Writing the number of expected events as $\lambda = \mu s + b$ with s as the theoretically predicted signal yield, the signal strength parameter μ can be used as parameter of interest in a statistical analysis, with $\mu = 0$ corresponding to

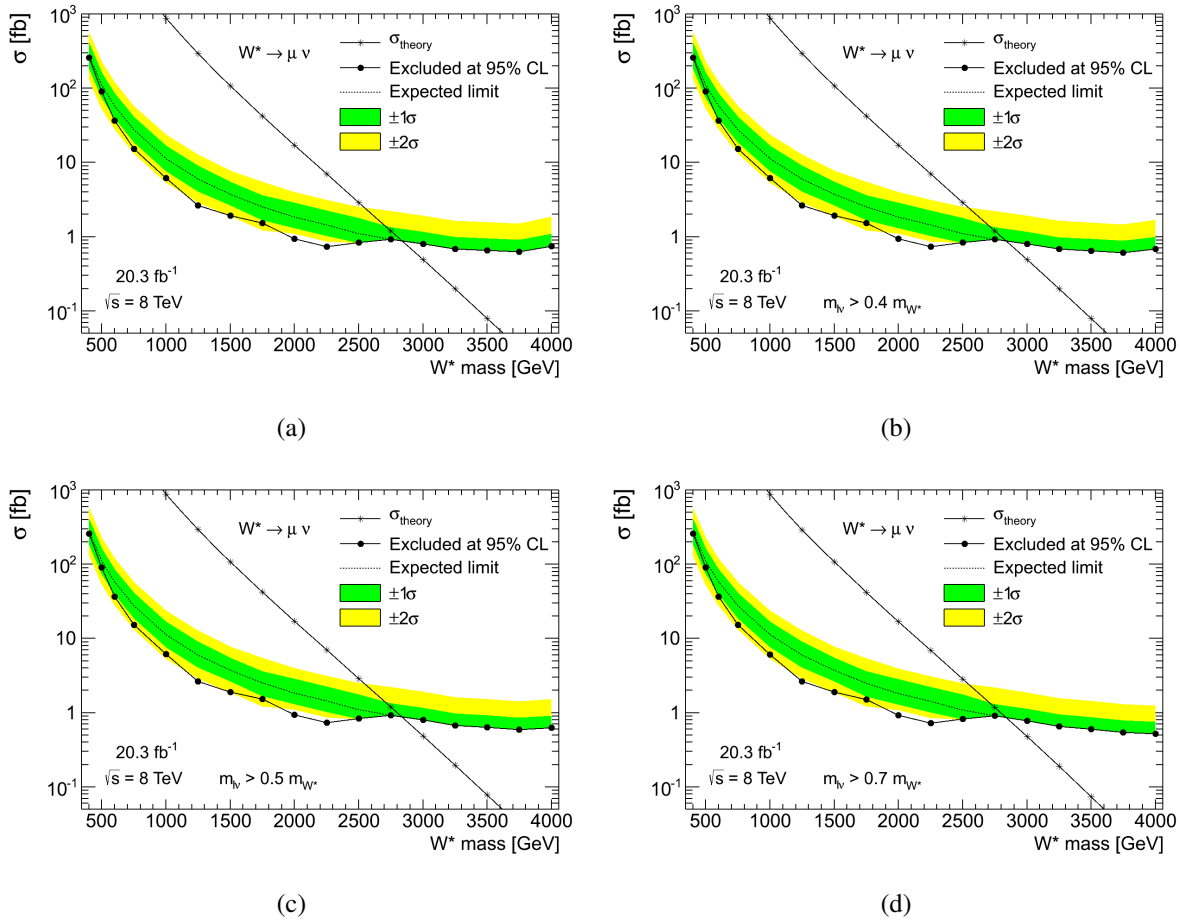

Figure 8.20: Limit plots for the W^* for four different invariant mass fiducial cuts. In (a) there is no fiducial cut and the results are the same as shown in fig. 8.8(d), but they are shown again here for convenience. In (b), (c), and (d), the relative cut values are $\kappa = 0.4$, $\kappa = 0.5$, and $\kappa = 0.7$ respectively.

Excluding the cross section uncertainty from the limit setting is, however, the recommendation of the ATLAS exotics working group. The motivation is presumably to keep the cross section limit a somewhat more "experimental" quantity, closer to what is actually measured and less affected by theoretical uncertainties which may change after the limits are published. Clearly, the fiducial cross section limits have this property to a much larger extent than total cross section limits, and we argue that the theoretical uncertainties, such as PDF uncertainties, are more appropriately associated to the signal cross section than the signal efficiency.

Limit plots for the W^* are shown in fig. 8.20, and it is clear that the application of the invariant mass fiducial cut hardly changes the appearance of the limit plots at all in the W^* case.

Full set of results for $\kappa = 0.4$

For the preliminary ATLAS results with the 2012 data, ref. [108], it was chosen to present results in terms of the fiducial cross section defined with an invariant mass cut at 40% of the

background (b) only and $\mu = 1$ corresponding to signal presence with the predicted yield. See e.g. ref. [115].

	$m_{W'}$ [TeV]		m_{W^*} [TeV]	
Channel	Expected	Observed	Expected	Observed
Electron	3.16	3.16	3.08	3.08
Muon	2.99	2.99	2.84	2.84
Combined	3.21	3.28	3.12	3.21

Table 8.15: Mass limits for the SSM W' (left) and the W^* (right) signal models as read from the fiducial cross section limit plots in fig. 8.21.

new boson mass, i.e. $\kappa = 0.4$. This choice provides an efficient reduction of the signal efficiency uncertainty while keeping the non-fiducial contribution to the final selection event sample at the level of only 3%. Limits were calculated without the fiducial cut in the numerator of the signal efficiency, and the corresponding set of results, including the electron channel and combination, is given here.

None of the limits presented here should be expected to be identical to those given in ref. [108] because of several small updates to the analysis. In particular, the beam energy uncertainty for signal and the application of the W' relative differential cross section uncertainties to the W^* were both added after the publication of ref. [108], and updates were also provided to the mass dependent k-factors and the W^* cross sections. The limits presented here correspond to the state of the analysis as in ref. [109], but with the parameter of interest in the limit setting chosen as in ref. [108].

The limit plots are shown in fig. 8.21, and the corresponding mass limits are given in table 8.15. The mass limits for the SSM W' are slightly higher than those given in table 8.12 because of the reduction of the signal efficiency uncertainty. Incidentally, the combined mass limit is exactly the same as that quoted by CMS [71]. The mass limits for the W^* are equal to those given in table 8.12, which corresponds to the fact that the fiducial cut has a smaller impact on the W^* model, and that the signal efficiency uncertainty is small for the W^* model in the mass limit region even when total cross sections are considered.

In section 8.7, it was mentioned that the effect of the nuisance parameter uncertainties on the SSM W' mass limit was of the order of 20-$50\,\mathrm{GeV}$, and that changing the theoretical cross section by its uncertainty would give a similar effect on the mass limit. In the case of the fiducial limits presented here, the effect of the nuisance parameter uncertainties is marginal, at the level of 5-$10\,\mathrm{GeV}$, while changing the theoretical cross section by its uncertainty would lead to a larger effect of 80-$90\,\mathrm{GeV}$. Tables with fiducial cross sections and other information related to the $\kappa = 0.4$ invariant mass fiducial cross section limits are given in section A.4 of appendix A.

Prior dependence

As is clear from fig. 7.2(a), the reduction of the signal efficiency uncertainty in the high mass region from up to 50-60% for total cross section limits to at most 20-25% for the fiducial cross section limits leads to a significant reduction of the dependence of the limits on the choice of prior for the signal efficiency. The dependence has been studied, and fiducial limits were found to be prior dependent at the level of $\pm 10\%$ taking into account both background and signal efficiency priors, while the prior dependence for the total cross section limits reached a factor of 2 for the highest SSM W' mass in the electron channel. The study was performed without correlation of the signal efficiency uncertainties and correlation of these with the background levels, but the results are expected to be representative also for the current set of limits.

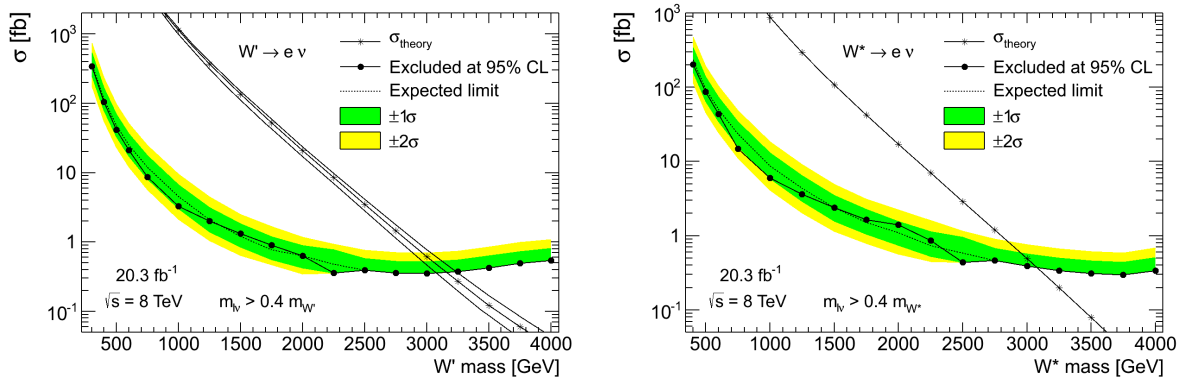

(a)

(b)

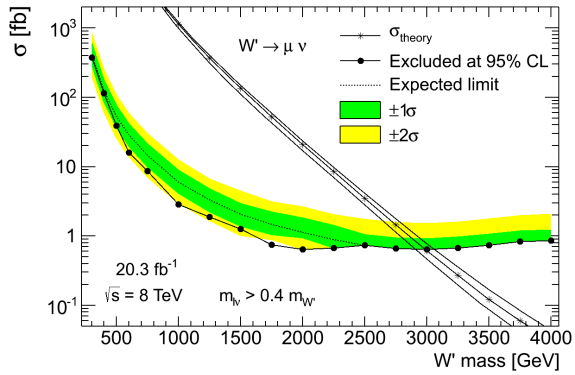

(c)

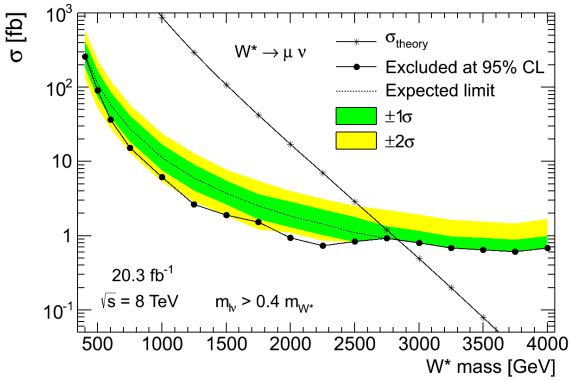

(d)

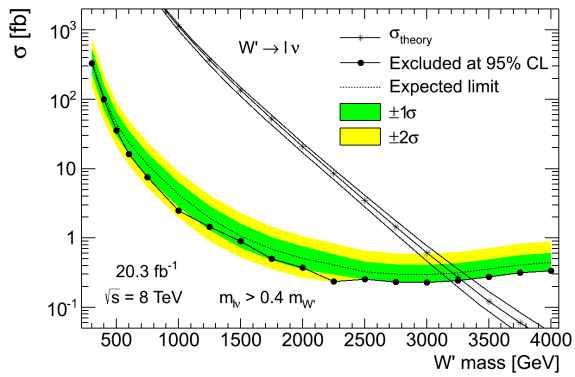

(e)

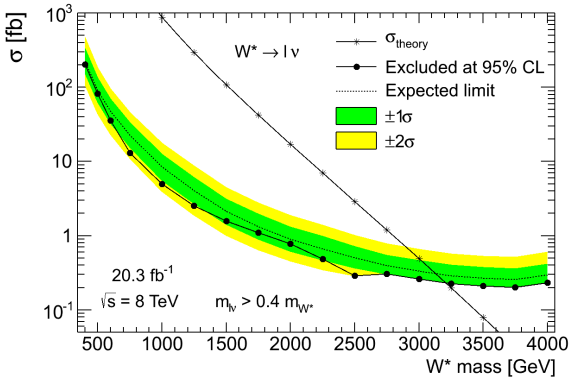

(f)

Figure 8.21: Limits on the fiducial cross sections defined with an invariant mass cut $m_{l\nu} > 0.4\, m_{W'/W^*}$ for the SSM W' ((a), (c), and (e)) and the W^* ((b), (d), and (f)). Limits are shown for the electron channel ((a) and (b)), the muon channel ((c) and (d)), and their combination ((e) and (f)). The parameter σ is here the fiducial cross section for W'/W^* production and decay to a single lepton generation, and the theory cross section σ_{theory} corresponds to tables A.3 and A.4, with the uncertainties in the SSM W' case represented by the band formed by the immediately adjacent curves to the central theory prediction.

The reduced prior dependence was an important motivation for the use of the invariant mass cut fiducial limits in ref. [108]. Concerns about prior dependence were later addressed with a comparison of the baseline cross section limits with log-normal priors to the frequentist limits calculated with the profile likelihood ratio test statistic. While one cannot get away from the arbitrary assignment of a PDF to describe each nuisance parameter uncertainty in the frequentist case, the resulting limits are less dependent on the choice. The baseline Bayesian limits with log-normal priors were found to agree with the frequentist limits within 10%. It was chosen to go back to the more conventional total cross section limits for ref. [109].

8.8.3 Transverse mass fiducial cut and model dependence

The total cross section limits shown in fig. 8.8 display an obvious difference between the SSM W' and W^* limits, with the high mass increase of the cross section limit in the SSM W' case being absent in the W^* case. As noted before, the difference is related to the low mass off-shell production tail, which is much more pronounced for the SSM W' than the W^*. In fig. 8.21, the difference at high mass is much less pronounced, and this is a first indication that fiducial cross section limits may be less model dependent than limits on the total cross section.

We compare directly the observed and expected cross section limits for the SSM W' and W^* models in the cases of total and invariant mass fiducial ($m_{l\nu} > 0.4\, m_{W'/W^*}$) cross section limits in fig. 8.22. It is clear that the choice of the invariant mass fiducial cross section as parameter of interest reduces the model dependence at high mass. We expect that the model dependence observed at high mass in ref. [39] could most likely be effectively reduced by a suitable fiducial cut on the dilepton invariant mass.

As one might expect, the invariant mass fiducial cut does not make much of an impact on the model dependence at lower mass, where the cross section is highly concentrated in the peak region both for the SSM W' and the W^*. Rather significant model dependence is observed also in this region, with the difference between the SSM W' and W^* limits exceeding a factor of 2 for the lowest masses. We expect that the model dependence in this region comes primarily from the differences in the SSM W' and W^* angular distributions rather than differences in the invariant mass distributions. The difference in angular distributions leads to a pronounced difference in the m_{T} distribution, as seen for example in fig. 3.5, and this difference is expected to manifest itself as a difference in signal efficiency when an m_{T} cut is imposed in the analysis selection. This motivates the study of a generator level m_{T} fiducial cut.

k-factor uncertainty

We have seen that the k-factor uncertainty on the signal efficiency can be reduced by imposing a fiducial cut that limits the denominator of the signal efficiency to a similar phase space region as the numerator. Since the most important analysis selection cut is on the reconstructed transverse mass, $m_{\mathrm{T}} > m_{\mathrm{T}}^{\mathrm{min}}$, it seems reasonable to believe that with a fiducial cut on the generator level transverse mass, $m_{\mathrm{T}}^{\mathrm{gen}} > m_{\mathrm{T}}^{\mathrm{min}}$, one may achieve an optimal reduction of the k-factor uncertainty. The generator level transverse mass $m_{\mathrm{T}}^{\mathrm{gen}}$ is calculated from the generator level lepton (i.e. muon) and neutrino labeled as final state particles. These are the particles as they appear after final state radiation, but before any interaction with the detector material and

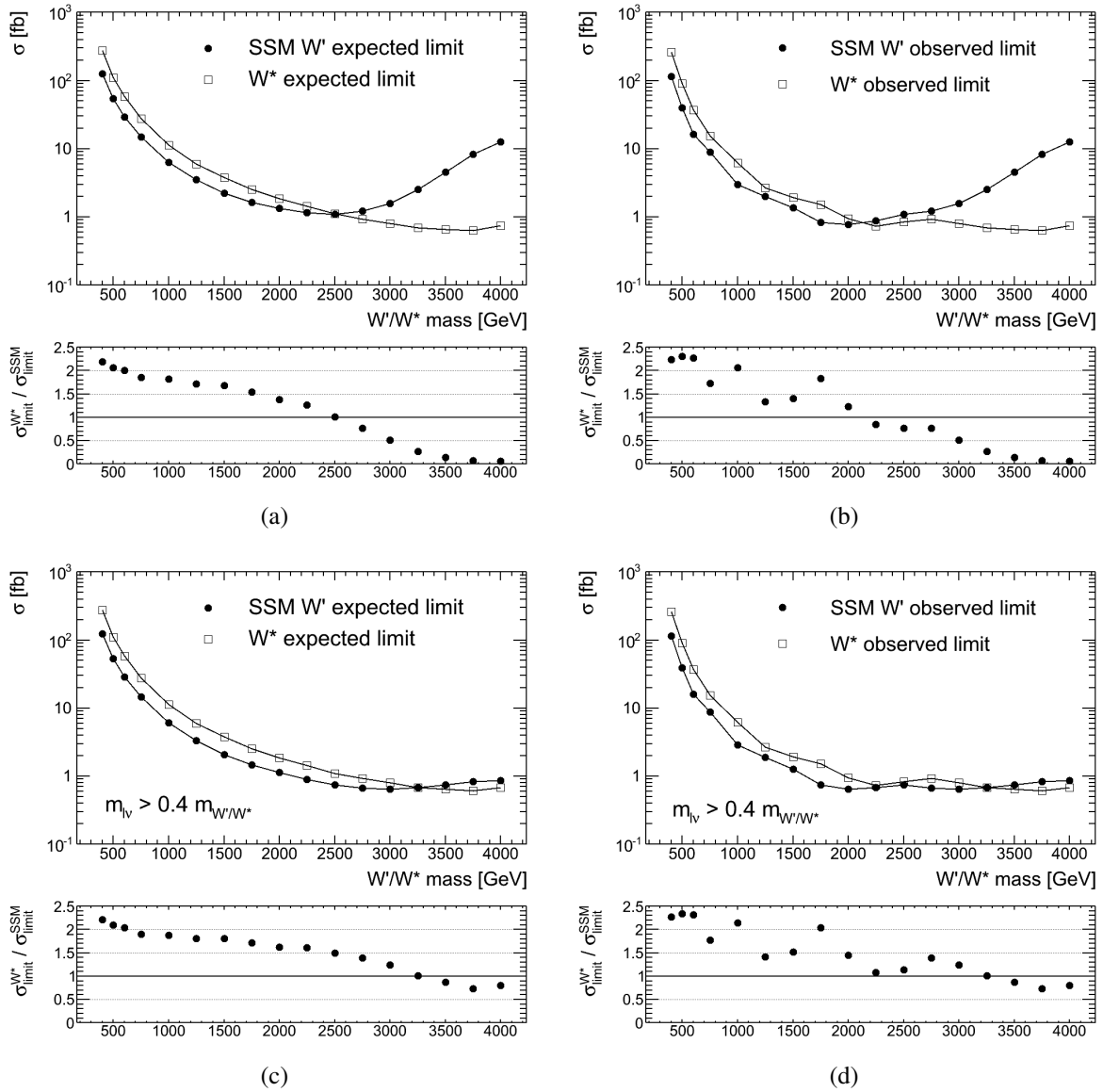

Figure 8.22: Comparison of the expected ((a) and (c)) and observed ((b) and (d)) cross section limits obtained for the SSM W' and W^* models. Results are shown for total cross section limits ((a) and (b)) and fiducial cross section limits defined with the invariant mass cut $m_{l\nu} > 0.4\, m_{W'/W^*}$ ((c) and (d)). The ratio of the W^* limit to the SSM W' limit is shown in the panel below each plot.

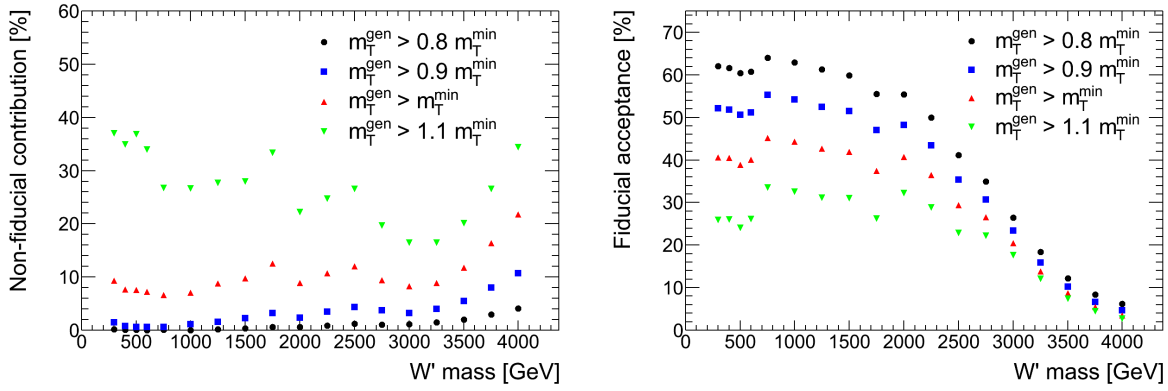

(a) (b)

Figure 8.23: The relative non-fiducial contribution to the final selection event sample (a) and the fiducial acceptance (b) for the SSM W' for fiducial cuts on the form $m_{\mathrm{T}}^{\mathrm{gen}} > \alpha m_{\mathrm{T}}^{\mathrm{min}}$.

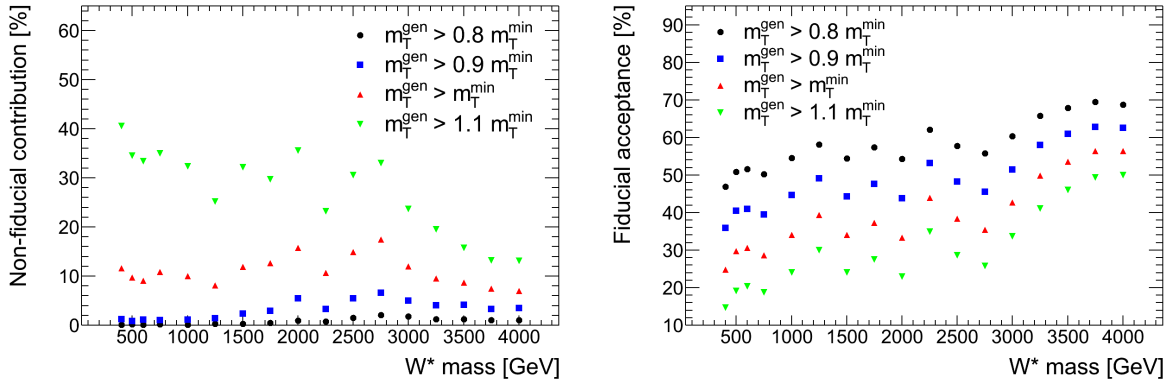

(a) (b)

Figure 8.24: The relative non-fiducial contribution to the final selection event sample (a) and the fiducial acceptance (b) for the W^* for fiducial cuts on the form $m_{\mathrm{T}}^{\mathrm{gen}} > \alpha m_{\mathrm{T}}^{\mathrm{min}}$.

magnetic field.

It is clear that with a cut $m_{\mathrm{T}}^{\mathrm{gen}} > m_{\mathrm{T}}^{\mathrm{min}}$, the finite muon momentum and $\not\!\!E_{\mathrm{T}}$ resolutions can lead to a potentially large contribution to the final selection event sample from outside the fiducial region, i.e. from events with $m_{\mathrm{T}}^{\mathrm{gen}} < m_{\mathrm{T}}^{\mathrm{min}}$. We focus therefore on the signal efficiency definition without the fiducial cut imposed in the numerator, and results correspond to this definition unless stated otherwise. The magnitude of the non-fiducial contribution to the final selection sample is shown for the SSM W' in fig. 8.23(a) and for the W^* in fig. 8.24(a) for different fiducial cuts on the form $m_{\mathrm{T}}^{\mathrm{gen}} > \alpha m_{\mathrm{T}}^{\mathrm{min}}$ with α as a constant. It is seen to be roughly 10-20% for the case $\alpha = 1$. We also show the fiducial acceptances in figs. 8.23(b) and 8.24(b). The fiducial acceptances are higher for the SSM W' than for the W^* at low mass because of the different angular distributions, and the SSM W' acceptances become very small at high mass, reflecting off-shell production tails.

The relative signal efficiency uncertainty due to the k-factor uncertainty is shown for the SSM W' and the W^* in fig. 8.25 for the class of fiducial cuts $m_{\mathrm{T}}^{\mathrm{gen}} > \alpha m_{\mathrm{T}}^{\mathrm{min}}$ with α as a constant. As expected, the m_{T} fiducial cut effectively reduces the k-factor uncertainty on the

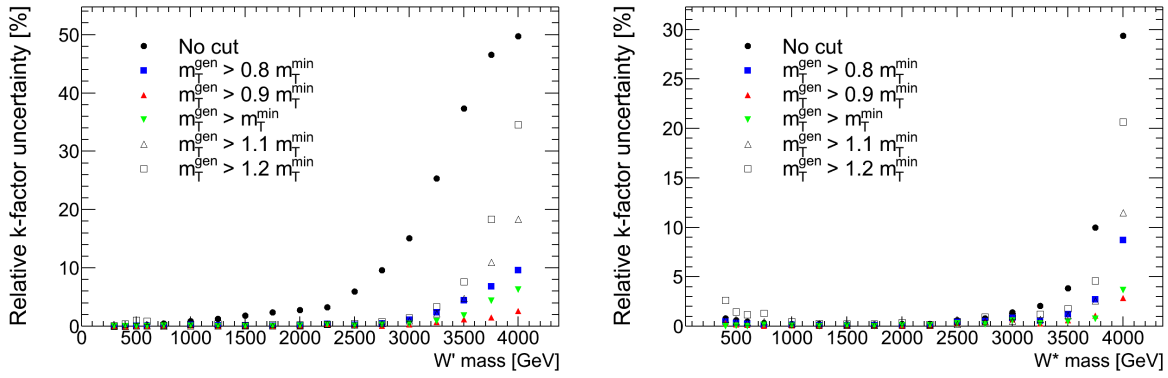

(a) (b)

Figure 8.25: The relative uncertainty on the signal efficiency due to the k-factor uncertainty obtained for the SSM W' (a) and the W^* (b) with fiducial cuts on the form $m_{\mathrm{T}}^{\mathrm{gen}} > \alpha m_{\mathrm{T}}^{\mathrm{min}}$.

signal efficiency. While one might have expected that $m_{\mathrm{T}}^{\mathrm{gen}} > m_{\mathrm{T}}^{\mathrm{min}}$ would be the optimal cut, it seems that a cut value slightly below $m_{\mathrm{T}}^{\mathrm{min}}$ is optimal, with $m_{\mathrm{T}}^{\mathrm{gen}} > 0.9\, m_{\mathrm{T}}^{\mathrm{min}}$ giving the lowest uncertainty among the possibilities shown in fig. 8.25. This is most likely because the final selection event sample receives a non-negligible contribution from events with $m_{\mathrm{T}}^{\mathrm{gen}} < m_{\mathrm{T}}^{\mathrm{min}}$ (see figs. 8.23(a) and 8.24(a)), so that a slightly wider fiducial region may better match the composition of the final selection sample.

Model dependence

Model dependence is the effect that cross section limits calculated for different models are in general not equal. The only inputs to the limit calculation that need to be evaluated in the context of a particular model are the signal efficiency and its uncertainty, and it is clear that model dependence enters the limit setting via these inputs. We have seen that the dominant signal efficiency uncertainty (that due to the k-factor) can be reduced to below 10% with a suitable m_{T} fiducial cut, and this leads to a very small impact on the evaluated cross section limit, as seen for a particular example case in fig. 7.2(a). It is therefore natural to assume that most model dependence enters via the signal efficiency itself, and we begin our investigation of model dependence by comparing directly signal efficiencies evaluated for the SSM W' and the W^*.

We expect that the most model independent limits are achieved with a fiducial region that matches as well as possible the final selection event sample, i.e. $m_{\mathrm{T}}^{\mathrm{gen}} > \alpha m_{\mathrm{T}}^{\mathrm{min}}$ with α close to unity. However, the optimal m_{T} thresholds differ between the SSM W' and W^* models, which leads to a mismatch between the fiducial regions defined for SSM W' and W^* bosons of the same mass. We argue, however, that a limit can be said to be model independent if one obtains the same limit value for different theories even if the limit for one of the theories is not the *optimal* one. The fact that the limit is not optimal for a given theory just means that the data could potentially be used to constrain that theory even more, not that the given contraint is not valid. We therefore compare signal efficiencies for the SSM W' and W^* models calculated with the same m_{T} thresholds, and both the optimal thresholds for the SSM W' and for the W^* are considered.

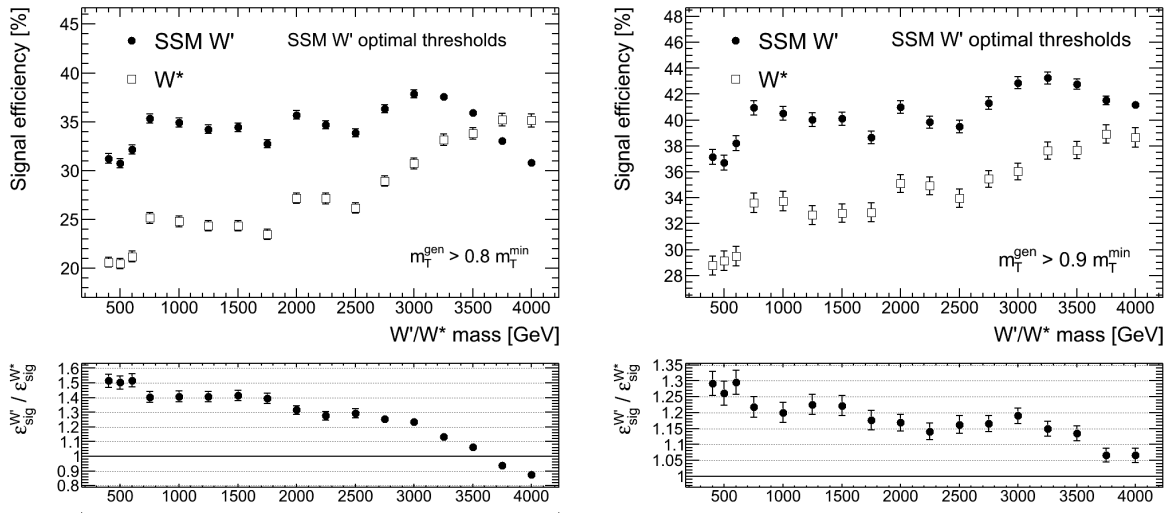

(a)

(b)

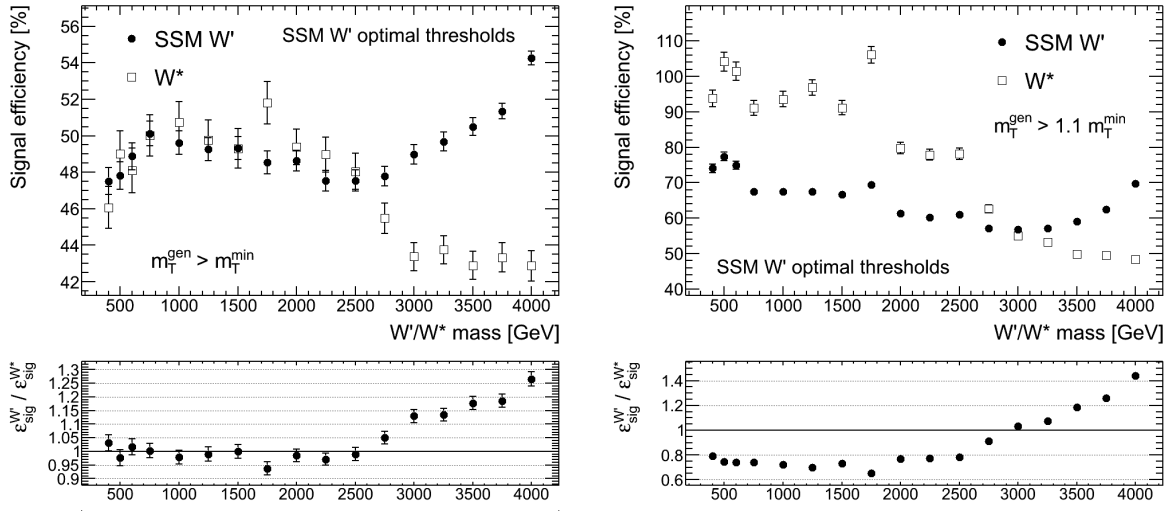

(c)

(d)

Figure 8.26: The signal efficiencies obtained for the SSM W' and W^* models with different fiducial cuts on the form $m_{\mathrm{T}}^{\mathrm{gen}} > \alpha m_{\mathrm{T}}^{\mathrm{min}}$. In (a), (b), (c), and (d), we have $\alpha = 0.8$, $\alpha = 0.9$, $\alpha = 1$, and $\alpha = 1.1$ respectively. The signal efficiencies are here evaluated with the optimal thresholds for the SSM W' model (see table 8.1). The ratio of the SSM W' to W^* signal efficiency is shown in the panel below each plot. The error bars represent statistical uncertainty.

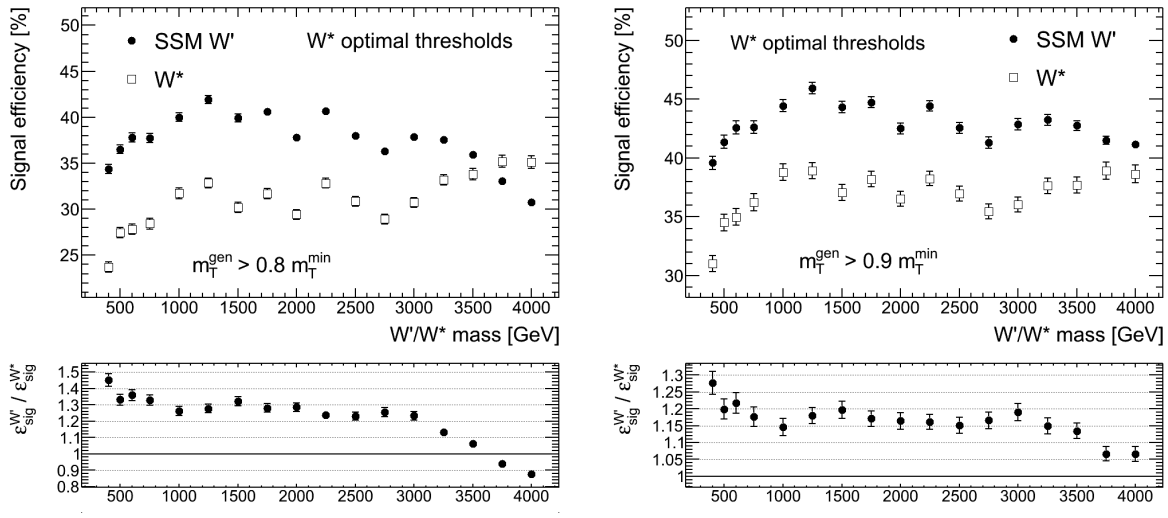

(a)

(b)

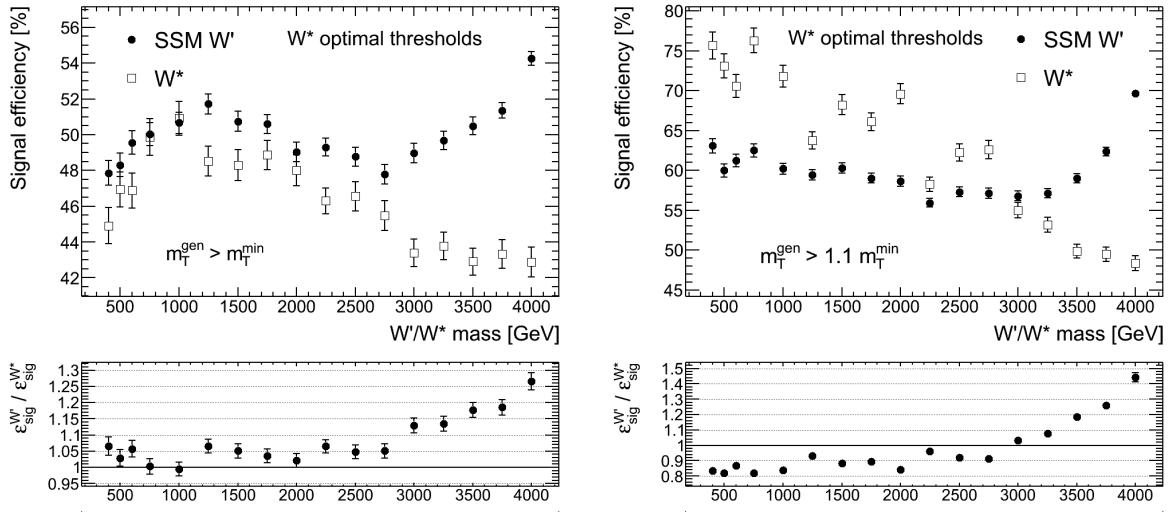

(c)

(d)

Figure 8.27: The signal efficiencies obtained for the SSM W' and W^* models with different fiducial cuts on the form $m_{\mathrm{T}}^{\mathrm{gen}} > \alpha m_{\mathrm{T}}^{\mathrm{min}}$. In (a), (b), (c), and (d), we have $\alpha = 0.8$, $\alpha = 0.9$, $\alpha = 1$, and $\alpha = 1.1$ respectively. The signal efficiencies are here evaluated with the optimal thresholds for the W^* model (see table 8.1). The ratio of the SSM W' to W^* signal efficiency is shown in the panel below each plot. The error bars represent statistical uncertainty.

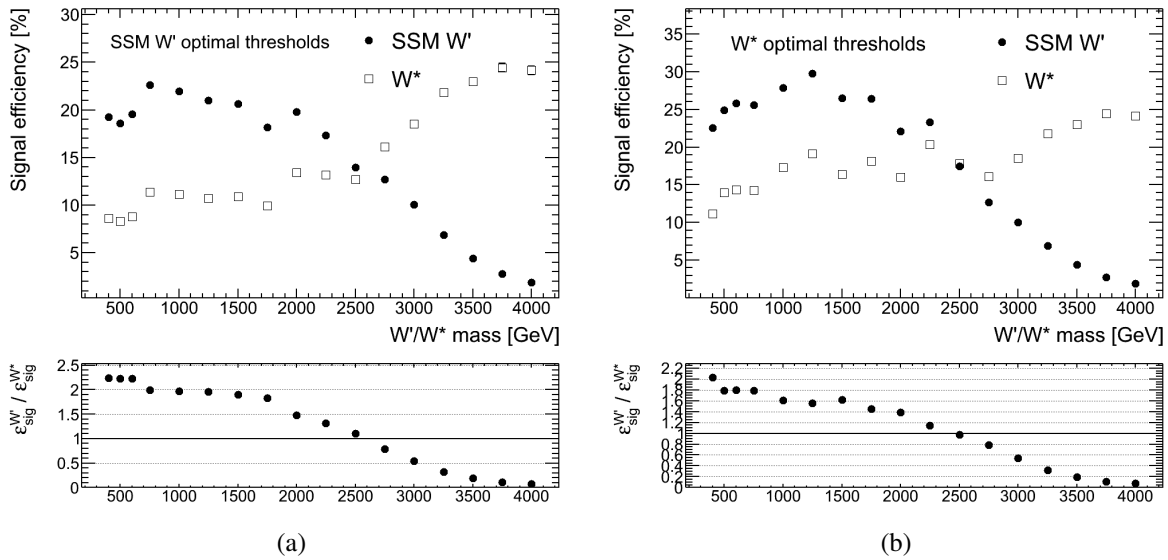

(a) (b)

Figure 8.28: The signal efficiencies obtained for the SSM W' and W^* models when considering total cross section limits. The signal efficiencies are evaluated with the optimal thresholds for the SSM W' model in (a) and for the W^* model in (b). The ratio of the SSM W' to W^* signal efficiency is shown in the panel below each plot. The error bars represent statistical uncertainty.

Signal efficiencies for the SSM W' and the W^* are compared with fiducial cuts on the form $m_{\mathrm{T}}^{\mathrm{gen}} > \alpha m_{\mathrm{T}}^{\mathrm{min}}$ in fig. 8.26 for the SSM W' optimal thresholds and in fig. 8.27 for the W^* optimal thresholds. The corresponding plots for total cross section limits are shown in fig. 8.28 for comparison. It is clear that the fiducial cuts on the form $m_{\mathrm{T}}^{\mathrm{gen}} > \alpha m_{\mathrm{T}}^{\mathrm{min}}$ with $\alpha \approx 1$ greatly reduce model dependence compared to total cross section limits. For $\alpha = 0.9$ and $\alpha = 1$, the SSM W' and W^* signal efficiencies differ by less than 30%, while the signal efficiencies corresponding to total cross section limits differ by up to a factor of 2 at low mass and more than a factor of 10 at the highest mass.

The intuitively correct choice of fiducial cut, $m_{\mathrm{T}}^{\mathrm{gen}} > m_{\mathrm{T}}^{\mathrm{min}}$, is seen indeed to provide the most model independent signal efficiencies over the majority of the mass range considered in the analysis. For the very highest masses, however, the SSM W' and W^* signal efficiencies are seen to diverge from each other. Here, the W^* signal efficiency seems to become almost constant while the SSM W' signal efficiency increases.

We argued in section 8.8.1 that the choice made in the ATLAS W' analysis to exclude the tau decay mode of the W' boson from the numerator of the signal efficiency in principle removes some model dependence because the resulting electron and muon channel limits are valid for models with different couplings to the different lepton generations as long as the width in the given model is comparable to the SSM W' width. Correspondingly, one might expect less model dependence with the fiducial cut imposed in the numerator of the signal efficiency when using an m_{T} fiducial cut, since the signal efficiency then only depends on the kinematics inside the fiducial region. While we argued that the non-fiducial contribution to the final selection event sample in the case of the fiducial cut $m_{\mathrm{T}}^{\mathrm{gen}} > m_{\mathrm{T}}^{\mathrm{min}}$ was too significant to be neglected, it is interesting to compare the model dependence of the signal efficiencies obtained with the fiducial cut imposed in the numerator to the baseline result. We perform this comparison for the

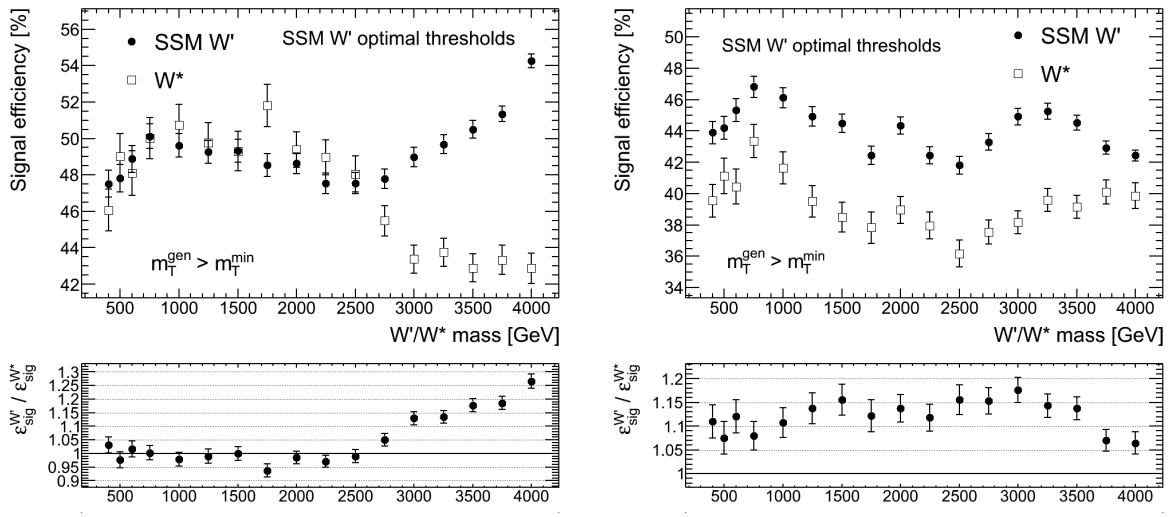

(a) (b)

Figure 8.29: The signal efficiencies obtained for the SSM W' and W^* models with the fiducial cut $m_{\mathrm{T}}^{\mathrm{gen}} > m_{\mathrm{T}}^{\mathrm{min}}$ without (a) and with (b) the fiducial cut imposed in the numerator of the signal efficiency. The signal efficiencies are here evaluated with the optimal thresholds for the SSM W' model. The ratio of the SSM W' to W^* signal efficiency is shown in the panel below each plot. The error bars represent statistical uncertainty.

SSM W' optimal thresholds in fig. 8.29.

Fig. 8.29(a) is the same as fig. 8.26(c), but is shown again for convenient comparison. We see that the signal efficiencies for masses up to $2.75\,\mathrm{TeV}$ are clearly more model independent in the case of *not* including the fiducial cut in the numerator of the signal efficiency, and this is understood as follows. Consider the m_{T} distributions shown for the $1\,\mathrm{TeV}$ mass in fig. 3.5, and recall that the SSM W' optimal threshold for this mass is $m_{\mathrm{T}}^{\mathrm{min}} \approx 800\,\mathrm{GeV}$. Clearly, the W^* model has more events close to $m_{\mathrm{T}}^{\mathrm{gen}} = m_{\mathrm{T}}^{\mathrm{min}}$ than the SSM W'. When including resolution effects, some of these events "migrate" from $m_{\mathrm{T}}^{\mathrm{gen}} > m_{\mathrm{T}}^{\mathrm{min}}$ to $m_{\mathrm{T}} < m_{\mathrm{T}}^{\mathrm{min}}$ and are thus excluded from the numerator of the signal efficiency due to the cut on the reconstructed transverse mass m_{T}. A lower signal efficiency can therefore be expected for the W^* than the SSM W' when the fiducial cut is imposed in the numerator of the signal efficiency, and this is indeed what is seen in fig. 8.29(b). When including also non-fiducial signal with $m_{\mathrm{T}}^{\mathrm{gen}} < m_{\mathrm{T}}^{\mathrm{min}}$ in the numerator, the loss of events due to migration from $m_{\mathrm{T}}^{\mathrm{gen}} > m_{\mathrm{T}}^{\mathrm{min}}$ to $m_{\mathrm{T}} < m_{\mathrm{T}}^{\mathrm{min}}$ can to some extent be compensated by migration from $m_{\mathrm{T}}^{\mathrm{gen}} < m_{\mathrm{T}}^{\mathrm{min}}$ to $m_{\mathrm{T}} > m_{\mathrm{T}}^{\mathrm{min}}$, i.e. exactly the events that are removed if the fiducial cut is imposed in the numerator, and this results in less model dependent signal efficiencies.

A similar argument may explain the increase in signal efficiency seen at very high mass for the SSM W' in fig. 8.29(a). For the highest W' masses, the threshold $m_{\mathrm{T}}^{\mathrm{min}} \approx 1.9\,\mathrm{TeV}$ is in a region where the m_{T} tail is increasing rapidly towards lower masses due to the off-shell production invariant mass tail (see fig. 3.7). There is thus more signal with $m_{\mathrm{T}}^{\mathrm{gen}} < m_{\mathrm{T}}^{\mathrm{min}}$ that has potential to migrate to $m_{\mathrm{T}} > m_{\mathrm{T}}^{\mathrm{min}}$ than vice versa, and the result is a higher signal efficiency. We note in this context the increase in the non-fiducial contribution to the final selection event sample seen in fig. 8.23(a) for the highest masses.

Limits

We proceed to compare directly the cross section limits obtained for the SSM W' and the W^* with the fiducial cut $m_{\mathrm{T}}^{\mathrm{gen}} > m_{\mathrm{T}}^{\mathrm{min}}$ in fig. 8.30. Comparisons are made both for expected and observed limits, and with the optimal thresholds for the SSM W' as well as for the W^*. The ratios of the SSM W' to W^* limits look identical for expected and observed limits. We recognize the ratio plots from figs. 8.26(c) and 8.27(c), and conclude that model dependence enters the limit setting primarily via the signal efficiency (central value) as expected.

The cross section limits for the SSM W' and the W^* shown in fig. 8.30 are equal within a few percent at low mass and within 25% at high mass. However, as already noted, the limits evaluated for the W^* model with the optimal thresholds for the SSM W' model are not optimal. The same goes for the limits on the SSM W' model evaluated with the optimal thresholds for the W^* model. We quantify the extent to which the limits are not optimal by comparing the ratio of the expected limit to the theoretical cross section between optimal and suboptimal thresholds in fig. 8.31. The ratio obtained with the suboptimal threshold is divided by the one obtained with the optimal threshold, and the resulting number exceeds unity by an amount that reflects the extent to which the suboptimal threshold is inferior to the optimal one. We see that the loss of sensitivity associated with using the m_{T} thresholds optimized for the "wrong" theory is in general below 15%, and below 20% in all cases. Starting from $m_{W'/W^*} = 2750\,\mathrm{GeV}$, there is no loss of sensitivity associated with changing thresholds, as the same threshold $m_{\mathrm{T}}^{\mathrm{min}} = 1888\,\mathrm{GeV}$ is optimal for both models.

In fig. 8.32, we show the observed limits evaluated for the SSM W' and the W^* with the fiducial cut $m_{\mathrm{T}}^{\mathrm{gen}} > m_{\mathrm{T}}^{\mathrm{min}}$ as well as the corresponding theoretical cross sections. We note that the theoretical cross section curves are not smooth because the m_{T} threshold $m_{\mathrm{T}}^{\mathrm{min}}$ is not a smooth function of the W'/W^* mass. Using the plots in fig. 8.32 we can read off the SSM W' (W^*) mass limit as the intersection of the SSM W' (W^*) theoretical cross section with the SSM W' (W^*) cross section limit curve. This gives the same muon channel mass limits as presented in table 8.15, because the further reduction of the signal efficiency uncertainty associated with the $m_{\mathrm{T}}^{\mathrm{gen}} > m_{\mathrm{T}}^{\mathrm{min}}$ fiducial cut as opposed to $m_{l\nu} > 0.4\,m_{W'/W^*}$ has practically no impact on the mass limit. We can also imagine reading off the mass limit for the SSM W' (W^*) as the intersection of the SSM W' (W^*) theoretical cross section with the W^* (SSM W') cross section limit curve, i.e. using the cross section limits derived for the "wrong" theory. This gives a mass limit that differs from the former by 1% in both the SSM W' and W^* cases.

We present finally standard limit plots for the fiducial limits with the cut $m_{\mathrm{T}}^{\mathrm{gen}} > m_{\mathrm{T}}^{\mathrm{min}}$ in fig. 8.33. We argued that the relatively flat limits observed at high mass in fig. 8.21 were a nice feature, demonstrating that the sensitivity to relevant signal was retained also for the highest masses. The limits presented in fig. 8.33 are certainly flat at high mass.

8.8.4 Discussion

We have argued that the use of the cross section as parameter of interest in a statistical analysis, as opposed to a theory parameter or a signal strength parameter, has the advantage that the parameter of interest is somewhat closer to the experimental observable, which is the number of events firing the necessary trigger(s) and passing the full event selection after reconstruction. With this in mind, we have investigated the use of fiducial cross sections limited to more rele-

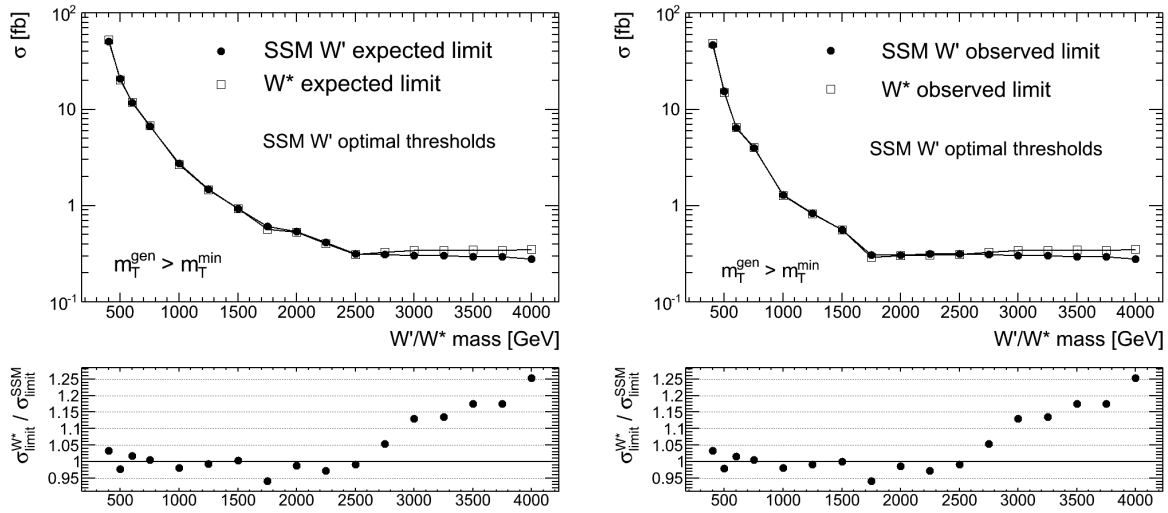

(a)

(b)

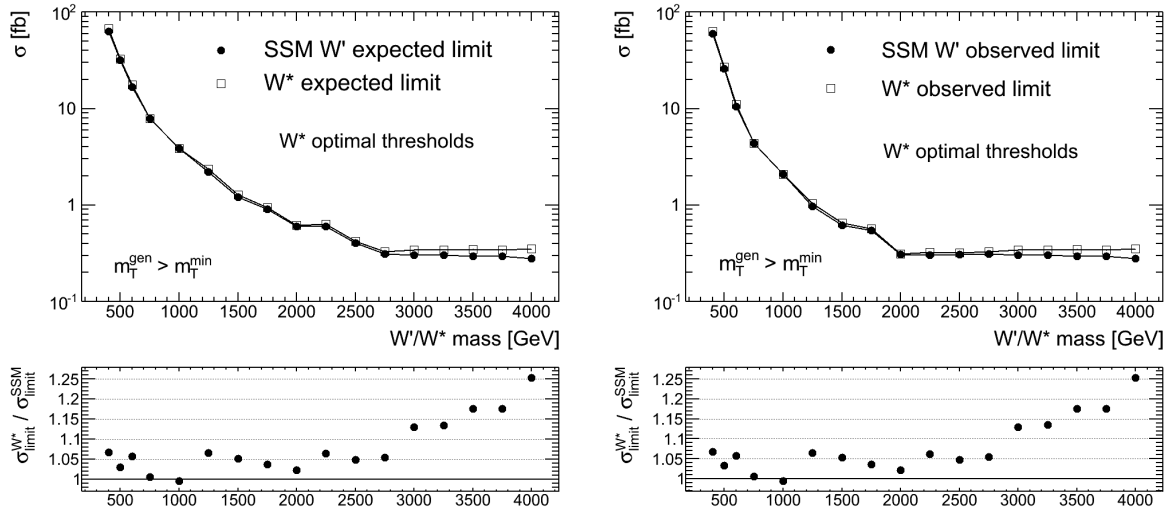

(c)

(d)

Figure 8.30: Comparison of the expected ((a) and (c)) and observed ((b) and (d)) cross section limits obtained for the SSM W' and W^* models with the fiducial cut $m_{\mathrm{T}}^{\mathrm{gen}} > m_{\mathrm{T}}^{\mathrm{min}}$. Limits are evaluated with the optimal thresholds for the SSM W' ((a) and (b)) and for the W^* ((c) and (d)). The ratio of the W^* limit to the SSM W' limit is shown in the panel below each plot.

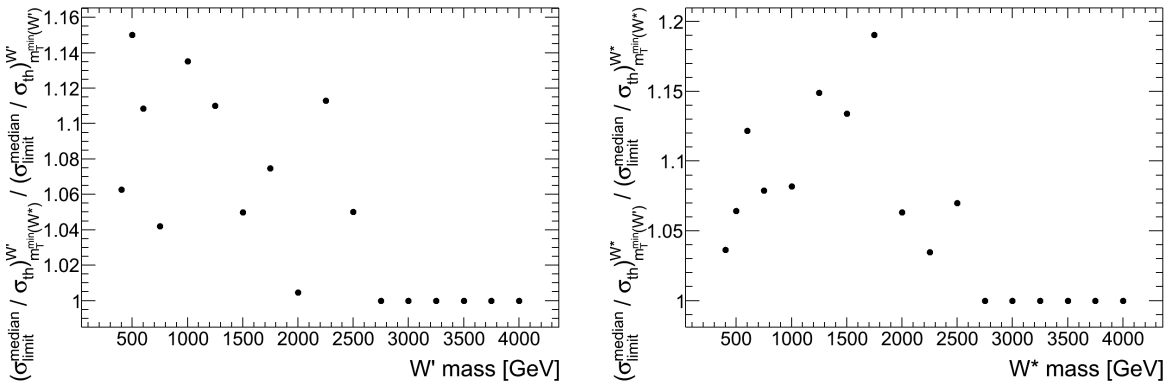

(a) (b)

Figure 8.31: The limit strength ratio $\sigma_{\rm limit}^{\rm median}/\sigma_{\rm theory}$ evaluated with the optimal $m_{\rm T}$ thresholds of the W^* (SSM W') model divided by the same ratio evaluated with the optimal $m_{\rm T}$ thresholds of the SSM W' (W^*) model for the SSM W' (a) (W^* (b)). The amount by which the numbers differ from unity quantifies the loss of sensitivity associated with evaluating cross section limits using the $m_{\rm T}$ thresholds optimized for the "wrong" theory. The limits are evaluated with the fiducial cut $m_{\rm T}^{\rm gen} > m_{\rm T}^{\rm min}$.

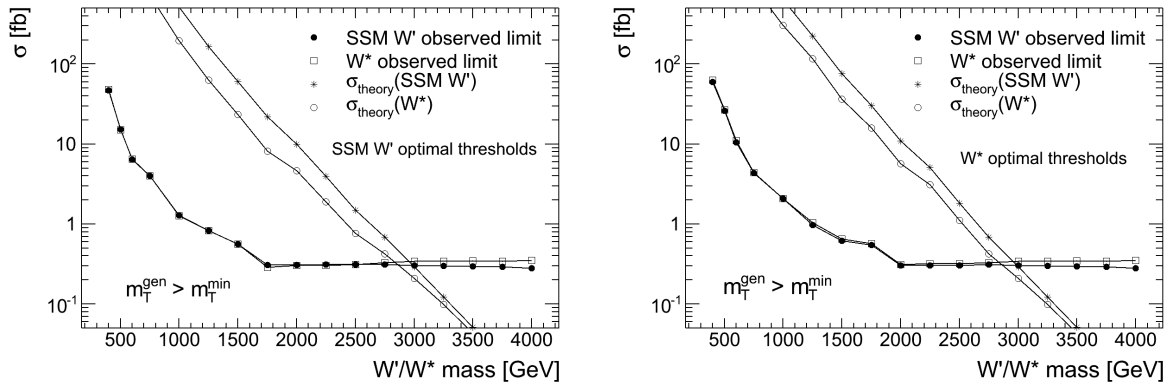

(a) (b)

Figure 8.32: Observed cross section limits and theoretical cross sections for the SSM W' and the W^* using the optimal thresholds for the SSM W' (a) and for the W^* (b). The limits are evaluated with the fiducial cut $m_{\rm T}^{\rm gen} > m_{\rm T}^{\rm min}$.

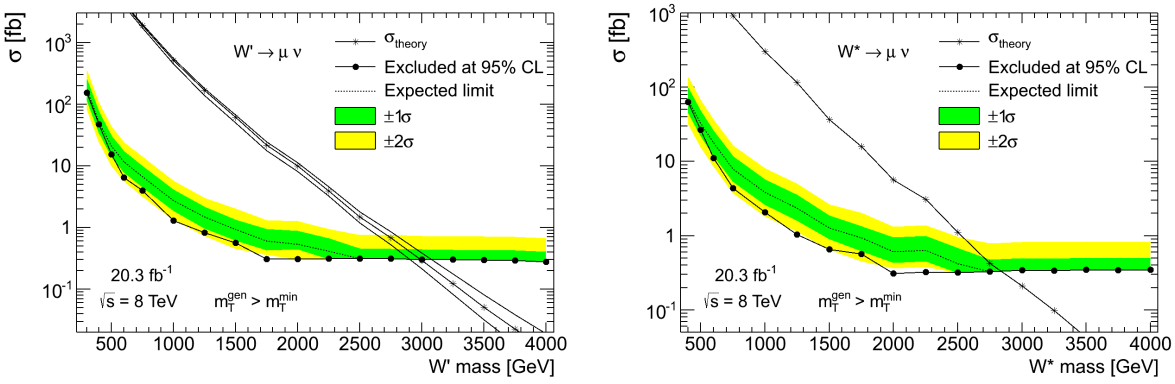

(a) (b)

Figure 8.33: Standard limit plots for the SSM W' and the W^*. The limits are evaluated with the fiducial cut $m_{\mathrm{T}}^{\mathrm{gen}} > m_{\mathrm{T}}^{\mathrm{min}}$.

vant parts of the total phase space. We find that the fiducial limits lead to a smaller theoretical uncertainty on the signal efficiency than the customary total cross section limits, and we argue that they better fulfill the ideal of being close to the experimental observable. The limit curves thus better represent the sensitivity to relevant signal as function of the new boson mass, and theoretical uncertainties affect to a larger extent the cross section rather than the signal efficiency. The shifting of the theoretical uncertainty to the cross section seems desirable, as it means that the signal efficiency is left a more experimental quantity, as one might intuitively expect it to be.

Model dependence has been investigated by comparing limits derived using the SSM W' and the W^* for the evaluation of the signal efficiency and its uncertainty. While a larger spectrum of models would be desirable for such a study, we expect that the comparison of these two models goes already a long way due to the striking differences in both the invariant mass distributions and the angular distributions. Studying the effect of varying the widths of both the SSM W' and W^* bosons would certainly be interesting, in particular if one could obtain a set of different theoretically motivated widths, as in the case of the ATLAS Z' analysis, ref. [39]. Such a study would be facilitated by the recent migration to the template sample reweighting technique. Using this technique, changing the width is just a matter of changing a parameter in the analysis code, and no new signal MC samples need to be produced.

To the extent that cross section limits are model independent, reinterpretation of the data in terms of a different model is merely a matter of calculating the theoretical cross section within the given model. Obviously, when limits are placed on a fiducial cross section, it is this fiducial cross section that must be calculated. We have found that model independence seems to be achieved in particular with the application of a generator level transverse mass fiducial cut with the same value as the analysis selection cut on the reconstructed transverse mass. Calculating fiducial cross sections for a given model should be trivial. In particular, an invariant mass fiducial cross section can be calculated in programs such as CalcHEP [61] and CompHEP [119]. The generator level transverse mass is not Lorentz invariant, and may be affected by a transverse boost of the new boson. Therefore, a parton shower generator, such as PYTHIA [59], HERWIG [88], or SHERPA [94], is in principle needed to calculate the fiducial

cross section defined by a transverse mass cut. However, the transverse mass is much less sensitive to parton shower effects than e.g. the lepton and neutrino transverse momenta, and one could probably obtain a reasonable approximation to the fiducial cross section even without a parton shower generator.

Obviously, completely model independent limits can be calculated by taking the expected number of signal events per unit of integrated luminosity at final selection, the "effective cross section", to be the parameter of interest in the limit setting. The drawback of such limits is that the calculation of this "effective cross section" necessarily involves the simulation of detector response to the generator level final state particles. While there are freely available generic detector simulation packages [120, 121], these can obviously never match the detail level and precision of the detector description that is used for simulation within the ATLAS collaboration. This description is not available outside the collaboration.

CMS seem to have chosen a hybrid approach for what they refer to as model independent limits in ref. [71]. They estimate so-called model independent contributions to the signal efficiency using the $W \rightarrow l\,\nu$ MC sample, and leave the acceptance of the main kinematic cuts, including the m_{T} threshold, to be calculated within a given model in the process of reinterpretation. It would seem that this acceptance must be estimated using some generic detector simulation to account for resolution effects. In this case, the acceptances evaluated for the electron and muon channels are not necessarily equal, and interpretation of the combined limit may be difficult.

We argue that fiducial cross section limits may be a way to facilitate the reinterpretation of ATLAS data without relying on generic detector simulation packages. We have seen that cross section limits evaluated using the same m_{T} thresholds for the SSM W' and the W^* can be made to agree within a few percent at low mass, and within 25% at high mass. While the SSM W' thresholds are not optimal for the W^* and vice versa, the loss of sensitivity associated with using the optimal thresholds for the "wrong" signal model is below 20% for all masses. However, we have produced fiducial cross section limits for both the SSM W' and the W^* models, and for a hypothetical reinterpretation, one could use the set of limits (thresholds) that would provide the strongest constraint on the given theory under study. To the extent that one really believes the model independence of the transverse mass fiducial limits, one could even use a threshold optimized for a different boson mass than the one under consideration. This is certainly possible in the case of the completely model independent limits on the "effective cross section", as these limits depend only on the m_{T} threshold without any reference to a boson mass or other theory parameters.

We note finally that our results on transverse mass fiducial limits are strongly dependent on the single bin counting experiment formalism. The fact that we can to a large extent isolate the final selection event sample already at the generator level is due to the use of the m_{T} cut to define the signal region in the analysis selection. This leads to a sharp cutoff, where the analysis is sensitive only to events with $m_{\mathrm{T}} > m_{\mathrm{T}}^{\mathrm{min}}$. In the case of a multi-bin analysis of the entire (or a large portion of the) m_{T} distribution, such as that performed for the SSM W' limits in ref. [71], the analysis would rather have a varying sensitivity as function of the m_{T}, governed by the varying background level. In this case, there is no obvious cut value to define a generator level transverse mass fiducial region.

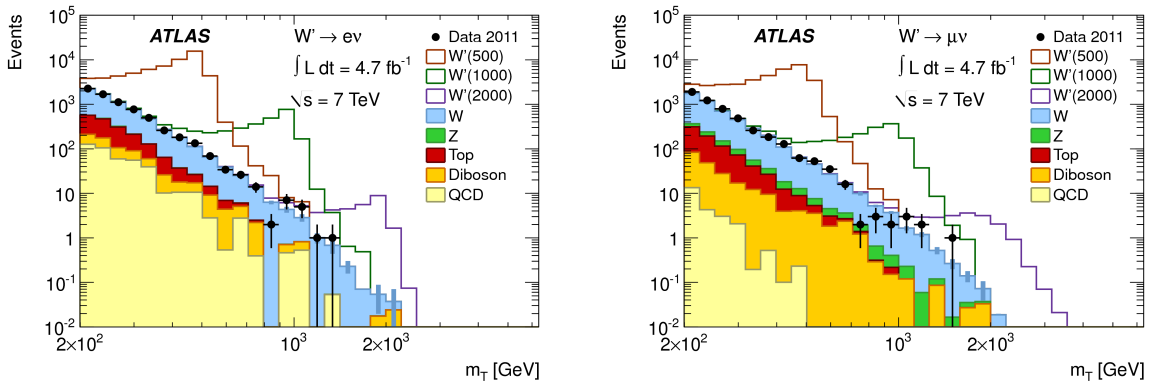

(a) (b)

Figure 8.34: Transverse mass distributions in the $\sqrt{s} = 7\,\mathrm{TeV}$ analysis in the electron (a) and muon (b) channels with example signal contributions from SSM W' bosons of different masses. The plots are from ref. [107].

8.9 Comparison to other searches

Before concluding this chapter, we proceed to compare the limits presented here to those presented in other publications. We begin by summarizing briefly the results of the $\sqrt{s} = 7\,\mathrm{TeV}$ ATLAS analysis.

8.9.1 ATLAS results at $\sqrt{s} = 7\,\mathrm{TeV}$

Also the data collected by the ATLAS detector at a pp center of mass energy $\sqrt{s} = 7\,\mathrm{TeV}$ was used to search for new physics in the one lepton and missing transverse energy final state, and we present the main results from the final analysis [107] with $4.7\,\mathrm{fb}^{-1}$ of integrated luminosity here. The $\sqrt{s} = 7\,\mathrm{TeV}$ analysis was performed using almost identical event selection and methodology as already described for the $\sqrt{s} = 8\,\mathrm{TeV}$ analysis. No significant excess of events over the background expectation was observed, and the Bayesian limit setting described in section 7.3 was employed to place limits on the cross sections for SSM W' and W^* production, although with Gaussian priors for all nuisance parameters.

We present the transverse mass distributions in the electron and muon channels in fig. 8.34. The data are observed to be in good agreement with the background expectation, and limits at 95% CL on the SSM W' and W^* cross sections are presented in fig. 8.35. Finally, the mass limits are shown in table 8.16. Comparing the expected combined mass limits, we see that the mass reach for the SSM W' and the W^* is extended by approximately $600\,\mathrm{GeV}$ and $700\,\mathrm{GeV}$ respectively in the $\sqrt{s} = 8\,\mathrm{TeV}$ analysis. In terms of the observed combined limit, the improvement is slightly higher because no events were observed in either channel above the highest m_T threshold at $\sqrt{s} = 8\,\mathrm{TeV}$, while one event was observed in the muon channel at $\sqrt{s} = 7\,\mathrm{TeV}$.

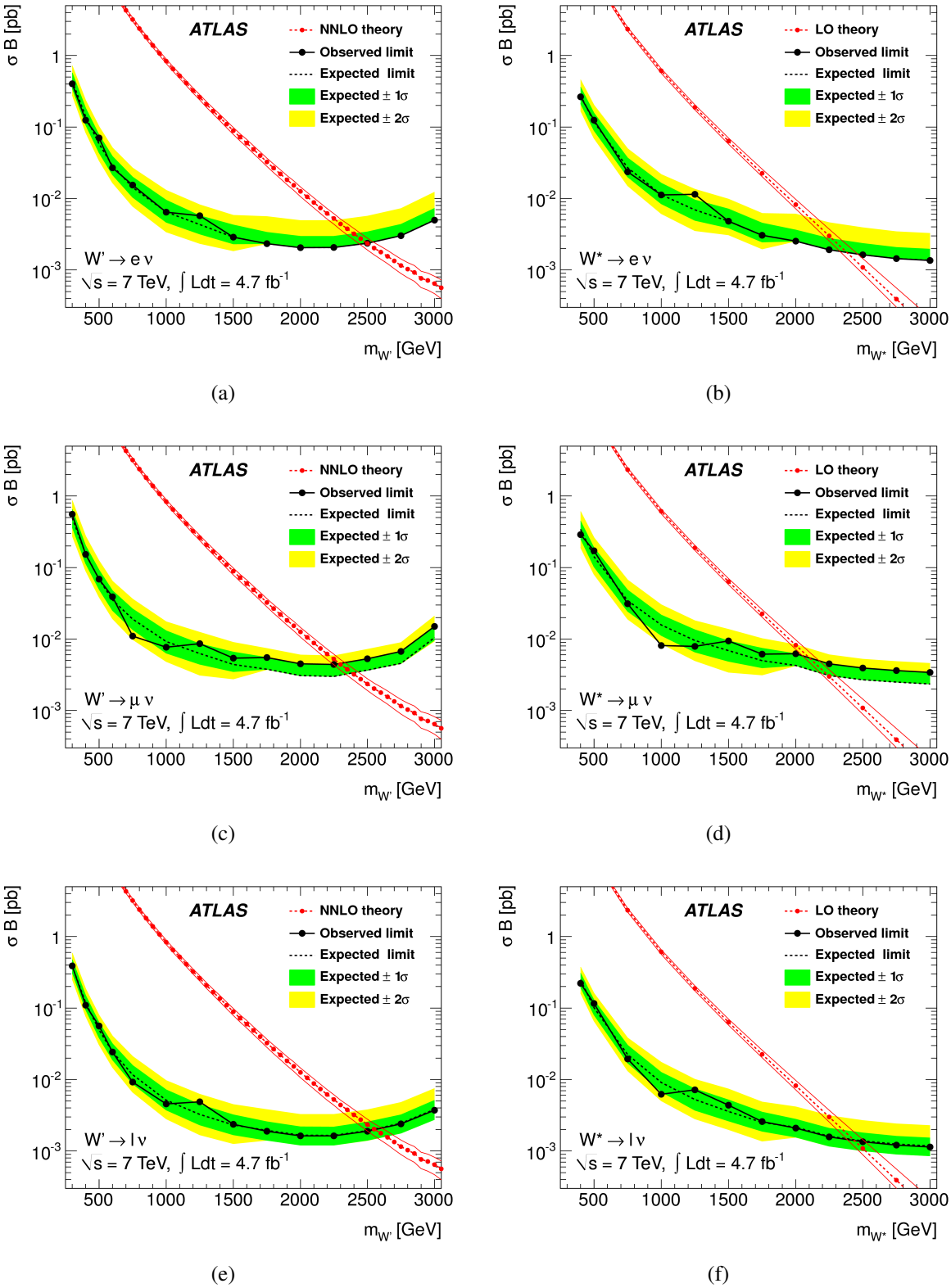

Figure 8.35: Limits on the cross sections for SSM W' ((a), (c), and (e)) and W^* ((b), (d), and (f)) production and decay to a single lepton generation at $\sqrt{s} = 7\,\text{TeV}$ using $4.7\,\text{fb}^{-1}$ of integrated luminosity. Limits are shown for the electron channel ((a) and (b)), the muon channel ((c) and (d)), and their combination ((e) and (f)). The parameter σB is here the total cross section for W'/W^* production and decay to a single lepton generation. The plots are from ref. [107].

Channel	$m_{W'}$ [TeV]		m_{W^*} [TeV]	
	Expected	Observed	Expected	Observed
Electron	2.50	2.50	2.38	2.38
Muon	2.38	2.28	2.25	2.09
Combined	2.55	2.55	2.42	2.42

Table 8.16: Mass limits for the SSM W' (left) and the W^* (right) signal models from the $\sqrt{s} = 7\,\mathrm{TeV}$ analysis.

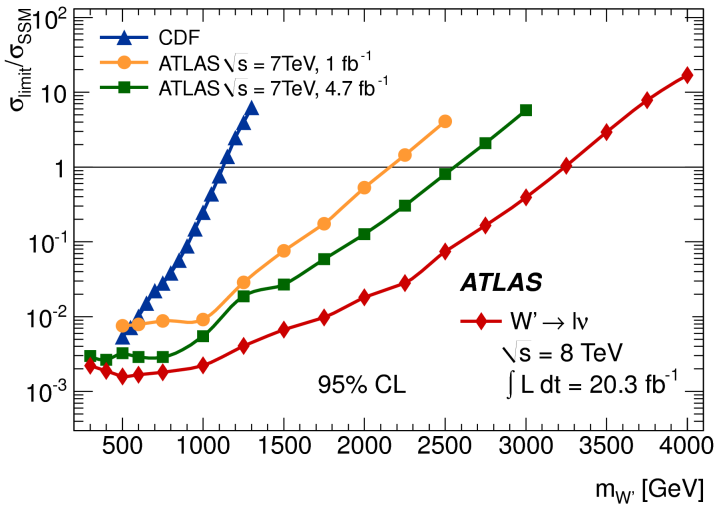

Figure 8.36: Comparison of limit strengths, quantified as the ratio $\sigma_{\mathrm{limit}}/\sigma_{\mathrm{theory}}$, between different ATLAS results [106, 107, 109] and the final CDF result [122] for the SSM W'. From the auxiliary material to ref. [109].

8.9.2 Sensitivity comparison as function of the W' mass

In fig. 8.36, we present a comparison of limit strengths, quantified as the ratio $\sigma_{\mathrm{limit}}/\sigma_{\mathrm{theory}}$, between different ATLAS results [106, 107, 109] and the final CDF result [122] for the SSM W'. The comparison is made as function of the W' mass, and the use of the ratio $\sigma_{\mathrm{limit}}/\sigma_{\mathrm{theory}}$ instead of just the cross section limit σ_{limit} makes results comparable between different center of mass energies and beam types.

The plot shown in fig. 8.36 was released by the ATLAS collaboration as auxiliary material to ref. [109], and contains obviously the official ATLAS limits. However, we have already mentioned that the combined limits on the total cross sections presented in section 8.7 agree with these to within 6%, and a variation of this magnitude would hardly be visible in fig. 8.36. The ATLAS limits based on the $\sqrt{s} = 8\,\mathrm{TeV}$ data provide the strongest bounds on the SSM W' model among the considered analyses for the whole mass range.

8.9.3 Mass limit comparison

We present finally mass limits for lepton channel W' searches at the Tevatron and the LHC in table 8.17. The limits are presented for the conventional SSM W' interpretation without interference with the W boson. Obviously, the significant increase in center of mass energy from the Tevatron to the LHC has drastically improved the mass reach for these searches, and the mass limits from the Tevatron experiments were already surpassed with the first $36\,\mathrm{pb}^{-1}$ of LHC data at $\sqrt{s} = 7\,\mathrm{TeV}$ [104, 124, 125]. The current best mass limits from the LHC experiments are close to $3.3\,\mathrm{TeV}$.

We mention also the W^* model, for which mass limits have not been presented by the other collaborations, but for which we have presented a mass limit of $3.21\,\mathrm{TeV}$. Finally, CMS have

Collaboration	Beams	Int. lum. [fb^{-1}]	$\sqrt{s}$ [TeV]	Channel	Mass limit [TeV]	Ref.
D0	$p+\overline{p}$	0.99	1.96	e	1.00	[123]
CDF	$p+\overline{p}$	5.3	1.96	e	1.12	[122]
CMS	$p+p$	5.0	7	$e+\mu$	2.5	[126]
ATLAS	$p+p$	4.7	7	$e+\mu$	2.55	[107]
CMS	$p+p$	19.7	8	$e+\mu$	3.28	[71]
ATLAS	$p+p$	20.3	8	$e+\mu$	3.24	[109]
ATLAS	$p+p$	20.3	8	$e+\mu$	3.28	Section 8.8.2

Table 8.17: Mass limits for lepton channel W' searches at the Tevatron and the LHC. The last row gives the mass limit obtained for the fiducial limits with an invariant mass cut $m_{l\nu} > 0.4\, m_{W'}$ presented in section 8.8.2.

also presented limits on the SSM model including interference, and give mass limits of $4.00\,\mathrm{TeV}$ in the case of same sign couplings (destructive interference) and $3.71\,\mathrm{TeV}$ in the opposite sign (constructive interference) case [71].

8.10 Summary

In this chapter, we have searched for new charged, heavy bosons and presented limits on new physics in the form of the SSM W' and W^* bosons. The SSM W' boson is found to be excluded for masses below $3.28\,\mathrm{TeV}$, and the corresponding mass limit for the W^* reference model is $3.21\,\mathrm{TeV}$. We have investigated different choices of the signal cross section used as parameter of interest in the limit setting, and find that constraining the cross section to more relevant parts of the total phase space can help separate experimental and theoretical uncertainties and reduce the model dependence of the calculated limits.

In section 3.2, we stressed that the search should in principle be thought of as a model independent search for any deviation from the SM in the one lepton and missing transverse energy transverse mass distribution. Indeed, heavy, charged bosons are not the only candidates for new physics to which our search is sensitive, and in the last chapter, we will interpret the search in terms of dark matter production.

Chapter 9

Search for dark matter production in association with a leptonically decaying W boson

The presence of dark matter (DM) as the dominant contribution to the total amount of matter in the universe is well established, but little is known about its nature. DM may be composed of weakly interacting massive particles (WIMPs) with tiny cross sections for non-gravitational interactions with ordinary matter. One such DM particle candidate is the lightest supersymmetric particle in R-parity conserving supersymmetry scenarios, which would be stable as R-parity conservation forbids its decay into two SM particles.

Many experiments search for DM particles directly by looking for signatures of their non-gravitational interactions in underground terrestrial experimental equipment. Others search indirectly for DM by searching for the products of WIMP annihilation or decay. Finally, collider experiments can search for DM particle production in association with SM particles [127–130]. Obviously, the DM particles do not interact significantly with the detector and escape undetected. This leads to missing transverse energy when the DM particles recoil against visible particles. In the case that DM particles are produced in association with a leptonically decaying W boson, the final state contains one lepton and missing transverse energy, and this analysis can thus be used to place limits on such signal.

9.1 Signal models

Results of searches for DM particles in collider experiments are usually interpreted in the context of effective field theories (EFTs). These theories are based on the assumption that the interaction of the DM particles with the SM particles occurs through the exchange of a particle that is much heavier than the typical momentum transfer of that interaction. The most relevant process in the context of hadron collider searches for DM is the annihilation of a quark and an antiquark into a heavy intermediate state which subsequently decays into a pair of DM particles (fig. 9.1 left). In this s-channel process, the invariant mass transferred in the heavy particle propagator must be much smaller than the mass of the heavy particle for the EFT approach to be valid. In this case, we can approximate the propagator as a constant in the invariant mass,

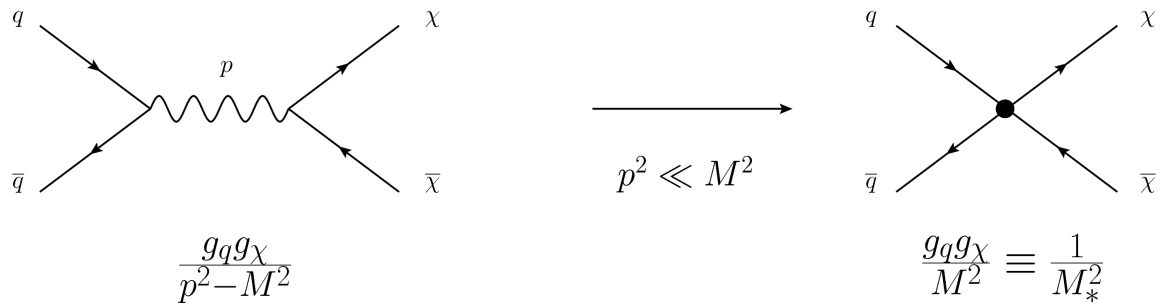

Figure 9.1: The figure shows schematically how the s-channel exchange of a heavy particle of mass M can be represented as a point coupling in an effective field theory in the limit of small momentum transfer, $p^2 \ll M^2$. The propagator becomes independent of p^2 in this limit, and becomes effectively a dimensionful coupling constant coupling the quarks to the DM particles χ/$\overline{\chi}$ directly.

Name	Interaction
D1	$\frac{m_q}{M_*^3}\overline{\chi}\chi\,\overline{q}q$
D5	$\frac{1}{M_*^2}\overline{\chi}\gamma^\mu\chi\,\overline{q}\gamma_\mu q$
D9	$\frac{1}{M_*^2}\overline{\chi}\sigma^{\mu\nu}\chi\,\overline{q}\sigma_{\mu\nu}q$

Table 9.1: The three EFTs considered in this analysis. The naming corresponds to ref. [130]. The symbols q and χ represent the Dirac spinors associated with the quarks and DM particles respectively, and the strength of the quark-DM interaction is governed by the parameter M_* with the dimension of mass. The presence of the quark mass m_q in the D1 interaction mitigates the contribution to flavor changing processes [130]. The matrix $\sigma^{\mu\nu}$ is defined as $\sigma^{\mu\nu} = (i/2)[\gamma^\mu, \gamma^\nu]$.

and the propagator is effectively replaced by a coupling (fig. 9.1 right).

Let us consider the non-interacting propagator of a particle of mass M transferring a four-momentum p. It has the form $1/(p^2 - M^2)$, and its magnitude reduces simply to $1/M^2$ in the limit $p^2 \ll M^2$. Connecting the SM quarks to the DM particles via such a propagator involves the couplings of the heavy mediator to the quarks and DM particles, and the resulting point coupling in the EFT depends both on the mass M and these couplings, as depicted schematically in fig. 9.1. In the effective field theory, then, the couplings and mediator mass come together as a dimensionful coupling, which can be defined simply in terms of a mass scale M_* as results evaluated in the EFT do not depend on the individual couplings and the mediator mass.

We consider only DM particles that are Dirac fermions, and we denote the DM particle χ with its respective antiparticle $\overline{\chi}$. The interaction of the mediator particle with quarks and DM particles is associated not only with the coupling constants, but also with a particular Dirac matrix structure, which affects the results in the EFT and must be specified. A large set of possibilities was considered in ref. [130], and the names defined therein are widely used. We consider the D1, D5, and D9 models, and the corresponding interaction Lagrangian terms are specified in table 9.1.

As noted in ref. [131], the mono-W process (the production of a W boson in association with a pair of DM particles) benefits from constructive interference in the case that the coupling of the DM particles to up and down type quarks have opposite sign. In this scenario, searches targeting the mono-W process can provide stronger limits than those targeting other mono-X processes, such as the mono-jet and mono-Z processes. Fig. 9.2 shows Feynman diagrams

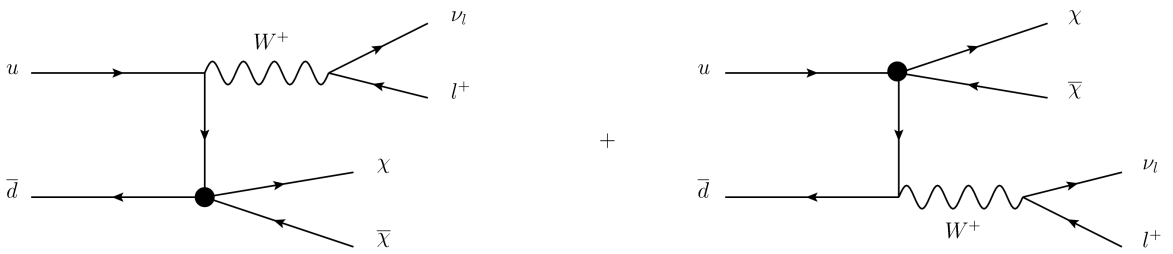

Figure 9.2: Feynman diagrams for a particular hard scattering process leading to the one lepton and $\not{E}_{\mathrm{T}}$ final state via the mono-W process. The plus sign indicates that the diagrams are added together in the cross section calculation, so that constructive or destructive interference may occur.

for a particular hard scattering process leading to the one lepton and $\not{E}_{\mathrm{T}}$ final state. The DM particles are seen to couple to different quarks in the two diagrams, so the interference may be constructive or destructive depending on the relative sign of the DM coupling to up and down quarks.

Because of the interference effects, we provide results for two different variants of the D5 EFT with different relative sign of the DM coupling to up and down quarks. In the case of opposite sign, the interference is constructive, and we refer to the corresponding EFT as D5c. The case of same sign couplings leads to destructive interference, and the corresponding EFT is labeled D5d. Interference effects are found not to be important in the cases of the D1 and D9 EFTs.

9.1.1 MC samples

Signal MC samples for DM production in association with a leptonically decaying W boson have been generated at the hard scattering level with MadGraph 5 [132] using the MSTW 2008 LO PDFs [26] and interfaced to PYTHIA 8 [27, 59] with the AU2 tune [60] and the MSTW 2008 LO PDFs for the parton shower, hadronization, and underlying event. In addition to the mass scale M_* in the EFT, the DM particle mass m_χ must be specified, and samples are generated for a selection of masses in the range from $1\,\mathrm{GeV}$ to $1.3\,\mathrm{TeV}$. All three leptonic decay channels of the W boson are included in the samples, which are listed in table 9.2. Fast detector simulation (Atlfast-II [64]) are used for all samples.

The parameter M_* in the EFT is set to $M_* = 1\,\mathrm{TeV}$ for all samples, and the cross sections given in table 9.2 correspond to this value. The choice is arbitrary, and affects only the cross section, not the kinematical distributions. The cross sections given in table 9.2 are only used as an intermediate step when converting an experimental cross section limit to a limit on M_*, and no results to be presented depend on the actual value of M_* used in the event generation.

A set of generator level cuts on the lepton, $p_{\mathrm{T}} > 10\,\mathrm{GeV}$ and $|\eta| < 2.5$, were applied at the time of event generation, and the cross sections given in table 9.2 correspond to events passing this selection.

EFT	m_χ [GeV]	σ_{gen} [fb]	EFT	m_χ [GeV]	σ_{gen} [fb]
D1	1	$4.39 \cdot 10^{-7}$	D5d	1	7.22
D1	100	$3.32 \cdot 10^{-7}$	D5d	100	7.08
D1	200	$2.01 \cdot 10^{-7}$	D5d	200	5.88
D1	400	$6.46 \cdot 10^{-8}$	D5d	400	3.29
D1	1000	$1.60 \cdot 10^{-9}$	D5d	1000	0.237
D1	1300	$2.13 \cdot 10^{-10}$	D5d	1300	0.0454
D9	1	96.6	D5c	1	60.8
D9	100	87.0	D5c	100	57.5
D9	200	69.5	D5c	200	48.8
D9	400	36.5	D5c	400	27.9
D9	1000	2.27	D5c	1000	1.92
D9	1300	0.412	D5c	1300	0.351

Table 9.2: Signal MC samples for DM particle production in association with a leptonically decaying W boson. The column labeled "σ_{gen}" contains the cross sections calculated by the generator. All cross sections are for the sum of the three leptonic W boson decay modes and correspond to the parameter value $M_* = 1\,\text{TeV}$ used in the event generation. All samples were generated with 40000 events.

9.1.2 Cross section scaling

As already mentioned, the choice of value for M_* in the event generation is unimportant, and affects only the cross section. Clearly, the cross section scales in a trivial way with M_*, as the point coupling vertex in the Feynman diagrams of fig. 9.2 is associated with a factor $1/M_*^n$ with $n = 2$ for D5 and D9 and $n = 3$ for D1. As the cross section is proportional to the squared Feynman amplitude, it scales as $\sigma \propto 1/M_*^{2n}$. Given an exclusion limit on the cross section, σ_{limit}, the corresponding limit on M_* is found by

$$M_*^{\text{limit}} = M_*^{\text{gen}} \left(\frac{\sigma_{\text{gen}}}{\sigma_{\text{limit}}} \right)^{\frac{1}{2n}} \tag{9.1}$$

with $M_*^{\text{gen}} = 1\,\text{TeV}$ as the value of M_* used in the event generation and σ_{gen} as the corresponding cross section given in table 9.2.

It is clear that the drastically lower cross sections in the D1 EFT is due to the additional factor m_q/M_* in the coefficient of the interaction term compared to the D5 and D9 models. As we will see, the proportionality of the coupling with the quark mass leads to a cross section which is dominated by processes involving the charm quark. The resulting cross section suppression factor $(m_c/M_*)^2$ is of the order 10^{-6} for $M_* = 1\,\text{TeV}$, and additional suppression of the D1 cross sections relative to the cross sections in the other models comes from the natural PDF suppression of charm quarks in the proton.

9.1.3 The mono-W signal at the generator level

We familiarize ourselves with the mono-W signal by plotting a few generator level quantities. We consider first the invariant mass of the four final state particles; the two DM particles, the

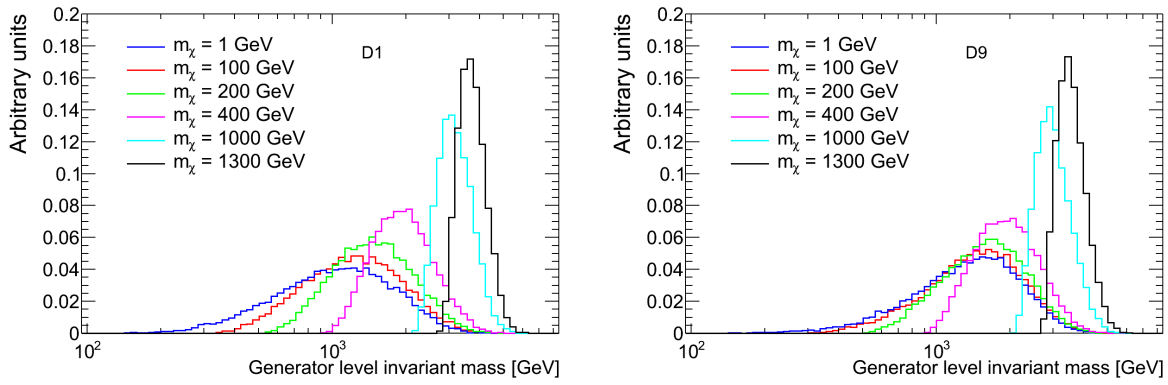

(a)

(b)

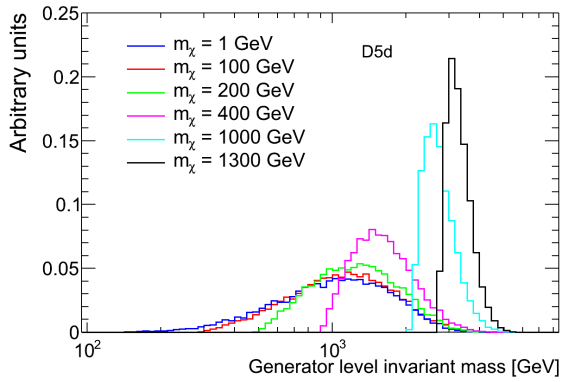

(c)

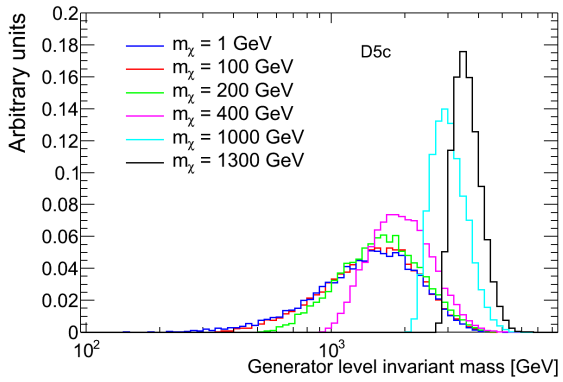

(d)

Figure 9.3: Distributions of the generator level invariant mass of the four final state particles of the mono-W signal; the two DM particles, the lepton, and the neutrino. The distributions are shown for the D1 (a), D9 (b), D5d (c), and D5c (d) signal models. The distributions corresponding to the different DM particle masses are normalized to the same area for a pure shape comparison.

lepton, and the neutrino. The distribution is shown for the different signal models in fig. 9.3. The distributions look rather similar in the different models, but have a strong DM particle mass dependence due to the threshold at the invariant mass $m_{\chi\bar{\chi}l\nu} = 2m_\chi + m_W$.

We proceed to consider the generator level lepton p_T, which is shown in fig. 9.4. Furthermore, we consider the generator level missing transverse energy in fig. 9.5, defined as the negative vector sum of the transverse momenta of the two DM particles and the neutrino, i.e.

$$\not{\mathbf{E}}_\mathrm{T}^\mathrm{gen} = -\left(\mathbf{p}_\mathrm{T}^\chi + \mathbf{p}_\mathrm{T}^{\overline{\chi}} + \mathbf{p}_\mathrm{T}^\nu\right). \tag{9.2}$$

We note that, although the higher DM particle masses lead to very high invariant masses, the distributions of the lepton p_T and the $\not{E}_\mathrm{T}$ are quite weakly dependent on the DM particle mass. The strongest DM particle mass dependence in these distributions is seen for the D1 signal model.

We consider next the generator level transverse mass, i.e. the transverse mass calculated from the generator level lepton $\mathbf{p}_\mathrm{T}$ and $\not{\mathbf{E}}_\mathrm{T}$, in fig. 9.6. It is clear that the transverse mass distribution in the mono-W events extends to quite large values. This means that a favorable

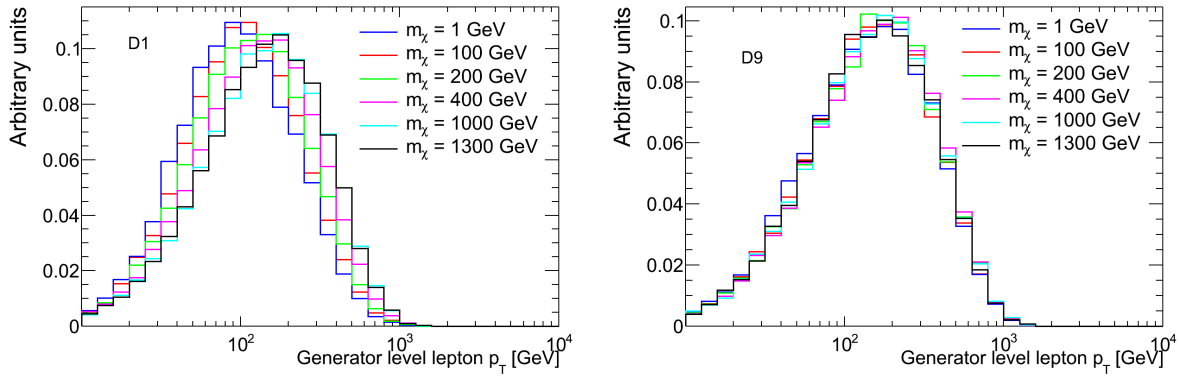

(a)

(b)

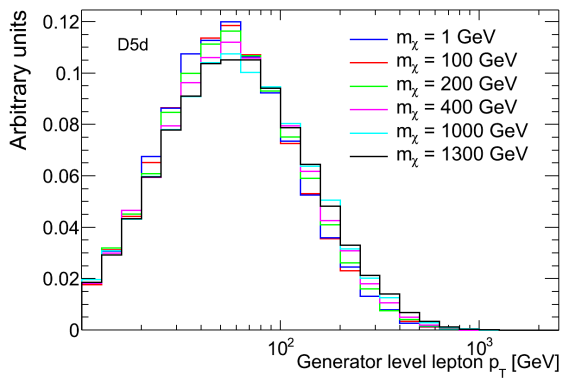

(c)

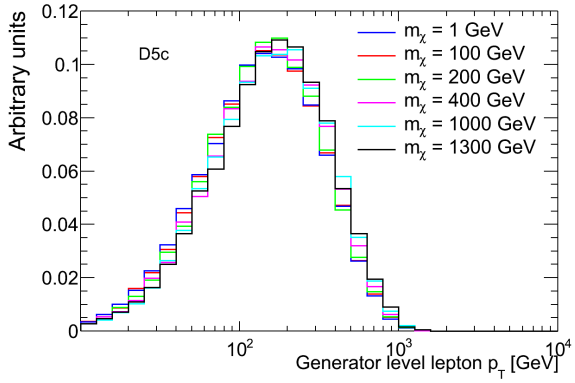

(d)

Figure 9.4: Distributions of the generator level lepton p_{T} for the mono-W signal. The distributions are shown for the D1 (a), D9 (b), D5d (c), and D5c (d) signal models. The distributions corresponding to the different DM particle masses are normalized to the same area for a pure shape comparison.

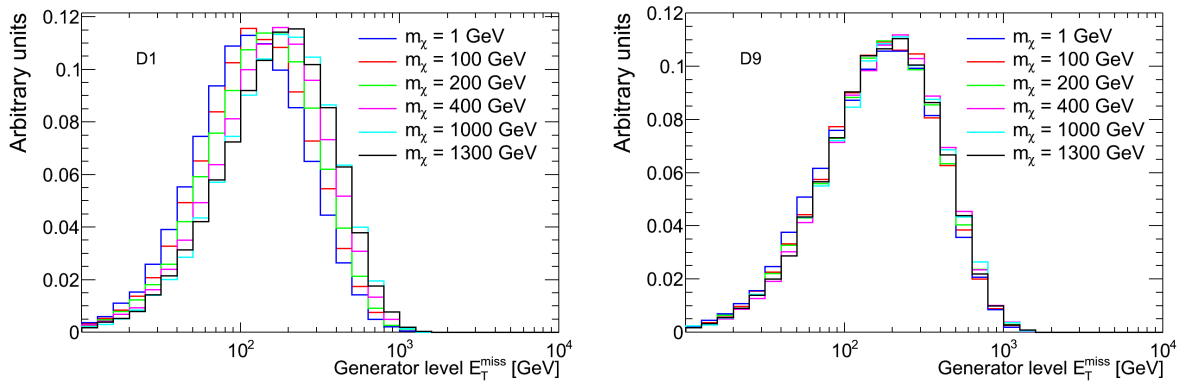

(a)

(b)

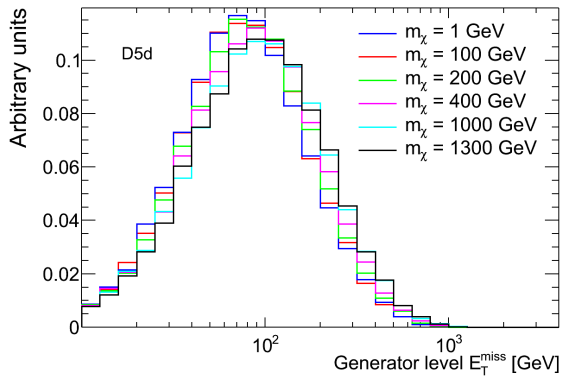

(c)

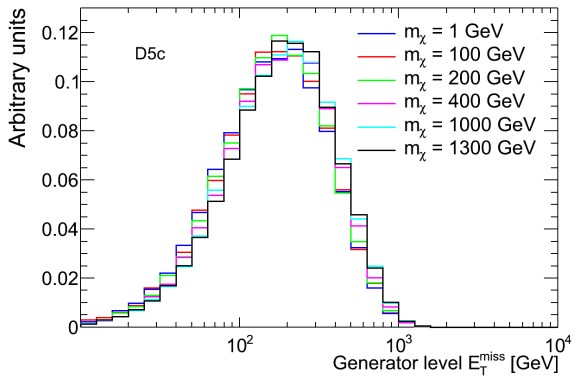

(d)

Figure 9.5: Distributions of the generator level $\not{E}_{\mathrm{T}}$ for the mono-W signal. The distributions are shown for the D1 (a), D9 (b), D5d (c), and D5c (d) signal models. The distributions corresponding to the different DM particle masses are normalized to the same area for a pure shape comparison.

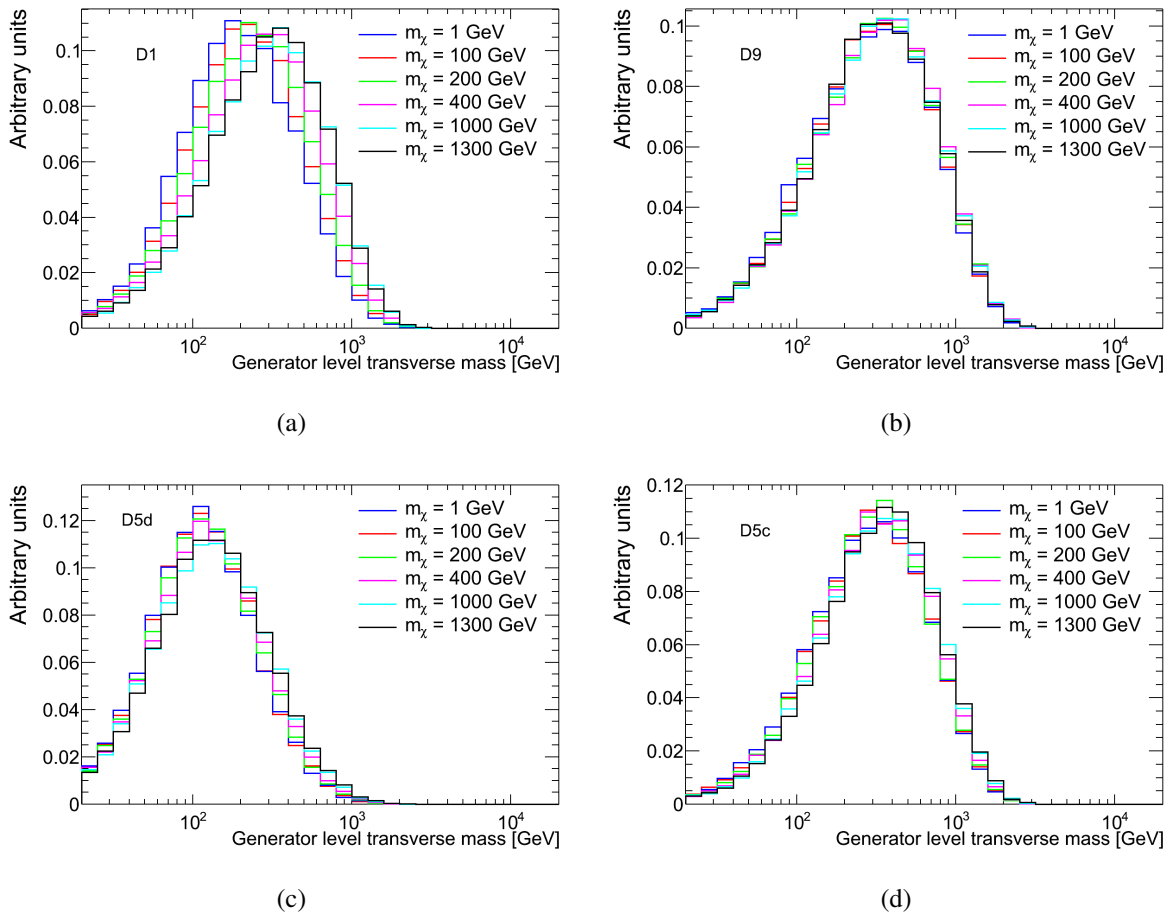

Figure 9.6: Distributions of the generator level transverse mass for the mono-W signal. The distributions are shown for the D1 (a), D9 (b), D5d (c), and D5c (d) signal models. The distributions corresponding to the different DM particle masses are normalized to the same area for a pure shape comparison.

signal-to-background ratio can be achieved with a transverse mass cut, and the mono-W signal is thus well suited to be constrained by this analysis. As the p_{T} and $\not{E}_{\mathrm{T}}$ distributions, also the transverse mass distribution is quite weakly dependent on the DM particle mass, with the strongest dependence seen for the D1 model.

Finally, we look at the quark flavor composition in the mono-W signal. The distribution of the interacting quark species identity is shown in fig. 9.7. The flavor composition is quite similar in the D9, D5d, and D5c signal models, with up and down quarks dominating as one would expect. We see that the positive charge combination $u + \overline{d}$ dominates over the negative combination $\overline{u} + d$ as expected from the valence quark content of the proton.

The situation is drastically different in the D1 case because of the proportionality of the coupling with the quark mass, which leads to a preference for the heavier quark species. We see that charm quarks are abundant because of their large mass. Looking in detail at the values in the histogram, we find that a c or $\overline{c}$ quark is present in more than 99% of the events for $m_\chi = 1\,\mathrm{GeV}$ and almost 97% of the events for $m_\chi = 1.3\,\mathrm{TeV}$. The lighter quarks are thus present almost exclusively to the extent to which they couple to the c and $\overline{c}$ quarks via the $q\,\overline{q'} \to W$ vertex. In particular, many s and $\overline{s}$ quarks are present because of the $c\,\overline{s} \to W^+$ and $\overline{c}\,s \to W^-$ vertices.

There is also a significant amount of d quarks due to the CKM suppressed $\bar{c}\,d \rightarrow W^-$ vertex, for which the corresponding mono-W process occurence is amplified by the valence d quark content in the proton.

We note some DM particle mass dependence of the flavor composition. Such dependence can be expected from differences in the momentum fraction dependencies of the different quark densities in the proton combined with the difference in invariant mass distributions between the different DM particle masses[1], but the dependence is not analyzed here in more detail.

Finally, it is worth noting that b quarks as initial state partons (proton constituents) must be explicitly turned on in MadGraph and that this was not done for the generation of the DM MC samples. While b quark initiated processes are usually negligible, the quark mass proportionality in the D1 model clearly warrants an estimate of the expected b quark initiated contribution to the cross section. The b ($\bar{b}$) quark must couple to the $\bar{c}$ (c) quark in the mono-W process, and the CKM matrix element V_{cb} enters ($|V_{cb}| \approx 0.04$ [1]). Taking into account the quark masses, the $c + b$ subprocess is already estimated to be at the level of 1-3% compared to $c + s$ before taking into account additional PDF suppression. The absence of b quark initiated processes is therefore assumed to be a negligible effect.

9.1.4 The direct detection cross section

Direct detection experiments are designed to detect the interaction of DM particles with the nuclei in the material of the experimental setup. At the fundamental level, such an interaction is between the quarks in the nucleus and the DM particle, and must hence be governed by the same physics as DM particle production at the LHC. It should thus be possible to convert a limit based on LHC data to a limit on the DM-nucleon scattering cross section, in terms of which direct detection limits are presented. Within the EFT approach, the scattering of a DM particle off a quark is described by the Feynman diagram obtained by rotating the right diagram of fig 9.1 by $90°$.

The DM-nucleon cross sections have been calculated within the EFTs considered in this analysis. They are presented in ref. [130] and based on ref. [133], and are given as[2]

$$\sigma^{\mathrm{D1}}_{\chi-N} = 1.60 \cdot 10^{-37}\,\mathrm{cm}^2 \times \left(\frac{\mu_\chi}{1\,\mathrm{GeV}}\right)^2 \left(\frac{20\,\mathrm{GeV}}{M_*}\right)^6 \tag{9.3}$$

for D1,

$$\sigma^{\mathrm{D9}}_{\chi-N} = 4.7 \cdot 10^{-39}\,\mathrm{cm}^2 \times \left(\frac{\mu_\chi}{1\,\mathrm{GeV}}\right)^2 \left(\frac{300\,\mathrm{GeV}}{M_*}\right)^4 \tag{9.4}$$

for D9,

$$\sigma^{\mathrm{D5d}}_{\chi-N} = 1.38 \cdot 10^{-37}\,\mathrm{cm}^2 \times \left(\frac{\mu_\chi}{1\,\mathrm{GeV}}\right)^2 \left(\frac{300\,\mathrm{GeV}}{M_*}\right)^4 \tag{9.5}$$

[1]The momentum fractions x_1 and x_2 of the interacting partons are related to the invariant mass m of the interaction via $m = \sqrt{x_1 x_2 s}$ with s as the squared pp center of mass energy.

[2]There was a typographical error in the expression for the D9 cross section in ref. [130], and the expression given here should be the correct one. Furthermore, the D5c case was not considered in ref. [130], and the corresponding cross section was provided for ATLAS by the authors of ref. [131].

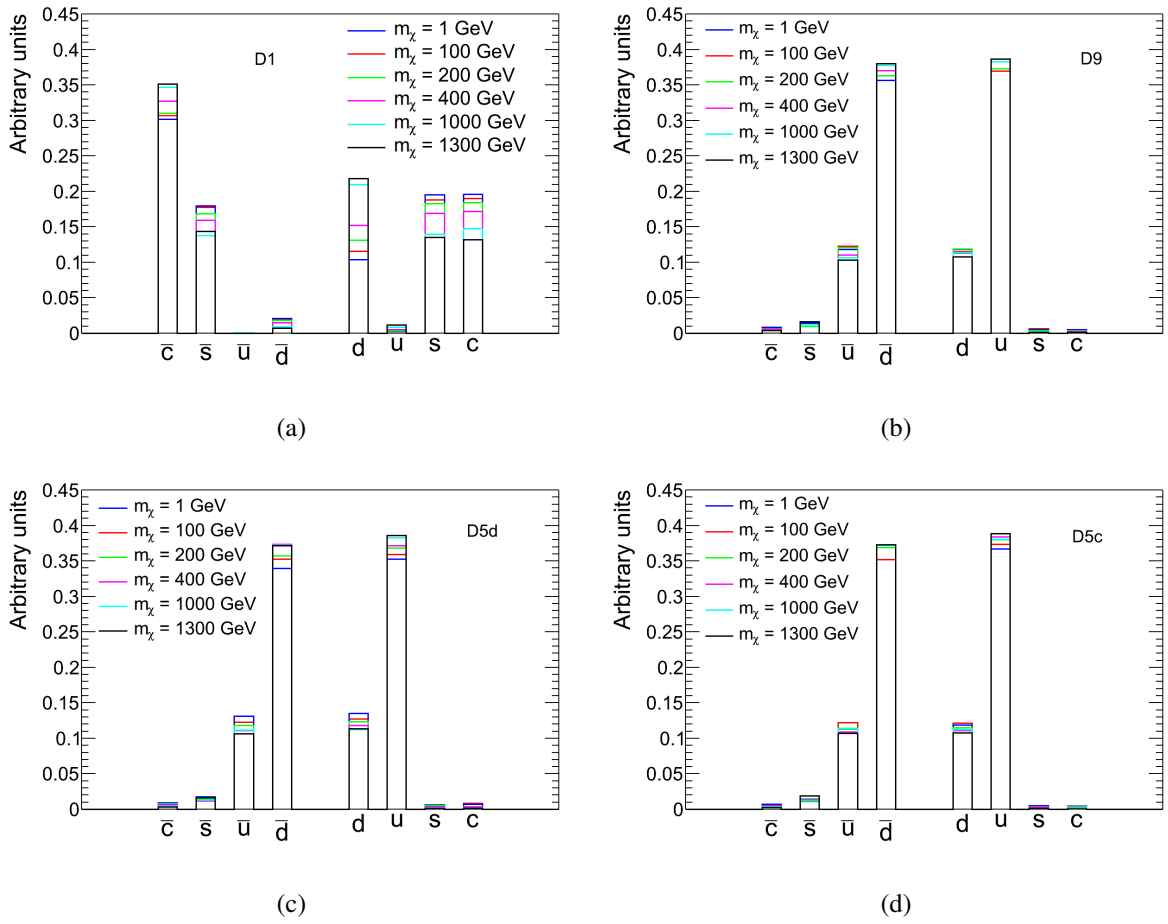

Figure 9.7: The quark flavor composition of the mono-W signal. The composition is shown for the D1 (a), D9 (b), D5d (c), and D5c (d) signal models. The histograms are normalized to sum to unity for all DM particle masses.

for D5d, and finally

$$\sigma_{\chi-N}^{\mathrm{D5c}} = 1.5 \cdot 10^{-38}\,\mathrm{cm}^2 \times \left(\frac{\mu_\chi}{1\,\mathrm{GeV}}\right)^2 \left(\frac{300\,\mathrm{GeV}}{M_*}\right)^4 \tag{9.6}$$

for D5c. In all these expressions, $\mu_\chi = (m_\chi^{-1} + m_N^{-1})^{-1}$ is the reduced mass of the DM-nucleon system, and we use the value $m_N = 939\,\mathrm{MeV}$ for the nucleon mass.

9.1.5 Validity of the effective field theory

The EFT approach is only valid when the four-momentum p transferred in the quark-DM point coupling is much smaller than the mass M of the particle mediating the interaction, i.e. $p^2 \ll M^2$. Only in this limit are results obtained in the EFT a good approximation to those obtained in the more complete theory containing the mediator particle of mass M explicitly. It is not obvious that the EFT description is adequate at the LHC due to the potentially large momentum transfers in the quark-DM vertex [134–136].

The validity of the EFT approximation has been studied in the context of the ATLAS mono-jet search [137]. In this study, it was found that the validity requirement for the EFT approxima-

tion could certainly be violated, but that there were also parts of the parameter space where good validity occured. The degree of validity depends in particular on the couplings of the mediator particle to quarks and DM particles in the underlying theory, for which there is not necessarily a theoretically motivated value. The validity also depends on the DM particle mass, as the minimum value of p^2 for s-channel production of two DM particles is $2m_\chi$, so that validity becomes a bigger concern for high DM particle masses.

Ref. [137] includes also a comparison of results obtained in a toy model with an explicitly included vector boson mediating the quark-DM interaction to the corresponding EFT results. As one expects, the EFT limits are found to coincide with the limits obtained in the toy model when the mediator mass becomes large. EFT limits are observed to be conservative in an intermediate mass range in which the mediator can be produced on-shell, meaning that the limits obtained in the toy model are stronger than the EFT limits in this region. Finally, for low mediator masses, the EFT is found to lead to an overestimated sensitivity. Results in the toy model are found to depend strongly on the mediator width. In particular, the increase in sensitivity due to on-shell production in the intermediate mediator mass range is much more pronounced for the lower choice of width, $\Gamma = M/(8\pi)$, than for the higher choice, $\Gamma = M/3$.

We do not make any attempt to study the EFT validity in this analysis. We note that the EFT is useful as a benchmark model for comparison between collider results even if it does not well approximate a particular underlying theory. When considering results on the DM-nucleon cross section, we should keep in mind that these results assume the EFT to be valid.

9.2 PDF uncertainty

In the case of the W' and W^* signal models, we saw that the dominant uncertainty on the signal efficiency at high mass came from the k-factor uncertainty, which was dominated by PDF uncertainties. Given the very high invariant masses probed in the DM signal models (see fig. 9.3), we expect that PDF uncertainties could become important for the DM signal efficiency as well. We evaluate this uncertainty using PDF reweighting and following the prescription of ref. [81] for Hessian PDF sets and asymmetric errors. The uncertainty is made symmetric in the usual way by taking the maximum of the upward and downward uncertainties as the final symmetric uncertainty.

The DM signal is generated with the MSTW 2008 LO PDFs. As mentioned in the context of the W^* signal model, LO PDF uncertainties are regarded as too optimistic, and we consider therefore some different possibilities for the PDF uncertainty. The obvious choice for a LO PDF is to reweight the signal efficiency to each of the accompanying PDF variations (so-called eigenvector variations) to obtain the corresponding uncertainty on the signal efficiency. Since LO PDF uncertainties are regarded as too optimistic, we consider also an additional possibility: reweighting first the central value of the efficiency to the MSTW 2008 NNLO PDFs and thereafter reweighting to all of the accompanying eigenvector variations to obtain an uncertainty. The *relative* signal efficiency uncertainty obtained with the NNLO PDF set is then taken to apply to the signal efficiency evaluated with the default LO PDF. Hence, the central value evaluated with the NNLO PDF set is used only as an intermediate step to obtain the relative uncertainty, while the signal efficiency evaluated with the LO PDF set is used as the central value, since a

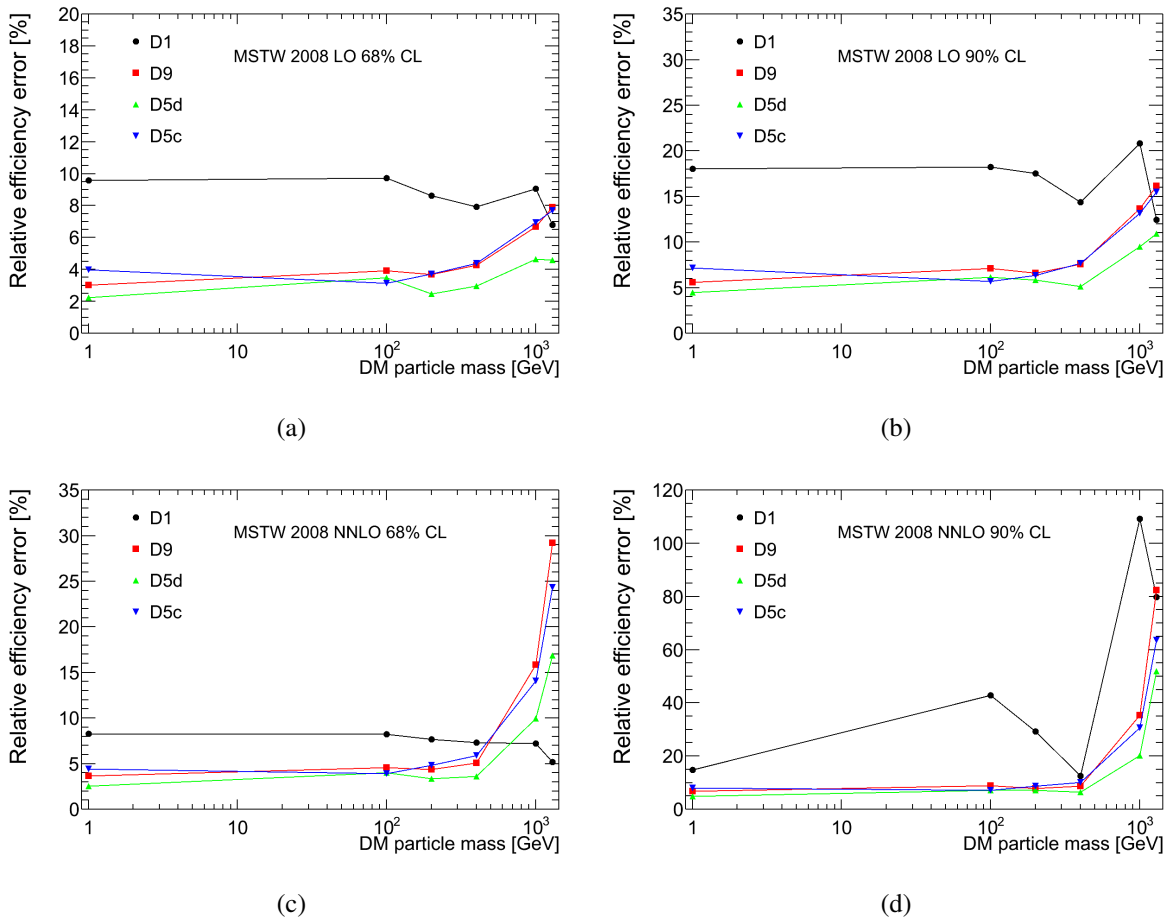

Figure 9.8: The relative signal efficiency uncertainties due to PDF uncertainties in the muon channel obtained with the MSTW 2008 LO ((a) and (b)) and NNLO ((c) and (d)) PDFs both for 68% CL ((a) and (c)) and 90% CL ((b) and (d)) eigenvector variations.

LO PDF is appropriate when generating signal at LO.

Fig. 9.8 shows the relative signal efficiency uncertainties in the muon channel obtained with the MSTW 2008 LO and NNLO PDFs both for 68% CL and 90% CL eigenvector variations. The uncertainties are evaluated for the optimal m_{T} thresholds shown in table 9.4, which are based on the optimization described in section 9.4. Several features should be noted in these plots. It is clear that the NNLO PDF uncertainties lead to larger signal efficiency uncertainties than the LO ones as expected. There is some lack of clear trends in some of the uncertainty curves, in particular for D1. The lack of clear trends may to some extent be due to statistical fluctuations because of limited statistics in the DM signal MC samples. Indeed, we will see that the DM signal samples are somewhat statistics limited, but the largest fluctuations are in general seen for the D5d model, while the largest fluctuations in fig. 9.8 occur for the D1 model. It thus seems that the large fluctuations for the D1 model may have a significant contribution besides limited MC statistics, and this is believed to come from features in the PDF variations for the charm and strange quarks in the proton. It is in any case natural to assume that the overall larger uncertainties observed for D1 than for the other models is due to the preference for heavier quarks in this model.

For the models other than D1, the PDF uncertainty on the signal efficiency is quite small

for low DM particle masses, with the uncertainty not significantly exceeding 10% for $m_\chi \leq 400\,\mathrm{GeV}$ even for the most conservative choice of NNLO uncertainties at 90% CL. For the highest masses, however, the uncertainty becomes substantially larger, reaching 80% for the D9 model at the highest DM particle mass in the case of NNLO uncertainties at 90% CL. The LO uncertainties at 68% CL were chosen for the DM limit calculations in order for this analysis to stay as consistent as possible with already published ATLAS results, and this choice is compared to the more conservative possibilities in section 9.7.

One may argue that, since any uncertainty will be interpreted as a 1σ variation in the statistical analysis, the 90% CL PDF uncertainties should be "scaled back to 1σ" by dividing by 1.645, since this is the "number of sigmas" corresponding to a 90% confidence interval. However, a pure statistical interpretation of PDF uncertainties is rendered impossible by the need for a scaling of the relevant $\Delta\chi^2$ thresholds due to e.g. apparent inconsistencies between the different data sets entering the fit, incorrectly estimated uncertainties, and/or insufficient flexibility in the PDF parametrization [81, 138, 139]. Therefore, we interpret the 90% CL uncertainties simply as more conservative estimates of the PDF uncertainty, and we do not scale back to 1σ, neither for the numbers of fig. 9.8 nor when these are propagated to the statistical analysis in section 9.7. We note that this was also the prescription followed for the PDF uncertainties on the invariant mass dependent k-factors (section 4.1.1).

We argued that correlation of the k-factor uncertainty between signal and background was warranted in the case of the W'/W^* interpretation of this analysis (see section 8.3.2). For the DM search, the signal and background processes occur at very different invariant masses (and hence momentum fractions) for the highest DM particle masses where the signal efficiency uncertainty is the largest. This can be understood by comparing the values of the m_T thresholds in table 9.4, characteristic of the invariant mass in the dominant $W \to l\,\nu$ background process, to the invariant mass distributions in fig. 9.3. Hence, it is not obvious that full correlation of the PDF uncertainty for the signal efficiency and background level is warranted for the DM signal. While some correlation might certainly be present, taking into account this kind of partial correlation can only be properly done with a more advanced statistical analysis where the different eigenvector variations of the PDFs are represented by different nuisance parameters whose variations are propagated properly to the signal efficiencies and background levels. It was chosen to assume no correlation between signal and background for the DM limit calculations. This was motivated by the separate mass scales of the background and signal as well as arguments of consistency with already published ATLAS results.

9.3 Limit setting for the dark matter signal

We calculate limits on the DM signal using the same procedure as for the W'/W^* limit calculations described in chapters 7 and 8. The signal efficiency and its uncertainty are calculated with the use of the DM signal MC samples, and the corresponding reconstruction level transverse mass distributions are shown for the muon channel in fig. 9.9. These look rather similar to the generator level distributions shown in fig. 9.6 except for the fact that the reconstruction level distributions have a threshold around $90\,\mathrm{GeV}$ due to the cuts on the muon p_T and the $\not{E}_\mathrm{T}$, both at $45\,\mathrm{GeV}$.

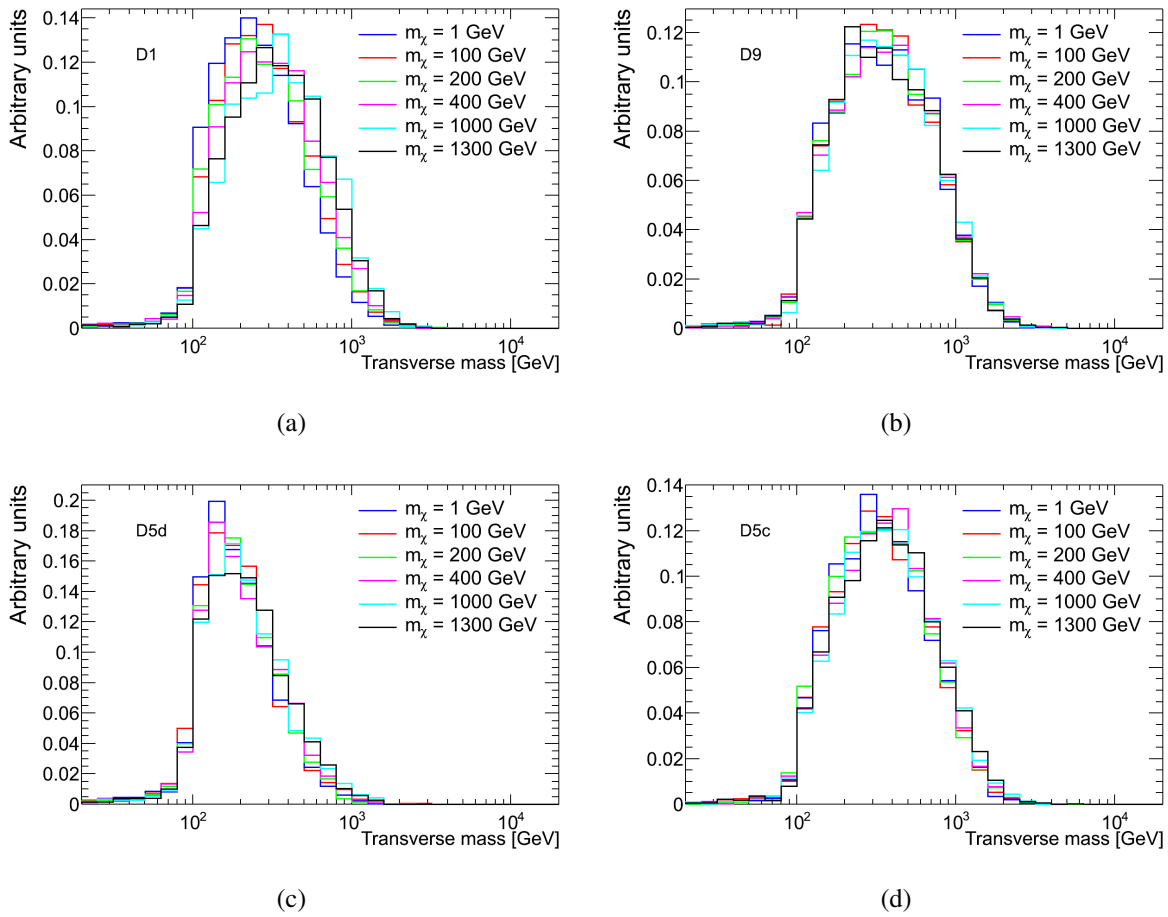

Figure 9.9: Distributions of the muon channel reconstructed transverse mass for the mono-W signal. The distributions are shown for the D1 (a), D9 (b), D5d (c), and D5c (d) signal models. The distributions corresponding to the different DM particle masses are normalized to the same area for a pure shape comparison.

Most of the signal efficiency uncertainties are calculated in exactly the same way for the DM search as for the W'/W^* search. The only exceptions are the k-factor uncertainty, which is essentially replaced by the PDF uncertainty described in section 9.2, and the beam energy uncertainty, which has not been evaluated for the DM signal. The PDF uncertainty is treated as correlated between the signal efficiencies in the electron and muon channels, but not correlated between signal efficiencies and background levels, as already discussed.

We take the parameter of interest in the limit setting to be the cross section for the mono-W process with the decay $W \rightarrow l\nu$ with l denoting a single lepton generation, i.e. the parameter of interest is not taken to be the inclusive cross section for the three leptonic W decay modes. However, we do allow the tau decays of the W boson with subsequent decay of the tau lepton to an electron or muon to contribute to the signal strength, i.e. these events are included in the numerator of the signal efficiency, eq. (8.2). We argue that there is no motivation for excluding such signal, as the W boson in the mono-W events is the usual SM particle, and its decays to all lepton generations are firmly established.

Fiducial cross section limits have not been studied in the context of the DM interpretation, although the PDF uncertainty on the signal efficiency could most likely be reduced with a

fiducial cut on the generator level transverse mass. However, the parameter of interest in the limit setting is the cross section within the phase space region defined by the generator level cuts on the lepton, $p_{\mathrm{T}} > 10\,\mathrm{GeV}$ and $|\eta| < 2.5$, not the total cross section.

While 95% CL limits are customary in high energy physics, 90% CL limits are typically reported by DM direct detection experiments and are therefore also widely used in collider searches for DM particles. All limits presented in this chapter are at 90% CL, and the difference wrt. 95% CL limits is quantified in section 9.8.

9.4 Transverse mass threshold optimization

The transverse mass threshold is optimized in the same way as for W'/W^*, with a separate optimization for each signal model and DM particle mass. Results presented here are for the muon channel. No separate optimization has been performed for the electron channel, and the same thresholds are used for the electron and muon channels.

A few example optimization plots for the D1, D5c, and D9 signal models are shown in fig. 9.10. The median limit does not appear completely smooth even for thresholds below $1\,\mathrm{TeV}$. In figs. 8.5 and 8.6, the median limit does look completely smooth in this region, and we argue that the lack of smoothness in fig. 9.10 is due to statistical fluctuations in the DM signal MC samples. The fact that the DM signal MC samples are statistically limited can be understood from the fact that the optimal thresholds around $800\,\mathrm{GeV}$ cut very hard into the transverse mass distributions shown in fig. 9.9, so that the number of events passing the transverse mass cut is relatively low. The situation is even worse for the D5d signal model, as the example optimization plots in fig. 9.11 illustrate. The complete set of optimization plots is given in section A.2 of appendix A.

The optimal thresholds obtained by the optimization procedure are shown in table 9.3. Considering first the D1, D9, and D5c signal models, we see that the optimal thresholds obtained for the different DM particle masses within a given model are quite close to each other, and that a single threshold is optimal for the majority of the DM particle masses within each model. Since the optimal threshold within a given model has no clear trend as function of the DM particle mass, we argue that the thresholds differing from the most frequently occuring one within each model are most likely due to statistical fluctuations, and we use the most frequently occuring threshold for the limit evaluation for all DM particle masses. We thus use $m_{\mathrm{T}}^{\mathrm{min}} = 843\,\mathrm{GeV}$ for the D9 and D5c models, and $m_{\mathrm{T}}^{\mathrm{min}} = 796\,\mathrm{GeV}$ for the D1 model. The impact on the median limit under the background-only hypothesis associated with this change of thresholds is about 5% for the D1 model with $m_\chi = 100\,\mathrm{GeV}$, 2% for D5c with $m_\chi = 1.3\,\mathrm{TeV}$, and below 2% for all m_χ in the D9 model.

Considering finally the D5d signal model, we note quite large fluctuations in the optimal threshold as function of the DM particle mass. There is not one frequently occuring threshold that sticks out, but we argue that choosing a single threshold is reasonable also for the D5d model, as the different optimal thresholds obtained for the different DM particle masses are clearly due to statistical fluctuations. We choose the threshold $m_{\mathrm{T}}^{\mathrm{min}} = 597\,\mathrm{GeV}$, and the corresponding impact on the median limit under the background-only hypothesis associated with this change of thresholds is about 25% for $m_\chi = 100\,\mathrm{GeV}$ and below 10% for the higher

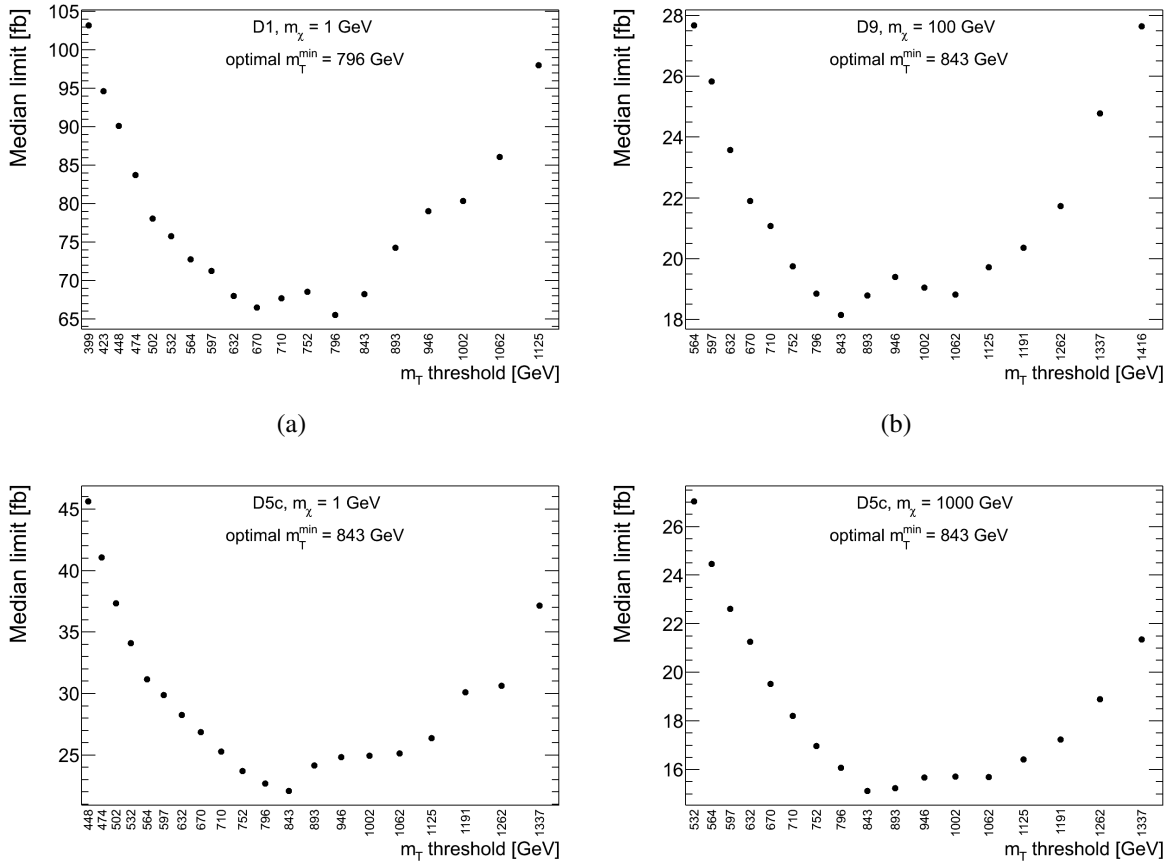

(a) (b)

(c) (d)

Figure 9.10: The median limit under the background-only hypothesis as function of the m_{T} threshold for the DM signal. The plot is shown for the D1 model with the DM particle mass $m_\chi = 1\,\mathrm{GeV}$ (a), the D9 model with $m_\chi = 100\,\mathrm{GeV}$ (b), and the D5c model with $m_\chi = 1\,\mathrm{GeV}$ (c) and $m_\chi = 1\,\mathrm{TeV}$ (d). The minimum median limit defines the optimal threshold.

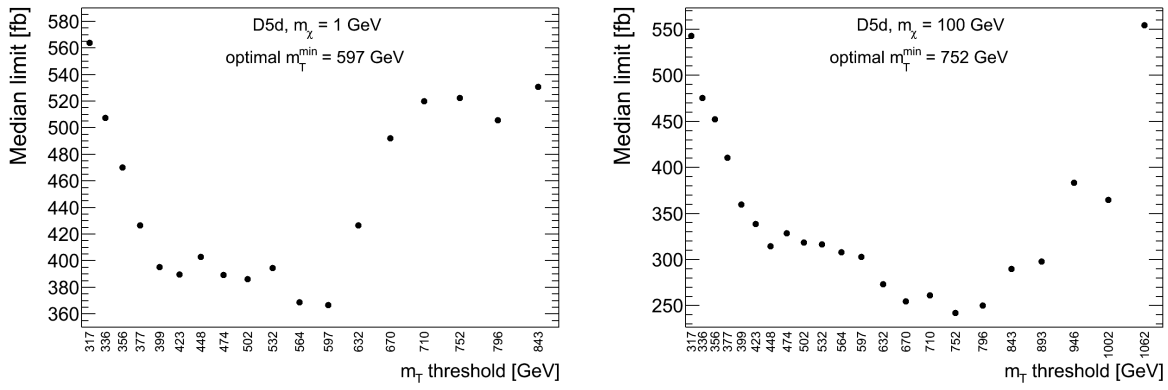

(a) (b)

Figure 9.11: The median limit under the background-only hypothesis as function of the m_{T} threshold for the DM signal. The plot is shown for the D5d model with the DM particle mass $m_\chi = 1\,\mathrm{GeV}$ (a) and $m_\chi = 100\,\mathrm{GeV}$ (b). The minimum median limit defines the optimal threshold.

EFT	m_χ [GeV]	Optimal threshold [GeV]	EFT	m_χ [GeV]	Optimal threshold [GeV]
D1	1	796	D5d	1	597
D1	100	843	D5d	100	752
D1	200	796	D5d	200	502
D1	400	796	D5d	400	423
D1	1000	796	D5d	1000	843
D1	1300	796	D5d	1300	670
D9	1	843	D5c	1	843
D9	100	843	D5c	100	843
D9	200	843	D5c	200	843
D9	400	1062	D5c	400	843
D9	1000	1002	D5c	1000	843
D9	1300	893	D5c	1300	1002

Table 9.3: The optimal transverse mass thresholds obtained by the standard optimization procedure. For each signal model and DM particle mass, the optimal threshold is defined as the one giving the lowest median limit under the background-only hypothesis.

EFT	D1	D5d	D5c	D9
Threshold [GeV]	796	597	843	843

Table 9.4: The chosen transverse mass thresholds to be used for limit calculations for the DM signal. A single threshold is used for all DM particle masses for a given signal model (EFT).

DM particle masses. The chosen thresholds for the different signal models are summarized in table 9.4.

9.5 Summary of systematic uncertainties

The systematic uncertainties on the DM signal efficiencies are presented in the same form as for the W'/W^* in tables 9.5-9.12. We note that the MC statistical uncertainty gives a significant contribution to the total uncertainty, as expected from considerations in the previous sections. The statistical uncertainty is largest for the D5d signal model, and this fits well with the fact that the largest fluctuations in the threshold optimizations were observed for this model.

As the m_{T} thresholds used for the DM search were also encountered in the W'/W^* searches, the background uncertainty tables 8.2 and 8.3 contain all background uncertainty information relevant also for the DM search. Finally, the inputs to the DM limit calculations are presented in tables 9.13-9.20.

Source	m_χ, $m_{\mathrm{T}}^{\mathrm{min}}$ [GeV]					
	1	100	200	400	1000	1300
	796	796	796	796	796	796
Efficiency	2.6	2.6	2.5	2.5	2.5	2.6
Resolution	0.71	0.75	0.59	0.42	0.26	1.1
Scale	3.8	1.6	3.4	1.2	1.8	1.3
$\not\!\!E_{\mathrm{T}}$	0.91	0.50	0.96	0.21	0.31	0.33
Jet resolution	1.1	0.38	0.57	0.78	0.23	0.40
Jet scale	0.68	0.87	0.48	0.38	0.084	0.39
All experimental	4.9	3.3	4.4	3.0	3.1	3.1
MC statistics	6.4	5.6	4.9	4.1	3.5	3.6
All uncorrelated	8.0	6.5	6.6	5.1	4.7	4.8
PDF	13	11	9.7	8.6	9.2	8.6
All correlated	13	11	9.7	8.6	9.2	8.6
Total	15	13	12	10	10	9.8

Table 9.5: Electron channel relative signal efficiency uncertainties in percent for the D1 signal model.

Source	m_χ, $m_{\mathrm{T}}^{\mathrm{min}}$ [GeV]					
	1	100	200	400	1000	1300
	597	597	597	597	597	597
Efficiency	2.7	2.6	2.5	2.5	2.4	2.5
Resolution	1.8	2.2	0.92	1.9	0.88	1.2
Scale	2.9	4.0	3.4	4.5	3.0	2.4
$\not\!\!E_{\mathrm{T}}$	0.88	2.3	0.82	1.4	0.92	0.28
Jet resolution	1.2	1.8	0.64	0.97	0.79	1.4
Jet scale	0.99	1.3	0.80	2.0	1.4	0.91
All experimental	4.7	6.2	4.5	6.1	4.4	4.0
MC statistics	9.1	8.9	9.0	7.8	6.6	6.5
All uncorrelated	10	11	10	9.9	8.0	7.7
PDF	4.4	3.0	2.9	3.5	4.2	5.6
All correlated	4.4	3.0	2.9	3.5	4.2	5.6
Total	11	11	10	10	9.0	9.5

Table 9.6: Electron channel relative signal efficiency uncertainties in percent for the D5d signal model.

Source	m_χ, $m_{\mathrm{T}}^{\mathrm{min}}$ [GeV]					
	1	100	200	400	1000	1300
	843	843	843	843	843	843
Efficiency	2.6	2.5	2.5	2.5	2.5	2.5
Resolution	0.49	0.14	0.47	0.41	0.24	0.11
Scale	1.9	1.7	1.4	2.2	1.7	1.6
$\not\!\!E_{\mathrm{T}}$	0.29	0.076	0.32	0.31	0.26	0.073
Jet resolution	0.16	0.50	0.084	0.39	0.13	0.17
Jet scale	0.15	0.11	0.020	0.19	0.083	0.16
All experimental	3.3	3.1	3.0	3.4	3.0	3.0
MC statistics	4.1	3.9	4.0	3.7	3.5	3.4
All uncorrelated	5.2	5.0	5.0	5.0	4.6	4.5
PDF	3.7	3.7	4.1	4.0	8.1	8.3
All correlated	3.7	3.7	4.1	4.0	8.1	8.3
Total	6.4	6.2	6.4	6.4	9.3	9.4

Table 9.7: Electron channel relative signal efficiency uncertainties in percent for the D5c signal model.

Source	m_χ, $m_{\mathrm{T}}^{\mathrm{min}}$ [GeV]					
	1	100	200	400	1000	1300
	843	843	843	843	843	843
Efficiency	2.5	2.5	2.5	2.5	2.5	2.5
Resolution	0.98	0.15	0.81	0.074	0.51	0.36
Scale	2.1	2.1	1.6	1.5	1.7	1.3
$\not\!\!E_{\mathrm{T}}$	0.27	0.29	0.42	0.11	0.15	0.31
Jet resolution	0.52	0.18	0.29	0.34	0.30	0.42
Jet scale	0.26	0.24	0.27	0.079	0.078	0.18
All experimental	3.5	3.3	3.2	3.0	3.1	2.8
MC statistics	3.8	3.6	3.4	3.4	3.4	3.4
All uncorrelated	5.1	4.8	4.7	4.5	4.6	4.5
PDF	3.6	3.4	3.7	4.6	7.3	9.0
All correlated	3.6	3.4	3.7	4.6	7.3	9.0
Total	6.3	5.9	6.0	6.4	8.6	10

Table 9.8: Electron channel relative signal efficiency uncertainties in percent for the D9 signal model.

Source	m_χ, $m_{\mathrm{T}}^{\mathrm{min}}$ [GeV]					
	1	100	200	400	1000	1300
	796	796	796	796	796	796
Efficiency	3.4	3.4	3.5	3.4	3.4	3.5
Resolution	1.1	1.2	2.2	1.3	0.43	0.52
Scale	0.88	3.0	0.51	0.62	1.6	0.48
$\not\!\!E_{\mathrm{T}}$	1.7	1.3	0.37	1.2	0.39	0.70
Jet resolution	0.85	1.3	0.65	0.50	1.2	0.60
Jet scale	1.1	0.42	$3 \cdot 10^{-5}$	0.70	0.33	0.83
All experimental	4.2	5.1	4.2	4.0	4.0	3.7
MC statistics	8.2	6.9	6.4	5.5	4.5	4.8
All uncorrelated	9.2	8.5	7.7	6.8	6.0	6.1
PDF	9.6	9.7	8.6	7.9	9.0	6.8
All correlated	9.6	9.7	8.6	7.9	9.0	6.8
Total	13	13	12	10	11	9.1

Table 9.9: Muon channel relative signal efficiency uncertainties in percent for the D1 signal model.

Source	m_χ, $m_{\mathrm{T}}^{\mathrm{min}}$ [GeV]					
	1	100	200	400	1000	1300
	597	597	597	597	597	597
Efficiency	3.3	3.4	3.4	3.6	3.5	3.3
Resolution	1.6	2.4	0.12	3.0	1.2	1.7
Scale	2.6	0.60	1.1	2.4	0.95	1.2
$\not\!\!E_{\mathrm{T}}$	1.5	0.0	1.8	1.9	0.68	0.91
Jet resolution	0.0	0.85	3.2	1.3	1.0	1.6
Jet scale	0.0	0.049	1.5	1.9	1.3	0.53
All experimental	4.7	4.3	5.4	6.1	4.2	4.4
MC statistics	13	11	12	10	8.5	8.6
All uncorrelated	13	12	13	12	9.4	9.6
PDF	2.2	3.5	2.5	2.9	4.7	4.6
All correlated	2.2	3.5	2.5	2.9	4.7	4.6
Total	14	13	13	12	11	11

Table 9.10: Muon channel relative signal efficiency uncertainties in percent for the D5d signal model.

Source	m_χ, $m_{\mathrm{T}}^{\mathrm{min}}$ [GeV]					
	1	100	200	400	1000	1300
	843	843	843	843	843	843
Efficiency	3.5	3.5	3.4	3.5	3.4	3.5
Resolution	0.56	2.8	1.2	1.2	0.87	0.87
Scale	1.4	1.0	1.3	0.74	0.24	1.1
$\not{E}_{\mathrm{T}}$	0.50	0.64	0.63	0.18	0.68	0.46
Jet resolution	0.85	0.55	0.80	0.47	0.37	0.33
Jet scale	0.32	0.76	0.70	0.18	0.16	0.41
All experimental	3.9	4.7	4.1	3.8	3.6	3.8
MC statistics	5.3	5.3	5.2	4.8	4.3	4.5
All uncorrelated	6.6	7.1	6.6	6.1	5.7	5.9
PDF	4.0	3.1	3.7	4.4	6.9	7.7
All correlated	4.0	3.1	3.7	4.4	6.9	7.7
Total	7.7	7.8	7.6	7.5	9.0	9.7

Table 9.11: Muon channel relative signal efficiency uncertainties in percent for the D5c signal model.

Source	m_χ, $m_{\mathrm{T}}^{\mathrm{min}}$ [GeV]					
	1	100	200	400	1000	1300
	843	843	843	843	843	843
Efficiency	3.4	3.4	3.5	3.4	3.4	3.4
Resolution	0.40	1.4	0.93	0.25	1.0	0.65
Scale	0.70	0.57	0.95	1.5	1.2	0.92
$\not{E}_{\mathrm{T}}$	0.25	0.31	0.35	0.44	0.67	0.33
Jet resolution	0.15	0.11	0.47	0.32	0.58	0.15
Jet scale	0.24	0.11	0.47	0.15	0.36	0.54
All experimental	3.5	3.7	3.8	3.7	3.9	3.6
MC statistics	4.9	4.8	4.7	4.6	4.5	4.6
All uncorrelated	6.0	6.1	6.0	5.9	5.9	5.9
PDF	3.0	3.9	3.7	4.3	6.7	7.9
All correlated	3.0	3.9	3.7	4.3	6.7	7.9
Total	6.7	7.2	7.1	7.3	8.9	9.8

Table 9.12: Muon channel relative signal efficiency uncertainties in percent for the D9 signal model.

m_χ [GeV]	$m_{\mathrm{T}}^{\mathrm{min}}$ [GeV]	$\overline{\varepsilon_{\mathrm{sig}}}$	$\frac{(\Delta\varepsilon_{\mathrm{sig}})_{\mathrm{uc}}}{\overline{\varepsilon_{\mathrm{sig}}}}$ [%]	$\frac{(\Delta\varepsilon_{\mathrm{sig}})_{\mathrm{c}}}{\overline{\varepsilon_{\mathrm{sig}}}}$ [%]	$\overline{L_{\mathrm{int}}}\,\overline{\sigma_{\mathrm{bg}}^{\mathrm{eff}}}$	$\frac{(\Delta\sigma_{\mathrm{bg}}^{\mathrm{eff}})_{\mathrm{uc}}}{\overline{\sigma_{\mathrm{bg}}^{\mathrm{eff}}}}$ [%]	$\frac{(\Delta\sigma_{\mathrm{bg}}^{\mathrm{eff}})_{\mathrm{c}}}{\overline{\sigma_{\mathrm{bg}}^{\mathrm{eff}}}}$ [%]	n_{obs}
1	796	0.0294	8.0	13	116	5.0	12	101
100	796	0.0396	6.5	11	116	5.0	12	101
200	796	0.0484	6.6	9.7	116	5.0	12	101
400	796	0.0709	5.1	8.6	116	5.0	12	101
1000	796	0.0989	4.7	9.2	116	5.0	12	101
1300	796	0.0964	4.8	8.6	116	5.0	12	101

Table 9.13: Electron channel inputs to the D1 limit calculation.

m_χ [GeV]	$m_{\mathrm{T}}^{\mathrm{min}}$ [GeV]	$\overline{\varepsilon_{\mathrm{sig}}}$	$\frac{(\Delta\varepsilon_{\mathrm{sig}})_{\mathrm{uc}}}{\overline{\varepsilon_{\mathrm{sig}}}}$ [%]	$\frac{(\Delta\varepsilon_{\mathrm{sig}})_{\mathrm{c}}}{\overline{\varepsilon_{\mathrm{sig}}}}$ [%]	$\overline{L_{\mathrm{int}}}\,\overline{\sigma_{\mathrm{bg}}^{\mathrm{eff}}}$	$\frac{(\Delta\sigma_{\mathrm{bg}}^{\mathrm{eff}})_{\mathrm{uc}}}{\overline{\sigma_{\mathrm{bg}}^{\mathrm{eff}}}}$ [%]	$\frac{(\Delta\sigma_{\mathrm{bg}}^{\mathrm{eff}})_{\mathrm{c}}}{\overline{\sigma_{\mathrm{bg}}^{\mathrm{eff}}}}$ [%]	n_{obs}
1	597	0.0148	10	4.4	456	4.7	8.7	414
100	597	0.0158	11	3.0	456	4.7	8.7	414
200	597	0.0147	10	2.9	456	4.7	8.7	414
400	597	0.0190	9.9	3.5	456	4.7	8.7	414
1000	597	0.0281	8.0	4.2	456	4.7	8.7	414
1300	597	0.0291	7.7	5.6	456	4.7	8.7	414

Table 9.14: Electron channel inputs to the D5d limit calculation.

m_χ [GeV]	$m_{\mathrm{T}}^{\mathrm{min}}$ [GeV]	$\overline{\varepsilon_{\mathrm{sig}}}$	$\frac{(\Delta\varepsilon_{\mathrm{sig}})_{\mathrm{uc}}}{\overline{\varepsilon_{\mathrm{sig}}}}$ [%]	$\frac{(\Delta\varepsilon_{\mathrm{sig}})_{\mathrm{c}}}{\overline{\varepsilon_{\mathrm{sig}}}}$ [%]	$\overline{L_{\mathrm{int}}}\,\overline{\sigma_{\mathrm{bg}}^{\mathrm{eff}}}$	$\frac{(\Delta\sigma_{\mathrm{bg}}^{\mathrm{eff}})_{\mathrm{uc}}}{\overline{\sigma_{\mathrm{bg}}^{\mathrm{eff}}}}$ [%]	$\frac{(\Delta\sigma_{\mathrm{bg}}^{\mathrm{eff}})_{\mathrm{c}}}{\overline{\sigma_{\mathrm{bg}}^{\mathrm{eff}}}}$ [%]	n_{obs}
1	843	0.0737	5.2	3.7	85.6	5.1	13	79
100	843	0.0798	5.0	3.7	85.6	5.1	13	79
200	843	0.0762	5.0	4.1	85.6	5.1	13	79
400	843	0.0857	5.0	4.0	85.6	5.1	13	79
1000	843	0.0987	4.6	8.1	85.6	5.1	13	79
1300	843	0.101	4.5	8.3	85.6	5.1	13	79

Table 9.15: Electron channel inputs to the D5c limit calculation.

m_χ [GeV]	$m_{\mathrm{T}}^{\mathrm{min}}$ [GeV]	$\overline{\varepsilon_{\mathrm{sig}}}$	$\frac{(\Delta\varepsilon_{\mathrm{sig}})_{\mathrm{uc}}}{\overline{\varepsilon_{\mathrm{sig}}}}$ [%]	$\frac{(\Delta\varepsilon_{\mathrm{sig}})_{\mathrm{c}}}{\overline{\varepsilon_{\mathrm{sig}}}}$ [%]	$\overline{L_{\mathrm{int}}}\,\overline{\sigma_{\mathrm{bg}}^{\mathrm{eff}}}$	$\frac{(\Delta\sigma_{\mathrm{bg}}^{\mathrm{eff}})_{\mathrm{uc}}}{\overline{\sigma_{\mathrm{bg}}^{\mathrm{eff}}}}$ [%]	$\frac{(\Delta\sigma_{\mathrm{bg}}^{\mathrm{eff}})_{\mathrm{c}}}{\overline{\sigma_{\mathrm{bg}}^{\mathrm{eff}}}}$ [%]	n_{obs}
1	843	0.0850	5.1	3.6	85.6	5.1	13	79
100	843	0.0950	4.8	3.4	85.6	5.1	13	79
200	843	0.104	4.7	3.7	85.6	5.1	13	79
400	843	0.103	4.5	4.6	85.6	5.1	13	79
1000	843	0.107	4.6	7.3	85.6	5.1	13	79
1300	843	0.102	4.5	9.0	85.6	5.1	13	79

Table 9.16: Electron channel inputs to the D9 limit calculation.

m_χ [GeV]	$m_{\mathrm{T}}^{\mathrm{min}}$ [GeV]	$\overline{\varepsilon_{\mathrm{sig}}}$	$\frac{(\Delta\varepsilon_{\mathrm{sig}})_{\mathrm{uc}}}{\overline{\varepsilon_{\mathrm{sig}}}}$ [%]	$\frac{(\Delta\varepsilon_{\mathrm{sig}})_{\mathrm{c}}}{\overline{\varepsilon_{\mathrm{sig}}}}$ [%]	$\overline{L_{\mathrm{int}}}\,\overline{\sigma_{\mathrm{bg}}^{\mathrm{eff}}}$	$\frac{(\Delta\sigma_{\mathrm{bg}}^{\mathrm{eff}})_{\mathrm{uc}}}{\overline{\sigma_{\mathrm{bg}}^{\mathrm{eff}}}}$ [%]	$\frac{(\Delta\sigma_{\mathrm{bg}}^{\mathrm{eff}})_{\mathrm{c}}}{\overline{\sigma_{\mathrm{bg}}^{\mathrm{eff}}}}$ [%]	n_{obs}
1	796	0.0179	9.2	9.6	84.2	5.4	11	58
100	796	0.0256	8.5	9.7	84.2	5.4	11	58
200	796	0.0292	7.7	8.6	84.2	5.4	11	58
400	796	0.0399	6.8	7.9	84.2	5.4	11	58
1000	796	0.0622	6.0	9.0	84.2	5.4	11	58
1300	796	0.0519	6.1	6.8	84.2	5.4	11	58

Table 9.17: Muon channel inputs to the D1 limit calculation.

m_χ [GeV]	$m_{\mathrm{T}}^{\mathrm{min}}$ [GeV]	$\overline{\varepsilon_{\mathrm{sig}}}$	$\frac{(\Delta\varepsilon_{\mathrm{sig}})_{\mathrm{uc}}}{\overline{\varepsilon_{\mathrm{sig}}}}$ [%]	$\frac{(\Delta\varepsilon_{\mathrm{sig}})_{\mathrm{c}}}{\overline{\varepsilon_{\mathrm{sig}}}}$ [%]	$\overline{L_{\mathrm{int}}}\,\overline{\sigma_{\mathrm{bg}}^{\mathrm{eff}}}$	$\frac{(\Delta\sigma_{\mathrm{bg}}^{\mathrm{eff}})_{\mathrm{uc}}}{\overline{\sigma_{\mathrm{bg}}^{\mathrm{eff}}}}$ [%]	$\frac{(\Delta\sigma_{\mathrm{bg}}^{\mathrm{eff}})_{\mathrm{c}}}{\overline{\sigma_{\mathrm{bg}}^{\mathrm{eff}}}}$ [%]	n_{obs}
1	597	0.00798	13	2.2	301	5.4	8.5	255
100	597	0.00961	12	3.5	301	5.4	8.5	255
200	597	0.00862	13	2.5	301	5.4	8.5	255
400	597	0.0113	12	2.9	301	5.4	8.5	255
1000	597	0.0179	9.4	4.7	301	5.4	8.5	255
1300	597	0.0167	9.6	4.6	301	5.4	8.5	255

Table 9.18: Muon channel inputs to the D5d limit calculation.

m_χ [GeV]	$m_{\mathrm{T}}^{\mathrm{min}}$ [GeV]	$\overline{\varepsilon_{\mathrm{sig}}}$	$\frac{(\Delta\varepsilon_{\mathrm{sig}})_{\mathrm{uc}}}{\overline{\varepsilon_{\mathrm{sig}}}}$ [%]	$\frac{(\Delta\varepsilon_{\mathrm{sig}})_{\mathrm{c}}}{\overline{\varepsilon_{\mathrm{sig}}}}$ [%]	$\overline{L_{\mathrm{int}}}\,\overline{\sigma_{\mathrm{bg}}^{\mathrm{eff}}}$	$\frac{(\Delta\sigma_{\mathrm{bg}}^{\mathrm{eff}})_{\mathrm{uc}}}{\overline{\sigma_{\mathrm{bg}}^{\mathrm{eff}}}}$ [%]	$\frac{(\Delta\sigma_{\mathrm{bg}}^{\mathrm{eff}})_{\mathrm{c}}}{\overline{\sigma_{\mathrm{bg}}^{\mathrm{eff}}}}$ [%]	n_{obs}
1	843	0.0437	6.6	4.0	64.4	6.2	11	40
100	843	0.0436	7.1	3.1	64.4	6.2	11	40
200	843	0.0462	6.6	3.7	64.4	6.2	11	40
400	843	0.0531	6.1	4.4	64.4	6.2	11	40
1000	843	0.0640	5.7	6.9	64.4	6.2	11	40
1300	843	0.0604	5.9	7.7	64.4	6.2	11	40

Table 9.19: Muon channel inputs to the D5c limit calculation.

m_χ [GeV]	$m_{\mathrm{T}}^{\mathrm{min}}$ [GeV]	$\overline{\varepsilon_{\mathrm{sig}}}$	$\frac{(\Delta\varepsilon_{\mathrm{sig}})_{\mathrm{uc}}}{\overline{\varepsilon_{\mathrm{sig}}}}$ [%]	$\frac{(\Delta\varepsilon_{\mathrm{sig}})_{\mathrm{c}}}{\overline{\varepsilon_{\mathrm{sig}}}}$ [%]	$\overline{L_{\mathrm{int}}}\,\overline{\sigma_{\mathrm{bg}}^{\mathrm{eff}}}$	$\frac{(\Delta\sigma_{\mathrm{bg}}^{\mathrm{eff}})_{\mathrm{uc}}}{\overline{\sigma_{\mathrm{bg}}^{\mathrm{eff}}}}$ [%]	$\frac{(\Delta\sigma_{\mathrm{bg}}^{\mathrm{eff}})_{\mathrm{c}}}{\overline{\sigma_{\mathrm{bg}}^{\mathrm{eff}}}}$ [%]	n_{obs}
1	843	0.0516	6.0	3.0	64.4	6.2	11	40
100	843	0.0531	6.1	3.9	64.4	6.2	11	40
200	843	0.0559	6.0	3.7	64.4	6.2	11	40
400	843	0.0581	5.9	4.3	64.4	6.2	11	40
1000	843	0.0618	5.9	6.7	64.4	6.2	11	40
1300	843	0.0581	5.9	7.9	64.4	6.2	11	40

Table 9.20: Muon channel inputs to the D9 limit calculation.

9.6 Limits on the dark matter production cross section

We proceed to present limits on the cross section for DM pair production in association with a leptonically decaying W boson. As mentioned already, the cross section is defined with restriction to a single lepton generation for the W decay and within the lepton phase space region $p_{\mathrm{T}} > 10\,\mathrm{GeV}$ and $|\eta| < 2.5$. It is not to be confused with the DM-nucleon scattering cross section $\sigma_{\chi-N}$.

The cross section limits are shown in fig. 9.12 for the D1 and D9 signal models and in fig 9.13 for the D5d and D5c signal models. We note that the limit plots look very different from those of the W' and W^* signal models presented in fig. 8.8. In the latter cases, the cross section limit varies by more than two orders of magnitude from low to intermediate masses because of the drastic decrease of the background level as the m_{T} threshold is increased. For the DM signal, the use of the same m_{T} threshold for all DM particle masses means that the evolution of the cross section limit as function of the DM particle mass is solely due to the change in the signal efficiency and its uncertainty. The signal efficiency does itself not change dramatically as function of the DM particle mass, which reflects the fact that the transverse mass distribution is relatively insensitive to the DM particle mass, and the result is a cross section limit which is relatively flat as function of the DM particle mass. In particular, the cross section limits are flat within about a factor of 2 for the D9, D5d, and D5c signal models, while slightly stronger DM particle mass dependence is seen for D1. We note the correspondence to figs. 9.6 and 9.9, where the strongest DM particle mass dependence is seen for D1.

All limits presented here are in good agreement with the corresponding ones presented in the ATLAS paper based on the 2012 data, ref. [109]. In particular, the electron channel limits all agree within 0.2%, i.e. within the precision of the limit calculation, as exactly the same limit inputs are used here as for the paper results. For the muon channel, the limit inputs are recalculated for this work, but the corresponding limits agree within 3% for the D1, D5c, and D9 models and within 6.5% for the D5d model. The combined limits agree within 1.5% for the D1, D5c, and D9 models and within 2.5% for the D5d model. The reasons for the small differences between this work and the official ATLAS results are detailed in section A.1 of appendix A.

The use of the same m_{T} threshold for all DM particle masses means that we expect the position of the observed limit relative to the expected limit and its one and two sigma bands to be approximately independent of the DM particle mass, and this is seen indeed to be the case. For the D9 and D5c models in the muon channel, the observed limit is below the lower edge of the yellow band, as limits for these models are evaluated with the threshold $m_{\mathrm{T}}^{\mathrm{min}} = 843\,\mathrm{GeV}$, corresponding to the most significant deficit of data compared to the expected background.

While it may not be clearly visible in fig. 9.12(c), the observed limit is actually slightly below the edge of the yellow band also in the D1 case for the muon channel. As the significance of a deviation of the data wrt. the expected background for a single channel does not depend on the signal model, this might appear to be in conflict with fig. 8.7(b), where the significance is slightly below 2 for the W' of mass $1\,\mathrm{TeV}$, for which the same threshold $m_{\mathrm{T}}^{\mathrm{min}} = 796\,\mathrm{GeV}$ is used as for the D1 model. The apparent discrepancy arises because the log-normal distribution is used for the background level in the limit setting, also when the background-only pseudo-experiments are generated for the green and yellow bands. This leads to slightly higher significances of downward deviations than for the Gaussian distribution which is used for fig. 8.7.

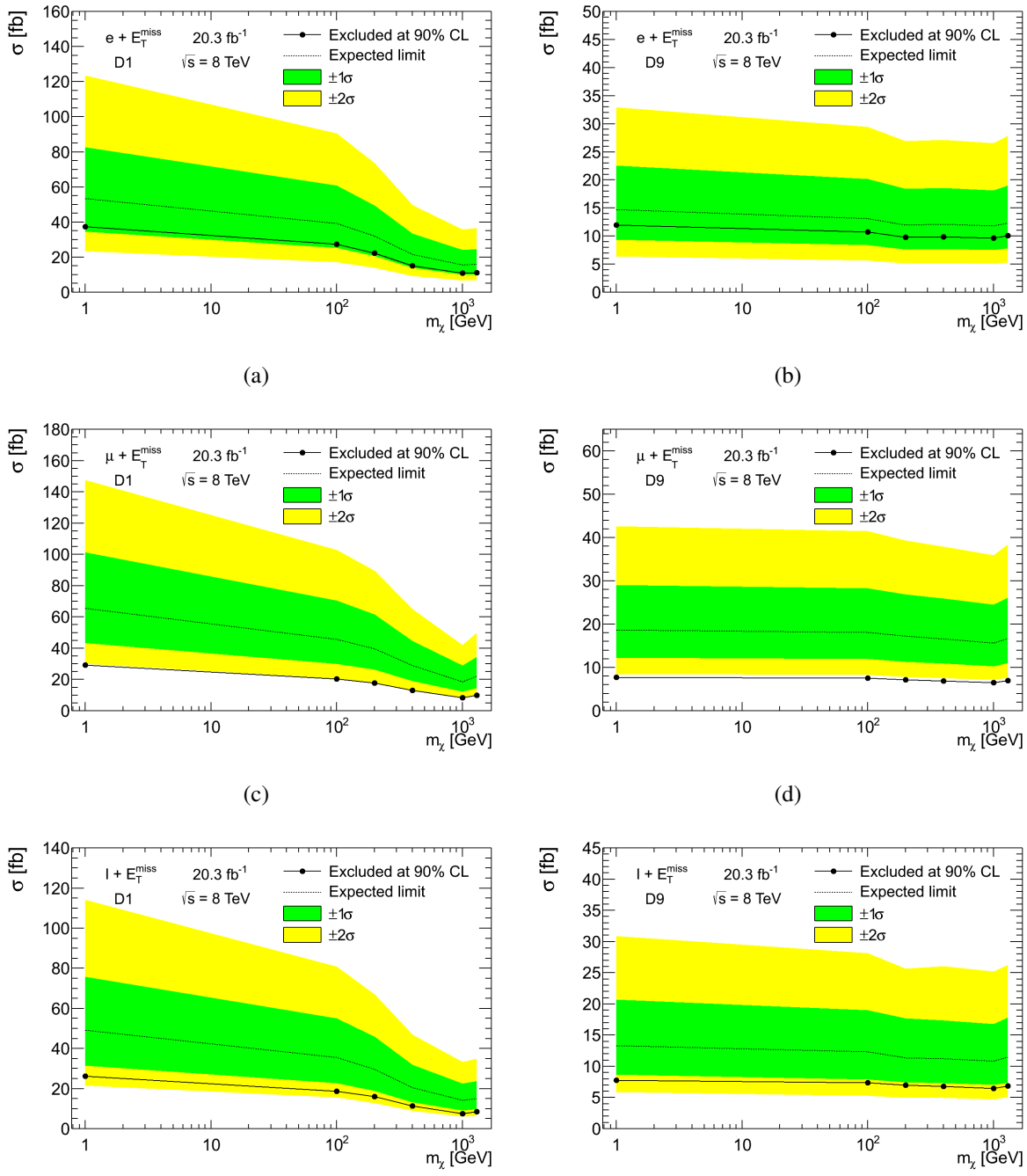

Figure 9.12: Limits on the cross section for DM pair production in association with a leptonically decaying W boson in the D1 ((a), (c), and (e)) and D9 ((b), (d), and (f)) signal models. Limits are shown for the electron channel ((a) and (b)), the muon channel ((c) and (d)), and their combination ((e) and (f)). The parameter σ is here the cross section defined with restriction to a single lepton generation for the W decay and within the lepton phase space region $p_{\mathrm{T}} > 10\,\mathrm{GeV}$ and $|\eta| < 2.5$.

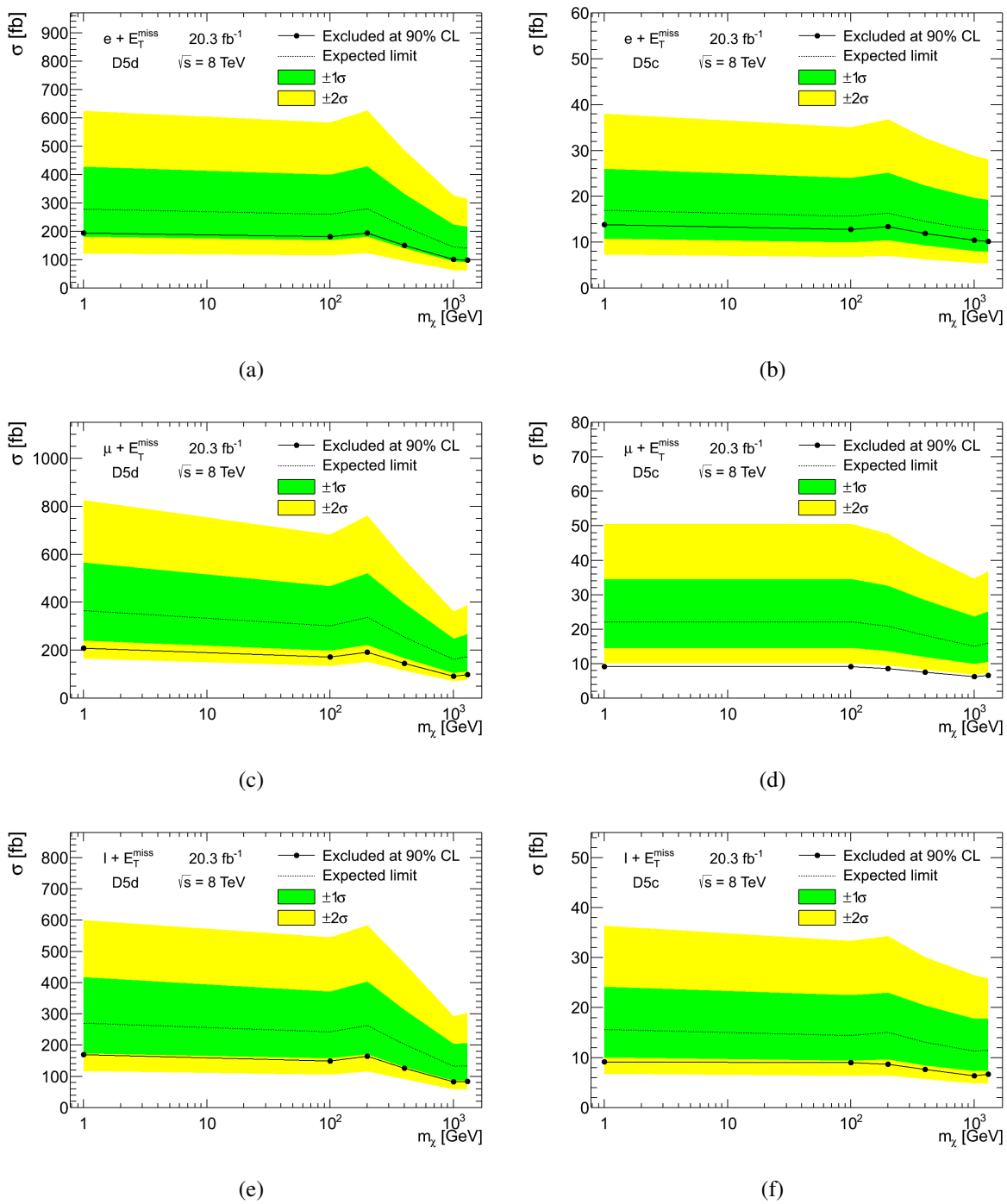

Figure 9.13: Limits on the cross section for DM pair production in association with a leptonically decaying W boson in the D5d ((a), (c), and (e)) and D5c ((b), (d), and (f)) signal models. Limits are shown for the electron channel ((a) and (b)), the muon channel ((c) and (d)), and their combination ((e) and (f)). The parameter σ is here the cross section defined with restriction to a single lepton generation for the W decay and within the lepton phase space region $p_{\mathrm{T}} > 10\,\mathrm{GeV}$ and $|\eta| < 2.5$.

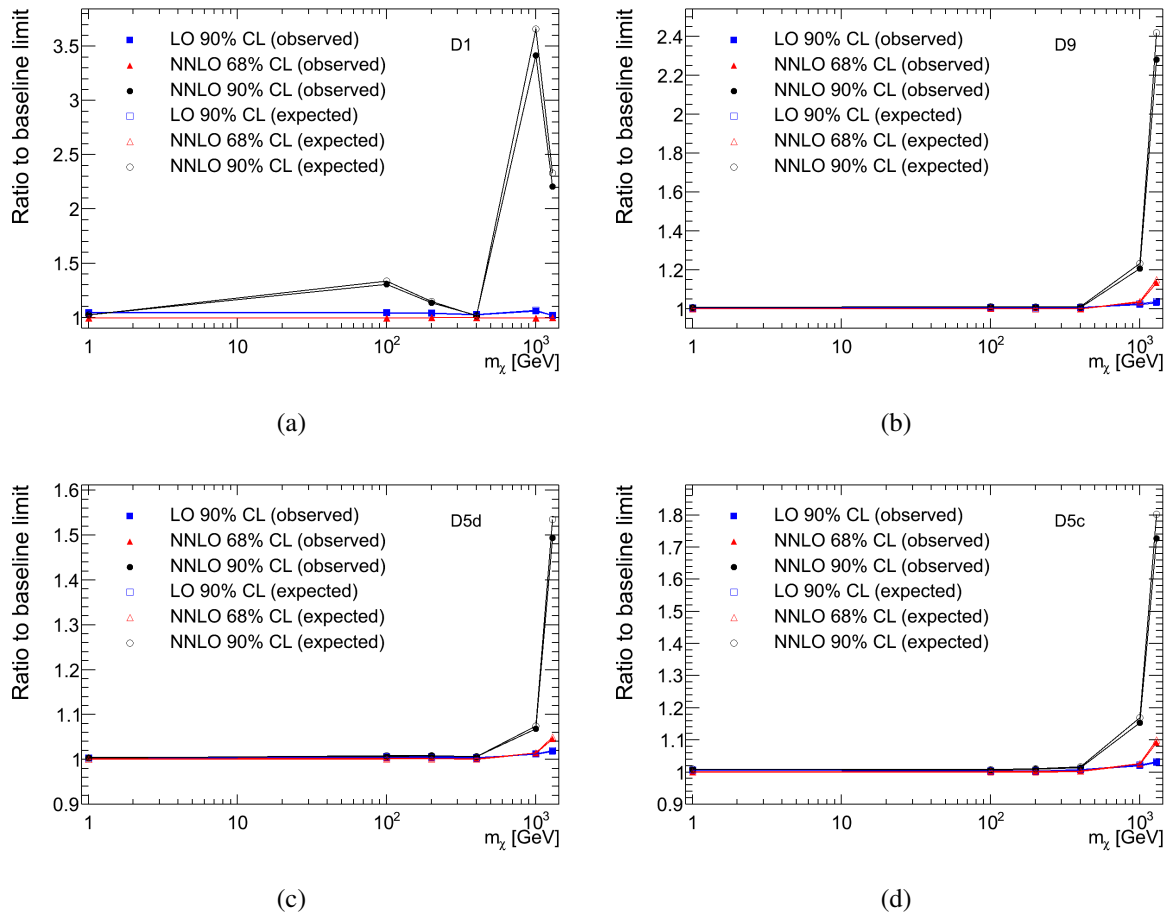

Figure 9.14: The ratios of muon channel cross section limits obtained with more conservative choices for the PDF uncertainty on the signal efficiency to the baseline cross section limits for the D1 (a), D9 (b), D5d (c), and D5c (d) signal models. The ratios are shown both in terms of observed and expected limits. The signal efficiency PDF uncertainties themselves are shown in fig. 9.8.

We note finally that for the D1, D5c, and D9 models, the observed limit is stronger in the muon channel than in the electron channel due to the low muon channel data event count compared to the background expectation. The expected limit is, however, stronger in the electron channel, which shows that this is the more sensitive channel.

9.7 More conservative PDF uncertainty choices

In section 9.2, different possibilities were considered for the evaluation of the PDF uncertainty on the signal efficiency for the DM signal. The most optimistic (least conservative) possibility of LO uncertainties at 68% CL was chosen for the official ATLAS analysis based on arguments of consistency with already published ATLAS results, and limits presented in this chapter are calculated with this choice. It is interesting to know how much this choice affects the presented limits, and we therefore proceed to compare the baseline limits to limits calculated with the other PDF uncertainty evaluations considered in section 9.2. The comparison is made for the muon channel only.

The results are presented in fig. 9.14 in the form of ratios of the limits calculated with the more conservative choices for the PDF uncertainty to the baseline limits both in terms of expected and observed limits. We see that the effect of the PDF uncertainty on the signal efficiency does not depend strongly on whether expected or observed limits are considered. The results for the D1 signal model seem a bit strange, presumably because of the sensitivity to the charm and strange quark contents of the proton, as already commented on in section 9.2. For the other models, limits are affected only marginally by the choice of PDF uncertainties, by at most 1-2%, for $m_\chi \leq 400\,\mathrm{GeV}$. For the two highest DM particle masses considered, the effect of the choice becomes more important, and large effects are seen in particular for the highest mass, $m_\chi = 1.3\,\mathrm{TeV}$, where limits are affected by more than a factor of 2 for the D9 model.

While the ratios in fig. 9.14 are calculated from the cross section limits corresponding to figs. 9.12 and 9.13, they are equally valid for the limits on the DM-nucleon scattering cross section $\sigma_{\chi-N}$ (to be presented in section 9.10) as is clear from eqs. (9.3)-(9.6) and (9.1). As is clear from eq. (9.1), the corresponding ratios of M_* limits can be obtained from the ratios in fig. 9.14 by raising them to the power $1/(2n)$ with $n = 3$ for D1 and $n = 2$ for the other models[3]. The M_* limits (to be presented in section 9.9) are thus less strongly affected by the PDF uncertainty choice than the cross section limits. For example, the more than a factor of 2 effect for the D9 model is approximately a 25% effect in terms of M_*.

We conclude that the choice of the most optimistic PDF uncertainties for the DM signal does not significantly affect the results for any $m_\chi \leq 400\,\mathrm{GeV}$ for the D5d, D5c, and D9 signal models. Even for $m_\chi = 1\,\mathrm{TeV}$, results with the most conservative choice differ from the baseline results by only 10-20% in terms of cross section limits, corresponding to a 2-5% effect in terms of M_* limits. A more significant effect is seen for $m_\chi = 1.3\,\mathrm{TeV}$. For the D1 model, a more extensive study of PDF effects seems warranted because of the sensitivity to the charm and strange quark content of the proton in this model, but such a study is not pursued here.

9.8 Comparison to 95% CL limits

All limits in this chapter are presented at 90% CL because the use of this confidence or credibility level is customary in DM searches. However, as 95% CL limits are customary in high energy physics searches in general, it is interesting to know how much difference there is between 95% and 90% CL limits. The ratios of 95% to 90% CL cross section limits are shown in fig. 9.15. As in section 9.7, we consider the cross section limits corresponding to figs. 9.12 and 9.13, and we note that the ratios are equally valid for limits on the DM-nucleon scattering cross section. The equivalent ratios for M_* limits can be obtained by raising the cross section limit ratios to the relevant powers.

We see that the difference between cross section limits at 95% and 90% CL is generally slightly less than 20% for expected limits and between 20% and 30% for observed limits. For the combined observed limits, the difference is about 23-25%. We note some statistical fluctuations at the level of 1-3% in the combined expected limit coming from the limited number of background-only pseudo-experiments. We note finally that the differences of 20-30% on cross

[3]The ratios in fig. 9.14 are alternative limits divided by baseline limits. Raising these to the relevant power, one obtains the inverse M_* limit ratio, i.e. the baseline limit divided by the alternative limit.

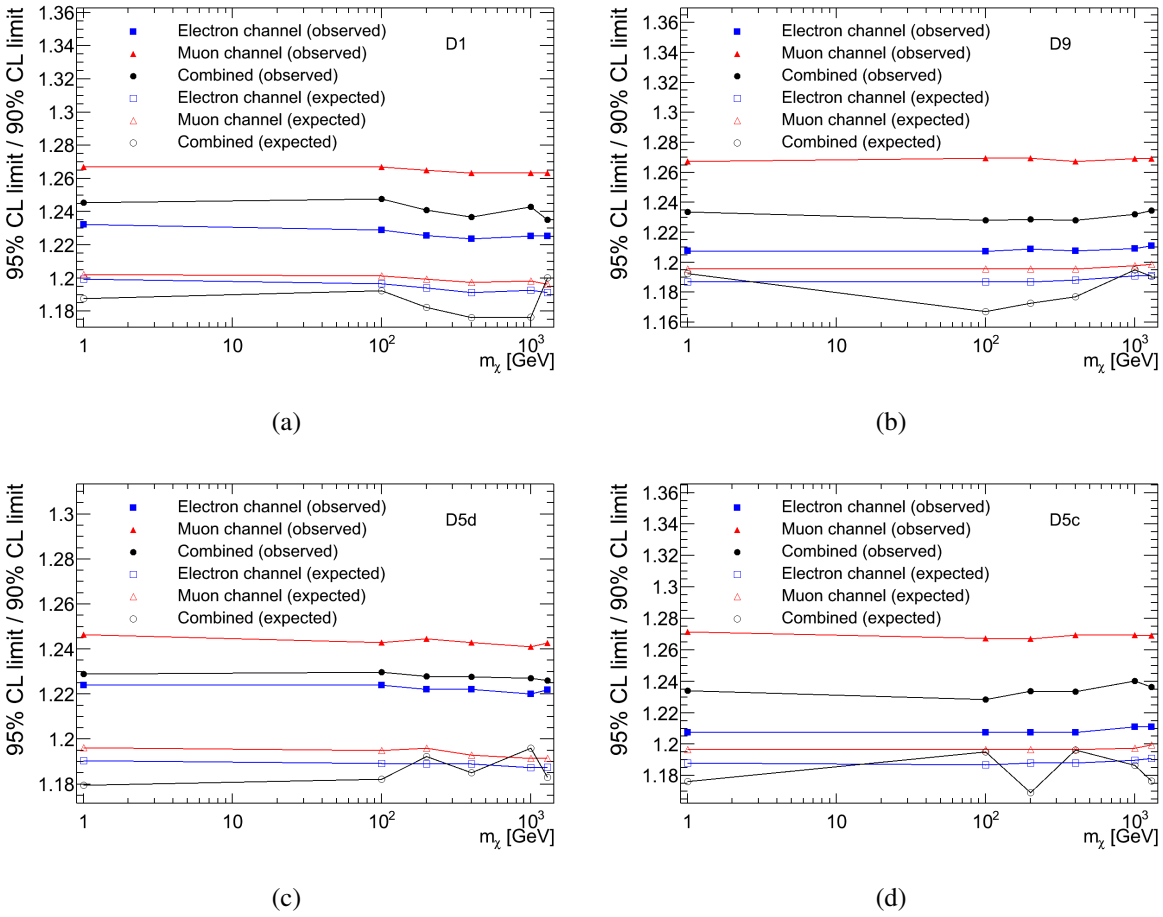

Figure 9.15: The ratio of cross section limits at 95% and 90% CL for the D1 (a), D9 (b), D5d (c), and D5c (d) signal models. The ratio is shown both in terms of observed and expected limits.

section limits correspond to M_* limit differences of 3-5% for the D1 model and 5-7% for the other models.

9.9 Limits on the mass scale M_* in the effective field theory

The (upper) cross section limits presented in section 9.6 are converted to (lower) limits on the parameter M_* with the dimension of mass which determines the strength of the point coupling between quarks and DM particles in the EFT. The conversion is done using eq. (9.1) and the cross sections of table 9.2[4]. We note that PDF uncertainties affect in principle the cross sections used in the conversion, and are analogous to the uncertainties on the theoretical cross section curves in figs. 8.8 and 8.21. The M_* limits are analogous to the mass limits for the W' and W^* models, and using the cross section values from table 9.2 directly without considering the corresponding uncertainties corresponds to reading the W'/W^* mass limits from the intersections of the central theory predictions with the observed limits. The uncertainty on the theoretical cross section is in the W' case displayed as a band around the theoretical cross section curve, and one could imagine representing the PDF uncertainty of the cross sections in table 9.2 as bands around the resulting M_* limits as function of the DM particle mass. On the other hand, we argued that it was unreasonable to quote LO PDF uncertainties on the W^* cross sections, and by extension of the argument, no band should therefore be shown around the M_* limits as also the DM signal is generated at LO.

The M_* limits as function of the DM particle mass are shown in fig. 9.16 for the D1 and D9 signal models and in fig 9.17 for the D5d and D5c signal models. Obviously, the position of the observed limit wrt. the expected limit and the green and yellow bands is "inverted" compared to figs. 9.12 and 9.13, as stronger limits correspond to higher values of M_*.

We note that the M_* limit is relatively flat at low DM particle mass, with roughly the same value at $m_\chi = 1\,\mathrm{GeV}$ and $m_\chi = 100\,\mathrm{GeV}$. As the DM particle mass is increased beyond $100\,\mathrm{GeV}$, the M_* limit starts decreasing rapidly. Even though the experimental sensitivity, quantified in terms of the signal efficiency or the cross section limit, typically improves a little in this region, the cross section for the mono-W process decreases and causes the overall decrease of the M_* limit. We can say that, in spite of the retained or even improved experimental sensitivity, the sensitivity to the underlying physics is reduced as we approach the kinematically inaccessible region as governed by the pp center of mass energy.

9.9.1 Comparison between ATLAS limits

We compare finally the observed M_* limits of this analysis to those obtained by the ATLAS searches in the final states with, in addition to missing transverse energy, a hadronically decayed W or Z boson [140], a leptonically decayed Z boson [141], or a jet [142]. All results are based on the full 2012 dataset, except for the mono-jet analysis, which is based on the 2011 dataset;

[4]Note that the cross sections in table 9.2 are given for the sum of the three leptonic W decay channels, while the cross section limits of figs 9.12 and 9.13 apply to the cross section for a single lepton generation. The appropriate factor of 3, assuming lepton universality of the W branching fractions, must be included when taking the ratio of the generated cross section and the cross section limit.

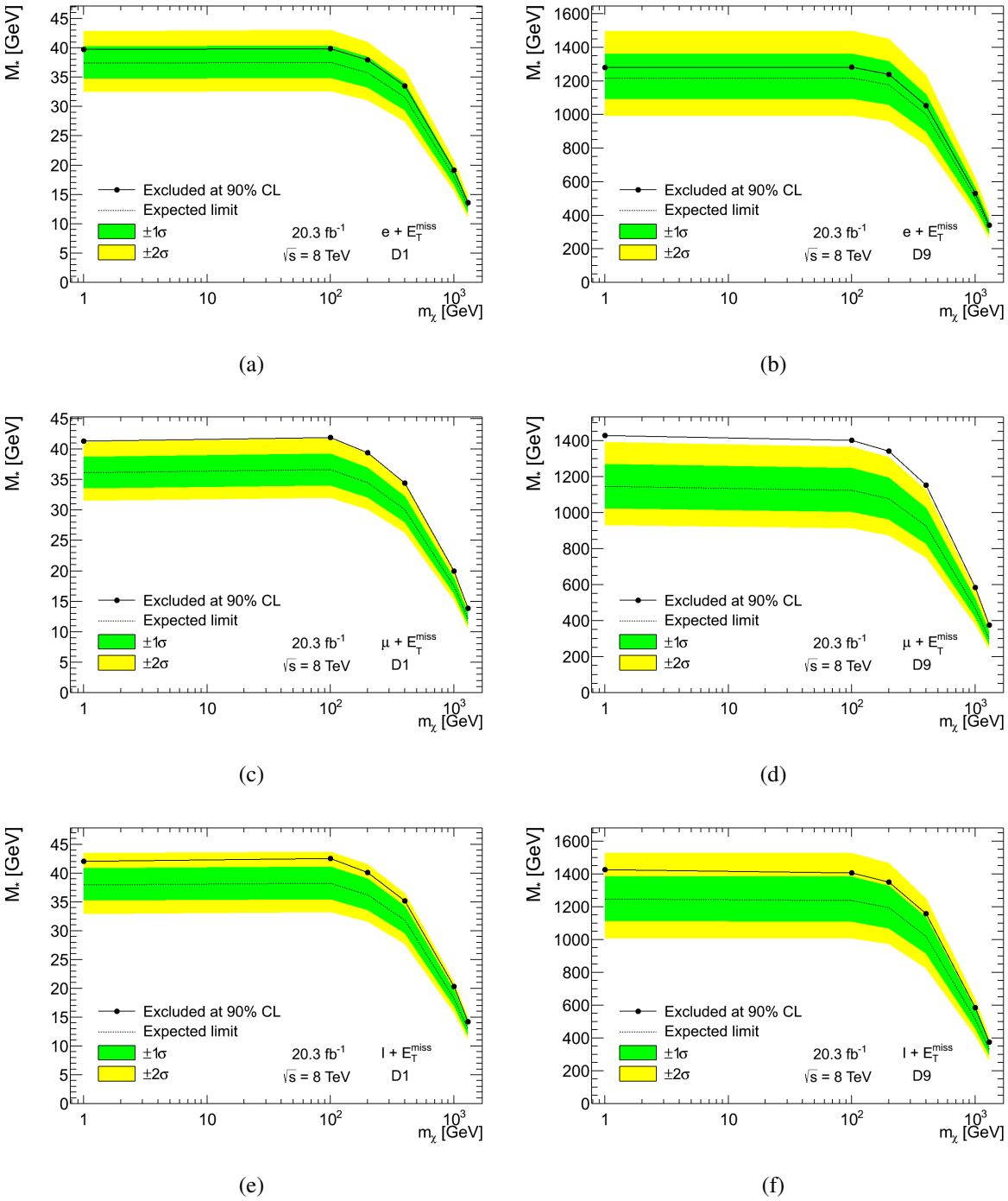

Figure 9.16: Limits on the parameter M_* with the dimension of mass which determines the strength of the point coupling between quarks and DM particles in the EFT for the D1 ((a), (c), and (e)) and D9 ((b), (d), and (f)) signal models. Limits are shown for the electron channel ((a) and (b)), the muon channel ((c) and (d)), and their combination ((e) and (f)).

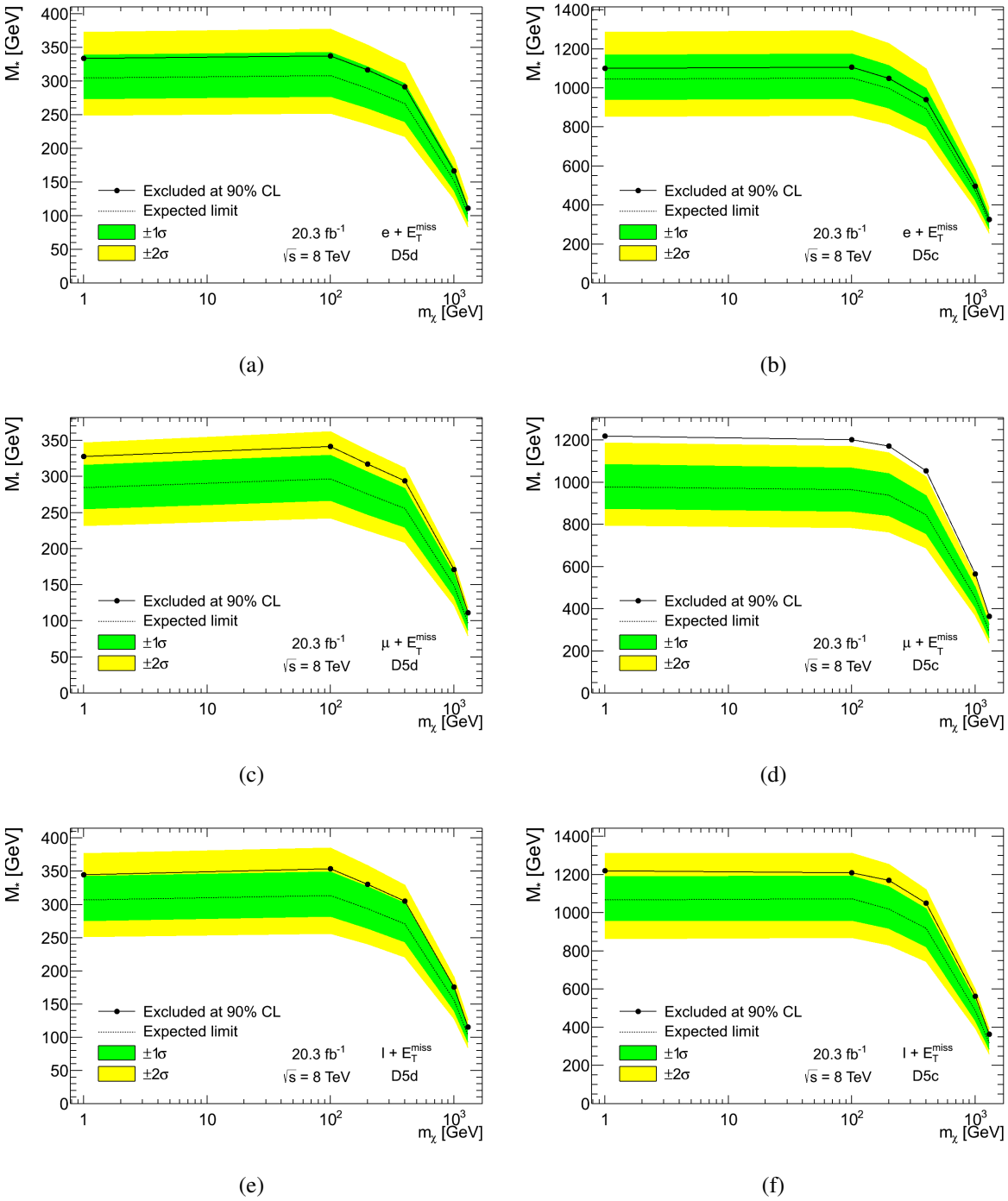

Figure 9.17: Limits on the parameter M_* with the dimension of mass which determines the strength of the point coupling between quarks and DM particles in the EFT for the D5d ((a), (c), and (e)) and D5c ((b), (d), and (f)) signal models. Limits are shown for the electron channel ((a) and (b)), the muon channel ((c) and (d)), and their combination ((e) and (f)).

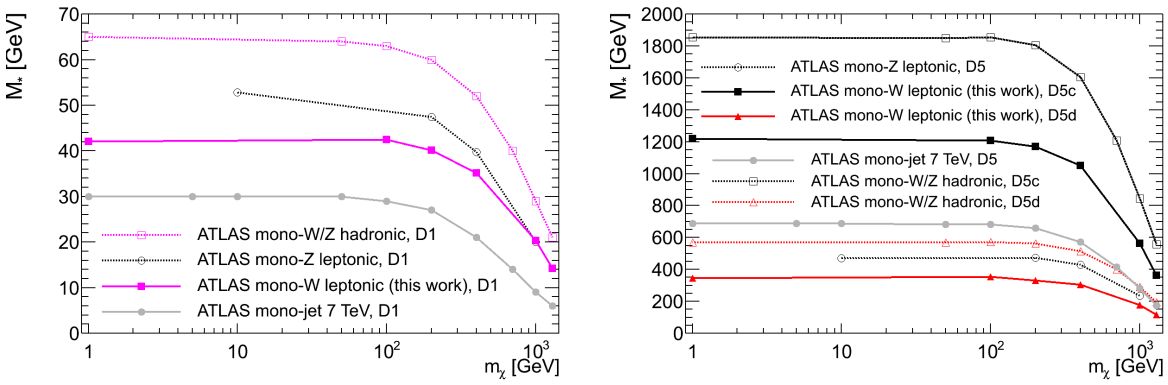

(a)

(b)

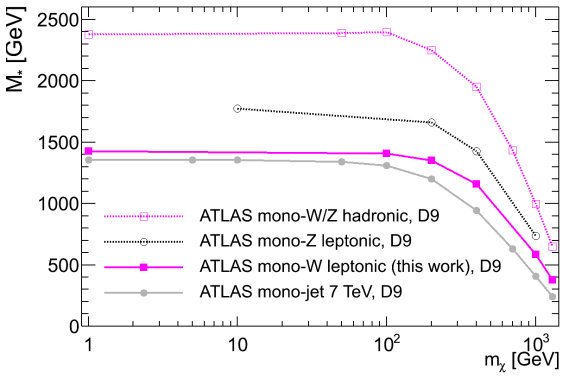

(c)

Figure 9.18: Limits on the mass scale M_* in the effective field theory as function of the DM particle mass for ATLAS DM searches in different final states for the D1 (a), D5 (b), and D9 (c) signal models. All results are based on the full 2012 dataset, except for the mono-jet analysis, which is based on the 2011 dataset. Each drawn point corresponds to a simulated DM particle mass, and the selection of masses differs between the different analyses.

$4.7\,\mathrm{fb}^{-1}$ of integrated luminosity at $\sqrt{s} = 7\,\mathrm{TeV}$. The M_* limits are compared for the different signal models in fig. 9.18.

For the D1 and D9 signal models, we see that all the $8\,\mathrm{TeV}$ results provide stronger bounds than the $7\,\mathrm{TeV}$ mono-jet result, although we note that the M_* limit for D9 from the analysis presented here is very close to the one from the $7\,\mathrm{TeV}$ mono-jet analysis, and that the latter analysis is in fact slightly more sensitive as quantified by the expected M_* limit. For the D5 signal models, all results are shown in one plot. The results from the interference insensitive mono-jet and mono-Z analyses are labeled just "D5" as in the corresponding publications, and the corresponding M_* limits should be valid regardless of the relative sign of the couplings of DM to up and down quarks. We see that the interference sensitive analyses can provide superior bounds on D5 interactions in the case of opposite sign couplings of DM to up and down quarks (constructive interference, D5c). For both the D1, D9, and D5c models, the mono-W/Z hadronic analysis provides the strongest ATLAS limits published to date, while the strongest limit for the D5d case comes from the mono-jet analysis.

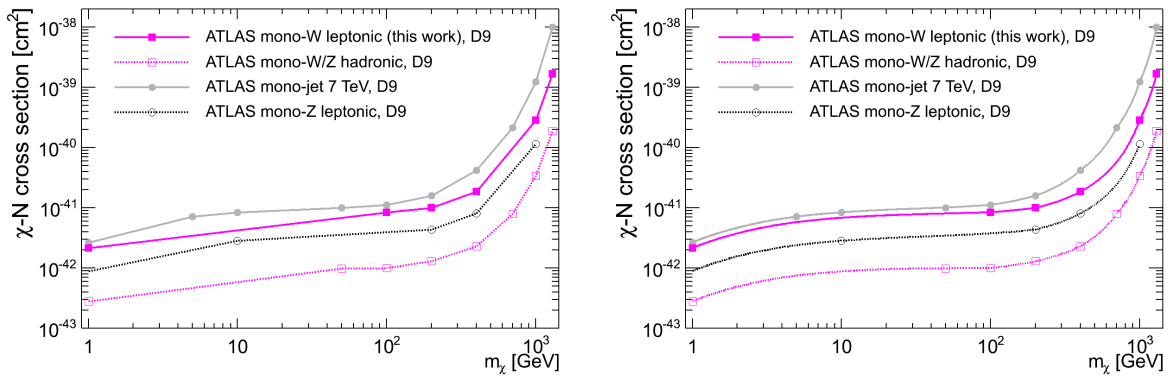

(a) (b)

Figure 9.19: DM-nucleon cross section limits as function of the DM particle mass for ATLAS DM searches in different final states. All results are based on the full 2012 dataset, except for the mono-jet analysis, which is based on the 2011 dataset. Each drawn point corresponds to a simulated DM particle mass, and interpolation between the simulated points is done by straight lines in the log-log plot in (a) and by linear interpolation of the M_* limit as function of the DM particle mass in (b). There is a "ghost point" at $m_\chi = 1\,\text{GeV}$ for the leptonic mono-Z analysis. This point was not simulated, but a value for the $\sigma_{\chi-N}$ limit was provided based on extrapolation.

9.10 Limits on the DM-nucleon scattering cross section

We finally convert the M_* limits to limits on the DM-nucleon scattering cross section $\sigma_{\chi-N}$ using eqs. (9.3)-(9.6). The limits are compared to other ATLAS results as well as to limits from direct detection experiments. When comparing to the direct detection limits, we keep in mind that the comparison is model dependent and only valid within the region of validity of the EFT approximation.

9.10.1 Interpolation

In refs. [140] (ATLAS mono-W/Z hadronic) and [141] (ATLAS mono-Z leptonic), the DM-nucleon cross section limit is presented as function of the DM particle mass in a log-log plot with a linear (in the log-log plane) interpolation between the points. We argue that this is an unfortunate presentation which leads to obvious problems in the low DM particle mass region. The problem is illustrated in fig. 9.19(a), where the DM-nucleon cross section limits are plotted as function of the DM particle mass for the different ATLAS analyses. The linear interpolation in the log-log plane is seen to lead to obvious shape mismatch between the different analyses at low DM particle mass because of the use of different mass point sets in the different analyses.

We noted in section 9.9 that the M_* limits were quite flat in the low DM particle mass region. In particular, the values for the combined limits at $m_\chi = 1\,\text{GeV}$ and at $m_\chi = 100\,\text{GeV}$ differ by less than 3% for all the signal models. On the other hand, the corresponding $\sigma_{\chi-N}$ limits differ by about a factor 3-4. Considering eqs. (9.3)-(9.6), it is clear that a few percent difference in the M_* value cannot lead to a factor 3-4 difference in the $\sigma_{\chi-N}$ value, so the evolution of the $\sigma_{\chi-N}$ limit in the low m_χ region must be governed primarily by the reduced mass μ_χ. Indeed,

we find $[\mu_\chi(m_\chi = 100\,\mathrm{GeV})/\mu_\chi(m_\chi = 1\,\mathrm{GeV})]^2 \approx 3.7$, which explains the factor 3-4 seen for the $\sigma_{\chi-N}$ limits.

As the M_* limit is almost constant in the low m_χ region, it seems well warranted to base the interpolation of the $\sigma_{\chi-N}$ limit on an interpolation of the underlying M_* limit, thus incorporating the exact analytical evolution of μ_χ. This is done in fig. 9.19(b), where the M_* limit is interpolated linearly in the M_* vs. m_χ plane. Clearly, the low m_χ region looks much better in this plot, with no obvious shape mismatches between the different ATLAS results.

In the high m_χ region, the reduced mass approaches a constant ($\mu_\chi = m_N$), and the evolution of the $\sigma_{\chi-N}$ limit is governed by the evolution of the M_* limit. In this region, there is no strong motivation for using the underlying linear M_* interpolation, but this approach is in any case not expected to do any worse than linear interpolation in the log-log $\sigma_{\chi-N}$ vs. m_χ plane. We therefore argue that using the underlying linear M_* interpolation is overall greatly preferred, and proceed with this approach.

9.10.2 Comparison to direct detection experiments

We finally compare the DM-nucleon cross section limits to the corresponding limits from the other ATLAS searches and from the direct detection detection experiments XENON100 [143], CDMS [144, 145], LUX [146], COUPP [147], SIMPLE [148], IceCube [149], CoGeNT [150], and PICASSO [151] in fig. 9.20. The direct detection limits are presented separately for so-called spin dependent and spin independent interactions. The D9 signal model leads to spin dependent interactions, while the D5 and D1 signal models lead to spin independent interactions, and the ATLAS limits are compared to the relevant direct detection limits.

For the interference insensitive ATLAS searches, results for the D5 model are presented as in the corresponding publications, with the label "D5". While the M_* limits obtained in these searches should be independent of the relative sign of the couplings of DM to up and down quarks, the conversion to the DM-nucleon cross section is made for the same sign coupling choice (D5d). As is clear from the comparison of eqs. (9.5) and (9.6), the DM-nucleon cross section limits from these searches would be improved by close to one order of magnitude if opposite sign couplings were considered. They would still not be able to compete with the interference sensitive searches in this scenario, as is also clear from the M_* limits in fig. 9.18(b).

Although we keep in mind that comparison between ATLAS and direct detection limits is model dependent and can be affected by problems with the validity of the EFT approach, we do note the fact that the ATLAS searches seem to have a unique sensitivity to spin dependent interaction models and very low DM particle masses. This is known to be a general feature in the comparison of collider DM searches to direct detection experiments.

9.11 Summary

In this chapter, we have interpreted the search in the one lepton and $\not{E}_\mathrm{T}$ final state as a search for DM production in association with a leptonically decaying W boson. As signal models, a set of standard EFT descriptions of the quark-DM interaction have been considered. Limits have been placed on the cross section for the mono-W process, and they have also been converted to limits on the dimensionful parameter M_* in the EFT. Finally, the M_* limits have been converted

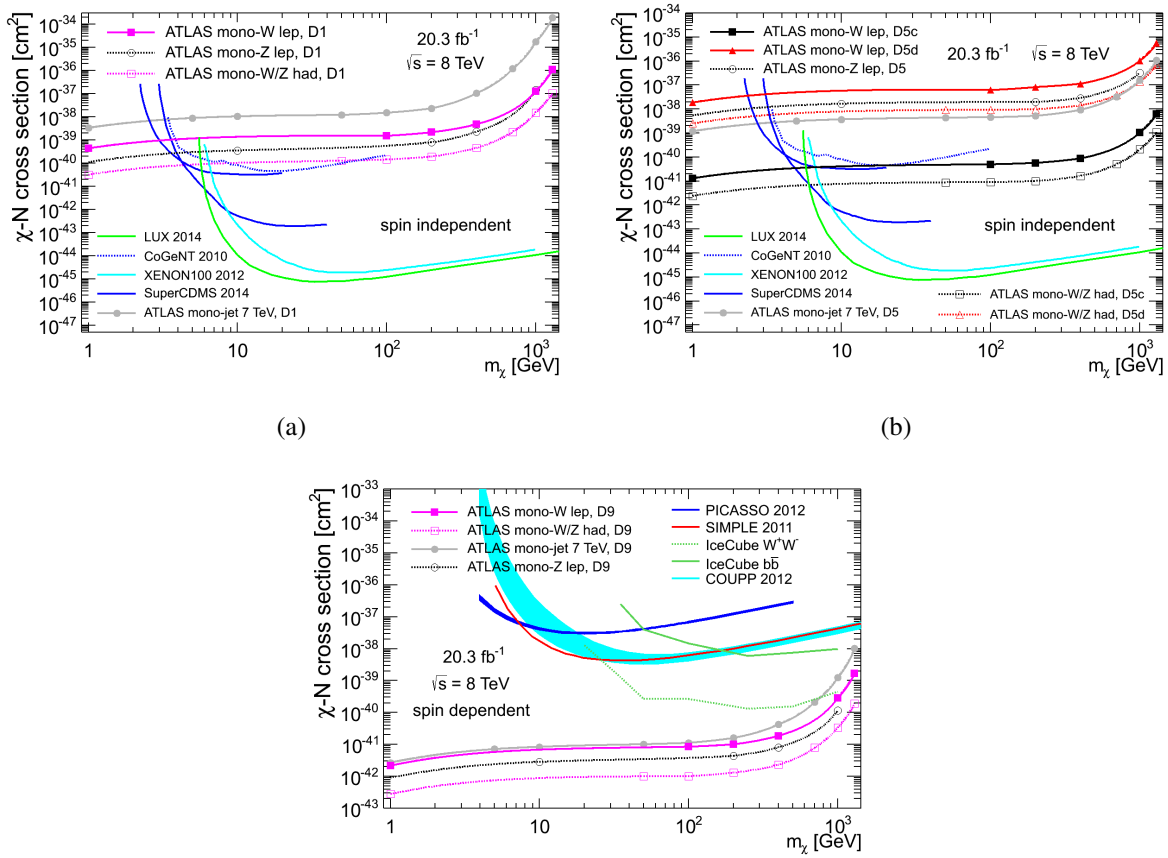

Figure 9.20: Limits on the DM-nucleon cross section as function of the DM particle mass for ATLAS DM searches and direct detection experiments for the D1 (a), D5 (b), and D9 (c) signal models. The abbreviations "lep" and "had" are used for leptonic and hadronic decays respectively in the legends. The "mono-W lep" results are from this analysis.

to limits on the DM-nucleon scattering cross section relevant for comparison to direct detection experiments.

Limits have been compared to those of other ATLAS searches in different final states. The most stringent ATLAS limits to date come in general from the analysis targeting hadronic decays of W and Z bosons. Both the analysis presented here and the mono-W/Z hadronic analysis benefit from constructive interference in the case of the D5 EFT if the coupling of the DM particles to up and down type quarks have opposite sign.

When comparing to direct detection limits, the usual conclusion is reached that the collider results are in general especially sensitive to low DM particle masses and spin dependent interactions.

Conclusions and outlook

In this thesis, a search for new physics in final states with one lepton and missing transverse energy has been presented. The observed transverse mass distribution in data is in good agreement with the Standard Model (SM) expectations, so no evidence of physics beyond the SM is found. The search has been interpreted in terms of the production of hypothetical heavy, charged bosons, and also in terms of the production of dark matter particles in association with a leptonically decaying W boson. Limits on the cross sections and relevant mass scales of these processes have been presented, and the mass limits for heavy, charged bosons extend up to $3.28\,\mathrm{TeV}$ for the Sequential Standard Model (SSM) W' and $3.21\,\mathrm{TeV}$ for the W^*. The SSM is a reference model for new gauge bosons arising from broken gauge symmetries, and the mass limit on this model is a vast improvement over Tevatron limits and matches the latest CMS mass limit based on the same LHC run. The W^* resonance appears in theories that address the hierarchy problem, and limits on the corresponding reference model have been provided only by ATLAS.

As a search for dark matter production, the analysis is found to be competitive with searches targeting the mono-jet, mono-Z leptonic, and mono-W/Z hadronic processes. In particular, good sensitivity is achieved for the case of constructive interference in the D5 effective field theory, although the mono-W/Z hadronic analysis also benefits from the interference and provides the strongest constraint on this model. The mono-W leptonic analysis (this work) is complementary to the other ATLAS searches, and provides in combination with the mono-W/Z hadronic and mono-Z leptonic searches excellent exploitation of the mono-W/Z processes as potential dark matter production signatures. Obviously, the inclusion of the analysis would improve a hypothetical ATLAS-wide combination of dark matter searches.

The first runs of the LHC at pp center of mass energies of $\sqrt{s} = 7\,\mathrm{TeV}$ and $\sqrt{s} = 8\,\mathrm{TeV}$ have been hugely successful. The discovery of the Higgs boson has completed the SM picture and triggered a Nobel Prize. All results so far indicate that the Higgs boson is accurately described by the SM, though it could still be just the first glimpse of an extended Higgs sector. The LHC data have so far not provided any major surprises, and no evidence of physics beyond the SM has been found. The nature of neutrino masses, dark matter, and dark energy, remains therefore as mysterious as ever, and the hierarchy problem is puzzling still. While the shortcomings of the SM indicate that deviations from the model will be encountered at some energy scale, the SM may provide an accurate description of physics up to energy scales well beyond the reach of the LHC now that the Brout-Englert-Higgs mechanism has been confirmed. Still, there are arguments, e.g. based on naturalness, indicating that the TeV scale may be special.

Experimental results are the only means to extend discussions of the shortcomings of the SM and their potential resolutions beyond theoretical speculation. The LHC still has plenty of

potential in this respect. With the first collisions at $\sqrt{s} = 13\,\mathrm{TeV}$ fast approaching[5], the next few years hold the potential to be every bit as exciting as the last few years have been, and the physicists in the LHC community prepare to venture into virgin territory once again. Initial studies in the ATLAS W' group suggest that the sensitivity of the $\sqrt{s} = 8\,\mathrm{TeV}$ analysis will already be superseded with the first $1\,\mathrm{fb}^{-1}$ of $\sqrt{s} = 13\,\mathrm{TeV}$ data, and that sensitivity to SSM W' bosons of mass $4.5\,\mathrm{TeV}$ will be achieved with only $10\,\mathrm{fb}^{-1}$. On a slightly longer timescale, upgrades of the LHC are foreseen to provide increased luminosity, and a total integrated luminosity of $3000\,\mathrm{fb}^{-1}$ is envisioned by approximately year 2035. On even longer timescales, the future is unclear and will most likely depend on the findings of the LHC at the design energy. It would seem that the increase in mass reach for new physics searches that will be achieved with the early $\sqrt{s} = 13\,\mathrm{TeV}$ LHC data within the next year or two is not likely to be paralleled for quite a while, and a critical time lies ahead of the particle physics community.

[5]The first physics collision data at $\sqrt{s} = 13\,\mathrm{TeV}$ are expected in May 2015.

Appendix A

Additional details

A.1 Differences wrt. the official ATLAS results in the muon channel

In chapters 8 and 9, we made use of electron channel inputs to the statistical analysis corresponding to the official ATLAS results presented in ref. [109]. For the muon channel, all inputs were recalculated for the thesis results. The final muon channel results are almost identical to those presented in ref. [109], and the magnitude of the differences are quantified in sections 8.7 and 9.6. In the interest of full disclosure, the reasons for the differences are given here, and some are also mentioned in the relevant sections of chapters 8 and 9.

While the muon channel optimal m_{T} thresholds presented in section 8.4 were exactly those obtained for the official ATLAS analysis, it was chosen to use a common set of thresholds for the electron and muon channels in the official analysis. The lower one of the electron and muon channel thresholds was used for each mass. In this thesis, we used instead the optimal threshold "out of the box" for the muon channel, leading to a slightly different threshold for the SSM W' of mass $600\,\mathrm{GeV}$ and the W^* of mass $2\,\mathrm{TeV}$. Only these two masses were affected because the threshold used in the official analysis came in most cases from the muon channel optimization in the first place.

Even disregarding the two mass points with differing m_{T} thresholds, small differences are observed between this thesis and the official results. The most important difference in terms of the effect on exclusion limits, is the use of some different background MC samples here and in the official results, leading to some 10-20% differences on cross section limits in the high statistics (low mass) region. For some of the mass and p_{T} filtered background MC samples, validation samples were produced using full detector simulation. In this thesis, we used consistently the fast simulation for all these samples, while the full simulation was used for the official results for all samples for which full simulation was available. The resulting estimated background levels are more or less consistent within statistical uncertainty, but the cross section limits are sensitive to small variations in the high statistics region.

The m_{T} thresholds are based on optimization with logarithmically spaced sample values. In both the official results and in this thesis, these are presented rounded to the nearest GeV. However, in the official results, the "exact" value is used for the statistical analysis, while the rounded value is used for the muon channel results in this thesis.

In this thesis, we have chosen to neglect an additional efficiency uncertainty due to "catastrophic energy loss" by radiation for high p_{T} muons, which is included in the official analysis. The uncertainty was in the first place included to be conservative, without there being a particular reason to expect that such energy loss was poorly modeled in the MC. Since it is in any case found to be negligible, and we have doubts about the parametrization of the uncertainty based on the results of a previous analysis, we neglect this uncertainty.

Small updates were made to the muon channel jet background estimate in the process of writing this thesis after the publication of ref. [109]. Changes in the extrapolated jet background levels were very small, and given the small impact of the jet background in the first place, the effect of the jet background change on cross section limits is miniscule. The change is nonetheless mentioned here for completeness.

Finally, there is a minor difference in the calculation of the dark matter signal efficiency. In this thesis, we follow the same prescription as for the W' and W^* signal, where the denominator of eq. (8.2) is the number of events[1] after the selection of muon decays of the W boson at the generator level. In the official analysis, it is taken to be the total number of events (including electron, muon, and tau decays) divided by three. As even the tau lepton mass is completely negligible compared to the W mass, the difference manifests itself only as statistical fluctuations.

A.2 Complete set of threshold optimization plots

Some example m_{T} threshold optimization plots for the muon channel were presented in sections 8.4 and 9.4. The full set of muon channel plots is given here for reference in figs. A.1-A.3 for the SSM W', figs. A.4-A.6 for the W^*, and figs. A.7-A.9 for the DM signal. For the DM signal, strange features are seen, which are assumed to be due to insufficient MC statistics, as discussed in section 9.4. Also the W' and W^* optimization plots are seen not to be smooth at high mass, but this is expected because of the discrete nature of the median ("expected") limit as discussed in section 8.4.

[1] As explained in the text around eq. (8.2), we consider weighted number of events both for the numerator and denominator of the signal efficiency. For the dark matter signal, this is not important when it comes to the denominator, as there is no k-factor and no Breit-Wigner weight. (When calculating the PDF uncertainty, the PDF weights must be included in both the numerator and the denominator, but these weights do not enter the calculation of the signal efficiency central value.) Other weights should average to unity at the initial selection stage, except for efficiency correction weights, which are only included in the numerator of the signal efficiency.

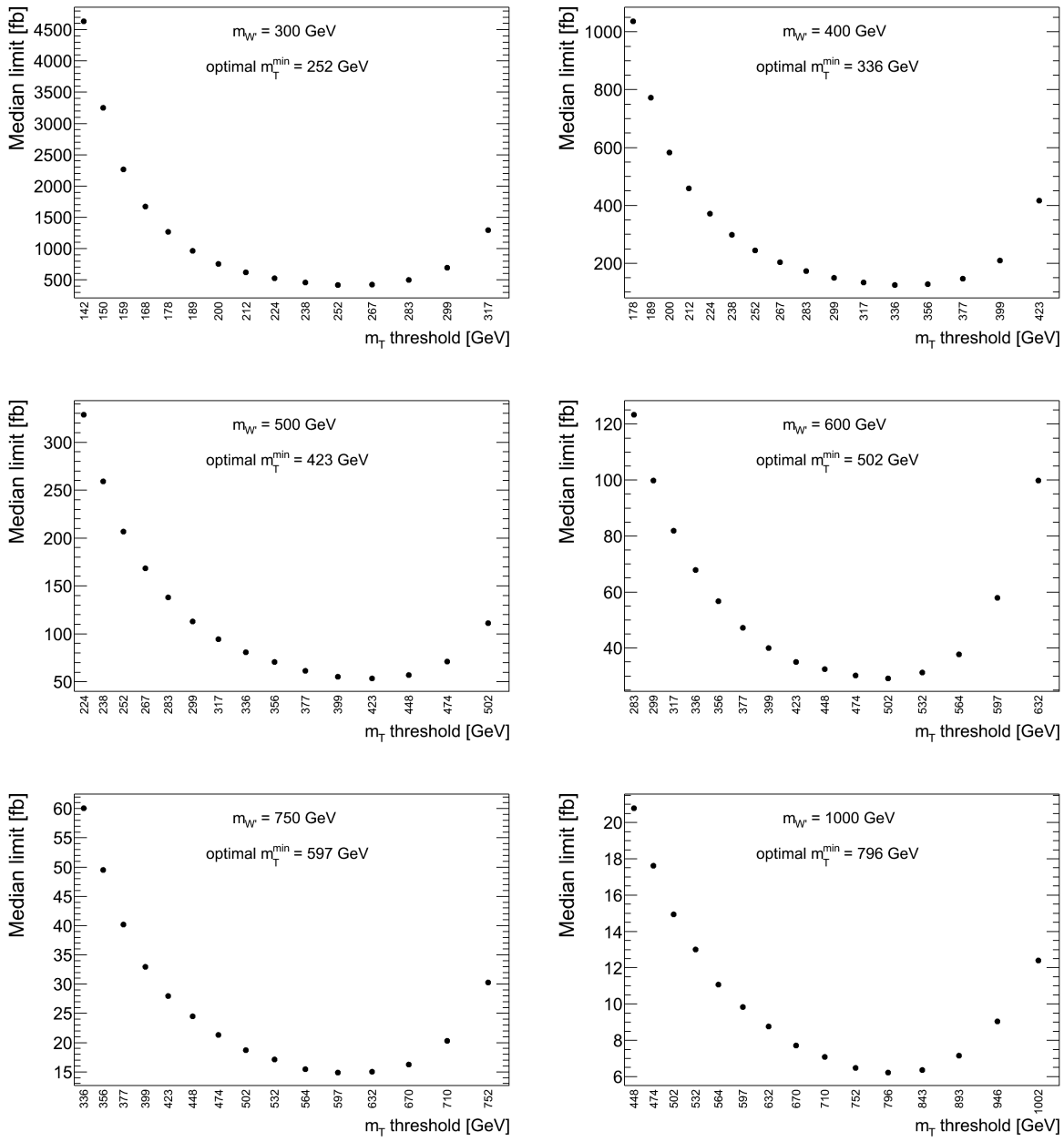

Figure A.1: The median limit under the background-only hypothesis as function of the m_{T} threshold for the SSM W' for different boson masses. The boson mass and the optimal threshold is given inside each plot frame.

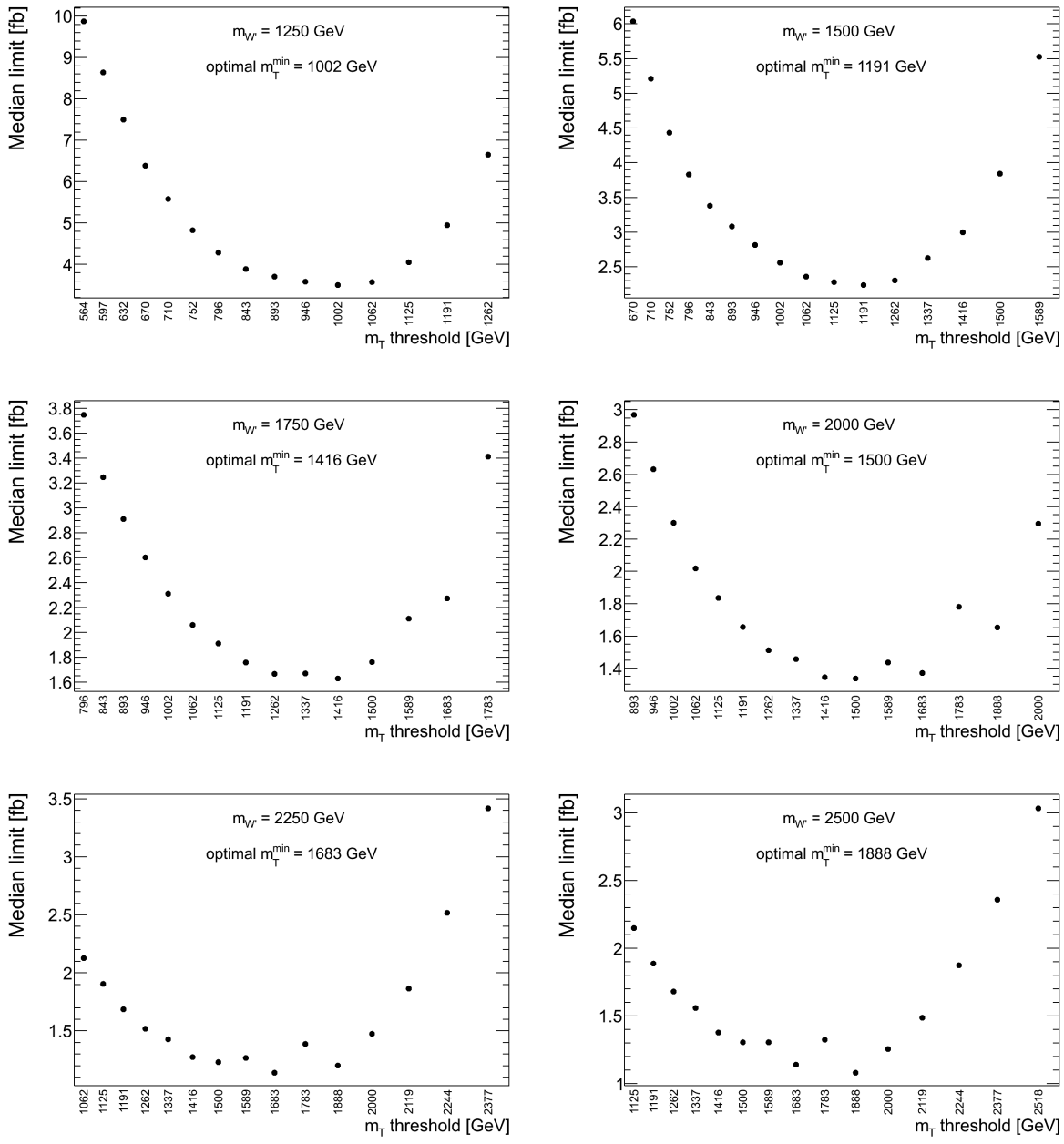

Figure A.2: The median limit under the background-only hypothesis as function of the m_{T} threshold for the SSM W' for different boson masses. The boson mass and the optimal threshold is given inside each plot frame.

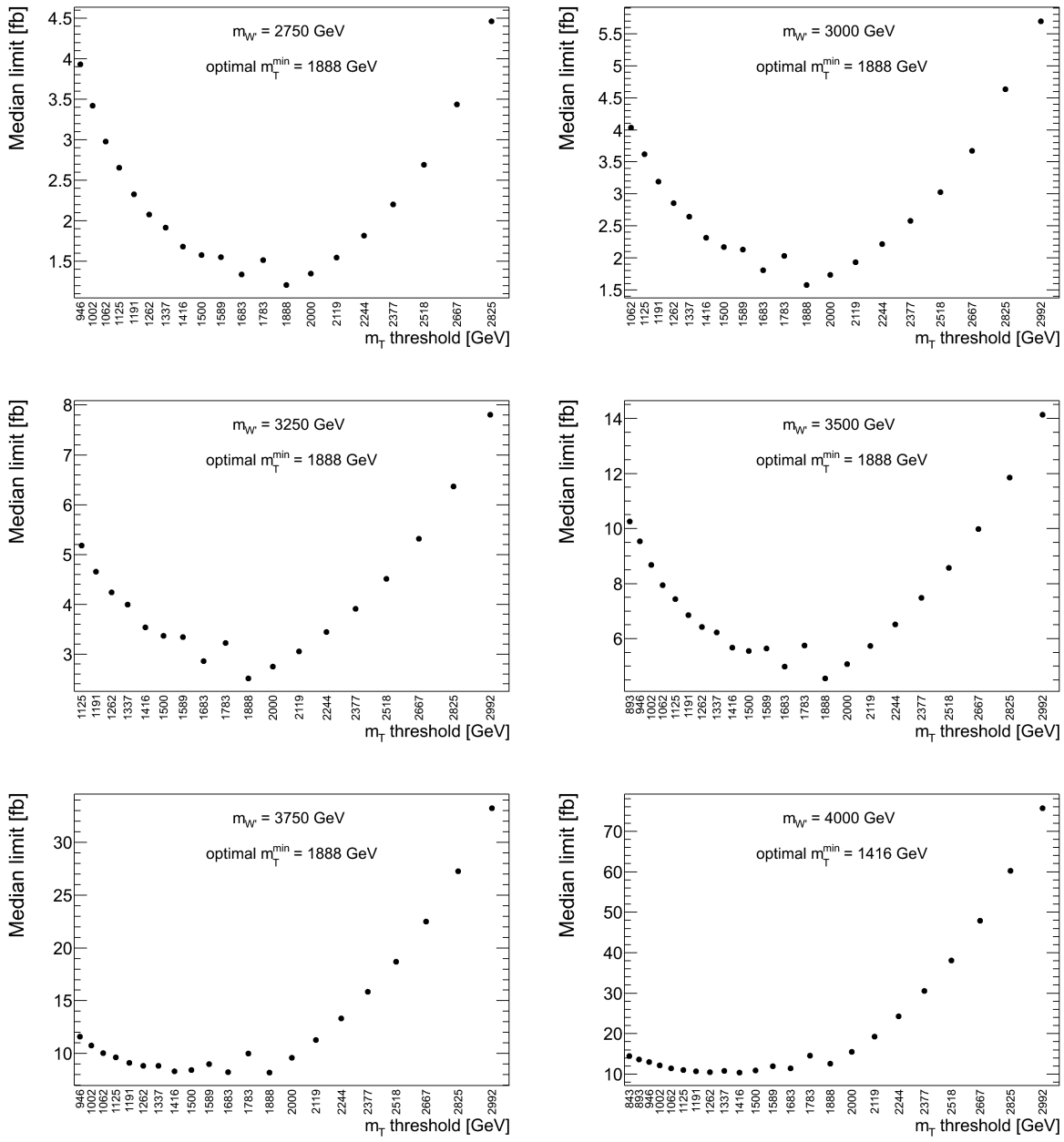

Figure A.3: The median limit under the background-only hypothesis as function of the m_{T} threshold for the SSM W' for different boson masses. The boson mass and the optimal threshold is given inside each plot frame.

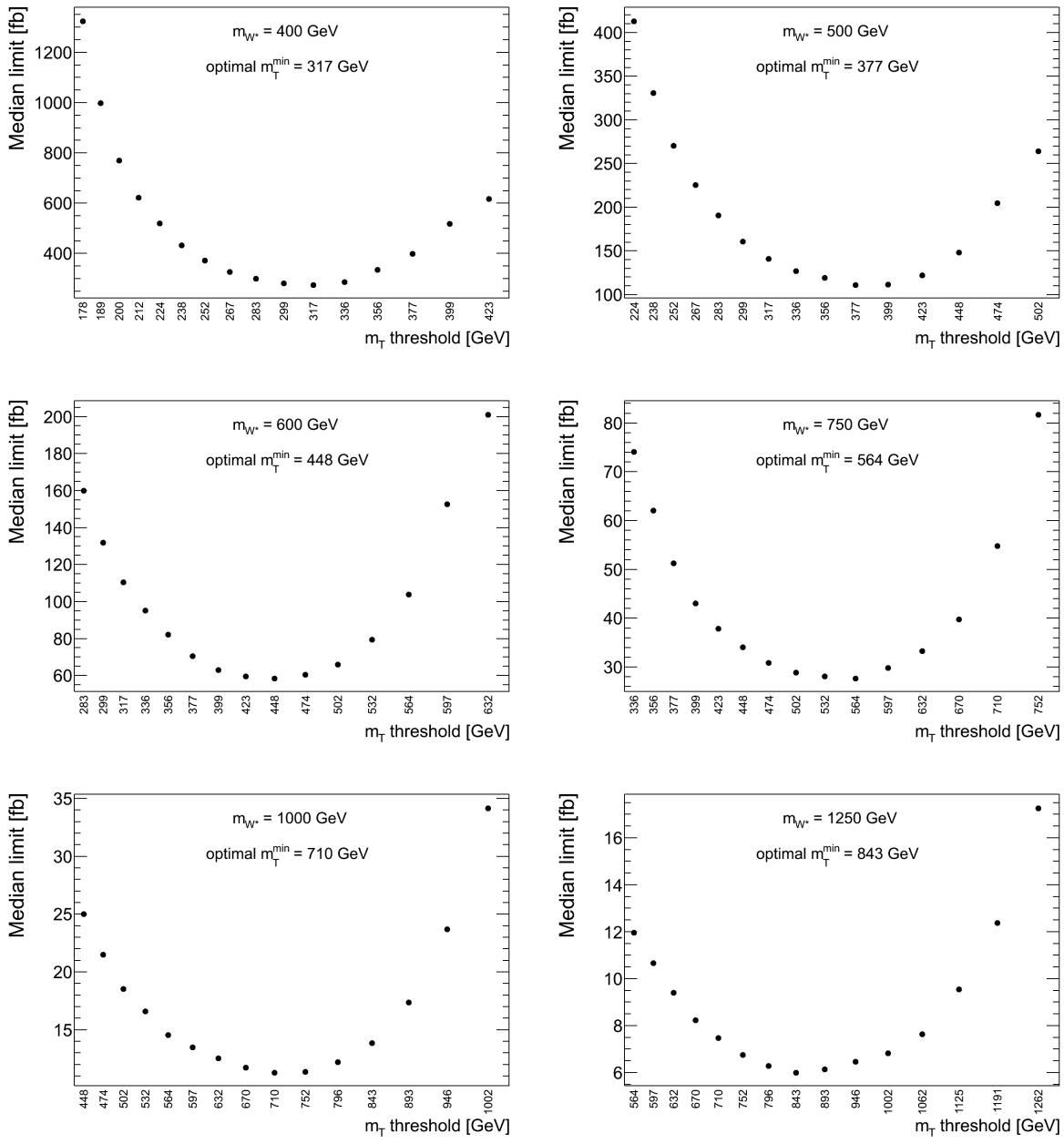

Figure A.4: The median limit under the background-only hypothesis as function of the m_{T} threshold for the W^* for different boson masses. The boson mass and the optimal threshold is given inside each plot frame.

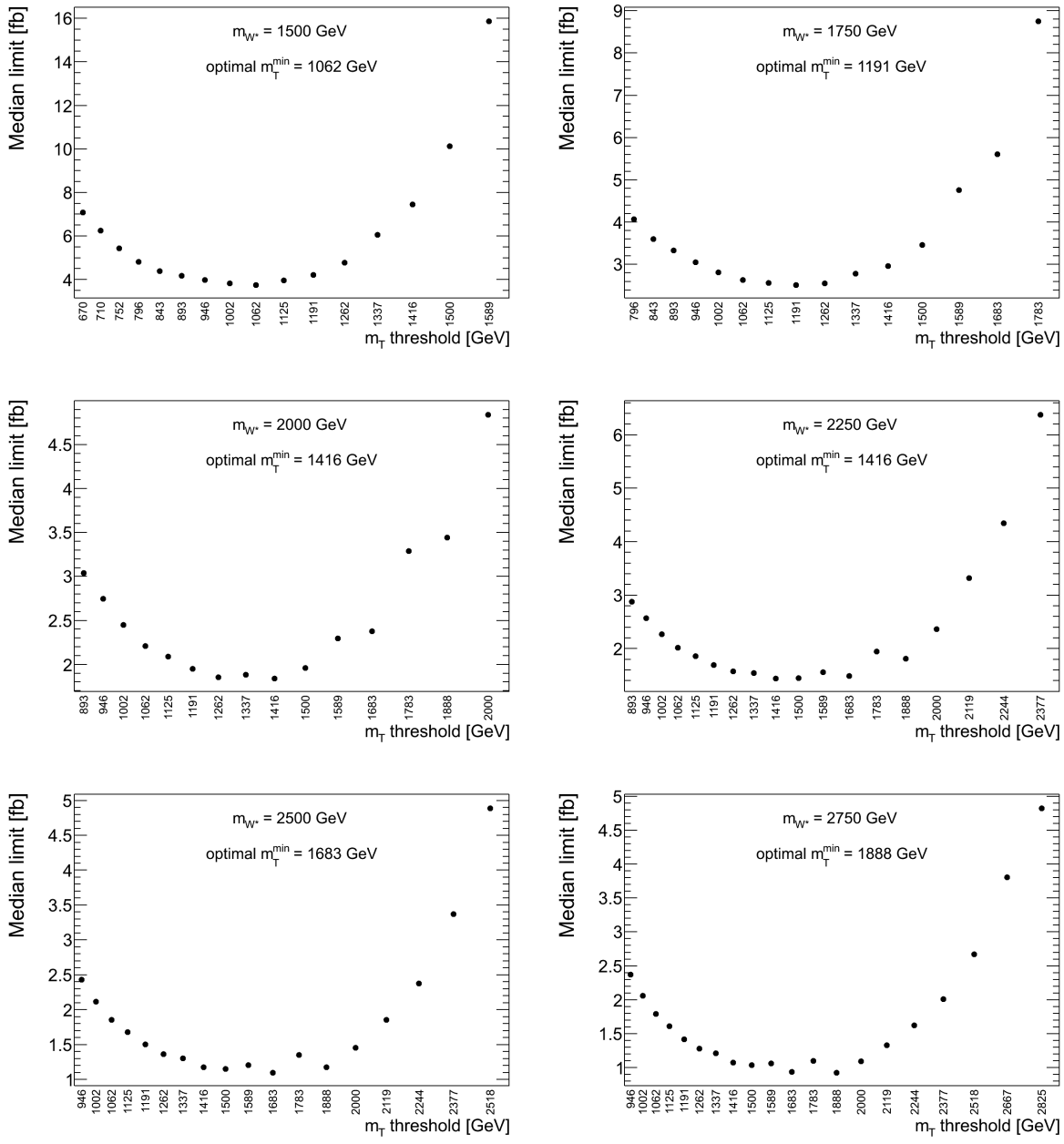

Figure A.5: The median limit under the background-only hypothesis as function of the m_{T} threshold for the W^* for different boson masses. The boson mass and the optimal threshold is given inside each plot frame.

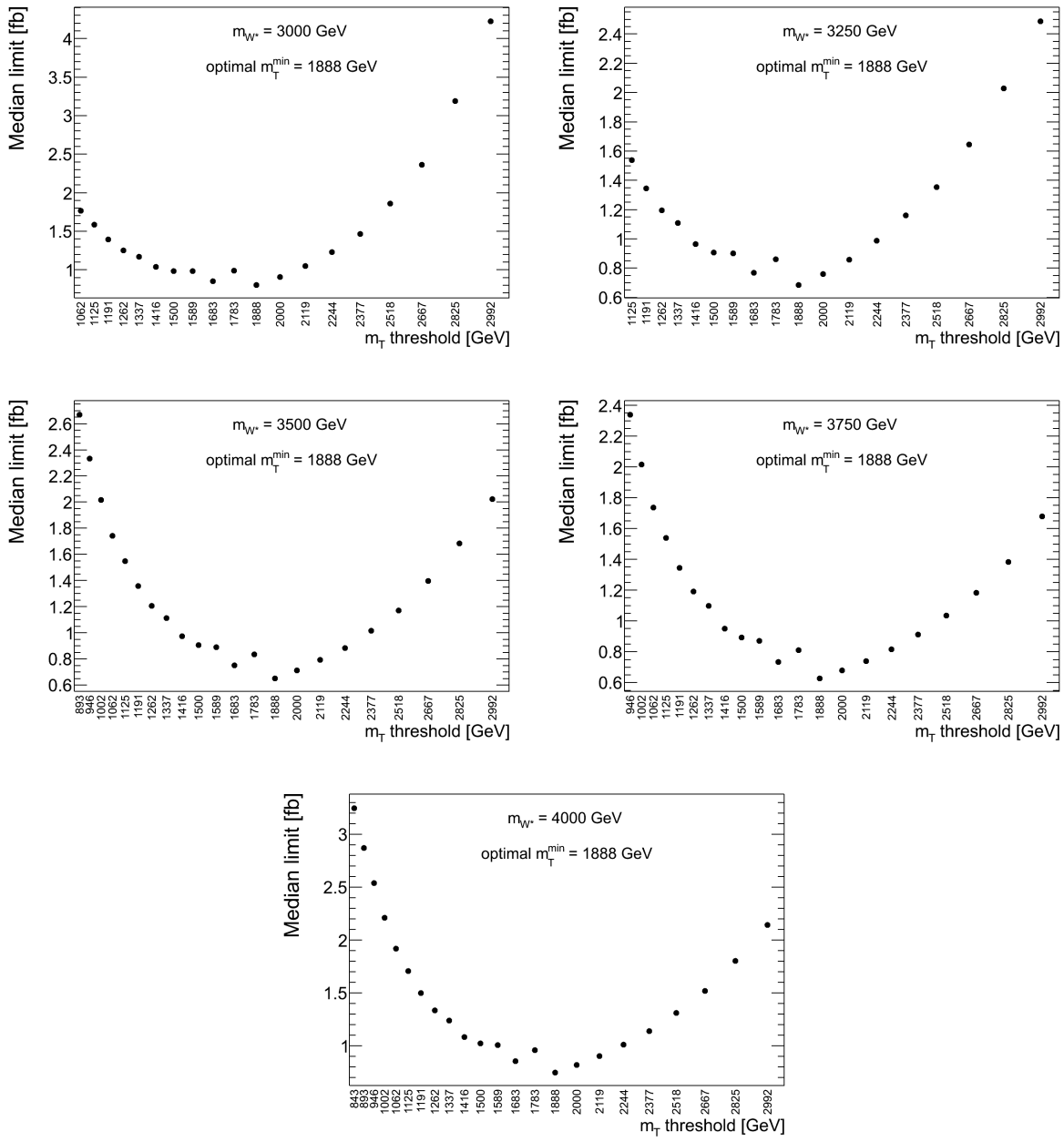

Figure A.6: The median limit under the background-only hypothesis as function of the m_{T} threshold for the W^* for different boson masses. The boson mass and the optimal threshold is given inside each plot frame.

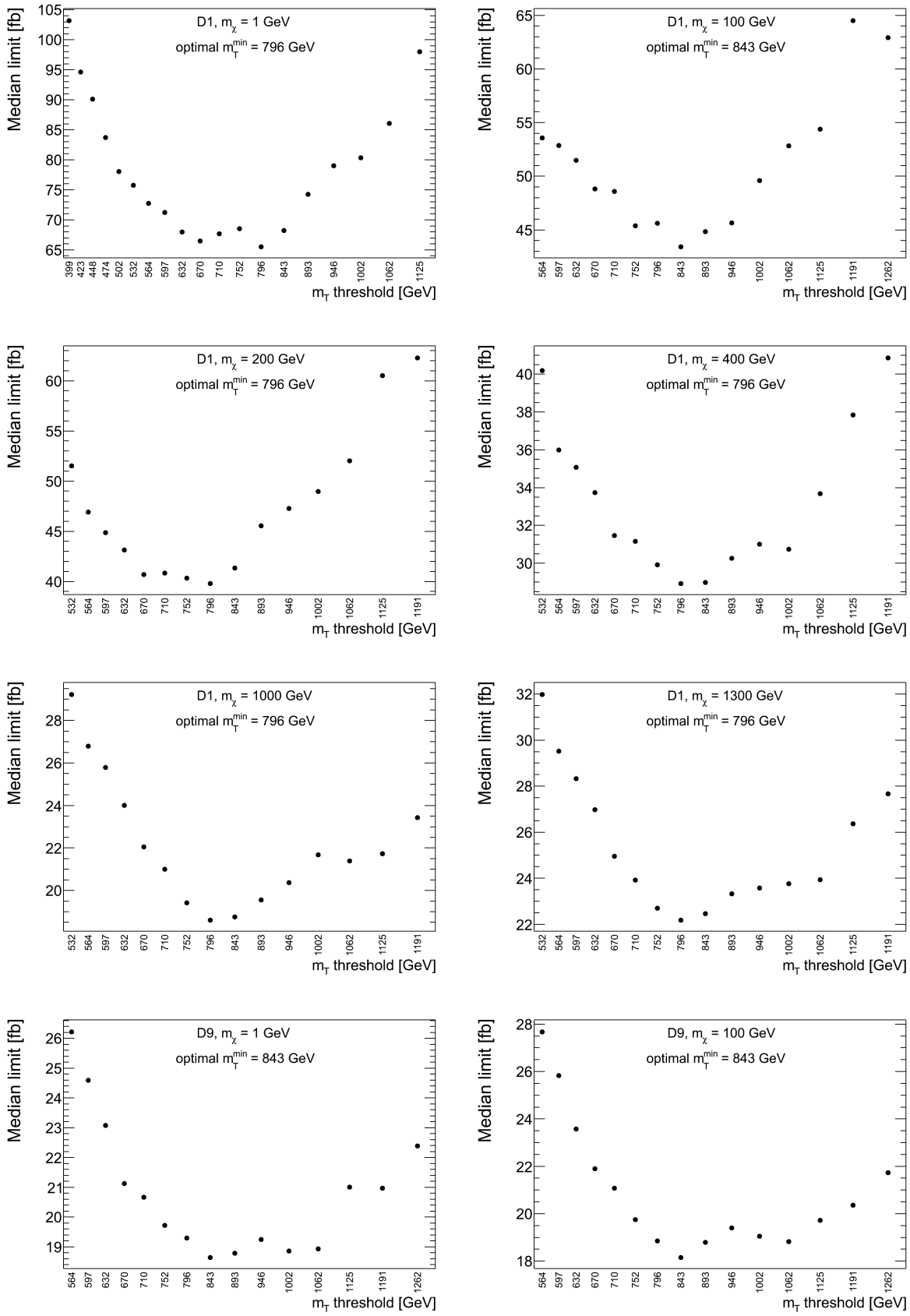

Figure A.7: The median limit under the background-only hypothesis as function of the m_{T} threshold for the DM signal for different signal models and DM particle masses. The signal model, DM particle mass, and optimal threshold is given inside each plot frame.

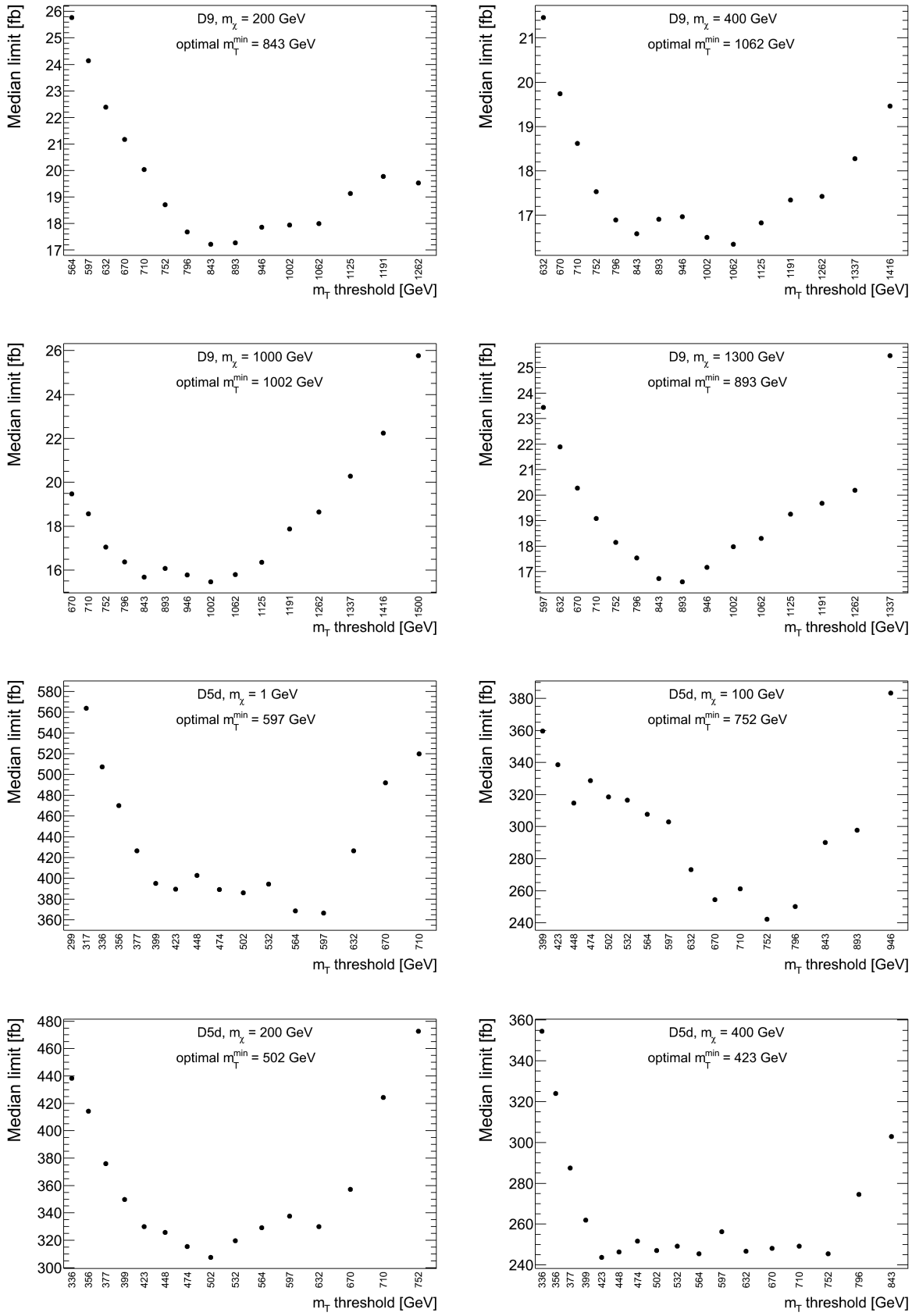

Figure A.8: The median limit under the background-only hypothesis as function of the m_{T} threshold for the DM signal for different signal models and DM particle masses. The signal model, DM particle mass, and optimal threshold is given inside each plot frame.

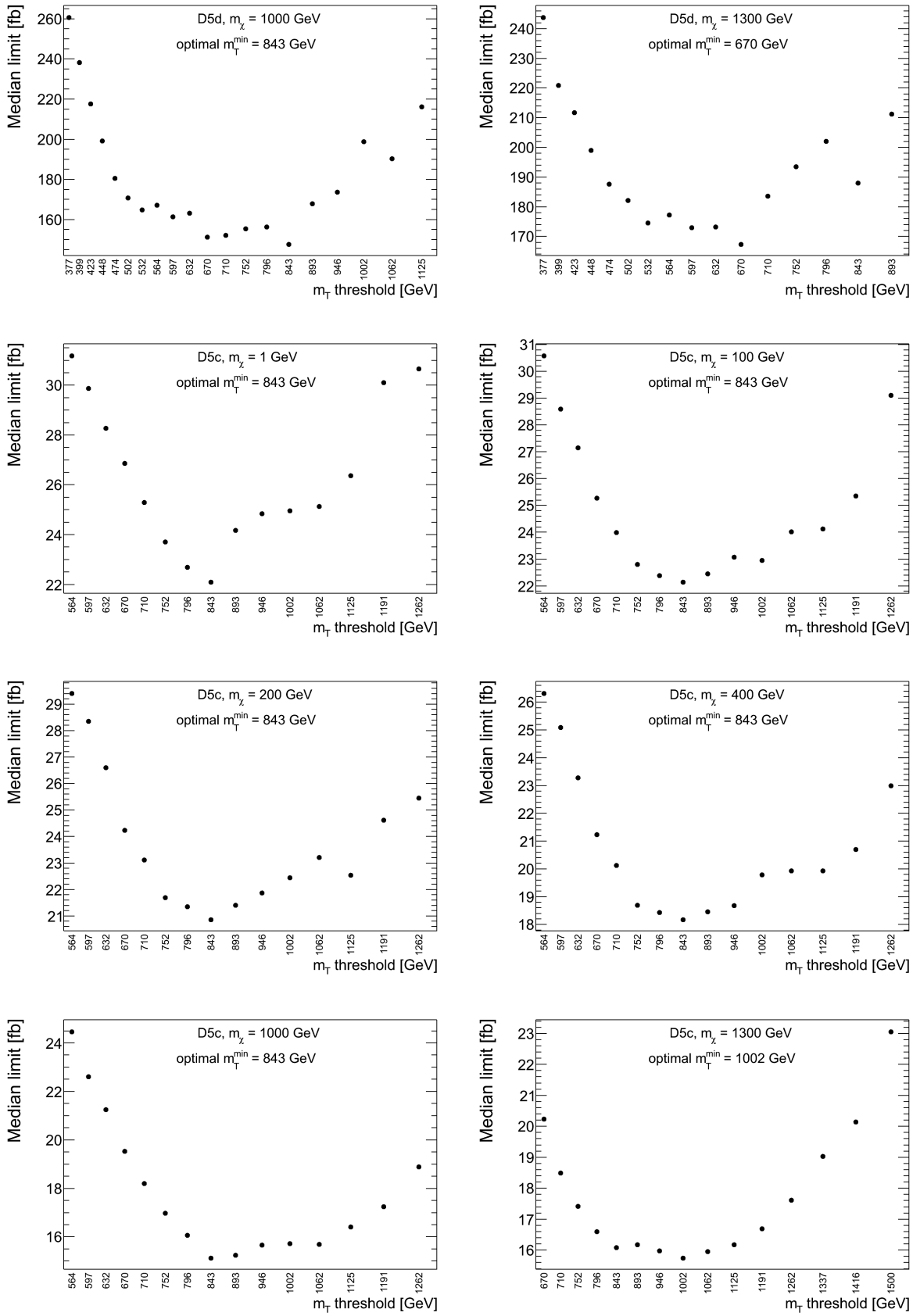

Figure A.9: The median limit under the background-only hypothesis as function of the m_{T} threshold for the DM signal for different signal models and DM particle masses. The signal model, DM particle mass, and optimal threshold is given inside each plot frame.

A.3 Background composition tables

The total background level for each transverse mass threshold is given in the limit input tables 8.8-8.11. The individual contributions to this total background level are given in tables A.1 and A.2. The W background is by far dominant, constituting approximately 80-95% of the total background in the electron channel and approximately 75-85% in the muon channel.

A.4 Additional tables related to fiducial cross section limits

In this section, additional tables related to the fiducial cross section limits with the cut $m_{l\nu} > 0.4\, m_{W'/W^*}$ are presented. The fiducial cross sections are presented in tables A.3 and A.4, corresponding to tables 3.2 and 3.3 for the total cross sections. The SSM W' cross sections in table A.3 are given at NNLO with estimated uncertainties. We note that the k-factor is below unity for the highest boson masses, reflecting that the LO cross sections give an optimistic estimate of the sensitivity to these masses. This effect is not evident from table 3.2, where the k-factors for the highest boson masses are dominated by the off-shell tail at low invariant mass. The W^* cross sections in table A.4 are given at LO only and without any uncertainty estimate as discussed in section 3.2.3.

The muon channel SSM W' and W^* signal efficiency uncertainties are summarized in tables A.5 and A.6 respectively, and these correspond to tables 8.5 and 8.7 for the total cross section limits. As one might have expected, only the beam energy and k-factor uncertainties are changed when going from total to fiducial cross sections. These are the uncertainties that affect the generator level invariant mass distribution. The corresponding tables for the electron channel are unfortunately not available, but the same conclusion should be valid for the electron channel as well.

The limit inputs are presented in tables A.7-A.10, corresponding to tables 8.8-8.11 for the total cross section limits. Changes are only seen in the columns for the efficiency and its correlated uncertainty[2]. Finally, the tables corresponding to 8.13 and 8.14 are A.11 and A.12. Obviously, the limit numbers themselves change, at high mass in particular, but besides this, the only important difference seen in these tables is a reduced impact of the signal efficiency uncertainty at high mass. In particular, the effect of this uncertainty reaches about 10% (compared to about 50% for total cross section limits) at the highest masses, with the effect of signal efficiency correlation also being at most about 10% (compared to about 45% for total cross section limits).

[2] A couple of the numbers for the predicted number of signal events differ in the last digit, but this is just a rounding effect.

$m_{\mathrm{T}}^{\mathrm{min}}$ [GeV]	W	Z	Dibosons	Top	Jets	Total
252	$1.02 \cdot 10^4 \pm 1.2 \cdot 10^2$	32.5 ± 2.1	444 ± 7.0	$1.52 \cdot 10^3 \pm 17$	682 ± 12	$1.29 \cdot 10^4 \pm 1.2 \cdot 10^2$
317	$5.20 \cdot 10^3 \pm 76$	21.7 ± 1.5	258 ± 5.4	778 ± 12	369 ± 8.4	$6.63 \cdot 10^3 \pm 77$
336	$4.16 \cdot 10^3 \pm 65$	17.9 ± 1.3	215 ± 5.0	593 ± 11	291 ± 7.3	$5.28 \cdot 10^3 \pm 67$
377	$2.66 \cdot 10^3 \pm 46$	11.3 ± 1.0	140 ± 4.1	335 ± 8.3	174 ± 5.2	$3.32 \cdot 10^3 \pm 47$
423	$1.70 \cdot 10^3 \pm 29$	8.02 ± 0.84	92.7 ± 3.3	179 ± 6.1	99.3 ± 3.7	$2.07 \cdot 10^3 \pm 30$
448	$1.34 \cdot 10^3 \pm 21$	6.25 ± 0.72	73.8 ± 3.0	135 ± 5.4	76.1 ± 3.1	$1.63 \cdot 10^3 \pm 22$
474	$1.05 \cdot 10^3 \pm 13$	4.61 ± 0.62	60.0 ± 2.7	93.2 ± 4.5	56.8 ± 2.6	$1.26 \cdot 10^3 \pm 15$
564	507 ± 4.9	1.61 ± 0.32	30.4 ± 2.0	32.1 ± 2.7	21.6 ± 1.4	593 ± 6.1
597	394 ± 4.3	1.36 ± 0.31	23.5 ± 1.8	20.7 ± 2.2	16.1 ± 1.1	456 ± 5.3
710	179 ± 2.9	0.351 ± 0.084	12.3 ± 1.4	6.73 ± 1.2	5.39 ± 0.53	203 ± 3.4
796	104 ± 2.1	0.173 ± 0.054	6.58 ± 0.90	2.66 ± 0.65	2.81 ± 0.29	116 ± 2.4
843	77.4 ± 1.8	0.134 ± 0.052	4.69 ± 0.80	1.28 ± 0.43	2.06 ± 0.17	85.6 ± 2.1
1002	32.2 ± 1.1	0.0277 ± 0.0027	2.30 ± 0.66	0 ± 0	0.727 ± 0.098	35.3 ± 1.3
1062	23.1 ± 0.91	0.0198 ± 0.0020	2.16 ± 0.66	0 ± 0	0.513 ± 0.081	25.8 ± 1.1
1191	12.2 ± 0.60	0.00820 ± 0.00069	0.705 ± 0.31	0 ± 0	0.257 ± 0.053	13.2 ± 0.68
1337	5.96 ± 0.33	0.00422 ± 0.00047	0.665 ± 0.31	0 ± 0	0.130 ± 0.033	6.75 ± 0.45
1416	4.12 ± 0.23	0.00264 ± 0.00033	0.346 ± 0.24	0 ± 0	0.0925 ± 0.025	4.56 ± 0.33
1500	2.65 ± 0.10	0.00163 ± 0.00022	0.270 ± 0.23	0 ± 0	0.0662 ± 0.020	2.99 ± 0.25
1683	1.09 ± 0.035	0.000562 ± 0.000072	0.254 ± 0.23	0 ± 0	0.0342 ± 0.011	1.38 ± 0.23
1888	0.414 ± 0.0078	0.000187 ± 0.000024	0 ± 0	0 ± 0	0.0179 ± 0.0066	0.432 ± 0.010

Table A.1: Background composition in the electron channel. For each transverse mass threshold, the individual contributions to the total background level are given with statistical uncertainty. All contributions are given in terms of expected event counts at final selection.

$m_{\mathrm{T}}^{\mathrm{min}}$ [GeV]	W	Z	Dibosons	$t\bar{t}$	Single top	Jets	Total
252	$8.12 \cdot 10^3 \pm 1.0 \cdot 10^2$	701 ± 9.8	409 ± 6.9	$1.54 \cdot 10^3 \pm 15$	223 ± 9.9	134 ± 25	$1.11 \cdot 10^4 \pm 1.1 \cdot 10^2$
317	$3.25 \cdot 10^3 \pm 58$	263 ± 5.0	172 ± 4.5	471 ± 8.4	74.3 ± 5.8	48.4 ± 13	$4.28 \cdot 10^3 \pm 61$
336	$2.58 \cdot 10^3 \pm 50$	206 ± 4.1	139 ± 4.1	343 ± 7.2	56.6 ± 5.1	37.4 ± 11	$3.36 \cdot 10^3 \pm 52$
377	$1.64 \cdot 10^3 \pm 35$	125 ± 2.5	88.0 ± 3.4	173 ± 5.1	34.7 ± 4.1	22.5 ± 7.6	$2.09 \cdot 10^3 \pm 37$
423	$1.04 \cdot 10^3 \pm 23$	77.4 ± 1.7	59.8 ± 2.9	85.1 ± 3.6	19.1 ± 2.7	13.5 ± 5.2	$1.30 \cdot 10^3 \pm 24$
448	843 ± 18	60.2 ± 1.3	48.3 ± 2.6	63.8 ± 3.1	16.8 ± 2.6	10.5 ± 4.2	$1.04 \cdot 10^3 \pm 19$
502	527 ± 9.0	37.9 ± 0.87	32.2 ± 2.2	29.0 ± 2.1	7.27 ± 1.7	6.33 ± 2.8	640 ± 10
564	319 ± 4.6	23.8 ± 0.65	21.0 ± 1.9	13.5 ± 1.4	2.05 ± 1.1	3.78 ± 1.9	383 ± 5.6
597	251 ± 3.8	18.6 ± 0.55	18.2 ± 1.8	8.87 ± 1.2	1.42 ± 0.97	2.94 ± 1.5	301 ± 4.8
710	117 ± 2.7	9.25 ± 0.35	9.87 ± 1.3	1.71 ± 0.49	0.640 ± 0.64	1.37 ± 0.79	140 ± 3.2
796	69.6 ± 2.1	5.51 ± 0.22	6.40 ± 1.2	1.22 ± 0.41	0.640 ± 0.64	0.823 ± 0.51	84.2 ± 2.6
843	53.0 ± 1.8	4.19 ± 0.17	5.23 ± 1.1	0.716 ± 0.33	0.640 ± 0.64	0.638 ± 0.41	64.4 ± 2.3
1002	23.1 ± 1.2	2.05 ± 0.16	3.36 ± 0.94	0 ± 0	0.0018 ± 0.0018	0.297 ± 0.21	28.8 ± 1.6
1062	17.2 ± 1.1	1.63 ± 0.16	3.10 ± 0.94	0 ± 0	0.0018 ± 0.0018	0.230 ± 0.17	22.2 ± 1.5
1191	8.61 ± 0.63	0.886 ± 0.11	1.46 ± 0.57	0 ± 0	0.0018 ± 0.0018	0.138 ± 0.11	11.1 ± 0.87
1416	3.41 ± 0.45	0.439 ± 0.11	0.576 ± 0.25	0 ± 0	0 ± 0	0.0641 ± 0.054	4.49 ± 0.53
1500	2.73 ± 0.43	0.370 ± 0.11	0.456 ± 0.23	0 ± 0	0 ± 0	0.0496 ± 0.043	3.60 ± 0.50
1683	1.16 ± 0.14	0.269 ± 0.11	0.131 ± 0.093	0 ± 0	0 ± 0	0.0297 ± 0.027	1.59 ± 0.20
1888	0.517 ± 0.063	0.108 ± 0.035	0 ± 0	0 ± 0	0 ± 0	0.0178 ± 0.017	0.643 ± 0.075

Table A.2: Background composition in the muon channel. For each transverse mass threshold, the individual contributions to the total background level are given with statistical uncertainty. All contributions are given in terms of expected event counts at final selection.

$m_{W'}$ [GeV]	σ_{LO} [fb]	k-factor	σ_{NNLO} [fb]	$(\Delta\sigma/\sigma)^{\mathrm{up}}_{\mathrm{NNLO}}$ [%]	$(\Delta\sigma/\sigma)^{\mathrm{down}}_{\mathrm{NNLO}}$ [%]
300	$1.13 \cdot 10^5$	1.31	$1.48 \cdot 10^5$	6.8	3.2
400	$3.79 \cdot 10^4$	1.31	$4.95 \cdot 10^4$	6.6	3.2
500	$1.62 \cdot 10^4$	1.30	$2.11 \cdot 10^4$	6.3	4.2
600	$7.94 \cdot 10^3$	1.29	$1.02 \cdot 10^4$	5.9	5.8
750	$3.20 \cdot 10^3$	1.27	$4.07 \cdot 10^3$	5.5	8.3
1000	902	1.25	$1.13 \cdot 10^3$	6.6	12
1250	303	1.22	371	8.2	16
1500	113	1.21	136	9.9	18
1750	44.5	1.18	52.6	12	19
2000	18.0	1.16	20.8	14	18
2250	7.56	1.12	8.49	16	18
2500	3.26	1.07	3.50	18	19
2750	1.42	1.03	1.46	21	22
3000	0.621	0.990	0.615	26	25
3250	0.289	0.932	0.270	32	27
3500	0.139	0.882	0.123	37	29
3750	0.0663	0.911	0.0604	40	30
4000	0.0347	0.909	0.0315	40	30

Table A.3: Fiducial cross sections with the invariant mass cut $m_{l\nu} > 0.4\, m_{W'}$ for the process $pp \to W' + X \to l\,\nu + X$ at a pp center of mass energy $\sqrt{s} = 8\,\mathrm{TeV}$. The cross sections are for a single decay channel, i.e. not a sum over the three lepton generations. Both the LO cross section, the NNLO cross section, and the ratio between the two (the k-factor) is shown. The uncertainties on the NNLO cross sections are derived from variations of the mass dependent k-factor as described in section 4.1.1 and are dominated by PDF uncertainties. They are presented here as relative uncertainties in percent.

m_{W^*} [GeV]	σ_{LO} [fb]	m_{W^*} [GeV]	σ_{LO} [fb]
400	$3.76 \cdot 10^4$	2250	6.99
500	$1.62 \cdot 10^4$	2500	2.90
600	$7.95 \cdot 10^3$	2750	1.20
750	$3.17 \cdot 10^3$	3000	0.488
1000	882	3250	0.198
1250	294	3500	0.0788
1500	108	3750	0.0311
1750	42.3	4000	0.0121
2000	17.1		

Table A.4: Fiducial cross sections with the invariant mass cut $m_{l\nu} > 0.4\, m_{W^*}$ for the process $pp \to W^* + X \to l\,\nu + X$ at a pp center of mass energy $\sqrt{s} = 8\,\mathrm{TeV}$. The cross sections are for a single decay channel, i.e. not a sum over the three lepton generations.

Source	$m_{W'}$, $m_{\mathrm{T}}^{\mathrm{min}}$ [GeV]								
	300	400	500	600	750	1000	1250	1500	1750
	252	336	423	502	597	796	1002	1191	1416
Efficiency	3.3	3.3	3.3	3.4	3.4	3.4	3.4	3.5	3.5
Resolution	0.15	0.21	0.12	0.95	0.44	0.98	0.69	0.44	1.2
Scale	0.53	0.48	0.84	0.81	0.79	1.1	1.4	1.8	2.4
$\not{E}_{\mathrm{T}}$	0.65	0.27	0.20	0.12	0.19	0.19	0.096	0.13	0.083
Jet resolution	0.44	0.065	0.38	0.30	0.18	0.11	0.15	0.065	0.21
Jet scale	0.19	0.015	0.12	0.041	0.034	0.023	0.15	0.13	0.18
All experimental	3.4	3.4	3.5	3.6	3.5	3.7	3.7	3.9	4.4
MC statistics	1.6	1.6	1.6	1.5	1.4	1.3	1.3	1.3	1.3
All uncorrelated	3.8	3.7	3.8	3.9	3.8	3.9	4.0	4.1	4.5
Beam energy	0.006	0.007	0.011	0.014	0.016	0.026	0.046	0.071	0.12
k-factor	0.002	0.031	0.13	0.22	0.34	0.58	0.60	0.72	0.64
All correlated	0.007	0.032	0.13	0.22	0.34	0.58	0.60	0.72	0.65
Total	3.8	3.7	3.8	3.9	3.8	4.0	4.0	4.2	4.6

Source	$m_{W'}$, $m_{\mathrm{T}}^{\mathrm{min}}$ [GeV]								
	2000	2250	2500	2750	3000	3250	3500	3750	4000
	1500	1683	1888	1888	1888	1888	1888	1888	1888
Efficiency	3.5	3.5	3.6	3.5	3.5	3.6	3.9	3.8	3.7
Resolution	1.4	0.74	1.3	0.92	1.1	0.60	0.40	0.40	1.3
Scale	1.8	2.3	2.8	2.3	1.9	1.9	2.1	2.5	3.3
$\not{E}_{\mathrm{T}}$	0.064	0.055	0.064	0.071	0.083	0.030	0.018	0.011	0.015
Jet resolution	0.038	0.023	0.051	0.060	0.017	0.006	0.047	0.023	0.036
Jet scale	0.039	0.033	0.099	0.096	0.054	0.051	0.028	0.024	0.032
All experimental	4.2	4.3	4.7	4.3	4.2	4.1	4.5	4.6	5.1
MC statistics	1.2	1.2	1.2	1.1	1.1	1.0	0.97	0.85	0.71
All uncorrelated	4.3	4.4	4.9	4.5	4.3	4.2	4.6	4.6	5.1
Beam energy	0.17	0.28	0.43	0.65	0.95	1.3	1.6	1.7	1.5
k-factor	0.63	0.92	1.5	2.5	4.7	8.4	13	17	18
All correlated	0.65	0.96	1.5	2.6	4.8	8.5	13	17	18
Total	4.4	4.5	5.1	5.2	6.5	9.5	14	17	19

Table A.5: Muon channel SSM W' relative signal efficiency uncertainties in percent for fiducial limits with the invariant mass cut $m_{l\nu} > 0.4\, m_{W'}$.

Source	m_{W^*}, $m_{\mathrm{T}}^{\mathrm{min}}$ [GeV]								
	400	500	600	750	1000	1250	1500	1750	2000
	317	377	448	564	710	843	1062	1191	1416
Efficiency	3.3	3.3	3.3	3.4	3.3	3.4	3.4	3.4	3.5
Resolution	0.76	0.59	0.19	0.58	0.19	0.88	0.30	0.90	0.86
Scale	0.94	0.54	0.46	0.86	0.86	1.2	1.5	2.1	2.8
$\not\!\!E_{\mathrm{T}}$	0.66	0.32	0.25	0.47	0.36	0.24	0.13	0.17	0.12
Jet resolution	0.29	0.62	0.19	0.22	0.17	0.075	0.14	0.14	0.090
Jet scale	0.27	0.41	0.009	0.22	0.22	0.12	0.030	0.033	0.10
All experimental	3.6	3.5	3.4	3.6	3.5	3.7	3.7	4.1	4.5
MC statistics	2.2	2.1	2.1	2.1	1.9	1.7	1.8	1.7	1.8
All uncorrelated	4.2	4.1	4.0	4.1	3.9	4.1	4.1	4.4	4.9
Beam energy	0.074	0.049	0.049	0.046	0.032	0.029	0.043	0.044	0.058
k-factor	0.79	0.60	0.45	0.35	0.24	0.23	0.17	0.17	0.24
All correlated	0.79	0.60	0.45	0.35	0.24	0.23	0.18	0.18	0.24
Total	4.3	4.1	4.0	4.1	3.9	4.1	4.1	4.4	4.9

Source	m_{W^*}, $m_{\mathrm{T}}^{\mathrm{min}}$ [GeV]							
	2250	2500	2750	3000	3250	3500	3750	4000
	1416	1683	1888	1888	1888	1888	1888	1888
Efficiency	3.5	3.5	3.5	3.5	3.8	3.8	3.7	3.6
Resolution	0.38	0.66	0.36	0.28	1.1	1.4	1.2	0.35
Scale	2.2	2.5	4.7	2.8	2.3	1.8	2.1	1.9
$\not\!\!E_{\mathrm{T}}$	0.26	0.099	0.12	0.057	0.052	0.15	0.11	0.17
Jet resolution	0.14	0.073	0.25	0.15	0.14	0.052	0.064	0.033
Jet scale	0.18	0.040	0.042	0.044	0.026	0.087	0.039	0.027
All experimental	4.1	4.3	5.9	4.6	4.6	4.4	4.4	4.1
MC statistics	1.6	1.7	1.8	1.8	1.8	1.8	1.8	2.0
All uncorrelated	4.4	4.7	6.2	4.9	4.9	4.7	4.8	4.6
Beam energy	0.062	0.082	0.13	0.15	0.23	0.30	0.48	0.67
k-factor	0.24	0.57	0.75	1.3	1.9	3.4	8.4	24
All correlated	0.24	0.58	0.76	1.3	1.9	3.4	8.5	24
Total	4.4	4.7	6.2	5.1	5.3	5.8	9.7	25

Table A.6: Muon channel W^* relative signal efficiency uncertainties in percent for fiducial limits with the invariant mass cut $m_{l\nu} > 0.4\, m_{W^*}$.

$m_{W'}$ [GeV]	$m_{\mathrm{T}}^{\mathrm{min}}$ [GeV]	$\overline{\varepsilon_{\mathrm{sig}}}$	$\frac{(\Delta\varepsilon_{\mathrm{sig}})_{\mathrm{uc}}}{\overline{\varepsilon_{\mathrm{sig}}}}$ [%]	$\frac{(\Delta\varepsilon_{\mathrm{sig}})_{\mathrm{c}}}{\overline{\varepsilon_{\mathrm{sig}}}}$ [%]	$\overline{L_{\mathrm{int}}}\,\overline{\varepsilon_{\mathrm{sig}}}\sigma_{\mathrm{th}}$	$\overline{L_{\mathrm{int}}}\,\overline{\sigma_{\mathrm{bg}}^{\mathrm{eff}}}$	$\frac{(\Delta\sigma_{\mathrm{bg}}^{\mathrm{eff}})_{\mathrm{uc}}}{\overline{\sigma_{\mathrm{bg}}^{\mathrm{eff}}}}$ [%]	$\frac{(\Delta\sigma_{\mathrm{bg}}^{\mathrm{eff}})_{\mathrm{c}}}{\overline{\sigma_{\mathrm{bg}}^{\mathrm{eff}}}}$ [%]	n_{obs}
300	252	0.230	4.1	0.12	$6.9 \cdot 10^5$	$1.29 \cdot 10^4$	3.3	5.4	12717
400	336	0.323	3.8	0.13	$3.2 \cdot 10^5$	$5.28 \cdot 10^3$	4.5	5.2	5176
500	423	0.330	4.1	0.20	$1.4 \cdot 10^5$	$2.07 \cdot 10^3$	5.0	5.3	2017
600	474	0.404	3.4	0.41	$8.4 \cdot 10^4$	$1.26 \cdot 10^3$	4.2	6.3	1214
750	597	0.402	3.3	0.39	$3.3 \cdot 10^4$	456	4.7	8.7	414
1000	796	0.398	3.1	0.39	$9.1 \cdot 10^3$	116	5.0	12	101
1250	1002	0.396	3.1	0.56	$3.0 \cdot 10^3$	35.3	6.1	15	34
1500	1191	0.402	3.1	0.77	$1.1 \cdot 10^3$	13.2	6.8	17	14
1750	1416	0.372	3.1	0.74	$4.0 \cdot 10^2$	4.56	8.8	18	5
2000	1500	0.431	2.9	0.62	$1.8 \cdot 10^2$	2.99	10	18	3
2250	1683	0.416	2.9	1.1	72	1.38	18	16	0
2500	1888	0.381	3.0	1.7	27	0.432	6.4	20	0
2750	1888	0.417	2.9	2.8	12	0.432	6.4	20	0
3000	1888	0.425	2.8	5.1	5.3	0.432	6.4	20	0
3250	1888	0.405	2.8	9.2	2.2	0.432	6.4	20	0
3500	1888	0.368	2.8	15	0.92	0.432	6.4	20	0
3750	1888	0.331	2.9	21	0.41	0.432	6.4	20	0
4000	1888	0.310	3.0	23	0.20	0.432	6.4	20	0

Table A.7: Electron channel inputs to the SSM W' limit calculation for fiducial limits with the invariant mass cut $m_{l\nu} > 0.4\,m_{W'}$.

$m_{W'}$ [GeV]	$m_{\mathrm{T}}^{\mathrm{min}}$ [GeV]	$\overline{\varepsilon_{\mathrm{sig}}}$	$\frac{(\Delta\varepsilon_{\mathrm{sig}})_{\mathrm{uc}}}{\overline{\varepsilon_{\mathrm{sig}}}}$ [%]	$\frac{(\Delta\varepsilon_{\mathrm{sig}})_{\mathrm{c}}}{\overline{\varepsilon_{\mathrm{sig}}}}$ [%]	$\overline{L_{\mathrm{int}}}\,\overline{\varepsilon_{\mathrm{sig}}}\sigma_{\mathrm{th}}$	$\overline{L_{\mathrm{int}}}\,\overline{\sigma_{\mathrm{bg}}^{\mathrm{eff}}}$	$\frac{(\Delta\sigma_{\mathrm{bg}}^{\mathrm{eff}})_{\mathrm{uc}}}{\overline{\sigma_{\mathrm{bg}}^{\mathrm{eff}}}}$ [%]	$\frac{(\Delta\sigma_{\mathrm{bg}}^{\mathrm{eff}})_{\mathrm{c}}}{\overline{\sigma_{\mathrm{bg}}^{\mathrm{eff}}}}$ [%]	n_{obs}
300	252	0.185	3.8	0.007	$5.6 \cdot 10^5$	$1.11 \cdot 10^4$	4.3	5.4	10886
400	336	0.195	3.7	0.032	$2.0 \cdot 10^5$	$3.36 \cdot 10^3$	4.3	5.5	3306
500	423	0.189	3.8	0.13	$8.1 \cdot 10^4$	$1.30 \cdot 10^3$	4.5	5.6	1214
600	502	0.199	3.9	0.22	$4.1 \cdot 10^4$	640	4.5	6.8	548
750	597	0.231	3.8	0.34	$1.9 \cdot 10^4$	301	5.4	8.5	255
1000	796	0.227	3.9	0.58	$5.2 \cdot 10^3$	84.2	5.4	11	58
1250	1002	0.220	4.0	0.60	$1.7 \cdot 10^3$	28.8	7.1	13	19
1500	1191	0.221	4.1	0.72	$6.1 \cdot 10^2$	11.1	16	14	6
1750	1416	0.201	4.5	0.65	$2.1 \cdot 10^2$	4.49	21	14	0
2000	1500	0.231	4.3	0.65	98	3.60	19	14	0
2250	1683	0.220	4.4	0.96	38	1.59	16	16	0
2500	1888	0.203	4.9	1.5	14	0.643	33	19	0
2750	1888	0.225	4.5	2.6	6.6	0.643	33	19	0
3000	1888	0.234	4.3	4.8	2.9	0.643	33	19	0
3250	1888	0.226	4.2	8.5	1.2	0.643	33	19	0
3500	1888	0.210	4.6	13	0.52	0.643	33	19	0
3750	1888	0.193	4.6	17	0.24	0.643	33	19	0
4000	1888	0.189	5.1	18	0.12	0.643	33	19	0

Table A.8: Muon channel inputs to the SSM W' limit calculation for fiducial limits with the invariant mass cut $m_{l\nu} > 0.4\,m_{W'}$.

m_{W^*} [GeV]	$m_{\mathrm{T}}^{\mathrm{min}}$ [GeV]	$\overline{\varepsilon_{\mathrm{sig}}}$	$\frac{(\Delta\varepsilon_{\mathrm{sig}})_{\mathrm{uc}}}{\overline{\varepsilon_{\mathrm{sig}}}}$ [%]	$\frac{(\Delta\varepsilon_{\mathrm{sig}})_{\mathrm{c}}}{\overline{\varepsilon_{\mathrm{sig}}}}$ [%]	$\overline{L_{\mathrm{int}}}\,\overline{\varepsilon_{\mathrm{sig}}}\sigma_{\mathrm{th}}$	$\overline{L_{\mathrm{int}}}\,\overline{\sigma_{\mathrm{bg}}^{\mathrm{eff}}}$	$\frac{(\Delta\sigma_{\mathrm{bg}}^{\mathrm{eff}})_{\mathrm{uc}}}{\overline{\sigma_{\mathrm{bg}}^{\mathrm{eff}}}}$ [%]	$\frac{(\Delta\sigma_{\mathrm{bg}}^{\mathrm{eff}})_{\mathrm{c}}}{\overline{\sigma_{\mathrm{bg}}^{\mathrm{eff}}}}$ [%]	n_{obs}
400	317	0.196	4.9	0.82	$1.5 \cdot 10^5$	$6.63 \cdot 10^3$	4.1	5.2	6448
500	377	0.246	4.3	0.59	$8.1 \cdot 10^4$	$3.32 \cdot 10^3$	4.0	5.3	3275
600	448	0.257	4.3	0.54	$4.1 \cdot 10^4$	$1.63 \cdot 10^3$	5.0	5.7	1582
750	564	0.248	4.2	0.50	$1.6 \cdot 10^4$	593	4.4	8.0	524
1000	710	0.302	4.2	0.25	$5.4 \cdot 10^3$	203	4.8	11	177
1250	843	0.337	3.9	0.16	$2.0 \cdot 10^3$	85.6	5.1	13	79
1500	1062	0.296	3.9	0.19	$6.5 \cdot 10^2$	25.8	6.4	16	26
1750	1191	0.324	3.9	0.20	$2.8 \cdot 10^2$	13.2	6.8	17	14
2000	1337	0.342	3.8	0.23	$1.2 \cdot 10^2$	6.75	9.1	17	9
2250	1416	0.391	3.6	0.26	55	4.56	8.8	18	5
2500	1683	0.338	3.8	0.47	20	1.38	18	16	0
2750	1888	0.323	3.9	0.86	7.8	0.432	6.4	20	0
3000	1888	0.384	3.6	1.3	3.8	0.432	6.4	20	0
3250	1888	0.440	3.5	2.0	1.8	0.432	6.4	20	0
3500	1888	0.479	3.4	3.4	0.77	0.432	6.4	20	0
3750	1888	0.508	3.3	9.0	0.32	0.432	6.4	20	0
4000	1888	0.505	3.3	26	0.12	0.432	6.4	20	0

Table A.9: Electron channel inputs to the W^* limit calculation for fiducial limits with the invariant mass cut $m_{l\nu} > 0.4\, m_{W^*}$.

m_{W^*} [GeV]	$m_{\mathrm{T}}^{\mathrm{min}}$ [GeV]	$\overline{\varepsilon_{\mathrm{sig}}}$	$\frac{(\Delta\varepsilon_{\mathrm{sig}})_{\mathrm{uc}}}{\overline{\varepsilon_{\mathrm{sig}}}}$ [%]	$\frac{(\Delta\varepsilon_{\mathrm{sig}})_{\mathrm{c}}}{\overline{\varepsilon_{\mathrm{sig}}}}$ [%]	$\overline{L_{\mathrm{int}}}\,\overline{\varepsilon_{\mathrm{sig}}}\sigma_{\mathrm{th}}$	$\overline{L_{\mathrm{int}}}\,\overline{\sigma_{\mathrm{bg}}^{\mathrm{eff}}}$	$\frac{(\Delta\sigma_{\mathrm{bg}}^{\mathrm{eff}})_{\mathrm{uc}}}{\overline{\sigma_{\mathrm{bg}}^{\mathrm{eff}}}}$ [%]	$\frac{(\Delta\sigma_{\mathrm{bg}}^{\mathrm{eff}})_{\mathrm{c}}}{\overline{\sigma_{\mathrm{bg}}^{\mathrm{eff}}}}$ [%]	n_{obs}
400	317	0.111	4.2	0.79	$8.5 \cdot 10^4$	$4.28 \cdot 10^3$	4.2	5.5	4227
500	377	0.140	4.1	0.60	$4.6 \cdot 10^4$	$2.09 \cdot 10^3$	4.3	5.6	2002
600	448	0.144	4.0	0.45	$2.3 \cdot 10^4$	$1.04 \cdot 10^3$	4.6	5.9	936
750	564	0.143	4.1	0.35	$9.2 \cdot 10^3$	383	4.8	8.0	321
1000	710	0.173	3.9	0.24	$3.1 \cdot 10^3$	140	6.0	10	109
1250	843	0.191	4.1	0.23	$1.1 \cdot 10^3$	64.4	6.2	11	40
1500	1062	0.164	4.1	0.18	$3.6 \cdot 10^2$	22.2	7.8	13	12
1750	1191	0.182	4.4	0.18	$1.6 \cdot 10^2$	11.1	16	14	6
2000	1416	0.160	4.9	0.24	55	4.49	21	14	0
2250	1416	0.204	4.4	0.24	29	4.49	21	14	0
2500	1683	0.179	4.7	0.58	10	1.59	16	16	0
2750	1888	0.162	6.2	0.76	3.9	0.643	33	19	0
3000	1888	0.186	4.9	1.3	1.8	0.643	33	19	0
3250	1888	0.220	4.9	1.9	0.88	0.643	33	19	0
3500	1888	0.232	4.7	3.4	0.37	0.643	33	19	0
3750	1888	0.250	4.8	8.5	0.16	0.643	33	19	0
4000	1888	0.251	4.6	24	0.062	0.643	33	19	0

Table A.10: Muon channel inputs to the W^* limit calculation for fiducial limits with the invariant mass cut $m_{l\nu} > 0.4\, m_{W^*}$.

$m_{W'}$		95% CL limit on the signal cross section [fb]						
[GeV]	Channel	none	S	SB	SBL	S_c	$(SB)_c$	$(SB)_cL$
	Electron	28.7	28.8	301	338	28.8	302	339
300	Muon	27.4	27.5	336	373	27.5	336	373
	Combined	16.1	16.1	222	272	16.1	290	331
	Electron	13.9	13.9	93.7	104	13.9	93.8	104
400	Muon	21.2	21.3	104	114	21.3	104	114
	Combined	10.1	10.1	69.1	82.6	10.1	87.6	98.9
	Electron	9.01	9.04	38.0	41.6	9.04	38.2	41.8
500	Muon	9.17	9.19	35.1	38.8	9.19	35.2	38.9
	Combined	5.27	5.27	24.5	29.3	5.27	31.6	35.7
	Electron	5.58	5.59	19.2	20.9	5.59	19.4	21.0
600	Muon	4.55	4.57	14.5	15.8	4.57	14.6	15.9
	Combined	2.82	2.83	10.6	12.5	2.83	14.7	16.4
	Electron	2.88	2.89	8.07	8.52	2.89	8.15	8.60
750	Muon	3.40	3.41	8.18	8.62	3.41	8.25	8.69
	Combined	1.73	1.73	5.13	5.70	1.73	6.97	7.48
	Electron	1.79	1.79	3.15	3.24	1.79	3.17	3.26
1000	Muon	1.80	1.81	2.74	2.83	1.81	2.78	2.86
	Combined	1.00	1.00	1.78	1.89	1.00	2.38	2.48
	Electron	1.56	1.56	1.97	1.99	1.56	1.98	2.01
1250	Muon	1.52	1.53	1.83	1.86	1.53	1.85	1.87
	Combined	0.936	0.937	1.21	1.24	0.937	1.43	1.46
	Electron	1.19	1.19	1.31	1.32	1.19	1.32	1.32
1500	Muon	1.12	1.12	1.24	1.25	1.12	1.25	1.26
	Combined	0.720	0.721	0.815	0.826	0.721	0.887	0.897
	Electron	0.872	0.874	0.897	0.901	0.874	0.901	0.904
1750	Muon	0.735	0.738	0.738	0.742	0.738	0.741	0.744
	Combined	0.471	0.472	0.482	0.485	0.472	0.501	0.505
	Electron	0.618	0.619	0.629	0.631	0.619	0.630	0.632
2000	Muon	0.639	0.642	0.642	0.644	0.642	0.643	0.646
	Combined	0.356	0.356	0.361	0.363	0.356	0.370	0.372
	Electron	0.356	0.356	0.356	0.357	0.356	0.357	0.358
2250	Muon	0.671	0.674	0.674	0.676	0.674	0.676	0.677
	Combined	0.233	0.233	0.233	0.234	0.233	0.234	0.235
	Electron	0.388	0.388	0.388	0.389	0.388	0.389	0.390
2500	Muon	0.730	0.733	0.733	0.735	0.733	0.735	0.736
	Combined	0.253	0.254	0.254	0.254	0.254	0.255	0.255
	Electron	0.354	0.356	0.356	0.356	0.356	0.356	0.357
2750	Muon	0.657	0.661	0.661	0.662	0.661	0.663	0.664
	Combined	0.230	0.231	0.231	0.231	0.231	0.232	0.233
	Electron	0.348	0.351	0.351	0.351	0.351	0.352	0.353
3000	Muon	0.632	0.638	0.638	0.639	0.638	0.642	0.643
	Combined	0.225	0.225	0.225	0.226	0.226	0.228	0.229
	Electron	0.366	0.372	0.372	0.373	0.372	0.375	0.376
3250	Muon	0.655	0.666	0.666	0.668	0.666	0.673	0.674
	Combined	0.235	0.236	0.236	0.237	0.239	0.243	0.243
	Electron	0.402	0.420	0.420	0.421	0.420	0.426	0.426
3500	Muon	0.703	0.731	0.731	0.732	0.731	0.741	0.743
	Combined	0.256	0.261	0.261	0.261	0.267	0.274	0.274
	Electron	0.446	0.486	0.486	0.486	0.486	0.493	0.494
3750	Muon	0.765	0.812	0.811	0.813	0.812	0.826	0.828
	Combined	0.282	0.292	0.292	0.292	0.303	0.314	0.315
	Electron	0.477	0.531	0.531	0.532	0.531	0.541	0.542
4000	Muon	0.782	0.838	0.838	0.839	0.838	0.854	0.856
	Combined	0.297	0.309	0.309	0.310	0.324	0.337	0.338

Table A.11: Fiducial cross section limits with the invariant mass cut $m_{l\nu} > 0.4\, m_{W'}$ for the SSM W' with different subsets of the nuisance parameter uncertainties included in the limit calculation.

m_{W^*}		95% CL limit on the signal cross section [fb]						
[GeV]	Channel	none	S	SB	SBL	S_c	$(SB)_c$	$(SB)_cL$
	Electron	20.7	20.8	180	201	20.8	183	204
400	Muon	44.3	44.5	232	255	44.5	235	259
	Combined	16.6	16.7	141	170	16.7	180	204
	Electron	17.3	17.3	78.1	86.5	17.3	79.0	87.5
500	Muon	18.0	18.0	81.5	90.0	18.0	82.5	91.1
	Combined	10.6	10.6	55.0	66.3	10.6	72.0	81.5
	Electron	10.4	10.4	40.0	43.5	10.4	40.4	43.9
600	Muon	8.61	8.63	32.9	36.4	8.63	33.2	36.7
	Combined	5.36	5.36	23.7	28.2	5.36	31.7	35.7
	Electron	4.23	4.25	13.8	14.7	4.25	13.9	14.9
750	Muon	5.48	5.50	14.3	15.3	5.50	14.4	15.4
	Combined	2.57	2.57	8.57	9.78	2.57	12.0	13.1
	Electron	2.69	2.70	5.75	5.97	2.70	5.79	6.01
1000	Muon	3.17	3.18	5.87	6.10	3.18	5.91	6.13
	Combined	1.61	1.61	3.58	3.85	1.61	4.77	5.02
	Electron	2.29	2.30	3.56	3.63	2.30	3.57	3.64
1250	Muon	1.80	1.81	2.56	2.63	1.81	2.58	2.65
	Combined	1.17	1.17	1.85	1.94	1.17	2.45	2.54
	Electron	1.99	2.00	2.36	2.38	2.00	2.36	2.39
1500	Muon	1.65	1.65	1.88	1.91	1.65	1.89	1.91
	Combined	1.11	1.11	1.34	1.37	1.11	1.55	1.58
	Electron	1.48	1.48	1.62	1.63	1.48	1.62	1.64
1750	Muon	1.36	1.36	1.51	1.52	1.36	1.51	1.52
	Combined	0.884	0.885	1.00	1.01	0.885	1.08	1.09
	Electron	1.34	1.34	1.39	1.40	1.34	1.39	1.40
2000	Muon	0.925	0.929	0.929	0.933	0.929	0.930	0.934
	Combined	0.718	0.719	0.732	0.739	0.719	0.771	0.776
	Electron	0.829	0.832	0.854	0.857	0.832	0.855	0.859
2250	Muon	0.725	0.728	0.728	0.732	0.728	0.729	0.732
	Combined	0.456	0.457	0.467	0.470	0.457	0.484	0.488
	Electron	0.437	0.439	0.439	0.440	0.439	0.439	0.440
2500	Muon	0.828	0.831	0.831	0.833	0.831	0.833	0.834
	Combined	0.286	0.287	0.287	0.288	0.287	0.288	0.288
	Electron	0.458	0.460	0.460	0.460	0.460	0.460	0.460
2750	Muon	0.915	0.922	0.922	0.924	0.922	0.923	0.924
	Combined	0.306	0.306	0.306	0.306	0.306	0.306	0.307
	Electron	0.386	0.387	0.387	0.387	0.387	0.387	0.388
3000	Muon	0.795	0.799	0.799	0.800	0.799	0.800	0.802
	Combined	0.260	0.260	0.260	0.261	0.260	0.261	0.262
	Electron	0.336	0.337	0.337	0.338	0.337	0.337	0.338
3250	Muon	0.673	0.677	0.677	0.679	0.677	0.679	0.680
	Combined	0.224	0.225	0.225	0.225	0.225	0.226	0.226
	Electron	0.308	0.310	0.310	0.311	0.310	0.311	0.311
3500	Muon	0.637	0.641	0.641	0.642	0.641	0.643	0.645
	Combined	0.208	0.208	0.208	0.209	0.209	0.210	0.211
	Electron	0.291	0.296	0.296	0.297	0.296	0.298	0.299
3750	Muon	0.593	0.604	0.604	0.605	0.604	0.610	0.611
	Combined	0.195	0.197	0.197	0.197	0.198	0.202	0.202
	Electron	0.293	0.333	0.333	0.333	0.333	0.339	0.340
4000	Muon	0.590	0.664	0.664	0.665	0.664	0.681	0.683
	Combined	0.195	0.207	0.207	0.208	0.221	0.232	0.232

Table A.12: Fiducial cross section limits with the invariant mass cut $m_{l\nu} > 0.4\, m_{W^*}$ for the W^* with different subsets of the nuisance parameter uncertainties included in the limit calculation.

Appendix B

Qualification task within the MC generators group

In order for a PhD student to appear on the author list of ATLAS publications, a so-called qualification task must be completed. Such a task should be valuable to (or necessary for) the collaboration, but should not be directly part of a physics analysis. I did my qualification task within the MC generators group, working on validation of the Herwig++ [152] parton shower generator, and in particular the use of Herwig++ for the showering of ALPGEN [153] events.

B.1 Multileg generators

A parton shower generator, such as PYTHIA [27, 59], provides in principle a complete description of a pp collision final state. The hard scattering process is calculated in perturbation theory, with quarks or gluons from the protons as initial state particles. For example, W^- production and subsequent decay to a muon and a muon antineutrino is in the hard scattering associated with the $(2 \rightarrow 2)$ Feynman diagram of fig. B.1(a) and similar diagrams with other initial state quarks, and initial state radiation of jets from the quarks is handled by the parton shower. However, when considering event topologies with several hard and well separated jets, this approach is found to give an unsatisfactory description of data.

In order to properly describe events with many hard and well separated jets, the partons giving rise to these jets need to be included in the hard scattering process. For the $W^- \rightarrow \mu^- \overline{\nu_\mu}$ example, one needs then to generate events and calculate cross sections not only corresponding to the Feynman diagrams such as the one in fig. B.1(a), but also to other Feynman diagrams, of which some examples are shown in figs. B.1(b)-(h), corresponding to higher jet multiplicities. Some jet radiation is then described in the hard scattering calculation, but the parton shower is still needed to evolve the final state partons into a set of colorless hadrons. A multileg event generator must therefore be interfaced to a parton shower generator, unless the same generator handles both multileg hard processes and parton shower, as in the case of SHERPA [94].

As the hard scattering process of fig. B.1(a) combined with a parton shower provides already a description of events with one or more jets, there is overlap between the jet phase space simulated with this hard process and with the hard processes corresponding to higher jet multiplicities. Obviously, the same kind of overlap occurs between all the different jet mul-

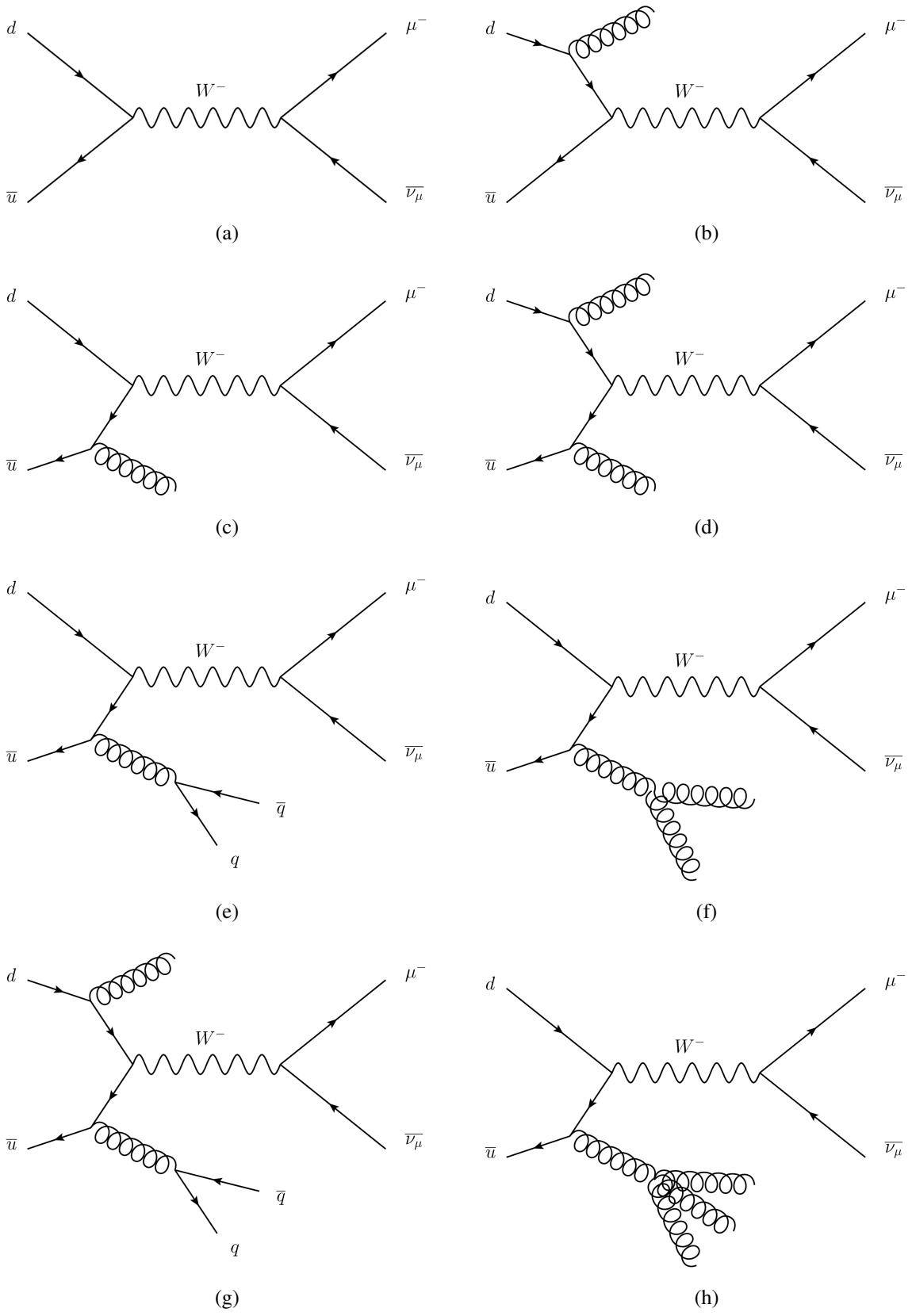

Figure B.1: Examples of Feynman diagrams for the production of the W^- with subsequent decay to a muon and a muon antineutrino. Different numbers of hard partons, which give rise to jets in the final state, are included. The number of hard partons ranges here from zero (a) to three ((g) and (h)).

tiplicities, and different prescriptions exist for the consistent merging of multileg events with parton shower generators [154].

B.1.1 ALPGEN and MLM matching

The ALPGEN event generator is capable of generating hard scattering processes with many hard partons, for example up to 6 hard partons in the case of W or Z boson production in association with jets. It can be interfaced to PYTHIA 6, PYTHIA 8, HERWIG, or Herwig++. Overlap in the jet phase space simulated with the different hard processes is removed with the "MLM matching" prescription [154].

The MLM matching procedure is based on the clustering of jets from the final state particles emerging from the parton shower, and the matching of these jets to the hard partons in the "final state" of the hard scattering process. A jet and a parton are said to match if their separation in the η,ϕ-plane is smaller than a cutoff related to the cone size used for the jet clustering. All the partons in the "final state" of the hard scattering are required to be matched to a jet, and if this is not the case, the event is rejected. Events are also rejected if they contain jets which are not matched to any of the partons in the "final state" of the hard scattering, as such events are better represented in the relevant higher parton multiplicity samples. The only exception is the case of the sample with the highest parton multiplicity, in which extra jets generated by the parton shower are allowed, as there is no higher multiplicity sample with which these events overlap. For a complete description of any process, all the samples corresponding to the different parton multiplicities must be included.

B.2 Validation of W and Z production with Herwig++'s internal POWHEG implementation

While the main focus of my qualification task was to set up and validate the showering of ALPGEN events with Herwig++ in ATLAS, I was initially asked to do some validation of Herwig++ standalone processes in order to get familiar with event generation in the ATLAS software and with Herwig++ in particular. The processes I looked at were W and Z production at NLO using the POWHEG method [72, 73] as implemented in Herwig++. This method is based on changing slightly the parton shower in such a way that the hardest emission is always the first in order to facilitate the consistent merging of the parton shower technique with a NLO hard scattering calculation. The CT10 NLO PDFs [75] were used. The results were compared, using Rivet[1], to previously validated samples generated with POWHEG BOX [74] using the CT10 NLO PDFs and showered in PYTHIA 8. The total cross sections agree within 3%. Reasonable agreement is also observed in lepton and gauge boson specific variables, as seen in the example plots of fig. B.2.

While there is reasonable agreement also in the shape of the leading jet p_{T}, fig. B.3(a), the subleading jet p_{T} displays an obvious problem with the Herwig++ samples. As shown in fig. B.3(b), this distribution has a sharp drop around $p_{\mathrm{T}} = 80\,\mathrm{GeV}$, which does not occur in the

[1]The Rivet project (Robust Independent Validation of Experiment and Theory) is a toolkit for validation of Monte Carlo event generators. See here: `http://rivet.hepforge.org/`

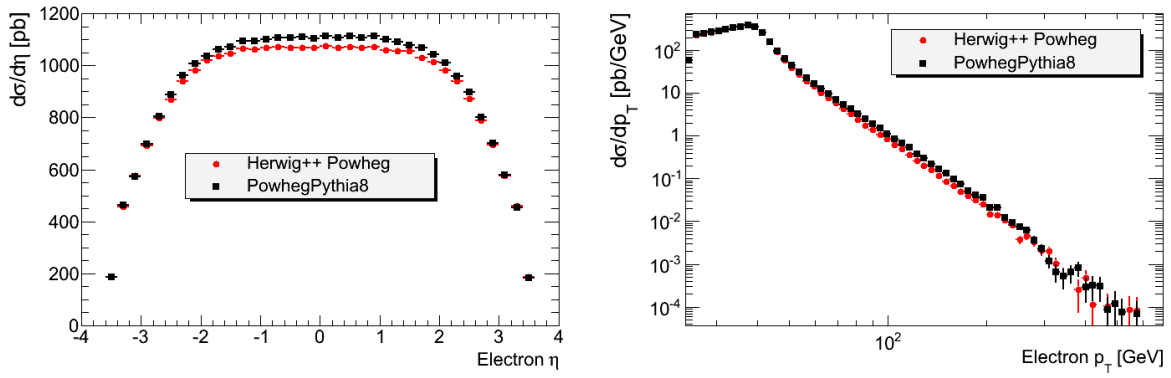

(a) (b)

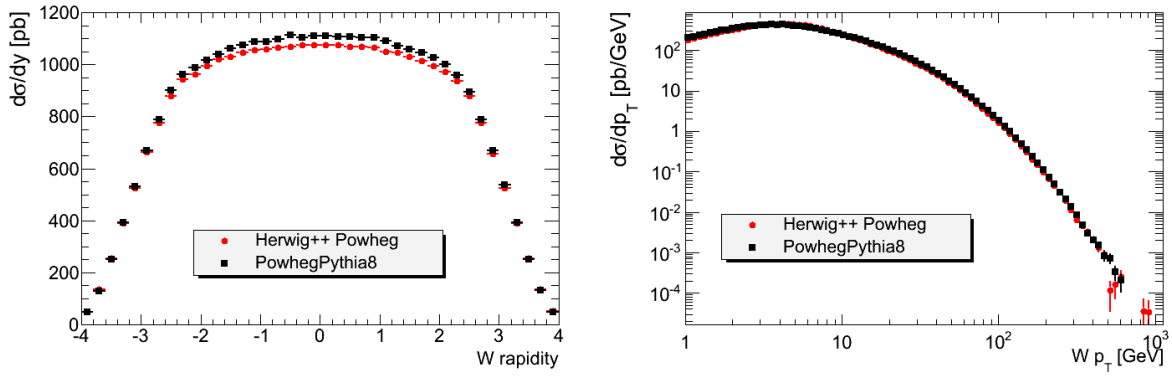

(c) (d)

Figure B.2: Distributions of the electron η (a), electron p_{T} (b), W boson rapidity (c), and W boson p_{T} (d) compared between Herwig++ and POWHEG BOX + PYTHIA 8 for the $W \to e\,\nu$ process in pp collisions at $\sqrt{s} = 7\,\mathrm{TeV}$. The Herwig++ results correspond to this generator's internal POWHEG implementation.

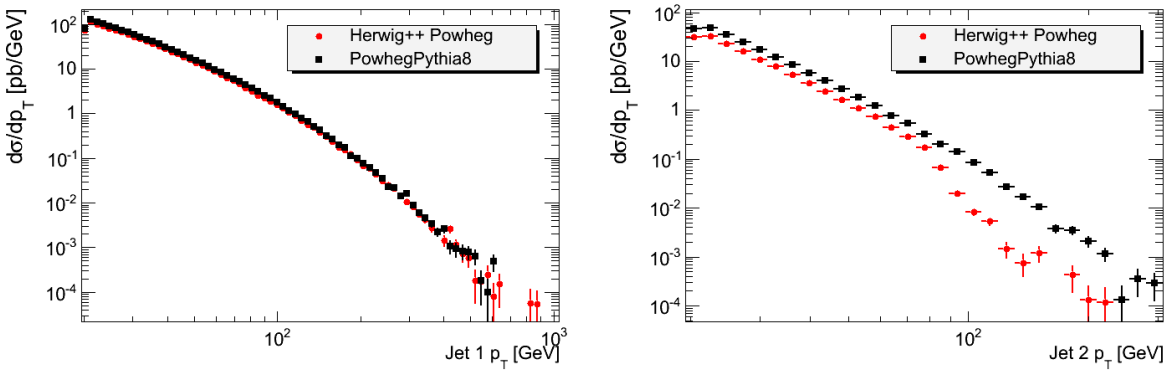

(a) (b)

Figure B.3: Distributions of the leading (a) and subleading (b) jet p_{T} compared between Herwig++ and POWHEG BOX + PYTHIA 8 for the $W \rightarrow e\,\nu$ process in pp collisions at $\sqrt{s} = 7\,\mathrm{TeV}$. The Herwig++ results correspond to the generator's internal POWHEG implementation.

POWHEG BOX + PYTHIA 8 case. According to the Herwig++ authors, the problem should be absent in Herwig++ version 2.6.3. The plots in fig. B.3 were made with version 2.6.1. Indeed, the subleading jet p_{T} looks much better in version 2.6.3, as demonstrated in fig. B.4.

B.3 Showering of ALPGEN events with Herwig++

While ALPGEN samples processed with the Fortran based parton shower generators PYTHIA 6 and HERWIG have long been used in ATLAS and are well validated, the processing of ALPGEN events with PYTHIA 8 and Herwig++ in ATLAS is just getting started. It is important to gain experience with such samples, as the more modern, C++ based, PYTHIA 8 and Herwig++ generators are expected to completely take over for their Fortran based counterparts in the long run.

The processing of ALPGEN events requires more than a simple interface that passes the hard scattering events to the parton shower generator. The MLM matching is performed in the shower stage, and a dedicated ALPGEN interface handling this is therefore required. Such an interface has existed for Herwig++ since version 2.6.0 [155].

To facilitate the processing of hard scattering events from a wide variety of generators in the available parton shower generators, a common file format has been agreed on for such events [156]. The XML-style files contain all the information agreed upon in the original Les Houches Accord [157], including event level information such as the event weight and coupling constants, and particle level information such as the identity and four-momentum for each particle. Unfortunately, the hard scattering event files produced by current versions of ALPGEN do not follow the file format defined in ref. [156], although all necessary information as defined in ref. [157] is present in the files. The ALPGEN interface to Herwig++ therefore comes with a standalone C++ code for converting the ALPGEN event file to the proper Les Houches format. In the conversion process, relevant configuration parameters are also read from an auxiliary ALPGEN output file, and a set of Herwig++ commands are written by the conversion code that

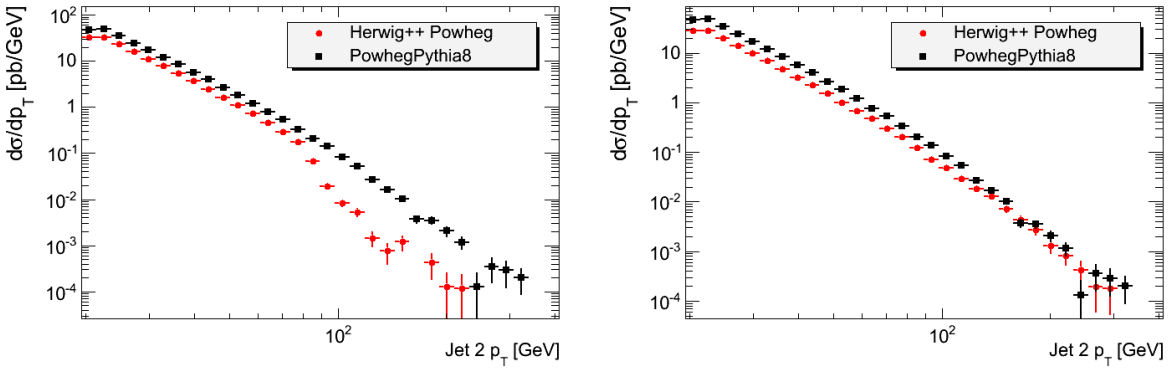

(a) (b)

Figure B.4: Distributions of the subleading jet p_{T} compared between Herwig++ and POWHEG BOX + PYTHIA 8 for the $W \to e\,\nu$ process in pp collisions at $\sqrt{s} = 7\,\mathrm{TeV}$. The Herwig++ results correspond to the generator's internal POWHEG implementation. Herwig++ version 2.6.1 is used in (a) while version 2.6.3 is used in (b).

easily allows the user to set up Herwig++ to process the converted event file.

For every ATLAS grid dataset containing ALPGEN hard scattering events, one could obviously run the conversion code and create a new dataset containing the same events in the format required by Herwig++. To facilitate the direct use of existing ALPGEN datasets and on-the-fly generation where ALPGEN and Herwig++ runs in the same job, the conversion code was instead modified to comply with ATLAS conventions and integrated in the ATLAS software. The resulting implementation allows the user to run Herwig++ directly on existing ALPGEN datasets after creating only a minimal job configuration file. However, an upcoming version of ALPGEN is foreseen to produce event files in the required format directly, and an additional interface in the ATLAS software has therefore been implemented for the processing of these files directly in Herwig++.

B.3.1 Physics validation

My work on the ALPGEN+Herwig++ combination in ATLAS extended beyond the purely technical aspect. A large part was devoted to validation in the form of the comparison of ALPGEN event samples processed in Herwig++ to the corresponding samples processed in PYTHIA 6 and in particular HERWIG. For all comparisons, existing ALPGEN samples generated with the CTEQ6L1 PDFs were used.

Herwig++ vs. HERWIG for W+jets at $\sqrt{s} = 8\,\mathrm{TeV}$

Initial comparisons were made between ALPGEN samples showered with Herwig++ and HERWIG without underlying event for W boson production in association with jets using the relevant pure MC Rivet analysis[2] (`MC_WJETS`). Such validation had initially been performed by

[2]For such pure MC comparisons, the yellow bands in the ratio plots represent only the statistical uncertainty of the MC result listed first in the legend. For comparisons to data, they represent the full uncertainty of the data points, including systematic uncertainty.

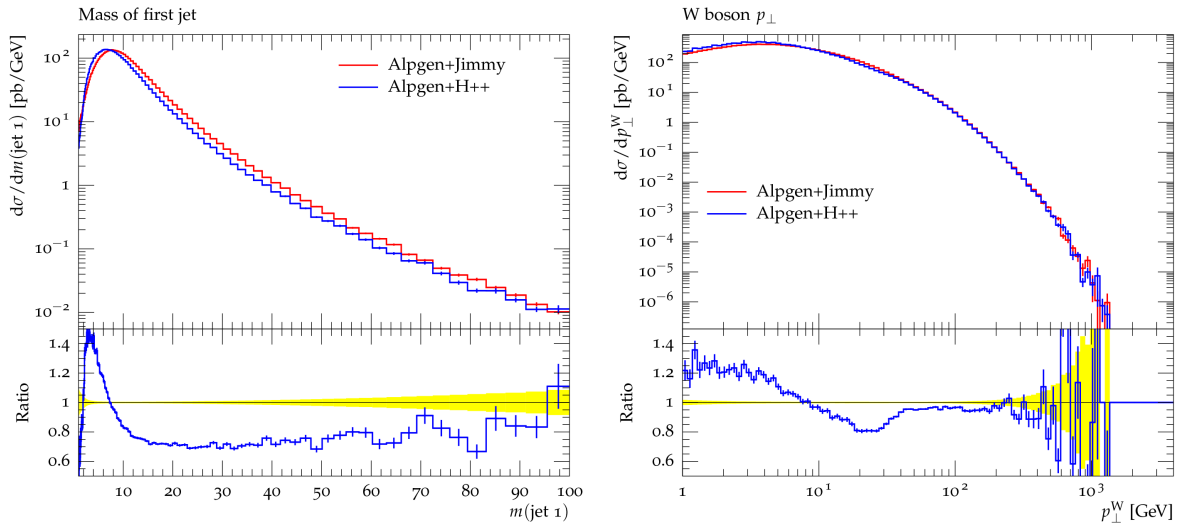

(a) (b)

Figure B.5: Distributions of the leading jet mass (a) and the W boson p_{T} (b) in W+jets events generated by ALPGEN. Results of showering and matching in HERWIG (labeled "Alpgen+Jimmy" following ATLAS nomenclature) are compared to those using Herwig++.

the author of the ALPGEN interface to Herwig++, and those results served as a cross check. Systematic differences were already in that study noted in the jet mass and W boson p_{T} distributions, and we observe the same discrepancies in fig. B.5.

In fig. B.6, ALPGEN samples processed with HERWIG and Herwig++ are compared in terms of the leading and subleading jet p_{T} for three different settings of Herwig++. In figs. B.6(a) and B.6(b), the default Herwig++ settings as defined by the ALPGEN interface are used. In particular, this means that the strong coupling constant in the shower is set consistently with what was used in ALPGEN, which is again determined by the PDF used, and corresponds in our case to a value $\alpha_{\mathrm{s}}(m_Z) = 0.13$ at the Z mass and running at the one loop order. It was already found in the study done by the interface author that better agreement could be achieved by forcing the strong coupling in Herwig++ to be the same as that used by default in HERWIG, corresponding to $\Lambda_{\mathrm{QCD}} = 180\,\mathrm{MeV}$ and running at the two loop order. The corresponding results are shown in figs. B.6(c) and B.6(d), and improved agreement is observed. Finally, we applied in addition the shower improvement [158] for wide angle gluon radiation introduced as an option in Herwig++ version 2.6.0, with the corresponding results shown in figs. B.6(e) and B.6(f). There is rather good agreement between HERWIG and Herwig++ with these settings.

Comparison to ATLAS data for W+jets at $\sqrt{s} = 7\,\mathrm{TeV}$

Rivet contains many analyses that allow quick comparison of generator level event samples to real experimental data. In fig. B.7, we compare ALPGEN samples processed in Herwig++, HERWIG, and PYTHIA 6 to real ATLAS data [159]. The samples include only electron decays of the W boson, and all the samples are normalized to the total cross section $10.46\,\mathrm{nb}$ by scaling each parton multiplicity sample with the same k-factor[3]. Good agreement is observed between

[3]Before applying the k-factor, each parton multiplicity sample is normalized to its cross section as obtained from the running of ALPGEN and Herwig++.

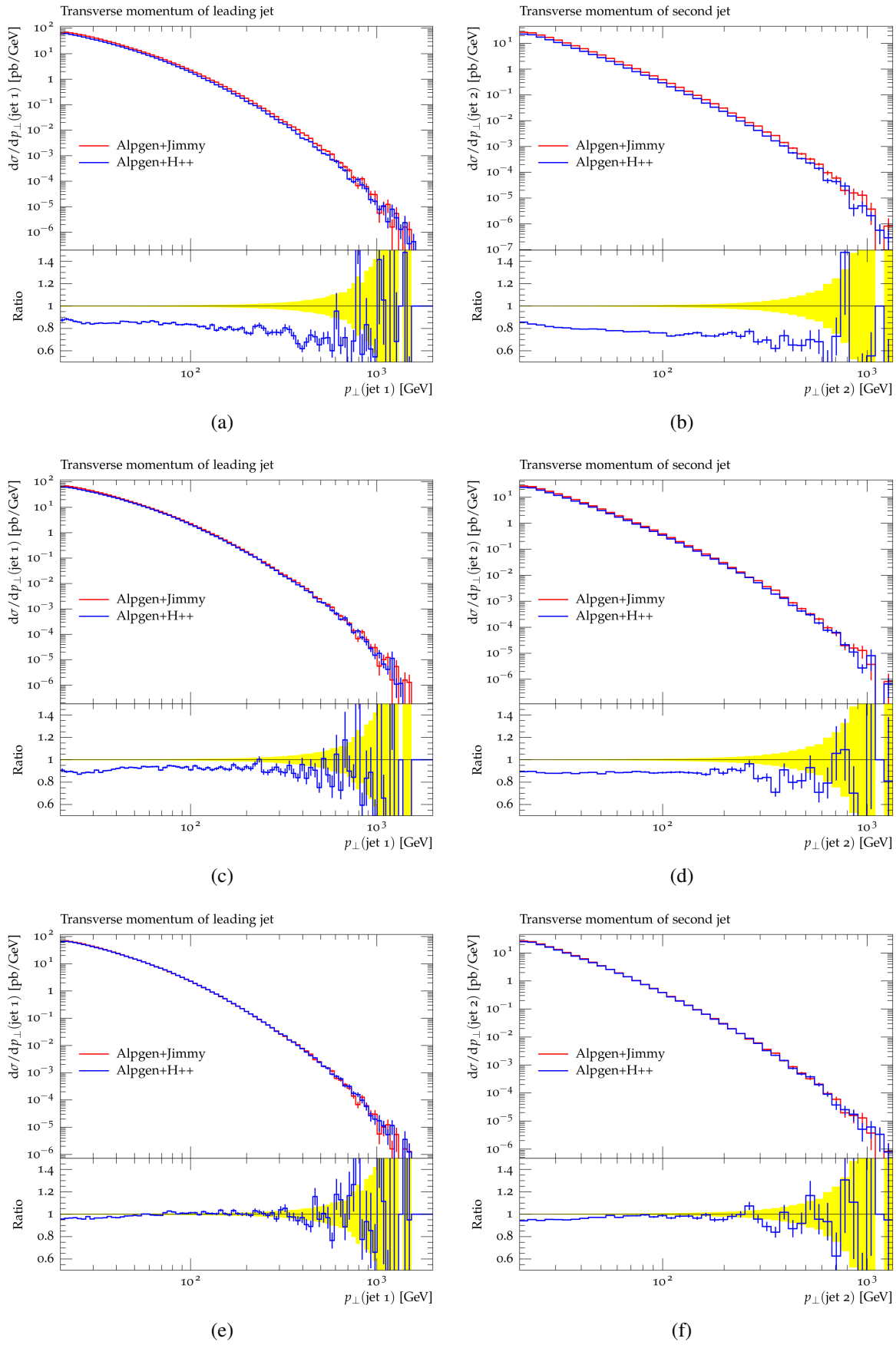

Figure B.6: Distributions of the leading ((a), (c), and (e)) and subleading ((b), (d), and (f)) jet p_{T} in W+jets events generated by ALPGEN. Results of showering and matching in HERWIG (labeled "Alpgen+Jimmy" following ATLAS nomenclature) are compared to those using Herwig++ with varying settings.

the different parton shower generator options and with data. The variable H_{T} is defined as the scalar sum of the p_{T} of the lepton, the neutrino, and all jets.

We compare also different settings for Herwig++ in fig. B.8. The settings that are changed were introduced in the previous section. The legend gives the setting for α_{s} as "default" or "two-loop" and for the shower improvement as "yes" (used) or "no" (not used). In general, no big differences are seen between the different settings in this analysis.

Comparison to ATLAS data for Z+jets at $\sqrt{s} = 7\,\mathrm{TeV}$

After my qualification was formally finished, I stayed on board the generators group as the contact person for ALPGEN+Herwig++ event generation in ATLAS. Also during this period, some validation was performed, and the Z+jets process was considered due to interest from the relevant ATLAS physics analysis group. We consider the Z boson p_{T} distribution [160] in fig. B.9(a), and various distributions from the ATLAS Z+jets analysis [161] in figs. B.9(b)-(f). The different MC results are for the $Z \to e^+e^-$ decay channel and are all normalized to the same total cross section $1.07\,\mathrm{nb}$ by scaling each parton multiplicity sample with the same k-factor.

Both of the choices for the strong coupling constant in Herwig++ are considered, with "LO" in the legend denoting the default choice with the one loop evolution. While the default choice provides a better description of the very low end of the Z p_{T} distribution, the jet distributions are in general better described when using the "HERWIG compatible" choice of strong coupling constant. It is worth noting in this context that the default setting in Herwig++, which matches the strong coupling to what was used in the hard scattering generation, can help to avoid inconsistencies and counter-intuitive results [162].

Comparison to ATLAS data for $t\bar{t}$ at $\sqrt{s} = 7\,\mathrm{TeV}$

The $t\bar{t}$ production process was finally considered due to interest from the ATLAS top working group. In the dileptonic decay channel, ATLAS data is available for validation in the form of the "gap fraction" analysis [163]. In this analysis, dileptonic $t\bar{t}$ events with two identified b-jets are selected, and they are vetoed if they contain significant additional jet activity (defined either as any one jet above a certain threshold or in terms of the scalar sum of jet p_{T}) in a central rapidity interval. The fraction of events surviving the veto is presented in fig. B.10 as function of the veto threshold for the different veto definitions. ALPGEN $t\bar{t}$ samples processed with HERWIG and Herwig++ are compared to ATLAS data. The "HERWIG" compatible choice of strong coupling constant is here used. The samples processed with HERWIG and Herwig++ are in good agreement, and these ALPGEN samples seem to describe the data very well.

B.3.2 Outlook

The processing (showering and MLM matching) of ALPGEN events with Herwig++ is now fully integrated in the ATLAS software with the possibility of running central production of such samples on the grid. Initial physics validation has been performed, and looks in general promising. Different settings for the strong coupling constant in the shower have been investigated, and, as one might expect, using in Herwig++ the same "inconsistent" setting which is

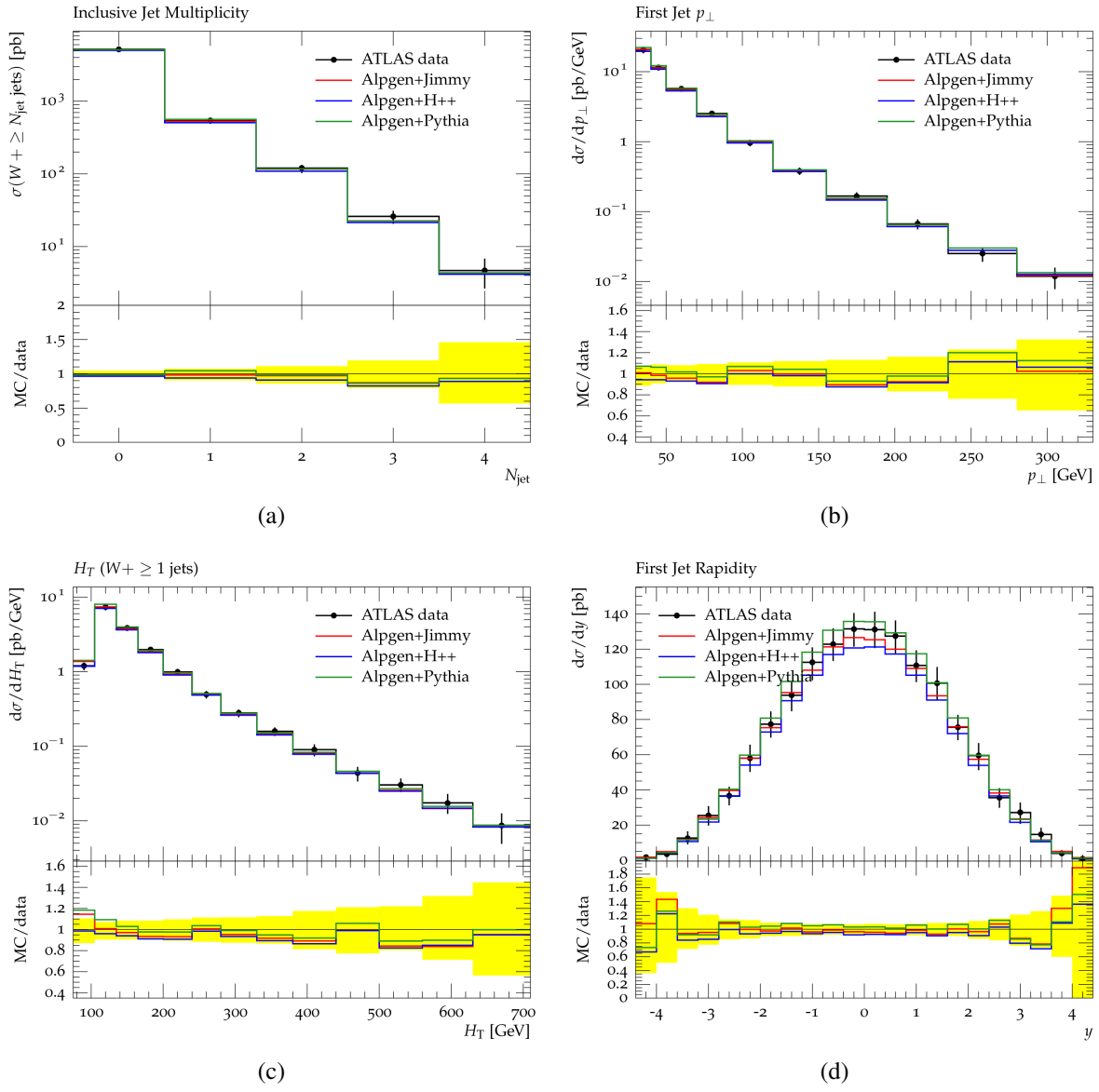

Figure B.7: The distributions of the jet multiplicity (a), leading jet p_{T} (b), H_{T} (c), and leading jet rapidity (d). The distributions obtained by processing ALPGEN events in Herwig++, HERWIG (labeled "Alpgen+Jimmy" following ATLAS nomenclature), or PYTHIA 6 are compared to ATLAS data.

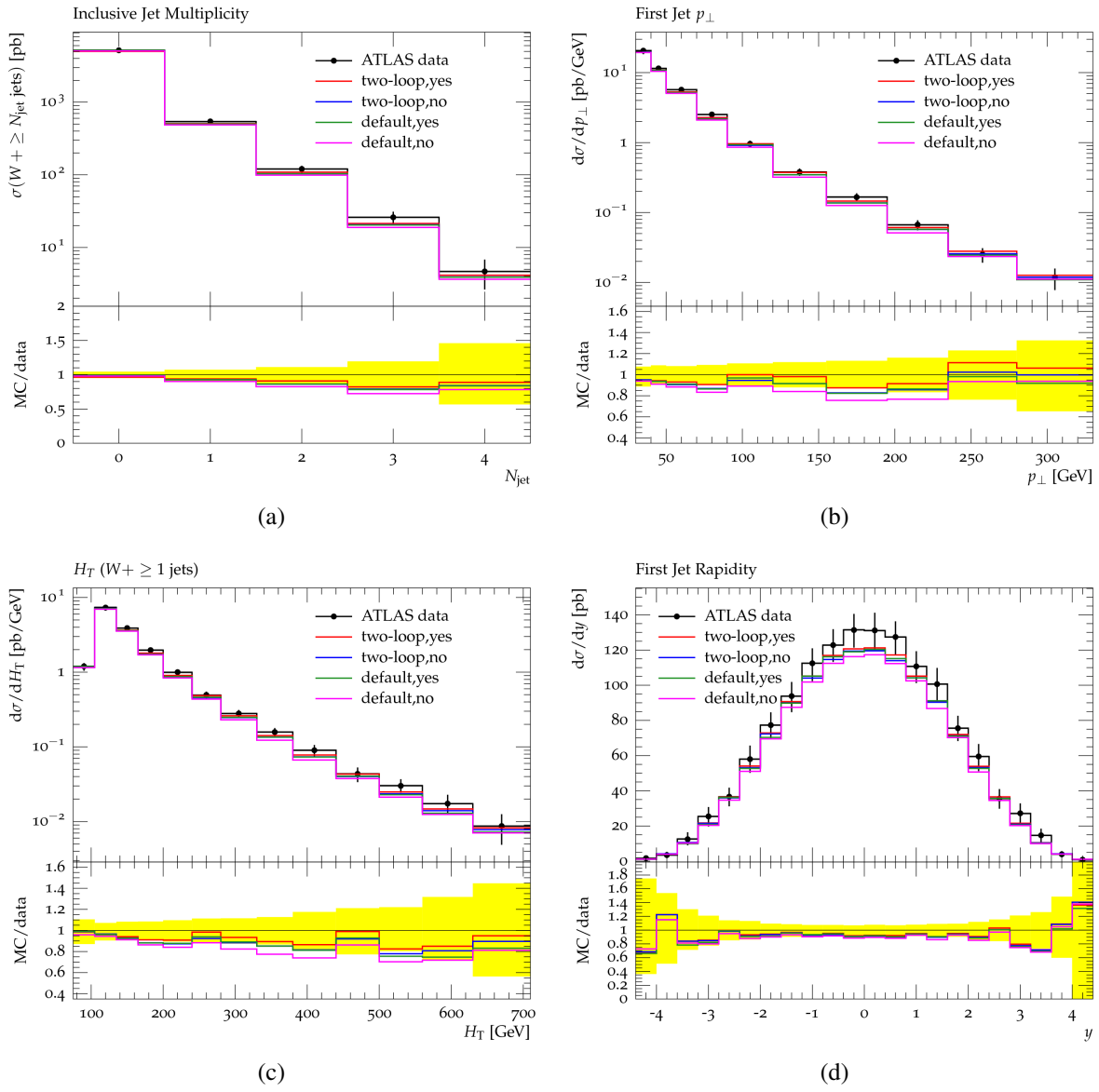

Figure B.8: The distributions of the jet multiplicity (a), leading jet p_{T} (b), H_{T} (c), and leading jet rapidity (d). The distributions obtained by processing ALPGEN events in Herwig++ using different settings are compared to ATLAS data. The setting for the strong coupling constant is given in the legend as "two-loop" ($\Lambda_{\mathrm{QCD}} = 180\,\mathrm{MeV}$ and running at the two loop order) or "default" ($\alpha_{\mathrm{s}}(m_Z) = 0.13$ and running at the one loop order). The shower improvement for wide angle gluon radiation is used ("yes") or not used ("no").

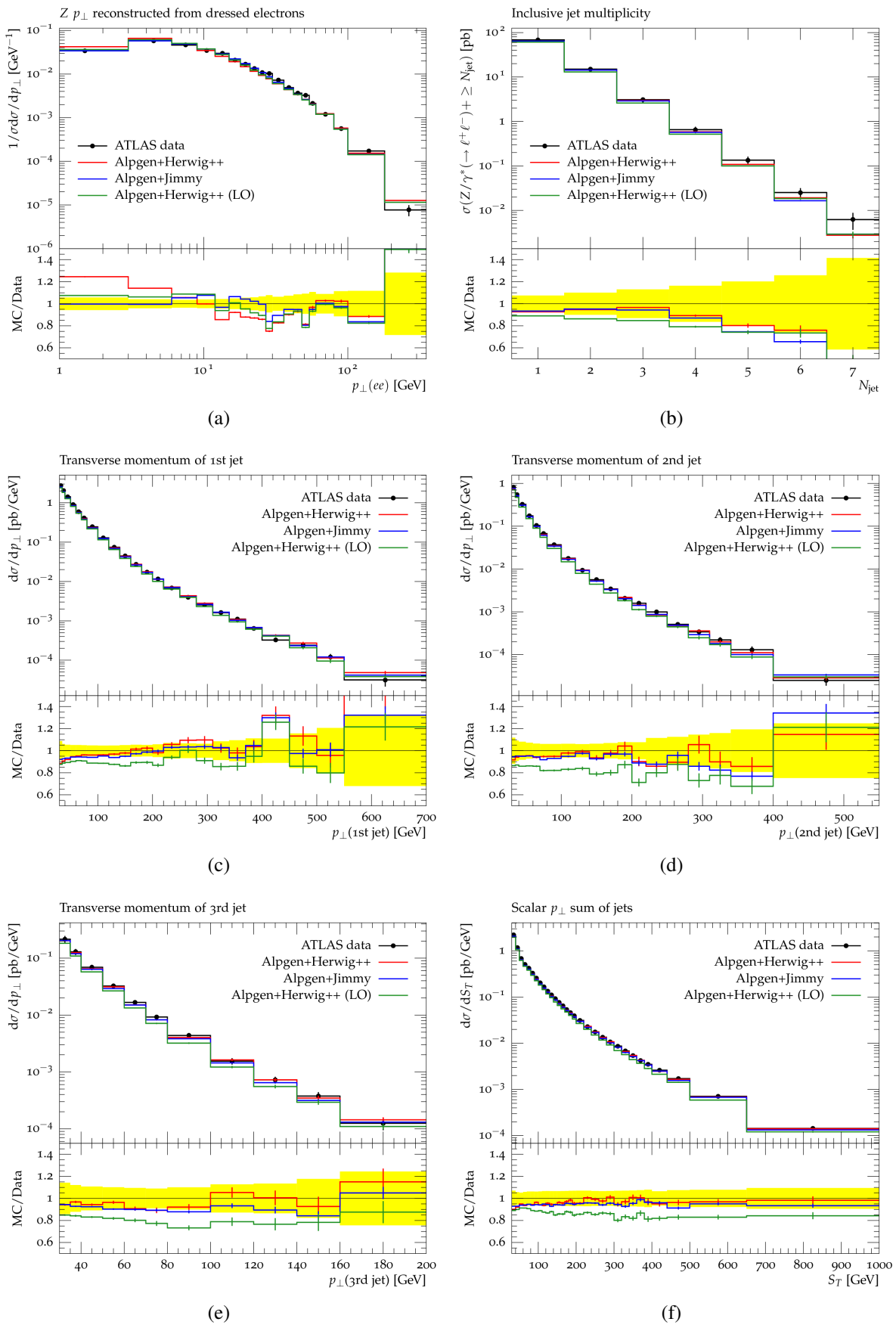

Figure B.9: Various distributions for the Z+jets process. The distributions obtained by processing ALPGEN events in Herwig++ or HERWIG (labeled "Alpgen+Jimmy" following ATLAS nomenclature) are compared to ATLAS data.

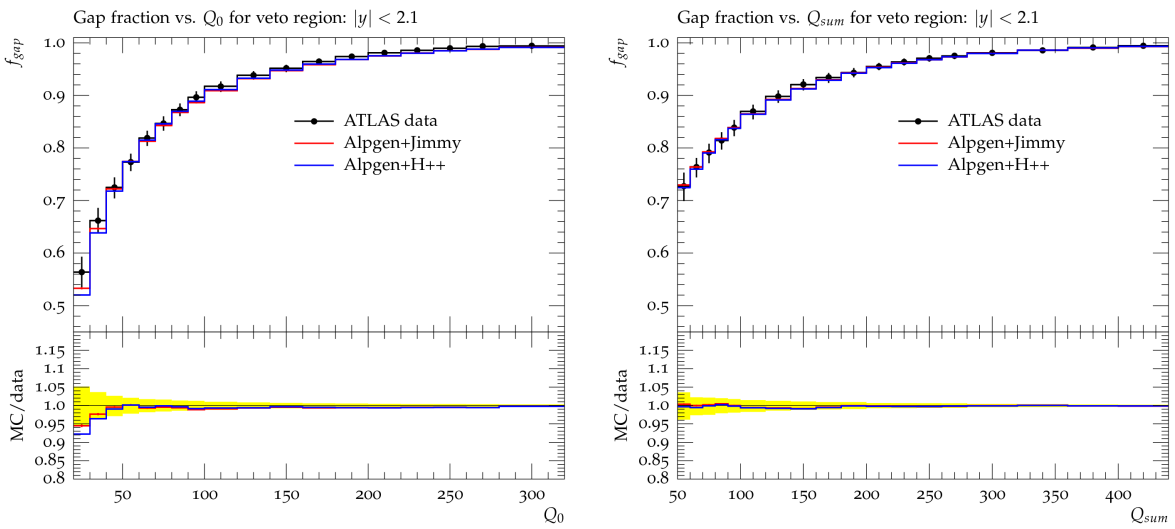

(a) (b)

Figure B.10: The fraction of events surviving the central jet activity veto as function of the veto threshold for the widest jet rapidity interval. The single jet veto definition is used in (a), while the scalar sum of jet p_{T} is used in (b). The fractions obtained by processing ALPGEN events in Herwig++ or HERWIG (labeled "Alpgen+Jimmy" following ATLAS nomenclature) are compared to ATLAS data.

used in HERWIG gives better agreement between the two. Such "inconsistent" setting of the strong coupling constant seems also to give a better description of data in terms of jet observables, and the corresponding ALPGEN+Herwig++ results are mostly within the uncertainties of the experimental data in the Rivet analyses considered here. It has been suggested that using a NLO PDF and corresponding strong coupling constant in ALPGEN may improve agreement with data, but this has not been studied in the context of the Herwig++ validation.

In order to achieve the eventual replacement of HERWIG by Herwig++ for the processing of ALPGEN samples in ATLAS, further validation work is needed. In particular, the natural next step would be the central production of some samples including detector simulation in order to take comparisons beyond the generator level. Involvement from the relevant physics working groups will be crucial in such an effort.

Appendix C

The International Masterclasses and the Z path measurement

In the Oslo group, we have been heavily involved in outreach work via the International Particle Physics Outreach Group (IPPOG)[1] and in particular the International Masterclasses (IMC)[2]. We have led the development of the Z path Masterclass measurement[3] [164–166], which will be presented in this appendix.

The IMCs provide an opportunity for 15- to 19-year-old school students to discover particle physics through hands-on measurements. The students spend a full day at their local university, where they first learn about particle physics theory and experimental particle physics through lectures, before applying the knowledge by analyzing real LHC data themselves. A video conference is organized with all the universities taking part in the IMC on the given day, so that the students can discuss their results, talk to scientists based at CERN, and get a feeling of what it is like to work in an international collaboration.

C.1 The Z path measurement

The first IMCs were arranged in the last half of the 1990s, using real LEP data. The students were presented with the task of identifying Z boson decays as electron, muon, tau, or quark decays by analyzing the Z events visually in an event display. The same measurement was performed by different students every year for more than a decade. After the arrival of the first LHC collision data, it was obviously desirable to create new measurements based on these data. Several measurements have been developed, among which two are based on ATLAS data. These are the W path [167] and Z path measurements, of which the latter was developed in the Oslo group, and will now be presented in more detail.

As the original IMC measurement based on LEP data, the Z path measurement is based on visual analysis of events in an event display. The event display program, called HYPA-

[1] http://ippog.web.cern.ch/

[2] http://physicsmasterclasses.org/

[3] M. Pedersen, F. Ould-Saada, M. K. Bugge, V. Morisbak, E. Gramstad, http://atlas.physicsmasterclasses.org/en/zpath.htm

TIA[4] [168], is based on the official ATLAS event display ATLANTIS[5], but is tailored for outreach purposes. The version used in the Z path Masterclass is in addition tailored specifically for this use.

The measurement is based on the invariant mass concept as a tool for identifying known and discovering new short lived particles. The students identify final state particles, and HYPATIA calculates the invariant mass of any set of particles selected by the students. In the original version of the measurement, the students were supposed to identify electrons/positrons and muons in the final states, and look at the invariant mass distribution of e^+e^- and $\mu^+\mu^-$ pairs. As the name "Z path" suggests, the rediscovery of the Z boson was a central goal. The students also had the opportunity to identify the J/ψ and Υ mesons, and even search for the "unknown": a new heavy gauge boson Z' with a mass of $1\,\mathrm{TeV}$ which was mixed in with the real data in the form of simulation[6].

With the discovery of the Higgs boson in 2012, the Z path measurement was updated in order to reflect this development. The idea was that the students should themselves search for the Higgs boson, and the analysis was extended to final states with two photons and with four leptons – the golden channels for Higgs detection at the LHC. For the 2013 Masterclasses, $1\,\mathrm{fb}^{-1}$ of ATLAS data was released for education purposes, and this amount was doubled the following year. Obviously, not even with the $2\,\mathrm{fb}^{-1}$ available for the 2014 Masterclasses could the students themselves really discover the Higgs boson, but the inclusion of the diphoton and four-lepton final states allowed the students to learn about how the Higgs boson was in fact discovered at the LHC.

The idea behind the Z path measurement is that the students should realize that they have mastered a "discovery tool". The inclusion of the simulated Z' events is crucial in this context, as these events really allow the students to discover something new and unexpected themselves. The students should also realize that the method they have learned could be used to discover the Higgs boson as well, and that it was in fact *exactly* this method that was employed to discover the Higgs boson at the LHC. They should understand that they may have identified real Higgs boson events, but that the amount of data available to them was not sufficient for them to actually make the discovery themselves.

C.2 Event identification in HYPATIA

During the practical measurement part of the Masterclass day, the students work in pairs and analyze events visually in the event display program HYPATIA. The goal is to identify electrons/positrons, muons, and photons in each event, and decide whether the event could fit into one of the following categories:

- dilepton (e^+e^- or $\mu^+\mu^-$),
- diphoton, or

[4] `http://hypatia.phys.uoa.gr/`

[5] `http://atlantis.web.cern.ch/atlantis/`

[6] The simulation was performed within the SSM Z' model, in which the new gauge boson has the same couplings to fermions as the familiar Z boson and no couplings to the W and Z bosons.

- four leptons ($e^+e^-e^+e^-$, $e^+e^-\mu^+\mu^-$, or $\mu^+\mu^-\mu^+\mu^-$).

If so, the relevant set of identified particles is selected by the students, and the particles are entered into a table where the corresponding invariant mass is calculated.

An example screenshot of HYPATIA, as it would appear to a student working on the Z path measurement, is shown in fig. C.1. The "Canvas Window" shows two projections of the ATLAS detector, which are zoomed to show primarily the innermost parts of the detector in this particular example. In the *transverse* projection (top left), the beam line is perpendicular to the plane of the paper, while in the *longitudinal* projection (bottom), the beam line is horizontal and in the plane of the paper. In the inner detector (grey), we see reconstructed tracks corresponding to the trajectories of charged particles. In the electromagnetic (green) and hadronic (red) calorimeters, yellow dots correspond to measured energy deposits. The "lego plot" (top right) shows the distribution of measured calorimeter energy in the η,ϕ-plane.

In this event, there are two pronounced clusters of energy deposits in the electromagnetic calorimeter. Since there are also tracks in the tracking detector pointing in the direction of these clusters, we identify this event as an electron-positron event. The assumed electron and positron have been selected and inserted into the "Invariant Mass Window" at the top. The invariant mass of the electron-positron pair in this event is $94\,\mathrm{GeV}$, so this is a typical Z boson candidate event. The currently selected track is highlighted (white) in both the transverse and longitudinal projections, and the corresponding rows in the "Track Momenta Window" and "Invariant Mass Window" are both highlighted as well.

Fig. C.2 shows two ATLAS event displays. In fig. C.2(a), we recognize a typical event with two muons. Muons are rather easily identifed in event displays, as they are the only particles that pass through the whole detector and are detected in the muon spectrometer (blue). Fig. C.2(b) shows a typical event with two photons. Photons deposit energy in the electromagnetic calorimeter just like electrons and positrons, but unlike the electrons and positrons, the photons do not leave tracks in the inner detector. While a couple of tracks are "almost" pointing towards the upper calorimeter deposit in the transverse projection, both photons are seen to be clearly isolated from track activity in the longitudinal projection in spite of the relatively large track multiplicity in the event[7].

We show finally an example of a four-lepton event with two electrons and two muons in fig. C.3(a), and an example of a diphoton event with one converted photon in fig. C.3(b). A photon conversion is the process $\gamma \rightarrow e^+\,e^-$, which is impossible in vacuum, but which can happen when the photon interacts with the detector material. There are two tracks very close together pointing in the direction of one of the electromagnetic calorimeter clusters in fig. C.3(b). It is seen that these are indeed two separate tracks in the transverse projection, but this is hardly visible in the longitudinal projection. The invariant mass of the two tracks is $0.7\,\mathrm{GeV}$, and such a low invariant mass supports the conversion hypothesis.

The four-lepton invariant mass in the event of fig. C.3(a) is $267\,\mathrm{GeV}$, rather far from $125\,\mathrm{GeV}$, so the event is not a Higgs boson candidate. The invariant mass of the e^+e^- pair is $89\,\mathrm{GeV}$, which is typical for the Z boson, and that of the $\mu^+\mu^-$ pair is $65\,\mathrm{GeV}$.

[7]Only tracks with $p_\mathrm{T} > 3\,\mathrm{GeV}$ are here shown, and the track p_T cut is adjustable in event displays such as HYPATIA. Turning the cut off completely makes visual event analysis impossible because of enormous track activity. It is useful that the students see how crowded the pp collision environment really is, before setting a reasonable track p_T cut to gain clarity.

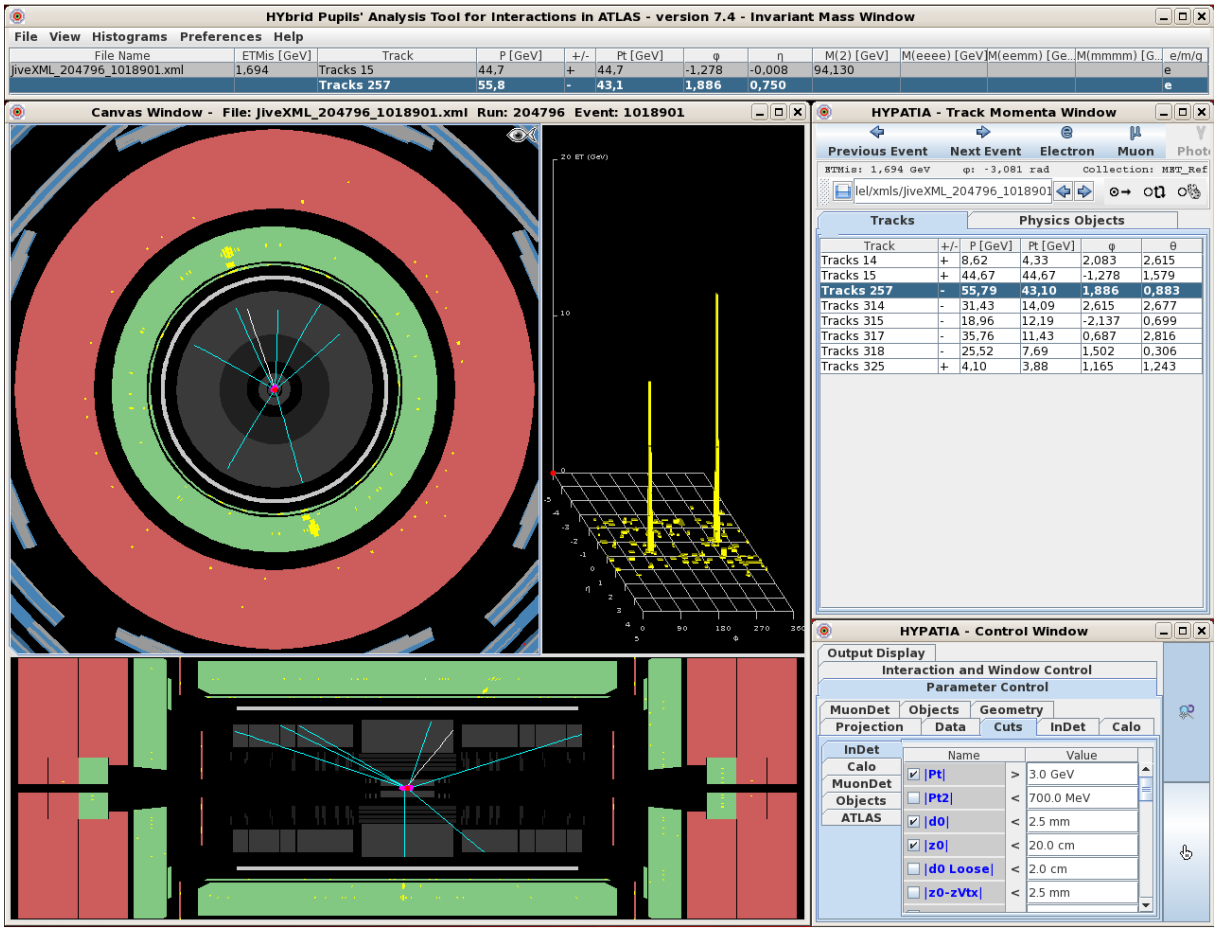

Figure C.1: A screenshot of the event display program HYPATIA as it would appear to a student doing the Z path measurement. This is a typical electron-positron event, with two pronounced clusters of energy deposits in the electromagnetic calorimeter and corresponding tracks in the tracking detectors. The measured charges corresponding to the two tracks can be checked in the "Track Momenta Window" to the right to verify that the two electron/positron candidates are indeed oppositely charged. The currently selected track is highlighted (white) in both the transverse and longitudinal projections, and the corresponding rows in the "Track Momenta Window" and "Invariant Mass Window" are both highlighted as well.

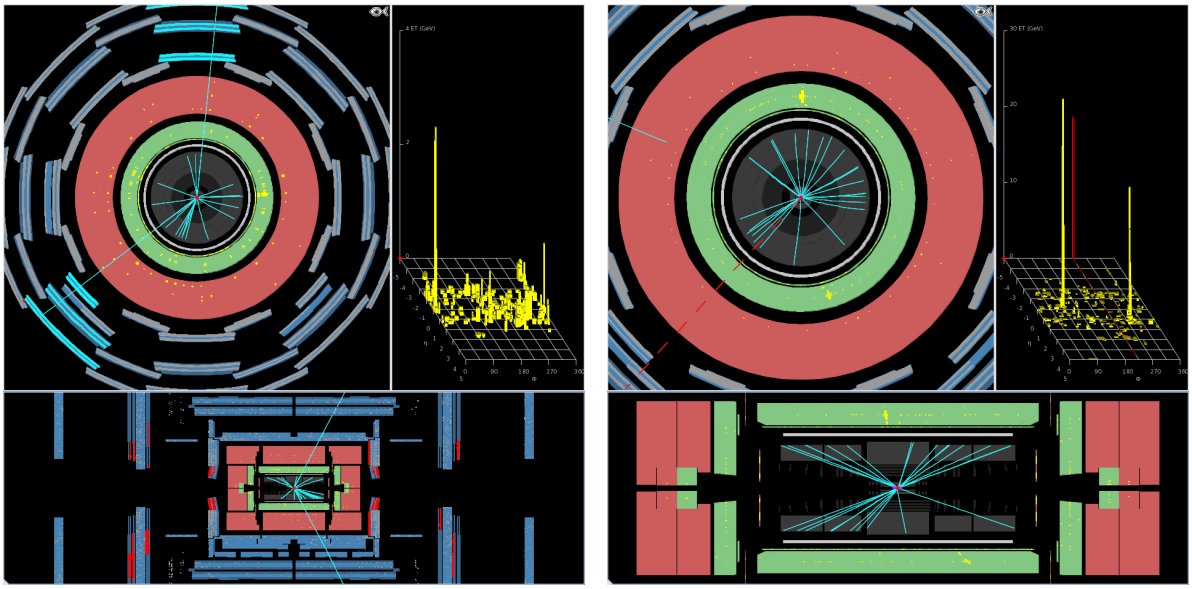

(a) (b)

Figure C.2: ATLAS event displays of a typical event with two muons (a) and a typical event with two photons (b).

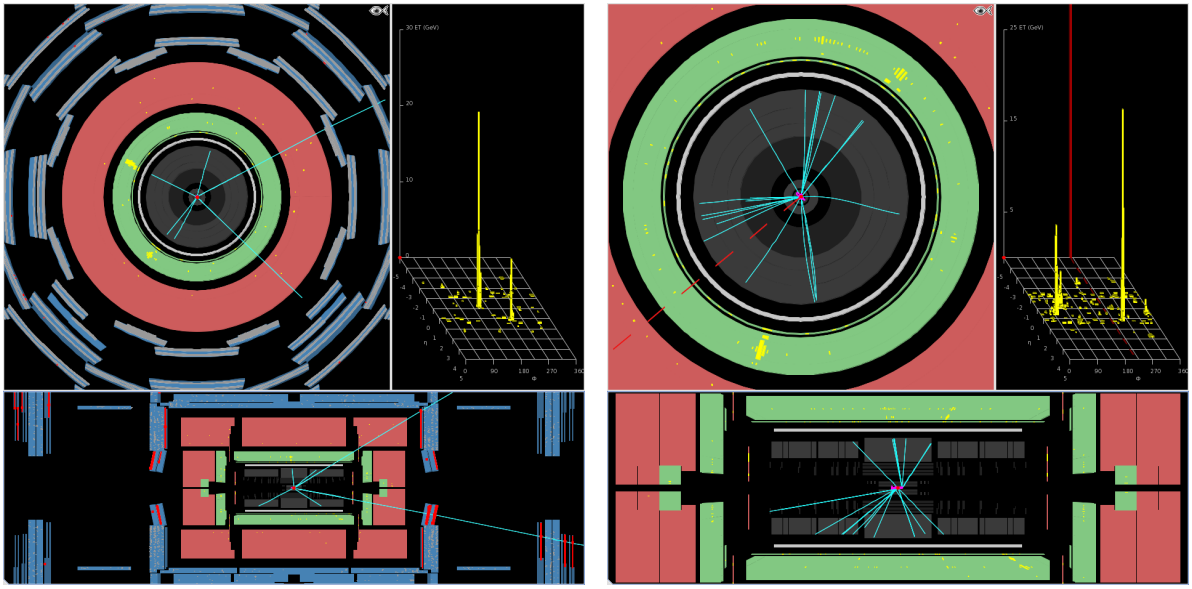

(a) (b)

Figure C.3: ATLAS event displays of an event with four leptons (a) and an event with two photons where one of the photons is converted (b).

Event type	Number of events	Fraction in mixture
$Z \to l^+l^-$	18 500	50%
$J/\psi \to l^+l^-$	1 850	5%
$\Upsilon \to l^+l^-$	1 850	5%
$Z' \to l^+l^-$	1 850	5%
Four-lepton	40	5%
Diphoton	11 100	30%

Table C.1: Details on the event mixture for the 2014 Z path Masterclasses. The numbers of events used from each category are shown, as well as the fraction of the given event type in the students' datasets. The numbers of events correspond in general to the relevant fractions, except in the case of four-lepton candidate events, which are replicated many times in the students' datasets to allow all students the possibility of discovering such events. For all categories of l^+l^- events, there is a democratic division between electron and muon pairs.

C.3 Event selection and mixture

Each pair of students analyzes a set of 50 events in the practical session of the Masterclass day. Such a sample of 50 events is a random mixture of events from a set of categories defined by offline event selection. The diphoton and four-lepton events used in the 2014 Masterclasses have been selected following the "official" selection of the relevant Higgs working groups in ATLAS. The dilepton events have been selected using a very minimal selection. The diphoton events are restricted to the invariant mass range $[100\,\mathrm{GeV}, 160\,\mathrm{GeV}]$, and the dilepton events are selected within invariant mass windows around the J/ψ, Υ, and Z resonances. For the Z' dilepton events, a lower invariant mass cut of $700\,\mathrm{GeV}$ is imposed to remove the region dominated by interference with the Z boson.

All the real data (everything except for the Z' events) used for the 2014 Masterclasses were selected from runs 204769-206971 (period B12-C6, $2\,\mathrm{fb}^{-1}$) recorded by ATLAS in June and July 2012. The events were mixed together in the groups of 50 analyzed by the students with the fractions of the different event categories as given in table C.1. For all categories of l^+l^- events, electron and muon events are included in equal amounts.

The above mentioned run range contains only 40 four-lepton events, as these events are very rare. In order to make the measurement more interesting to the students, we wanted all students to have the possibility to encounter at least one or two such events, and we therefore chose to duplicate these events many times in order to have 2-3 such events in each group of 50. Except for the four-lepton events, each dataset of 50 events should be unique. With the event category fractions defined in table C.1, the total number of datasets is then limited to 740 by the amount of available diphoton events. This was the number of datasets prepared for the 2014 Masterclasses, and it was sufficient to accomodate even the biggest Masterclass events of 2014.

Converted photons are particularly hard to identify for the students. Because of this, the fraction of unconverted photon events is enhanced in the first 411 datasets, and the remaining 329 datasets contain only events in which at least one of the photons has been identified as a conversion by the ATLAS software. These last datasets are meant to be used only in the case of

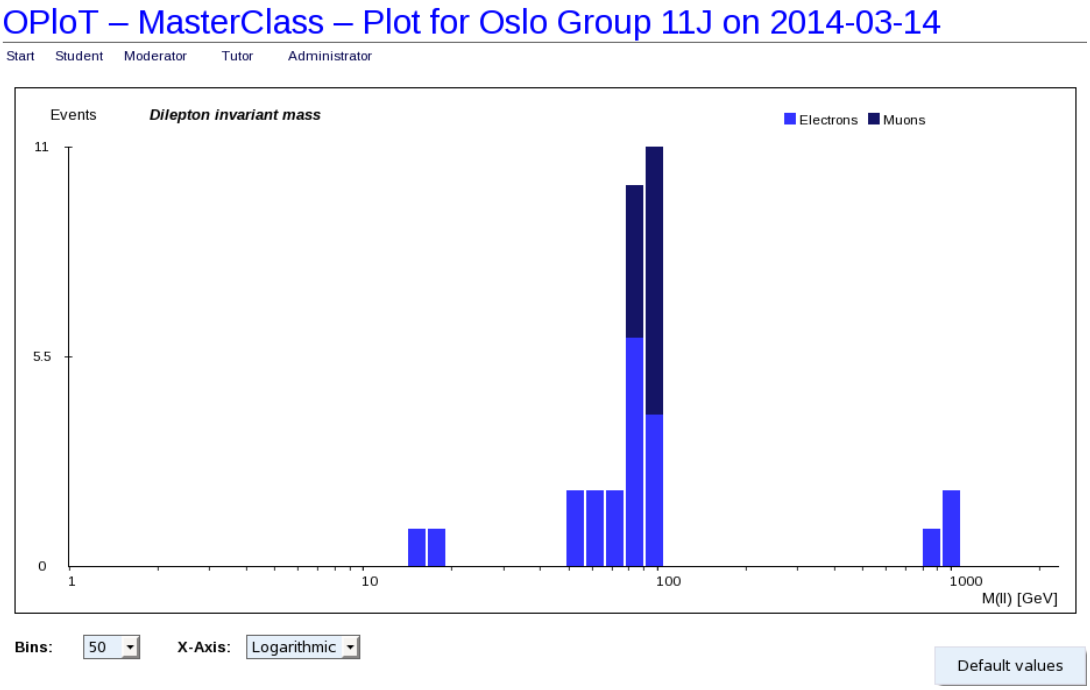

Figure C.4: The dilepton invariant mass distribution obtained by a particular pair of students in the Z path Masterclass on the 14th of March 2014. The figure shows the distribution as presented by OPloT with a logarithmic invariant mass axis.

particularly large Masterclass events and/or by more advanced students[8], and tapping into these datasets was in fact not necessary for any of the 2014 Masterclass events.

In the 2014 Z path Masterclass data, about 60 Higgs events are expected in the diphoton final state. In the four-lepton final state, between one and two Higgs events are expected, but there are several candidates in the range 120-130 GeV.

C.4 Plotting tool and discussion of results

After a pair of students has finished analyzing their 50 events, they export a plain text file of invariant masses from HYPATIA which they subsequently upload to the online plotting tool OPloT[9] (Oslo Plotting Tool). Immediately after uploading their file, the students can study their own results in the form of invariant mass histograms. They can interactively change the invariant mass axis range, choose between linear and logarithmic binning, and set the number of bins. The distributions of the invariant mass of two charged leptons, two photons, and four charged leptons can be viewed individually and together. When results are discussed in a plenary session at each institute and in the following video conference, OPloT can be set to display results of combining all submitted data from a given university or all submitted data from all universities taking part in the Z path Masterclass on the given day.

[8]The handiness of the XML event format combined with the fact that the data used for the Masterclasses is released for education purposes, facilitates the use of the Masterclass data also in teaching at the university level. For this purpose, a program has been developed that allows students to run automated analysis of large numbers of events much like real ATLAS physicists.

[9]V. Morisbak, M. Pedersen, F. Ould-Saada, http://cernmasterclass.uio.no/OPloT/index.php

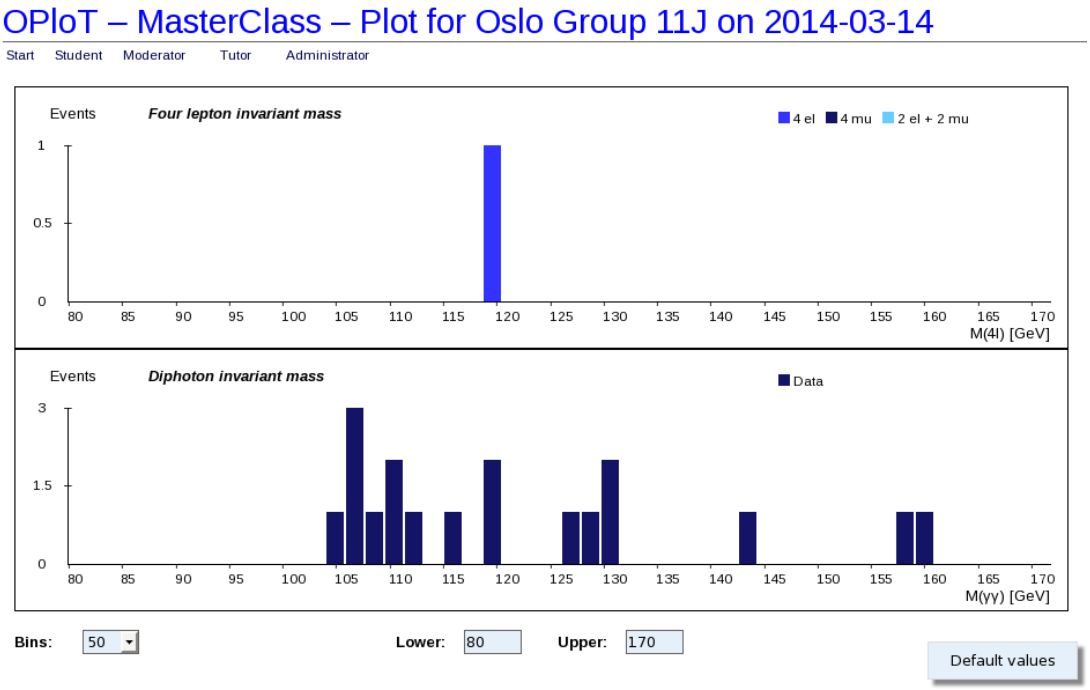

Figure C.5: The four-lepton and diphoton invariant mass distributions obtained by a particular pair of students in the Z path Masterclass on the 14th of March 2014. The figure shows the distributions as presented by OPloT. It has here been chosen to view the two distributions simultaneously with identical invariant mass axes and binning for the two distributions.

The dilepton invariant mass distribution obtained by a particular pair of students in the Z path Masterclass on the 14th of March 2014 is shown in fig. C.4. There is no doubt that this pair of students has identified the Z boson, with almost 20 candidates in the two bins just around $90\,\mathrm{GeV}$. There are three exciting candidates with very high invariant mass just around $1\,\mathrm{TeV}$. As seen from the point of view of the students at this point, this is a hint that something special might be going on around that mass. When the students later see the combined results with the other students' data, it becomes clear that a new particle is discovered. In contrast, the two events these students have identified around 15-$20\,\mathrm{GeV}$ are at the combination stage seen to blend into a dreary background, and no particle is discovered at this mass.

The four-lepton and diphoton invariant mass distributions obtained by the same pair of students are shown in fig. C.5. These students seem to have done an excellent job with their event identification. They have identified 18 diphoton candidates, which fits nicely with the expectation for a 50 event dataset, and the invariant mass of the four-electron candidate event identified by the students fits with one of the four-electron events identified by the official ATLAS analysis. The students may thus have identified a real Higgs boson event, and this is in fact quite likely because of the high signal-to-background ratio in the four-lepton invariant mass distribution. The diphoton events identified by these students between 125 and $130\,\mathrm{GeV}$ are also excellent Higgs candidates, but these events have probabilities to be real signal at the level of only a few percent because of the relatively low signal-to-background ratio in the diphoton search channel.

Fig. C.6 shows the invariant mass distributions resulting from the combination of all submitted results from all universities taking part in the Z path Masterclass on the 14th of March

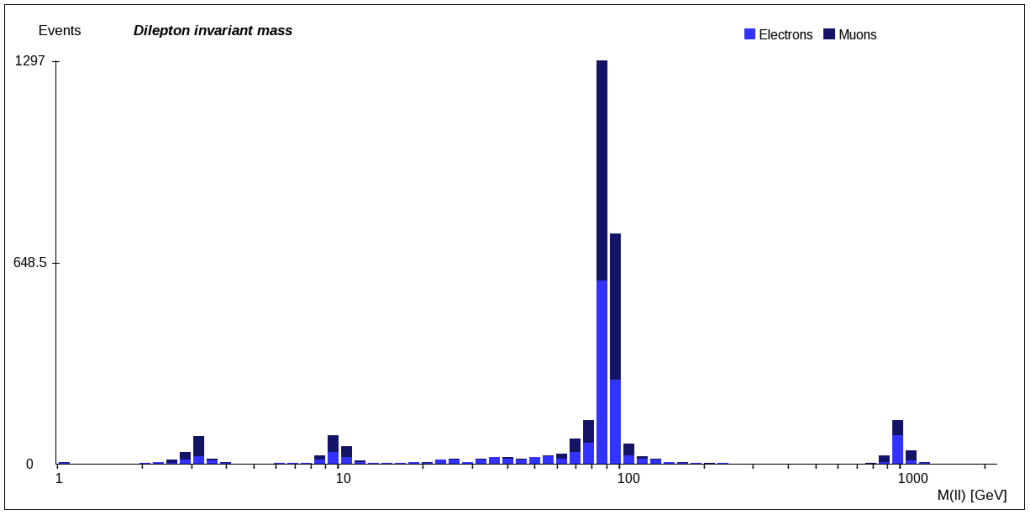

(a) The combined dilepton invariant mass distribution.

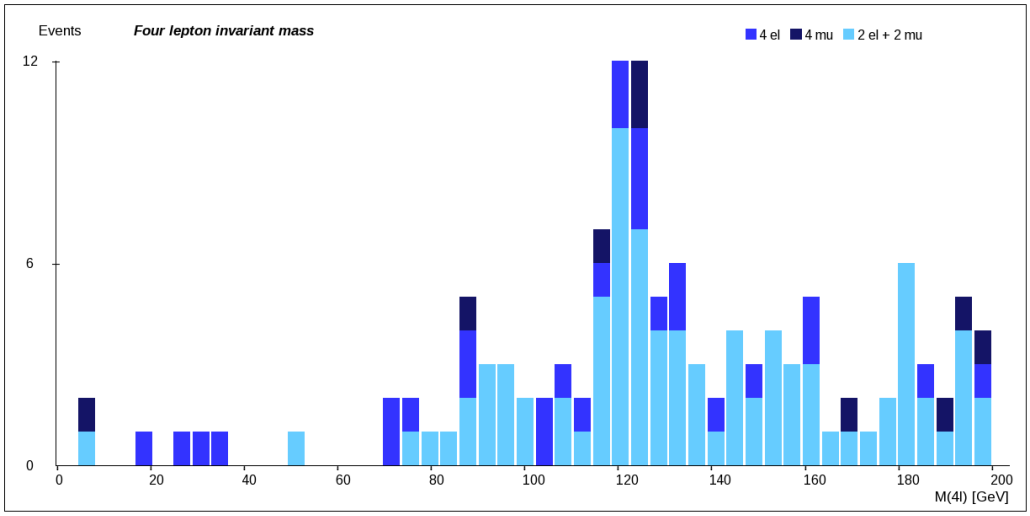

(b) The combined four-lepton invariant mass distribution.

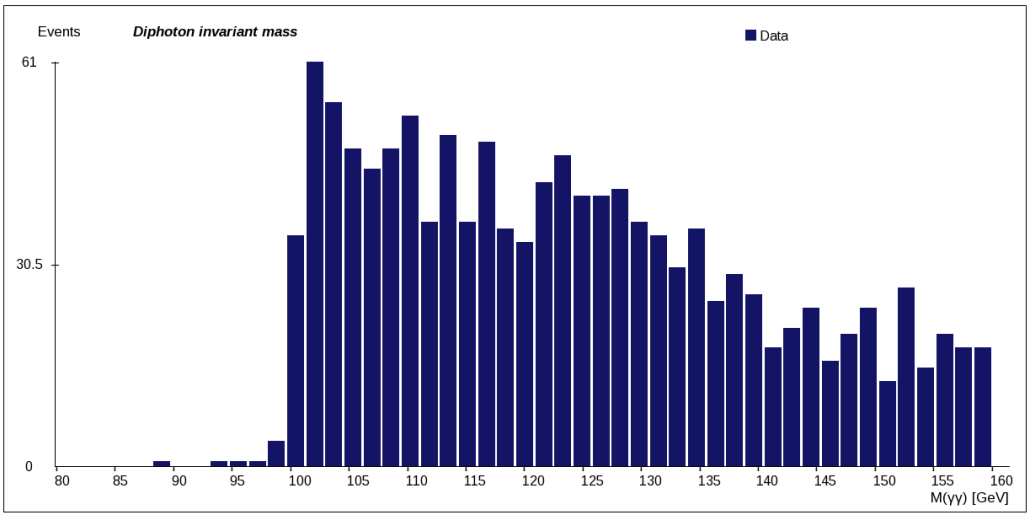

(c) The combined diphoton invariant mass distribution.

Figure C.6: The invariant mass distributions resulting from the combination of all submitted results from all universities taking part in the Z path Masterclass on the 14th of March 2014. The dilepton (a), four-lepton (b), and diphoton (c) invariant mass distributions are shown.

2014. The dilepton invariant mass distribution in fig. C.6(a) shows clear evidence of the J/ψ and Υ mesons as well as the Z boson. It is also clear that the students have discovered a new particle with a mass of $1\,\mathrm{TeV}$. Although this is because of the simulated events mixed in with the real data, it allows the students to see what the discovery of a new particle would look like, and helps them realize that they have mastered a discovery technique. Obviously, it is explained to the students during the results session that the peak at $1\,\mathrm{TeV}$ is due to the simulated events. We also observe a smooth "continuum" distribution between the peaks. This must be coming primarily from misidentification by the students, as dilepton events outside the invariant mass peak windows were not mixed into the students' data. It is interesting to note that e^+e^- events dominate completely the regions between the peaks, as expected from the fact that an electron-like experimental signature is more easily mimicked by hadrons, of which there are always plenty in pp collision events.

The four-lepton invariant mass distribution in fig. C.6(b) shows that the students are very eager to look for such events, and possibly that they should be more critical in their particle identification. Although only 40 four-lepton events were selected and mixed into the event samples for the 2014 Masterclasses, the students have identified more than 200. We note the dominance of events of the type $e^+e^-\mu^+\mu^-$, which could be due to the misidentification of hadrons as electrons and positrons in events with a real muon pair.

The diphoton invariant mass distribution in fig. C.6(c) looks pretty much as expected, but the statistical fluctuations are clearly too large for a small peak due to the Higgs boson to be discovered. It is important that the students understand that this is a limitation of the size of the data sample, and that the diphoton invariant mass distribution was in fact a key ingredient in the Higgs discovery at the LHC. This is discussed in the plenary results session and the video conference, and to aid the discussion, one can in OPloT choose to display simulated data corresponding to different data sample sizes in order to show how a Higgs peak becomes more apparent as the amount of data increases. The simulated data corresponding to a large data sample ($25\,\mathrm{fb}^{-1}$ of integrated luminosity) is shown in fig. C.7. Here, it should be possible to convince oneself that the peak due to the Higgs boson would be visible even if it were the same color as the background.

Even though examples are not shown here, there are further interesting possibilities in OPloT for the diphoton invariant mass distribution. One can choose to compare the students' distribution to simulated background and signal distributions corresponding to the size of the data sample analyzed by the students. Doing so for the results of the 14th of March 2014, we find that the students have only identified about half as many diphoton events as expected. A significant part of the mismatch between expected and observed event counts is assumed to be due to student pairs that do not manage to analyze all their 50 events within the available time. The student data can also be replaced by the "correct" distribution, resulting from the selection of events using ATLAS software analysis procedures. The interested reader can try out all of OPloT's capabilities interactively online[10].

Finally, we show in fig. C.8 the dilepton and overall statistics of the Masterclass on the 14th of March 2014 as presented by OPloT. In the dilepton statistics table (fig. C.8(a)), four invariant mass regions "R1"-"R4" are defined. These are adjustable by the user, and correspond here

[10]Please contact epf-mc@fys.uio.no if you have any questions about OPloT or the Z path Masterclass measurement in general.

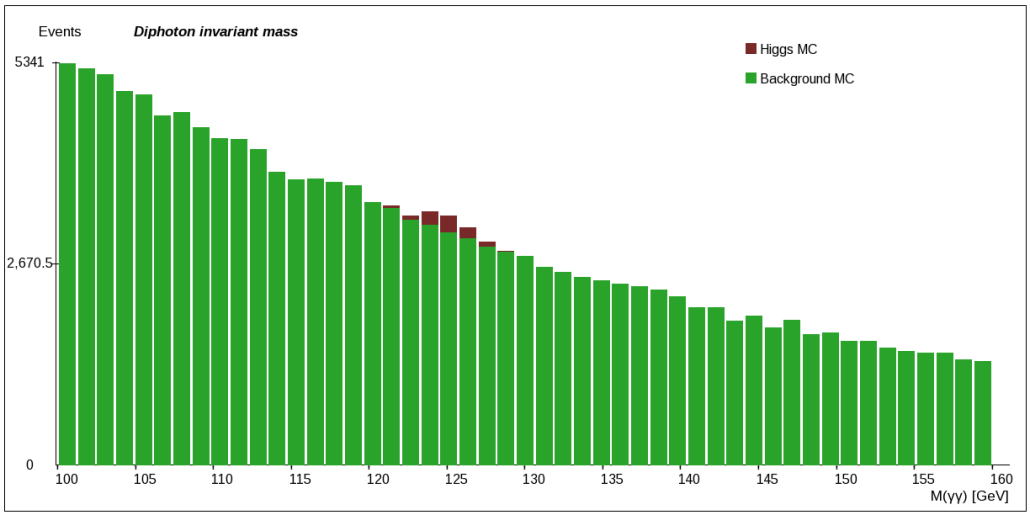

Figure C.7: The diphoton invariant mass distribution presented by OPloT when set to display simulated background and Higgs signal corresponding to an integrated luminosity of $25\,\mathrm{fb}^{-1}$.

Dilepton statistics

	Electrons			
Region	R1	R2	R3	R4
Events	80	100	868	107
Mean	3.05	9.80	89.82	993.71
Width	0.48	1.14	3.48	33.69

	Muons			
Region	R1	R2	R3	R4
Events	111	105	1186	83
Mean	3.04	9.85	90.50	1,000.42
Width	0.27	0.72	3.58	51.83

(a)

Number of events

	Student distribution	Expected
ll	3392	5038
4l	218	40
γγ	1274	2325
Sum	4884	7403

(b)

Figure C.8: OPloT's presentation of the dilepton (a) and overall (b) statistics resulting from the combination of all submitted results from all universities taking part in the Masterclass on the 14th of March 2014. Values in the "Mean" and "Width" rows of (a) are in GeV.

to windows around the J/ψ, Υ, Z, and Z' masses. For each region, the mean and standard deviation of the invariant mass distribution inside the region are shown, which serve as simple estimates of the mass and width of the different resonances. Clearly, the width estimate is affected by resolution, and can not be expected to coincide precisely with the natural width. However, the electron channel estimate of the Z' width is in fact quite close to the correct value of $30\,\mathrm{GeV}$ [39].

In the overall statistics table (fig. C.8(b)), the numbers of events in the different categories are compared to the expected numbers based on the number of student groups that have uploaded their results. For the four-lepton category, we note the excess of events found by the students as already discussed. The deficit of events in the other two categories is most likely due to a combination of the facts that students do not necessarily correctly recognize all events and that they do not necessarily manage to go through all their 50 events in the allocated time.

C.5 Outlook

The Z path measurement has evolved alongside the LHC physics program. After the rediscovery of the Z boson and other SM particles in 2010, school students could already in the spring of 2011 look at the first handful of dilepton events. In the spring of 2012, ten thousand events were already available for the students to analyze, and results could for the first time be analyzed in the online plotting tool OPloT. In the summer of 2012, the discovery of the Higgs boson was announced by the ATLAS and CMS collaborations, and already in the spring of 2013 were school students all around the world themselves searching for the Higgs boson in a subset of the very data used for the actual discovery. For the 2014 Masterclasses, the student datasets were revised to consist exclusively of $\sqrt{s} = 8\,\mathrm{TeV}$ data from 2012, and expanded because the amount of data released for education and outreach purposes was doubled.

School students all around the globe may soon get their hands on $\sqrt{s} = 13\,\mathrm{TeV}$ collision data. Only time will tell what the students will be searching for in these data, as the Z path measurement will certainly be updated to reflect any major discovery made at the LHC. Perhaps will we at some point replace the simulated Z' data with real events from a newly discovered resonance, or we may need to introduce final states involving missing transverse energy to reflect the discovery of a W' boson or supersymmetry. In any case, the Z path measurement will be kept "fresh" and closely related to the latest LHC results.

Appendix D

Assorted event displays

Through my work with the Z path Masterclass measurement described in appendix C, I have gained a certain enthusiasm for event displays. In this appendix, some event displays will be presented from the various selection regions encountered in this thesis. In particular, we consider final selection (i.e. signal-like) events, events from the "fake" muon control region, and tag and probe (Z-like) events. Within the final selection region, we pay special attention to the events with the highest transverse masses.

The events presented here are selected from a sample of approximately 200 events, about 40 events from each of the following categories:

- final selection events with no m_{T} cut,
- "fake" muon control region events in which the muon is not tight (i.e. not isolated),
- "fake" muon control region events in which the muon is tight (i.e. isolated),
- tag and probe events,
- final selection events with $m_{\mathrm{T}} > 843\,\mathrm{GeV}$, i.e. the signal region for the W^* of mass $1250\,\mathrm{GeV}$.

All these events were analyzed visually in the ATLANTIS event display. Note that the number of events in the last category is exactly 40, and all of these events were analyzed visually.

In the longitudinal projection of the ATLANTIS event display, the upward and downward directions are separated by a plane containing the beam line. Obviously, there is a priori no preferred orientation of this plane, and the default ATLANTIS behavior is to have this plane as the x,z-plane, i.e. so that anything in the upper "hemisphere" of the transverse projection is also going upwards in the longitudinal projection. However, if there is significant activity along the horizontal direction in the transverse projection, e.g. if there are jets or other objects close to $\phi = 0$ or $\phi = \pi$, one may want to adjust the angle of the "splitting plane". This is done in a few of the event displays shown here, and to avoid confusion, it is mentioned in the relevant figure captions. For the rest of the event displays, the "splitting plane" is horizontal, i.e. the x,z-plane.

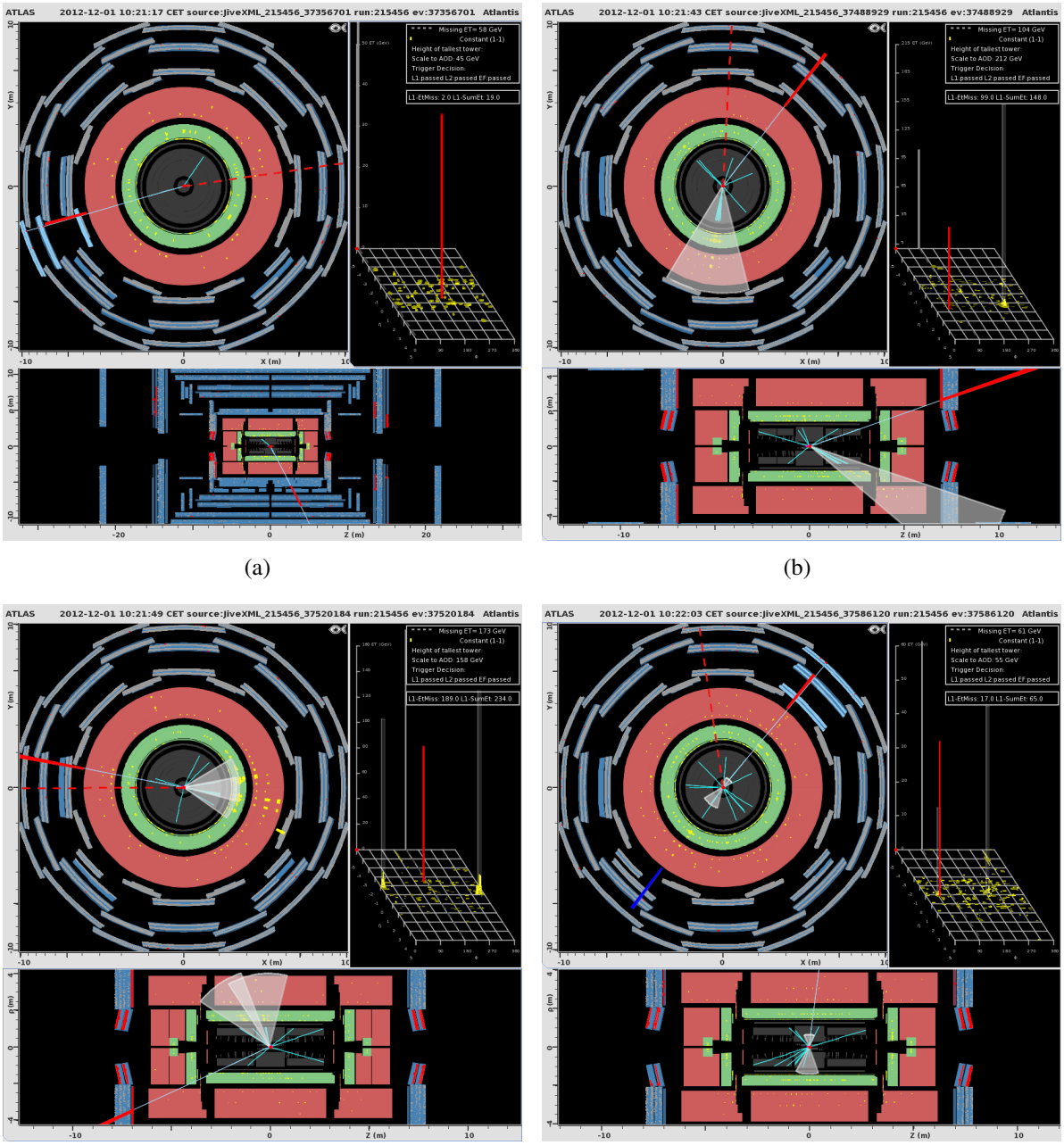

Figure D.1: ATLANTIS event displays of events from the final selection event sample. A representative "clean" event (a) is shown, as well as two events ((b) and (c)) where the muon and neutrino recoil against significant jet activity. Finally, in (d), the muon is within a reconstructed jet cone and recoiling against a b-tagged jet, suggesting that the muon may be "fake". Note that in (c), the "splitting plane" is vertical, i.e. the y,z-plane.

D.1 Final selection events

Fig. D.1 shows event displays of four events from the final selection event sample[1]. The event of fig. D.1(a) is a representative example of a "clean" event with no significant activity other than the muon and the $\not{E}_{\mathrm{T}}$. The red "pole" which is seen along the muon track is an object indicator corresponding to the muon. The $\not{E}_{\mathrm{T}}$ (dashed line in the transverse projection) is seen to be almost "back to back" with the muon ($\Delta\phi_{\mu,\not{E}_{\mathrm{T}}} \approx \pi$) in the transverse plane, as will necessarily be the case when there is no significant calorimeter activity. The inner detector track p_{T} cut is $5\,\mathrm{GeV}$, and only one track passes this cut except for the muon track. This cut value will be used for all events shown in this appendix.

In figs. D.1(b) and D.1(c), the muon and neutrino are recoiling against significant jet activity, and are therefore not "back to back". Reconstructed jets are shown as transparent cones in the displays. In fig. D.1(b) the muon and neutrino are recoiling against a single "textbook" jet with many collimated tracks and significant calorimeter deposits in both the electromagnetic and hadronic calorimeters. The p_{T} of the jet is $210\,\mathrm{GeV}$. In fig. D.1(c) the muon and neutrino are recoiling against two hard jets with transverse momenta of $160\,\mathrm{GeV}$ and $130\,\mathrm{GeV}$ respectively. In these and many other displays, the longitudinal projection is zoomed to show more clearly the inner detector tracks, jets, and calorimeter deposits, at the cost of not seeing the complete muon track in the muon spectrometer[2]. It should be easy to determine from the direction of the muon track in this projection whether the muon is in the end-cap or barrel part of the muon spectrometer. For example, the muons of fig. D.1(b) and D.1(c) are both end-cap muons, while fig. D.1(d) shows a barrel muon.

Finally, the muon in fig. D.1(d) is close to the axis of a jet which recoils against a b-tagged jet. The b-tagged jet is shown as a transparent cone with a blue object indicator. The relatively low transverse mass of this event, $42\,\mathrm{GeV}$, corresponds to a region where the estimated jet background constitutes about 6% of the total background, and it is not impossible that this muon is indeed "fake". Note that b-tagging is not within my area of expertise, and that I am here simply relying on default ATLANTIS settings.

D.2 "Fake" muon control region

We proceed to show some event displays of events from the "fake" muon control region in figs. D.2 and D.3. The muons in the events of fig. D.2 do not pass the track based isolation cut, i.e. are not tight, and those in fig. D.3 do pass the cut.

The event of fig. D.2(a) contains two b-tagged jets which are "back to back" in the transverse plane. Both these jets contain a muon, but the event still passes our selection, as the muon going downwards to the right in the transverse projection has a p_{T} of $9\,\mathrm{GeV}$, below the cut of $20\,\mathrm{GeV}$

[1] Readers who are not too familiar with ATLAS event displays (or event displays in general) are referred to the discussion in appendix C.

[2] The "problem" is that the muon spectrometer constitutes such a large part of the total detector volume because of the long "lever arm" needed for a realiable measurement of high p_{T} muons. In the transverse projection, the problem is neatly solved by the "fish eye" transformation (indicated by the symbol in the top right corner of this projection), which inflates the inner detector and compresses the muon spectrometer. Using the "fish eye" transformation on the longitudinal projection leads to more obvious distortion, and is not done in any display shown here.

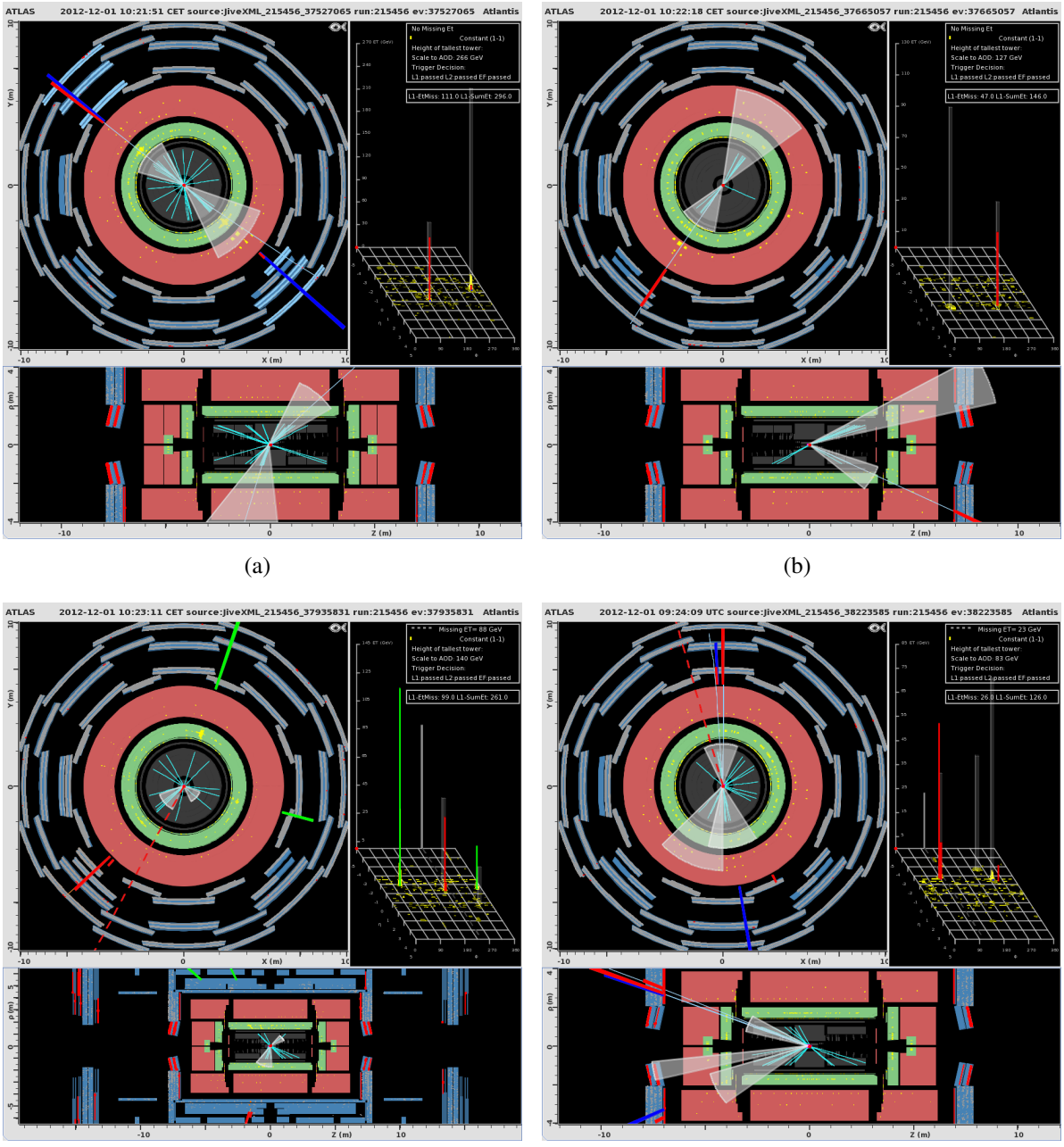

(a) (b)

(c) (d)

Figure D.2: ATLANTIS event displays of events from the "fake" muon control region. These events do not pass the track based isolation cut, i.e. they are not tight as defined in the context of the data driven jet background estimate. Note that in (c), the "splitting plane" is vertical, i.e. the y,z-plane.

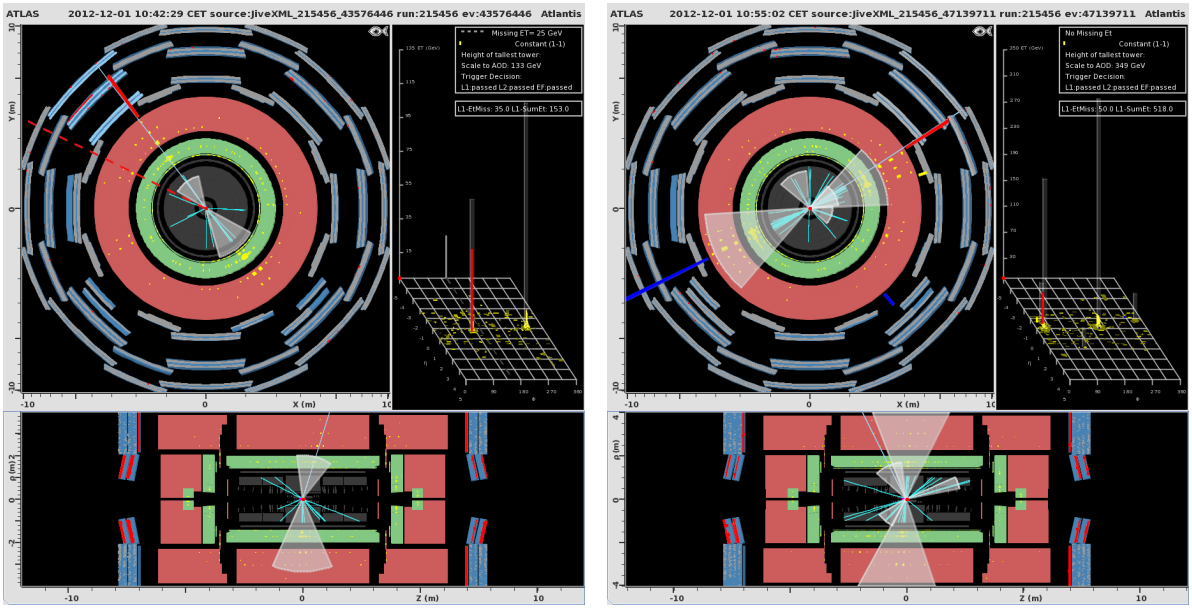

(a) (b)

Figure D.3: ATLANTIS event displays of events from the "fake" muon control region. These events do pass the track based isolation cut, i.e. they are tight as defined in the context of the data driven jet background estimate.

used for additional muons in the vetoing of dimuon events. It seems indeed that b-tagged jets are very common in the "fake" muon control region, which is reasonable based on the findings in ref. [98]. This could be kept in mind for the analysis of the higher energy LHC data to come, as b-tagging variables could potentially be useful in defining the "fake" muon control region. The event of fig. D.2(b) is a typical dijet event.

The event of fig. D.2(c) is quite interesting. This event contains two oppositely charged electrons (green object indicators) which pass even the tightest electron identification criteria, and the invariant mass of the electron pair is $94\,\mathrm{GeV}$. The event seems thus to have a Z boson decaying to electrons, and our selected muon candidate is found within a jet recoiling against the Z boson (against the electron pair). There is no combined fit muon track corresponding to our selected muon, so the muon spectrometer stand-alone track is shown instead, but it is mostly hidden underneath the corresponding muon object indicator.

Finally, the event of fig. D.2(d) contains again two b-tagged jets. One of these jets contains two muons, of which one is our selected muon and the other one has a p_{T} of $17\,\mathrm{GeV}$, below the dimuon veto threshold. The invariant mass of the muon pair is $3.2\,\mathrm{GeV}$, suggesting that it may be the result of a J/ψ meson decay.

We proceed to consider the muons of fig. D.3, which do pass the track based isolation cut, i.e. they are tight as defined in the context of the data driven jet background estimate. The event of fig. D.3(a) is a typical "back to back" dijet event. The muon in the event is close to the axis of a jet with a p_{T} of $80\,\mathrm{GeV}$, but the jet contains practically no track activity, and the muon passes the track based isolation cut. The event of fig. D.3(b) has very hard jet activity, with leading and subleading jet p_{T} of $350\,\mathrm{GeV}$ and $230\,\mathrm{GeV}$ respectively. The muon is close to the axis of a jet with a p_{T} of $60\,\mathrm{GeV}$, but is again seen to be very isolated in terms of track activity.

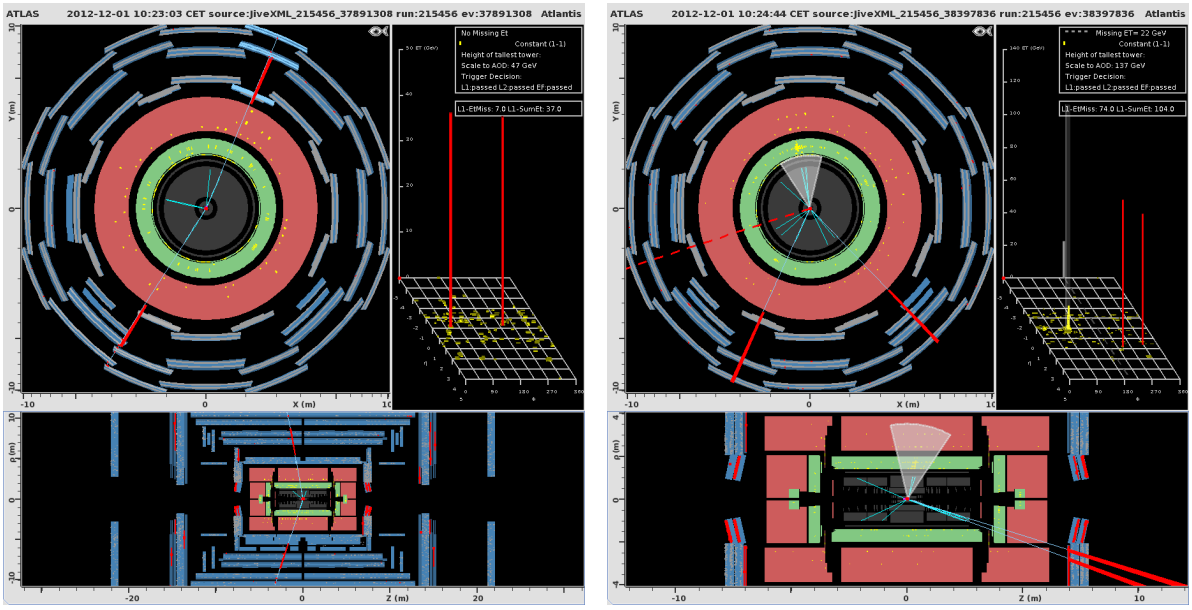

(a) (b)

Figure D.4: ATLANTIS event displays of events from the tag and probe selection.

D.3 Tag and probe selection

Events from the tag and probe region contain two selected muons with an invariant mass in the range $[86\,\mathrm{GeV}, 110\,\mathrm{GeV}]$. Two examples are shown in fig. D.4. Fig. D.4(a) shows a typical "clean" dimuon event where the muons are almost "back to back" in the transverse plane, while fig. D.4(b) shows an event where the muon pair recoils against a jet with a p_{T} of $140\,\mathrm{GeV}$.

D.4 High transverse mass events

We turn our attention finally to the "most interesting" events in the analysis, namely those with the highest transverse masses. All the 40 events above $m_{\mathrm{T}} = 843\,\mathrm{GeV}$ were analyzed visually, and eight of them are presented here. These are the six highest mass candidates, and two events that are included because they are of special interest. The six events with the highest transverse masses are presented in figs. D.5 and D.6. The values of the transverse mass, muon p_{T}, and $\not{E}_{\mathrm{T}}$ are given below each display. The values given correspond to our analysis, and they may differ from information readable from the event displays themselves. In particular, the $\not{E}_{\mathrm{T}}$ shown in ATLANTIS is the default one, not including the muon specific changes used in our analysis, and the ATLAS software version used to produce the event displays may differ from the one used to reconstruct the data for our analysis.

Clearly, the event with the highest transverse mass, shown in fig. D.5(a), is worth some discussion. While this event is seen in our analysis as a single muon event with large $\not{E}_{\mathrm{T}}$, the ATLANTIS display shows two muons and negligible $\not{E}_{\mathrm{T}}$. Both the muons shown in ATLANTIS are combined, as is seen from the fact that the tracks extend all the way from the inner detector through the calorimeters and the muon spectrometer. It would thus seem that the event should not be selected by our analysis, but the second muon fails the STACO combination, and there is

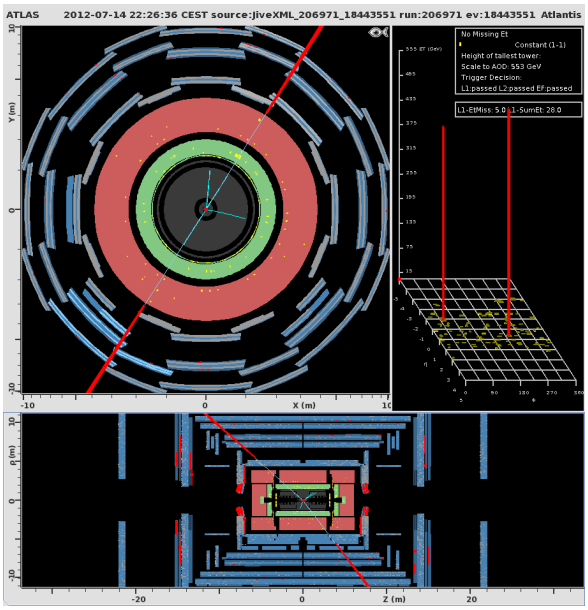

(a) $m_{\mathrm{T}} = 1380\,\mathrm{GeV}$, $p_{\mathrm{T}}^{\mu} = 700\,\mathrm{GeV}$, $\not{E}_{\mathrm{T}} = 680\,\mathrm{GeV}$

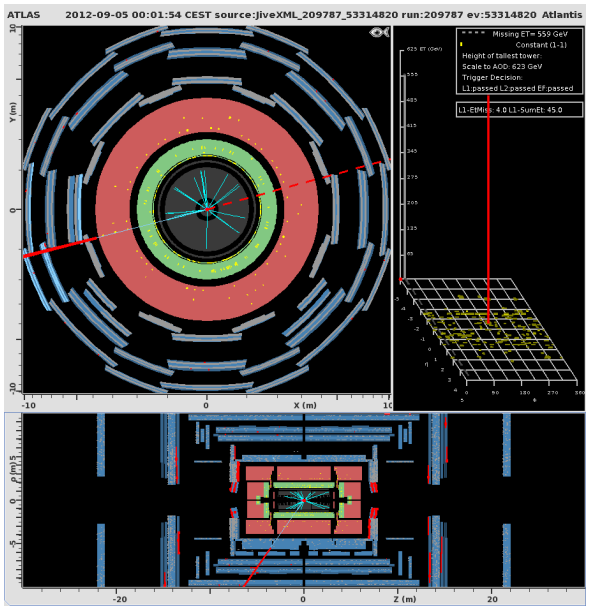

(b) $m_{\mathrm{T}} = 1370\,\mathrm{GeV}$, $p_{\mathrm{T}}^{\mu} = 700\,\mathrm{GeV}$, $\not{E}_{\mathrm{T}} = 670\,\mathrm{GeV}$

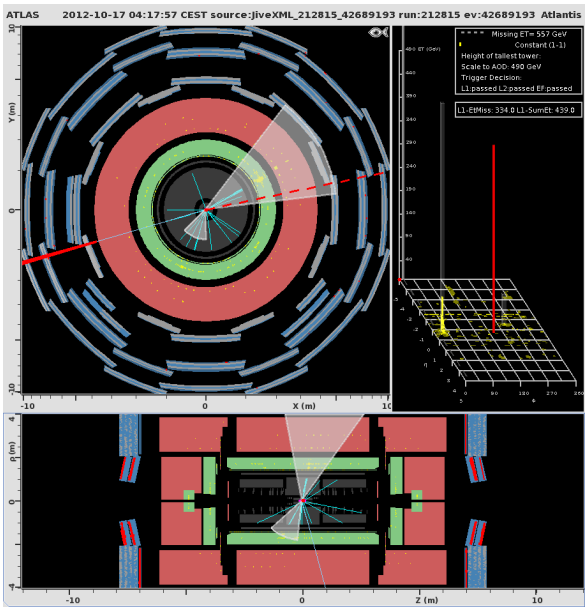

(c) $m_{\mathrm{T}} = 1350\,\mathrm{GeV}$, $p_{\mathrm{T}}^{\mu} = 940\,\mathrm{GeV}$, $\not{E}_{\mathrm{T}} = 480\,\mathrm{GeV}$

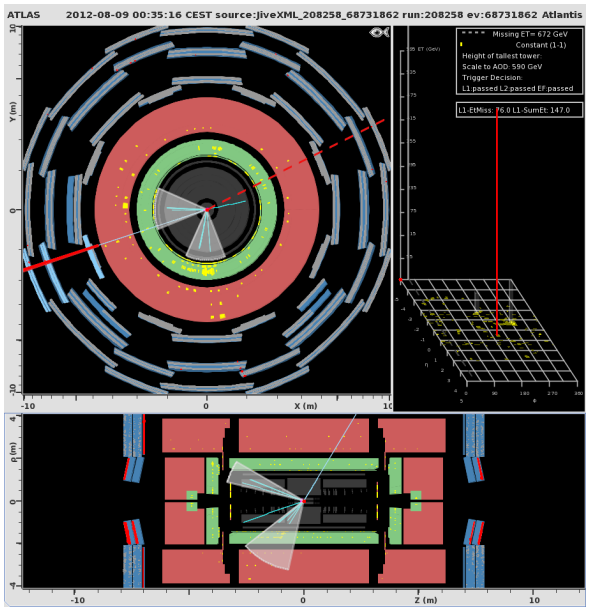

(d) $m_{\mathrm{T}} = 1320\,\mathrm{GeV}$, $p_{\mathrm{T}}^{\mu} = 630\,\mathrm{GeV}$, $\not{E}_{\mathrm{T}} = 700\,\mathrm{GeV}$

Figure D.5: ATLANTIS event displays of the four events with the highest transverse masses. Note that in (d), the "splitting plane" is along $\phi = \pi/4$ (or $\phi = 5\pi/4$), i.e. between the jets.

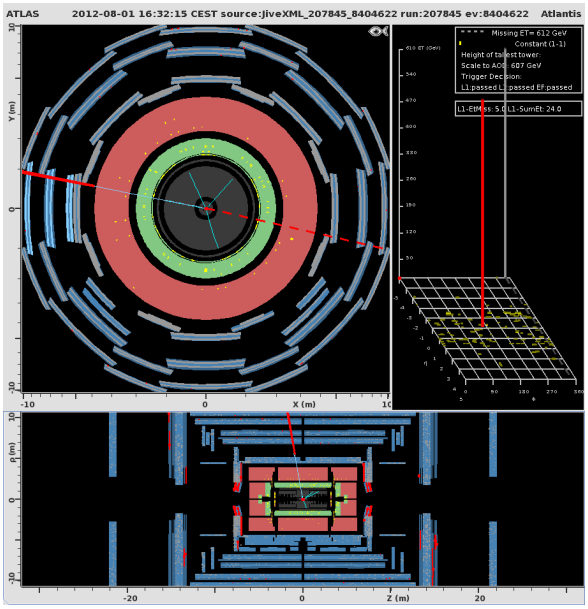

(a) $m_{\mathrm{T}} = 1230\,\mathrm{GeV}$, $p_{\mathrm{T}}^{\mu} = 610\,\mathrm{GeV}$, $\not{E}_{\mathrm{T}} = 610\,\mathrm{GeV}$

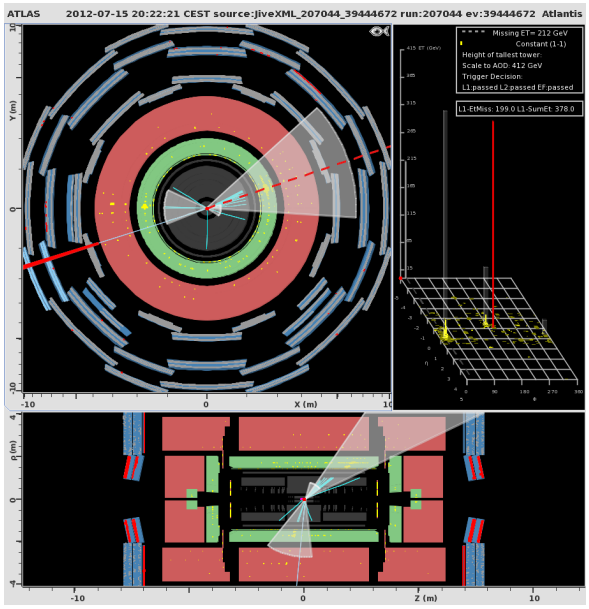

(b) $m_{\mathrm{T}} = 1220\,\mathrm{GeV}$, $p_{\mathrm{T}}^{\mu} = 800\,\mathrm{GeV}$, $\not{E}_{\mathrm{T}} = 460\,\mathrm{GeV}$

Figure D.6: ATLANTIS event displays of the fifth and sixth highest transverse mass events. Note that in (b), the "splitting plane" is vertical, i.e. the y,z-plane.

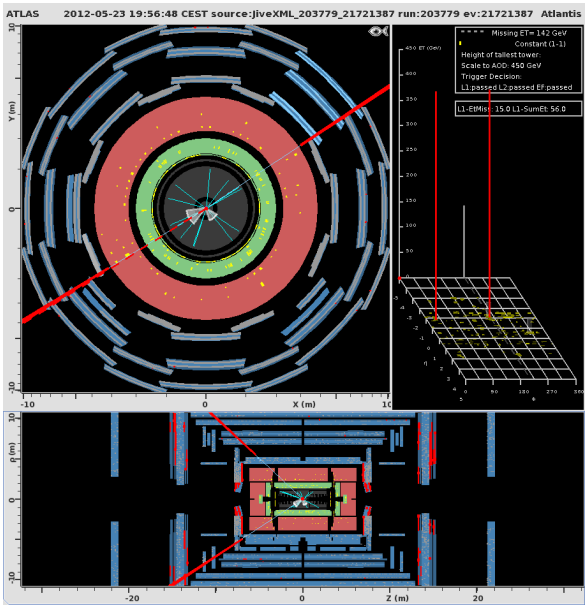

(a) $m_{\mathrm{T}} = 850\,\mathrm{GeV}$, $p_{\mathrm{T}}^{\mu} = 450\,\mathrm{GeV}$, $\not{E}_{\mathrm{T}} = 400\,\mathrm{GeV}$

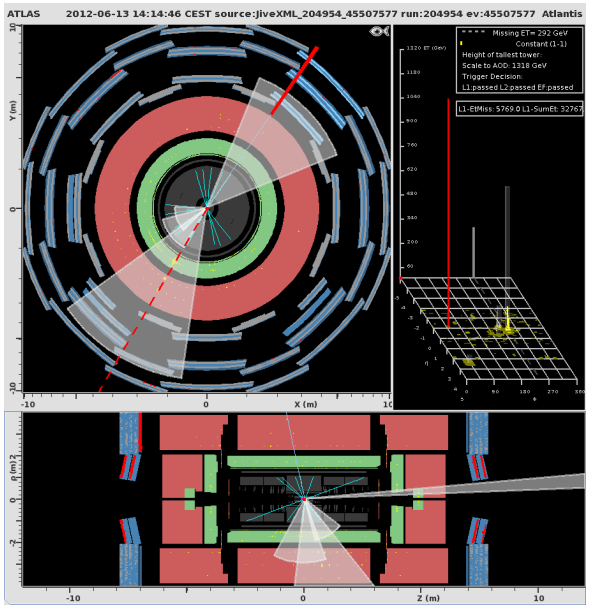

(b) $m_{\mathrm{T}} = 1060\,\mathrm{GeV}$, $p_{\mathrm{T}}^{\mu} = 1220\,\mathrm{GeV}$, $\not{E}_{\mathrm{T}} = 230\,\mathrm{GeV}$

Figure D.7: ATLANTIS event displays of two additional events from the search region $m_{\mathrm{T}} > 843\,\mathrm{GeV}$.

only one combined muon in the event as seen from the STACO point of view. The other muon thus effectively disappears, and large $\not{E}_{\mathrm{T}}$ arises because we do not include this muon in the $\not{E}_{\mathrm{T}}$ calculation.

If we were to use the MuID algorithm, both the muons in this event would be combined, and we would not have selected the event. The fact that both muons pass the MuID combination is also the reason why they are seen to have combined fit tracks in the ATLANTIS display. While it may seem awkward that our highest transverse mass event seems in fact to be a high mass dimuon event, this is completely unproblematic as long as the dimuon background is properly accounted for in the total background estimate. Among the 40 events above $m_{\mathrm{T}} = 843\,\mathrm{GeV}$, we find one additional event of the same kind, which appears as a dimuon event in ATLANTIS. This event is shown in fig. D.7(a).

Among the remaining events of the six highest transverse mass candidates, we find two examples of very "clean" events in figs. D.5(b) and D.6(a), and three examples of events with some jet activity in figs. D.5(c), D.5(d), and D.6(b). In the events of figs. D.5(c) and D.6(b), the leading jet has a p_{T} of $490\,\mathrm{GeV}$ and $410\,\mathrm{GeV}$ respectively, and the significant jet activity is reflected in the asymmetry between the muon p_{T} and the $\not{E}_{\mathrm{T}}$. The jet activity in the event of fig. D.5(d) is much softer, with a leading jet p_{T} of $110\,\mathrm{GeV}$.

The event shown in fig. D.7(b) was included because of very hard jet activity. The three jets going in the opposite direction of the muon in the transverse plane have transverse momenta of $830\,\mathrm{GeV}$, $120\,\mathrm{GeV}$, and $60\,\mathrm{GeV}$ respectively. The total (vector sum) transverse momentum of the muon and the neutrino ($\not{E}_{\mathrm{T}}$) in this event is $980\,\mathrm{GeV}$.

Bibliography

[1] J. Beringer et al. (Particle Data Group), *Review of Particle Physics*, Phys. Rev. D 86, 010001 (2012), http://journals.aps.org/prd/abstract/10.1103/PhysRevD.86.010001

[2] ATLAS Collaboration, *Observation of a new particle in the search for the Standard Model Higgs boson with the ATLAS detector at the LHC*, Phys. Lett. B 716 (2012) 1-29, arXiv:1207.7214, http://arxiv.org/abs/1207.7214

[3] CMS Collaboration, *Observation of a new boson at a mass of 125 GeV with the CMS experiment at the LHC*, Phys. Lett. B 716 (2012) 30, arXiv:1207.7235, http://arxiv.org/abs/1207.7235

[4] W. N. Cottingham, D. A. Greenwood, *An Introduction to the Standard Model of Particle Physics*, Second Edition, Cambridge

[5] F. Mandl, G. Shaw, *Quantum field theory*, Revised Edition, WILEY

[6] Goldstein, Poole, Safko, *Classical Mechanics*, Third Edition, Addison Wesley

[7] M. Peskin, D. Schroeder, *An Introduction to Quantum Field Theory*, Westview

[8] D. Griffiths, *Introduction to Elementary Particles*, Second, Revised Edition, WILEY-VCH

[9] Y. Aharonov, D. Bohm, *Significance of Electromagnetic Potentials in the Quantum Theory*, Phys. Rev. 115, 485-491 (1959), http://link.aps.org/doi/10.1103/PhysRev.115.485

[10] Quang Ho-Kim, Xuam-Yem Pham, *Elementary Particles and Their Interactions: Concepts and Phenomena*, Springer

[11] UA1 Collaboration, *Experimental observation of isolated large transverse energy electrons with associated missing energy at* $\sqrt{s} = 540\,\mathrm{GeV}$, Phys. Lett., 122B (1983), p. 103, http://www.sciencedirect.com/science/article/pii/0370269383911772

[12] UA2 Collaboration, *Observation of Single Isolated Electrons of High Transverse Momentum in Events with Missing Transverse Energy at the CERN* $\overline{p}p$ *Collider*, Phys. Lett., 122B (1983), p. 476, http://www.sciencedirect.com/science/article/pii/0370269383916052

[13] UA1 Collaboration, *Experimental observation of lepton pairs of invariant mass around* $95\,\mathrm{GeV}/c^2$ *at the CERN SPS collider*, Phys. Lett. B 126 (1983) 398-410, http://www.sciencedirect.com/science/article/pii/0370269383901880

[14] UA2 Collaboration, *Evidence for* $Z^0 \to e^+e^-$ *at the CERN* $\overline{p}p$ *collider*, Phys. Lett. B 129 (1983) 130-140, http://www.sciencedirect.com/science/article/pii/037026938390744X

[15] ATLAS Collaboration, *Measurement of the Higgs boson mass from the* $H \to \gamma\gamma$ *and* $H \to ZZ^* \to 4l$ *channels with the ATLAS detector using* $25\,\mathrm{fb}^{-1}$ *of pp collision data*, Phys. Rev. D 90, 052004 (2014), arXiv:1406.3827 [hep-ex], http://arxiv.org/abs/1406.3827

[16] CMS Collaboration, *Precise determination of the mass of the Higgs boson and studies of the compatibility of its couplings with the standard model*, CMS-PAS-HIG-14-009, https://cds.cern.ch/record/1728249

[17] Joan Solà, *Cosmological constant and vacuum energy: old and new ideas*, J. Phys.: Conf. Ser. 453 012015, http://iopscience.iop.org/1742-6596/453/1/012015

[18] ATLAS Collaboration, *Evidence for the spin-0 nature of the Higgs boson using ATLAS data*, Phys. Lett. B 726 (2013) 120, arXiv:1307.1432 [hep-ex], http://arxiv.org/abs/1307.1432

[19] ATLAS Collaboration, *Measurement of Higgs boson production in the diphoton decay channel in pp collisions at center-of-mass energies of 7 and 8 TeV with the ATLAS detector*, arXiv:1408.7084 [hep-ex], http://arxiv.org/abs/1408.7084

[20] ATLAS Collaboration, *Measurements of Higgs boson production and couplings in the four-lepton channel in pp collisions at center-of-mass energies of 7 and 8 TeV with the ATLAS detector*, arXiv:1408.5191 [hep-ex], http://arxiv.org/abs/1408.5191

[21] ATLAS Collaboration, *Observation and measurement of Higgs boson decays to* WW^* *with ATLAS at the LHC*, ATLAS-CONF-2014-060, http://cds.cern.ch/record/1954714

[22] ATLAS Collaboration, *Evidence for Higgs boson Yukawa couplings in the* $H \to \tau\tau$ *decay mode with the ATLAS detector*, ATLAS-CONF-2014-061, https://cds.cern.ch/record/1954724

[23] ATLAS Collaboration, *Search for the Standard Model Higgs boson decay to* $\mu^+\mu^-$ *with the ATLAS detector*, Phys. Lett. B 738 (2014) 68-86, arXiv:1406.7663 [hep-ex], http://arxiv.org/abs/1406.7663

[24] ATLAS Collaboration, *Measurements of Higgs boson production and couplings in diboson final states with the ATLAS detector at the LHC*, Phys. Lett. B 726 (2013) 88, arXiv:1307.1427 [hep-ex], http://arxiv.org/abs/1307.1427

[25] CLIC Physics Working Group, *Physics at the CLIC Multi-TeV Linear Collider: report of the CLIC Physics Working Group*, arXiv:hep-ph/0412251, http://arxiv.org/abs/hep-ph/0412251

[26] A. Martin, W. Stirling, R. Thorne, G. Watt, *Parton distributions for the LHC*, Eur. Phys. J. C 63 (2009) 189, arXiv:0901.0002, http://arxiv.org/abs/0901.0002

[27] T. Sjöstrand, S. Mrenna, P. Skands, *PYTHIA 6.4 Physics and Manual*, JHEP 05 (2006) 026, http://iopscience.iop.org/1126-6708/2006/05/026

[28] ALICE Collaboration, *Measurement of inelastic, single- and double-diffraction cross sections in proton–proton collisions at the LHC with ALICE*, arXiv:1208.4968 [hep-ex], http://arxiv.org/abs/1208.4968

[29] G. Gabrielse et al., *New Determination of the Fine Structure Constant from the Electron g Value and QED*, Phys. Rev. Lett. 97, 030802 (2006), http://journals.aps.org/prl/abstract/10.1103/PhysRevLett.97.030802

[30] R. Davis Jr., D.S. Harmer, K.C. Hoffman, *Search for Neutrinos from the Sun*, Phys. Rev. Lett., 20 (1968), p. 1205, http://journals.aps.org/prl/abstract/10.1103/PhysRevLett.20.1205

[31] SNO Collaboration, *Direct Evidence for Neutrino Flavor Transformation from Neutral-Current Interactions in the Sudbury Neutrino Observatory*, Phys. Rev. Lett. 89, 011301 (2002), http://journals.aps.org/prl/abstract/10.1103/PhysRevLett.89.011301

[32] S. Hatakeyama et al., *Measurement of the Flux and Zenith-Angle Distribution of Upward Through-Going Muons in Kamiokande II + III*, Phys. Rev. Lett. 81:2016-2019 (1998), arXiv:hep-ex/9806038, http://arxiv.org/abs/hep-ex/9806038

[33] D. Clowe et al., *A direct empirical proof of the existence of dark matter*, Astrophys. J. 648:L109-L113 (2006), arXiv:astro-ph/0608407, http://arxiv.org/abs/astro-ph/0608407

[34] Ø. Grøn, S. Hervik, *Einstein's General Theory of Relativity*, Springer

[35] G. D. Coughlan, J. E. Dodd, B. M. Gripaios, *The Ideas of Particle Physics*, Third Edition, Cambridge

[36] H. Georgi, S. L. Glashow, *Unity of All Elementary-Particle Forces*, Phys. Rev. Lett. 32, 438 (1974), http://journals.aps.org/prl/abstract/10.1103/PhysRevLett.32.438

[37] P. Langacker, *The Physics of Heavy Z' Gauge Bosons*, Rev. Mod. Phys. 81, 1199-1228 (2008), arXiv:0801.1345 [hep-ph], http://arxiv.org/abs/0801.1345

[38] D. London, J. L. Rosner, *Extra gauge bosons in E_6*, Phys. Rev. D 34, 1530 (1986), http://journals.aps.org/prd/abstract/10.1103/PhysRevD.34.1530

[39] ATLAS Collaboration, *Search for high-mass dilepton resonances in pp collisions at* $\sqrt{s} = 8\,\mathrm{TeV}$ *with the ATLAS detector*, Phys. Rev. D. 90, 052005 (2014), arXiv:1405.4123 [hep-ex], http://arxiv.org/abs/1405.4123

[40] CMS Collaboration, *Search for Resonances in the Dilepton Mass Distribution in pp Collisions at* $\sqrt{s} = 8\,\mathrm{TeV}$, CMS-PAS-EXO-12-061, http://cds.cern.ch/record/1519132

[41] A. Djouadi, *The anatomy of electroweak symmetry breaking Tome II: The Higgs bosons in the Minimal Supersymmetric Model*, Physics Reports 459 (2008), http://www.sciencedirect.com/science/article/pii/S0370157307004346

[42] G. Senjanovic, R. N. Mohapatra, *Exact left-right symmetry and spontaneous violation of parity*, Phys. Rev. D12, 1502 (1975), http://journals.aps.org/prd/abstract/10.1103/PhysRevD.12.1502

[43] R. N. Mohapatra, G. Senjanovic, *Neutrino Mass and Spontaneous Parity Nonconservation*, Phys. Rev. Lett. 44, 912 (1980), http://journals.aps.org/prl/abstract/10.1103/PhysRevLett.44.912

[44] O. S. Brüning et al., *LHC Design Report Vol. I: The LHC Main Ring*, CERN-2004-003-V1, https://cds.cern.ch/record/782076 and https://ab-div.web.cern.ch/ab-div/Publications/LHC-DesignReport.html

[45] J. D. Jackson, *Classical Electrodynamics*, Second Edition, Wiley

[46] J. M. Leinaas, *Classical Mechanics and Electrodynamics*, lecture notes in the course FYS3120 given at the University of Oslo, http://www.uio.no/studier/emner/matnat/fys/FYS3120/v12/LectureNotes3120.pdf

[47] *LEP Design Report Vol. II: The LEP Main Ring*, CERN-LEP-84-01, https://cds.cern.ch/record/102083

[48] T. Behnke et al., *ILC Technical Design Report*, https://www.linearcollider.org/ILC/Publications/Technical-Design-Report

[49] M. Aicheler et al., *A Multi-TeV Linear Collider based on CLIC Technology: CLIC Conceptual Design Report*, https://edms.cern.ch/document/1234244

[50] D. Green, *High* P_{T} *Physics at Hadron Colliders*, Cambridge

[51] ATLAS Collaboration, *The ATLAS Experiment at the CERN Large Hadron Collider*, 2008 JINST 3 S08003, https://cdsweb.cern.ch/record/1129811

[52] ATLAS Collaboration, *ATLAS detector and physics performance, Technical Design Report*, Volume I, ATLAS TDR 14, CERN/LHCC 99-14, (1999), https://cds.cern.ch/record/391176

[53] ATLAS Collaboration, *Performance of missing transverse momentum reconstruction in proton-proton collisions at 7 TeV with ATLAS*, Eur. Phys. J. C 72 (2012) 1844, arXiv:1108.5602 [hep-ex], http://arxiv.org/abs/1108.5602

[54] G. Altarelli, B. Mele, M. Ruiz-Altaba, *Searching for new heavy vector bosons in $p\overline{p}$ colliders*, Z. Phys. C 45 (1989) 109, http://link.springer.com/article/10.1007%2FBF01556677

[55] H. E. Haber, *Signals Of New W's And Z's*, SLAC-PUB-3456, http://inspirehep.net/record/205064/

[56] ATLAS Collaboration, *Search for heavy neutrinos and right-handed W bosons in events with two leptons and jets in pp collisions at $\sqrt{s} = 7\,\mathrm{TeV}$ with the ATLAS detector*, Eur. Phys. J. C72 (2012) 2056, arXiv:1203.5420 [hep-ex], http://arxiv.org/abs/1203.5420

[57] M. V. Chizhov, G. Dvali, *Origin and Phenomenology of Weak-Doublet Spin-1 Bosons*, Phys. Lett. B 703:593-598 (2011), arXiv:0908.0924, http://arxiv.org/abs/0908.0924

[58] M. V. Chizhov, *A Reference Model for Anomalously Interacting Bosons*, arXiv:1005.4287, http://arxiv.org/abs/1005.4287

[59] T. Sjöstrand, S. Mrenna, P. Skands, *A Brief Introduction to PYTHIA 8.1*, Comput. Phys. Comm. 178 (2008) 852, arXiv:0710.3820 [hep-ph], http://arxiv.org/abs/0710.3820

[60] ATLAS Collaboration, *Summary of ATLAS Pythia 8 tunes*, ATL-PHYS-PUB-2012-003, http://cds.cern.ch/record/1474107

[61] A. Belyaev, N. D. Christensen, A. Pukhov, *CalcHEP 3.4 for collider physics within and beyond the Standard Model*, arXiv:1207.6082, http://arxiv.org/abs/1207.6082

[62] J. Pumplin, D. R. Stump, J. Huston, H. L. Lai, Pavel M. Nadolsky, W. K. Tung, *New generation of parton distributions with uncertainties from global QCD analysis*, JHEP 0207 (2002) 012, arXiv:hep-ph/0201195, http://arxiv.org/abs/hep-ph/0201195

[63] S. Agostinelli et al., *Geant4 – a simulation toolkit*, Nucl. Instr. Meth. Phys. Res. A 506 250-303, http://www.sciencedirect.com/science/article/pii/S0168900203013688

[64] W. Lukas, *Fast Simulation for ATLAS: Atlfast-II and ISF*, J. Phys.: Conf. Ser. 396 022031, http://iopscience.iop.org/1742-6596/396/2/022031

[65] P. Golonka, Z. Was, *PHOTOS Monte Carlo: a precision tool for QED corrections in Z and W decays*, Eur. Phys. J. C 45 (2006) 97-107, arXiv:hep-ph/0506026, http://arxiv.org/abs/hep-ph/0506026

[66] M. V. Chizhov, *On the two kinds of vector particles*, arXiv:hep-ph/0008187, http://arxiv.org/abs/hep-ph/0008187

[67] M. V. Chizhov, V. A. Bednyakov, J. A. Budagov, *Proposal for chiral bosons search at LHC via their unique new signature*, Phys. Atom. Nucl. 71:2096-2100, 2008, arXiv:0801.4235, http://arxiv.org/abs/0801.4235

[68] E. Boos et al., *Interference between W' and W in single-top quark production processes*, Physics Letters B 655 (2007) 245-250, http://www.sciencedirect.com/science/article/pii/S0370269307004157

[69] T. G. Rizzo, *The determination of the helicity of W' boson couplings at the LHC*, JHEP 05 (2007) 037, http://iopscience.iop.org/1126-6708/2007/05/037/

[70] E. Accomando et al., *Interference effects in heavy W'-boson searches at the LHC*, arXiv:1110.0713 [hep-ph], http://arxiv.org/abs/1110.0713

[71] CMS Collaboration, *Search for physics beyond the standard model in final states with a lepton and missing transverse energy in proton-proton collisions at $\sqrt{s} = 8\,\mathrm{TeV}$*, arXiv:1408.2745 [hep-ex], http://arxiv.org/abs/1408.2745

[72] P. Nason, *A New Method for Combining NLO QCD with Shower Monte Carlo Algorithms*, JHEP 0411:040 (2004), arXiv:hep-ph/0409146, http://arxiv.org/abs/hep-ph/0409146

[73] S. Frixione, P. Nason, C. Oleari, *Matching NLO QCD computations with Parton Shower simulations: the POWHEG method*, J. High Energy Phys. 0711 (2007) 070, arXiv:0709.2092, http://arxiv.org/abs/0709.2092

[74] S. Alioli, P. Nason, C. Oleari, E. Re, *A general framework for implementing NLO calculations in shower Monte Carlo programs: the POWHEG BOX*, JHEP 1006:043 (2010), arXiv:1002.2581 [hep-ph], http://arxiv.org/abs/1002.2581

[75] H.-L. Lai, M. Guzzi, J. Huston, Z. Li, P. M. Nadolsky, Jon Pumplin, C.-P. Yuan, *New parton distributions for collider physics*, Phys. Rev. D82 (2010) 074024, arXiv:1007.2241, http://arxiv.org/abs/1007.2241

[76] R. Hamberg, W. L. van Neerven, T. Matsuura, *A complete calculation of the order α_s^2 correction to the Drell-Yan K-factor*, Nucl. Phys. B 359 (1991) 343-405; Erratum-ibid. 644 (2002) 403, http://www.sciencedirect.com/science/article/pii/0550321391900645

[77] C. Anastasiou, L. Dixon, K. Melnikov, F. Petriello, *High-precision QCD at hadron colliders: electroweak gauge boson rapidity distributions at NNLO*, Phys. Rev. D 69 (2004) 094008, arXiv:hep-ph/0312266, http://arxiv.org/abs/hep-ph/0312266

[78] K. Melnikov, F. Petriello, *Electroweak gauge boson production at hadron colliders through $O(\alpha_s^2)$*, Phys. Rev. 74 (2006) 114017, arXiv:hep-ph/0609070, http://arxiv.org/abs/hep-ph/0609070

[79] R. Gavin, Y. Li, F. Petriello, S. Quackenbush, *FEWZ 2.0: A code for hadronic Z production at next-to-next-to-leading order*, Comput. Phys. Commun. 182 (2011) 2388, arXiv:1011.3540 [hep-ph], http://arxiv.org/abs/1011.3540

[80] S. G. Bondarenko, A. A. Sapronov, *NLO EW and QCD proton-proton cross section calculations with mcsanc-v1.01*, Comput. Phys. Commun. 184 (2013) 2343-2350, arXiv:1301.3687, http://arxiv.org/abs/1301.3687

[81] S. Alekhin, S. Alioli, R. D. Ball, V. Bertone, J. Blumlein, et al., *The PDF4LHC Working Group Interim Report*, arXiv:1101.0536 [hep-ph], http://arxiv.org/abs/1101.0536

[82] R. D. Ball, V. Bertone, S. Carrazza, C. S. Deans, L. Del Debbio, S. Forte, A. Guffanti, N. P. Hartland et al., *Parton distributions with LHC data*, arXiv:1207.1303 [hep-ph], http://arxiv.org/abs/1207.1303

[83] S. Alekhin, J. Blumlein, S. Moch, *Parton distribution functions and benchmark cross sections at NNLO*, arXiv:1202.2281 [hep-ph], http://arxiv.org/abs/1202.2281

[84] V. Radescu for the H1, ZEUS Collaborations, *Hera Precision Measurements and Impact for LHC Predictions*, arXiv:1107.4193, http://arxiv.org/abs/1107.4193 HERAPDF 1.5 NLO and NNLO preliminary, H1prelim-11-042, ZEUS-prel-11-002, Proceedings of Moriond 2011. See also here: https://www.desy.de/h1zeus/combined_results/index.php?do=proton_structure

[85] ATLAS Collaboration, *ATLAS tunes of PYTHIA 6 and Pythia 8 for MC11*, ATL-PHYS-PUB-2011-009, https://cds.cern.ch/record/1363300

[86] B. P. Kersevan, E. Richter-Was, *The Monte Carlo event generator AcerMC versions 2.0 to 3.8 with interfaces to PYTHIA 6.4, HERWIG 6.5 and ARIADNE 4.1*, Comput. Phys. Commun. 184 (2013) 919-985, http://www.sciencedirect.com/science/article/pii/S001046551200375X (see also arXiv:hep-ph/0405247, http://arxiv.org/abs/hep-ph/0405247)

[87] S. Frixione, B. R. Webber, *Matching NLO QCD computations and parton shower simulations*, JHEP 06 (2002) 029, arXiv:hep-ph/0204244, http://arxiv.org/abs/hep-ph/0204244

[88] G. Corcella et al., *HERWIG 6.5: an event generator for Hadron Emission Reactions With Interfering Gluons (including supersymmetric processes)*, JHEP 01 (2001) 010, arXiv:hep-ph/0011363, http://arxiv.org/abs/hep-ph/0011363

[89] J. M. Butterworth, M. H. Seymour, *Multi-parton Interactions in HERWIG*, http://projects.hepforge.org/jimmy

[90] M. Czakon, A. Mitov, *Top++: a program for the calculation of the top-pair cross-section at hadron colliders*, arXiv:1112.5675 [hep-ph], http://arxiv.org/abs/1112.5675

[91] N. Kidonakis, *NNLL resummation for s-channel single top quark production*, Phys. Rev. D 81, 054028 (2010), arXiv:1001.5034 [hep-ph], http://arxiv.org/abs/1001.5034

[92] N. Kidonakis, *Next-to-next-to-leading-order collinear and soft gluon corrections for t-channel single top quark production*, Phys. Rev. D 83, 091503 (2011), arXiv:1103.2792 [hep-ph], http://arxiv.org/abs/1103.2792

[93] N. Kidonakis, *Two-loop soft anomalous dimensions for single top quark associated production with a W^- or H^-*, Phys. Rev. D 82, 054018 (2010), arXiv:1005.4451 [hep-ph], http://arxiv.org/abs/1005.4451

[94] T. Gleisberg, S. Hoeche, F. Krauss, M. Schonherr, S. Schumann, et al., *Event generation with SHERPA 1.1*, JHEP 02 (2009) 007, arXiv:0811.4622 [hep-ph], http://arxiv.org/abs/0811.4622

[95] J. M. Campbell, R. K. Ellis, *An update on vector boson pair production at hadron colliders*, Phys. Rev. D 60, 113006 (1999), arXiv:hep-ph/9905386, http://arxiv.org/abs/hep-ph/9905386

[96] ATLAS Collaboration, *Measurement of multi-jet cross sections in proton-proton collisions at a 7 TeV center-of-mass energy*, Eur. Phys. J. C71 (2011) 1763, arXiv:1107.2092 [hep-ex], http://arxiv.org/abs/1107.2092

[97] Eirik Gramstad, *Searches for Supersymmetry in Di-Lepton Final States with the ATLAS Detector at $\sqrt{s} = 7\,\mathrm{TeV}$*, PhD thesis, University of Oslo (2013), http://urn.nb.no/URN:NBN:no-39806

[98] Maiken Pedersen, *Fake lepton determination, Supersymmetry searches in di-lepton final states, and sharing ATLAS research with young students*, PhD thesis, University of Oslo (2014), http://urn.nb.no/URN:NBN:no-44688

[99] ATLAS Collaboration, *Improved luminosity determination in pp collisions at $\sqrt{s} = 7\,\mathrm{TeV}$ using the ATLAS detector at the LHC*, Eur. Phys. J. C 73 (2013) 2518, arXiv:1302.4393 [hep-ex], http://arxiv.org/abs/1302.4393

[100] ATLAS Collaboration, *Selection of jets produced in proton-proton collisions with the ATLAS detector using 2011 data*, ATLAS-CONF-2012-020, http://cds.cern.ch/record/1430034

[101] ATLAS Collaboration, *Preliminary results on the muon reconstruction efficiency, momentum resolution, and momentum scale in ATLAS 2012 pp collision data*, ATLAS-CONF-2013-088, http://cds.cern.ch/record/1580207

[102] M. Cacciari, G. P. Salam, G. Soyez, *The anti-k_t jet clustering algorithm*, JHEP 0804:063 (2008), arXiv:0802.1189 [hep-ph], http://arxiv.org/abs/0802.1189

[103] ATLAS Collaboration, *Search for high-mass states with electron plus missing transverse energy using the ATLAS Detector at* $\sqrt{s} = 7\,\mathrm{TeV}$, ATLAS-CONF-2010-089, http://cds.cern.ch/record/1299104

[104] ATLAS Collaboration, *Search for high-mass states with one lepton plus missing transverse momentum in proton-proton collisions at* $\sqrt{s} = 7\,\mathrm{TeV}$ *with the ATLAS detector*, Phys. Lett. B 701:50-69 (2011), arXiv:1103.1391 [hep-ex], http://arxiv.org/abs/1103.1391

[105] ATLAS Collaboration, *Search for high-mass states with one muon plus missing transverse momentum in proton-proton collisions at* $\sqrt{s} = 7\,\mathrm{TeV}$ *with the ATLAS detector*, ATLAS-CONF-2011-082, http://cds.cern.ch/record/1356189

[106] ATLAS Collaboration, *Search for a heavy gauge boson decaying to a charged lepton and a neutrino in* $1\,\mathrm{fb}^{-1}$ *of pp collisions at* $\sqrt{s} = 7\,\mathrm{TeV}$ *using the ATLAS detector*, Phys. Lett. B 705 (2011) 28-46, arXiv:1108.1316 [hep-ex], http://arxiv.org/abs/1108.1316

[107] ATLAS Collaboration, *ATLAS search for a heavy gauge boson decaying to a charged lepton and a neutrino in pp collisions at* $\sqrt{s} = 7\,\mathrm{TeV}$, Eur. Phys. J. C (2012) 72: 2241, arXiv:1209.4446 [hep-ex], http://arxiv.org/abs/1209.4446

[108] ATLAS Collaboration, *Search for high-mass states with one lepton plus missing transverse momentum in pp collisions at* $\sqrt{s} = 8\,\mathrm{TeV}$ *with the ATLAS detector*, ATLAS-CONF-2014-017, http://cds.cern.ch/record/1692660

[109] ATLAS Collaboration, *Search for new particles in events with one lepton and missing transverse momentum in pp collisions at* $\sqrt{s} = 8\,\mathrm{TeV}$ *with the ATLAS detector*, JHEP 09 (2014) 037, arXiv:1407.7494 [hep-ex], http://arxiv.org/abs/1407.7494

[110] A. L. Read, *Presentation of search results: the* CL_s *technique*, J. Phys. G: Nucl. Part. Phys. 28 (2002) 2693-2704, http://iopscience.iop.org/0954-3899/28/10/313

[111] T. Junk, *Confidence Level Computation for Combining Searches with Small Statistics*, Nucl. Instrum. Meth. A434 (1999) 435-443, arXiv:hep-ex/9902006, http://arxiv.org/abs/hep-ex/9902006

[112] L. Demortier, *Bayesian Treatments of Systematic Uncertainties*, in *Proceedings of the Conference on Advanced Statistical Techniques in Particle Physics* edited by M. R. Whalley and L. Lyons (University of Durham, Durham, 2002), pp. 145-151 (Durham Report No. IPPP/02/39, 2002), http://citeseerx.ist.psu.edu/viewdoc/summary?doi=10.1.1.205.7146

[113] L. Demortier, S. Jain, H. B. Prosper, *Reference priors for high energy physics*, Phys. Rev. D 82, 034002 (2010), arXiv:1002.1111 [stat.AP], http://arxiv.org/abs/1002.1111

[114] L. Smestad, *The Search for the Standard Model Higgs Boson in $H \to \gamma\gamma$ Decays with the ATLAS Detector in $4.9\,\mathrm{fb}^{-1}$ of 2011 Data at $\sqrt{s} = 7\,\mathrm{TeV}$*, PhD thesis, University of Oslo (2013), http://urn.nb.no/URN:NBN:no-39113

[115] G. Cowan, K. Cranmer, E. Gross, O. Vitells, *Asymptotic formulae for likelihood-based tests of new physics*, Eur. Phys. J. C 71:1554 (2011), arXiv:1007.1727 [physics.data-an], http://arxiv.org/abs/1007.1727

[116] O. Vitells, A. L. Read, *A comment on estimating sensitivity to neutrino mass hierarchy in neutrino experiments*, arXiv:1311.4076 [hep-ex], http://arxiv.org/abs/1311.4076

[117] E. Ciuffoli, J. Evslin, X. Zhang, *Sensitivity to the Neutrino Mass Hierarchy*, arXiv:1305.5150 [hep-ph], http://arxiv.org/abs/1305.5150

[118] J. Wenninger, *Energy Calibration of the LHC Beams at 4 TeV*, CERN-ATS-2013-040, http://cds.cern.ch/record/1546734

[119] E. Boos et al, *CompHEP 4.4 – Automatic Computations from Lagrangians to Events*, Nucl. Instrum. Meth. A534 (2004) 250, arXiv:hep-ph/0403113, http://arxiv.org/abs/hep-ph/0403113

[120] J. Conway et al., *PGS 4: Pretty Good Simulation of high energy collisions*, http://www.physics.ucdavis.edu/~conway/research/software/pgs/pgs4-general.htm

[121] S. Ovyn, X. Rouby, V. Lemaitre, *Delphes, a framework for fast simulation of a generic collider experiment*, arXiv:0903.2225 [hep-ph], http://arxiv.org/abs/0903.2225

[122] CDF Collaboration, *Search for a New Heavy Gauge Boson W' with Electron + $\not\!\!E_{\mathrm{T}}$ Event Signature in $p\bar{p}$ collisions at $\sqrt{s} = 1.96\,\mathrm{TeV}$*, Phys. Rev. D 83:031102 (2011), arXiv:1012.5145 [hep-ex], http://xxx.lanl.gov/abs/1012.5145

[123] D0 Collaboration, *Search for W' Bosons Decaying to an Electron and a Neutrino with the D0 Detector*, Phys. Rev. Lett. 100, 031804 (2008), http://journals.aps.org/prl/abstract/10.1103/PhysRevLett.100.031804

[124] CMS Collaboration, *Search for a W' boson decaying to a muon and a neutrino in pp collisions at $\sqrt{s} = 7\,\mathrm{TeV}$*, CMS-EXO-10-015, Phys. Lett. B 701 (2011), arXiv:1103.0030 [hep-ex], http://arxiv.org/abs/1103.0030

[125] CMS Collaboration, *Search for a heavy gauge boson W' in the final state with an electron and large missing transverse energy in pp collisions at $\sqrt{s} = 7\,\mathrm{TeV}$*, Phys. Lett. B 698 (2011), arXiv:1012.5945 [hep-ex], http://arxiv.org/abs/1012.5945

[126] CMS Collaboration, *Search for leptonic decays of W' bosons in pp collisions at $\sqrt{s} = 7\,\mathrm{TeV}$*, JHEP 08 (2012) 023, arXiv:1204.4764 [hep-ex], http://arxiv.org/abs/1204.4764

[127] A. Birkedal, K. Matchev, M. Perelstein, *Dark Matter at Colliders: a Model-Independent Approach*, Phys. Rev. D 70:077701 (2004), arXiv:hep-ph/0403004, http://arxiv.org/abs/hep-ph/0403004

[128] J. Goodman et al., *Constraints on Light Majorana Dark Matter from Colliders*, Phys. Lett. B 695:185-188 (2011), arXiv:1005.1286 [hep-ph], http://arxiv.org/abs/1005.1286

[129] Y. Bai, P. J. Fox, R. Harnik, *The Tevatron at the Frontier of Dark Matter Direct Detection*, JHEP 1012:048 (2010), arXiv:1005.3797 [hep-ph], http://arxiv.org/abs/1005.3797

[130] J. Goodman et al., *Constraints on Dark Matter from Colliders*, Phys. Rev. D 82, 116010 (2010), arXiv:1008.1783 [hep-ph], http://arxiv.org/abs/1008.1783

[131] Y. Bai, T. M. P. Tait, *Searches with Mono-Leptons*, Phys. Lett. B 723:384-387 (2013), arXiv:1208.4361 [hep-ph], http://arxiv.org/abs/1208.4361

[132] J. Alwall et al., *MadGraph 5 : Going Beyond*, arXiv:1106.0522 [hep-ph], http://arxiv.org/abs/1106.0522

[133] G. Belanger, F. Boudjema, A. Pukhov, A. Semenov, *Dark matter direct detection rate in a generic model with micrOMEGAs2.2*, Comput. Phys. Commun. 180:747-767 (2009), arXiv:0803.2360 [hep-ph], http://arxiv.org/abs/0803.2360

[134] G. Busoni, A. De Simone, E. Morgante, A. Riotto, *On the Validity of the Effective Field Theory for Dark Matter Searches at the LHC*, Phys. Lett. B 728 (2014) 412-421, arXiv:1307.2253 [hep-ph], http://arxiv.org/abs/1307.2253

[135] G. Busoni, A. De Simone, J. Gramling, E. Morgante, A. Riotto, *On the Validity of the Effective Field Theory for Dark Matter Searches at the LHC, Part II: Complete Analysis for the s-channel*, arXiv:1402.1275 [hep-ph], http://arxiv.org/abs/1402.1275

[136] G. Busoni, A. De Simone, T. Jacques, E. Morgante, A. Riotto, *On the Validity of the Effective Field Theory for Dark Matter Searches at the LHC Part III: Analysis for the t-channel*, arXiv:1405.3101 [hep-ph], http://arxiv.org/abs/1405.3101

[137] ATLAS Collaboration, *Sensitivity to WIMP Dark Matter in the Final States Containing Jets and Missing Transverse Momentum with the ATLAS Detector at 14 TeV LHC*, ATL-PHYS-PUB-2014-007, https://cds.cern.ch/record/1708859

[138] D. Stump et al., *Uncertainties of Predictions from Parton Distribution Functions I: the Lagrange Multiplier Method*, Phys. Rev. D 65:014012 (2001), arXiv:hep-ph/0101051, http://arxiv.org/abs/hep-ph/0101051

[139] J. Pumplin et al., *Uncertainties of predictions from parton distribution functions II: the Hessian method*, Phys. Rev. D 65:014013 (2001), arXiv:hep-ph/0101032, http://arxiv.org/abs/hep-ph/0101032

[140] ATLAS Collaboration, *Search for dark matter in events with a hadronically decaying W or Z boson and missing transverse momentum in pp collisions at* $\sqrt{s} = 8\,\mathrm{TeV}$ *with the ATLAS detector*, Phys. Rev. Lett 112, 041802 (2014), arXiv:1309.4017 [hep-ex], http://arxiv.org/abs/1309.4017

[141] ATLAS Collaboration, *Search for dark matter in events with a Z boson and missing transverse momentum in pp collisions at* $\sqrt{s} = 8\,\mathrm{TeV}$ *with the ATLAS detector*, Phys. Rev. D. 90, 012004 (2014), arXiv:1404.0051 [hep-ex], http://arxiv.org/abs/1404.0051

[142] ATLAS Collaboration, *Search for dark matter candidates and large extra dimensions in events with a jet and missing transverse momentum with the ATLAS detector*, JHEP 1304 (2013) 075, arXiv:1210.4491 [hep-ex], http://arxiv.org/abs/1210.4491

[143] E. Aprile et al., XENON Collaboration, *Dark Matter Results from 225 Live Days of XENON100 Data* , Phys. Rev. Lett. 109 (2012) 181301, arXiv:1207.5988 [astro-ph.CO], http://arxiv.org/abs/1207.5988

[144] R. Agnese et al., SuperCDMS Collaboration, *CDMSlite: A Search for Low-Mass WIMPs using Voltage-Assisted Calorimetric Ionization Detection in the SuperCDMS Experiment*, Phys. Rev. Lett. 112 (2014) 041302, arXiv:1309.3259 [physics.ins-det], http://arxiv.org/abs/1309.3259

[145] R. Agnese et al., SuperCDMS Collaboration, *Search for Low-Mass WIMPs with SuperCDMS*, arXiv:1402.7137 [hep-ex], http://arxiv.org/abs/1402.7137

[146] D. Akerib et al., LUX Collaboration, *First results from the LUX dark matter experiment at the Sanford Underground Research Facility*, Phys. Rev. Lett. 112 (2014) 091303, arXiv:1310.8214 [astro-ph.CO], http://arxiv.org/abs/1310.8214

[147] E. Behnke et al., COUPP Collaboration, *First dark matter search results from a 4-kg* CF_3I *bubble chamber operated in a deep underground site*, Phys. Rev. D 86 (2012) 052001, arXiv:1204.3094 [astro-ph.CO], http://arxiv.org/abs/1204.3094

[148] M. Felizardo et al., SIMPLE Collaboration, *Final Analysis and Results of the Phase II SIMPLE Dark Matter Search*, Phys. Rev. Lett. 108 (2012) 201302, arXiv:1106.3014 [astro-ph.CO], http://arxiv.org/abs/1106.3014

[149] M. G. Aartsen et al., IceCube Collaboration, *Search for dark matter annihilations in the Sun with the 79-string IceCube detector*, Phys. Rev. Lett. 110 (2013) 131302, arXiv:1212.4097 [astro-ph.HE], http://arxiv.org/abs/1212.4097

[150] C. E. Aalseth et al., CoGeNT Collaboration, *Results from a Search for Light-Mass Dark Matter with a P-type Point Contact Germanium Detector*, Phys. Rev. Lett. 106 (2011) 131301, arXiv:1002.4703 [astro-ph.CO], http://arxiv.org/abs/1002.4703

[151] S. Archambault et al., PICASSO Collaboration, *Constraints on Low-Mass WIMP Interactions on* ^{19}F *from PICASSO*, Phys. Lett. B 711 (2012) 153-161, arXiv:1202.1240 [hep-ex], http://arxiv.org/abs/1202.1240

[152] M. Bahr et al., *Herwig++ Physics and Manual*, Eur. Phys. J. C 58 (2008) 639-707, arXiv:0803.0883 [hep-ph], http://arxiv.org/abs/0803.0883

[153] M. L. Mangano, M. Moretti, F. Piccinini, R. Pittau, A.D. Polosa, *ALPGEN, a generator for hard multiparton processes in hadronic collisions*, JHEP 0307 (2003) 001, arXiv:hep-ph/0206293, http://arxiv.org/abs/hep-ph/0206293

[154] J. Alwall et al., *Comparative study of various algorithms for the merging of parton showers and matrix elements in hadronic collisions*, Eur. Phys. J. C 53 (2008) 473-500, arXiv:0706.2569 [hep-ph], http://arxiv.org/abs/0706.2569

[155] K. Arnold, A. Papaefstathiou et al., *Herwig++ 2.6 Release Note*, arXiv:1205.4902 [hep-ph], http://arxiv.org/abs/1205.4902

[156] J. Alwall et al., *A standard format for Les Houches Event Files*, Comput. Phys. Commun. 176 (2007) 300-304, arXiv:hep-ph/0609017, http://arxiv.org/abs/hep-ph/0609017

[157] E. Boos et al., *Generic User Process Interface for Event Generators*, arXiv:hep-ph/0109068, http://arxiv.org/abs/hep-ph/0109068

[158] A. Schofield, M. H. Seymour, *Jet vetoing and Herwig++*, arXiv:1103.4811 [hep-ph], http://arxiv.org/abs/1103.4811

[159] ATLAS Collaboration, *Study of jets produced in association with a W boson in pp collisions at* $\sqrt{s} = 7\,\mathrm{TeV}$ *with the ATLAS detector*, Phys. Rev. D 85 (2012) 092002, arXiv:1201.1276 [hep-ex], http://arxiv.org/abs/1201.1276

[160] ATLAS Collaboration, *Measurement of the transverse momentum distribution of Z/*γ^* *bosons in proton-proton collisions at* $\sqrt{s} = 7\,\mathrm{TeV}$ *with the ATLAS detector*, Phys. Lett. B 705 (2011) 415-434, arXiv:1107.2381 [hep-ex], http://arxiv.org/abs/1107.2381

[161] ATLAS Collaboration, *Measurement of the production cross section of jets in association with a Z boson in pp collisions at* $\sqrt{s} = 7\,\mathrm{TeV}$ *with the ATLAS detector*, JHEP 07 (2013) 032, arXiv:1304.7098 [hep-ex], http://arxiv.org/abs/1304.7098

[162] B. Cooper, J. Katzy, M. L. Mangano, A. Messina, L. Mijovic, P. Skands, *Monte Carlo tuning in the presence of Matching*, arXiv:1109.5295 [hep-ph], http://arxiv.org/abs/1109.5295

[163] ATLAS Collaboration, *Measurement of* $t\bar{t}$ *production with a veto on additional central jet activity in pp collisions at* $\sqrt{s} = 7\,\mathrm{TeV}$ *using the ATLAS detector*, Eur. Phys. J. C 72 (2012) 2043, arXiv:1203.5015 [hep-ex], http://arxiv.org/abs/1203.5015

[164] F. Ould-Saada, *International Particle Physics Masterclasses – Bringing LHC data into the Classroom*, PoS ICHEP2012 (2013) 559, http://inspirehep.net/record/1257275/files/ICHEP2012_559.pdf

[165] M. K. Bugge, E. Gramstad, V. Morisbak, F. Ould-Saada, M. Pedersen, S. H. Raddum, *ATLAS Masterclasses – W and Z path physics and presentation of the Z path measurement*, EPJ Web of Conferences 71 (2014), http://www.epj-conferences.org/articles/epjconf/pdf/2014/08/epjconf_icnfp2013_00024.pdf

[166] M. Pedersen, F. Ould-Saada, M. K. Bugge, *Sharing ATLAS data and research with young students*, ATL-COM-OREACH-2014-001, https://cds.cern.ch/record/1957124, to be published in the proceedings of ICHEP 2014, Nuclear Physics B – Proceedings Supplements (NUPHBP) (see also https://indico.ific.uv.es/indico/contributionDisplay.py?sessionId=33&contribId=656&confId=2025)

[167] U. Bilow, C. Hasterok, K. Jende, M. Kobel, C. Rudolph, J. Woithe, *ATLAS W path – real data from the LHC for high school students*, EPJ Web of Conferences 71 (2014), http://www.epj-conferences.org/articles/epjconf/pdf/2014/08/epjconf_icnfp2013_00018.pdf

[168] S. Vourakis, *Bringing high energy physics to the classroom with HY.P.A.T.I.A.*, EPJ Web of Conferences 71 (2014), http://www.epj-conferences.org/articles/epjconf/pdf/2014/08/epjconf_icnfp2013_00137.pdf